EXPERIMENTAL ELEMENT-PARTITIONING AND PHASE-EQUILIBRIUM STUDIES RELEVANT TO SUBDUCTION ZONES

Harriet Alice Randle

PhD
The University of Edinburgh
1994

DECLARATION

I declare that the work presented in this thesis is my own, except where otherwise stated.

ABSTRACT

Melting in subduction zones is thought to take place in the mantle wedge, triggered by influx of fluid from the subducting slab. Although the isotopic composition of island arc volcanics (IAV) indicates that there is some recycling of the subducted oceanic crust, there is no consensus as to its relative importance or mode of incorporation into the mantle-derived melts. One major obstacle to the development of models for magma genesis in subduction zones is a scarcity of experimental data relevant to the partitioning of trace elements between melts, fluids, and residual phases during melting or dehydration of the mantle or the slab. The aims of this project were: a) to determine experimentally the major- and trace-element compositions of partial melts and residual phases of hydrous peridotite; and b) to calculate the partition coefficients between hydrous fluid and basaltic melt, produced at high pressure and temperature.

Using solid-media apparatus, synthetic trace-element-doped peridotitic starting materials were equilibrated between 1.8 GPa and 2.8 GPa, and 970°C and 1150°C under water-saturated conditions at an fO_2 equal to the Ni/NiO buffer. Melt compositions were calculated from analyses of melt inclusions trapped in an olivine crystal included in the capsule. However, analysis by secondary ion mass spectrometry (SIMS) showed that many of these experiments had been contaminated by boron from the surrounding boron-nitride sleeve, apparently via holes which formed and subsequently sealed. Water had not always been lost from contaminated capsules, and hence their failure had not previously been suspected. Comparison with uncontaminated experiments shows that boron fluxes melting and thus invalidates the results from the contaminated runs. This may be a general experimental problem, affecting past studies. Some experiments performed at 1.8 GPa were not contaminated and showed that with increasing temperature, the solidus is encountered, followed by the amph-out, ilm-out, ru-out, cpx-out and opx-out curves, consistent with previous studies. Calculated melt compositions were tested by reversal, i.e. equilibration of the melt composition under similar conditions to the original experiment. A forward experiment conducted at 1.8 GPa, 1020°C produced ol, opx, cpx, amph, ru, ilm, sp, and basaltic melt (53.6% SiO_2, 22.7% Al_2O_3). However the phases on the liquidus of the calculated melt composition were opx, cpx, gt, amph, and were more aluminous than the original phases. In reversal experiments performed without a separate olivine crystal, an *extra* 20 wt% forsterite

component was necessary to stabilise olivine. The calculated melt is therefore deficient in olivine component and is more aluminous than the true melt.

In order to maximise fluid-phase quench products for analysis, a basaltic composition was equilibrated with up to 50 wt% water at ~2.0 GPa and 1010°C. A salt cell was used to avoid contamination. Mass balance, coupled with textural and compositional evidence, suggests that the small glass spheres are quenched representatives of the fluid at equilibrium. Glass spheres and melt were analysed by SIMS for Li, Be, B, Na, K, Ti, Rb, Sr, Y, Zr, Nb. Cs, Ba, REE, Hf, Ta, Pb, and U, and assuming a value of 12.7 wt% solute in the fluid, values of D (fluid/melt) were determined, and, with the exception of Cs, are less than unity. The lowest values are exhibited by the REE and Y. There is a positive relationship between D (fluid/melt) and ionic radius for the 1+ ions, and negative relationships for the 3+ and 4+ ions. There is no obvious relationship for the 2+ ions, although Be, with the smallest ion, has the largest value of D (fluid/melt). D (fluid/melt) is greater for Ta than for Nb, and both values are less than those of the 1+ ions. Values of D (olivine/fluid) were derived from analysis of olivine and coexisting glass spheres.

D (mineral/fluid) was calculated by combining D (fluid/melt) with published D (mineral/melt) values. The compositions of melts and fluids in equilibrium with the slab and the mantle have been calculated for a variety of possible compositions and mineralogies. Although the trace-element composition of IAV can be reproduced by mixing slab- and mantle-derived melts, it is thought that this is due to the similarities between IAV and subducted sediment. A more likely scenario, considering that the slab is thought to lose much of its mobile-element budget during metamorphism, is that the mantle melts after metasomatism by a LILE-rich slab-derived fluid. The main conclusion is that the trace-element contents of IAV can be reproduced by this model if the mantle wedge is of a depleted MORB-source composition.

ACKNOWLEDGEMENTS

The three original supervisors of this project were John Dixon, Godfrey Fitton, and Colin Graham. I thank them for their time, interest, and advice throughout.
Nic Odling's expertise and enthusiasm in the lab were invaluable, and prompted me to co-opt him onto the supervisorial board. I thank him for all his help as an XP colleague and as a supervisor .

This project has not always gone smoothly, and I would especially like to thank John Craven for his oblique encouragement, and for being susceptible to bribes! Without his help on the ion probe, there would be few useful results in this thesis.

The experimental petrology labs in Edinburgh are run by Steve Elphick who was also a source of much encouragement and help. I thank Damian Carrington and Dave Draper for advice in the lab, and Rob Brown for machining parts, often at short notice. Jon Turner and several passing males are thanked for saving my back from further damage by lifting heavy solid-media apparatus.

Stuart Kearns and Pete Hill gave much-appreciated help and advice with the electron probe, beyond the call of duty.

Thanks also to Shane for sorting out computing problems, and to Diane Baty for developing my black and white film.

This project has benefited from useful discussions with many people besides those named above, especially Chris Hawkesworth, John Holloway, Bruce Watson, Paul Beattie, Ann Bebout, and Richard Hinton.

I am very grateful to the NERC for funding this project.

TABLE OF CONTENTS

LIST OF ABBREVIATIONS USED IN THE THESIS

Minerals and phases

amph	amphibole	chl	chlorite	cpx	clinopyroxene
gt	garnet	ilm	ilmenite	ol	olivine
plag	plagioclase	ru	rutile	sp	spinel
fq	fluid quench	ign	ignorite - Mg, Cr, Al borate (see Chapter 6)		

Mg no.	Mg/(Mg+Fe)	wt%	weight percent

Abbreviations regarding analytical techniques

c/s	counts per second	n.d.	not determined
EPMA	electron probe microanalysis	SIMS	secondary ion mass spectrometry
XRD	X-ray diffraction	psi	pounds per square inch
GPa	gigapascals (1 GPa = 10 kilobars)		

Oxygen buffers

HM	hematite-magnetite	IW	iron-wüstite
NNO	nickel-nickel oxide	MW	magnetite-wüstite
QFM	quartz-fayalite-magnetite	QIF	quartz-iron-fayalite

The fO_2's of these buffers at 1.5 GPa are shown in Figure 3.5 (Chapter 3).

Geological terms

IAB	island arc basalt	IAT	island arc tholeiite
IAV	island arc volcanic(s)	MORB	mid-ocean ridge basalt(s)
OIB	ocean island basalt(s)	myr	million years

In this thesis, a **forward** experiment is one which contains a peridotitic starting material which is partially melted. A **reversal** experiment contains the estimated melt composition from a forward experiment, run under similar conditions to the forward experiment.

Terminology for trace-element partitioning was taken from Beattie *et al.* (1993).

CHAPTER 1

INTRODUCTION

CHAPTER 1: INTRODUCTION

1.1 BACKGROUND

It is widely recognised that the volcanics erupted above subduction zones are geochemically and isotopically distinct from rocks erupted at different settings such as mid-ocean ridges or ocean islands. In particular, island arc volcanics (IAV) are characterised by high abundances of large ion lithophile elements (LILE) such as Sr, K, Rb, and low abundances of high field strength elements (HFSE) such as Ti, Zr, Nb, relative to mid-ocean ridge basalts (MORB). See Fig. 1.1. They also exhibit, to varying extents, elevated $^{87}Sr/^{86}Sr$, $^{10}Be/Be$, and $^{207}Pb/^{204}Pb$, and lower $^{143}Nd/^{144}Nd$, relative to MORB.

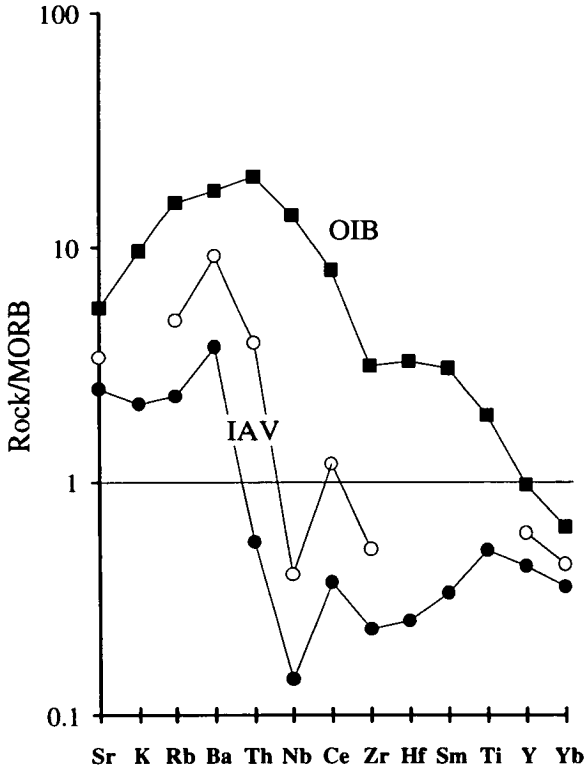

Figure 1.1: MORB-normalised incompatible-element abundances of typical ocean-island basalts (OIB) and IAV, using the plotting order and normalisation constants of Pearce (1983). OIB composition is taken from Sun & McDonough (1989); open circles denote an average arc basalt (Hawkesworth *et al.*, 1991); filled circles denote the composition of a basalt from the New Britain Arc, Papua New Guinea (Woodhead & Johnson, 1993).

Although it is agreed that the origin of this distinctive signature must be attributed in some way to the presence of the hydrated subducted slab, there is no consensus as to the processes by which these rocks are formed or, in particular, the compositions and

relative sizes of the contributions from the mantle and from the slab. One major obstacle to the development of models of magma genesis in subduction zones is a scarcity of experimental data relating to the partitioning of trace elements during melting or dehydration of hydrous mantle or of the slab. This project aimed to provide some more experimental data relevant to the behaviour of trace elements during the production of IAV, and to use these data to further constrain the processes responsible for the formation of these rocks.

Although some early workers (e.g. Fitton, 1971) suggested that IAV may be a direct product of melting of the slab, it is now more generally accepted that the majority, if not all, of the melting takes place in the mantle, triggered by the influx of fluid from the slab (e.g. Hawkesworth *et al.*, 1991; Davies & Bickle, 1991; Tatsumi, 1989; Stolper & Newman, 1994 - see Chapter 2 for a discussion of these and other studies). The identification of components involved in the production of this melt has been the objective of many geochemical studies of IAV. Within-suite variations in trace-element and isotopic compositions of arc rocks suggest that there are at least two sources in their genesis (e.g. Ellam & Hawkesworth, 1988; Lin *et al.*, 1990; Francalanci *et al.*, 1993). That one of these sources lies in the subducting slab is implied by the isotopic composition of the volcanics. Perhaps the most convincing evidence for this is the presence in some arc rocks of ^{10}Be, a short-lived cosmogenic nuclide which is not present in the mantle, but is found in the uppermost oceanic sediments (Morris *et al.*, 1990). Other similarities in isotopic composition between the sediments and the erupted volcanics also support the hypothesis that sediment can be recycled through subduction zones; for example, the lead isotopic compositions of IAV generally fall between those of MORB and locally subducted sediments (Arculus & Powell, 1986; Hickey *et al.*, 1986; Woodhead, 1989). There is some doubt, however, that the same component is responsible for both the sediment-like isotopic character of IAV, and the high-LILE, low-HFSE signature: in many arcs it has been found that there is no correlation between the LILE enrichment and the shift in the isotopic ratios (e.g. Ellam & Hawkesworth, 1988; Lin *et al.*, 1990; Francalanci *et al.*, 1993). This suggests that production of IAV is more complicated than the melting of a simple mixture of the mantle wedge and a slab component. Nevertheless, although complicated, it is clear that there is transfer of material from the subducted slab to the mantle wedge, and ultimately, to the IAV. There is no consensus, however, as to the method of incorporation of slab material into the magmas. It has been suggested that small amounts of slab-derived melts may mix with mantle melts (e.g. Ryerson & Watson, 1987; Yogodzinski, 1994). However,

comparison of the theoretical temperature regime in subduction zones with experimentally-determined melting curves suggests that the slab is unlikely to melt in most arcs (Peacock *et al.*, 1994), and therefore, a more likely scenario is that material is transported by fluids released by the breakdown of hydrous minerals in the slab. In order to establish whether this is the case, it is necessary to model the compositions of such fluids. It was the current lack of data pertaining to the high-pressure partitioning of trace elements between hydrous fluids and residual phases that was the motivation for this project.

A major unknown in the question of melt production in subduction zones is the extent to which the trace-element signature of IAV results from the presence of water in the mantle wedge. As well as stabilising new phases such as amphibole and phlogopite, water is known to have a significant effect on the phase relations of peridotite (Chapter 3). Furthermore, as there is a difference in major-element composition between melts of hydrous and anhydrous peridotite, it would not have been surprising to discover that there was also a difference in trace-element contents. However, to date there had been few experiments to investigate the trace-element contents of melts and coexisting phases in equilibrium with hydrous peridotite. The determination of such data was one of the aims of this project. It was hoped that this information could throw some light on the question of the origin of the anomalously low HFSE contents of IAV. This has been the subject of much debate, and is intimately connected with another contentious issue: the composition of the mantle wedge. The similarity in trace-element and isotopic composition between IAV and OIB has been used by some authors as evidence that OIB-source mantle is present beneath arcs (e.g. Morris & Hart, 1983; Ito & Stern, 1985/86). They suggest that during melting of such mantle, the HFSE may be held back by a residual phase, possibly stabilised due to the presence of water. Other authors argue that the mantle wedge composition is similar to the MORB source, or to the MORB source which has already been depleted by melt extraction (White & Patchett, 1984; Plank & Langmuir, 1988; McCulloch & Gamble, 1991). If the mantle wedge were composed of either of these compositions, the development of the IAV signature would require metasomatism of the mantle by a fluid or melt from the slab, enriched in elements other than the HFSE. One of the aims of this study was to ascertain whether this proposed slab input is necessary to cause the relatively low HFSE content in melts, or whether hydrous melting without metasomatism can by itself account for the HFSE signature.

In summary, from current knowledge it is not clear at which points in the production of IAV the anomalous geochemical signature develops. Figure 1.2 shows a schematic cartoon of a subduction zone and highlights six major areas at which trace-element fractionation may occur. The purpose of this project was to provide experimental data relevant to steps b, c, and d, i.e. the behaviour of trace elements during dehydration of the slab, the interaction of slab-derived fluids with the mantle, and melting of the mantle.

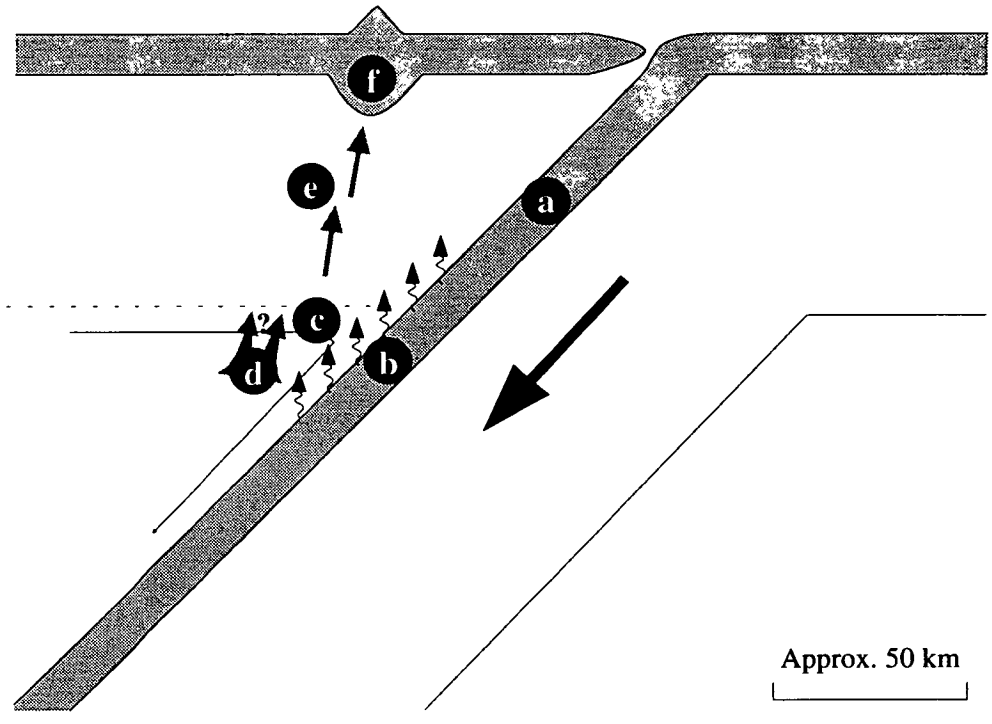

Figure 1.2: Schematic cartoon of a subduction zone. Six major areas at which the fractionation of trace elements may occur are shown.

a. *Metamorphism of the subducting slab.* Evidence from metamorphic rocks suggests that as the slab is subducted, it may lose a substantial proportion of its mobile-element budget (e.g. Moran *et al.*, 1992; Bebout *et al.*, 1993 - see Chapter 2).
b. *Dehydration or melting of the slab.*
c. *Fluid/mantle interaction,* i.e. metasomatism of the mantle by fluids in equilibrium with the slab and/or the mantle; formation of hydrous phases such as amphibole or phlogopite.
d. *Melting of the mantle.*
e. *Movement of melts through the mantle wedge and possible equilibration of melt with wall rocks.*
f. *Fractional crystallisation, assimilation etc. in the crustal magma reservoirs.*

1.2 AIMS OF THE PROJECT

The broad aims of this project were to perform experiments to determine the extent of trace-element fractionation during

1) dehydration of the slab
2) interaction of fluids with the mantle
3) melting of the hydrous mantle.

The complexities of the changes in temperature and composition across the slab-mantle interface ensured that it was not possible to design a single experiment to address all of the above aims. Therefore the problem was approached from more than one direction, with a view to amalgamating all the data gathered.

The presence of water in the mantle wedge is one critical difference between melting in subduction zones and in other settings, and as the effect of water on the trace-element composition of melts is relatively unknown, it was reasoned that only after ascertaining the composition of mantle melts could the significance of trace-element transport by fluids into the mantle wedge be deduced. A set of experiments was therefore performed, designed to produce partial melts of peridotite under hydrous conditions. Although such studies have been carried out before, the emphasis had previously been on the determination of phase equilibria and of major-element rather than trace-element compositions of melts and residual phases. Furthermore, as hydrous melt undergoes considerable modification during quenching, the determination of the true equilibrium melt composition in previous studies had been fraught with difficulties (see Chapter 3). In this project a different technique for determination of melt composition was employed. Developed by Odling (*accepted*), this method involves the use of an *in situ* olivine crystal to trap melt as inclusions. Subsequent analyses of these melt inclusions by electron probe microanalysis (EPMA) can be used to calculate the equilibrium melt composition. In detail, the objectives of the partial melting experiments were:

i) To determine the major-element composition of partial melts of hydrous peridotite over a range of pressures and temperatures, using the new technique.
ii) To determine the trace-element composition of partial melts of hydrous peridotite over a range of pressures and temperatures. It was of particular interest to compare the trace-element contents of melts produced with and without various residual phases such as rutile and amphibole.

iii) To measure partition coefficients between amphibole and melt. One major difference between a dry mantle and a hydrous mantle is the presence of amphibole. Partition coefficients between pargasitic amphibole and melt are necessary for a thorough assessment of the potential influence of residual amphibole during melting of the mantle.

Experiments were performed in solid-media apparatus over a range of pressures (1.8 GPa to 2.8 GPa) and temperatures (970°C to 1150°C) under water-saturated conditions. This pressure range was chosen partly to enable coexisting amphibole and melt to be produced, for the calculation of partition coefficients. It is likely that some melting in the mantle wedge takes place at higher pressures (Fig. 1.2) and it would therefore be appropriate for future work to extend these experiments to 4.0 GPa. Major-element compositions of melts and residual phases were determined by EPMA, and the calculated melt compositions were tested by means of liquidus experiments. In addition, it was intended to measure trace-element contents of melts and amphibole crystals by secondary ion mass spectrometry (SIMS).

However, the project was severely disrupted after the discovery, by SIMS, of high levels of boron in experimental run products. Unfortunately, as boron cannot be detected by EPMA, this problem was not discovered until the beginning of the third year of the project; the first time at which ion-probe time became available. Subsequent analysis of many run products revealed that the extent of contamination varied between experiments, although it was often very severe, with B_2O_3 contents reaching up to 30 wt% in the melt from some experiments. In three experiments, ingress of boron was so severe that crystals of Mg-Cr-Ti-Al-borate had formed. The boron is thought to have been derived from the boron nitride components in the experimental cell, and may have entered through holes or rips in the capsule walls. Because many of the contaminated capsules had retained their water throughout the experiment (one criterion traditionally used to confirm that an experiment has been successful), this discovery may have significant results for similar experiments, past, present and future. Therefore, although it is not relevant to subduction zones, it was felt that the problem deserved further investigation. This involved a thorough assessment of the extent of contamination of run products, and a comparison of major-element compositions of phases developed in experiments contaminated to varying extents. Results (Chapter 6) suggest that boron can sufficiently alter the phase relations and compositions of phases to render many of the experimental results unusable. Fortunately, there were some experiments which had not been contaminated. Most of these were performed at 1.8 GPa - the lowest pressure

studied. Major-element compositions of phases are therefore still valid, as are the phase relations deduced at this pressure. However, due to the small number of uncontaminated experiments, trace-element data are insufficient to derive any consistent trends with temperature. Furthermore, it is unfortunate that the experiments that produced crystals of amphibole large enough to analyse by SIMS, from trace-element doped starting materials had been severely contaminated.

Returning to the problem of subduction zones, another main objective of this project was to determine the trace-element compositions of hydrous fluid in equilibrium with mantle rocks and melts. Previous work (Chapter 3) is relatively scarce and seldom includes many trace elements. It was therefore decided to determine, by SIMS, partition coefficients between fluid and melt for a wider range of elements than have been studied before. Because of the extensive set of published IAV compositions, it was considered important to include all naturally-occurring REE as well as the LILE (Cs, Rb, K, Ba, Sr, Th, Pb, U) and the HFSE (Ti, Zr, Hf, Nb, Ta). In addition to this, the behaviour of B and Be was of particular interest, as B and ^{10}Be are thought to reflect the slab component. Previous methods for the experimental determination of fluid composition have included the analysis of fluid quench material trapped between an inner and an outer capsule (Schneider & Eggler, 1986), or the calculation of the fluid composition from the compositions of phases prior to and following fluid loss (e.g. Tatsumi *et al.*, 1986). In the present study, fluid quench products (glass spheres ranging from 10 μm to 100 μm) were analysed directly by EPMA and SIMS. Data were derived from some uncontaminated run products from the partial melting experiments, as well as from a new set of liquidus experiments, designed to produce melt, fluid, and rare large crystals of other phases such as olivine. Results show that there are complex, but consistent, relationships between partition coefficients (between fluid and melt, or fluid and olivine), ionic radius, and ionic charge. The melt produced in these experiments was basaltic in composition, and is an analogue for a low degree partial melt of hydrated mantle. Results, therefore, are appropriate for the calculation of partition coefficients between melt and fluid in equilibrium with the mantle; and, when used in conjunction with published D (mineral/melt), the calculation of partition coefficient between fluids and mantle minerals. It was originally intended to use the same experimental technique to derive partition coefficients between fluids and the slab. Unfortunately, although it was anticipated that this might have been relatively easy, it was not possible to achieve this in the time available. Instead, to infer the partitioning of trace elements between hydrous fluids and the slab, mineralogies for the slab have been assumed, and partition

coefficients have been calculated from D (fluid/melt) determined from this study and D (mineral/melt) from the literature. The results are subject to some error due to uncertainties concerning the mineralogy of the slab at the point of dehydration, and difficulties in obtaining values of D (mineral/melt) pertinent to the low temperatures in the slab. Nevertheless, it is still possible to assess the subsequent effect on melting of a fluid derived from the slab with or without various residual phases.

1.3 LAYOUT OF THE THESIS

The geochemistry of IAV and some of the models put forward for their genesis are discussed in Chapter 2. Many of these models invoke slab-derived, trace-element-rich fluids to produce the LILE enrichments seen in IAV. Experimental results necessary to assess these hypotheses are discussed in Chapter 3. This project involves the execution of partial melting experiments and liquidus experiments in which the major- and trace-element compositions of fluid and melt are determined. Previous experimental approaches to these problems are discussed in Chapter 3, and in light of this, a rationale behind the experimental approach adopted in this study is presented. A more detailed discussion of the techniques used to execute the required experiments and to analyse the run products is given in Chapter 4, along with an assessment of the inherent errors in these techniques.

Three separate experimental studies are reported in this thesis: the partial melting of hydrous peridotite, an investigation into contamination of experiments by boron, and experimental determination of the composition of hydrous fluids in equilibrium with mantle minerals and melt. The partial melting experiments were designed to enable measurement of the major-element and trace-element composition of melts and residual phases, and in particular to measure partition coefficients between amphibole and coexisting melt. However, many of these experiments were found to have been contaminated by boron. The major-element results from uncontaminated experiments are presented in Chapter 5, with an appraisal of the new technique used for the calculation of the melt composition. Unfortunately, the trace-element results from these few experiments are inconsistent and will not be presented. The experiments which were contaminated by boron, and a discussion of the possible reasons for the contamination and its wider implications, are presented in Chapter 6. Because of the varying extents of contamination, it has been possible to use results to

form a study into the effects of boron on the phase equilibria and phase compositions in this system. This is the second experimental study in the thesis. In Chapter 7, the third study is presented: the determination of the composition of hydrous fluid in equilibrium with basaltic melt, and the calculation of partition coefficients between fluid, melt, and olivine. Major-element and trace-element compositions of phases are presented, and it is argued that the compositions of the fluid quench products are truly representative of the fluid at equilibrium. Calculated partition coefficients are presented and correlations between partition coefficients, ionic radius, and ionic charge are highlighted.

Thus, the experimental results of the study consist of major-element compositions of residual phases and partial melts of hydrated peridotite, and partition coefficients between hydrous fluid, melt, and olivine. In Chapter 8, the partition coefficients are used in conjunction with measured D (mineral/melt) to calculate the likely partitioning of trace elements into fluids and melts in equilibrium with the slab and the mantle. Various models for the formation of IAV are tested using these data. The conclusions of the thesis are drawn together in Chapter 9.

CHAPTER 2

THE GEOCHEMISTRY OF ISLAND ARC VOLCANICS

CHAPTER 2: THE GEOCHEMISTRY OF ISLAND ARC VOLCANICS

2.1 INTRODUCTION

The distinctive geochemical characteristics of IAV have been well established by numerous studies, although their origin is still hotly debated. This chapter contains a review of the geochemical features of IAV, and a discussion of the models proposed to explain their genesis.

A description of the major-element, trace-element and isotopic compositions of IAV is presented in Section 2.2. As this project is concerned with the genesis of *primary* magmas in arcs, I have included minimal discussion of rocks that are the products of fractional crystallisation, a process which is thought to exert considerable influence over the major- and trace-element compositions of arc volcanics (Pearce & Norry, 1979; Gill, 1981; Foden, 1983).

By examining the variation in composition of arc basalts, many authors have attempted to characterise and identify the components involved in the genesis of subduction-related magmas (see Section 2.3). These studies show that there is good evidence that some subducted sediment is recycled through subduction zones. Whilst scrutiny of the compositions of IAV can yield information regarding the components involved in their origin, a comprehensive model for the genesis of these rocks must explain how these components interact. A general consensus reached by previous workers is that melting takes place in the mantle wedge, triggered by influx of fluid from the slab. However there is little agreement concerning the mode of incorporation of slab material into the mantle, and the trace-element fractionation processes that may be occurring at various stages of the process (see discussion in Section 2.4). There are a number of unresolved questions that will be addressed in this thesis. These include:

- How is material transported from the slab to the mantle melting zone? Can slab-derived fluids significantly modify the composition of the mantle wedge?
- Why in some arcs is there an apparent decoupling between isotopic compositions and incompatible-element abundances and ratios (see Section 2.3.2)? Is there more than one slab component to account for this decoupling? Is part of the LILE signature derived from fluids in equilibrium with the mantle?

- What is the composition of the mantle wedge? Is it more similar to OIB source, MORB source, or MORB source which has been depleted in incompatible elements by previous melt extraction?
- Do the low HFSE contents in IAV reflect low HFSE contents in their source, or are they a result of retention of these elements in a residual phase during partial melting?

Despite many attempts to answer them, these questions remain highly contentious. Some of the discrepancies between conclusions reached by separate studies may reflect genuine differences between the processes in operation in different arcs, or even in different regions of the same arc. However, much of the disagreement stems from the fact that it is impossible to constrain many of these models due to a lack of relevant experimental data, relating in particular to the compositions of melts and fluids in equilibrium with the slab and the mantle. In this chapter it will be established that the experimental evidence used by many authors to support their hypotheses is inadequate for that purpose, and needs to be extended. A detailed critique of relevant previous experimental work is deferred until Chapter 3.

2.2 GEOCHEMISTRY OF ISLAND ARC VOLCANICS

2.2.1 Major elements

Rocks erupted at island arcs encompass a wide range of compositions from basalts to dacites. Compositions generally fall into two main categories: a calc-alkaline series and a tholeiitic series. The former are characterised by their higher Al_2O_3 and K_2O contents relative to the tholeiitic rocks. Rocks within each series follow continuous compositional trends, and are thought to be genetically related (Cawthorn *et al.*, 1973; Gill, 1981). During differentiation, tholeiitic rocks show a marked enrichment in iron (Fig. 2.1).

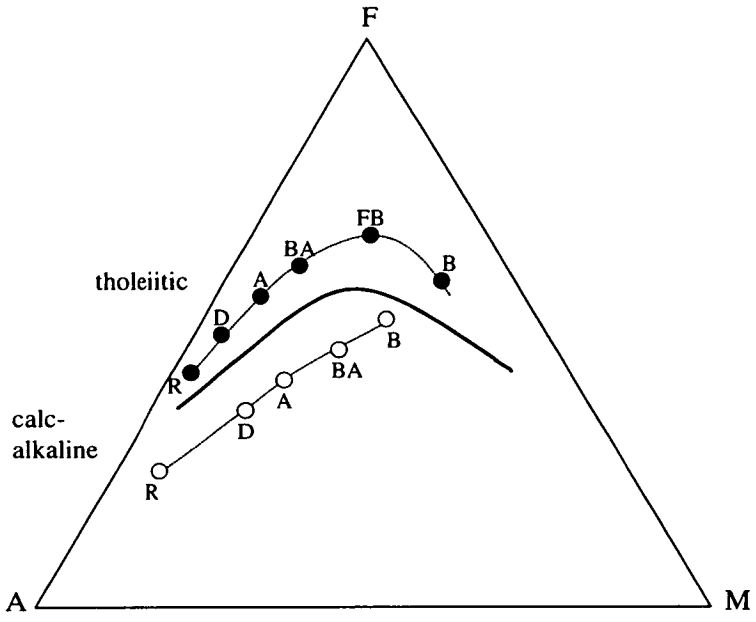

Figure 2.1: AFM diagram showing typical tholeiitic and calc-alkaline trends.

Key

A	$Na_2O + K_2O$
F	$FeO + Fe_2O_3$
M	MgO
B	basalt
FB	ferro basalt
BA	basaltic andesite
A	andesite
D	dacite
R	rhyolite

Evolved rocks from island arcs are very different from those erupted at mid-ocean ridge spreading centres, probably as a result of their different fractional crystallisation histories: the low-pressure fractional crystallisation residue of MORB is plag+ol or cpx+plag (Walker *et al.*, 1979), whereas the fractionating assemblage during the production of IAV is usually cpx (+ol) (Perfit *et al.*, 1980). In contrast to the evolved rocks, the most primitive rocks from island arcs are remarkably similar to MORB in terms of major elements (Perfit *et al.*, 1980; Arculus & Powell, 1986), although IAV generally contain more K_2O and sometimes less TiO_2 than MORB.

2.2.2 Trace elements

A large number of trace elements are of interest to geochemists studying IAV petrogenesis. These include REE, LILE (defined for these purposes as Cs, Rb, K, Ba, Pb, Sr), HFSE (defined for these purposes as Zr, Hf, Ti, Nb, Ta), Li, Be, B, P, Y, Th, U and some of the transition metals. This project is not concerned with the behaviour of P or the transition metals, and I shall therefore exclude discussion of them. There is an enormous amount of published data relating to the trace-element composition of arc rocks. These show that the majority of rocks possess fairly similar geochemical signatures, although there is a wide variation in absolute trace-element contents. Because of this variation, it would be dangerous to illustrate a typical IAV composition by combining data from different sources. Unfortunately,

there are few published analyses incorporating the full range of useful trace elements. Commonly analysed elements include K, Ti, Rb, Sr, Y, Zr, Nb, Ba, REE, Pb. There is some doubt regarding the accuracy of published Nb contents due to the low abundances of this element and the difficulties inherent in its analysis (Thirlwall *et al.*, 1994). Surprisingly, given that depletion in Ta is a widely-quoted characteristic of IAV, there is a scarcity of published Ta data for arc rocks. In addition, there are few analyses of Li or Cs. Although there are an increasing number of investigations of B and Be contents in arc rocks, these studies do not generally report B and Be data in conjunction with other trace elements. There is therefore a pressing need for further analyses of IAV incorporating a very wide range in trace elements. To illustrate the trace-element characteristics of IAV, I have selected analyses of basalts from the Sunda arc (Stolz *et al.*, 1990), The Aleutians (Yogodzinski *et al.*, 1994), The New Britain Arc (Woodhead & Johnson, 1993), a typical arc tholeiite (Sun, 1980) and a typical calc-alkaline basalt (Sun, 1980). Included for comparison are the compositions of basalts from two continental arcs (arcs overlying continental crust): the Aeolian Arc (Francalanci *et al.*, 1993) and Chile (Hickey *et al.*, 1986). All analyses were selected primarily because they incorporated a wide range of trace elements.

Trace-element compositions of IAV can be illustrated effectively using a multi-element diagram normalised to MORB (a spidergram). The ordering of elements on the abscissa has been the subject of some debate (McCulloch & Gamble, 1991; Rollinson, 1993; Wilson, 1989), as it can affect the appearance, and the superficial interpretation of the diagram. Pearce (1983) chose to plot the mobile elements on the left-hand side of the diagram, arranged in order of increasing incompatibility in garnet lherzolite. The right-hand side of the axis consisted of the immobile elements, arranged in order of decreasing incompatibility in garnet lherzolite. Those elements with ionic potential (the ratio of ionic charge to ionic radius) greater than 12 and less than 3 were defined as mobile. Figure 2.2 illustrates the differences in trace-element contents between typical OIB and several arc basalts, using the same element array (excluding P) and plotting order of Pearce (1983).

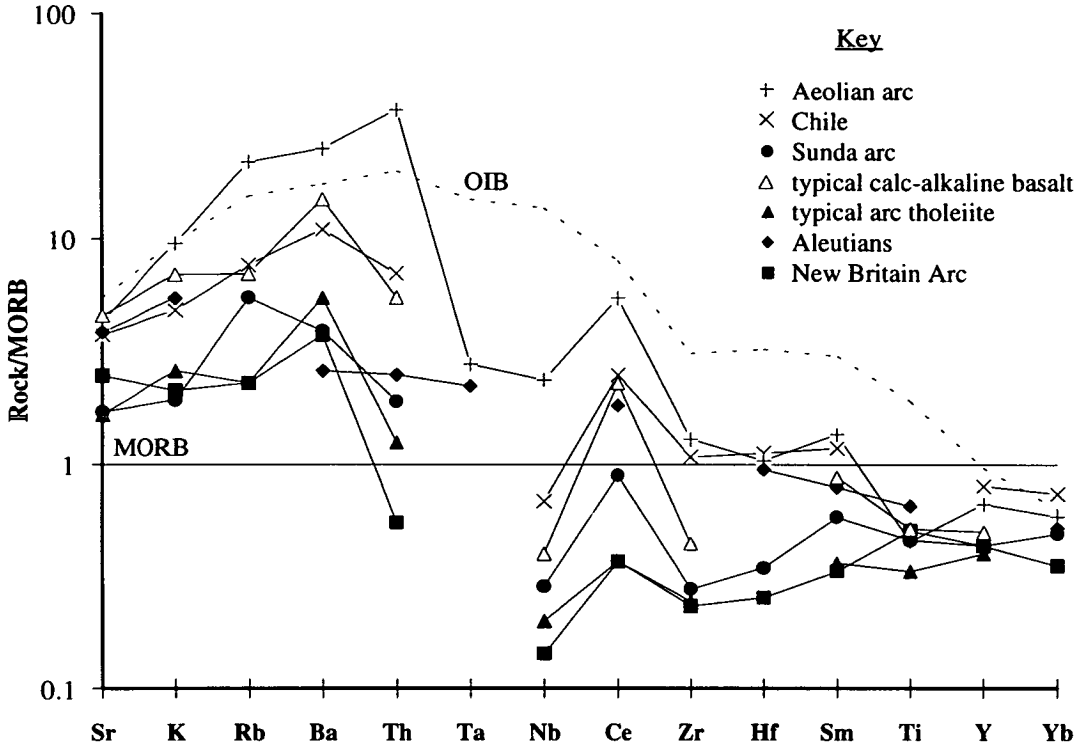

Figure 2.2: Spidergram showing the trace-element contents of typical OIB (Sun & McDonough, 1989); IAV from the Sunda arc (Stolz *et al.*, 1990), the Aleutians (Yogodzinski *et al.*, 1994), the New Britain Arc (Woodhead & Johnson, 1993) and typical arc tholeiitic and calc-alkaline basalts (Sun, 1980). Elements are plotted using the normalisation constants and plotting order of Pearce (1983).

As the set of elements for which there are data is larger than that illustrated in Figure 2.2, I have devised a new plot incorporating the additional elements Li, Be, B, Na, Cs, La, Pr, Nd, Eu, Gd, Tb, Dy, Ho, Er, Tm, Lu, Pb, and U, and normalising to the MORB composition of Hofmann (1988). Elements have been classed as mobile or immobile according to their ionic potential, with immobile elements defined as those with ionic potential between 2 and 12 (using octahedral ionic radii from Whittaker & Muntus, 1970). Following the rules of Pearce (1983), the ordering of elements is based on their relative incompatibility in a melt in equilibrium with garnet lherzolite. The bulk partition coefficients used are presented in Chapter 8 (Table 8.6), and have been calculated from values of D (mineral/melt) compiled from the literature, assuming the garnet lherzolite mineralogy suggested by McKenzie & O'Nions (1991) (Table 8.4). The full set of elements of interest in this project are arranged in the new order in Figure 8.3. To avoid unnecessary confusion, whilst at the same time presenting essential data, I have selected a group of twenty elements to illustrate the trace-element contents of IAV (Fig. 2.3). Comparison of Figures 2.2 and 2.3 shows that one result of using these newly-compiled values of bulk partition coefficients is

a slight alteration to the order used by Pearce (1983): Nb and Ta are now separated by Ce, and Y now plots after Yb.

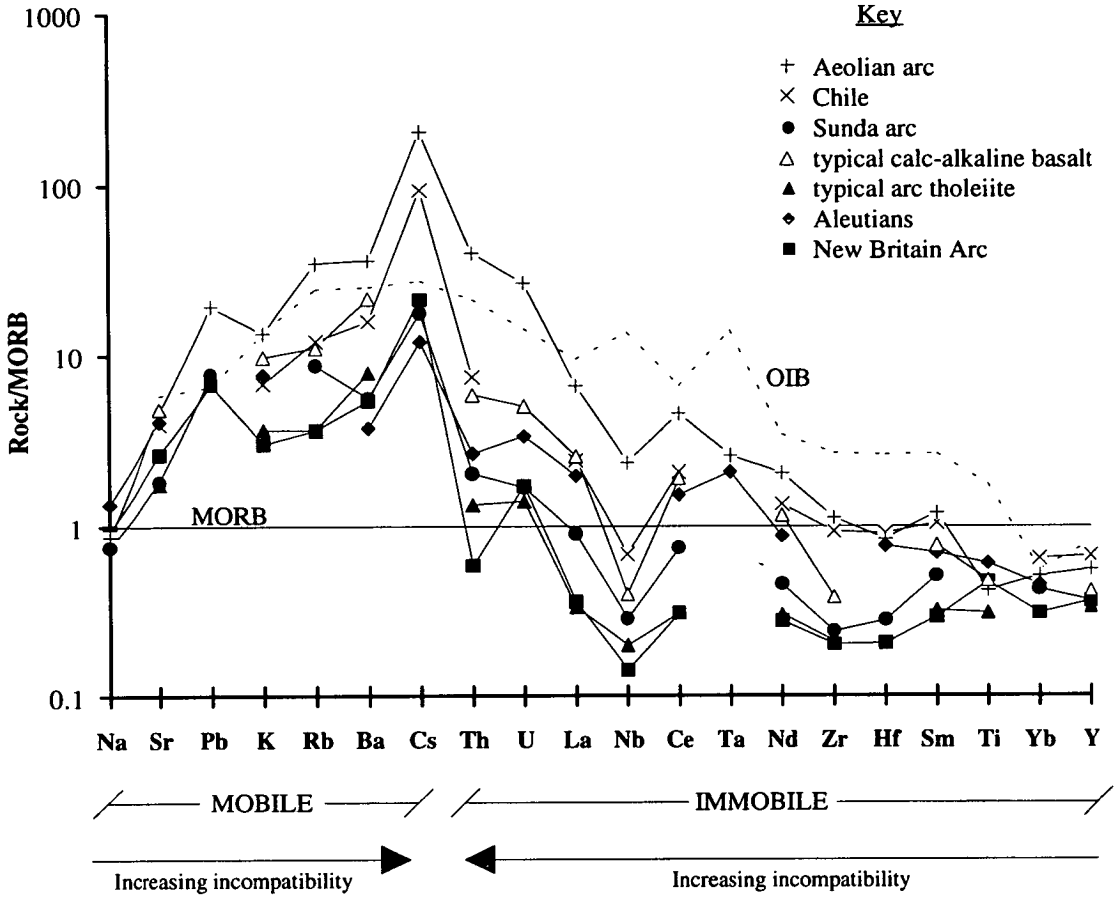

Figure 2.3: Spidergram normalised to MORB (Hofmann, 1988) showing the trace-element contents of typical OIB (Sun & McDonough, 1989); IAV from the Sunda arc (Stolz *et al.*, 1990), the Aleutians (Yogodzinski *et al.*, 1994), the New Britain Arc (Woodhead & Johnson, 1993) and typical arc tholeiitic and calc-alkaline basalts (Sun, 1980). The logic behind the plotting order (see text) is also summarised.

There is a wide variety of absolute trace-element abundances amongst the compositions illustrated. Note that the two most enriched compositions are taken from the Aeolian arc (Francalanci *et al.*, 1993) and Chile (Hickey *et al.*, 1986). These arcs lie on continental crust, and the volcanics may thus contain a contribution from the upper plate. It is therefore less complicated to consider the compositions of IAV, which lie on oceanic crust. The differences between trace-element contents of typical calc-alkaline and tholeiitic basalts are also illustrated. In general, calc-alkaline basalts are more enriched in trace elements than are tholeiitic basalts. This is also seen in Figure 2.6.

An immediately striking feature of Figure 2.3 is the relative enrichment in IAV of the elements plotted on the left-hand side of the diagram, i.e. the mobile elements. Cs is the most enriched of all elements examined, followed by Pb, Ba, Rb, K, and Sr. Th and U are also slightly enriched. The immobile elements (with the exception of Th and U), in contrast, are generally depleted relative to MORB. The HFSE and heavy rare earth elements (HREE) are particularly depleted, whilst there appears to be a relatively higher content of light rare earth elements (LREE). In Figures 2.2 and 2.3, Nb plots in a trough relative to its neighbouring elements. This is more pronounced in Figure 2.2 in which the neighbouring elements are Th (in the absence of Ta data) and Ce. Figure 2.4 shows the same data plotted in the order suggested by McCulloch & Gamble (1991). Here, there is no Nb trough, and the composition of IAV merely appears to be enriched in all elements other than the HFSE, Y, or Yb.

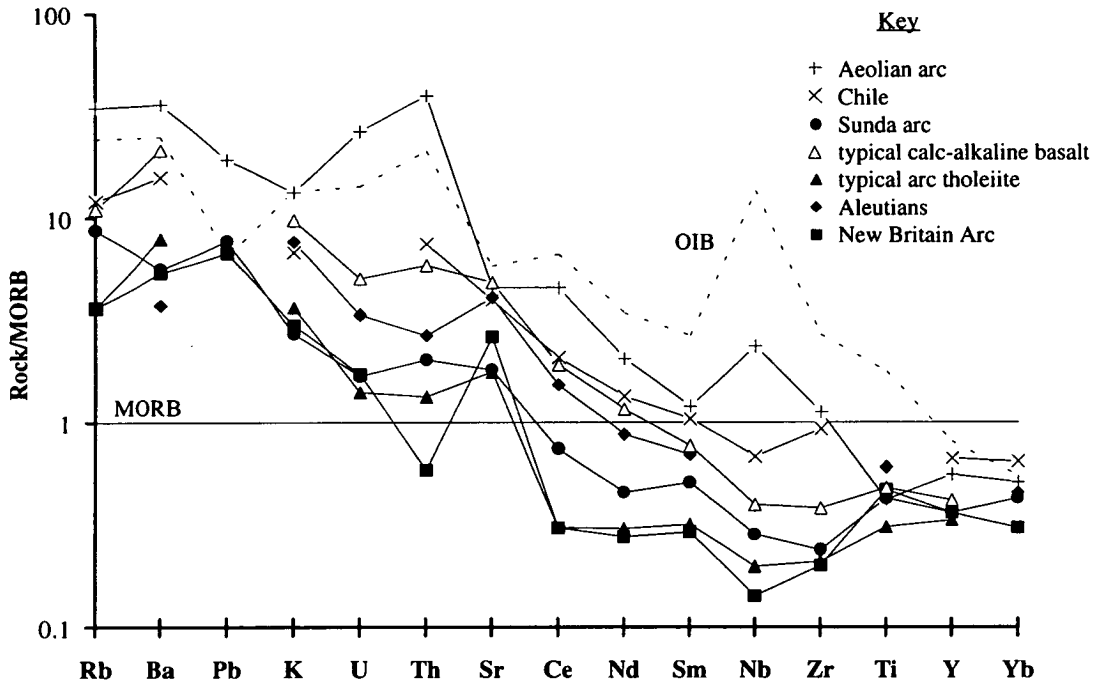

Figure 2.4: Spidergram normalised to MORB (Hofmann, 1988) showing the trace-element contents of typical OIB (Sun & McDonough, 1989); IAV from the Sunda arc (Stolz *et al.*, 1990), the Aleutians (Yogodzinski *et al.*, 1994), the New Britain Arc (Woodhead & Johnson, 1993) and typical arc tholeiitic and calc-alkaline basalts (Sun, 1980), using the plotting order suggested by McCulloch & Gamble (1991).

Besides illustrating the fairly obvious point that a new plotting order will change the appearance of the spidergram, this is not, in my opinion, a useful diagram as the order was derived by assuming that fluid-dominated processes were important, and is

roughly based on the mobility of elements inferred from experimental data and from the compositions of the IAV themselves. In the rest of the thesis, I have opted to use the order illustrated in Figure 2.3, as this is based on the ionic potential of elements, and one set of partition coefficients, and was not chosen with any preconceived ideas in mind.

Whichever way the elements are plotted, it is clear that the HFSE contents of IAV are considerably lower than OIB. There is a substantial overlap in HFSE contents between the range of IAV and MORB compositions (McCulloch & Gamble, 1991; Hildreth & Moorbath, 1988). McCulloch & Gamble (*op. cit.*) reported average Nb contents of continental arc basalts (3.3±1.6), IAB (1.5±1.0), MORB (2.8±1.6), and NMORB (2.0±1.0). Analyses which include both Nb and Ta show that Nb/Ta is fairly constant in arcs, and is not dissimilar to that in OIB (Gill, 1981). Nb and Ta depletion is not, however a feature common to all arc rocks. For example, leucite basanites from Muriah, Java are depleted relative to MORB in Ti, but not Ta or Nb, suggesting that Ta and Nb may be decoupled from Ti (Stolz *et al.*, 1990). Hawkesworth *et al.* (1993a) noted that high LILE/HFSE ratios were best developed in rocks which possessed low abundances of HFSE.

The REE are extremely useful in geochemical studies, as they possess similar properties, and they contain the radioactive decay scheme of ^{147}Sm to ^{143}Nd. Figure 2.5 shows the REE patterns, normalised to MORB (Hofmann, 1988) for a number of arc basalts, OIB and MORB (shown in Figures 2.2-2.4).

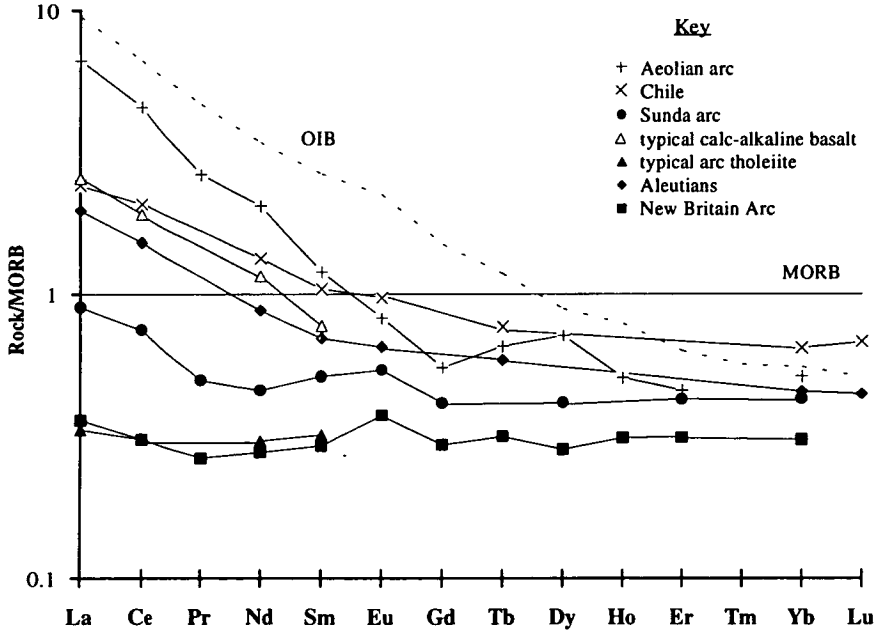

Figure 2.5: REE patterns, normalised to MORB (Hofmann, 1988) for a number of arc basalts (see caption to Figure 2.4), and OIB (Sun & McDonough, 1989).

In general, arc basalts are enriched in LREE relative to HREE, although the extent of this enrichment varies. Continental arc rocks are characterised by higher LILE/HREE ratios than are IAV, within which the calc-alkaline basalts have higher LREE/HREE ratios than do tholeiitic basalts. Hawkesworth and coworkers have divided all IAV into two groups: one group is characterised by high Ce/Yb ratios and diverse isotopic compositions. The other group possesses lower Ce/Yb ratios and is thought to be more isotopically 'normal' (Hawkesworth *et al.*, 1991, 1993a,b). They suggest that the low Ce/Yb IAV are formed by the simpler island arc systems, whereas the high Ce/Yb IAV reflect more complicated tectonic processes. Other trace-element features of IAV include occasional negative cerium anomalies (White & Dupré, 1986), and negative europium anomalies (Hawkesworth & Ellam, 1988), although the latter may be due to removal of plagioclase during low pressure fractionation (Woodhead, 1988).

Several recent studies have focused on the B and Be contents in IAV. Levels of B in IAV are highly variable, ranging from 1 to 60 ppm, and 1 to 30 ppm in basalts (Ryan & Langmuir, 1988). Comparison with the NMORB value of 0.34-0.74 ppm (Chaussidon & Jambon, 1994) shows that IAV can be extremely enriched in B. Be abundances in IAV are much less variable, and are comparable to levels in MORB (Ryan & Langmuir, 1988). The interest in these elements is partly connected with the discovery in some arc rocks of elevated ^{10}Be levels, which have been attributed to the recycling of sediments from the downgoing slab (Tera *et al.*, 1986; Morris & Tera, 1990, see Section 2.2.3), and the observation of positive correlations between $^{10}Be/Be$ and B (Morris *et al.*, 1990; Leeman *et al.*, 1994). The variation in B content has been attributed to variations in the slab-derived fluid flux, which is inferred to be rich in B. Volcanics from behind the volcanic front possess significantly lower B contents than volcanic front rocks, suggesting that B is not subducted to depth (Morris *et al.*, 1990). These ideas will be discussed further in Section 2.4.1.

There is much disagreement surrounding the origin of the high-LILE, low-HFSE signature seen in arc volcanics. Some authors have noted that the trace-element signature of IAV is closer in composition to OIB than to MORB (e.g. Morris & Hart, 1983). Thus it has been suggested that IAV magmas are a product of partial melting of OIB-source mantle, and the depletion in HFSE relative to OIB has been attributed to the retention of these elements in a residual mineral(s), stabilised due to the hydrous conditions in the mantle wedge. Certainly, there is a similarity between IAV and OIB in terms of inter-element ratios such as K/Rb, K/Ba, K/Sr (Morris & Hart, 1983; Arculus & Powell, 1986), although in IAV K/Cs is lower, Ba/La is higher

(Gill, 1981), and B contents are considerably higher than OIB Ryan & Langmuir, 1988).

Other workers have advocated that the mantle is of MORB-source composition, and that the most depleted elements in IAV are derived entirely from the mantle, whereas more enriched elements are inferred to be partially derived from other reservoirs, such as the slab (e.g. Pearce, 1983; Yogodzinski *et al.*, 1994; Tatsumi *et al.*, 1986) or enriched portions of the mantle (Arculus & Powell, 1986; Hawkesworth & Ellam, 1989; Hawkesworth *et al.*, 1991). The proportion of trace elements inferred to be derived from sources other than the mantle has been termed the subduction component (Pearce, 1983), and is illustrated in Figure 2.6.

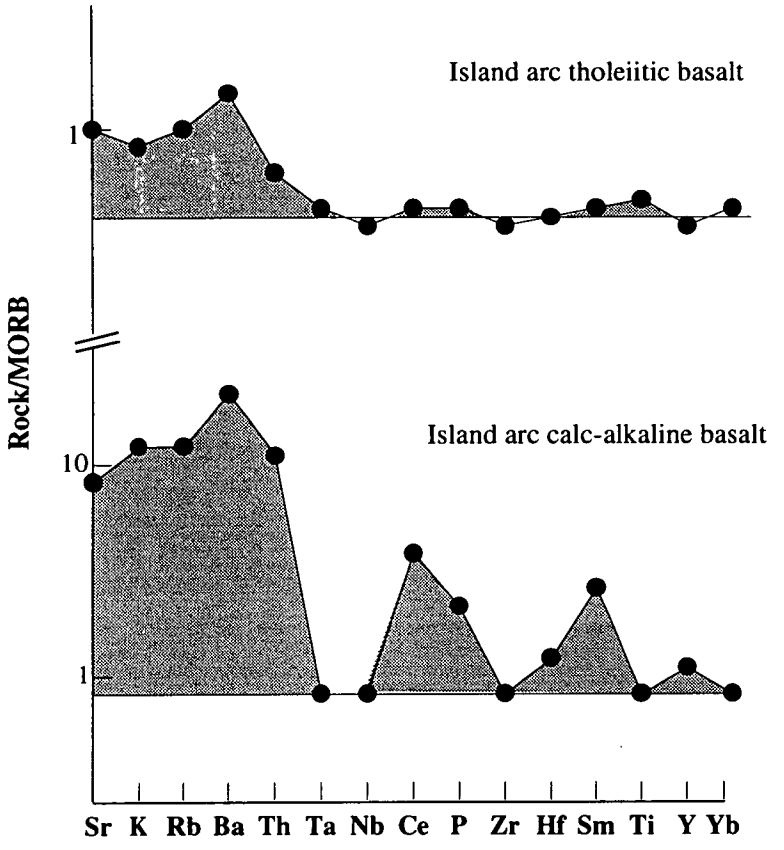

Figure 2.6: MORB-normalised trace-element patterns for a tholeiitic basalt from the South Sandwich arc and a calc-alkaline basalt from the New Hebrides arc. The subduction component (shaded area) is the area above a line drawn through the unenriched portion of the spidergram and extrapolated to Sr. This line represents the inferred composition of a partial melt of the mantle without addition of the subduction component (Pearce, 1983).

The unenriched portion of the spidergram is often depleted relative to MORB (Figs. 2.2-2.4). To account for this, it has been suggested that the degree of melting is

higher in the mantle wedge than under mid-ocean ridges, or alternatively, the mantle wedge had already been depleted in trace elements by previous melt extraction (Stolz *et al.*, 1990; McCulloch & Gamble, 1991; Pearce *et al.*, 1994). Mass-balance calculations indicate that for a typical tholeiitic basalt, the percentage subduction component for individual elements is 85% for Ba, 76% for Rb, 65% for Sr, 64% for K, 56% for Th, whereas the other elements in Figure 2.6 are derived entirely from the mantle (Pearce, 1983).

In summary, there are two principal opposing scenarios to explain the trace-element signature of IAV:

1. Melting of an OIB-source mantle composition, with retention of HFSE in the residue.
2. Melting of a MORB-source or depleted MORB-source mantle composition, after addition of an extra component, present due to the subducting slab.

Evidence to judge these hypotheses is presented in Section 2.3.

2.2.3 Isotopes

Isotopes are extremely useful tools for tracing sources of magmas and have been extensively studied in IAV. Figure 2.7 shows a Sr-Nd isotopic plot for various arcs, OIB and MORB. IAV generally possess elevated $^{87}Sr/^{86}Sr$ and low $^{143}Nd/^{144}Nd$ relative to MORB. The wide range in composition exhibited by all arcs only occasionally falls outside that of OIB; a fact that has been used as evidence that they are from a similar source (Morris & Hart, 1983; Ito & Stern, 1985/86). However it has been pointed out that given the extremely wide range in isotopic composition of OIB, the isotopic overlap of IAV with OIB is not particularly surprising (Woodhead, 1989). In some arcs, such as the Lesser Antilles, or Banda, the $^{87}Sr/^{86}Sr$ ratios are very high, possibly due to incorporation of isotopically enriched sediments from the slab (Arculus & Powell, 1988; Ellam & Hawkesworth, 1988).

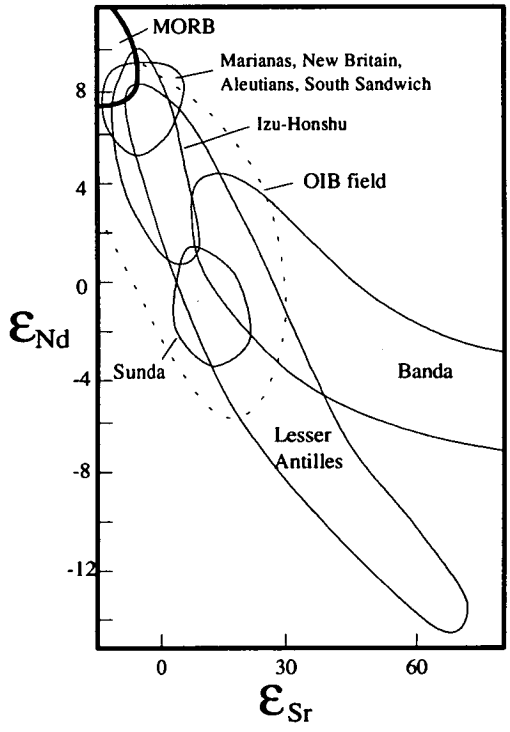

Figure 2.7: Variation of $^{143}Nd/^{144}Nd$ (or ε_{Nd}) and $^{87}Sr/^{86}Sr$ (or ε_{Sr}) for island arcs compared to the range in OIB and MORB. Redrawn from Wilson (1989) after Arculus & Powell (1986).

Lead isotopes are particularly sensitive indicators of slab involvement due to the high concentrations and distinctive isotopic signature of lead in oceanic sediments. The

lead isotope ratios of IAV generally fall between MORB and the local sediments (Arculus & Powell, 1986; Hickey *et al.*, 1986; Woodhead, 1989). See Fig. 2.8.
A strong correlation between the lead isotopic compositions of local sediment along the trench and the corresponding eruption products in the Lesser Antilles arc (White & Dupré, 1986) provides further evidence that the volcanics contain a component derived from the subducted sediments.

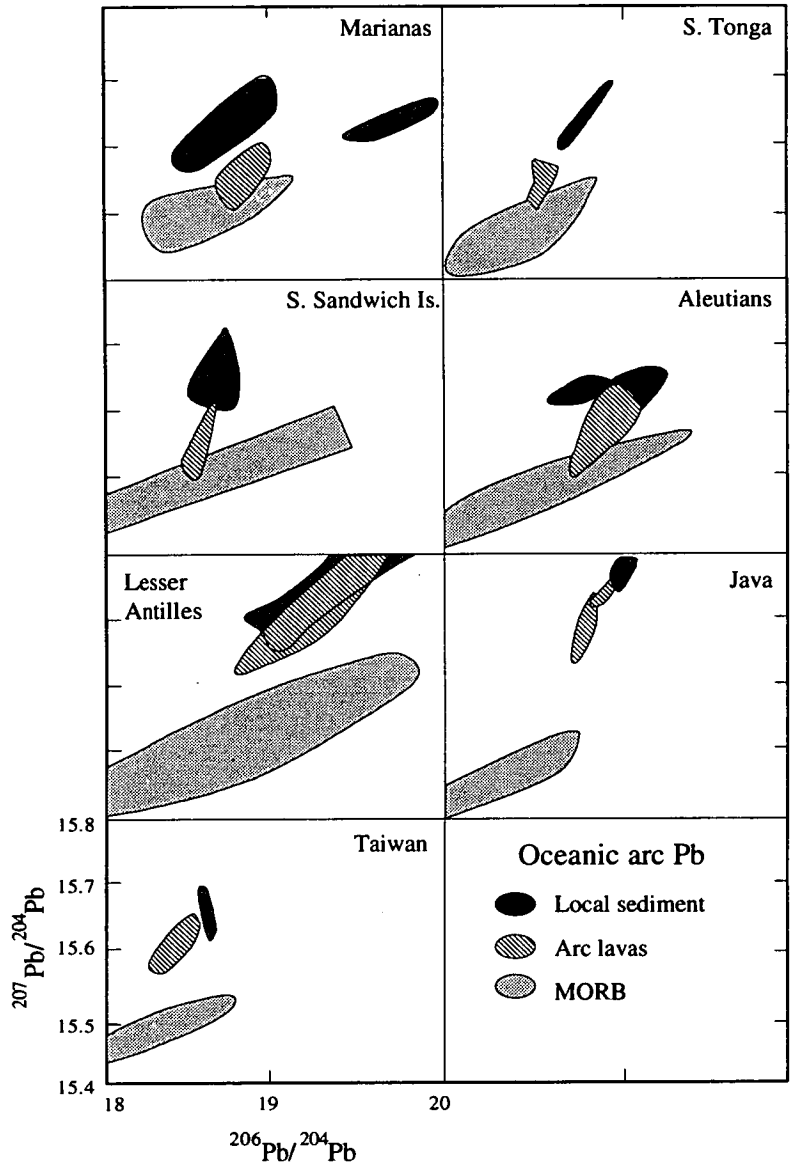

Figure 2.8: Pb isotope data for a number of oceanic arcs. From Woodhead (1989). Lava compositions are confined between MORB and local sediment composition, despite obvious regional variations in the latter.

Perhaps the most persuasive evidence of sediment recycling is provided by beryllium isotopes. ^{10}Be, a cosmogenic nuclide formed by spallation of nitrogen and oxygen in the atmosphere, is found in abundance ($>10^9$ atoms g^{-1}) in oceanic sediments, whereas it is relatively depleted in MORB ($<10^6$ atoms g^{-1}) and mantle rocks. This discrepancy, combined with its short half-life (1.5 myr) makes it an excellent tracer of recent sediment recycling through subduction zones. High levels of ^{10}Be have been found in some arc basalts and have been attributed to an input from sediments in the downgoing slab (Tera *et al.*, 1986). Whilst the appearance of ^{10}Be appears to be a sensitive indicator of sediment involvement, its absence does not rule it out. It is known that the isotope only resides in the top 50 m of sediment (Ryan & Langmuir, 1988) which is the most likely portion of the downgoing slab to be scraped off and thereby avoid deep subduction. Therefore, in many arcs ^{10}Be may not be subducted. For example, the ^{10}Be concentration in lavas from the Marianas is negligible (Woodhead & Fraser, 1985) and there is no positive ^{10}Be anomaly in the Lesser Antilles, probably because the sediments are scraped off in the accretionary prism (White & Dupré, 1986). It is also conceivable that magma may pond underneath an arc for long enough to lose any ^{10}Be signature (Feigenson & Carr, 1986). Similar studies have been performed using other isotopes. For example, Palmer (1991) found that the $\delta^{11}B$ values of Indonesian lavas were much higher than those of MORB. As altered MORB and subducted sediments possess relatively high values of $\delta^{11}B$, the involvement of a slab-derived component in the source of the lavas is implicated.

The uranium disequilibrium series has been studied in some arcs and can give information regarding the U/Th ratio of the source. Data from the Aleutians show that the source is characterised by a $^{230}Th/^{238}U$ ratio less than unity, indicative of addition of uranium to the mantle (Newman *et al.*, 1984). This approach has been applied to other arcs with the same results (e.g. McDermott & Hawkesworth, 1991).

Before there can be any conclusions based upon the isotopic evidence reviewed above, it is necessary to ensure that the isotopic anomalies are not due to assimilation of crust by magmas at high level. Evidence that some high-level crustal assimilation can occur includes the presence of metasediment xenoliths in IAV (White & Dupré, 1986). However, the rare xenoliths from the mantle wedge possess a similar geochemical signature to that of the erupted products (e.g. Maury *et al.*, 1992). The $^{10}Be/Be$ ratio is identical in the phenocrysts and the ground mass from within individual IAV samples, and thus this signature is inferred to have been acquired before magmas entered the magma chamber (Morris & Tera, 1990). This observation, coupled with the fact that OIB do not have elevated ^{10}Be despite being

erupted through oceanic crust, suggests that the $^{10}Be/Be$ signature is inherited from the melt source. It is therefore considered that, in general, the isotopic and trace-element signatures of IAV have been derived from the melt source and not from crustal assimilation.

In summary, the isotopic data from arc rocks provide unequivocal evidence that there is some recycling of material from the downgoing slab. In many cases there are strong correlations between separate isotopic ratios. For example, the Nicaraguan lavas in the Central American arc are characterised by high $^{10}Be/Be$ as well as low $^{143}Nd/^{144}Nd$ and high $^{87}Sr/^{86}Sr$, all indicative of sediment involvement (Feigenson & Carr, 1986). In the Aleutians, high $^{10}Be/Be$ ratios are associated with lead and neodymium isotopic trends consistent with incorporation of a sediment-derived component (Ryan & Langmuir, 1988). In many arcs there is a negative correlation between Δ7/4 (the displacement to high $^{207}Pb/^{204}Pb$ above the Northern Hemisphere Reference Line, Hart, 1984) and $^{143}Nd/^{144}Nd$ (Ellam & Hawkesworth, 1988), suggesting that there may be mixing between a relatively low $^{207}Pb/^{204}Pb$, high $^{143}Nd/^{144}Nd$ mantle composition, and a component derived from subducted sediments, which possess relatively high $^{207}Pb/^{204}Pb$ and low $^{143}Nd/^{144}Nd$. Further inferences derived from such correlations will be discussed in Section 2.3.

2.3 SOURCE COMPONENTS OF ISLAND ARC VOLCANICS

2.3.1 Introduction

It is becoming increasingly clear that the genesis of IAV may involve a number of sources from within the subducting plate and the overlying mantle. In order to quantify the proportions and compositions of mantle and slab components, it is necessary to identify end-member compositions by examining the variations in isotopic and trace-element compositions of IAV. It is acknowledged, however, that many within-suite correlations in trace-element contents and ratios could arise from variations in the degree of melting of the mantle and/or variations in the extent of equilibration of individual elements with the mantle wedge during ascent of the melt (e.g. Navon & Stolper, 1987; McKenzie & O'Nions, 1991). Therefore, for the purposes of identification of end-member compositions it is simplest to use isotopic ratios or trace-element ratios involving elements of similar compatibility. There

remain many disagreements that have not been resolved by these studies. These include questions relating to the composition of the mantle wedge, the exact source of the slab-derived component and its mode of transport to the mantle, and the origin of the low HFSE contents in IAV. These will be addressed in sections 2.3.3, 2.3.4, and 2.3.5, respectively.

2.3.2 Geochemical variations in IAV composition

Variations in IAV geochemistry both across and along an arc have been documented in a number studies (see also Gill, 1981). Examination of these compositional trends can provide information relating to the characteristics and relative importance of the various geochemical components involved in magma genesis.

Across arc

In many arcs there is a consistent increase in most incompatible element concentrations (relative to a constant SiO_2 content) away from the plate boundary. Included in this are Rb, Ba, Sr, REE, Th, U, Zr, Hf, Nb, Ta, sometimes Pb, and particularly K_2O, for which a positive correlation with distance from the arc front in many arcs has long been recognised (e.g. Dickinson & Hatherton, 1967; Saunders *et al.*, 1980). Some element ratios also change consistently across an arc. For example, Rb/K and Ba/K are often elevated in the back-arc side volcanoes (Gill, 1981; Tatsumi *et al.* 1991). Boron, in contrast to other incompatible elements, becomes progressively depleted with increasing distance from the plate boundary (Morris *et al.*, 1990), and is therefore inferred to behave in a different manner to other elements during the genesis of magmas. In Chapter 8, the compositions of volcanics from the front and the back of the New Britain arc (Woodhead & Johnson, 1993) will be examined, and results of this project will be used to comment on the differences between their respective petrogenesis.

Along arc

The compositions of lavas can vary greatly along an arc (e.g. Hildreth & Moorbath, 1988; Feigenson & Carr, 1986; Francalanci *et al.*, 1993), and even between neighbouring volcanoes (Miller *et al.*, 1992). By utilising these geochemical variations, many studies have aimed to identify mixing curves between different components involved in IAV genesis. To avoid unnecessary confusion, it is easiest to choose element or isotopic ratios that are independent of the degree of melting. It

has already been shown that the $^{87}Sr/^{86}Sr$, $^{143}Nd/^{144}Nd$ and Pb isotopic compositions of IAV often fall between the isotopic compositions of MORB and of subducted sediment, although some authors consider that the similarity in isotopic composition between IAV and OIB is more significant. Combining isotopic data with trace-element ratios highlights often complex relationships involving more than one component (Figure 2.9).

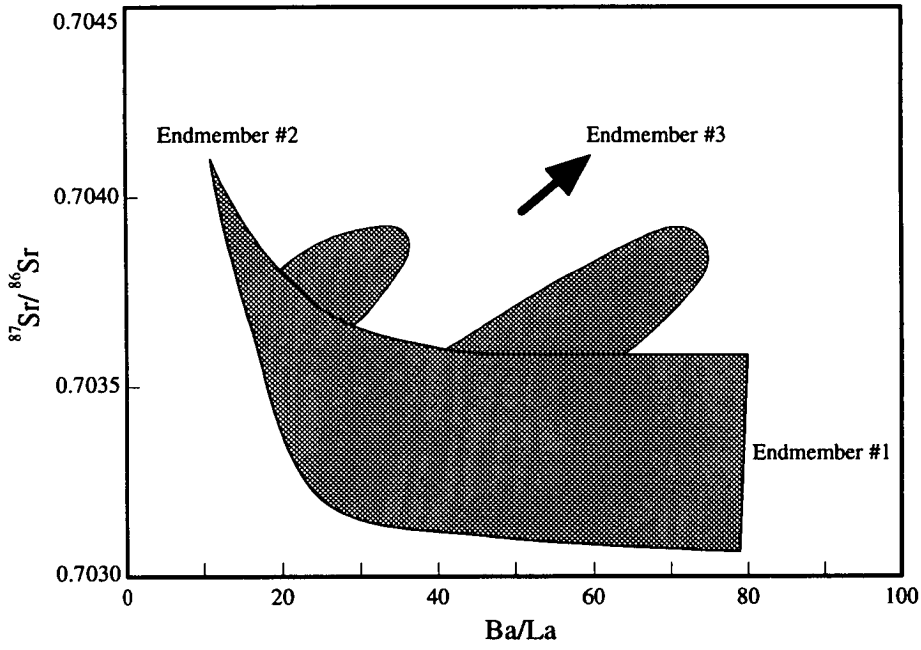

Figure 2.9: $^{87}Sr/^{86}Sr$ v Ba/La for lavas from the Marianas arc (from Lin *et al.*, 1990). Three end members have been identified:
#1 has high Ba/La, low $^{87}Sr/^{86}Sr$, low La/Yb, high ε_{Nd}.
#2 has low Ba/La, high $^{87}Sr/^{86}Sr$, high La/Yb, low ε_{Nd}.
#3 is rich in LILE and low in REE with high $^{87}Sr/^{86}Sr$.

Figure 2.9 illustrates one of the enigmas of island arc volcanism, namely that the enriched isotopic component thought to be derived from the subducted sediments, is not necessarily responsible for the elevated LILE seen in IAV. Similar 'decoupling' between isotopic compositions and incompatible-element abundances and ratios has been observed in many arcs (Ellam & Hawkesworth, 1988; Francalanci *et al.*, 1993). Lin *et al.* (1990) suggested that the end members involved in the genesis of Marianas lavas (Fig. 2.9) corresponded to metasomatised MORB-source mantle (end member #1), OIB-source mantle (end member #2), and a LILE-rich fluid derived from sediments (end member #3). However other authors disagree with this interpretation and suggest that there may be more than one slab component as well as MORB-source mantle. Further difficulties arise from attempts to constrain the proportions of material derived from each source. Isotopic data suggest that the contribution from

subducted sediment is considerably lower than the estimates calculated on the basis of minor and trace elements (Hawkesworth *et al.*, 1991). Possible resolutions of this problem include dilution of isotopic signatures by the mantle, or derivation of some of the high LILE 'subduction component' from the mantle wedge (Arculus & Powell, 1986; Hawkesworth & Ellam, 1989).

Combining Be isotopic data with B/Be ratios highlights well-defined mixing lines between two end members, one with high B/Be and high ^{10}Be/Be, and the other with low B/Be and low ^{10}Be/Be (Morris *et al.*, 1990). See Fig. 2.10. As ^{10}Be/Be and B/Be are extremely low in both MORB-source and OIB-source mantle, the B-Be systematics of arc lavas are relatively insensitive to the chemical variations in the mantle.

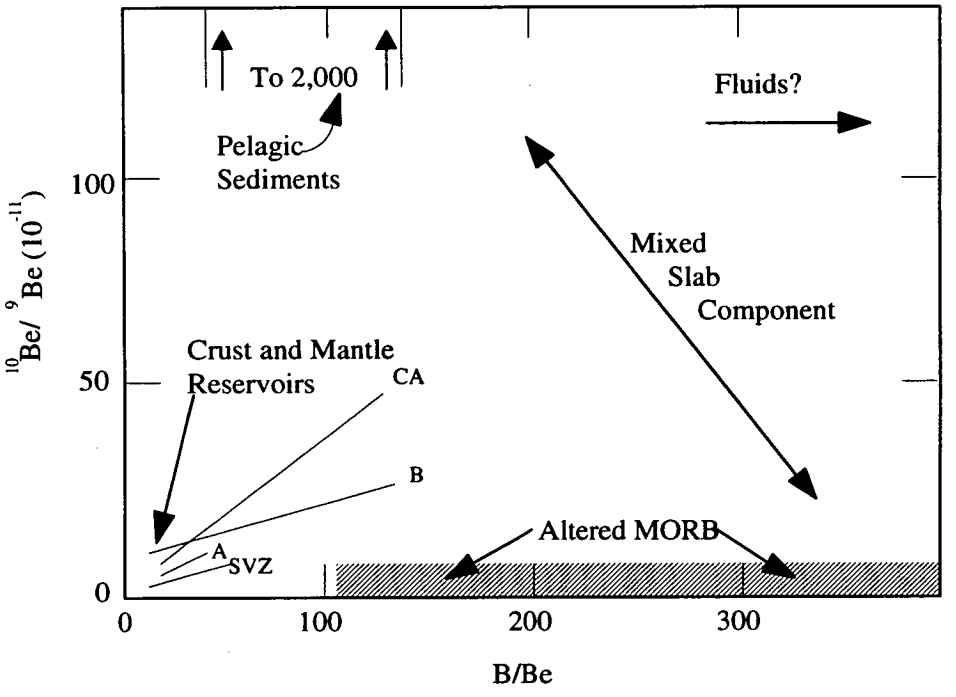

Figure 2.10: ^{10}Be/Be ratio versus B/Be for selected arcs, fields for mantle and crustal reservoirs (OIB, MORB, continental crust), pelagic sediments and altered MORB (from Morris *et al.*, 1990). Arc data from Central America arc (CA); Bismarck arc (B); Southern Volcanic zone, Southern Chile (SVZ); Andes (A). See text for interpretations.

The low B/Be, low ^{10}Be/Be component is inferred to be derived from the mantle, whereas the high B/Be, high ^{10}Be/Be is likely to be from the slab, which contains ^{10}Be-rich sediments, and B-rich altered MORB. According to Figure 2.10, the IAV compositions could be reproduced by mixing a combined slab component (consisting of sediments and altered MORB) with the mantle. In theory, a sediment-derived fluid with preferential partitioning of boron into the fluid is also an acceptable end

member (Morris *et al.*, 1990). The feasibility of these models will be discussed in Section 2.4.

Other useful information regarding processes of fluid release and partial melting can be gleaned from examination of the relationship between the physical nature of subduction and the associated IAV geochemistry. In a recent study, Leeman *et al.* (1994) demonstrated that there is a two-fold variation in the B/La ratio along the Central American Arc. As B contents are positively correlated with $^{10}Be/Be$, the variation in B/La is likely to be due to changes in the proportion of sediment-derived component involved in magma genesis along the arc. They suggest that B is released by fluids, and that the depth and magnitude of fluid release is governed by the temperature regime and geometry of the subduction zone. The areas of the arc with high B/La ratios are found to be underlain by colder, more steeply dipping slab than are the areas with low B/La. It is conceivable that the relatively low temperatures of this steeply dipping slab will facilitate retention of hydrous phases to greater depths, leading to dehydration of the slab underneath the arc and incorporation of the high-B slab signature into the arc magmas. In contrast, the warmer, shallow-dipping slab may dehydrate at shallower levels, thus limiting the fluid-related metasomatism of the sub-arc mantle, which could account for the lower B contents in related arc magmas.

Whilst the geochemical variations discussed above can indicate the end-member compositions, other variations can provide information regarding the relative compatibility of trace elements during melting. In an effort to determine the cause of the low HFSE in IAV, many authors have attempted to infer the behaviour of HFSE during melting. For example, McCulloch & Gamble (1991) have shown that the Nb/Zr ratios of lavas from five Pacific arcs are approximately constant and independent of Nb concentration (Fig. 2.11). A similar relationship can be seen for MORB, indicating that the geochemical behaviour of Nb and Zr are very similar in both environments. This is very strong evidence against the presence of a Nb-bearing phase such as rutile in the source of arc magmas. It should, however, be remembered that Nb contents are not easy to determine, and the reliability of much of the published data is questionable.

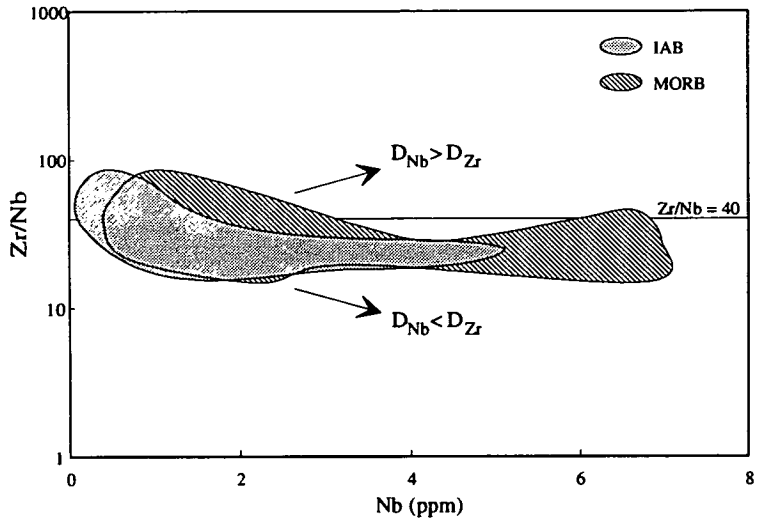

Figure 2.11: Zr/Nb versus Nb in arcs and primitive MORB. Data were taken from five Pacific arcs. Redrawn from McCulloch & Gamble (1991).

In a recent study of high-MgO lavas from the Lesser Antilles, Thirlwall *et al.* (1994) documented variations in HFSE content in relation to LREE enrichment (LREE/HREE decreases with increasing melting, and is a useful petrogenic indicator). As these lavas are extremely primitive, the observed relationships are thought to reflect the behaviour of these elements during melting, rather than fractional crystallisation. Lavas from St. Vincent were found to possess fairly constant Ti/Eu, Zr/Sm, and Nb/La ratios, implying that the elements within each of these pairs had similar bulk partition coefficients, $\bar{D}$, during the melting process. Where measured, the Zr/Sm and Nb/La ratios from other parts of the arc were similar to St. Vincent. However, the relationship between Ti/Yb and Eu/Yb for lavas from St. Vincent was not seen in the lavas from Grenada, Carriacou, or Petit Martinique, which were found to possess similar Ti/Yb values for a range of Eu/Yb (Fig. 2.12). This indicates that values of $\bar{D}$ for Ti and Yb were similar during melting, and both were greater than $\bar{D}$ for Eu. In comparison to melting at ocean ridges or islands, $\bar{D}$ for Ti was extremely high (Thirlwall *et al.*, 1994). To account for these observations, it seems likely that in the production of lavas from Grenada, Carriacou and Petit Martinique, a residual phase retained Ti in preference to Eu, without causing any particular change to the Zr/Sm or Nb/La ratios. The presence of amphibole in the smaller-degree partial melts may account for the observed depletion in Ti, and the lack of Ti depletion in lavas from St. Vincent may be due to the elimination of amphibole at the relatively high degrees of melting suggested by the low LREE/HREE ratios. In order to evaluate this hypothesis, it is necessary to obtain accurate measurement of the partition coefficients between amphibole and melt, and

to see whether they could account for the inferred depletion in Ti coupled with the constant Zr/Sm and Nb/La in these arc lavas. One of the objectives of this project was to perform such a study.

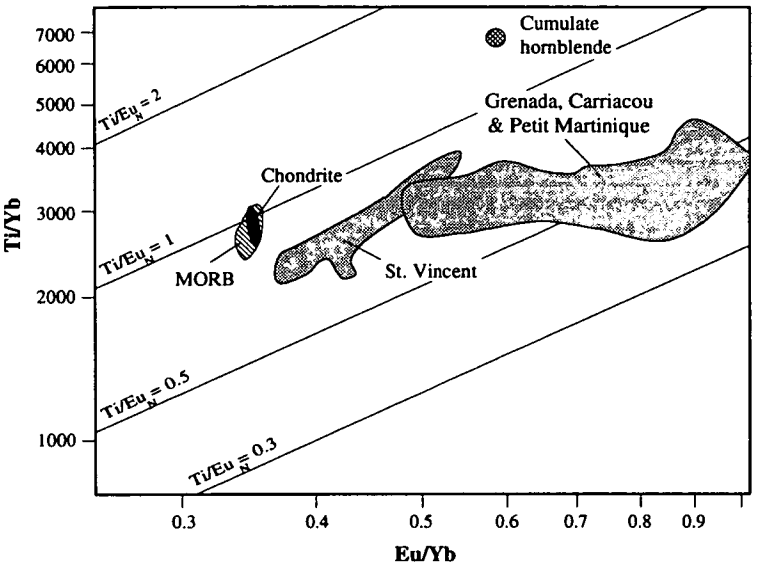

Figure 2.12: Ti/Yb versus Eu/Yb for high-MgO lavas from the Lesser Antilles. Redrawn from Thirlwall *et al.* (1994). With increasing degrees of melting Eu/Yb is inferred to decrease. This is accompanied by a decrease in Ti/Yb for the St. Vincent lavas, but no decrease in Ti/Yb for the lavas from Grenada, Carriacou, or Petit Martinique.

Ba/La is negatively correlated with La/Sm in many arcs (Perfit *et al.*, 1980; Francalanci *et al.*, 1993; Lin *et al.*, 1989). Figure 2.13a shows the relationship between these ratios for volcanics from the Aeolian arc (Francalanci *et al., op. cit.*).

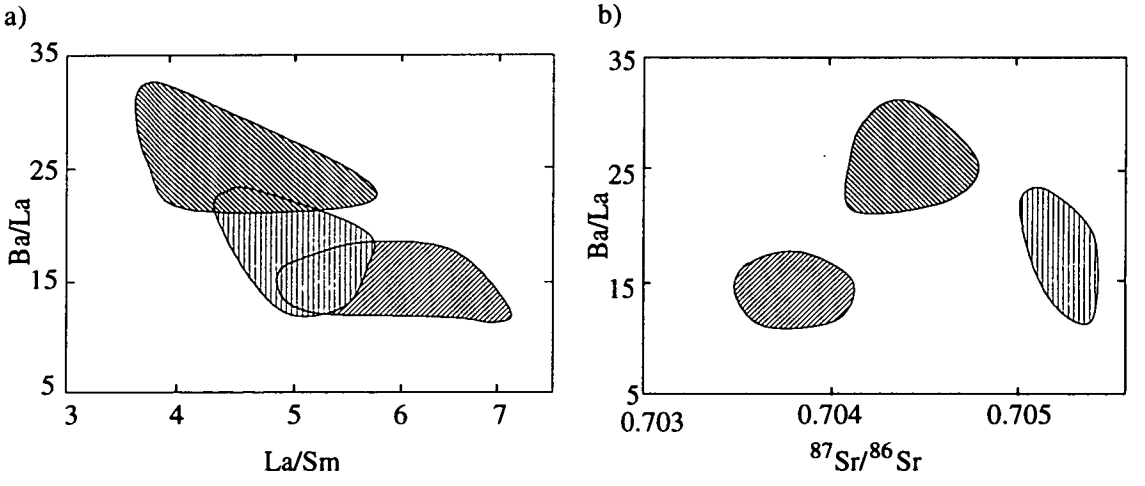

Figure 2.13: a) Ba/La versus La/Sm, b) Ba/La versus $^{87}Sr/^{86}Sr$ for samples from the Aeolian arc. From Francalanci *et al.* (1993). Individual shaded areas represent samples from different parts of the arc.

It is plausible that the volcanics with low La/Sm and high Ba/La were formed by high degrees of melting, triggered by high fluxes of Ba-rich fluid. If this fluid were derived from the slab (which has high $^{87}Sr/^{86}Sr$), and if the mantle were of MORB-source composition (this has low $^{87}Sr/^{86}Sr$), then a positive correlation between Ba/La and $^{87}Sr/^{86}Sr$ would be expected. However, this is not found (Fig. 2.13b). Any explanation must therefore involve more than one slab component or more than one mantle component or even both.

In summary, geochemical variations in IAV have allowed constraints to be placed on the behaviour of trace elements during melting, and the compositions of end members involved in magma genesis. There is strong evidence against the theory that residual rutile retains HFSE during melting, although it is possible that some geochemical characteristics of some IAV may be caused by residual amphibole in the source. Mixing curves inferred from a combination of isotopic and trace-element ratios indicate that there are at least two components involved in the genesis of IAV. Although there is much disagreement surrounding the interpretation of such curves, isotopic evidence has proved beyond doubt that a component derived from the subducted sediments is involved. A discussion of some of the principal controversies follows.

2.3.3 Mantle-wedge composition

Contrasting ideas have been proposed to explain the geochemical mixing curves described above. Some authors have suggested that the isotopically enriched end member corresponds to OIB-source mantle, possibly present as local hot spots (Lin *et al.*, 1990) or veins in the mantle wedge (Arculus & Powell, 1986). Evidence used to support these claims include the strong isotopic similarities between OIB and IAV (e.g. Morris & Hart, 1983; Ito & Stern, 1985/86). However, if IAV were derived from OIB-source mantle, there must be some process causing strong depletions in HFSE. Furthermore, it would be difficult to explain why the volcanics erupted in nearby back-arc basins are of MORB-like composition (White & Patchett, 1984). The broad similarity in major-element composition between MORB and IAV and the similar degrees of melting inferred for the formation of both (Plank & Langmuir, 1988) has been used as evidence that they share the same source. Were this the case, it would require higher degrees of melting or previous depletion in incompatible elements by prior melt extraction, to explain the low abundances of HFSE in IAV

relative to MORB. In addition, there must be a process causing selective enrichments in trace LILE and LREE.

Because of a) the similarity in major-element composition between IAV and MORB, b) the presence of MORB-like volcanics in back-arc basins, and c) the evidence against the presence of residual HFSE-bearing minerals during melting, it seems reasonable that the mantle wedge is more likely to be of MORB-source or depleted-MORB-source composition, although there may be some subduction zones in which local hot spots are incorporated. The similarity in isotopic and trace-element composition between IAV and OIB may result from incorporation of subducted material in the OIB source (White & Patchett, 1984; Ringwood, 1990).

2.3.4 Slab component

Isotopes provide unambiguous evidence for the recycling of some elements from oceanic sediments. Furthermore, to a first approximation, where the sediment flux into a trench is high for a particular element, the associated volcanics are enriched in that element (Plank & Langmuir, 1993). It is clear therefore that subducted sediments play an important role in the genesis of IAV. However, mass balance calculations indicate that the slab component cannot correspond to sediments alone, as these are too isotopically enriched (Davidson, 1987). One possible explanation for this enigma is that part of the slab component is derived from the rocks underneath the sediments, such as altered MORB or the ultramafic portion of the slab. It would be difficult to positively identify the involvement of unaltered ultramafics from the slab as these are unlikely to be very different from ultramafics in the overlying plate. However, sediments and altered MORB are isotopically and compositionally distinct, and it should be possible to distinguish between these two sources in the genesis of IAV. By extrapolation of two-component mixing curves to high B/Be ratios, Edwards *et al.* (1993) have estimated the isotopic composition of the slab component involved in production of IAV in the Sunda arc (Fig. 2.14). Mass balance calculations suggest that this inferred slab component could correspond to a mixture of 20% sediment and 80% altered MORB.

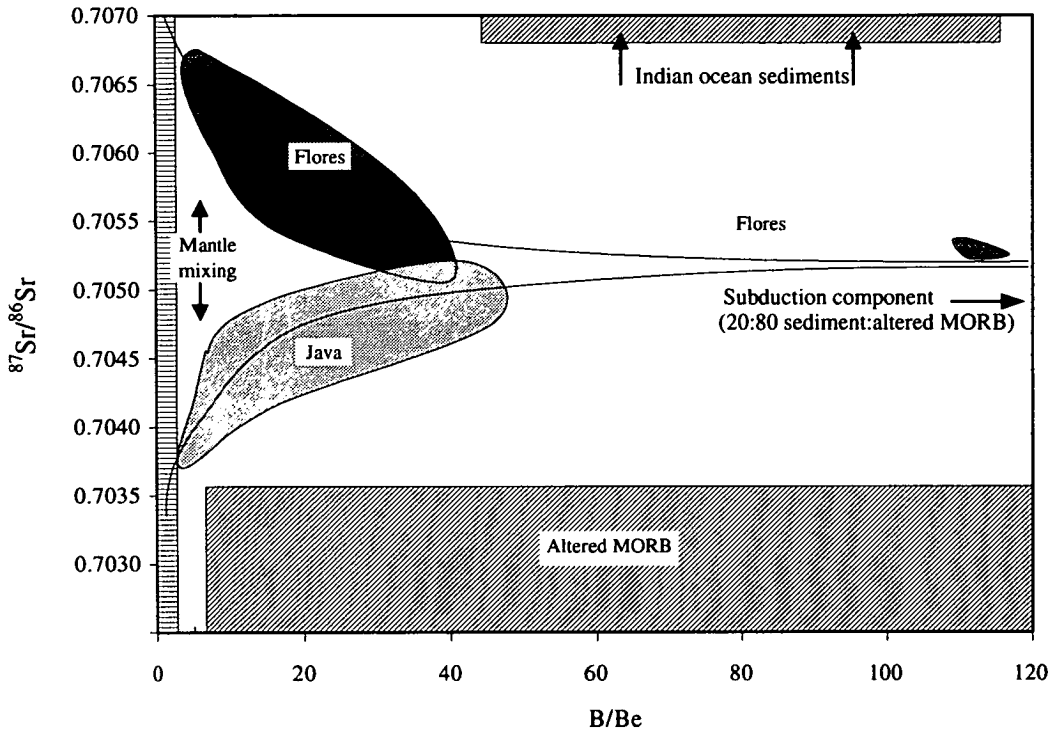

Figure 2.14: The range in $^{87}Sr/^{86}Sr$ and B/Be ratio for calc-alkaline lavas from Java (light shading) and Flores (dark shading). Mixing curves between a mantle and a slab component are shown. The inferred slab end member consists of 20% oceanic sediment and 80% altered MORB. Redrawn from Edwards *et al.* (1993).

The slab end member inferred from two-component mixing lines between $^{10}Be/Be$ and B/Be (Morris *et al.*, 1990) could also be caused by mixture of the mantle with a combination of altered MORB and sediments or a fluid therefrom (Fig. 2.10). Thus, there is good evidence that subducted sediments and altered MORB play some part in the genesis of IAV. However, the mode of transport of material from the slab to the mantle is still hotly debated (see Section 2.3.6).

2.3.5 The origin of the low HFSE contents

There is still much debate over whether the low HFSE in IAV result from retention of these elements in a residual phase during melting, or whether they reflect relatively low concentrations of these elements in the mantle wedge. If the mantle wedge were of OIB-source composition, a HFSE-bearing residual phase must be invoked. If the mantle wedge were of MORB-source or depleted MORB-source composition, relative enrichment of the mantle wedge by elements other than the HFSE must be invoked.

It has been proposed by many workers that the HFSE are retained in a mantle phase which is stabilised as a result of the subduction process (e.g. Morris & Hart, 1983; Foley & Wheller, 1990). Suggestions have included titaniferous minerals such as rutile or ilmenite, which possess high partition coefficients for Nb and Ta (Green & Pearson, 1987). However, experiments conducted by Ryerson & Watson (1987) show that the TiO_2 contents of hydrous rutile-saturated melts are much higher than those measured in IAV. For example they find that the TiO_2 content of a basalt in equilibrium with rutile is 5-7 wt%: far in excess of the levels found in IAB. Foley & Wheller (1990) contested these conclusions arguing that the effects of high pressure and high f_{O_2} may be sufficient to reduce the TiO_2 content of rutile-saturated melts to more feasible values. However, comparison between the variations in Nb and Zr contents in IAV and MORB indicates that the bulk partition coefficients for these elements are similar during the production of IAV and MORB. Furthermore, if rutile were a residual phase during melting, then one would expect to see fractionation of Nb from Ta owing to their different partition coefficients (Green & Pearson, 1987). However, available data, although scarce, suggests that Nb/Ta in IAV is constant and is apparently decoupled from Ti (Briqueu *et al.*, 1984). Other possible residual phases include Ti-rich clinopyroxene or amphibole (Hofmann, 1988). Some IAV from the Lesser Antilles display trace-element variations indicative of the retention of Ti by a residual phase, possibly amphibole, although these depletions in Ti are not accompanied by depletion in Nb (Thirlwall *et al.*, 1994).

An alternative explanation is that the depletion in HFSE existed in the mantle wedge prior to melting and that there was selective enrichment in other elements such as the LILE. Lavas from the Lesser Antilles possess constant subchondritic Zr/Sm and Nb/La ratios (Thirlwall *et al.*, 194) suggesting that Zr and Sm were depleted prior to melting. Woodhead *et al.* (1993), using Zr as a melting indicator, examined the ratios Ti/Zr, V/Ti and Sc/Y in arc lavas. They concluded that the original source of the lava was depleted in incompatible elements (possibly by extraction of a back arc melt). The enrichment of LILE and LREE in IAV may be due to an input from the slab, which could possibly contain residual rutile.

Finally, another proposed explanation for low HFSE abundances in IAV is that they arise during movement of melt through the mantle (Kelemen *et al.*, 1990, 1993). Experimental results obtained by these authors have indicated that partition coefficients between mantle minerals (in particular olivine, opx, garnet and spinel) are higher for many of the HFSE than for other incompatible elements. It is suggested that melts in subduction zones are more likely than magmas in other settings to equilibrate with the mantle through which they pass because of a) the

suggested slow ascent of these magmas, and b) the inverted geotherm in the mantle wedge which may cause melts to heat up past their liquidi. If the partition coefficients measured are correct, and there is no reason to suppose them to be inaccurate, it is conceivable that reaction of melts with wall rock could produce depletions in HFSE. However, the movement of melt in the mantle is still relatively unconstrained (Section 2.4.4) and as a consequence these hypotheses cannot be fully evaluated. In summary, the idea that HFSE depletions arise during ascent of melts cannot be ruled out, although it shall not be investigated further in this project.

2.3.6 Discussion

Isotopic mixing curves provide good evidence that material from subducted sediments and altered MORB is involved in the petrogenesis of IAV. Although there is still some debate, it seems likely that prior to infiltration by slab-derived material, the mantle wedge was of MORB-source composition. To account for the low abundances of some trace elements (e.g. the HFSE) relative to MORB it is inferred that either a) the generation of IAV involves higher degrees of melting than the generation of MORB, b) the mantle wedge had been depleted in incompatible elements by previous melt extraction, or both of these options. It is possible that this will vary from arc to arc, depending on, among other factors, the temperature regime and the presence of a back-arc basin.

Mixing curves inferred from the variation in IAV compositions indicates that IAV are not sourced simply from a mixture of one mantle component and one isotopically-enriched, high-LILE slab-derived component. A number of authors have observed that there is an apparent decoupling between isotopic compositions and incompatible-element abundances and ratios in many arcs: it appears as though there is more than one component to account for the isotopic enrichment and the high-LILE characteristics of IAV.

In order to explain the observations made from a study of IAV compositions, it is necessary to establish how much of the discrepancy between MORB and IAV composition is due to the melting of hydrous as opposed to anhydrous mantle. It is also necessary to quantify the compositions of the slab-derived component in order to ascertain how much of the trace-element signature can be attributed to this. The method of incorporation of the slab component into the mantle is still a matter of debate, with authors advocating transport in fluids (e.g. Tatsumi *et al.*, 1986; Hawkesworth *et al.*, 1991), melts (e.g. Pearce, 1983; Yogodzinski *et al.*, 1994) or

even carbonatite melts (Wallace & Green, 1988; Green & Wallace, 1988). In the following section possible processes involved in the genesis of IAV will be discussed.

2.4 PROCESSES INVOLVED IN THE PRODUCTION OF ISLAND ARC VOLCANICS

In the last section it was shown that there are at least two components involved in the generation of IAV, and there is some recycling of material from the slab to the overlying mantle. A general consensus reached by previous workers is that melting takes place in the mantle, triggered by influx of fluids from the slab. The entire process of subduction and melt generation is extremely complex and involves metamorphism, fluid release, and possible melting of the slab, followed by infiltration of slab-derived fluids into the mantle, melting of the mantle and movement of these melts through the mantle wedge. Finally, magmas can undergo extensive fractional crystallisation in the magma chamber. For a schematic summary of these stages see Figure 1.2. There follows discussion of the trace-element fractionation processes in operation at each of these stages.

2.4.1 Metamorphism of the downgoing slab

Water is present in oceanic crust both as a free phase and locked up in minerals. As the slab sinks and heats up it loses water, first by expulsion of pore waters during compaction, and later by a series of dehydration reactions. There is a growing realisation that loss of mobile elements in these fluids can significantly alter the bulk composition of the slab, and as a consequence the composition of the slab beneath the arc may be different to that being newly subducted. Bulk Cs and B contents in rocks from the Catalina schist show a marked decrease with increasing metamorphic grade: their concentration is calculated to fall by 75% between 0.5 GPa, 300°C and 1.1 GPa, 750°C (Bebout *et al.*, 1993; Bebout *et al.*, in prep.). These elements are inferred to have been scavenged by hydrous fluids. The high mobility of boron (and consequent early loss of boron from the slab) may explain observations by Ryan & Langmuir (1993) that the boron content in IAV decreases with increasing depth to

the slab. It is possible that Rb, K, and Pb are also lost to shallow fluids, as there is a decrease in bulk rock contents of these elements with increasing metamorphic grade (Sighinolfi & Gorgoni, 1978). Beryllium also is inferred to be mobile in subduction zone fluids, although less mobile than boron. These studies have suggested that mobile elements can be lost from the slab at relatively shallow levels (less than 40 km). However the change in composition of the slab with depth still remains very poorly constrained. Furthermore, although it is thought that some of these shallow fluids will be expelled back through the accretionary prism (You *et al.*, 1993) and so play no part in magma genesis, it is not known whether some fluid will travel into the mantle wedge, and be dragged down by the action of subduction. In short, this is an area of considerable uncertainty.

The change in mineralogy of the slab with progressive subduction is also a major unknown. This is very important as it could influence the composition of fluids or melts released from the slab. For example, the presence or absence of rutile in the slab could have significance for the Ti, Nb, and Ta contents of slab-derived fluids or melts. Hydrous eclogites generally consist of garnet, clinopyroxene, and amphibole. However there may be up to thirty additional phases in metabasaltic eclogites and fifty additional phases in metasedimentary eclogites (Mottana *et al.*, 1990) depending on a number of variables including the bulk composition, water content, pressure and temperature. It had been hoped that this project could have involved experiments to simulate metamorphism and fluid release from the slab. Unfortunately there was no time for this to be achieved, and it remains an important task for the future.

2.4.2 Dehydration or melting of the slab?

In order to ascertain the depths at which water is lost from the slab and to decide whether the slab will melt, it is necessary to combine theoretical models for the temperature regime in subduction zones with relevant high P,T experimental data. There have been many models of the thermal structure of subduction zones (e.g. McKenzie, 1969; Hasebe *et al.*, 1970; Andrews & Sleep, 1974; Schubert *et al.*, 1975; Anderson *et al.*, 1978; Peacock, 1990b) based on geophysical constraints and estimates of the following: frictional heating, heat released by exothermic reactions and required by endothermic reactions, convective flow of the asthenosphere, advection of heat by fluids, radiogenic heating. Recent models (e.g. Davies & Stevenson, 1992; Peacock *et al.*, 1994) combined with experimentally deduced solidi indicate that the slab is only capable of melting if it is young (<5 Ma) and hence

relatively hot. The arcs above those slabs that *are* hot enough to melt often contain adakites (high-Al andesitic to dacitic rocks inferred to be derived from the melting of oceanic crust, Defant & Drummond, 1990). Using PS-waves, a thin low-velocity layer has been detected in the top of the descending slab beneath the north-eastern Japan arc (Matsuzawa *et al.*, 1986). The relatively high implied Q values of this layer suggest that it is unlikely to be partially molten. In this subduction zone therefore, there is good evidence that the slab does not melt. In summary, theoretical calculations, supported by some seismic evidence, suggest that in the majority of cases the slab is too cool to melt and thus the main mechanism of transfer of material from the slab to the mantle wedge is via hydrous fluids.

There are few reliable data concerning the subsolidus phase relations of hydrated metabasalts and metasediments, partly because of the difficulties of performing low-pressure experiments. A number of hydrous minerals may be present in the subducted crust, such as amphibole, epidote or chlorite in metabasalt; talc or chlorite in metasediments. The dehydration reactions for these minerals are shown in Figure 2.15. With the possible exception of water retained in chlorite, most of the water is likely to have been released prior to the slab descending beneath the arc (Tatsumi, 1989). It is possible that this fluid infiltrates the mantle and is dragged down to the zone of melt generation by convection induced by the movement of the slab (Tatsumi, *op. cit.*). Mass balance calculations indicate that an order of magnitude more water is subducted than can be accounted for in arc volcanics (Peacock, 1990a). It is possible that this can be explained by retention of water in high-pressure hydrous phases in the slab, such as ellenbergerite (Chopin, 1986) or dense hydrous magnesian silicates (Akimoto & Akaoigi, 1980; Liu, 1989). It is also possible that water may be retained in high-pressure hydrous phases in the mantle. In summary, details of the behaviour of the subducting slab are largely unknown. In order to model the compositions of slab-derived fluids and melts, it is necessary to determine the mineralogy of the slab at the point(s) of fluid release or melting; and the composition of the slab at this time.

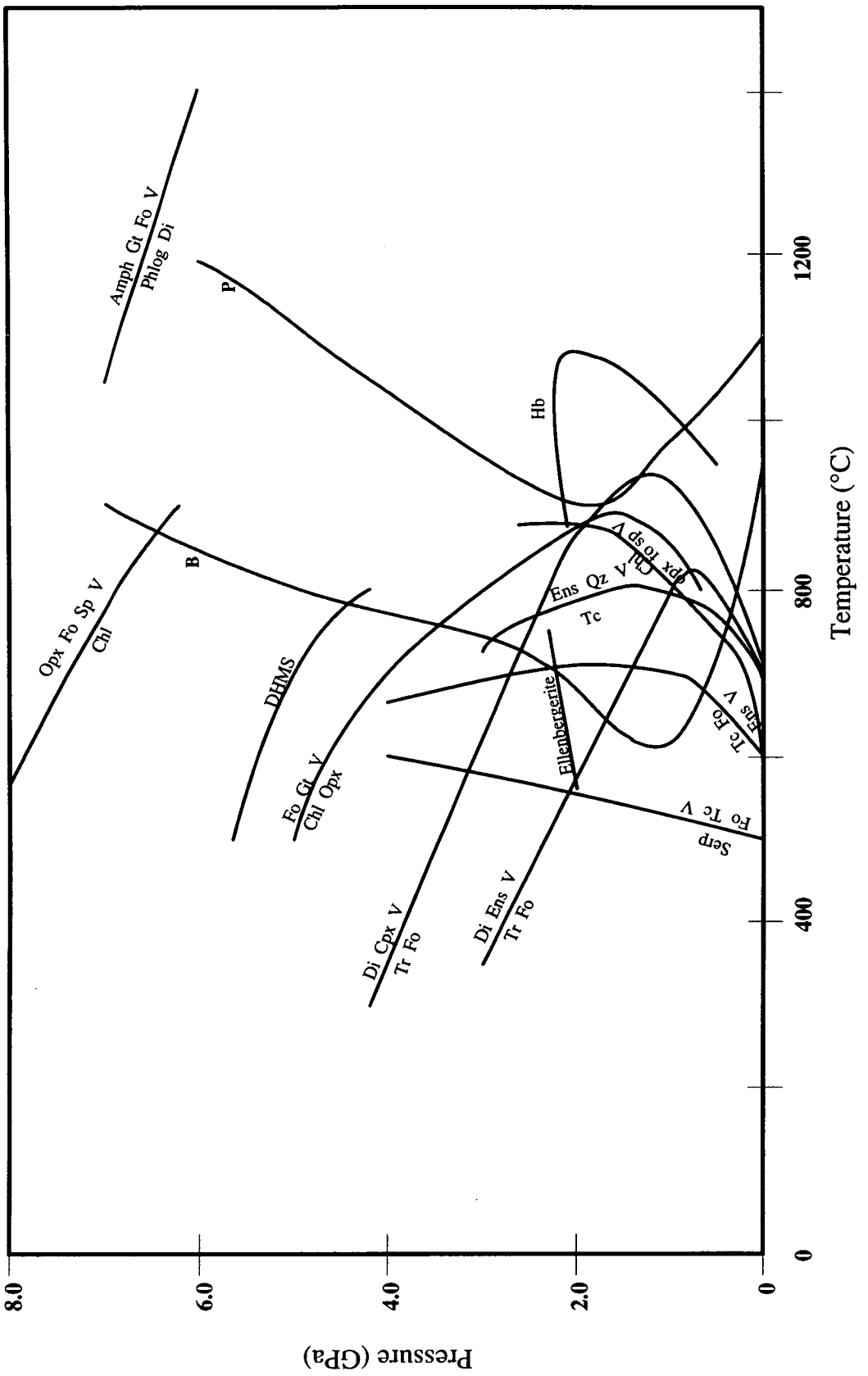

Figure 2.15: Possible dehydration reactions in the subducting slab and mantle wedge. See following page.

Figure 2.15 (preceding page): Possible dehydration reactions in the subducting slab and mantle wedge.
Key to symbols: Amph = amphibole; Chl = chlorite; Di = diopside; Ens = enstatite; Fo = forsterite; Gt = garnet; Opx = orthopyroxene; Phlog = phlogopite; Qz = quartz; Serp = serpentine; Sp = spinel; Tc = talc; Tr = tremolite; V = vapour.
Reactions: Tc = Ens + Qz + V (Chernosky Jr. *et al.*, 1985); Chl = 2 Cpx + Fo + Sp + V (Jenkins & Chernosky Jr., 1986; Delany & Helgeson, 1978); Tr = 2 Di + 3 Cpx + V (Delany & Helgeson, 1978); Tc + Fo = 5 Ens + V (Kitahara *et al.*, 1966); Tr + Fo = 2 Di + 5 Ens + V (Delany & Helgeson, 1978); Chl + Opx = Fo + Gt + V (Goto & Tatsumi, 1990); Phlog + Di = Amph + Gt + Fo + V (Sudo & Tatsumi, 1990).
The water-saturated solidi for basalt and peridotite are labelled B and B, respectively.
The curves labelled Hb marks the upper stability of hornblende in basalt (Allen *et al.*, 1975) and the curves labelled ellenbergerite and DHMS mark the lower stability limits of ellenbergerite (Chopin, 1986) and Dense Hydrous Magnesian Silicates (Akimoto & Akaoigi, 1980).

2.4.3 Composition of hydrous fluids in subduction zones

The idea that fluid-dominated processes may be responsible for the trace-element characteristics of IAV stems in part from the observation that the concentration in IAV of an element is strongly correlated with its ionic potential (e.g. Woodhead, 1989), a property thought to control an element's mobility in a fluid (e.g. Tatsumi *et al.*, 1986). The high-LILE and low-HFSE characteristics of IAV are often considered to result from interaction with the mantle of a LILE-rich slab-derived fluid (e.g. Tatsumi *et al.* 1986; Hawkesworth *et al.*, 1991) or from fluid scavenging the mantle for these elements (Arculus & Powell, 1986; Hawkesworth & Ellam, 1989). In order to evaluate these theories it is necessary to establish the composition of hydrous fluids in equilibrium with the slab and the mantle at relevant pressures and temperatures. The reduction in Cs, B, (and to less extent Rb, K, Pb, and Be) abundances in rocks with increasing metamorphic grade indicates that these elements are mobile in fluids released from these rocks (Bebout *et al.*, 1993; Sighinolfi & Gorgoni, 1978; Domanik *et al.*, 1993). More accessible fluids such as those at hydrothermal vents have been investigated by many authors, and the relative mobility of trace elements in these fluids is relatively well known. However these studies may not be relevant to high pressure fluid release. Fluid compositions have been inferred indirectly from observed geochemical correlations in IAV. However, it would require circular reasoning to argue that this inferred composition can prove that fluid-dominated processes are important! Therefore, the most relevant data needed to model the influence of slab-derived fluids come from experiments performed under appropriate conditions. Prior to this project there had been a few, although not many experimental studies of hydrous fluids in equilibrium with

peridotite or basalt. A critique of the methods employed and the results from these studies is given in Section 3.2.1.

A very large number of authors have used the experimental results of Tatsumi *et al.* (1986) to model the relative trace-element concentrations of slab-derived fluids. The elements investigated by Tatsumi *et al.* (*op. cit.*) consisted of Cs, Rb, Ba, Sr, La, Sm, Tb, Y, Yb, and Nb, and the results referred to the relative mobility of each element in a fluid derived from serpentine at 1.0 GPa. There is a broad negative correlation between mobility and ionic radius. This has been used by some authors e.g. Hawkesworth *et al.* (1993a) to infer the mobility of unmeasured elements such as Th, U, Ce, Pb, Nd, Zr, B, and Be, although the correlation between mobility and ionic radius is by no means proven. Data referring to the mobility of a trace element in fluid derived from serpentine is not, however, strictly relevant to the partitioning of an element between a fluid phase and the eclogitic slab, due to differences in mineralogy of the residue. Partition coefficients have been established for a small set of trace elements (Cs, Ba, Sr, Na, Ce, Gd, Yb) between olivine and fluid at 2.0 GPa (Brenan & Watson, 1992), and there appears to be a negative correlation between D (olivine/fluid) and ionic radius. Measurements and inferences from these studies suggest that the solubility of HFSE is much lower than LILE or REE, an observation that has led authors to presume that the solubility of an element is governed by its ionic potential. However, they are contradicted by a recent high-pressure experimental study by Ayers & Watson (1991) in which it was found that rutile and zircon (both HFSE minerals) can be significantly more soluble in water than can the REE mineral, monazite. As well as the experimental results of Ayers & Watson (1991), evidence for high solubility of HFSE includes the discovery of rutile and zircon in fluid inclusions from palaeosubduction zones (Phillipot & Selverstone, 1991). Boron and the HFSE have relatively small ionic radii and extrapolation of the relationship between ionic radii and mobility (or partitioning) suggests that these elements would be relatively immobile in hydrous fluids (Tatsumi *et al.*, 1986). However, boron is extremely mobile in hydrothermal fluids, and furthermore, evidence from metamorphic rocks suggests that boron is lost very early by release of fluids.

In summary, experimental results prior to this project are conflicting, and not strictly relevant to partitioning of elements into slab-derived fluids or fluids in equilibrium with the mantle. One of the aims of this project, therefore, was to measure partition coefficients between hydrous fluid and mantle and slab phases. Unfortunately this was not achieved entirely. Partition coefficients between fluid and basaltic melt and fluid and olivine were measured and have been combined with published

D(mineral/melt) to infer the bulk partition coefficients between hydrous fluid and the slab (see Chapter 8).

2.4.3 Fluid/mantle interaction

It is likely that fluids released from the slab will infiltrate the mantle and form a number of hydrous phases such as serpentine, chlorite, talc, amphibole and phlogopite (Tatsumi, 1989). The following pressure-dependent reactions may be important in the mantle wedge:

amph $\leftrightarrow$ cpx + gt + water

opx + chl $\leftrightarrow$ ol + gt + water

Although there is some slight variation between arcs, the depth from the arc to the Wadati-Benioff Zone (WBZ) is approximately 112 km. As a results of the higher Mg no. of the mantle, amphibole is stable to greater depths in the mantle than in the slab (Millholen *et al.*, 1974), and dehydrates at ~3.0 GPa (Green, 1973; Mysen & Boettcher, 1975). Chlorite dehydration could take place over a range of depths, depending on the temperature regime in the subduction zone. The breakdown of these minerals is thus inferred to take place at a depth corresponding to the base of the mantle wedge beneath the arc (Tatsumi, 1989). Davies & Bickle (1990) propose that water released from the breakdown of mantle amphibole will percolate upwards until it intersects and reacts with dry peridotite. They suggest that the amphibole peridotite produced will then be dragged down by forced convection until it reaches the dehydration pressure again, at which point the process will be repeated. The net result is a horizontal zone of amphibole peridotite extending into the mantle wedge (Fig. 2.16). Once this crosses the solidus (approximately 1000°C in Figure 2.16), melting will begin. They suggest that there will be a zone in which melt and amphibole coexist, as a result of the small degree partial melts being unable to separate from the matrix. Convection in the mantle wedge, however, is a poorly constrained area. Many authors (e.g. Spiegelman & McKenzie, 1987) have suggested that the movement of the slab will induce convection in the asthenospheric mantle wedge. However, as the base of the mechanical boundary layer is normally ~100 km, and amphibole dehydration takes place at ~90 km, all mantle amphibole is likely to be restricted to the lithosphere. It has not been established that this convects although it is possible that the asthenospheric mantle convection and the presence of melt may effectively reduce the mechanical boundary layer thickness. Assuming that the model presented in Figure 2.16 is correct, it is conceivable that the slab-derived

fluid may equilibrate with the mantle and thus lose its original composition, unless the hydration and dehydration process can transfer dissolved slab-derived components as well as water. The slab could thus play a much less important role than advocated by many studies, although isotopic evidence from IAV (presented above) suggests that the slab is nevertheless important. It is necessary to quantify the compositions of fluids in the mantle, and to judge whether they would be capable of producing enrichments in LILE, as proposed by Ellam & Hawkesworth (1988) and Arculus & Powell (1986). This was one of the aims of this project.

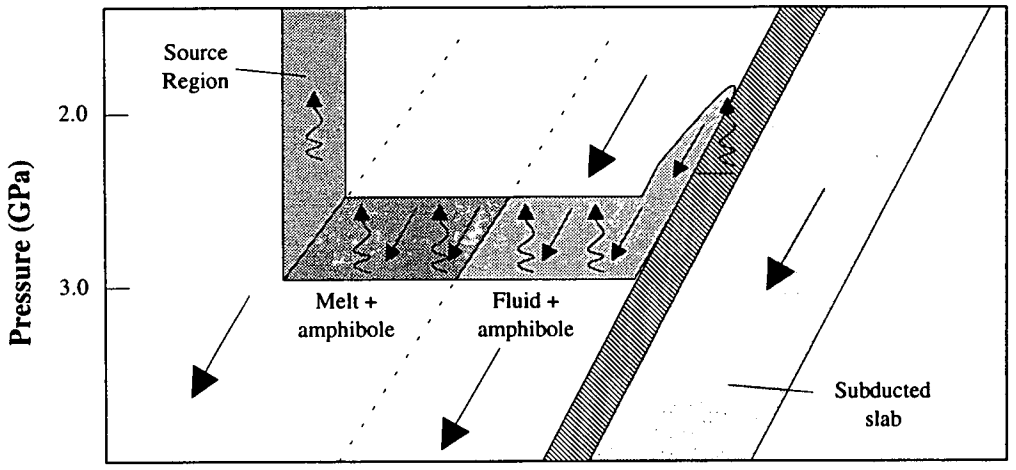

Figure 2.16: Schematic cross section of the mantle wedge illustrating a proposed mechanism for transport of fluid from the slab to the zone of melt generation (Davies & Bickle, 1990). The straight arrows represent the motion of the matrix while the wiggly arrows represent the motion of either melt or fluid.

2.4.4 Melting of the mantle

The general consensus of most authors is that melting in subduction zones takes place in the mantle and is triggered by the influx of slab-derived fluids. This is reasonable given the good experimental evidence to suggest that the melting point of mantle is likely to be lowered significantly by the input of water (see Chapter 3). The compositions of partial melts of a hydrous mantle are relatively unknown in comparison to melts of anhydrous mantle. There are very few estimates of major-element composition, and even fewer estimates of trace-element compositions of hydrous melts. One major difference between hydrous and anhydrous mantle is the presence of amphibole (below ~3.0 GPa) in the former. According to the models of Davies & Bickle (1990) and Tatsumi (1989), melting occurs when amphibole peridotite is dragged over its solidus (see Fig. 2.16). Whether amphibole is retained

in the residue is dependent on the degree of melting undergone. There are authors who have claimed to see the geochemical consequences of amphibole in the source. For example, numerical inversion of the REE contents of arc suites led McKenzie & O'Nions (1991) to invoke residual amphibole in the source region of magmas. In the Lesser Antilles there may be amphibole in the source region of some of the volcanics, which were inferred to have been produced by relatively low degrees of melting (Thirlwall *et al.*, 1994), although in the majority of volcanics, no residual amphibole was invoked.

2.4.5 Behaviour of fluids and melts

The path taken by melt produced in a subduction zone can be complex because to reach the surface it must move against the mantle wedge which is being dragged down by the slab. Melt paths can be modelled by analogy with a two-dimensional system of melt flowing through a deformable matrix (Spiegelman & McKenzie, 1987). It is found that the flow of melt is governed by small changes in the piezometric pressure near the corner of the mantle wedge. As a consequence, melt is channelled to a region in the corner of the mantle wedge approximately 100-200 km above the Benioff zone. An important ramification of this is that melt is not necessarily representative of the mantle directly beneath the arc, but potentially from a considerable part of the mantle wedge. A quiet zone with no volcanism is predicted further out from the primary arc followed by a broad region of diffuse magmatism. The volcanism observed in many arcs is consistent with this. The finer details of the flow paths are dependent on the geometry of the subduction zone and the permeability of the matrix as well as the correctness of the relations between viscosity, depth and temperature adopted for melt and matrix (Fig. 2.17).

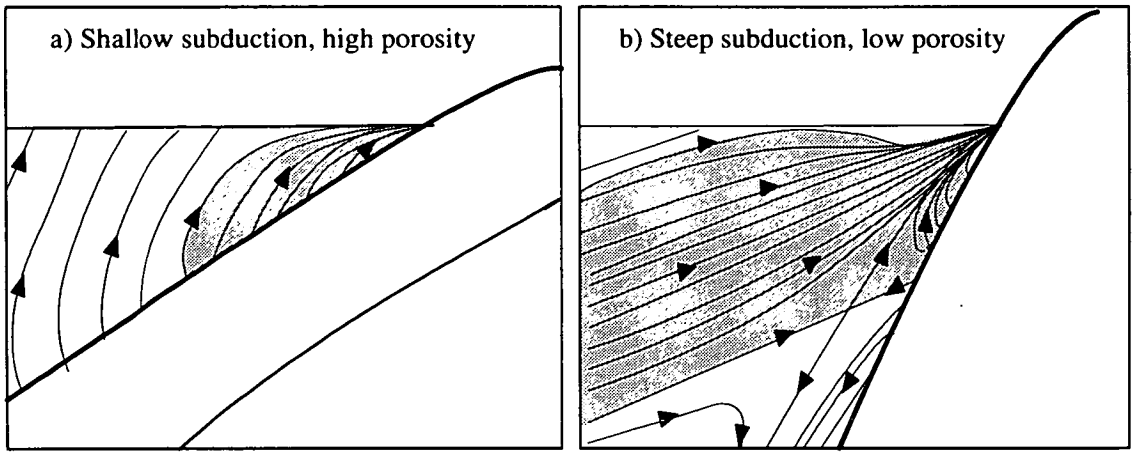

Figure 2.17: Melt streamlines in the asthenospheric mantle wedge. a) shallow subduction and relatively high porosity, b) steep subduction and relatively low porosity. The shaded region is the melt extraction zone containing all streamlines from depth that connect to the wedge corner. The streamlines denote the direction of flow of the melt should it be present. It is not implied that there is melt present throughout the shaded region. From Spiegelman & McKenzie (1987).

The behaviour of an individual trace element is not so straightforward to predict. A number of authors have noted that elements will be fractionated while travelling in a melt phase through a matrix. The mantle can be thought of as an ion exchange column (Navon & Stolper, 1987). Consider the upward movement of melt through a column of mantle. As melt rises it endeavours to equilibrate with the mantle through which it passes and so the melt will change in composition. Different elements will equilibrate at different rates depending on their partition coefficients, and if equilibrium is not attained, on the diffusion kinetics of each species. With time, if the mantle is not replenished, the melt will begin to recover its original composition. As an element moves up, a front is formed above which the element has the concentration of a liquid in equilibrium with the matrix and below which the element retains its original concentration in the melt. Fronts of different elements move at different speeds, that of the most incompatible element moving at the greatest speed. Thus trace elements can be fractionated from one another, analogous to separation of elements using an ion exchange column. In a subduction zone the matrix is continually replenished by fresh mantle circulating in the wedge. The melt will rise due to buoyancy. As the melt percolates through the wedge the positions of the element fronts can be predicted from the speed of the matrix relative to the moving melt, and the distribution coefficient of the element, assuming that equilibrium has been reached. The more incompatible element fronts will move faster and thus the element front will reach the top of the column rather than be carried away by the matrix. Thus some of the original signature will be preserved for the most incompatible elements. The less incompatible element fronts will move more slowly

and some will fail to reach the top of the column. There is a critical value of D above which an element is too compatible for the original melt signature to be preserved. This is given by:

$D^{crit} = G / \{LV_s\}$ (Navon & Stolper, 1987)

where G is the flux of the melt, which should be equal to the growth rate of the arc; L is a length scale and V_s is the speed of the matrix.

Thus for elements with D above this critical value, the concentration in the melt will reflect the concentration in the mantle matrix and not the original melt. In this case:

$C_m = C_s^o / D$

where C refers to the concentration of the element in the melt (subscript m) and the mantle (subscript s). The original concentrations are denoted by a superscript o. For $D < D^{crit}$ the concentration in the emerging melt is related to the original concentration in the following way:

$C_m = C_m^o + \{C_s - DC_m^o\}/D^{crit}$

This approach has been combined with the two-phase flow equations of Spiegelman & McKenzie (1987) to predict the flow paths for individual elements (McKenzie & O'Nions, 1991). See Figure 2.18.

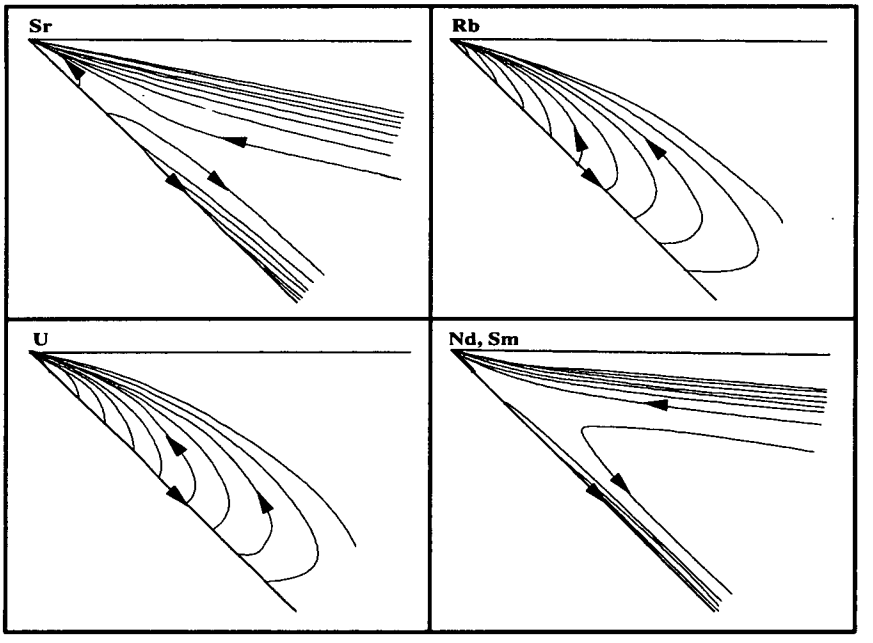

Figure 2.18: Streamlines for Sr, Rb, U, Nd, Sm in melts in subduction zones assuming amphibole peridotite in the source region. From McKenzie & O'Nions (1991).

In summary, the flow paths for individual elements are dependent on the speed of the fluid or melt, and the distribution coefficient of the element. Hawkesworth *et al.* (1993a) suggested that fluid flow in the mantle wedge was governed by processes such as the one proposed above. They suggest that the LILE, which they infer to be the most mobile elements, are more likely to reach equilibrium values, and that this can account for the observation that even though IAV are relatively enriched in LILE, the LILE abundances vary less than the HFSE. In summary, there is a growing realisation that the complex processes involved in fluid or melt movement through the mantle wedge can cause dispersion in inter-element ratios, certainly between elements with differing compatibilities. Hence, the situation is more complicated than that suggested by models of melt generation involving batch melting of a source composed of constant proportions of end members.

2.4.6 High-level processes

The rocks erupted above subduction zones are more diverse and, on average, richer in SiO_2 than those erupted at other settings. Identification of primary magmas is fundamental to the understanding of subduction zones. One method by which this can be done is to experimentally equilibrate a natural rock under mantle conditions and see whether there are any mantle phases on the liquidus. This was done for andesites, the most voluminous rock type and an early candidate for the parental melts. Results, although contentious, show that it is unlikely that andesite is formed as a direct partial melt of the mantle at depths greater than 40 km (Wyllie, 1982). Rather, andesites are likely to be formed by fractional crystallisation of a more mafic parental magma. High-alumina basalts are a potential primary magma: these are found in many arcs. Gust & Perfit (1987) showed experimentally that a high-Mg arc basalt was not formed in equilibrium with lherzolite. They suggested that the primitive melt is even more mafic. Johnston & Draper (1992) showed that a high magnesia basalt (from the Aleutians) had been in equilibrium with dry mantle at 1.2 GPa, 1300°C. This they inferred was either the point at which the mantle melted, or the last point at which the magma equilibrated with mantle. Generally, primitive magmas are calculated from IAV by addition of fractionated phases until the calculated melt composition is in equilibrium with mantle mineralogy (e.g. Woodhead, 1988). This has produced estimated mantle melts of picritic composition. Natural picrites have been discovered in a few arcs: Ramsay *et al.* (1984) found arc picrites to be similar to the postulated primary melt composition at

mid-ocean ridges, but enriched in K, Rb, Sr, Ba and LREE. Their scarcity in most arcs has been attributed to difficulty in ascending unaltered to the surface. The presence of picrites in some arcs should not, however, be taken as evidence that they are a universal primary melt. There still remains considerable disagreement as to the true primary melt composition in many arcs.

2.5 DISCUSSION

In order to explain the compositions and correlations between compositions of IAV, it is necessary to model the processes in operation within a subduction zone, and in particular to establish how material from the slab is incorporated into the magmas. This task is not easy as there are a multitude of unknowns surrounding many of the processes in operation within a subduction zone. In my opinion, there are three principal areas that could usefully benefit from experimental investigation.

1. *Metamorphism of the slab.* In order to model the compositions of fluids (or melts) released from the slab, it is essential to establish the mineralogy of the slab over the region of dehydration or melting. Useful experimental work could include an investigation into the phase relations and compositions of slab analogues along a typical slab P, T trajectory. There may be some difficulties with equilibration in studies of the type proposed, due to the relatively low temperatures experienced by the slab.
2. *Partitioning of elements into hydrous fluids.* Both slab- and mantle-derived fluids have been invoked to be the cause of the LILE enrichment observed in IAV. However, the experimental evidence to support such theories is sparse, often conflicting and not always strictly relevant. The measurement of partition coefficients between fluids and minerals, or fluids and melts could enable calculation of the bulk partition coefficients between fluid and the slab, or fluid and the mantle. For an accurate estimation of slab-derived fluid composition, it would, of course, be necessary to establish the mineralogy of the slab.
3. *Partition coefficients relevant to melting of hydrous mantle.* Partition coefficients have been determined for dry melting of the mantle, but may be very different for wet melting. This is implied by the difference in major-element composition of melts of anhydrous and hydrous melting (see Chapter 3). In addition, hydrous mantle can contain hydrous phases such as amphibole or

chlorite. In order to establish the influence of amphibole as a residual phase during melting in the mantle wedge, it is necessary to determine accurate partition coefficients between amphibole and melt. Furthermore, determination of the relevant partition coefficients can allow evaluation of how much of the IAV signature is due simply to the presence of water. Partition coefficients are also needed to investigate the effects of chromatographic processes operating on melts as they rise through the mantle.

These suggested experimental studies are obviously more than can be attempted in one PhD study! In this project it was decided to concentrate on a) the major- and trace-element systematics of hydrous melting of the mantle and b) the partitioning of trace elements into hydrous fluids in equilibrium with the mantle.

CHAPTER 3

EXPERIMENTAL RATIONALE

CHAPTER 3: EXPERIMENTAL RATIONALE

In Chapters 1 and 2, it was shown that in order to further constrain the processes responsible for the formation of IAV it is necessary to obtain experimental data relevant to the partitioning of trace elements during dehydration of the slab, interaction of fluids with the mantle, and melting of the hydrous mantle. The specific aims of this project were therefore

a) to determine experimentally the major- and trace-element compositions of melts and residual phases of hydrous peridotite over a range of pressures and temperatures.

b) to calculate the partition coefficients between hydrous (aqueous) fluid, basaltic melt and coexisting mineral phases produced at high pressures and temperatures.

Although there have been many previous studies of the phase relations and compositions of partial melts of hydrous peridotite, results are still subject to much debate. In particular there is disagreement over the major-element compositions of partial melts of water-undersaturated and water-saturated peridotite. The trace-element compositions of such melts have not previously been studied. Relevant previous work is discussed in detail in Section 3.1.1 and the approach adopted in this project will be outlined in Section 3.1.2.

Previous to this project, there had been few investigations of the composition of hydrous fluids in equilibrium with mantle rocks. Of these studies, fewer still had investigated the behaviour of trace elements. The methods used in these studies, and the results obtained, are discussed in Section 3.2.1 and the approach adopted in this project is introduced in Section 3.2.2.

3.1 MELTING OF HYDROUS PERIDOTITE

3.1.1 Previous work

Phase relations

It is well established that water influences the phase relations of peridotite: in particular with increasing water content, the solidus temperature decreases until

water saturation is reached (Wyllie, 1979 *and references therein*). Most previous work has been concentrated on the phase relations of water-saturated peridotite because water-undersaturated systems are more difficult to study (e.g. Green, 1973; Millholen *et al.*, 1974). For water-saturated conditions at pressures less than 5.0 GPa, subsolidus phases consist of olivine, orthopyroxene, clinopyroxene and amphibole (below the pressure of amphibole dehydration), an aluminous phase (plagioclase, spinel or garnet, also depending on pressure) and various accessory phases such as rutile or ilmenite. Amongst the majority of studies (e.g. Green, 1973; Millholen *et al.*, 1974; Mysen & Boettcher, 1975a), there is general agreement concerning the order of disappearance of phases with increasing temperature above the solidus. Where pressures are appropriate for subsolidus amphibole, this is the first phase to disappear completely, followed by ilmenite, clinopyroxene and then orthopyroxene. At higher pressures garnet disappears before clinopyroxene. Olivine is stable up to the liquidus. There is less agreement concerning the absolute conditions in P, T space at which these reactions take place. For example, there are a number of conflicting estimates for the position of the solidus (Fig. 3.1).

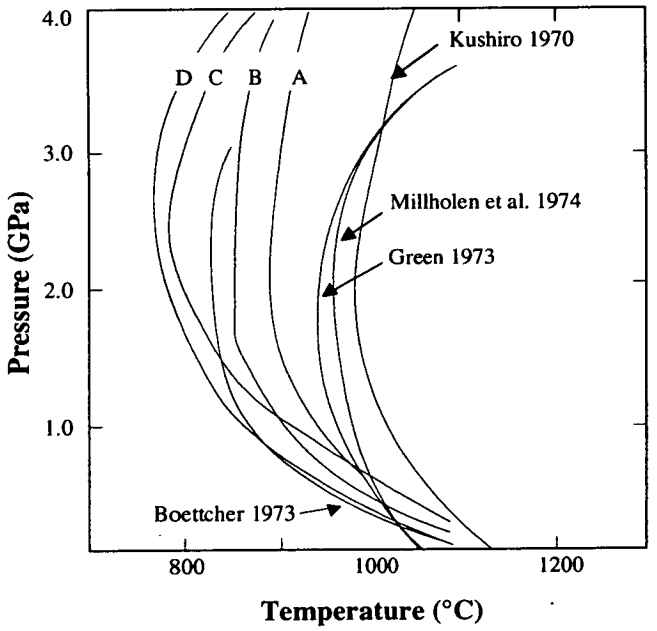

Figure 3.1: Comparison of results from several experimental studies on the solidus curve of peridotites in the presence of excess water. Data from Kushiro (1970); Boettcher (1973); Green (1973); Millholen *et al.* (1974); Mysen & Boettcher (1975a) - A, B, C, D have Mg nos. of 93, 88, 89, 83, respectively.

Whilst some of this variation may be due to the different starting materials used[1], the way in which the solidus is recognised is open to some debate (Green, 1976). The majority of authors positioned the solidus just below the temperature at which

[1]The solidus temperature decreases with decreasing Mg no. of the starting material at constant CaO/Al_2O_3, and with decreasing CaO/Al_2O_3 at constant Mg no. (Mysen & Boettcher, 1975b).

optically-identified melt was first produced. However, it may not be possible to detect by optical means extremely-small-degree partial melts. A more accurate method, in my opinion, is the one used by Green (1973). He documented changes in amphibole composition over a range of temperatures and found that there was an abrupt change in composition at one temperature, which he interpreted to be the solidus[2]. Optical evidence supported this assumption.

Figure 3.2 shows some estimates for the position of the amphibole-out curve. Again there is considerable variation which may be partly due to differences in the starting materials used[3] (Gilbert *et al.*, 1982), but could also be a consequence of inter-laboratory differences, and of subjective methods for determining the presence or absence of very small amounts of equilibrium amphibole.

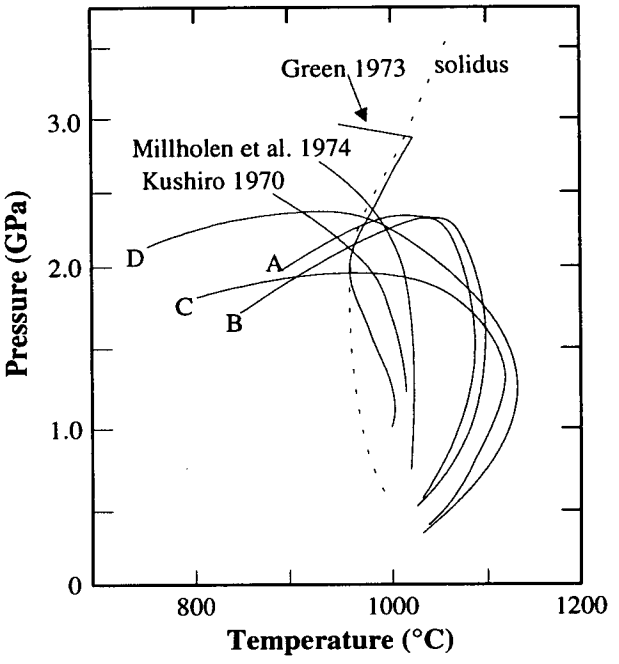

Figure 3.2: Comparison of results from several experimental studies on the P, T stability of amphibole in peridotites in the presence of excess water. Data from Kushiro (1970); Green (1973); Millholen *et al.* (1974); Mysen & Boettcher (1975a) - A, B, C, D have Mg nos. of 93, 88, 89, 83, respectively.

Possible reasons for discrepancies between experimental results include:

- failure to detect phases when present in small quantities and/or to distinguish between equilibrium and quench minerals.
- incomplete reaction of phases, possibly due to the large grain size of the starting material in some studies : For example, Green (1976) criticised experiments by Mysen & Boettcher (1975a) in which the starting material contained grains of up to 70μm diameter.

---

[2]The higher temperature amphiboles, interpreted to be supersolidus contain less K_2O

[3]Amphibole stability is enhanced by TiO_2, FeO, K_2O (Gilbert *et al.*, 1982).

- development of more refractory compositions due to progressive iron loss from the capsule: Green (1976) claimed that their cylindrical capsules were less susceptible to iron loss than the pillow-shaped capsules of Mysen & Boettcher (1975a) and co workers.
- variation in oxygen fugacity: the majority of these experiments were not buffered.

In summary, it is clear that these types of studies contain many inherent difficulties, and therefore in designing the experiments in this project, I have tried to avoid the pitfalls highlighted by previous work.

Melt composition

Early workers suggested that glass produced by partial melting of hydrous peridotite was highly siliceous. For example, an experiment at 2.6 GPa, 1190°C yielded glass with a reported SiO_2 content of 67.8% (Kushiro *et al.*, 1972). See table 2.1. Thus it was claimed that andesites and dacites could be produced by direct partial melting of the mantle under water-saturated conditions (Kushiro *et al.*, 1968; Kushiro *et al.*, 1972). There followed a long and controversial dispute concerning the pressures to which silica-rich magmas could be produced. Green (1973) performed experiments with similar results to Kushiro and co workers. However he proposed that the glass was not representative of the equilibrium melt, suggesting that on quenching there had been significant fractionation. This was supported by the occurrence of quench crystals in charges, and the observation that the glass was too iron rich to be in equilibrium with the olivine composition according to known experimental relationships (Roeder & Emslie, 1970). Furthermore, it was not possible to reconstruct the starting material by mass balance if the melt were andesitic. Green (1973) calculated the melt composition by addition of fractionating phases to the measured glass composition until the Fe/Mg olivine/melt exchange relationship of Roeder & Emslie (1970) was re-established. For high degrees of melting at 1.0 GPa and 2.0 GPa ($T > 1100°C$) the calculated melt compositions ranged from olivine tholeiite to magnesian quartz tholeiite - substantially more mafic than andesite. Mysen & Kushiro (1974) and Mysen & Boettcher (1975b) repeated partial melting experiments and claimed that no quench phases were produced. They reasserted their view that andesites can be produced by direct melting of the mantle at high pressures. Melt compositions derived from a number of studies are given in Table 3.1.

Table 3.1: Compositions of some experimentally-produced partial melts of peridotite in the presence of H_2O.

	Kushiro *et al.* (1972)	Green (1976)		Kushiro (1990)			
P (GPa)	2.6	1.0	1.0	1.2	1.2	1.6	2.0
T (°C)	1190	1200	1100	1200	1150	1150	1250
% H_2O in melt	n.d.	n.d.	n.d.	10.7	4.4	n.d.	4.6
SiO_2	67.8	53.8	55.5	52.75	49.62	54.55	47.85
TiO_2	0.6	2.0	2.5	0.54	0.76	0.4	0.76
Al_2O_3	16.1	9.7	12.3	12.7	16.76	13.16	14.6
Fe_2O_3		0.3	0.5				
FeO	1.1	9.1	6.8	9.51	9.92	9.76	10.7
MnO	0.1	0.2	0.1	0.19	0.16	0.25	0.17
MgO	0.6	14.1	9.3	13.69	9.29	11.14	12.67
CaO	10.2	8.6	10.4	8.86	11.13	8.41	11.31
Na_2O	3.1	1.7	2.0	1.42	2.04	1.95	1.71
K_2O	0.3	0.4	0.5	0.18	0.21	0.37	0.17
Cr_2O_3	n.d.	0.1	0.1	0.14	0.1	n.d.	0.09

All analyses are recalculated as 100% anhydrous. Kushiro *et al.* (1972) analysed an experimentally-produced glass by electron microprobe; Green (1976) derived melt compositions by means of a liquidus study on suggested melt compositions from Green (1973); Kushiro (1990) produced and analysed thick layers of glass (up to 100μm) in sandwich experiments with a starting assemblage consisting of a natural tholeiitic basalt sandwiched by a natural lherzolite.

In order to evaluate the accuracy of calculated melt compositions it is necessary to test them by reversal experiments. This involves re-equilibrating a synthetic mix of the calculated melt composition under the same conditions as the original experiment. In theory, the original residual phases should be present at or just below the liquidus. Nicholls & Ringwood (1973) tested the dacite glass composition of Kushiro *et al.* (1972). They found that the liquidus was 250°C lower than the temperature at which it had formed. Furthermore, olivine was not stable at or just below the liquidus. Thus they claimed that it could not represent the equilibrium melt composition in the original experiment. This approach was criticised by Mysen & Kushiro (1974), who claimed that the absence of olivine from the liquidus was not adequate proof that the liquid was not in equilibrium with olivine at its formation. They suggested that a reaction relationship may exist whereby orthopyroxene is precipitated as a result of reaction between olivine and a quartz-normative liquid. Nicholls (1974) performed experiments at various pressures using natural andesite compositions, adding olivine until it persisted. The composition of the final liquid was then estimated by electron probe analyses. Results suggested that andesitic magmas are only likely to be produced by direct partial melting of hydrous peridotite

at pressures less than 1.0 GPa, i.e. liquids produced by partially melting hydrous peridotite at pressures higher than 1.0 GPa are less siliceous than andesite: a conclusion in disagreement with the work of Mysen & Kushiro (1974). Furthermore, andesites produced at low pressures were found to be more magnesian and poorer in alkalis than natural andesites. Nicholls (1974) therefore concluded that natural andesites are unlikely to represent partial melts of the mantle. Green (1976) also tested his calculated melt compositions (Green, 1973) by means of liquidus experiments, and found that only minor adjustments to these relatively mafic compositions were needed in order to reproduce the phases present in the original experiments.

The results of previous workers were combined by Wyllie (1979, 1982) to produce a summary of the composition of liquids formed at different pressures (Fig. 3.3). Although there is still considerable disagreement over the depth of the boundaries, the trends with pressure and temperature are fairly well established.

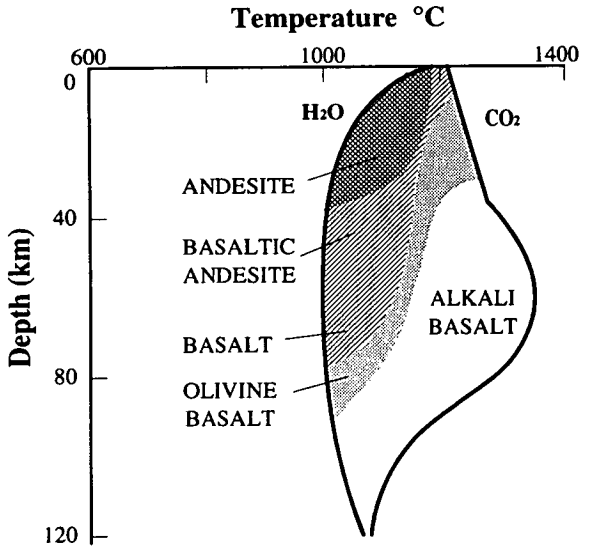

Figure 3.3: Compositions of near-solidus, vapour-saturated partial melts in the system peridotite-H_2O-CO_2. Redrawn from the modification by Wilson (1989) of a diagram by Wyllie (1982).

Summary

Experiments have shown that the presence of water lowers the solidus temperature of peridotite and causes an expansion of the olivine phase field to higher pressures (e.g. Nicholls & Ringwood, 1973; Kushiro, 1990). It is also well established that the presence of water elevates the SiO_2 content of melts produced, with SiO_2 content correlated negatively with pressure and positively with temperature (Fig. 3.3) and correlated positively with water content (for water undersaturated conditions, Kushiro, 1990). However, there are very few reported and tested analyses of partial

melts of water-saturated and water-undersaturated peridotite, and there is no agreement concerning the accuracy of these estimated compositions. This stems mainly from the problem of extensive fractionation of liquids during quenching, a phenomenon that is not so marked in anhydrous systems. There is therefore a need for further experiments in which the major-element and trace-element composition of melt is documented over a range of pressures and temperatures.

Finally, it should be noted that there is a recently-developed technique for the measurement of melt composition in anhydrous systems (Hirose & Kushiro, 1993; Baker & Stolper, 1994). This involves the inclusion in the capsule of finely-ground diamond powder, into which melt migrates. The melt quenches to form an unfractionated glass which is representative of the composition of the equilibrium melt. Although this may be a very useful technique in many future experimental studies, it cannot be applied here, as the inclusion of diamond in the capsules would cause saturation in carbon and thereby introduce another degree of freedom into the system.

3.1.2 The present study

It is clear that previous workers have encountered great difficulties in the measurement of the major-element composition of partial melts of hydrated peridotite. One of the motives for further investigation of this difficult subject in the present study was the development of a new technique for the determination of melt composition (Odling, *accepted*). This technique, which is described in more detail in Chapters 4 and 5, involves the production during the experiment of melt inclusions in a crystal of olivine that is present in the capsule. It is thought that during quenching the only quench crystals to form in these melt inclusions are olivines that coat the sides of the inclusion. The glass composition in the melt inclusions should therefore be depleted in olivine component relative to the equilibrium melt composition. It is a relatively simple matter to reconstruct the equilibrium melt composition by addition of the equilibrium olivine composition to the melt inclusion composition until the Fe/Mg olivine/liquid exchange relationship of Roeder & Emslie (1970) is re-established.

As the phase relations of hydrous peridotite have been well documented by Green (1973), it was decided to use his results as a starting point. Figures 3.4a and 3.4b show the phase diagrams derived by Green (1973) for water-saturated and water-undersaturated conditions, respectively. The starting composition used in the present

study is identical in terms of major elements to that of Green (1973), and in addition it was doped with a number of trace elements. In order to minimise the problems of equilibration encountered by previous workers (Section 3.1.1) experiments were performed using synthetic fine-grained starting materials (gels, sintered oxides, or mixtures of both). Iron loss was minimised by use of cylindrical capsules and the olivine bucket surrounding the starting material.

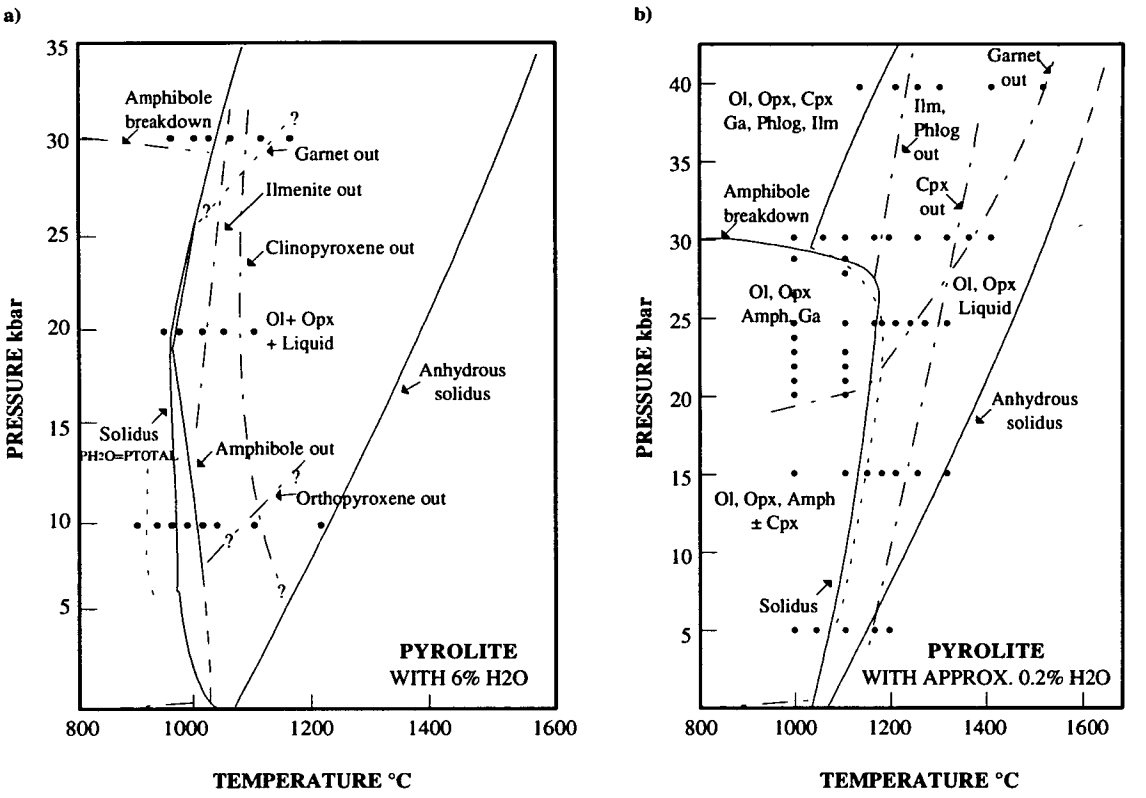

Figure 3.4: Phase relations of a peridotite composition under a) water-saturated and b) water-undersaturated conditions. Experiments were carried out on (pyrolite minus 40% olivine) composition with a) 10% water added and b) a water content equivalent to 0.2% in pyrolite; data points are shown as small circles in the diagrams. From Green (1973).

Besides the determination of the major-element and trace-element composition of partial melts, it was planned to use the results from these experiments to calculate partition coefficients between amphibole and melt. It was therefore decided to perform experiments initially within the pressure range in which mantle amphibole is stable (Fig. 3.4). Experiments were performed at pressures of 1.8 GPa, 2.3 GPa and 2.8 GPa and at temperatures ranging from subsolidus (966°C) to well above the solidus (1150°C). In order to analyse crystals by SIMS (see Chapter 4) it is necessary to produce crystals that are at least 40 μm x 40 μm in cross section.

However, in a typical partial melting experiment, crystals are smaller than this (approximately 10x15 μm). Efforts were made to grow larger crystals of amphibole (see Chapter 5), but they were not successful. Partition coefficients between amphibole and melt were therefore not measured. Originally it had been intended to extend this study to higher pressures (up to 4.0 GPa) in order to more accurately simulate the conditions at which melting is thought to take place in the mantle wedge (see Section 2.4.4). However this did not prove possible in the time available. Conditions of all experiments were water oversaturated, although it had been hoped to contrast the behaviour of water-saturated and water-undersaturated systems.

Finally, oxygen fugacity is an extremely important parameter in experiments as it governs the oxygen state of iron, and can influence the P/T position of the solidus and the composition of melts and fluids. However, despite its undoubted importance, the oxygen fugacity of the mantle wedge remains relatively unknown. The oxygen fugacity of the mantle can be estimated from thermodynamic models (e.g. O'Neill & Wall, 1987; Mattioli & Wood, 1988) using analyses of the ferric and ferrous iron content of minerals in xenoliths or in volcanics. As the oxidation state of iron in minerals is also dependent on the pressure and temperature of formation, it is necessary to incorporate estimates of these parameters into calculations. Although there have been many studies of this type, results are often spurious, possibly due to differences in the thermodynamic models and the geobarometers and geothermometers employed. Results are generally quoted with reference to the oxygen fugacity of standard synthetic buffers (Fig. 3.5).

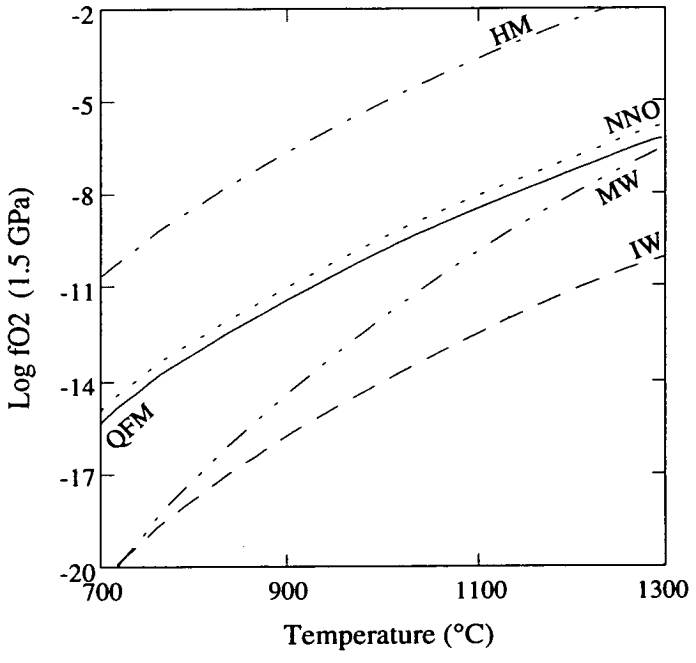

Figure 3.5: log fO_2's of synthetic buffers at 1.5 GPa.
HM is hematite - magnetite
NNO is nickel - nickel oxide
MW is magnetite - wüstite
QFM is quartz-fayalite-magnetite
IW is iron - wüstite.
All from Mattioli *et al.* (1989) except NNO (O'Neill, 1987).

Calculated fO_2's for the mantle (encompassing a range of environments) fall within ±2 log units of QFM (Mattioli *et al.*, 1989). In general, xenoliths and volcanics from subduction zone environments indicate that the oxygen fugacity of the mantle wedge is at the higher end of the range of oxygen fugacities of the mantle. For example, fO_2's in the mantle wedge have been calculated as 1 or 2 log units above NNO (Arculus & Wills, 1980), between QFM and NNO (Barsdell & Berry, 1990), 0 to 1.2 log units above QFM (Wood & Virgo, 1989), approximately QFM (Mattioli *et al.*, 1989), and approximately 2 log units above QFM (Ballhaus *et al.*, 1990, 1991). Therefore, although there is a range of estimates of the fO_2 of the mantle wedge, most authors suggest that it is above QFM and below HM. I consider that a good approximation for the oxygen fugacity in the mantle wedge is the NNO buffer, and therefore experiments will be buffered to NNO.

The results of the partial melting experiments, and the reversal experiments performed to test the calculated melt compositions, are presented in Chapter 5.

3.2 COMPOSITION OF HYDROUS FLUIDS IN EQUILIBRIUM WITH MANTLE ROCKS

3.2.1 Previous work

Solubility data suggest that fluid-saturated basaltic melts can coexist with a separate melt-saturated H_2O-rich fluid to pressures of at least 4.0 GPa (Eggler, 1987 *and references therein*). Major-element, and some trace-element concentrations in H_2O-rich fluids have been determined, either by collecting and analysing the solute (Holloway, 1971; Schneider & Eggler, 1986; Zielinski & Frey, 1974; Cullers *et al.* 1970; Cullers *et al.* 1973) or by mass balance, using the compositions of coexisting phases before and after an experiment (Mysen, 1979; Tatsumi *et al.* 1986; Brenan & Watson, 1991). Although these studies were performed under a range of conditions with different starting materials, they show that the solute is composed mainly of SiO_2 and Al_2O_3 with relatively high alkalis and low FeO, MgO, and TiO_2 (see Table 3.2).

With increasing pressure the composition of the fluid solute has been found to change, becoming less quartz normative and more aluminous (Schneider & Eggler, 1986). The solute content also rises markedly with pressure (Holloway, 1971;

Schneider & Eggler, 1986) although values remain very low. Holloway (1971) using a double-capsule technique with a basaltic starting material found that at 0.2-0.8 GPa, the solute content in H_2O-CO_2 fluid ranged from 0.5 wt% to 2 wt%. Data from higher pressures are relatively scarce: Schneider & Eggler (1986) measured solute contents of up to 12 wt% in fluids in equilibrium with phlogopite peridotite at pressures of up to 2.0 GPa. At these pressure the solute contents of fluids in equilibrium with amphibole peridotite were less (up to 5 wt%), possibly because these experiments were performed at lower temperatures than those producing phlogopite. However, Holloway (1971) observed a slight decrease in the solute content with increasing temperature. Claims that fluids at 3.0 GPa are K rich, with solubility of K_2O up to 25 wt% (Ryabchikov & Boettcher, 1981), have been treated with some scepticism (Schneider & Eggler, 1986; Eggler, 1987), although no further experiments have been performed at these pressures.

Table 3.2: Major element compositions of experimentally-produced fluids.

	A	B
SiO_2	63.88	66.5
TiO_2	1.27	3.0
Al_2O_3	13.87	10.2
FeO*	1.22	3.7
MgO	0.13	6.3
CaO	9.53	6.0
Na_2O	3.67	2.9
K2O	3.49	1.5
MnO	2.72	
Cr_2O_3	0.018	
NiO	0.073	

A : H_2O-CO_2 fluid in equilibrium with basalt at 0.8 GPa, 800°C. From Holloway (1971).
B -: H_2O fluid in equilibrium with amphibole peridotite at 1.7 GPa, 900°C. From Schneider & Eggler (1986).

* Total Fe as FeO

Perhaps the most widely quoted trace-element data are those of Tatsumi *et al.* (1986) who performed a set of dehydration experiments at 1.2 GPa, 850°C in which a predoped synthetic serpentine composition was contained in a gold capsule, perforated to allow the fluid phase to escape. The trace-element concentrations in both the starting material and the run product, which consisted of forsterite and enstatite, were determined by mass spectrometry. From this information, the relative mobilities of trace elements were calculated. Percentage mobility (%M) was defined as:

$$M \equiv \frac{R_x^{STM} - R_x^{RP}}{R_x^{STM}} \times 100(\%)$$

R_X^{STM} is the ratio of the element to Nb in the starting material and R_X^{RP} is the same ratio in the run product.

The concentrations were ratioed to Nb as it was found that the Nb concentration in the run product was very similar to that in the starting material, i.e. Nb was extremely immobile in the fluid. Cs and Rb contents in the run products were substantially lower than those in the starting material, and therefore it was deduced that these elements were relatively mobile in the fluid. The results are plotted against ionic radius in Figure 3.6. These results are worthy of comment as they have been used to support many models of IAV petrogenesis (e.g. Woodhead, 1989; Hawkesworth *et al.*, 1991; Francalanci *et al.*, 1993). In particular, these results have been used to argue that the high-LILE signature seen in IAV results from the preferential transport of these elements in slab-derived fluids.

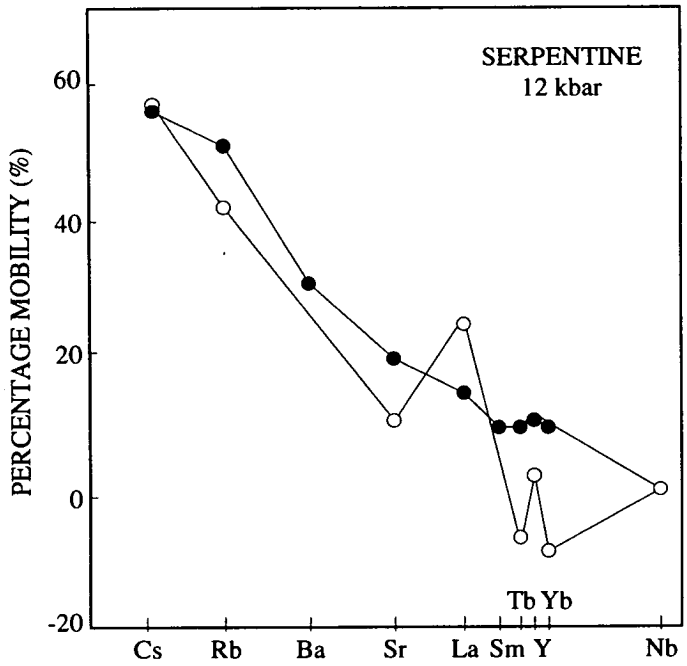

Figure 3.6: Mobility of incompatible elements in the fluid phase released from serpentine: filled circles, unwashed serpentine; open circles, washed serpentine. Ionic radius decreases to the right. From Tatsumi *et al.* (1986).

Close reference to the results shows that there does indeed appear to be a strong relationship between mobility and ionic radius, although this relationship is far less distinct for serpentine that had been washed in acid prior to the experiment to remove loosely bound elements. Some authors (e.g. Hawkesworth *et al.*, 1993a) have used the apparent relationship between mobility (in fluids derived from unwashed starting material) and ionic radius, and have extrapolated this relationship to estimate the mobility of unmeasured elements. However, later work by Tatsumi & Isoyama (1988), although seldom quoted, suggests that this apparent relationship does not

hold for smaller ions. They find that Be, despite its smaller ionic radius, is more mobile than Ti. It should also be noted that these results refer to the mobility of an element in a fluid in equilibrium with orthopyroxene and olivine (the residue left after dehydration of serpentine). As the residual phases in the slab are likely to be garnet, clinopyroxene (plus possible amphibole and some accessory minerals), the mobility of trace elements in a slab-derived fluid may be very different to those shown in Figure 3.6. Therefore it is somewhat dangerous to apply these results to the dehydration of the slab, and even more dangerous to extrapolate the observed relationship seen to predict the mobility of unmeasured elements.

More recently, Brenan & Watson (1991) determined the partition coefficients of several elements between olivine and aqueous fluid at 1.0 GPa and 1000°C. Experimental charges consisted of olivine and a fluid phase and were doped to known composition by radiotracers of Ce, Gd, Yb, Ba, Sr, Cs, and Na. Partition coefficients, calculated by mass balance from the compositions of the starting material and of olivine in the run product, show a rough negative correlation with ionic radius (Fig. 3.7), similar to the results of Tatsumi *et al.* (1986). The extremely low D (olivine/fluid) for sodium is thought to be due to the formation of Na-Al complexes in the fluid.

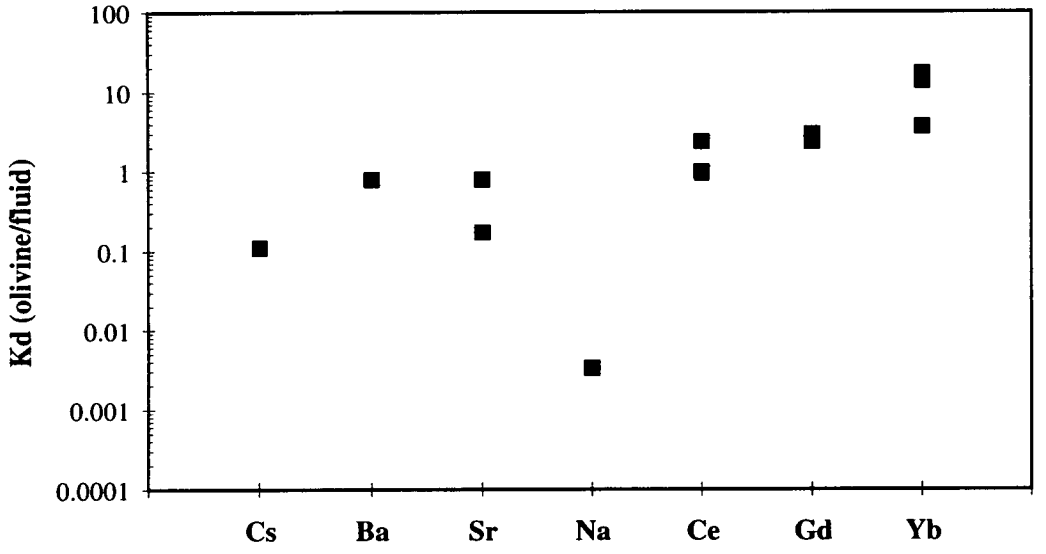

Figure 3.7: Olivine/fluid partitioning coefficients for hydrous fluid. From Brenan & Watson (1991).

Results are similar to those obtained by Cullers *et al.* (1973) who performed experiments at low pressure (< 0.1 GPa), in which water doped with known concentrations of REE and REE tracers was heated with either synthetic forsterite,

diopside or enstatite, or natural plagioclase or basaltic glass. Partition coefficients were derived from the measured concentrations of REE in crystals (or glass) and coexisting solutions. A decrease in the value of D (forsterite/water) was observed with increasing temperature, whereas D (diopside/water) showed the opposite effect. All compiled values of D (olivine/fluid) for the REE are shown in Figure 3.8. There is general agreement that LREE partition slightly more favourable into the fluid than do HREE. The values of D (olivine/fluid) measured by Mysen (1979) are noticeably lower than the others shown, possibly because they were derived from experiments performed at a higher pressure (2.0 GPa). It was claimed by Mysen (1979) that D (mineral/fluid) decreases rapidly with increasing pressure, a conclusion in agreement with the work of Ayers & Watson (1991) who showed that the solubility of monazite (a REE accessory mineral) and rutile increased with increasing pressure.

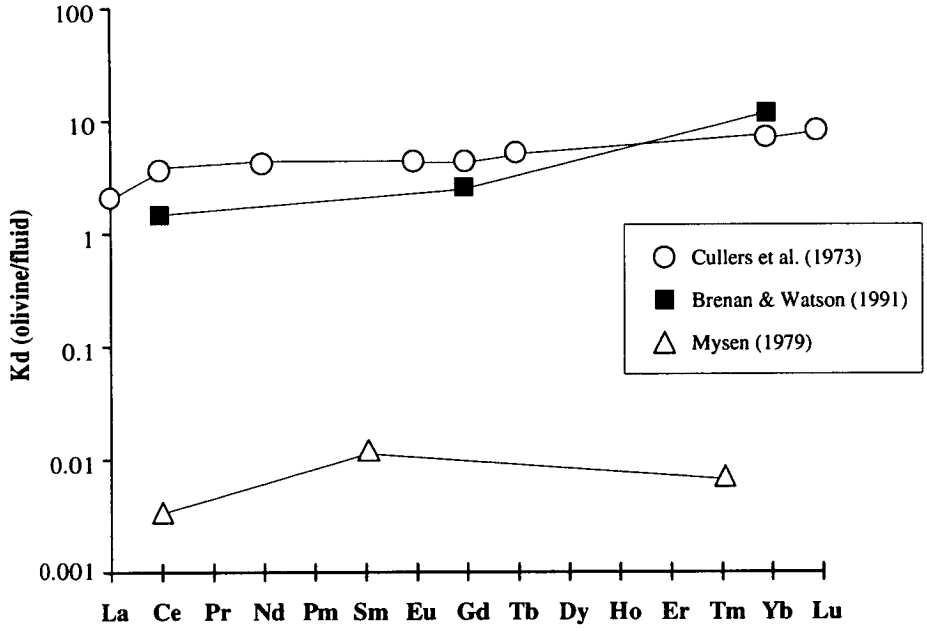

Figure 3.8: Olivine/fluid partitioning data for REE.

All of the results discussed above refer to the mobility of fluid in pure water. Experiments involving other fluid species have also been performed and have often highlighted the importance of the fluid composition in determining the absolute, and to some extent relative, solubility of elements. It is generally agreed that CO_2-rich fluid is less capable of dissolving all elements (with the exception of Ti) than is pure water (Eggler, 1987 *and references therein*; Schneider & Eggler, 1986; Brenan & Watson, 1991). Furthermore, the solute in CO_2-bearing fluids appears to be more alkali rich than that in pure H_2O. This has been attributed to the suppression, by

CO_2, of the SiO_2, or SiO_2-Al_2O_3 complexes prevalent in H_2O fluids (Schneider & Eggler, 1986). When anions such as chloride are introduced, a variety of complexes can form, leading to increased solubility of many elements (Brenan & Watson, 1991).

3.2.2 The present study

Previous studies have shown that fluid composition can significantly affect the solubility of trace elements. The choice of a relevant fluid composition is therefore critical to the accurate determination of partition coefficients between fluid and residual phases in the slab or the mantle wedge. Possible sources of fluid include 1) pore fluids in the subducting sediment or crust, which are likely to be saline due to the incorporation of sea water, 2) fluids derived from dehydration of minerals, and 3) decarbonation of calcareous phases and the decomposition of organic matter to yield CO_2-rich fluid. However, there is little evidence, and consequently much conjecture, concerning the composition of fluids released from the slab at high pressures. The presence of Fl and Cl in some mantle xenolith amphiboles has been taken as indirect evidence that salt-bearing fluids are present within the subcontinental mantle (Brenan & Watson, 1991). In addition, fluid inclusions from high-pressure Alpine eclogites have been reported to contain up to 40 wt% NaCl, suggesting that dissolved salts may be present at depth in the slab (Phillipott & Selverstone, 1991). However, the Alpine eclogites are from old continental crust and are not representative of typical subducting oceanic plate. Metasedimentary and metaigneous rocks from a Cretaceous oceanic subduction zone are preserved in the Catalina Schist, California (e.g. Sorenssen & Grossman, 1989; Bebout & Barton, 1989), and can yield information regarding the composition of fluids released from the subducting slab between depths of 25 km and 45 km. Fluid inclusions from these rocks, coupled with trace-element systematics (e.g. Bebout, 1991; Bebout & Fogel, 1992) suggest that C-O-H-S-N fluid was present, with a mole fraction of H_2O estimated to be greater than 0.98 (Bebout, 1991; Bebout *et al.*, 1993). However, it is unclear whether the fluid involved in the Catalina Schist rocks is an appropriate analogue for fluids released at much higher pressures into the subarc mantle. In the absence of better constraints, I decided to use pure water as an analogue for fluid released from the slab. In the future it may be useful to repeat the experiments with inclusion of dissolved salts and/or CO_2.

The purpose of this part of the project was therefore to determine the partitioning of trace elements into H_2O-rich fluids at high pressures and temperatures. The method used is described in full in Chapter 7. Briefly, experiments were performed in which fluid, melt and mineral phases coexisted at equilibrium. Fluid quench products, which are thought to be representative of the fluid at equilibrium, were analysed for a range of trace elements by SIMS. To derive D (fluid/mineral) it is necessary to determine the trace-element compositions of the coexisting crystals. Unfortunately, for all minerals except olivine, the relatively small crystal sizes (smallest dimension < 40 μm) precluded analysis by SIMS. Instead, coexisting basaltic melt was analysed by SIMS, and D (fluid/melt) was calculated. In Chapter 8, values of D (fluid/melt) derived from this study are combined with published D (mineral/melt) to derived estimates for D (fluid/mineral). The inherent errors and assumptions in this approach are discussed in Section 8.2 (Chapter 8).

As temperature, and particularly pressure, can have a strong effect on the partitioning of trace elements into fluids (Mysen, 1979; Ayers & Watson, 1991), the selection of relevant P, T conditions is extremely important. The region of dehydration of the slab is not well known as it unclear whether fluid is released into the subarc mantle, or whether fluid released at shallower depths hydrates the mantle and is dragged down to subarc depths by forced convection (Tatsumi, 1989). Ideally, experiments should be performed over a range of pressures up to approximately 3.0 GPa. In this project initial experiments were performed at approximately 2.0 GPa, because they were also designed to test the calculated melt composition of a melt produced from an experiment at 1.8 GPa. It had been intended to extend the experiments to higher pressures. However, this was not achieved in the time available and is an important priority for any future work.

The results presented in this thesis (Chapter 7) therefore relate to the partitioning of trace elements between hydrous fluid and basaltic melt at approximately 2.0 GPa.

3.3 CONCLUSIONS

The broad aims of this project were to constrain the behaviour of trace elements during dehydration of the slab, interaction of fluids with the mantle wedge, and melting of the hydrous mantle wedge.

As a starting point, it was decided to perform a set of partial melting experiments of hydrated peridotite with a view to 1) documenting the major-element and trace-element compositions of partial melts, and 2) measuring partition coefficients between amphibole and melt. Similar studies performed by previous workers have established the phase relations of hydrated peridotite. However there has been little agreement on the compositions of partial melts. In this project, it was hoped that the use of a new technique that involved the growth and subsequent analysis of melt inclusions in an *in situ* crystal of olivine, would enable partial melt compositions to be calculated accurately. Experiments were performed using a starting composition of Hawaiian pyrolite - 40% olivine (Green, 1973) at pressures ranging from 1.8 GPa to 2.8 GPa and at temperatures ranging from 966°C to 1150°C in water-oversaturated conditions. The oxygen fugacity was buffered to NNO, which is near the middle of the range of estimates for the fO_2 of the mantle wedge. Melt compositions were tested by reversal (liquidus) experiments. It should be noted that the failure to grow amphibole crystals of a size large enough to enable analysis by SIMS prevented the measurement of partition coefficients between amphibole and melt. Furthermore, many of these experiments were contaminated by boron (Chapter 6) and hence it was not possible to document the trace-element compositions of melts. The results of the uncontaminated partial melting and reversal experiments are presented in Chapter 5.
Prior to this project there were conspicuously few data regarding the partitioning of many trace elements into hydrous fluids. It was therefore decided to measure partition coefficients between fluid and coexisting phases for a wide range of trace elements. Liquidus experiments (at approximately 2.0 GPa and 1000°C) containing basaltic compositions and pure water, produced fluid and melt with and without coexisting mineral phases. Partition coefficients between fluid and basaltic melt were calculated from analyses by SIMS of fluid quench products and quenched melt. Results are presented in Chapter 7.

It is acknowledged that in order to more accurately simulate the conditions operating in a subduction zone it would be useful to extend these experiments to higher pressures. Unfortunately this proved impossible in the time available. For any future work, one priority would be to measure partition coefficients between fluid and melt at 3.0 GPa, and to document the melt compositions at this pressure.

CHAPTER 4

EXPERIMENTAL AND ANALYTICAL TECHNIQUES

CHAPTER 4: EXPERIMENTAL AND ANALYTICAL TECHNIQUES

The core of this project involved the execution of high pressure, high temperature experiments in solid-media apparatus, and the subsequent characterisation and analysis of run products. In this chapter I shall describe the techniques used to perform these experiments and to analyse the run products for major and trace elements. A summary of all experiments is given in Appendix A.

4.1 EXPERIMENTAL RATIONALE

One original experimental objective of this project was to perform a set of partial melting experiments on hydrous peridotite, and to measure the compositions of partial melts and coexisting phases over a range of pressures and temperatures. Of particular interest were the trace-element contents of amphiboles and coexisting melt. Therefore, it was hoped to produce crystals which were large enough to analyse by SIMS. The starting composition chosen for the forward experiments was Hawaiian Pyrolite - 40% (HAW), the phase relations of which have already been documented under water-saturated and water-undersaturated conditions (Green, 1973). Bearing this previous work in mind an initial pressure of 1.8 GPa was chosen to aid the production of coexisting amphibole and melt. In the past, one of the main problems with hydrous partial melting experiments has been the measurement of the melt composition (see Section 3.1.1). Here, we employed the method of Odling (*accepted*), which uses an olivine crystal to trap melt as inclusions (see 5.2.4 for a detailed discussion of this method). Conditions were water oversaturated, and experiments were maintained at an oxygen fugacity of NNO by means of an internal buffer. The cell chosen was ½" talc/boron nitride. Individual phases in all run products were analysed by EPMA. The calculated melt composition from one experiment (performed at 1.8 GPa and 1020°C) was tested by several reversal (liquidus) experiments, in which the estimated melt composition (and variants on this) were equilibrated under similar conditions to the original (forward) experiment. Several reversal experiments were performed using identical capsules and cells to the

forward experiments. One of the aims of these experiments was also to produce large crystals of amphibole. In addition, reversal experiments without using an olivine crystal were performed. In these it was an advantage to run more than one composition at identical conditions. Therefore, three capsules were run in a salt cell. Another objective of this project was to measure partition coefficients between fluid and coexisting phases. The reversal experiments run in salt cells contained trace-element doped starting materials as well as water, and produced melt and fluid with and without other mineral phases. Fluid quench, melt and olivine from these run products were analysed by SIMS, and D (fluid/melt) and D (olivine/fluid) were calculated.
All experiments were performed in solid-media piston-cylinder apparatus (Boyd & England, 1960).

4.2 STARTING MATERIALS

In all experiments the starting material was composed not of natural minerals, but of a synthetic composition in the form of a gel or a sintered oxide. Because the grain size of a gel is approximately ten times smaller[1] than that of a sintered oxide, it is relatively more reactive and more homogeneous. In addition, the gel-making process can produce homogeneous compositions, even for trace elements doped to a few parts per million. It was therefore advantageous to use gels as often as possible. However, the gel-making process is time consuming and it was not possible to make a gel for each new composition required in the reversal experiments. Therefore, for most reversal experiments the starting material was made from sintered oxides. The problem of doping a reversal composition was overcome by making a stock gel (doped with a range of trace elements) to which sintered oxides were added in order to make the required composition. All starting materials were glassed[2] and analysed by electron microprobe to check their compositions.

[1]Examination of a gel using a scanning electron microscope shows that the grain-size is 100 nm (Odling, *pers. comm.*)
[2]Starting materials are melted by passing a current through a platinum wire with which the materials are in contact (Odling, 1994).

4.2.1 Gels

Gels were prepared following the method of Hamilton & Henderson (1968). Constituents were dissolved in nitric acid and the resulting solutions were mixed in the required proportions. SiO_2 was then added as liquid tetraethyl orthosilicate (TEOS), and a gel was precipitated by the addition of concentrated ammonium hydroxide. After drying carefully for several days at increasing temperature, this was ground in a tungsten carbide grinding mill for at least ten minutes and ground further in an agate pestle and mortar.

Table 4.1: Actual and target compositions of gels used in this study.

	Hawaiian Pyrolite - 40%ol		Stock gel		
	mean	target*	mean (9)	s.d.	target**
SiO_2	47.86	48.25	57.10	0.38	55
TiO_2	1.25	1.21			
Al_2O_3	5.95	5.96	17.26	0.25	18
Cr_2O_3	0.49	0.71			
FeO	8.14	8.28	7.10	0.13	7
MgO	29.78	28.97	7.34	0.05	8
CaO	5.23	5.15	11.19	0.07	12
Na_2O	0.94	0.96			
K_2O	0.22	0.22			
MnO	0.09	0.10			
NiO	0.06	0.20			
Mg no.	86.7	86.2	64.8		67.1

* Composition used by Green (1973)
** Rough target composition. Although it was necessary for this gel to be homogeneous, the exact composition was immaterial.
All analyses were performed by EPMA, and have been normalised to 100% total. The total number are shown in parentheses, s.d. denotes standard deviation.

Iron oxide in the gel is thought to be predominantly ferric (3^+), as the gel-making process involves heating in open air. Manganese is also likely to be in a high oxidation state. However, in order to simulate the conditions in the mantle wedge as closely as possible, oxygen fugacity of NNO was required in the experiments (Section 3.1.2). Starting materials were therefore reduced so that the iron was predominantly in the ferrous (2^+) state. Gels were pressed into pellets and fired at 900°C for at least 16 hours in a one atmosphere furnace through which CO_2 and H_2O were passed. The ratio of CO_2 to H_2O was set to 0.65:0.35 which produces and oxygen fugacity roughly equivalent to the iron - wüstite buffer.

Two gels were used in this study. One was of composition HAW, and the other was a stock gel, designed to be used in conjunction with oxides to form the required compositions. The gel-making process can be extremely accurate, and the resulting compositions are homogeneous (Table 4.1).

4.2.2 Sintered oxides

The components used were analytical grade oxides and carbonates. Care had to be taken to keep all constituents dry, especially the hygroscopic carbonates. Using a high-precision balance, oxides of silicon, titanium, aluminium, chromium, magnesium and nickel were weighed out and placed in a clean agate mortar. Iron and manganese were added as Fe_2O_3 and Mn_3O_4 respectively, and the alkalis (calcium, sodium, potassium) were added as carbonates. The mixture was ground under acetone for approximately forty minutes and then dried.

Table 4.2: Actual and target compositions of sintered oxide mixes used in this study.

	ED143M3			ED143W1			ED143M5*			Fo90		
	mean (9)	s.d.	*target*	mean (6)	s.d.	*target*	mean (4)	s.d.	*target*	mean (3)	s.d.	*target*
SiO_2	53.02	1.16	*53.63*	48.77	0.59	*46.82*	51.02	0.71	*53.02*	41.22	0.18	*40.87*
TiO_2	1.38	0.06	*1.33*	1.82	0.08	*1.82*	1.49	0.08	*1.38*	0.02	0.00	*0*
Al_2O_3	22.61	0.70	*22.75*	11.52	0.20	*12.48*	23.13	0.62	*22.61*	0.09	0.00	*0*
Cr_2O_3	0.05	0.02	*0.02*	0.62	0.12	*0.73*	0.07	0.00	*0.05*	0.02	0.00	*0*
FeO	3.81	0.12	*3.53*	6.26	0.37	*6.12*	3.87	0.08	*3.81*	9.60	0.25	*9.77*
MgO	4.07	0.12	*4.35*	18.41	0.15	*20.11*	4.15	0.08	*4.07*	48.92	0.44	*49.36*
CaO	12.15	0.35	*11.73*	10.22	0.12	*9.78*	12.57	0.12	*12.15*	0.01	0.01	*0*
Na_2O	1.94	0.07	*1.78*	1.67	0.02	*1.45*	2.62	0.31	*1.94*	0.05	0.01	*0*
K_2O	0.70	0.03	*0.66*	0.38	0.02	*0.39*	0.73	0.09	*0.7*	0.05	0.01	*0*
MnO	0.17	0.02	*0.13*	0.11	0.01	*0.1*	0.20	0.02	*0.17*	0.01	0.01	*0*
NiO	0.11	0.03	*0.1*	0.21	0.02	*0.19*	0.15	0.02	*0.11*	0.00	0.01	*0*
Mg no.	65.52	0.01	*68.71*	83.98	0.85	*85.42*	65.62	0.39	*65.56*	90.08	0.31	*90.00*

* ED143M5 is a sintered oxide/gel mixture made using the stock gel (Table 4.1).
All analyses were performed by EPMA, and have been normalised to 100% total. The total number are shown in parentheses; s.d. denotes standard deviation.
ED143M3 is the melt composition from ED143; ED143W1 is a composition weighted towards amphibole and melt components; ED143M5 is a sintered oxide/gel mixture using the stock gel; Fo90 is a forsteritic composition. See Appendix B for details of all starting materials used.

In a similar manner to the gels, the resulting powder was made into a pellet and reduced at an fO_2 approximately equivalent to iron - wüstite at 900°C for at least sixteen hours, during which time all CO_2 was driven from the carbonates. The

reduced pellet was ground under acetone and made into a glass for analysis, as before (Odling, 1994). Three sintered oxide compositions, analysed by EPMA, are shown in Table 4.2 with the target compositions for comparison. Also shown is a sintered oxide/gel mixture, made using the stock gel (Table 4.1). Results suggest that the sintered-oxide-making process is reasonably accurate, although less so for the minor oxides such as sodium, potassium or nickel. A fairly high degree of homogeneity is obtained.

4.2.3 Trace-element doping

Homogeneous trace-element doped starting materials were necessary for many experiments in this project. The most efficient method of achieving this was to add acid solutions of trace-element oxides or carbonates to the major-element gel solutions prior to the gel precipitation stage. Because all constituents were added in solution, total mixing could be achieved efficiently.

Table 4.3: Trace element content of ED143M5 (a sintered mixture of the stock gel and oxides).

	representative analyses						average	s.d.	% error
B	6.47	6.71	9.29	7.59	8.02	7.33	**7.6**	1.0	13
Rb	402	451	399	434	380	389	**407**	22	5
Sr	305	292	293	279	279	281	**289**	9	3
Y	114	123	117	110	115	110	**115**	5	4
Zr	210	238	213	209	224	210	**217**	12	5
Nb	91.7	96.3	92.9	86.3	86.5	89.7	**90.6**	3.9	4
Ba	278	202	196	203	194	199	**212**	33	15
La	757	798	810	715	726	744	**758**	38	5
Ce	144	151	152	134	138	138	**143**	7	5
Nd	337	359	364	321	327	335	**341**	17	5
Sm	37.8	38.1	40.5	35.9	36	37.6	**37.7**	1.7	4
Eu	115	119	122	106	107	110	**113**	6	6
Yb	32.8	34	34.9	30.4	29.6	30.8	**32.1**	2.1	7
Hf	138	150	141.3	127	131	137	**137**	8	6
Ta	31.4	32.1	30.6	27.8	29.2	28.4	**29.9**	1.7	6

All values are in ppm, and were derived by SIMS; s.d. denotes standard deviation.

Table 4.3 shows trace-element contents, analysed by SIMS, in a mixture of the stock gel and sintered oxides. The standard deviation from the mean is relatively small i.e. the composition is extremely homogeneous. The stock gel was doped with 22 trace elements. However, in addition to these, the behaviour of Be, Li, Cs, Pb, U, and Th was also of interest. These elements were included in some starting materials in the

form of natural minerals: uraninite (UO_2) and beryl ($Be_3Al_2[Si_6O_{18}]$). Uraninite is radioactive, containing daughter Pb isotopes and presumably some Th. As well as containing 13% BeO, beryl often contains alkalis: Cs_2O can be present at levels of up to a few weight percent, with lesser amounts of Li_2O (Deer *et al.*, 1962). Small quantities of these minerals were ground and added to the sintered oxide/gel reversal composition (ED143M5), which was then reground for at least forty minutes before glassing and analysing. Results show that the new elements appear to have been well distributed (Table 4.4). Unfortunately, the concentration of Th was below the detection limit of the ion probe.

Table 4.4: Concentrations of gel doped with uraninite and beryl.

						average	s.d.
Be	301	314	301	308	327	**310**	11
Cs	9.22	12.59	10.74	10.66	11.2	**11**	1
Pb*	108	227	202	149	206	**178**	49
U	1880	2520	2790	2620	2680	**2498**	359

* The exact amount of lead cannot be determined by SIMS because the isotope ratios in this particular mineral are not known. However the relative variation in measured lead content is accurate.
All values are in ppm; five analyses are shown (performed by SIMS).

4.2.4 Olivine buckets

Olivine buckets were used to contain the starting mix in the majority of experiments. It was desirable to use a relatively pure natural olivine with an appropriately high Mg number. San Carlos olivine was used (see Table 4.5). Clear crystals, free from visible inclusions were selected.

Table 4.5: Composition, determined by EPMA, of San Carlos olivine buckets.

	mean	s.d.		mean	s.d.
SiO_2	40.46	0.19	**Na_2O**	0.02	0.01
TiO_2	0.02	0.02	**K_2O**	0.01	0.01
Al_2O_3	0.03	0.01	**MnO**	0.13	0.02
Cr_2O_3	0.04	0.01	**NiO**	0.38	0.04
FeO	9.10	0.62			
MgO	49.74	0.65	**Total**	100.01	0.41
CaO	0.09	0.02			
			Mg no.	90.64	0.63

s.d. denotes standard deviation.

4.2.5 Source of water

All experiments required the presence of water. Many forward experiments (see Appendix A) contained a hydrated gel of Hawaiian pyrolite - 40% olivine (the gel had been hydrated with 6% H_2O in a gas bomb at 900°C and 0.4 GPa for 5 days, and then ground up and used in these experiments). Other experiments contained free water in the capsule: double deionised and distilled water was added to the bottom of the capsule (one end welded) using a syringe. The amount of water added was checked by weighing.

In later experiments brucite, $Mg(OH)_2$, was added instead of free water. At run pressures, this dehydrates at less than 700°C to produce MgO and H_2O (Meyer & Chi-Sun Yang, 1962). As the brucite was added at the base of the capsule beneath the olivine bucket, the extra MgO did not come into contact with the starting material. For 1 mg of water to be produced, it was necessary to add 3.25 mg of brucite.

4.3 EXPERIMENTS USING OLIVINE BUCKETS

In all forward experiments and many reversal experiments the charge consisted of a 4 mm diameter platinum capsule containing an olivine bucket with a hole drilled into the top, in which the starting material was packed. Underneath this olivine bucket, NiO was included, to buffer the oxygen fugacity during the experiment. A ½" talc/boron nitride cell was used because the relatively high pressures of interest (up to 2.8 GPa) precluded the use of a ¾" cell, and high temperatures prevented the use of salt (perhaps the easiest and cheapest material) as a pressure medium.

4.3.1 Capsules

The geometry of the capsules varied between experiments (see Fig. 4.2), although in all cases capsules contained the starting mix in an olivine bucket, and NiO powder. The olivine bucket was made by coring a cylinder of diameter 3 mm from a single crystal of San Carlos olivine. After grinding this cylinder to a length of 2.5 mm, a hole of diameter 2 mm and depth 2 mm was drilled into one end. During the drilling

process it was necessary to secure the crystal, with beeswax, onto a metal plate. Sharp edges on the bucket were smoothed using a diamond grinding wheel. The bucket was then cleaned in methanol in an ultrasonic bath and inspected for any sign of wax or dirt.

Capsules were made from platinum tubing of 4 mm outer diameter and 0.1 mm thickness[3]. To produce one capsule, a length of tube of approximately 12 mm was used. After annealing, one end of the tube was made into a three-way crimp and arc welded. It was then squashed carefully in a pin press so that the base was almost flat[4].

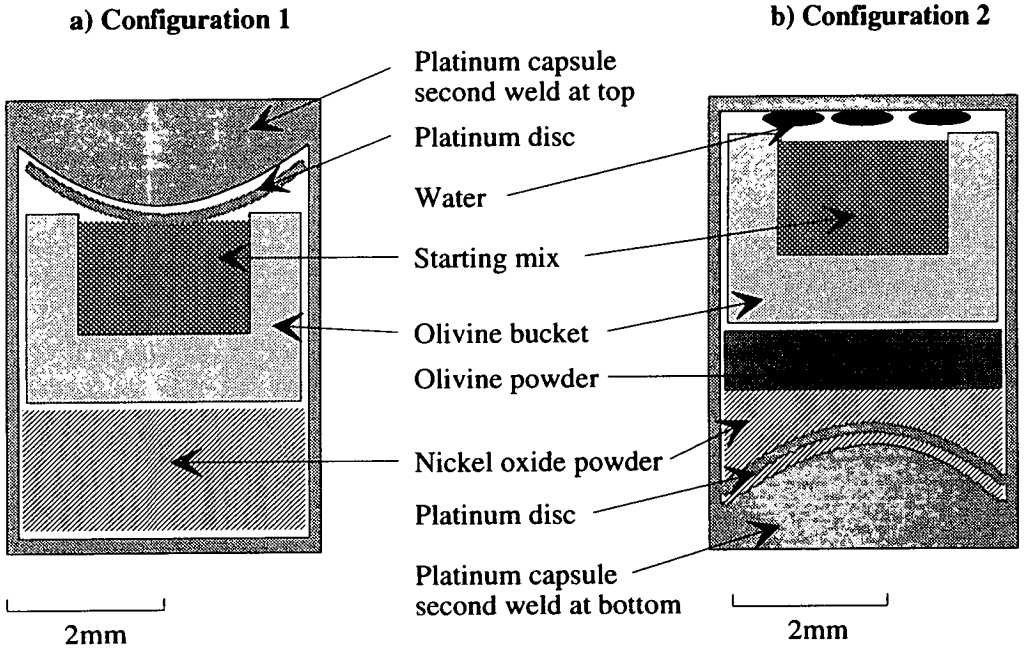

Figure 4.1: Capsule geometry for experiments involving olivine buckets: a) configuration 1; b) configuration 2.

In the initial experiments (configuration 1 in Figure 4.1), capsules were loaded with NiO powder followed by the olivine bucket (previously filled with the starting material). In some cases olivine powder (San Carlos) was added next. A disk of platinum was then inserted. After clearing away any powder, a three-way crimp was made and the capsule was welded. At all stages the weight was recorded. Hence, the capsule could be discarded if any water was lost during the welding process. The capsule was then squashed carefully in a pin press. Although this resulted in a flat end to the capsule, the longer length of the second crimp meant that the platinum was

[3]In experiments ED315, ED339, ED340, capsules were made from thick-walled (0.2 mm) platinum tubing. It was hoped that this would solve the problem of boron contamination (see Chapter 5).
[4]Thick-walled platinum was too strong to be squashed in a pin-press.

thicker at this end. Capsules made from thicker-walled platinum did not undergo this process because of their greater strength.

After concerns about the distance between the thermocouple and the starting mix due to the long second crimp (see Section 4.3.4), I decided to load the capsule so that the larger second weld was at the bottom (configuration 2). In this case the olivine bucket was loaded first, upside down, followed by a layer of olivine powder. This was necessary to ensure that the NiO powder did not fall down the gap between the olivine bucket and the platinum wall, and so contaminate the starting mix.

Welded capsules were tested for holes. If free water was present, the capsule was weighed before and after being left in an oven at 110°C for at least twenty minutes. The capsule was discarded if any weight had been lost. Capsules without free water were left in acetone for at least an hour. Any weight gain was assumed to be due to absorption of acetone through a hole in the capsule, and therefore the capsule was discarded.

Capsules of both configurations were typically 6-7 mm long and contained 10-15 mg of starting material.

4.3.2 Cell

All experiments involving olivine buckets were run using a 1/2" talc/boron nitride cell shown in Figure 4.2. Capsules were burnished with hardened steel to remove any sharp edges, and then slipped into a boron nitride sleeve of 5 mm length. This was placed in a graphite furnace, above a boron nitride spacer. Boron nitride powder was packed into any void space. On top of the capsule was an alumina disc of approximately 0.25 mm thickness, and a pyrophyllite bush. The lengths of all components were such that the middle of the capsule coincided with the centre of the graphite furnace i.e. the predicted hot-spot generated by passing current through the furnace. The furnace was fitted into a boron nitride sleeve which was enclosed by a talc sleeve.

A platinum/platinum-rhodium thermocouple was used, enclosed in a two-bore sheath made from pyrophyllite (early experiments) or mullite (later experiments). The thermocouple was inserted through a hole in the pyrophyllite bush so that it rested on the alumina disk, as close as possible to the top of the capsule.

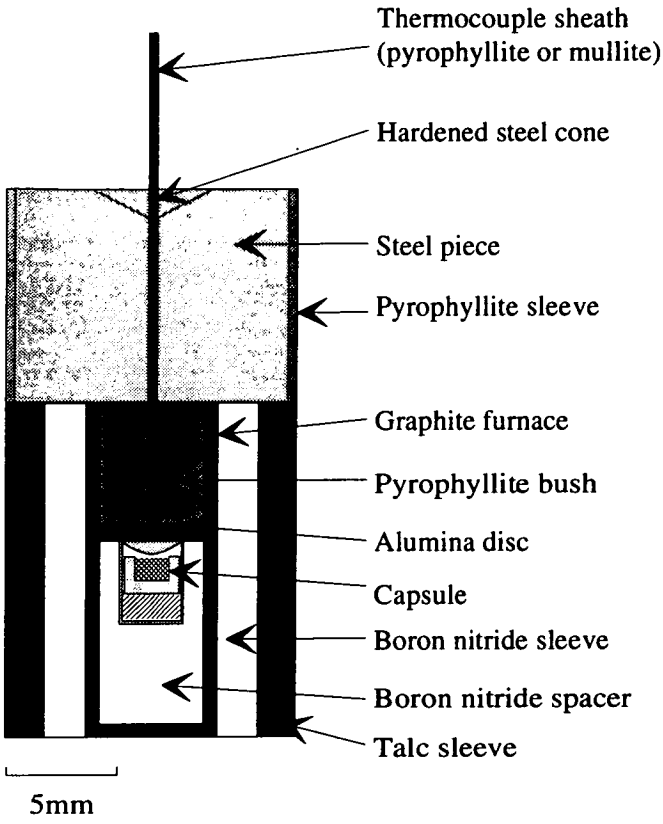

Figure 4.2: A schematic section of the ½" talc/boron nitride cell used in solid-media experiments.

4.3.3 Run up to pressure and temperature

In all experiments the hot piston-in method was employed. Pressure was increased by the hydraulic pumping of a small ram which pushed up a tungsten carbide base piece and piston. Temperature was increased by passing current through the graphite furnace by means of a controller.

After applying a confining force of 150 tons to stabilise the apparatus, the small ram was pumped to 2000 psi (equivalent to 1.0 GPa) and left for at least two hours for the cell to compact before heating began. Temperature and pressure were then increased simultaneously such that the temperature at which the final pressure was reached was approximately 200°C less than the final run temperature. Temperature was then increased and controlled electronically so that it did not exceed its programmed maximum. More power than was necessary was given to the controller in case it was required because of changes to the cell during the run. Experiments were monitored throughout and quenched by turning the power off. The temperature dropped to less that 100°C in a few seconds, with pressure dropping concurrently to a certain point beyond which the oil was bled off very slowly.

4.3.4 Pressure and temperature determination

Applied pressure was measured using an oil-filled Heise gauge. In practise it has been found that some cells do not transmit all of the applied pressure to the charge: frictional drag and inhomogeneity of shear strength can lead to variation in effective pressure across the cell. This effect varies according to the pressure medium used in the cell. Pressure corrections for the talc/boron nitride cell have been calculated by Welch (1987), by comparison of results of experiments conducted over a range of pressures using albite, jadeite and quartz, against the phase diagram determined by Holland (1980). The corrections adopted in this study are based on Welch (1987): the cell requires no pressure correction for experiments at 1.8 GPa and 2.3 GPa; and a -5% correction to runs at the nominal pressure of 2.8 GPa. The errors inherent in the measurement of pressure include uncertainties in this correction, pressure fluctuations, and gauge error. Effective pressures are quoted as ±0.05 GPa of the calculated pressure.

Temperature was calculated from the emf across a $Pt/Pt_{87}Rh_{13}$ thermocouple. One end was against the alumina disc in the cell, and the other was maintained at 0°C in an ice and water mixture. No correction was made for the unquantifiable effect of pressure on emf, which adds a degree of uncertainty. One potential problem with this type of thermocouple is the possibility of poisoning by other metals such as iron. Under reducing conditions such as those present in solid-media apparatus, thermocouple poisoning has been documented at 1200°C (Holloway & Wood, 1984), the consequence of which is a decrease in emf and apparent temperature. I have analysed, by EPMA, thermocouples from these experiments and have detected no iron contamination. Hence I do not think that these runs are long enough or at high enough temperatures for this to be a problem. Therefore, errors in temperature readings are due to the limitations of the voltmeter and the electronic controller. The uncertainty in temperature is ±3°C.

Thermal gradients

In order to subject the capsules to a constant temperature, and to record accurately that temperature by the thermocouple, capsules were positioned in the middle of the graphite furnace, directly underneath a thin (~0.25 mm) alumina disc, underneath the thermocouple bead.

Figure 4.3 shows a typical temperature gradient generated by a graphite furnace in a ½" talc/boron nitride cell (Odling, *pers. comm.*). Although there is some uncertainty in the shape of the thermal profile, and there may be some difference between the

profiles generated by individual furnaces, the data suggest that capsules do experience a thermal gradient, with the buffer section at a lower temperature than that recorded by the thermocouple. This, however, is not thought to be critical. Much more important is any thermal gradient within the starting mixture. It is not clear from the data whether the starting mixture in capsules of configuration 1 is at a constant temperature. However, slight changes in mineralogy and mineral composition with height in these capsules (see Section 5.2.3) led to concerns that there may have been some temperature gradient, and prompted the change to capsule configuration 2, in which the starting material is almost certainly at a constant temperature (Fig. 4.3).

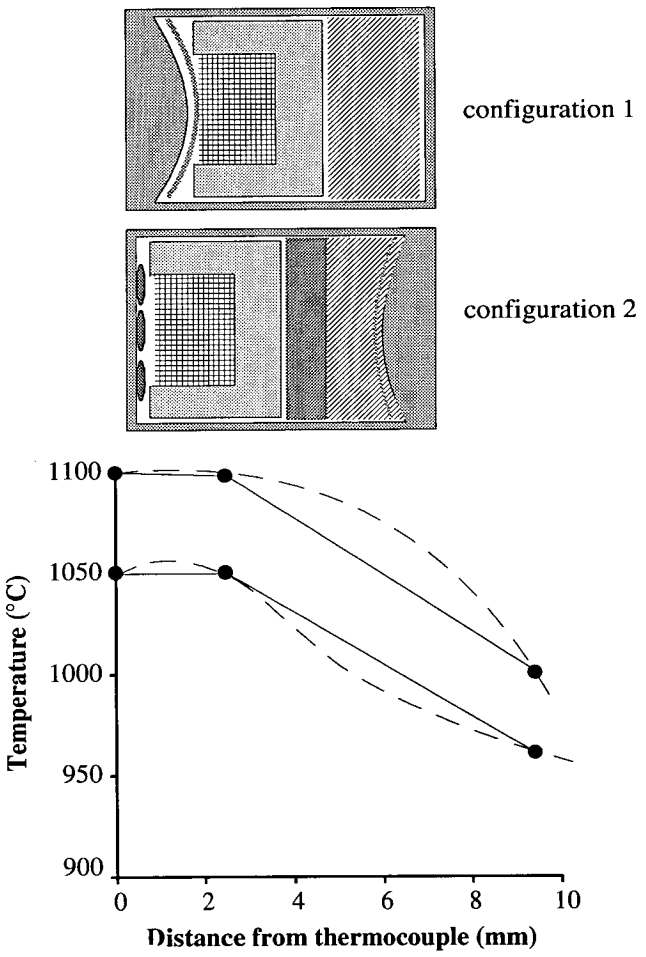

Figure 4.3: Vertical thermal profile of the hot spot generated by the graphite furnace in a ½" talc/boron nitride cell. Data for two nominal temperatures are shown, along with two possible extrapolations. The positions of the components in capsules (configurations 1 and 2) are shown using the same scale.

In conclusion, uncertainties are

Pressure: ±0.05 GPa

Temperature at the top of the capsule: ±3°C

Temperature (including the uncertainties regarding thermal gradients): ±10°C

4.3.5 Oxygen fugacity

The oxygen fugacity is of great importance, as this controls the valence of iron. For water-saturated experiments, it is possible to constrain this by several methods, one of which is to employ a solid buffer. The buffer chosen for these experiments was NNO (see Section 3.1.2). Nickel oxide was included in the capsule although it did not come into contact with the starting material. Hydrogen, which is present in talc, permeates easily through the platinum and reacts with the nickel oxide in the capsule to form nickel and water. Whilst nickel, nickel oxide and water are all present, the oxygen and hydrogen fugacities under constant pressure and temperature are fixed (equations 1, 2 3 and 4).

$$Ni + \tfrac{1}{2}O_2 = NiO \qquad (1)$$

$$k = \frac{a_{NiO}}{a_{NiO} \times fo_2^{1/2}} \qquad (2)$$

$$\Rightarrow fo_2^{1/2} = \frac{1}{k} \qquad (3)$$

$$H_2 + \tfrac{1}{2}O_2 = H_2O \qquad (4)$$

where k is the equilibrium constant for equation 1.

The effectiveness of the buffer relies on the presence of both nickel and nickel oxide throughout the run. Run products were checked after the experiment to ensure that both of these components were still present. In most cases it was found that the nickel oxide had been reduced to nickel in patches near the platinum walls and directly under the olivine bucket (see Plate 4.1). In the experiment shown in Plate 4.1, the initial buffer content[5] was 82 mg. Making a rough estimate based on the area exposed in cross section, there is approximately 10% nickel in the buffer after the experiment. A simple calculation indicates that approximately 2 mg of water was produced from the buffer during the experiment.

[5]The initial buffer consists of analytical grade nickel oxide. X-ray diffraction of this shows that there is a small amount of nickel present.

PLATE 4.1

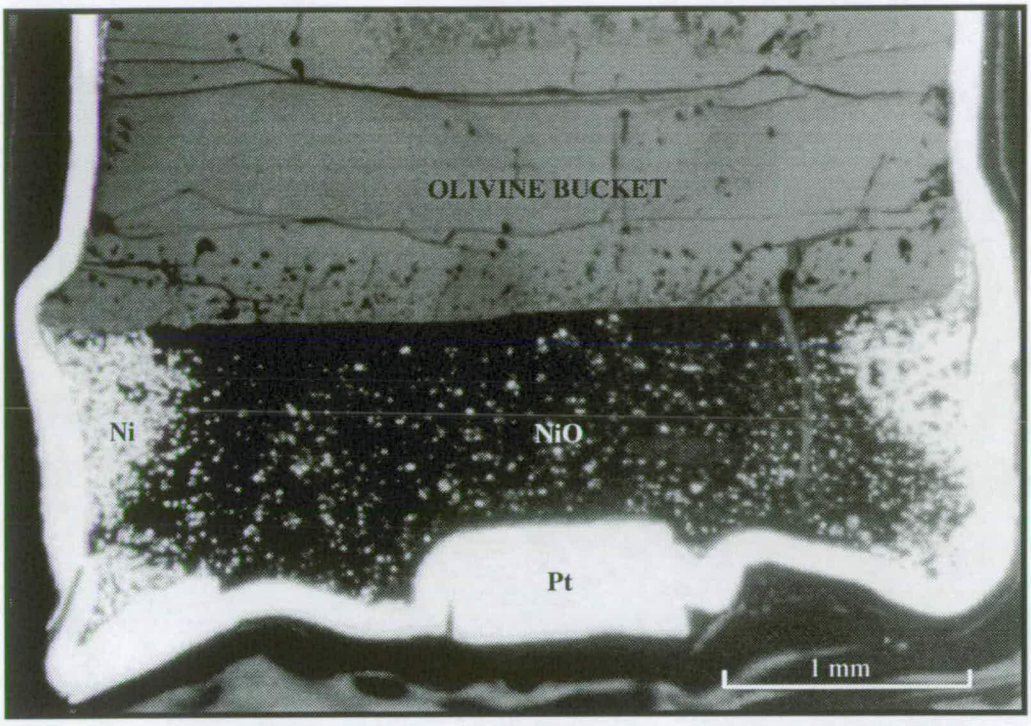

Reflected light photomicrograph showing part of a polished longitudinal cross secion of ED253. The NiO has been reduced to Ni near the walls of the capsule, underneath the olivine bucket.

PLATE 4.2

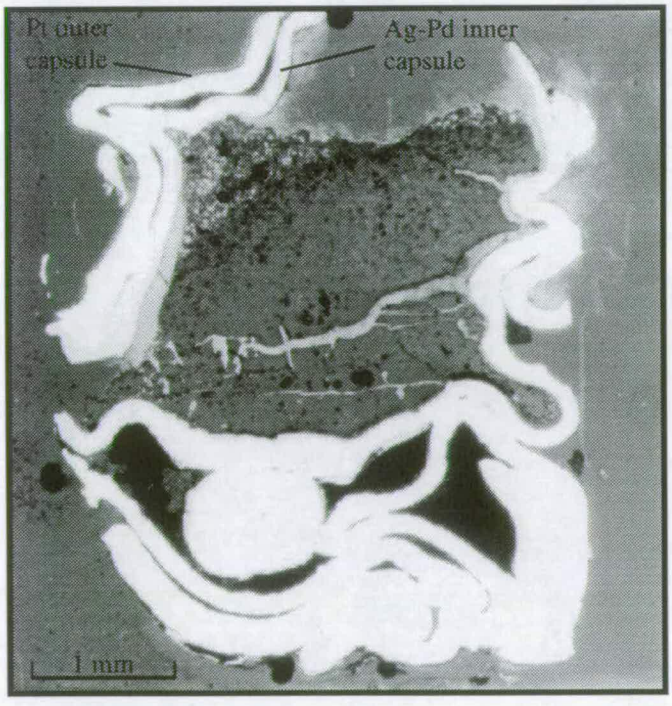

Reflected light photomicrograph of a polished longitudinal section of ED231. The two capsules can be seen, often welded together. The darker material in the middle is the run product.

4.4 REVERSAL EXPERIMENTS IN SALT CELLS

A set of reversal experiments was performed in which a number of different starting materials were equilibrated with water (between 10 wt% to 50 wt% of total). No olivine bucket was required and therefore smaller capsules could be used. Because I wanted to compare the behaviour of different compositions under identical conditions, I opted for a cell in which more than one capsule could be run at a time. The cell chosen was the ¾" salt cell developed by Carrington (1994) which can accommodate three capsules of 2 mm diameter. Experiments were conducted at approximately 1.8-1.9 GPa (near the upper limit for a ¾" cell) and 1020°C (near the melting point of salt at this pressure) and therefore the cell was not robust.

4.4.1 Capsules

Gold was used as a capsule material in preference to platinum. In the forward experiments this had not been possible due to the low melting point of gold. To overcome welding difficulties with capsules containing a large amount of water, the following method was found to be successful. After annealing a 12.5 mm length of gold tubing, one end was made into a straight crimp, welded and squeezed slowly so that it could fit into a hole of 2 mm diameter. After annealing again, water (double deionised and distilled) was added to the bottom of the capsule using a pipette. The mix was then added carefully. After removing any adhering powder from the upper part of the capsule, the top was squeezed shut with pliers and a crimp of approximately 5 mm in length was made. With the crimp secured in a vice, and the bottom of the capsule resting in cold water to inhibit evaporation, the second weld was made quickly. At all points during this process the weight was recorded and the capsule was rejected if any water was lost during the welding. After a successful weld, the long crimp was squeezed longitudinally and folded over so that the length of the capsule was approximately 8 mm. It then required more squeezing before the final capsule was of the necessary shape to fit into the holes in the cell. All capsules were tested for leaks by re-weighing after leaving them in the oven at 110°C for approximately 20 minutes. Finished capsules were approximately 8 mm in length and contained up to 11 mg of mix and 6.7 mg of water.

4.4.2 Cell

This cell (Fig. 4.4) was developed and tested in Edinburgh (Carrington, 1994). The dimensions of the internal components were such that the hot spot generated by the graphite furnace coincided with the centre of capsules of 5 mm length. In these experiments the capsules, which were slightly longer due to the very long second crimp, were inserted top first so that the hot spot coincided with the centre of the starting material.

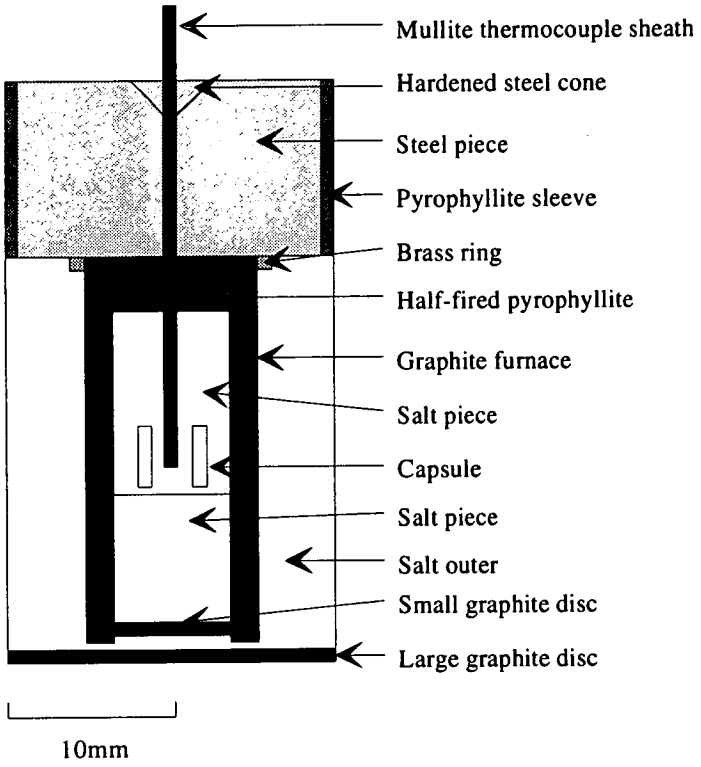

Figure 4.4: Schematic section of the ¾" salt cell used in solid-media experiments

4.4.3 Run up to pressure and temperature.

The salt cell is not very robust and therefore pressure and temperature were increased slowly and carefully. After a confining force of 150 tons was applied to the apparatus, the pressure was increased to 6000 psi (approximately equivalent to 1.0 GPa). This was calculated so that upon heating, the pressure would rise simultaneously with temperature until run conditions were met. After leaving the cell to settle for at least three hours, power was applied. The small ram did not need

to be pumped further, as the temperature rise was sufficient to increase pressure to the required value.

4.4.4 Pressure and temperature determination

No pressure correction is needed for this cell (Carrington, 1994), and therefore any errors in the pressure reading were inherent in the gauge. Temperature was measured by a $Pt/Pt_{87}Rh_{13}$ thermocouple with one end maintained at 0°C. No correction was made for the pressure effect on emf, and no thermocouple poisoning was detected. The vertical and horizontal temperature gradients, although not determined explicitly, are thought to be minimal (Carrington, 1994).

In conclusion, uncertainties are
Pressure: ± 0.05 GPa
Temperature: ± 5°C.

4.4.5 Oxygen fugacity

In an attempt to control the oxygen fugacity by the use of a solid buffer in the first of these experiments, one of the three capsules was filled with NiO and water, and the other two capsules contained the starting material and water. Although it was by no means certain that this method would be successful, in practice it proved impossible because the nickel alloyed with the gold and melted it. An attempt to contain the buffer in a platinum capsule was also unsuccessful for the same reason[6]. Therefore, the experiments remained buffered to the natural oxygen fugacity of the cell. This has been estimated, tentatively, as one to two log units below QFM at pressures up to 1.2 GPa (Carrington, 1994).

[6]It is inferred that the high-pressure melting points of Au-Ni and Au-Pt alloys are lower than Au or Pt, respectively. The capsules used in forward experiments contained Ni in contact with the platinum walls. Somewhat surprisingly, these did not melt, even thought the experiments were performed under similar conditions. The reason for the contrasting behaviour is not clear.

4.5 OTHER EXPERIMENTS

4.5.1 Double capsules

These were designed to trap fluid solute between a perforated inner capsule which contained the starting material, and a sealed outer capsule. In ED231 (Fig. 4.5), the perforated inner capsule contained an olivine disc and HAW. To avoid the use of a powdered starting material which was likely to escape through the perforations in the inner capsule, the powder was pressed into a pellet. The inner capsule and 38 mg of water (double deionised and distilled) were sealed in an outer platinum capsule of 4 mm diameter. Due to the large amount of water, the final weld was made under a stream of argon which had been cooled in a liquid nitrogen/ethanol mixture. This extremely cold gas stream froze the water in the capsule and made it possible to complete the weld before the water could escape. The capsule was run in a ½" talc/boron nitride cell. After the experiment the capsule was retrieved, weighed, pierced and put in an oven at 110°C. Approximately 6.5 mg of water was driven off. Therefore, the experiment had been partially successful in that some water had been retained. However, the original aim was not achieved because the capsules had pressure welded to each other in places and therefore could not be separated (see Plate 4.2).

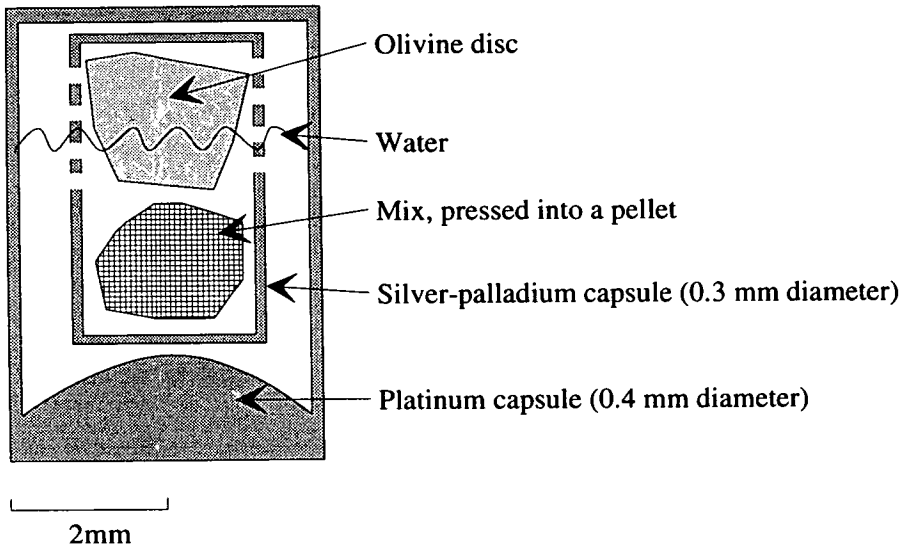

Figure 4.5: A schematic section of the double capsule used in ED231.

ED300 had a similar aim. The starting composition was made into glass beads and put into the inner capsule (gold) which was crimped but not sealed. The inner

capsule was sealed into an outer gold capsule with water, and run in a salt cell. Unfortunately, it lost its water during the run.

4.5.2 "Super capsule"

Ayers *et al.* (1992) reported a new solid-media capsule technique in which the sample is contained in a platinum capsule which fits inside a rigid metal bucket. The capsule is not welded shut. Instead, a lid is placed on top of the capsule. This was found to form a water-tight seal with the capsule walls during cold pressurisation. Upon heating, the metal anneals to form a permanent seal. It is claimed that this technique is particularly useful for experiments which contain a large proportion of water. I attempted to use this technique with a basaltic starting material and a water: rock ratio of 1:1 (Fig. 4.6).

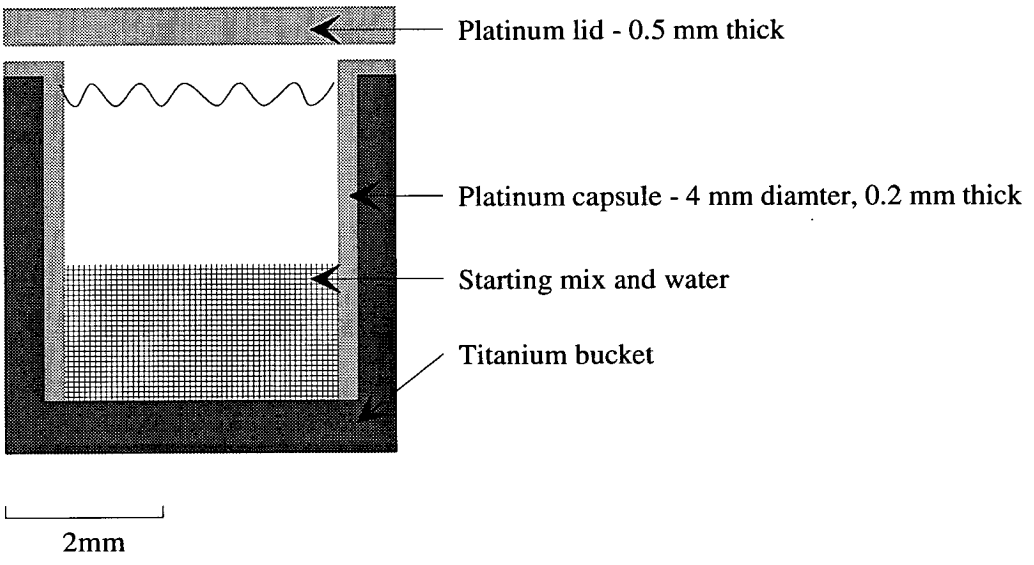

Figure 4.6: Schematic section of the "super capsule" used in ED312 (after Ayers *et al.*, 1992).

The experiment was run using a ½" talc/boron nitride cell which was cold pressurised to 0.5 GPa before increasing pressure and temperature such that the volume of water did not expand significantly at any stage. After the experiment, which was run for three hours, the capsule was retrieved and punctured (with some difficulty). No more than 2 mg of water was left in the capsule: at some point during the experiment the water had escaped from the capsule. Examination of a polished section of the run product revealed that the lid had not alloyed with the sides of the capsule: melt was found between them. However there was some evidence that fluid had been present

at some stage: the run product consisted of melt which contained some crystals, and fluid quench products (see Chapter 7). The fluid quench was in a roughly ellipsoidal void in the middle of the capsule, now filled by epoxy resin used to prepare the capsule for analysis. A crude calculation can indicate how much water would have been present in this cavity at run pressure and temperature: the dimensions of the cavity are approximately 2.5x2.5x1.5 mm i.e. 9.4×10^{-9} m^3. At 1.8 GPa and 1000°C one mole of H_2O occupies approximately 18 cm^3 (Taylor, 1985). Therefore, the cavity was occupied by 9.4 mg of water. There is also some water dissolved in the melt. However this still cannot account for the initial water content of 25 mg. In conclusion, this approach has potential, but time did not allow the technique to be perfected.

4.6 FAILED EXPERIMENTS

In this section I shall discuss those experiments which failed to reach run conditions or to maintain them for the required time. This is distinct from those experiments which failed as a result of contamination of the run products or loss of water from the capsule.

Of all sixty-four solid-media experiments conducted, twelve of them are classed as failures. Table 4.6 summarises the likely causes of all failures. All experiments which failed were run in talc/boron nitride cells.

Two failures (ED106 and ED135) occurred after at least ten hours at run pressure and temperature. They are attributed to surges in power and subsequent breaking of the thermocouple. All other failures occurred during the run up to pressure and temperature and are likely to have been caused by some imperfection in the cell, the thermocouple or the alignment of components. During the course of this project there were three stages at which the failure rate was high: April 1991; June 1991 and May-Oct. 1992.

Table 4.6: Details of experiments which failed.

Experiment	Date	Failure point	Potential causes
ED106	March 1991	after 19 hours	Power surge
ED116	April 1991	2000 psi; 600°C	Thermocouple bead broke
ED117	April 1991	4000 psi; 800°C	Thermocouple bead broke
ED130	June 1991	3000 psi; 900°C	Material forced up thermocouple sheath
ED130B	June 1991	after a few minutes	Material forced up thermocouple sheath
ED135	July 1991	after 10 hours	Power surge
ED227	May 1992	4000 psi; 1020°C	Not properly aligned
ED237	May 1992	2000 psi; 150°C	Thermocouple wire sheared
ED243	June 1992	2000 psi	Thermocouple wire sheared
ED255	July 1992	2000 psi; 150°C	Thermocouple wire sheared
ED276	Oct. 1992	2000 psi; 50°C	Thermocouple wire sheared
ED277	Oct. 1992	2000 psi	Thermocouple wire sheared

In April 1991 two experiments (ED116 and ED117) failed due to the thermocouple bead shearing and a thermocouple leg breaking respectively, probably due to too much void space in the cell. Afterwards I ensured that all void space was packed with boron nitride powder.

In June 1991, ED130 failed whilst pumping. Examination of the cell showed that powdered material from the cell components had been forced up one of the holes in the thermocouple sheath and had broken the platinum wire. The purpose of the pyrophyllite bush surrounding the thermocouple (Fig. 4.2) is to grip the thermocouple wires at pressure, and so prevent movement. It appeared as though this had not been achieved, and that the material had been too soft. A pyrophyllite bush, similar to the one used in ED130, which was the first experiment to fail in the manner described, was examined by XRD and found to contain talc and silica, i.e. not pyrophyllite. In order to harden the material, a bush was fired at 850°C for several hours prior to use in the following experiment. The thermocouple wire was also changed from 0.2 mm diameter to 0.3 mm diameter. However, this experiment also failed due to material being forced up the holes in the thermocouple sheath. The pyrophyllite bushes were therefore fired at a higher temperature (1100°C) for six hours, after which they contained some glassy material (detected by XRD). ED132 employed a fired, glassy bush. The experiment was successful. Using these fired pyrophyllite bushes and mullite thermocouple sleeves (to prevent the slight thermocouple extrusion that was evident in some early experiments), most experiments between June 1991 and May 1992 were successful.

From May until October 1992 five out of seventeen experiments failed. In all cases the platinum leg of the thermocouple had sheared at some point near the top of pyrophyllite bush. This group of failures coincided with the use of a new batch of

pyrophyllite bushes, in which it was found that the axial hole was sometimes slightly misaligned. No further failures occurred subsequently.
In summary, the majority of runs which failed were as a result of using pyrophyllite bushes which were either too soft (hence the material flowed up the holes in the thermocouple sheath and broke the thermocouple wire) or asymmetrical (and hence there was a shear component exerted during pressurisation which broke the thermocouple wire). From this account, it can be seen that the success of the equipment is extremely dependent on the use of materials with the correct properties, and the accuracy of machining.

4.7 PROCEDURE FOR THE EXAMINATION OF RUN PRODUCTS

4.7.1 Test for capsule failure

Capsules were retrieved carefully from the cell, either by removing adhering material with a scalpel, or by dissolving the salt in warm water. The cleaned capsule was examined optically for signs of holes, and then weighed.
A capsule from a salt cell was judged to have failed if it had lost weight during a run. In principle, the same could be true of a capsule from a talc/boron nitride cell, although in practice it was impossible to remove all adhering boron nitride or alumina and so the weight loss (if any) during an experiment could not easily be determined. Instead, these capsules were judged to have succeeded if there was free water present in the capsule after the experiment. This was determined by a loss of weight after piercing the capsule and leaving it in an oven at 110°C for approximately half an hour. Prior to piercing, capsules were frozen in liquid nitrogen to prevent explosive loss of volatiles.

4.7.2 Mounting, sectioning and polishing

The majority of capsules from talc/boron nitride cells were placed in a plastic tube (of diameter and length slightly greater than the capsule) which was then filled with epoxy resin. As the capsules had previously been pierced, the epoxy resin impregnated the run product. After this had set, the plastic was removed and the

epoxy resin block containing the capsule was sectioned longitudinally using a diamond saw. Each section was mounted in epoxy resin and ground down on a series of carborundum papers. The samples were then polished using alumina paste (early experiments) or diamond (the majority of experiments, including all samples analysed by SIMS).

Capsules from salt cells were smaller and were therefore not cut with a saw. Instead they were impregnated with epoxy resin; mounted in epoxy resin; and ground and polished as above.

4.8 ANALYSIS BY ELECTRON MICROPROBE

Major-element analyses of run products were made by electron probe microanalysis (EPMA) using a Cameca Camebax microprobe in the Department of Geology and Geophysics, University of Edinburgh. Samples were coated by a thin layer of carbon prior to analysis to prevent charge build up.

A back-scattered electron imaging system is incorporated into the instrument and was useful for positioning the sample. When used in conjunction with the energy dispersive system, rapid identification of phases could be achieved. Quantitative analyses were made using four wavelength dispersive spectrometers. Generally, elements were counted for 30 seconds and background was counted for 15 seconds. Count rates for the unknowns were compared to count rates for a set of standards and corrected for matrix effects using the PAP correction, before being converted to oxide contents. Table 4.7 gives a summary of crystal type and standards for each element analysed. See Reed (1993) for a detailed description of EPMA.

Beam conditions were chosen for optimum accuracy and precision without increasing the excitation volume beyond a reasonable size. An accelerating potential of 20 kV was used for all analyses, with the beam current at 20 nA for most crystalline phases. This yielded a beam size of 1-2 μm diameter. Due to problems of alkali mobilization the beam current was lowered to 5 nA for the analysis of glasses (Section 4.8.2). This produced a beam of less than 1 μm in diameter, which was also used to analyse particularly small crystals such as some spinels.

Table 4.7: Analysis by electron microprobe - details of crystal, spectrometer and standard used for each element.

Element	Spectrometer	Crystal	Standard
Na	1	TAP	jadeite
Mg	1	TAP	periclase
Al	2	TAP	corundum
Si	2	TAP	wollastonite
K	3	PET	orthoclase
Ca	3	PET	wollastonite
Ti	3	PET	rutile
Cr	3	PET	chromium metal
Mn	4	LIF	manganese metal
Fe	4	LIF	iron metal
Ni	4	LIF	nickel metal

TAP is thallium acid phthalate, PET is penta erythritol; LIF is lithium fluoride.

4.8.1 Errors

The detection limit (D.L.) and percentage error in precision (E) (see Norrish & Chappell, 1977) are given by:

$$D.L. = \frac{3}{M}\sqrt{\frac{R_B}{T_B}} \qquad E = \frac{100}{\sqrt{T}\left(\sqrt{R_P} - \sqrt{R_B}\right)}$$

where, for any one element,

R_P is the peak count-rate,

R_B is the background count-rate,

T is the peak counting time,

T_B is the background counting time,

M is counts/second/% element in the standard.

In Table 4.8 the detection limit and percentage error in precision are shown for representative analyses of all crystalline phases. With very few exceptions (such as K_2O in clinopyroxene, garnet and ilmenite), the measured oxide content in crystalline phases exceeds the detection limits. The error in precision can be very large e.g. a 72% error on the Na_2O content in olivine; a 66% error on the NiO content in garnet. However, the absolute abundances of these oxides are extremely small. For oxides present in quantities greater than 0.5% the error on the precision is seldom greater than 10%, and is frequently less. Absolute errors rarely exceed 0.1 wt% for each oxide.

	Olivine			Olivine bucket			Orthopyroxene			Clinopyroxene		
	oxides	D.L.	E (%)	oxides	D.L.	E (%)	oxides	D.L.	E (%)	oxides	D.L.	E (%)
SiO_2	39.71	0.00	0.5	40.62	0.00	0.2	52.50	0.00	0.2	51.66	0.00	0.2
TiO_2	0.08	0.00	28.6	0.02	0.00	40.3	0.40	0.00	3.2	0.70	0.00	2.2
Al_2O_3	0.05	0.00	60.6	0.04	0.00	23.0	5.01	0.00	0.6	4.15	0.00	0.5
Cr_2O_3	0.07	0.00	32.8	0.04	0.01	24.9	0.74	0.01	2.1	0.81	0.01	2.0
FeO	11.59	0.01	1.3	8.47	0.01	0.7	8.44	0.01	0.7	3.57	0.01	1.1
MgO	47.43	0.00	0.4	49.81	0.00	0.2	31.18	0.00	0.2	16.33	0.00	0.3
CaO	0.13	0.00	14.4	0.08	0.01	10.2	1.12	0.01	1.4	21.54	0.01	0.3
Na_2O	0.03	0.00	71.9	0.03	0.01	31.7	0.13	0.01	9.4	0.50	0.01	3.6
K_2O	0.00	0.00	-80.8	0.01	0.01	69.8	0.01	0.01	51.4	0.00	0.01	896.4
MnO	0.08	0.00	46.4	0.12	0.01	13.0	0.09	0.01	15.8	0.06	0.01	25.5
NiO	0.47	0.01	10.1	0.35	0.02	5.5	0.17	0.02	9.7	0.09	0.02	17.4
Total	99.65			99.58			99.79			99.40		

	Garnet			Amphibole			Spinel			Ilmenite		
	oxides	D.L.	E (%)	oxides	D.L.	E (%)	oxides	D.L.	E (%)	oxides	D.L.	E (%)
SiO_2	42.18	0.00	0.2	43.51	0.01	0.4	0.19	0.00	6.7	0.48	0.01	7.5
TiO_2	0.84	0.00	1.9	2.18	0.01	2.3	0.64	0.00	2.2	55.64	0.01	0.4
Al_2O_3	22.88	0.00	0.3	12.78	0.01	0.8	23.87	0.00	0.3	0.59	0.01	6.7
Cr_2O_3	0.63	0.01	2.4	0.43	0.01	7.4	46.83	0.01	0.2	0.43	0.02	7.9
FeO	7.03	0.01	0.8	5.24	0.03	2.1	10.56	0.02	0.6	27.96	0.04	0.8
MgO	21.18	0.00	0.3	17.93	0.01	0.7	17.07	0.00	0.4	12.77	0.01	1.0
CaO	4.37	0.01	0.6	10.86	0.02	0.9	0.07	0.01	12.0	0.41	0.02	6.1
Na_2O	0.02	0.01	47.7	2.35	0.02	3.0	0.01	0.01	150.0	0.08	0.02	46.4
K_2O	0.00	0.01	157.7	0.58	0.02	5.2	0.01	0.01	56.6	0.01	0.03	243.3
MnO	0.22	0.01	7.8	0.07	0.01	47.5	0.20	0.01	9.0	0.26	0.02	16.8
NiO	0.02	0.02	66.1	0.16	0.03	23.6	0.12	0.02	15.4	0.42	0.04	11.7
Total	99.37			96.09			99.56			99.05		

Table 4.8: Representative analyses by EPMA of crystalline phases: oxide content, detection limit (D.L.), and percentage error in precision (E).

4.8.2 Analysis of glasses

Analysis of glass materials by EPMA is often of poor precision due to the mobilization of alkalis (sodium in particular) out of the excitation volume during analysis (Hunt & Hill, 1993). This effect is enhanced by the presence of water in a glass. In this project, EPMA was used to determine the compositions of starting materials which had been melted in a heated stage and mounted as anhydrous glass beads. Quenched hydrous melt inclusions and melt pools were also analysed by EPMA as were small glass spheres interpreted to be fluid quench products.
For all types of glass, count rates under different beam conditions were monitored over time, and the effects of beam current and raster size were investigated.

Anhydrous glass beads
Count rates were monitored over a time interval of 450 seconds (Fig. 4.7). At 20 nA a focused beam caused the sodium count rate to drop exponentially from 300 counts/second to 110 counts/second. However, no significant sodium loss was produced by rastering over an area of 5x5 μm with the same beam current.

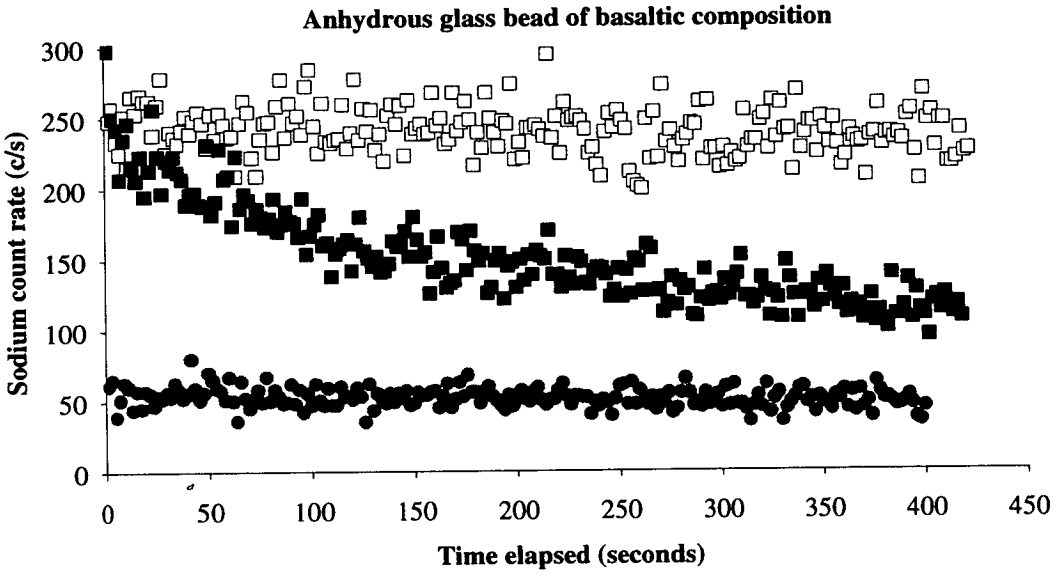

Figure 4.7: Sodium count rate from an anhydrous glass analysed using a beam current of 20 nA, focused (solid squares), rastered over an area of 5x5 μm (open squares), or using a beam current of 5 nA rastered over an area of 5x5 μm (circles).

Hydrous melt

Glass inclusions and pools derived from partial melts of hydrous peridotite were analysed over time under different beam conditions. The drop off in sodium count rates was minimised, although certainly not eradicated, by use of a beam current of 5 nA and a raster of 10x10 μm. Higher beam currents and/or smaller raster sizes produced significant sodium depletions in the resultant analysis (Fig. 4.8). Repeated analyses of the same melt inclusion resulted in a decrease in measured Na_2O and K_2O, and a consequent increase in measured SiO_2 content (see Table 4.9). Therefore, melt inclusions were analysed only once.

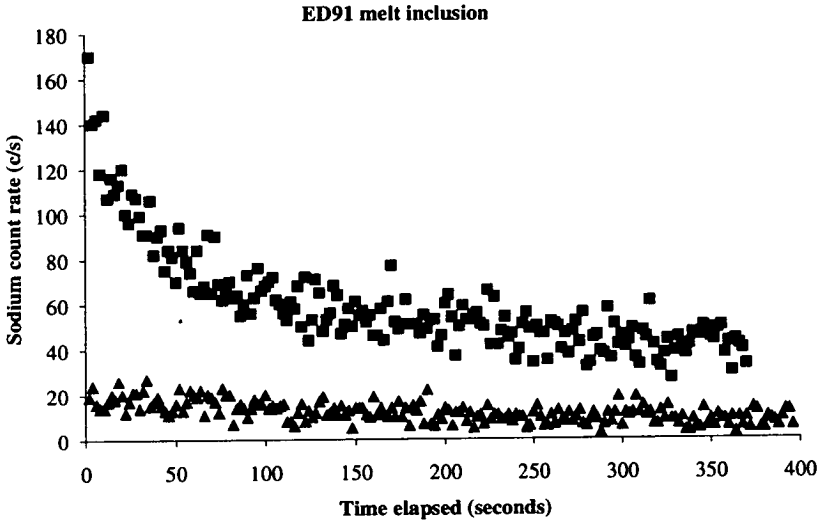

Figure 4.8: Sodium count rate from a melt inclusion in ED91 analysed using a beam rastered over an area of 5x5 μm of current 20 nA (squares) or 5 nA (triangles).

Table 4.9: One melt inclusion from ED137, analysed successively.

SiO_2	40.04	42.14	42.69	46.39
TiO_2	1.31	1.33	1.32	1.27
Al_2O_3	3.83	3.29	3.35	3.48
Cr_2O_3	0.04	0.03	0.03	0.01
FeO	3.50	3.53	3.51	3.37
MgO	20.67	20.46	20.84	22.58
CaO	9.29	9.81	9.87	10.39
Na_2O	1.62	0.52	0.30	0.17
K_2O	0.98	0.97	0.86	0.58
MnO	0.03	0.09	0.09	0.10
NiO	0.15	0.08	0.12	0.09
TOTAL	81.46	82.24	82.97	88.42

Note that the measured Na_2O and K_2O contents decrease, whereas the measured SiO_2 and CaO contents increase in successive analyses.

Fluid quench products

Small glass spheres quenched from the fluid phases were prone to major alkali loss even when beam currents were low (Fig. 4.9). Lowering the beam current below 5 nA was not practicable, because this yielded analyses of poor precision. Alkali loss was minimised by rastering the beam over a 6x6 μm area (Fig. 4.10). Count times for sodium and potassium were also reduced to 10 seconds for some analyses. Although this reduced alkali loss to a minimum, some drop in count rates with time remains.

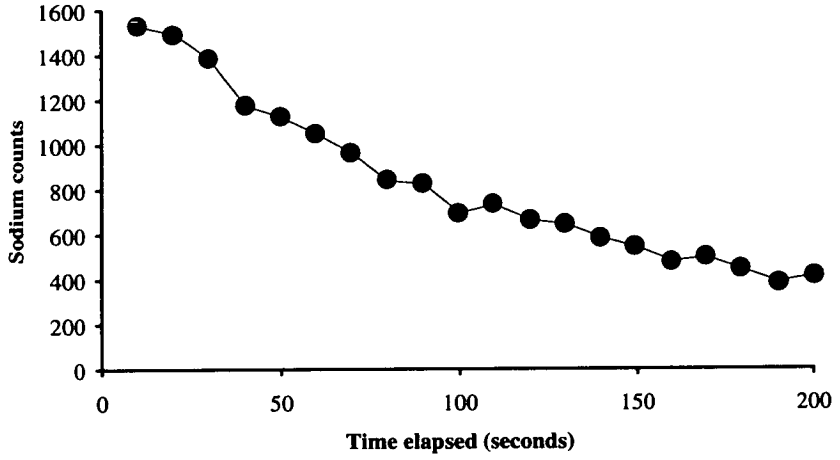

Figure 4.9: Sodium counts from a glass sphere, interpreted to be a fluid quench product. The beam (5 nA) was rastered over an area of 5x5 μm.

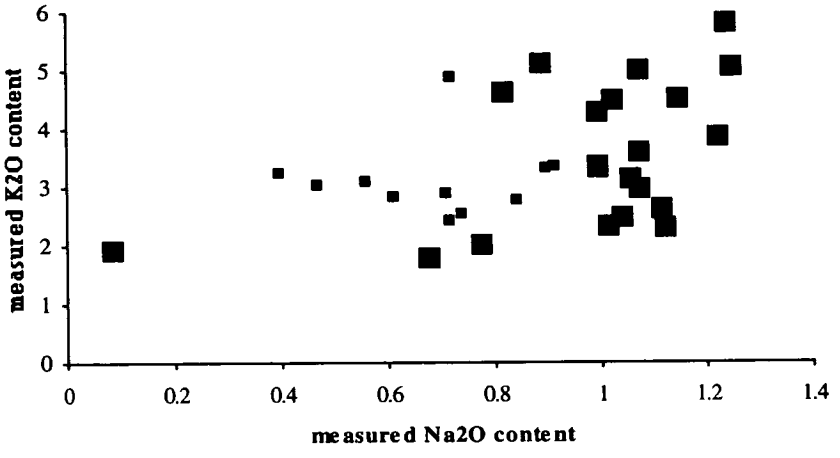

Figure 4.10: Alkali contents in fluid quench products from ED234, measured using a beam current of 5 nA. The beam was rastered over an area of 4x4 μm (small squares) or 6x6 μm (large squares).

In summary, mobilization of alkali elements out of the excitation volume during analysis, and consequent underestimation of the concentrations of these elements, can be minimised by use of a rastered beam of low current, coupled with low count times for Na and K. A decrease in beam current and increase in beam size will, however, produce analyses of lower precision (Table 4.10). Beam conditions were therefore chosen to strike a balance between alkali loss and good precision. Anhydrous glass beads of starting materials did not suffer particularly from alkali loss, and were analysed using a beam current of 20 nA and a raster of 5x5 μm. Sodium mobilization was more marked in hydrous glasses, which were therefore analysed using low beam currents (approximately 5 nA) and raster areas of up to 10x10 μm. Unfortunately these conditions did not prevent some loss of sodium during analysis of glass spheres quenched from the fluid. Hence, measured sodium contents in fluid quench products should be treated with caution.

Table 4.10: Melt inclusion from ED137, analysed with two different beam currents.

Melt inclusion		*5 nA*			*20 nA*	
	oxides	*D.L. (wt%)*	*E (%)*	*oxides*	*D.L. (wt%)*	*E (%)*
SiO_2	40.04	0.01	0.5	42.14	0.00	0.2
TiO_2	1.31	0.01	3.2	1.34	0.00	1.5
Al_2O_3	20.66	0.01	0.6	20.46	0.00	0.3
Cr_2O_3	0.04	0.01	53.1	0.03	0.01	38.6
FeO	3.50	0.03	2.7	3.53	0.01	1.3
MgO	3.83	0.01	1.7	3.29	0.00	0.9
CaO	9.29	0.02	1.0	9.81	0.01	0.4
Na_2O	1.62	0.03	3.9	0.52	0.01	3.8
K_2O	0.98	0.02	3.6	0.97	0.01	1.7
MnO	0.03	0.01	95.4	0.09	0.01	18.8
NiO	0.15	0.04	25.9	0.08	0.02	21.8
Total	81.46			82.24		

D.L. denotes detection limit; E denoted error on the precision. Note that the higher beam current gives a more accurate analysis with a lower measured Na_2O content.

4.9 ANALYSIS BY SECONDARY ION MASS SPECTROMETRY (SIMS)

Trace-element contents in run products were measured using a Cameca ims 4f ion microprobe[7] in the Department of Geology and Geophysics, University of Edinburgh. Analyses are performed by bombarding the sample with a primary beam of O^- ions which has been focused by a series of apertures and lenses. Secondary ions, sputtered from the surface of the specimen, are accelerated onto the entrance slit of a mass spectrometer. By varying the strength of the magnetic field, ions of specific mass/charge ratios can be selected, and counted using an electron multiplier. A primary beam current of 8 nA was selected to strike a satisfactory balance between a small beam size and a large ion yield from the sample. The beam spot was typically less than 25 μm in diameter.

One isotope was measured for each element required. This was usually the most abundant isotope, although it was sometimes an advantage to choose less abundant isotopes to minimise mass interferences. A maximum of 26 masses were recorded in any one analysis. During analysis, the magnetic field was changed to pre-set positions in order to record counts from the required masses. At each position, high energy ions[8] were recorded for five seconds. The magnetic field cycled through all masses a total of ten times. A drop or rise in the counts from any one element relative to another with successive cycles suggested that the sample was heterogeneous, and the analysis should not be used.

Raw data were converted into deadtime-corrected, background-corrected counts per second. These were then corrected for isotopic abundance and mass interference.

4.9.1 Mass interference

The sputtering process produces molecular species as well as atomic ions. In some cases it is impossible to distinguish between the mass of a molecular species and an atomic ion of another element. Although the selection of high energy ions minimises this problem[9], it is still necessary to perform some corrections. For the elements used in this study, the main interferences are listed overleaf (Table 4.11).

---

[7]The fore-runner to this instrument (the ims 3f) is described by Slodzian (1980).

[8]High energy ions at a nominal offset of 75 eV were selected. The energy window was ±19 eV. See Zinner & Crozaz (1986).

[9]Molecular ions tend to disassociate if ejected at high energies, whereas atomic ions possess a tail extending to relatively high energies (Reed, 1989).

Table 4.11: Mass interferences for isotopes measured.

Isotope measured	Interferences	Isotope measured	Interferences
^{85}Rb	$^{57}Fe^{28}Si$; $^{56}Fe^{29}Si$	^{165}Ho	$^{149}Sm^{16}O$ (13)
^{93}Nb	$^{92}Zr^{1}H$	^{167}Er	$^{151}Eu^{16}O$ (47)
^{153}Eu	$^{137}Ba^{16}O$ (11)	^{169}Tm	$^{153}Eu^{16}O$ (52)
^{157}Gd	$^{141}Pr^{16}O$ (100)	^{172}Yb	$^{156}Gd^{16}O$ (20)
^{158}Tb	$^{142}Ce^{16}O$ (11)	^{175}Lu	$^{159}Tb^{16}O$ (100)
	$^{142}Nd^{16}O$ (27)	^{179}Hf	$^{163}Dy^{16}O$ (24)
^{161}Dy	$^{145}Nd^{16}O$ (8)	^{181}Ta	$^{165}Ho^{16}O$ (100)

The number in parentheses is the percentage abundance of the isotope of the cation in the oxide.

Rare earth element data were corrected by assuming a ratio of atomic/oxide ion yield for each element concerned. The ratios (Table 4.12) were derived from analyses of standard NBS-610. The interference of an FeSi molecule with ^{85}Rb was corrected for by measuring the count rate for mass 84 (predominantly $^{56}Fe^{28}Si$). Similarly, the count rate at mass 95 (predominantly $^{94}Zr^{1}H$) was used to correct for $^{92}Zr^{1}H$ interference on ^{93}Nb. Background was monitored at a nominal mass of 130.

Table 4.12: Ratios of the yield of atomic ions to oxide ions for Ba and REE.

Oxide	Element:oxide ratio	Oxide	Element:oxide ratio
BaO	0.062	**TbO**	0.107
LaO	0.176	**DyO**	0.078
CeO	0.21	**HoO**	0.0758
PrO	0.158	**ErO**	0.075
NdO	0.12	**TmO**	0.06
SmO	0.0653	**YbO**	0.0564
EuO	0.0548	**LuO**	0.0623
GdO	0.108		

Derived from standard NBS-610.

4.9.2 Derivation of concentration

The ion yields vary with operating conditions, and therefore, a standard was read twice at the beginning of each day. Relative ion yields (RIY) for each element, x, were calculated:

$$RIYx = \frac{\left(cps/conc\right)_{x}^{std}}{\left(cps/conc\right)_{ref}^{std}}$$

where cps is corrected counts per second, ref is the reference element, usually silicon. The standard used was a silicate glass (NBS-610).

To calculate the concentration of x in the sample, the silicon content in the sample must be known. This can be determined by electron microprobe. Assuming that the relative ion yield for each element is identical in the standard and the sample, the concentration of element, x, in the sample is:

$$[x] = \frac{cps_x \times [Si]}{cps_{Si} \times RIY_x}$$

4.9.3 Errors

The calculations above rely on the assumption that relative ion yields are identical for standard and sample. In this project the phases analysed consist of glass approximating to a basaltic composition, silicate glass quenched from the fluid (SiO_2 contents from 55% to 65%), glassed starting materials, and olivine crystals (Table 4.13). The standard used is a glass (NBS-610: major element composition shown in Table 4.13).

It has been shown (Bottazzi *et al.*, 1991) that ion yields from crystals and their glassed equivalents are the same within error, suggesting that any difference in ion yields between the samples and the standard in this study will be due to the difference in composition. Fortunately, this matrix effect is minimised by the selection of high energy ions (Reed, 1989) and is likely to be eclipsed by counting errors which are thought to be the most significant area of uncertainty.

Table 4.13: Major-element compositions of the phases to be analysed by SIMS in this study, compared with the standard (NBS-610).

	melt	fluid quench	fluid quench	olivine	NBS-610
SiO_2	45.7	60.3	53.5	40.7	70.0
TiO_2	1.2	0.5	0.9	0.1	
Al_2O_3	18.8	16.9	18.5	0.1	2.0
FeO	1.8	0.6	1.6	8.4	
MgO	2.9	0.8	2.3	50.1	
CaO	10.6	2.9	6.3	0.3	11.7
Na_2O	1.2	1.9	2.0	0.0	13.6
K_2O	0.5	2.2	1.6	0.0	
TOTAL	82.7	85.9	86.7	99.6	97.3

Compositions were determined by EPMA. Note that standard NBS-610 also includes approximately 500 ppm of many other elements.

In Figure 4.11, percentage counting errors are shown for all elements analysed.

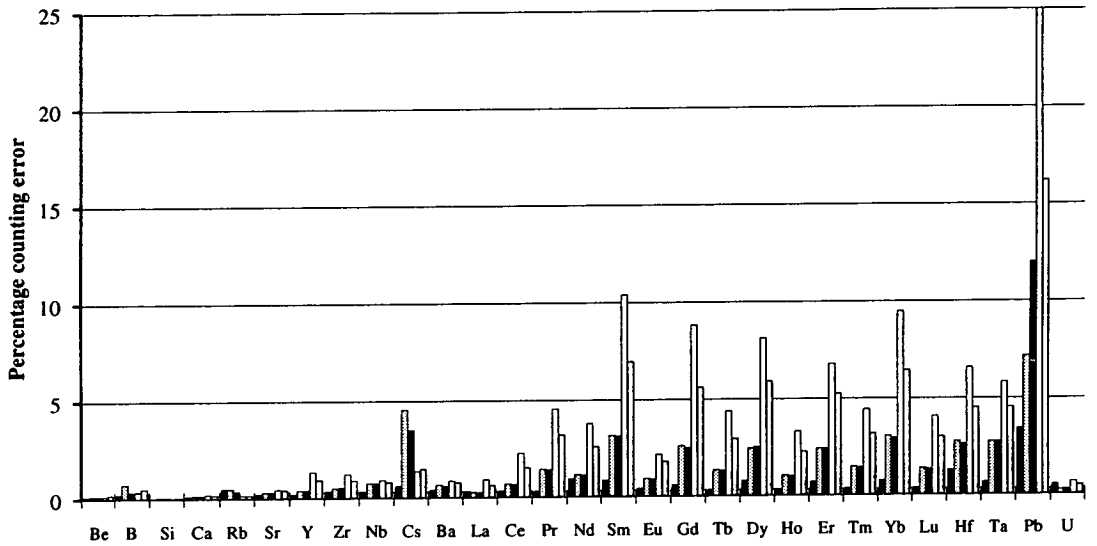

Figure 4.11: Percentage counting errors for each element in typical analyses of the standard, a starting composition, a melt and a glass sphere (columns 1, 2, 3, and 4, respectively).

Note that the glass sphere analysis has the highest errors for most elements. This is not surprising due to the low trace-element concentrations in this phase (see Chapter 7).

4.10 CONCLUSIONS

1. Experiments were performed in solid-media apparatus using either a ½" talc/boron nitride cell or a ¾" salt cell which could accommodate three capsules. The uncertainties in measurement of pressure and temperature for each cell are given in Table 4.14.

Table 4.14: Uncertainties in pressure and temperature determinations for the two cells used.

Uncertainties	*Talc/boron nitride cell*	*Salt cell*
Pressure	±0.05 GPa	±0.05 GPa
Temperature	±10°C	±5°C

2. The majority of experiments that were performed in the ½" talc/boron nitride cell used a platinum capsule which contained an olivine crystal holding the starting

mixture, and NiO powder. The starting mixture was either a gel, a hydrated gel, a sintered oxide, or a mixture of sintered oxide and gel. The gels contained small amounts of trace elements, distributed homogeneously. Free water was included in all capsules, except in those that contained a hydrated gel, or those that contained brucite. The oxygen fugacity was maintained at NNO.

3. The experiments that were performed in salt cells consisted of three gold capsules, each containing water and starting mixture (gel/sintered oxide mixture). The oxygen fugacity was not buffered.
4. Run products were often sectioned longitudinally, mounted in epoxy resin, and ground and polished prior to analysis by EPMA or SIMS.
5. Errors inherent in the analytical procedures were dependent on the concentration of the element of interest, the efficiency with which the element could be analysed, and the nature of the phase being analysed. Particularly large errors were associated with analysis by EPMA of Mn, Cr, or Ni in many phases; analysis by EPMA of Na in hydrous glass; and analysis by SIMS of Pb.

CHAPTER 5

PARTIAL MELTING OF HYDROUS PERIDOTITE - EXPERIMENTAL RESULTS

CHAPTER 5: PARTIAL MELTING OF HYDROUS PERIDOTITE - EXPERIMENTAL RESULTS

5.1 INTRODUCTION

One significant difference between the mantle wedge in a subduction zone and the mantle at other settings is the presence of slab-derived water in the mantle wedge. In order to evaluate the influence of water on the phase relations and melt compositions of peridotite, a set of experiments was performed in which a peridotite composition was partially melted over a range of pressures and temperatures under water-saturated conditions. The detailed aims of these experiments were:

i) to determine the major-element compositions of partial melts of hydrous peridotite over a range of pressures and temperatures.

ii) to determine the trace-element compositions of partial melts of hydrous peridotite over a range of pressures and temperatures, and to compare the composition of melts produced with and without various residual phases such as rutile or amphibole.

iii) to measure partition coefficients between amphibole and melt, as the presence of amphibole is another important difference between the mantle wedge and the mantle at other settings.

Although there have been previous studies of the phase relations of peridotite under water-saturated and water-undersaturated conditions (e.g. Kushiro 1970; Green, 1973; Millholen *et al.*, 1974; Mysen & Boettcher, 1975), there has been much disagreement over the major-element composition of partial melts (see Chapter 3). This is partly due to exsolution of quench phases from hydrous melt and the consequent modification of the melt composition during quenching. In this project the melt composition is determined by a new technique (Odling *et al.*, *submitted*) which involves the use of an *in situ* olivine crystal to trap melt as inclusions. Assuming that the only crystals to form in the melt inclusions during quenching are olivines, and that this is an equilibrium process, it should be possible to reconstruct the equilibrium melt composition from the melt inclusion composition by addition of an olivine component until an experimentally-determined Fe/Mg olivine/melt exchange relationship is re-established (Roeder & Emslie, 1970).

In Chapter 3, a rationale for the present experiments was presented. It was decided to perform the initial set of experiments between 1.8 GPa and 2.8 GPa over a range of temperatures from subsolidus to well over the solidus (past the clinopyroxene-out curve). This would yield a range of partial melts with various residual assemblages. The starting composition for the initial runs was Hawaiian pyrolite - 40% olivine[1]. Although it is acknowledged that Hawaiian pyrolite is not representative of the mantle wedge, which is thought to be of MORB-source or depleted MORB-source composition (see Chapter 2 and Chapter 8), it was anticipated that the use of this peridotite composition, which has relatively high alkalis and titanium contents, would promote the formation of amphibole, thus facilitating the measurement of partition coefficients between amphibole and melt. The experiments were buffered to NNO, which is within the range of estimates for the oxygen fugacity of the mantle wedge (Section 3.1.2). Twenty-six forward experiments were conducted at three separate pressures (1.8 GPa, 2.3 GPa, 2.8 GPa) over a range of temperatures. For the experimental details see Section 4.3. Run products were analysed for major elements by EPMA, and melt compositions were calculated from analyses of melt inclusions in the olivine bucket.

In order to test a calculated melt composition, it is often useful to perform a 'reversal' experiment, in which the starting material has the composition of the calculated melt, and the conditions are similar to the original (forward) experiment in which the partial melt was produced. In theory, if the melt composition has been calculated correctly, the run product should consist predominantly of melt, with some crystals of the same phases and compositions as those produced in the forward experiment. There are, however, some problems associated with reversal experiments. For example, there can be reactions between the melt and some crystalline phases that were stable in the forward experiment, e.g. spinel reacts with melt to form other phases such as orthopyroxene and olivine, and therefore spinel is not formed in these reversal experiments. Despite these problems, reversal experiments should give some indication of whether the calculated melt composition is correct. In this project, the calculated composition of a small-degree partial melt (from ED143) was tested by several reversal experiments using a similar capsule geometry to the forward experiments.

Textural evidence from the run products of reversals experiments that involved the use of an olivine bucket suggested that in many of these experiments, the olivine

[1] As the experiments were expected to be olivine saturated (Green, 1973) 40% olivine was subtracted from the Hawaiian pyrolite composition in order to reduce the amount of olivine component produced.

bucket had reacted with the melt to form orthopyroxene and sometimes clinopyroxene. Therefore, further reversal experiments without using an olivine bucket were conducted. The starting compositions in these experiments consisted of the calculated melt composition plus varying amounts of olivine component (Fo_{90}), as well as varying amounts of water. Four experiments, each containing three capsules without olivine buckets, were performed. One other aim of these experiments was to produce large amounts of fluid quench products for analysis by EPMA and SIMS (see Chapter 7).

As it was intended to measure the trace-element contents of melts and amphiboles by SIMS, the starting materials in the forward experiments had been doped with trace elements (see Chapter 4). In order to be confident that the ion beam does not overlap onto surrounding phases, it is advisable to analyse crystals that are at least 40x40 μm in cross-sectional area (Craven, *pers. comm.*). Typical amphibole crystals in forward experiments, however, are 10x10 μm, and 15x20 μm at the largest. Amphibole crystals in reversal experiments were usually larger than this (e.g. 15x50 μm). Considerable effort was directed towards the growth of larger crystals. This involved the execution of several further reversal experiments in olivine buckets, in which various parameters (temperature, water content, composition of the starting material) were changed to promote the growth of large amphibole crystals. Twenty of such experiments were performed.

Unfortunately, after the execution of a large proportion of the experiments in this study, analysis of the run products by SIMS revealed that many experiments had been contaminated by boron, derived from the boron nitride components in the solid-media cell. Further investigation showed that the mineralogical affects of this contamination are similar to those expected from an increase in temperature, and therefore the results from contaminated experiments cannot be used (see Chapter 6). There are, however, some experiments that have not been contaminated. The majority of these were performed at 1.8 GPa, the lowest pressure studied. Phase relations, and major-element compositions of minerals and melts from uncontaminated experiments at 1.8 GPa are presented in this chapter. The results from contaminated experiments (forward and reversal) are presented in Chapter 6.

One corollary of the contamination problems is that many of the original objectives of the project could not be achieved. For example, although some trace-element contents of melts from uncontaminated experiments have been measured, results from these few experiments are not consistent and will not be presented, although it is still considered that this may be a useful approach in future. The largest amphibole

crystals were produced in reversal experiments (see Section 5.5). Although these were still smaller than the recommended minimum area (40x40 μm) for analysis by SIMS, it was hoped that analyses could be performed. Unfortunately, the majority of reversal experiments which produced large amphiboles had either not been doped with trace elements or had been contaminated by boron (or both). It was therefore not possible to measure partition coefficients between amphibole and melt in the time available. In addition, it was not possible within the time available to extend the partial melting experiments to higher pressures, or to repeat the experiments using a more realistic starting material.

This Chapter contains the results of experiments performed at 1.8 GPa which were not contaminated by boron. The results of forward experiments are presented first, and the technique for the calculation of melt composition is discussed. Results of the reversal experiments performed on one calculated melt composition (from ED143 at 1020°C) are presented in Section 5.3. An appraisal of the technique for determination of melt composition is given in Section 5.3.3 and the estimated melt compositions are discussed in Section 5.4.

Experimental details and mineralogy of all run products are given in Appendix A.

5.2 FORWARD EXPERIMENTS

The results from six forward experiments uncontaminated by boron are shown in Table 5.1. Two experiments (ED91, ED101) were performed at much higher temperatures than the others. These were the first two experiments conducted, and were placed at these temperatures to coincide with the predicted solidus for water-undersaturated melting (Green, 1973). However, from the results it became apparent that due to the production of water in the buffer (see Section 4.3.5), run conditions were water saturated and the solidus was consequently at a lower temperature than originally anticipated. Therefore the following experiments were placed at intervals from 966°C to 1060°C. Unfortunately experiments conducted at 1040°C and 1060°C were contaminated by boron and the results are not presented in this chapter.

5.2.1 Mineralogy

The mineralogies produced by the experiments discussed in this chapter are given in Table 5.1.

Table 5.1: Mineralogy of forward experiments at 1.8 GPa.

Expt.	Temp. (°C)	melt	ol	opx	cpx	amph	sp	ru	ilm	fq
ED121	980		•	•	•	•	(•)	•	•	
ED133	1010	(•)	•	•	•	•	•		•	
ED143	1020	•	•	•	•	•	•	•	•	
ED137	1032	•	•	•	•	•	•	•		
ED101	1125	•	•	•	(•)		•			
ED91	1150	•	•	(•)			•			•

(Melt, olivine, orthopyroxene, clinopyroxene, amphibole, spinel, rutile, ilmenite, fluid quench).

- Two runs (ED111 at 966°C and ED121 at 980°C) were judged to have been subsolidus whilst the remaining runs contained melt. In ED133 (at 1010°C) very small amounts of melt were observed in interstices between crystals, although no melt inclusions were found in olivine. Run products from higher temperature experiments contained more melt, and it was possible to analyse melt inclusions in the olivine bucket.
- The results of these experiments constrain the amphibole-out curve to lie between 1032°C and 1125°C. However, the amphibole crystals produced at 1032°C are substantially smaller than those produced at 1020°C and may indicate that the breakdown temperature of amphiboles at this pressure is not far above 1032°C.
- The rutile-out curve was also constrained to lie between 1032°C and 1125°C.
- Ilmenite was identified in run products of experiments performed at 1020°C and lower temperatures, but not at 1032°C.
- Clinopyroxene was present in all experiments except ED91 (at 1150°C). At 1125°C, crystals were very small and only found in the cores of orthopyroxenes, implying that the clinopyroxene-out curve was between 1125°C and 1150°C.
- Orthopyroxene and olivine were present in all runs, although orthopyroxene crystals were rare in ED91 (1150°C).

5.2.2 Mineral compositions

Several analyses of all mineral phases from each experiment were performed by EPMA (see Section 4.8 for a discussion of this technique). Although the sample was positioned carefully and the electron beam was usually small compared to the crystals, all analyses were checked to ensure that they were pure, i.e. the electron beam had not overlapped onto surrounding phases. This involved comparison of the stoichiometry of the analysis with that expected from each phase. Data were examined and rejected if the oxide content or cation totals were significantly (1% for olivine, 2% for pyroxenes and garnet, 5% for amphiboles) different from the expected values for these phases, or if there was any obvious non-stoichiometry. The stoichiometries of all crystalline phases are discussed in the following sections. The average composition and standard deviation[2] of all minerals from each experiment are shown in Tables 5.2 - 5.8.

Olivine

As well as comprising the bucket, olivine was used in powder form at the top of the charges in all the forward experiments discussed in this chapter. It is therefore difficult to distinguish equilibrium crystals of olivine from those that were derived from fragmentation of the olivine bucket, or from the olivine powder. In most run products there is a bimodal distribution of olivine compositions, with one group coinciding with the olivine bucket composition in terms of Mg no., CaO content, and NiO content. The other group of compositions corresponds to smaller crystals (approximately 15 μm across) present in the main part of the charge, and is assumed to represent the equilibrium olivine composition.

[2]The standard deviations quoted are calculated in the following manner assuming that the arguments (number of arguments, n of value, x) are a sample of a population:

$$\sqrt{\frac{n\sum x^2-\left(\sum x\right)^2}{n(n-1)}}$$

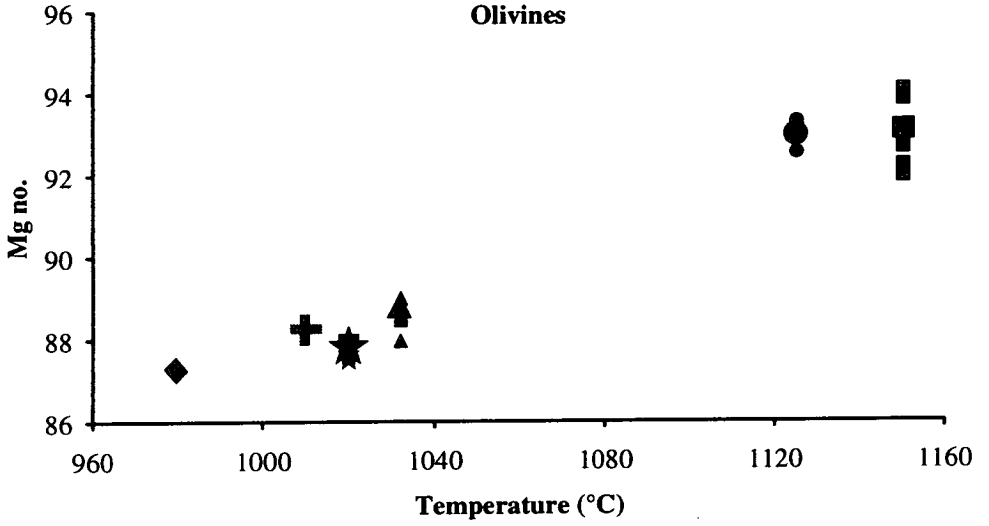

Figure 5.1: Mg no. of olivines as a function of the temperature of the experiments at 1.8 GPa. Average values are denoted by larger symbols.

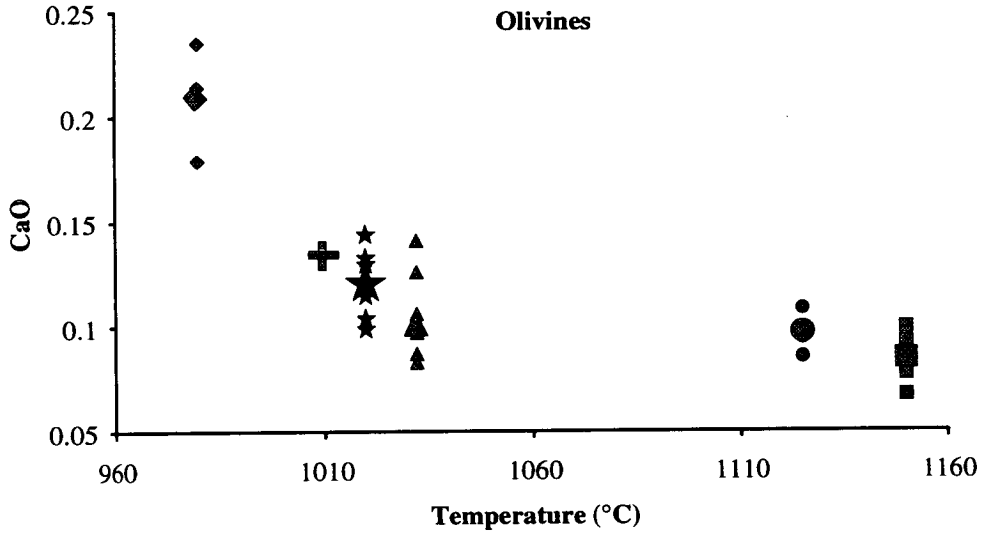

Figure 5.2: CaO content of olivines as a function of the temperature of the experiments at 1.8 GPa. Average values are denoted by larger symbols.

Cation contents were calculated on the basis of 4 oxygens per unit cell and were in agreement with the olivine stoichiometry: $(Mg,Fe)_2SiO_4$. Within each experiment there is a variation in olivine composition. This was particularly evident at the highest temperature (1150°C - ED91): olivines are zoned with Mg no. increasing from the cores outwards (see Table 5.2). Average olivine compositions from each experiment are shown in Table 5.3. Mg no. increases steadily with temperature from 87.3±0.09 at 980°C to 93.1±0.85 at 1150°C (Fig. 5.1).

Table 5.2: Typical analyses of a core and a rim of olivine in ED91.

OLIVINES FROM ED91

	rim	core	rim	core	average	s.d.
SiO_2	40.967	40.159	40.937	40.381	**41.203**	(0.696)
TiO_2	0.03	0.027	0.035	0.032	**0.032**	(0.007)
Al_2O_3	0.028	0.045	0.013	0.015	**0.017**	(0.009)
Cr_2O_3	0.124	0.123	0.118	0.133	**0.116**	(0.008)
FeO	6.007	8.034	6.077	7.543	**6.721**	(0.765)
MgO	51.574	49.445	51.772	49.638	**50.866**	(0.944)
CaO	0.083	0.084	0.067	0.071	**0.084**	(0.010)
Na_2O	0.015	0.005	0.013	0	**0.009**	(0.007)
K_2O	0.004	0	0.005	0.004	**0.007**	(0.003)
MnO	0.133	0.116	0.116	0.128	**0.131**	(0.013)
NiO	0.344	0.394	0.354	0.38	**0.366**	(0.028)
TOTAL	99.308	98.433	99.508	98.325	99.552	(0.590)
based on 4 oxygens:						
Si	1.00	0.99	0.99	1.00	1.00	(0.010)
Ti	0.001	0.001	0.001	0.001	0.001	(0.000)
Al	0.001	0.001	0.001	0.001	0.000	(0.000)
Cr	0.002	0.002	0.002	0.003	0.003	(0.000)
Fe	0.12	0.17	0.12	0.16	0.002	(0.000)
Mg	1.87	1.83	1.87	1.83	0.14	(0.016)
Ca	0.002	0.002	0.002	0.002	1.84	(0.029)
Na	0.001	0.000	0.001	0.000	0.002	(0.000)
K	0.000	0.000	0.000	0.000	0.000	(0.000)
Mn	0.003	0.002	0.002	0.003	0.000	(0.000)
Ni	0.007	0.008	0.007	0.008	0.007	(0.001)
TOTAL	3.00	3.00	3.01	3.00	3.00	(0.01)
Mg no.	93.87	91.65	93.82	92.14	93.09	(0.85)

The average and standard deviation (s.d.) were calculated from 7 analyses of the cores of olivine crystals.

Table 5.3: Average composition and standard deviation of olivines from forward experiments at 1.8 GPa.

OLIVINES

Expt.	**ED121**		**ED133**		**ED143**		**ED137**		**ED101**	
Temp	**980°C**		**1010°C**		**1020°C**		**1032°C**		**1125°C**	
	[3]	s.d.	[1]	s.d.	[6]	s.d.	[10]	s.d.	[5]	s.d.
SiO_2	39.845	(0.176)	40.009	(0.190)	39.724	(0.141)	39.919	(0.383)	41.139	(0.713)
TiO_2	0.096	(0.066)	0.235	(0.067)	0.061	(0.026)	0.058	(0.029)	0.027	(0.011)
Al_2O_3	0.165	(0.096)	0.062	(0.038)	0.041	(0.022)	0.071	(0.081)	0.045	(0.025)
Cr_2O_3	0.123	(0.028)	0.020	(0.007)	0.072	(0.010)	0.085	(0.026)	0.074	(0.007)
FeO	12.031	(0.159)	11.216	(0.151)	11.762	(0.194)	11.030	(0.258)	6.899	(0.237)
MgO	46.249	(0.280)	47.308	(0.198)	47.705	(0.325)	48.942	(0.823)	51.353	(0.677)
CaO	0.209	(0.028)	0.134	(0.019)	0.121	(0.018)	0.101	(0.023)	0.097	(0.008)
Na_2O	0.035	(0.020)	0.036	(0.026)	0.011	(0.013)	0.023	(0.040)	0.023	(0.018)
K_2O	0.006	(0.003)	0.020		0.005	(0.008)	0.003	(0.002)	0.006	(0.006)
MnO	0.123	(0.016)	0.154	(0.072)	0.107	(0.044)	0.111	(0.023)	0.126	(0.020)
NiO	0.580	(0.029)	0.400	(0.041)	0.485	(0.033)	0.387	(0.034)	0.306	(0.055)
TOTAL	99.463	(0.429)	99.595		100.094	(0.252)	100.731	(1.121)	100.093	(0.511)
based on 4 oxygens:										
Si	1.00	(0.005)	0.99		0.99	(0.004)	0.98	(0.004)	1.00	(0.012)
Ti	0.002	(0.001)	0.004		0.001	(0.000)	0.001	(0.001)	0.000	(0.000)
Al	0.005	(0.003)	0.002		0.001	(0.001)	0.002	(0.002)	0.001	(0.001)
Cr	0.002	(0.001)	0.000		0.001	(0.000)	0.002	(0.001)	0.001	(0.000)
Fe	0.25	(0.003)	0.23		0.24	(0.004)	0.23	(0.007)	0.14	(0.006)
Mg	1.72	(0.007)	1.75		1.76	(0.009)	1.79	(0.009)	1.85	(0.025)
Ca	0.006	(0.001)	0.004		0.003	(0.000)	0.003	(0.001)	0.003	(0.000)
Na	0.002	(0.001)	0.002		0.001	(0.001)	0.001	(0.002)	0.001	(0.001)
K	0.000	(0.000)	0.001		0.000	(0.000)	0.000	(0.000)	0.000	(0.000)
Mn	0.003	(0.000)	0.003		0.002	(0.001)	0.002	(0.000)	0.003	(0.000)
Ni	0.011	(0.001)	0.008		0.010	(0.001)	0.008	(0.001)	0.006	(0.001)
TOTAL	3.00	(0.00)	3.00		3.01	(0.00)	3.02	(0.00)	3.00	(0.01)
Mg no.	87.26	(0.09)	88.26		87.85	0.21	88.77	0.38	92.99	0.30

The number of analyses are shown in square brackets; s.d. is standard deviation. Olivine from ED91 is shown in Table 5.2. In ED133 only one olivine analysed was judged to have formed at equilibrium (as opposed to olivine powder included in the charge initially). The error quoted from this analysis is derived from the counting statistics of the electron microprobe.

CaO content also shows a marked temperature dependency, falling from 0.209±0.03 at 980°C to 0.084±0.01 at 1150°C (Fig. 5.2). Other oxide contents do not appear to be strongly controlled by temperature, although as the counting errors for some elements are relatively high, it is possible that there are other trends which are not recognised.

Pyroxenes

Coexisting orthopyroxene (typically 10x20 μm) and clinopyroxene (typically 10x5 μm) were formed in all experiments up to and including ED137 at 1032°C. In ED101 (1125°C) clinopyroxene crystals were small (2 μm across), subhedral and present in the cores of orthopyroxene, which suggests that this temperature is close to the clinopyroxene-out reaction. Analyses of these small crystals could not be obtained. Orthopyroxene crystals in the highest temperature experiment (ED91 at 1150°C) could not be analysed for a similar reason. Tables 5.4 and 5.5 show average orthopyroxene and clinopyroxene compositions respectively, derived from acceptable analyses in which the oxide and cation totals are good.

The pyroxene formula can be denoted as XYZ_2O_6 (Morimoto, 1988) where Z is filled with silicon and tetrahedrally co-ordinated aluminium, Al(IV). Y is then filled with octahedral aluminium, titanium, chromium and magnesium until the total is 1. Remaining magnesium is assigned to the X site with all iron, manganese, calcium, sodium and potassium. This should total approximately 2. It was assumed that the analysis was faulty if the full cation total deviated from 4±0.03. In Figure 5.3 the average compositions from each experiment are plotted on the quadrilateral for Ca-Fe-Mg pyroxenes.

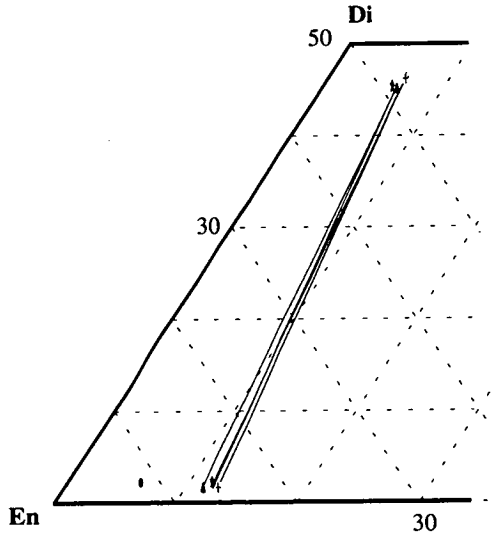

Figure 5.3: Part of the pyroxene quadrilateral showing the compositions of coexisting orthopyroxene and clinopyroxene formed at 1.8 GPa.

Table 5.4: Composition of average orthopyroxene from forward experiments at 1.8 GPa.

ORTHOPYROXENES

Expt.	**ED121**		**ED133**		**ED143**		**ED137**		**ED101**	
Temp	**980°C**		**1010°C**		**1020°C**		**1032°C**		**1125°C**	
	[4]	s.d.	[5]	s.d.	[8]	s.d.	[7]	s.d.	[4]	s.d.
SiO_2	53.374	(0.196)	53.019	(0.583)	53.988	(0.240)	54.030	(0.447)	57.931	(0.626)
TiO_2	0.390	(0.019)	0.341	(0.034)	0.374	(0.015)	0.376	(0.032)	0.160	(0.031)
Al_2O_3	4.092	(0.251)	3.624	(0.208)	3.210	(0.446)	3.376	(0.245)	1.172	(0.349)
Cr_2O_3	0.532	(0.052)	0.552	(0.038)	0.448	(0.106)	0.646	(0.053)	0.897	(0.224)
FeO	7.838	(0.148)	8.348	(0.338)	8.113	(0.360)	7.618	(0.550)	4.061	(0.189)
MgO	31.222	(0.332)	31.384	(0.479)	31.919	(0.322)	32.555	(0.381)	34.640	(0.568)
CaO	1.078	(0.216)	0.839	(0.040)	0.912	(0.104)	0.869	(0.078)	1.151	(0.297)
Na_2O	0.051	(0.040)	0.031	(0.020)	0.042	(0.026)	0.035	(0.022)	0.036	(0.008)
K_2O	0.024	(0.012)	0.013	(0.010)	0.006	(0.005)	0.006	(0.009)	0.008	(0.006)
MnO	0.106	(0.049)	0.100	(0.022)	0.128	(0.022)	0.104	(0.022)	0.136	(0.014)
NiO	0.172	(0.028)	0.120	(0.048)	0.134	(0.034)	0.123	(0.015)	0.088	(0.010)
TOTAL	98.879	(0.037)	98.373	(1.068)	99.273	(0.330)	99.739	(0.639)	100.279	(0.616)
based on 6 oxygens:										
Si	1.887	(0.008)	1.888	(0.006)	1.902	(0.010)	1.891	(0.009)	1.978	(0.019)
Al (IV)	0.113	(0.008)	0.112	(0.006)	0.098	(0.010)	0.109	(0.009)	0.022	(0.019)
Total	2		2		2		2		2	
Al (VI)	0.057	(0.007)	0.040	(0.006)	0.035	(0.011)	0.030	(0.007)	0.025	(0.006)
Ti	0.010	(0.001)	0.009	(0.001)	0.010	(0.000)	0.010	(0.001)	0.004	(0.001)
Cr	0.015	(0.001)	0.016	(0.001)	0.013	(0.003)	0.018	(0.002)	0.025	(0.006)
Mg(M1)	0.917	(0.008)	0.935	(0.007)	0.943	(0.013)	0.941	(0.008)	0.946	(0.006)
Total	1		1		1		1		1	
Mg(M2)	0.728	(0.014)	0.731	(0.012)	0.733	(0.015)	0.757	(0.015)	0.817	(0.019)
Fe	0.232	(0.004)	0.249	(0.011)	0.239	(0.011)	0.223	(0.016)	0.116	(0.005)
Mn	0.003	(0.001)	0.003	(0.001)	0.004	(0.001)	0.003	(0.001)	0.004	(0.000)
Ca	0.041	(0.008)	0.032	(0.002)	0.034	(0.004)	0.033	(0.003)	0.042	(0.011)
Na	0.003	(0.003)	0.002	(0.001)	0.003	(0.002)	0.002	(0.001)	0.002	(0.001)
K	0.001	(0.001)	0.001	(0.000)	0.000	(0.000)	0.000	(0.000)	0.000	(0.000)
Total	1.008	(0.006)	1.017	(0.006)	1.014	(0.006)	1.018	(0.006)	0.982	(0.009)
TOTAL	4.013	(0.006)	4.021	(0.005)	4.017	(0.006)	4.022	(0.006)	3.984	(0.009)
Mg no.	87.65	(0.28)	87.01	(0.54)	87.52	(0.56)	88.40	(0.79)	93.83	(0.34)

The number of analyses are shown in square brackets; s.d. is standard deviation.

Table 5.5: Composition of average clinopyroxene from forward experiments at 1.8 GPa.

CLINOPYROXENES

Expt.	**ED111**		**ED121**		**ED133**		**ED143**		**ED137**	
Temp	**966°C**		**980°C**		**1010°C**		**1020°C**		**1032°C**	
	[6]	s.d.	[3]	s.d.	[8]	s.d.	[10]	s.d.	[9]	s.d.
SiO_2	50.310	(0.423)	49.599	(0.151)	49.512	(0.336)	50.551	(0.811)	50.514	(0.443)
TiO_2	0.888	(0.094)	1.151	(0.013)	1.072	(0.080)	1.041	(0.215)	1.055	(0.128)
Al_2O_3	4.551	(0.316)	5.157	(0.050)	5.361	(0.504)	4.286	(0.844)	4.460	(0.509)
Cr_2O_3	0.082	(0.029)	0.818	(0.041)	0.825	(0.079)	0.743	(0.238)	0.903	(0.193)
FeO	3.532	(0.202)	3.769	(0.292)	3.779	(0.395)	3.659	(0.217)	3.688	(0.256)
MgO	16.493	(0.437)	15.915	(0.244)	15.971	(0.378)	16.519	(0.594)	16.433	(0.346)
CaO	21.975	(0.579)	21.690	(0.204)	21.634	(0.387)	21.299	(0.648)	21.200	(0.270)
Na_2O	0.275	(0.025)	0.281	(0.031)	0.359	(0.044)	0.410	(0.053)	0.476	(0.045)
K_2O	n.a.	n.a.	0.013	(0.012)	0.010	(0.012)	0.007	(0.008)	0.010	(0.011)
MnO	0.671	(0.138)	0.088	(0.006)	0.091	(0.029)	0.084	(0.033)	0.066	(0.028)
NiO	0.071	(0.017)	0.121	(0.008)	0.071	(0.018)	0.105	(0.040)	0.066	(0.029)
TOTAL	98.846	(0.331)	98.601	(0.437)	98.683	(0.575)	98.703	(0.361)	98.870	(0.358)
based on 6 oxygens:										
Si	1.863	(0.011)	1.842	(0.006)	1.837	(0.008)	1.870	(0.025)	1.866	(0.014)
Al (IV)	0.137	(0.011)	0.158	(0.006)	0.163	(0.008)	0.130	(0.045)	0.134	(0.026)
Total	2		2		2		2		2	
Al (VI)	0.061	(0.006)	0.067	(0.007)	0.071	(0.018)	0.057	(0.014)	0.060	(0.009)
Ti	0.025	(0.003)	0.032	(0.000)	0.030	(0.002)	0.029	(0.006)	0.029	(0.004)
Cr	0.002	(0.001)	0.024	(0.001)	0.025	(0.002)	0.022	(0.007)	0.027	(0.006)
Mg(M1)	0.912	(0.008)	0.876	(0.007)	0.874	(0.016)	0.892	(0.019)	0.884	(0.015)
Total	1		1		1		1		1	
Mg(M2)	-0.002	(0.019)	0.005	(0.005)	0.009	(0.013)	0.019	(0.021)	0.021	(0.008)
Fe	0.109	(0.006)	0.117	(0.009)	0.117	(0.012)	0.113	(0.007)	0.114	(0.008)
Mn	0.021	(0.004)	0.003	(0.000)	0.003	(0.001)	0.003	(0.001)	0.002	(0.001)
Ca	0.872	(0.026)	0.863	(0.009)	0.860	(0.014)	0.844	(0.026)	0.839	(0.011)
Na	0.020	(0.002)	0.020	(0.002)	0.026	(0.003)	0.029	(0.004)	0.034	(0.003)
K	n.a.	n.a.	0.001	(0.001)	0.000	(0.001)	0.000	(0.000)	0.000	(0.001)
Total	1.020	(0.006)	1.008	(0.007)	1.015	(0.008)	1.009	(0.034)	1.010	(0.003)
TOTAL	4.022	(0.005)	4.012	(0.007)	4.017	(0.008)	4.012	(0.002)	4.012	(0.003)
Mg no.	89.273	(0.583)	88.273	(0.893)	88.294	(1.062)	88.951	(0.381)	88.814	(0.771)

The number of analyses are shown in square brackets; s.d. is standard deviation.

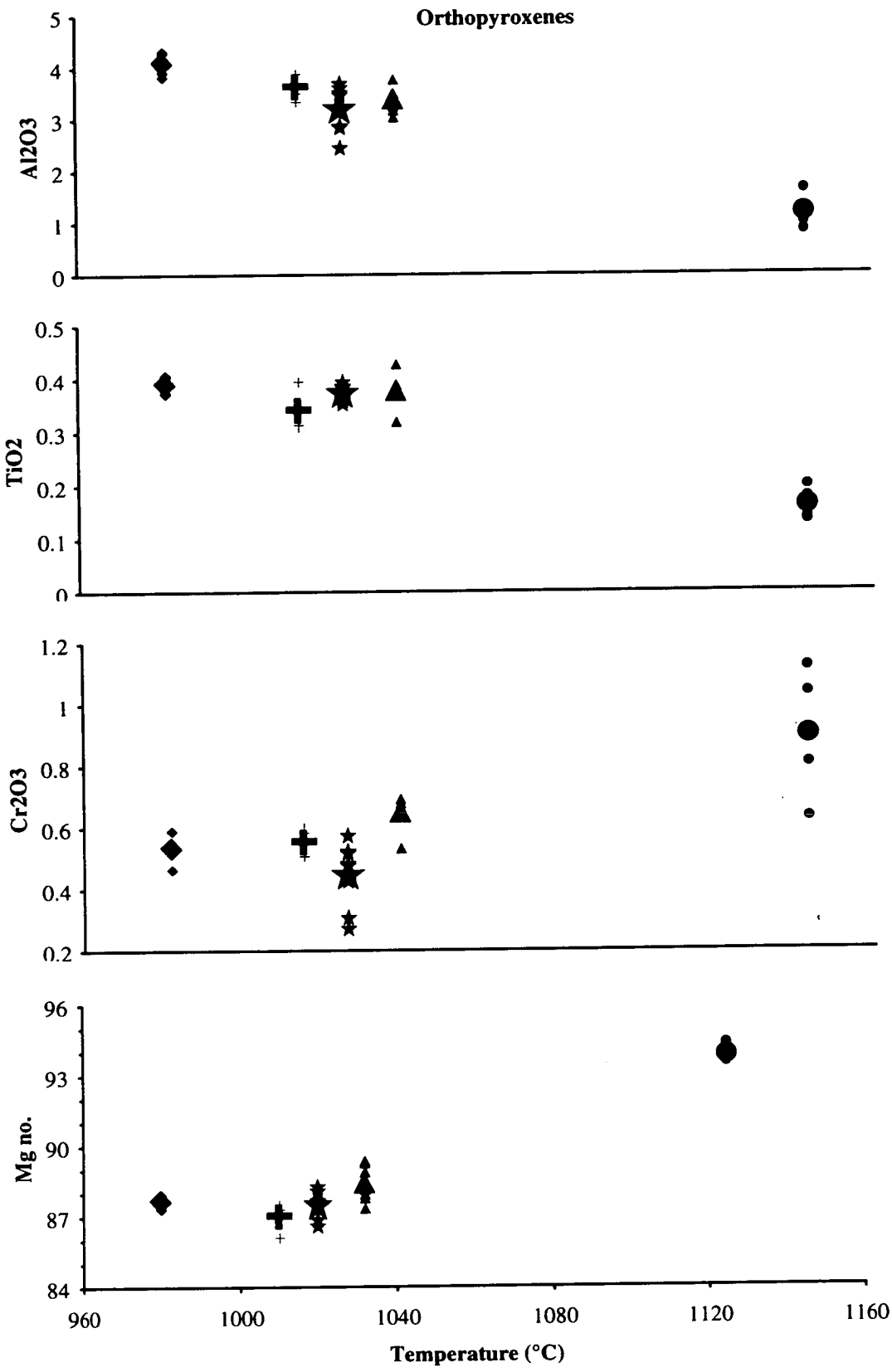

Figure 5.4: Orthopyroxenes from forward experiments at 1.8 GPa: composition as a function of temperature. Average values are denoted by the larger symbols.

The orthopyroxenes are chromian aluminian enstatites (Morimoto, 1988) and are typically zoned with Fe-rich rims. There is also some variation in composition between individual crystals within a single experiment. However it is still possible to see trends with temperature (Fig. 5.4). For example Mg no. increases with temperature, as does Cr_2O_3 content. TiO_2 and Al_2O_3 both decrease with temperature.

The clinopyroxenes fall in the diopside field and are all classified as chromian aluminian diopsides (Morimoto, 1988). There is a relatively larger spread in clinopyroxene compositions within an experiment, reflected in the larger standard deviations. Average Mg no. increases with temperature (Fig. 5.5) although this trend is not particularly marked. There is a strong correlation, however, between Na_2O content and temperature (Fig. 5.6) with values rising from 0.275±0.025 at 980°C to 0.476±0.045 at 1032°C.

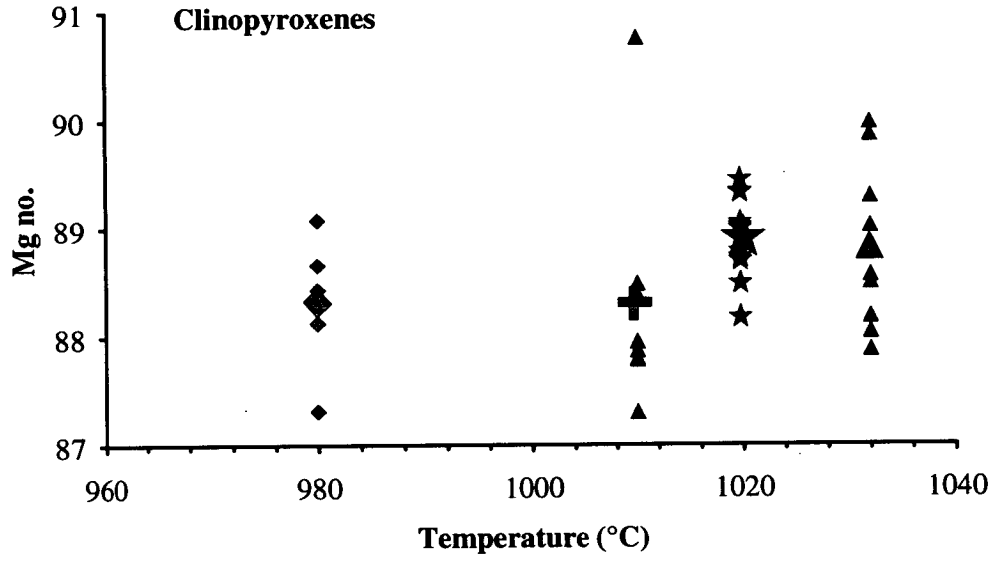

Figure 5.5: Mg no. of clinopyroxenes at 1.8 GPa as a function of the temperature of the experiment. Average values are denoted by larger symbols.

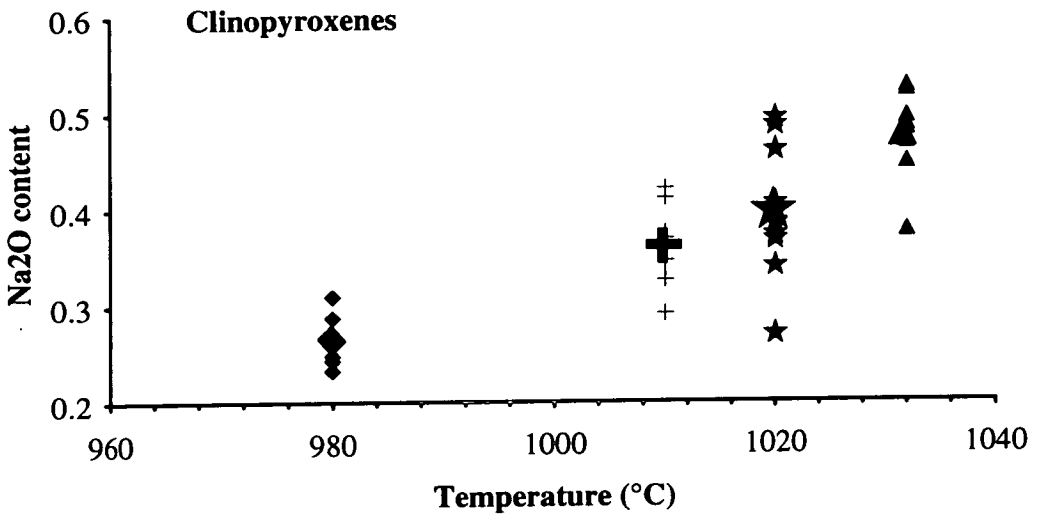

Figure 5.6: Na_2O content of clinopyroxenes at 1.8 GPa as a function of the temperature of the experiment. Average values are denoted by larger symbols.

Other oxide contents do not appear to be strongly correlated with temperature.
In addition to the replacement of Fe by Mg in the X site, important substitutions in pyroxenes include the Tschermak (1) and the Ti-tschermak (2) substitutions:

$$Mg + Si \leftrightarrow Al(VI) + Al(IV) \quad (5.1)$$
$$Mg + 2Si \leftrightarrow Ti + 2Al(IV) \quad (5.2)$$

In these experiments both orthopyroxene and clinopyroxene show some coupling of Al(IV) and Al(VI) (Fig. 5.7) which suggests that the Tschermak substitution is in operation, with Al content decreasing with increasing temperature. There is also limited correlation between Ti and Al(IV) in orthopyroxenes (Fig. 5.8) suggesting that the Ti-tschermak substitution is also driven to the left (Equation 5.1) by an increase in temperature. I can find no coupled substitution to explain the increase in Na_2O content in clinopyroxene with temperature.

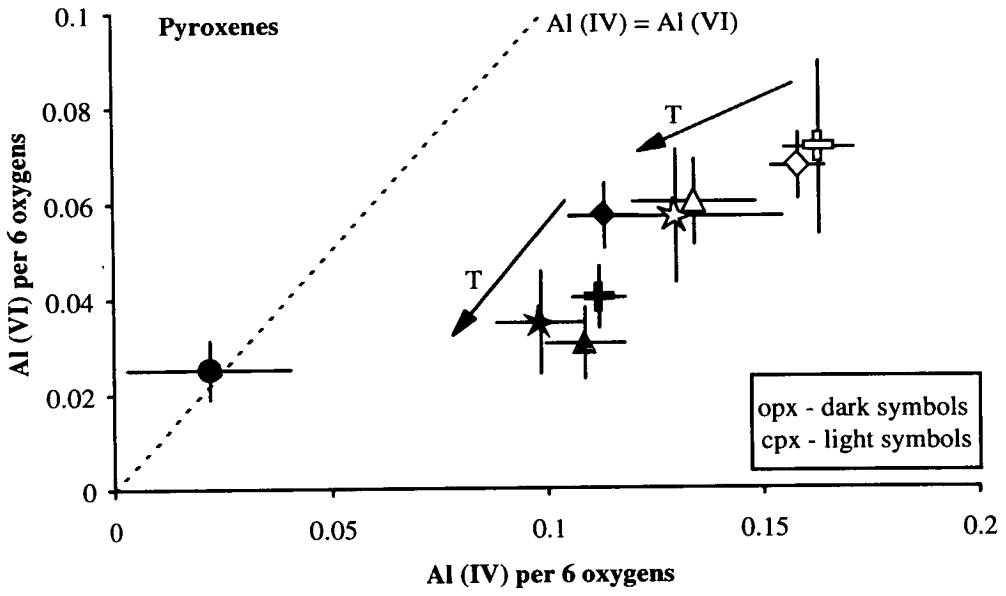

Figure 5.7: Al(VI) versus Al(IV) content of average pyroxenes from each experiment at 1.8 GPa. Filled symbols represent orthopyroxene whereas open symbols represent clinopyroxene. The tschermak substitution ideally proceeds along the dotted line. Arrows show the change in composition with increasing temperature. Symbols for each experiment are:
ED121(980°C)=diamond; ED133(1010°C)=cross; ED143(1020°C)=star;
ED137(1032°C)=triangle;
ED101(1125°C)=circle.

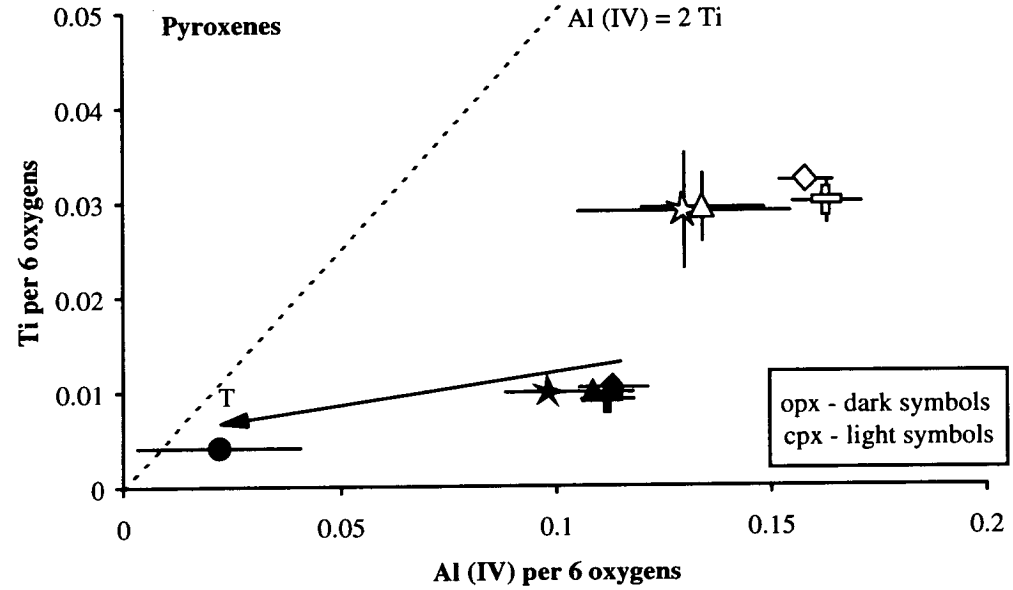

Figure 5.8: Ti versus Al(IV) in pyroxenes. Symbols are as in figure 5.7. The Ti-tschermak substitution ideally proceeds along dotted line. The arrow shows the change in composition with increasing temperature.

Amphiboles

Amphiboles were produced in all experiments up to and including ED137 at 1032°C. Crystals are typically euhedral and approximately 10x10 μm in ED121, ED133, and ED143. However in ED137 the crystals are much smaller (approximately 8x3 μm) and consequently difficult to analyse. Therefore many analyses were discarded due to poor stoichiometry. Cations were calculated on the basis of 23 oxygens per unit cell and were allocated to sites assuming a formula of $A_{0-1}X_2Y_5Z_2O_{22}(OH)_2$. The Z site was filled by silicon and tetrahedral aluminium, Al(IV). All remaining aluminium was assumed to be octahedral and allocated to the Y site with titanium, magnesium, manganese and iron until the total in the Y site was 5. Any remaining iron (and manganese and magnesium) was allocated to the X site with calcium and sodium until the total was 2. Any remaining sodium, and all potassium were assumed to be present in the [A] site. The average compositions and cation contents from all experiments are shown in Table 5.6. According to the nomenclature of Leake (1978), all amphiboles in these experiments are pargasitic hornblendes. In contrast to orthopyroxene, clinopyroxene and olivine, the Mg no. of amphibole decreases with temperature from 87.76±0.19 at 980°C to 84.03±1.8 at 1032°C. Cr_2O_3 content, and to a lesser extent CaO and Na_2O, are also negatively correlated with temperature (Fig. 5.9).

Tremolite, $Ca_2(Mg,Fe)_5[Si_8O_{22}](OH)_2$, can undergo a number of coupled substitutions:

$Mg + Si \leftrightarrow Al(VI) + Al(IV)$	(5.3)	Tschermak
$Mg + 2Si \leftrightarrow Ti + 2Al(IV)$	(5.4)	Ti-tschermak
$[\,] + Si \leftrightarrow Na[A] + Al(IV)$	(5.5)	Edenitic
$[\,] + Ca \leftrightarrow Na[A] + Na(M4)$	(5.6)	
$Ca + Mg \leftrightarrow Na(M4) + Al(VI)$	(5.7)	

as well as:

$Mg^{2+} \leftrightarrow Fe^{2+}$

$Ca^{2+} \leftrightarrow Fe^{2+}$

$Na^{+} \leftrightarrow K^{+}$

The amphiboles from these experiments lie on a rough positive trend on a plot of Al(IV) versus Al(VI), although there is no simple correlation with temperature (Fig. 5.10). There is a correlation between Al(IV) and Ti, with values for both parameters

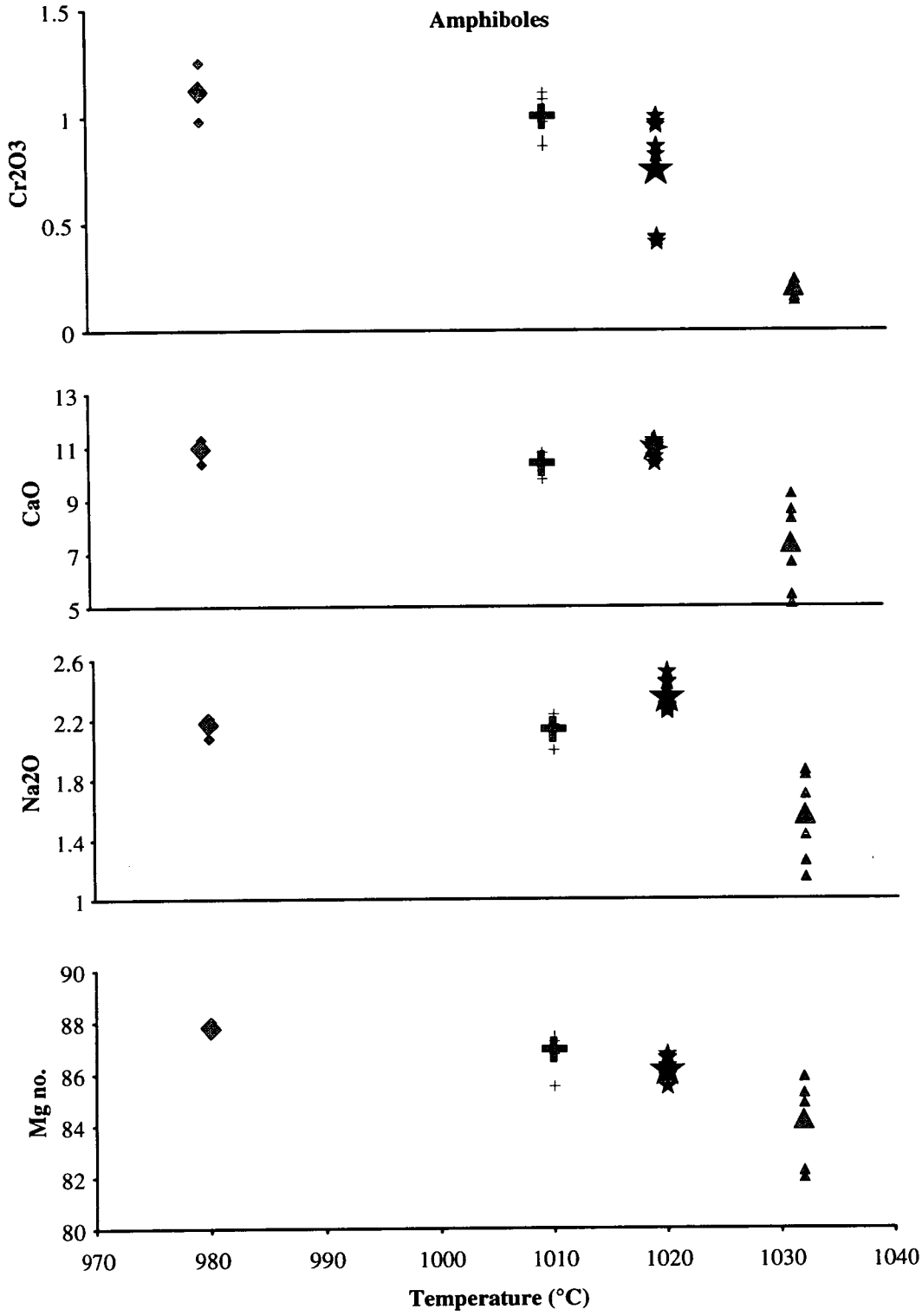

Figure 5.9: Amphiboles from forward experiments at 1.8 GPa: composition as a function of temperature. Average values are denoted by larger symbols.

Table 5.6: Composition of average amphibole from forward experiments at 1.8 GPa.

AMPHIBOLES

Expt.	**ED121**		**ED133**		**ED143**		**ED137**	
Temp	**980°C**		**1010°C**		**1020°C**		**1032°C**	
	[4]	s.d.	[6]	s.d.	[9]	s.d.	[5]	s.d.
SiO_2	43.967	(0.741)	44.013	(0.827)	43.591	(0.568)	44.936	(0.961)
TiO_2	1.867	(0.034)	2.115	(0.893)	2.123	(0.096)	1.851	(0.451)
Al_2O_3	12.139	(0.485)	11.824	(0.776)	12.057	(0.929)	12.975	(1.817)
Cr_2O_3	1.117	(0.112)	0.998	(0.107)	0.751	(0.250)	0.197	(0.042)
FeO	4.616	(0.107)	5.247	(0.211)	5.204	(0.198)	7.410	(0.229)
MgO	18.560	(0.259)	19.534	(0.499)	18.143	(0.438)	22.093	(2.606)
CaO	10.932	(0.394)	10.355	(0.355)	10.935	(0.283)	7.329	(1.915)
Na_2O	2.169	(0.062)	2.131	(0.079)	2.348	(0.099)	1.557	(0.335)
K_2O	0.427	(0.026)	0.377	(0.077)	0.549	(0.078)	0.268	(0.045)
MnO	0.084	(0.024)	0.067	(0.023)	0.070	(0.044)	0.117	(0.022)
NiO	0.163	(0.061)	0.172	(0.018)	0.148	(0.045)	0.113	(0.046)
TOTAL	96.039	(0.874)	96.834	(0.913)	95.918	(0.406)	98.846	(0.832)
based on 23 oxygens:								
Si	6.346	(0.063)	6.312	(0.125)	6.326	(0.089)	6.169	(0.006)
Al (IV)	1.654	(0.063)	1.688	(0.125)	1.674	(0.089)	1.831	(0.006)
Total in Z	8		8		8		8	
Al (VI)	0.412	(0.049)	0.309	(0.094)	0.388	(0.077)	0.537	(0.081)
Ti	0.203	(0.003)	0.228	(0.097)	0.232	(0.010)	0.244	(0.024)
Mg	3.993	(0.038)	4.175	(0.098)	3.924	(0.094)	4.089	(0.139)
Mn	0.010	(0.003)	0.008	(0.003)	0.009	(0.005)	0.015	(0.003)
Fe (Y)	0.382	(0.057)	0.279	(0.065)	0.448	(0.043)	0.116	(0.079)
Total in Y	5		5		5		5	
Fe (X)	0.175	(0.052)	0.350	(0.042)	0.184	(0.052)	0.776	(0.097)
Ca	1.691	(0.059)	1.591	(0.050)	1.700	(0.045)	1.314	(0.082)
Na (X)	0.134	(0.014)	0.059	(0.053)	0.116	(0.026)	0.000	(0.000)
Total in X	2		2		2		2.090	(0.015)
Na xs	0.472	(0.018)	0.534	(0.062)	0.545	(0.047)	0.502	(0.012)
K	0.079	(0.004)	0.069	(0.014)	0.102	(0.014)	0.054	(0.008)
Total in [A]	0.551	(0.017)	0.602	(0.069)	0.646	(0.055)	0.556	(0.020)
Cr	0.130	(0.014)	0.115	(0.012)	0.088	(0.029)	0.019	(0.004)
Ni	0.019	(0.007)	0.019	(0.002)	0.017	(0.005)	0.008	(0.000)
TOTAL	15.699	(0.032)	15.737	(0.075)	15.751	(0.039)	15.686	(0.035)
Mg no.	87.757	(0.188)	86.895	(0.724)	86.137	(0.465)	84.029	(1.803)

The number of analyses are shown in square brackets; s.d. is standard deviation.

increasing with temperature (Fig. 5.11). Na content in the [A]-site also increases with temperature for the three lower temperature experiments (Fig. 5.12).

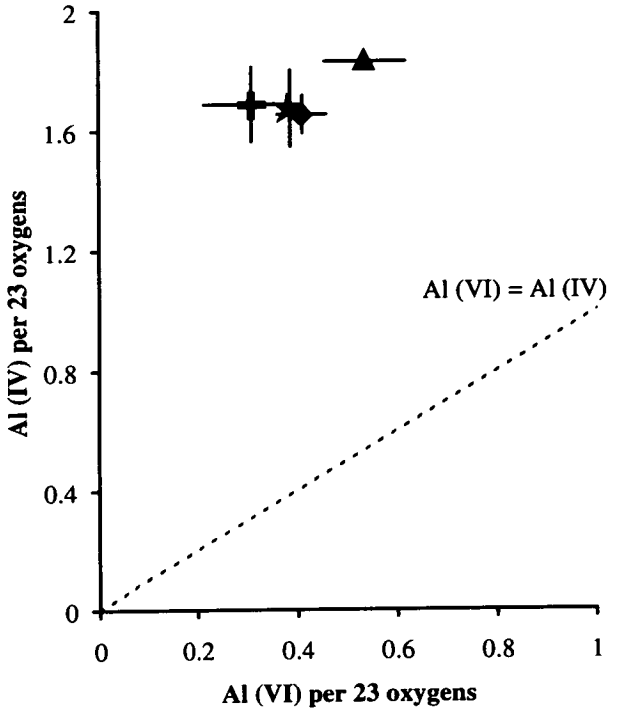

Figure 5.10: Al(VI) versus Al(IV) in amphiboles from forward experiments at 1.8 GPa. The average amphibole composition (and error) from each experiment is shown using the following symbols: ED121 (980°C) = diamond; ED133 (1010°C) = cross; ED143 (1020°C) = star; ED137 (1032°C) = triangle.

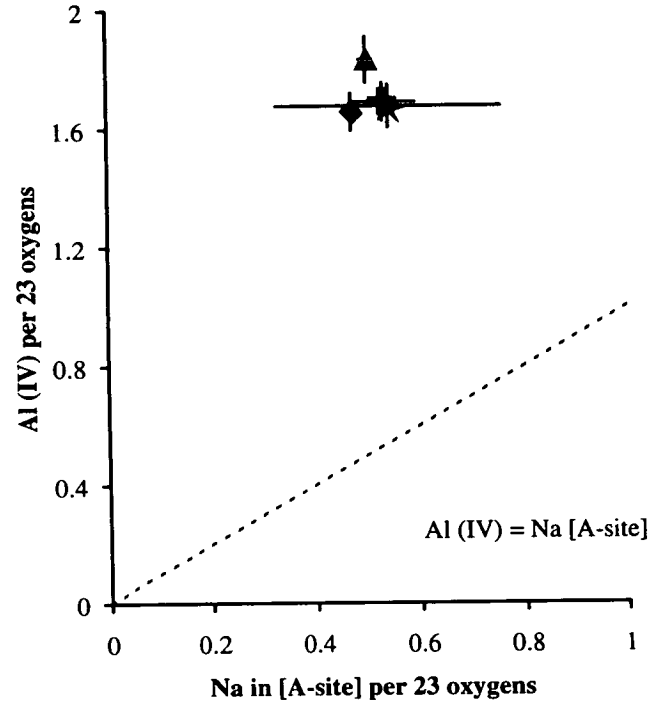

Figure 5.11: Al(VI) versus Na in [A] site in amphiboles from forward experiments at 1.8 GPa. The average amphibole composition (and error) from each experiment is shown using the following symbols: ED121 (980°C) = diamond; ED133 (1010°C) = cross; ED143 (1020°C) = star; ED137 (1032°C) = triangle.

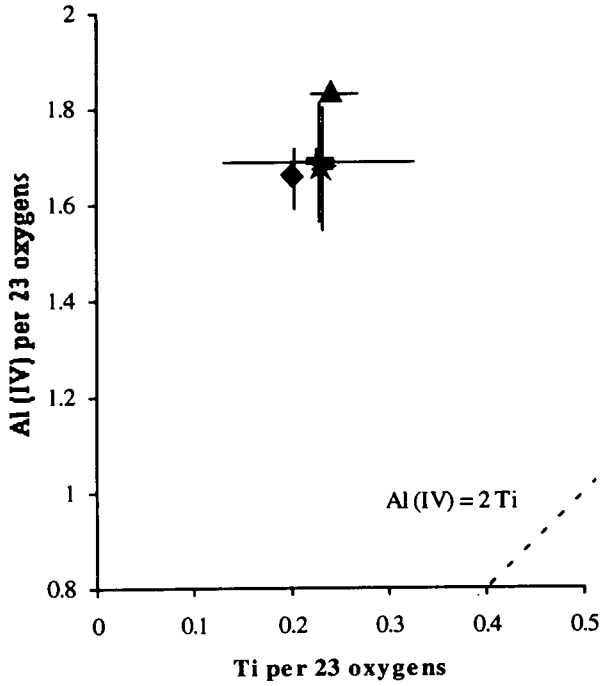

Figure 5.12: Al(IV) versus Ti in amphiboles from forward experiments at 1.8 GPa. The average amphibole composition (and error) from each experiment is shown using the following symbols: ED121 (980°C) = diamond; ED133 (1010°C) = cross; ED143 (1020°C) = star; ED137 (1032° C) = triangle.

As temperature increases, the amphiboles become more pargasitic-edenitic, and the Ti-tschermak substitution is driven. No correlation between Na[A], Na(M4) and Al(VI) can be found, from which it may be deduced that substitutions (5.6) and (5.7) are not important here.

Spinel

A cubic oxide mineral in the spinel series was formed in all experiments, although crystals in the lower-temperature experiments were very small and difficult to analyse. Overlap of the electron beam onto other phases during analysis was a major problem due to the small size of crystals in all experiments[3]. To overcome this problem, several analyses were performed on a number of crystals, and the results were regressed to achieve a SiO_2-free composition. This method produced relatively large errors for some elements (Table 5.7). In ED133 only one analysis was performed and so the method of regression to 0% SiO_2 could not be used. Although the SiO_2 content in this analysis was high (7.2%) it was decided to include this composition bearing in mind that the errors are very large.

[3]Spinels are 5x5μm on average: larger in higher-temperature experiments (up to 10x8 μm) and smaller in lower-temperature experiments (3x3 μm).

Table 5.7: Composition of spinels from forward experiments at 1.8 GPa.

SPINELS

	ED133 1010°C		ED143 1020°C		ED137 1032°C		ED101 1125°C		ED91 1150°C	
SiO_2	7.17	(0.48)	0		0		0		0	
TiO_2	0.60	(0.01)	0.62	(0.09)	1.14	(0.90)	1.20	(0.04)	1.80	(0.05)
Al_2O_3	42.94	(90.12)	52.50	(2.14)	39.20	(1.80)	11.30	(0.53)	15.80	(1.02)
Cr_2O_3	16.30	(0.03)	13.40	(1.56)	25.00	(1.50)	58.00	(1.18)	53.60	(1.17)
FeO	11.71	(0.07)	12.25	(0.26)	14.00	(0.20)	11.70	(0.19)	12.70	(0.11)
MgO	22.45	(0.08)	19.10	(0.77)	17.40	(0.10)	15.50	(1.37)	16.00	(0.38)
CaO	0.03	(0.00)	0.12	(0.01)	0.20	(0.05)	0.18	(0.01)	0.05	(0.01)
Na_2O	0.11	(0.17)	0.03	(0.01)	0.04	(0.01)	0.07	(0.02)	0.05	(0.02)
K_2O	0.01	(0.00)	0.00	(0.00)	0.00		0.01	(0.00)	0.02	(0.01)
MnO	0.19	(0.02)	0.11	(0.04)	0.15	(0.01)	0.23	(0.01)	0.22	(0.04)
NiO	0.27	(0.04)	0.75	(0.05)	0.19	(0.03)	0.08	(0.02)	0.20	(0.05)
TOTAL	101.79		98.88		97.32		98.27		98.63	
based on 4 oxygens:										
Si	0.19		0		0		0		0	
Ti	0.01		0.01		0.02		0.03		0.04	
Al	1.31		1.66		1.33		0.43		0.58	
Cr	0.34		0.29		0.58		1.51		1.34	
Fe	0.25		0.27		0.34		0.32		0.33	
Mg	0.87		0.76		0.75		0.75		0.74	
Ca	0.00		0.00		0.01		0.01		0.00	
Na	0.01		0.00		0.00		0.00		0.00	
K	0.00		0.00		0.00		0.00		0.00	
Mn	0.00		0.00		0.00		0.01		0.01	
Ni	0.01		0.02		0.00		0.00		0.00	
TOTAL	2.99		3.02		3.04		3.04		3.04	
Mg no.	77.35		73.54		68.90		70.25		69.19	

The spinel composition from ED133 represents one analysis, whereas the compositions from the other experiments were derived by extrapolation of analyses to 0% SiO_2. The errors have been estimated.

Most members of the spinel series found in igneous rocks may be plotted using a mulitcomponent spinel prism[4] (Haggerty, 1976). The compositions of spinels from these experiments, projected onto two rectangular faces of the spinel prism in Figure 5.13, fall between spinel ($MgAl_2O_4$) and picrochromite ($MgCr_2O_4$) with lesser amounts of hercynite ($FeAl_2O_4$) and chromite ($FeCr_2O_4$). With increasing temperature the spinel composition evolves towards picochromite-chromite compositions, with a slight increase in relative Ti, indicating a spinel ($MgAl_2O_4$) to ulvöspinel (Fe_2TiO_4) reaction.

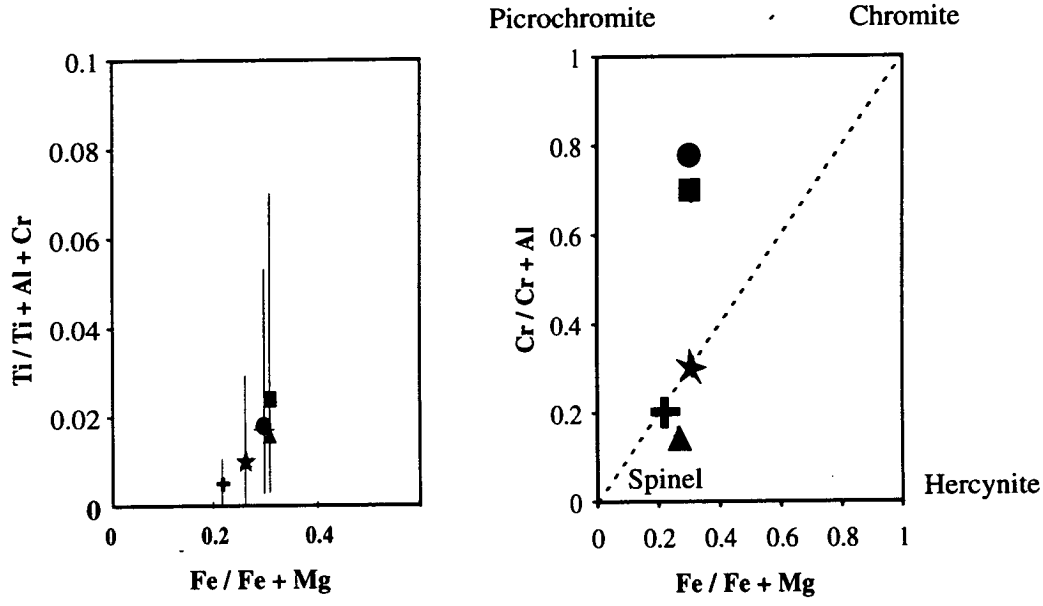

Figure 5.13: Compositions (with error bars) of spinels from forward experiments at 1.8 GPa, plotted on two projections of the spinel prism (see text). The symbols are: ED133 (1010°C) = cross; ED143 (1020°C) = star; ED137 (1032°C) = triangle; ED101 (1125°C) = circle; ED91 (1150°C) = square.

Rutile and Ilmenite

Ilmenite occurs in run products from experiments performed at temperatures up to 1020°C (ED143). Rutile is found in two experiments: ED143 and ED137 (1032°C). Crystals are larger in the higher temperature runs reaching sizes of approximately 10x10 μm (rutile) and 5x8 μm (ilmenite). However, in most cases crystals are anhedral and present difficulties similar to those encountered in spinel analysis. Hence many analyses have been made, the majority of which have been discarded. Compositions fall mid way between the ilmenite end member ($FeTiO_3$) and geikilite

[4]The front of the prism has end-members Mg_2TiO_4, $MgAl_2O_4$ and $MgCr_2O_4$, and the back of the prism has end-members Fe_2TiO_4, $FeAl_2O_4$, $FeCr_2O_4$ for Fe^{2+}+Ti spinels or Fe_3O_4, $FeAl_2O_4$, $FeCr_2O_4$ for Fe^{3+} spinels. For the spinels in these experiments it is assumed that Fe^{2+} predominates over Fe^{3+}.

Table 5.8: composition of ilmenites and rutiles produced in forward experiments at 1.8 GPa

	ILMENITES						RUTILES			
Expt.	**ED121**		**ED133**		**ED143**		**ED143**		**ED137**	
Temp.	**980°C**		**1010°C**		**1020°C**		**1020°C**		**1032°C**	
	[1]	s.d.	[5]	s.d.	[3]	s.d.	[4]	s.d.	[6]	s.d.
SiO_2	2.094	(0.434)	5.796	(3.189)	0.668	(0.534)	0.320	(0.211)	0.333	(0.140)
TiO_2	53.904	(0.174)	49.050	(4.142)	55.352	(0.650)	93.315	(0.585)	93.248	(0.507)
Al_2O_3	1.051	(0.081)	1.209	(0.398)	0.611	(0.065)	0.854	(0.033)	0.756	(0.026)
Cr_2O_3	0.321	(0.123)	1.551	(0.113)	1.113	(0.595)	2.737	(0.145)	3.533	(0.187)
FeO	25.564	(0.207)	25.014	(1.279)	26.690	(1.302)	0.934	(0.032)	0.838	(0.065)
MgO	15.281	(0.159)	15.803	(1.594)	13.682	(1.082)	0.281	(0.144)	0.248	(0.049)
CaO	0.356	(0.055)	0.907	(0.404)	0.320	(0.106)	0.295	(0.117)	0.371	(0.126)
Na_2O	0.039	(0.044)	0.094	(0.105)	0.041	(0.042)	0.000	(0.000)	0.025	(0.029)
K_2O		(0.044)	0.018	(0.017)	0.007	(0.001)	0.003	(0.003)	0.009	(0.003)
MnO	1.215	(0.044)	0.265	(0.012)	0.269	(0.026)	0.026	(0.022)	0.018	(0.019)
NiO	0.303	(0.040)	0.346	(0.044)	0.539	(0.102)	0.037	(0.028)	0.023	(0.033)
TOTAL	100.12		100.04	(1.377)	99.292	(0.235)	98.802	(0.318)	99.400	(0.404)
based on 3 oxygens:							**based on 2 oxygens:**			
Si	0.047		0.128	(0.070)	0.015	(0.012)	0.004	(0.003)	0.004	(0.002)
Ti	0.912		0.817	(0.081)	0.955	(0.020)	0.953	(0.006)	0.948	(0.004)
Al	0.028		0.032	(0.010)	0.017	(0.002)	0.014	(0.001)	0.012	(0.000)
Cr	0.006		0.028	(0.002)	0.020	(0.011)	0.030	(0.001)	0.038	(0.002)
Fe	0.481		0.464	(0.030)	0.512	(0.030)	0.011	(0.000)	0.009	(0.001)
Mg	0.512		0.522	(0.047)	0.468	(0.032)	0.006	(0.004)	0.005	(0.001)
Ca	0.009		0.022	(0.009)	0.008	(0.003)	0.004	(0.001)	0.005	(0.002)
Na	0.002		0.004	(0.004)	0.002	(0.002)	0.000	(0.000)	0.001	(0.001)
K	0.000		0.001	(0.000)	0.000	(0.000)	0.000	(0.000)	0.000	(0.000)
Mn	0.023		0.005	(0.000)	0.005	(0.001)	0.000	(0.000)	0.000	(0.000)
Ni	0.005		0.006	(0.001)	0.010	(0.002)	0.000	(0.000)	0.000	(0.000)
TOTAL	2.025		2.028	(0.010)	2.012	(0.005)	1.022	(0.002)	1.024	(0.002)
Mg no.	51.584		52.965	(3.702)	47.720	(3.157)	34.862	(11.796)	34.517	(0.545)

The number of analyses is shown in square brackets; s.d. is standard deviation.

($MgTiO_3$). A small proportion of the manganese end member, pyrophanite ($MnTiO_3$), is also present. No systematic change in composition is evident with change in temperature.

Rutiles contain between 93 and 94% TiO_2 with lesser amounts of Cr_2O_3 and less than 1% of Al_2O_3, FeO, CaO, MgO.

5.2.3 Discussion

Before interpreting this data, it is necessary to assess whether the minerals analysed were formed at equilibrium or whether they are metastable phases formed during quenching. Quench phases are, by their nature, formed below run temperature and it has been established that they reflect this in their compositions. For example, Mg nos. of quench crystals are lower than Mg nos. of equilibrium crystals of the same mineral. In one experiment reported by Green (1973), clinopyroxene crystals formed at equilibrium had a Mg no. of 88.5 (similar to orthopyroxene) whereas quench clinopyroxene had a much lower Mg no. of 77.5. Quench amphibole was also found in some experiments (Green, *op. cit.*). This had a very low Mg no. of 65 in contrast to the equilibrium amphibole at the same pressure (Mg no. 86.1). Thus, it is often possible to identify quench phases by their distinctive composition. In addition, quench phases are usually feathery in texture. In the experiments performed in the present study, no recognisable quench minerals were identified. Most crystals are relatively large (at least 5x5 μm) and euhedral (Plate 5.1). Crystals generally become smaller at higher temperatures, possibly because they are reaching the limits of their stability. However, all Mg nos. are consistent with formation at equilibrium. It has been widely documented (Chapter 3) that partial melts of hydrous peridotite tend to exsolve quench crystals. It is therefore likely that in the present experiments, quench overgrowths have grown on equilibrium crystals and have modified the composition of the melt during cooling (Section 5.2.4). However, the quench crystals are too small to be detected by the electron microprobe, and consequently all phases analysed by EPMA are thought to have formed at equilibrium.

Although one function of the olivine bucket was to separate the starting material from the capsule walls and so prevent loss of iron into the platinum, the consistent zoning of most minerals from Fe-rich in the core to Fe-poor in the rim is almost certainly due to some progressive iron loss. The extent of this has not been quantified as the run products were not analysed in bulk.

PLATE 5.1

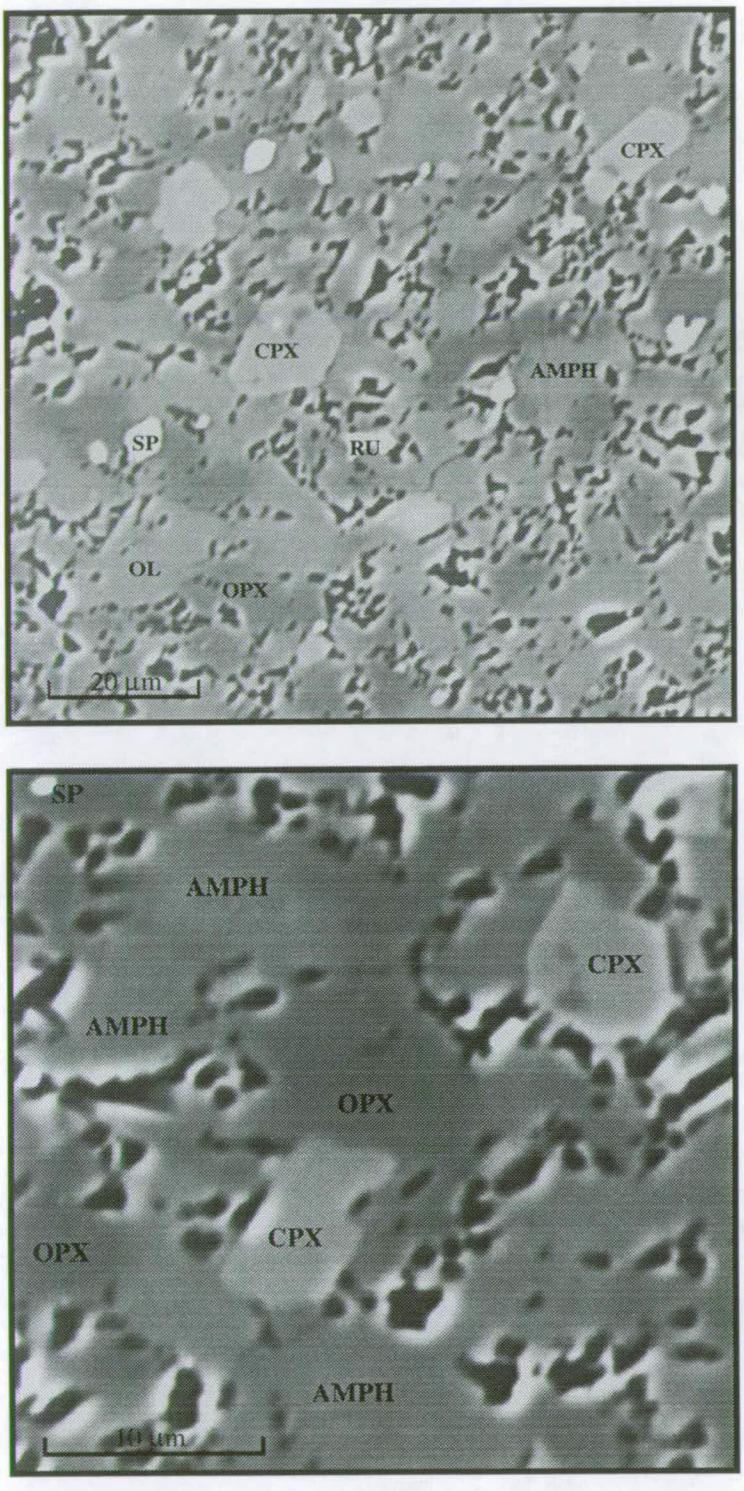

Back-scattered electron images of a polished section of ED143 showing crystals of olivine (OL), orthopyroxene (OPX), clinopyroxene, (CPX), amphibole (AMPH), spinel (SP), and rutile (RU). The interstices contain melt.

Comparison with other studies

These experiments are very similar to those performed by Green (1973). His data suggest that the solidus at 1.8 GPa lies between 970°C and 980°C, only a few degrees below the amphibole-out curve. At approximately 1010°C ilmenite disappears followed by clinopyroxene at just under 1100°C. The orthopyroxene curve has not been extrapolated, but is inferred to fall at a higher temperature than clinopyroxene-out. Mineralogical boundaries inferred from the present study are at a consistently higher temperature (by 20°C to 50°C) than those of Green (*op. cit.*), even though the major element composition of the starting material in both sets of experiments is identical (see Table 5.9). Although the data from Green (*op. cit.*) were derived from interpolation of results at other pressures, the errors inherent from these estimates are not enough to explain the discrepancy.

Table 5.9: The position of the main mineralogical boundaries for water-saturated peridotite at 1.8 GPa: a comparison of Green (1973) with the present study.

Mineralogical boundary	Green (1973)	The present study
Solidus	970°C - 980°C	≈1010°C
Amphibole-out	980°C - 990°C	≈1032°C
Ilmenite-out	1010°C	1020°C - 1032°C
Rutile-out	n.a.	1032°C - 1125°C
Clinopyroxene-out	≈1100°C	≈1125°C
Orthopyroxene-out	>1100°C	≈1150°C

Green (1973): values were interpolated from experiments conducted at 1.0 GPa, 2.0 GPa and 3.0 GPa. This study: boundaries were inferred from the presence or absence of certain phases in run products. In some cases the presence of very small anhedral crystals was taken to imply that the break-down temperature had almost been reached.

It is possible that I have failed to detect melting in the lower temperature experiments, and that Green (1973) produced but did not find amphiboles in higher temperature experiments. However, the consistency of the discrepancy suggests that it is significant: reactions occur at a higher nominal temperature in the present study. This could be explained by poor temperature calibration, although as no poisoning of the thermocouple was detected in these experiments, it is unlikely that the nominal temperature is incorrect. However, in the experiments referred to in Table 5.9, the thermocouple was positioned further away from the starting mixture than in later experiments[5]. Therefore it is possible that the thermocouple bead was in the hot spot

[5]This is because the capsules used in these experiments were filled in such a way that the long second crimp was at the top of the capsule (see Section 4.3.1). In addition, very slight thermocouple extrusion was observed in some experiments, but was rectified by changing the thermocouple sleeve material. It was felt that the extrusion was insignificant (<0.5 mm).

of the furnace whereas the charge was positioned beneath the hot-spot 'plateau', and consequently experienced a lower temperature than the thermocouple. For an independent measure of temperature, the two-pyroxene thermometer of Wells (1977) is used. Results are given in Table 5.10. The temperature calculated from the pyroxenes is higher than the nominal temperature for ED121, although it is within error. It is also within error of the nominal temperature in ED143. For the two other run products that produced measurable orthopyroxene-clinopyroxene pairs, the calculated temperature is approximately 30°C lower than the nominal temperature, although errors are relatively large.

Table 5.10: Comparison of nominal temperature of forward experiments with temperature calculated from pyroxene compositions using the method of Wells (1977).

Experiment	Temperature	
	nominal	**inferred from pyroxenes**
ED121	980±3°C	990±10°C
ED133	1010±3°C	978±28°C
ED143	1020±3°C	1008±47°C
ED137	1032±3°C	1007±15°C

If the charge were positioned beneath the temperature plateau then as well as experiencing a lower temperature it would be in a temperature gradient (see Section 4.3.4). If this were the case it would be likely to be reflected in the mineralogy and mineral chemistry of the run product. Although these capsules were not sectioned longitudinally, a record was made of the position in the capsule from which each mounted and polished section was obtained. Any amphibole from experiments is generally present towards the base of the charge along with clinopyroxene, whereas the more refractory olivine and orthopyroxene are usually present at the top. It is not clear whether this zoning in mineralogy is controlled by changes in temperature. Melt, when present, appears to be distributed throughout the charge and there is no evident relationship between mineral compositions and height within the charge, suggesting that any temperature gradient is relatively small and probably not responsible for the observations noted (Lesher & Walker, 1988).

In summary, capsules at the same nominal temperature appear to have undergone less melting in this study relative to that of Green (1973). It is possible that this may be because the capsule is positioned out of the hot spot generated by the furnace. However, this is unlikely, and is not supported by any mineralogical evidence.

Despite these uncertainties, the observations regarding mineral compositions are still valid. The main compositional changes caused by increasing temperature are summarised in Table 5.11.

Table 5.11: Summary of changes in mineral compositions with increasing temperature of experiment.

Mineral	Changes with increasing temperature
Olivine	Mg no. ⇑
	CaO ⇓
Orthopyroxene	Mg no. ⇑
	Cr_2O_3 ⇑
	Al_2O_3 ⇓
	TiO_2 ⇓
Clinopyroxene	Mg no. ⇑
	Na_2O ⇑
Amphibole	Mg no. ⇓
	Cr_2O_3 ⇓
	CaO ⇓
	Na_2O ⇓
Spinel	TiO_2 ⇑
	Al_2O_3 ⇓
	Cr_2O_3 ⇑

The Mg no. of olivine, orthopyroxene and to a lesser extent clinopyroxene all increase with increasing temperature. This is in contrast to amphibole which becomes less magnesian with increasing temperature. Cr_2O_3 increases in orthopyroxene and spinel, but decreases in amphibole. Na_2O also decreases in amphibole whereas it increases in clinopyroxene. There is a decrease in Al_2O_3 in both orthopyroxene and spinel, and a decrease in CaO in both olivine and amphibole. However, as the proportions of each mineral also change with temperature, these observations on their own cannot lead us to infer the melt composition. Nevertheless, there have been some studies which have derived relationships between melts and residual phases from which we can predict some properties of the melt in these experiments:

- perhaps the most widely used relationship between olivine and melt is that found by Roeder & Emslie (1970) who measured the composition of olivine and coexisting melt from a number of experiments and derived an exchange relationship between the Fe^{2+}/Mg ratio in the melt and in coexisting olivine. This relationship is used in the method of calculation of melt composition in these experiments. See Section 5.2.4.

- Jurewicz & Watson (1988) measured the calcium distribution coefficient between many experimental olivine/melt pairs, and found that it was dependent on the oxygen fugacity of the system and the calcium content of the melt, whereas temperature did not appear to have much effect. The partition coefficient for calcium (weight ratio of calcium in the olivine to that of the melt) is given by:

  $$D = 0.01\ \{(-0.08\pm0.015)(\%fo)+(9.5\pm0.2)\} \qquad (5.8)$$

  where %fo is the molar percentage of forsterite in the equilibrium olivine. The distribution coefficient translates to a value of approximately 0.02 in these experiments. In the present study the calcium content in the equilibrium olivine decreases with temperature (Fig. 5.2). Therefore the calcium content in the melt is also expected to decrease.

Major-element mineral-mineral distribution coefficients derived from these experiments are shown in Table 5.12, along with some values yielded by previous studies. The counting errors for some elements are so high as to render the results of little use. For example K content in orthopyroxene is so low that the errors on the value of D (amph/opx) can be greater than 100%. Nevertheless, the majority of calculated distribution coefficients in Table 5.12 have relatively small errors. Sodium and potassium partition strongly into hornblende[6] as do titanium and chromium (although to a lesser extent). However manganese and nickel favour olivine and orthopyroxene. Some partition coefficients show clear trends with temperature reflecting the changes in mineral composition already noted. For example, D (amph/cpx) and D (amph/opx) for Cr both decrease with increasing temperature mirroring the decrease in chromium content in amphibole. The simultaneous increase in sodium content in clinopyroxene and decrease in sodium content in amphibole with temperature are represented by the large drop in D (amph/cpx) for sodium.

[6]The value for D (amph/cpx) reported in this study is higher than those measured previously in ultramafic compositions (Gilbert *et al.* 1982).

Table 5.12: Partition coefficients of minor elements between coexisting mineral phases in these forward experiments at 1.8 GPa.

	ED121 980°C		ED133 1010°C		ED143 1020°C		ED137 1032°C		From literature
D (amph/cpx)									
Ti	1.62	(0.04)	1.97	(0.85)	2.04	(0.43)	1.75	(0.48)	1.3-7.1
Na	7.71	(0.87)	5.93	(0.76)	5.73	(0.78)	3.27	(0.77)	2.0-3.4
Mn	0.95	(0.28)	0.74	(0.34)	0.83	(0.61)	1.78	(0.82)	0.2-0.8
Cr	1.37	(0.15)	1.21	(0.17)	1.01	(0.47)	0.22	(0.07)	0.13-1.3
Ni	1.33	(0.50)	2.39	(0.65)	1.39	(0.68)	1.69	(1.01)	
D (amph/opx)									
Ti	4.79	(0.25)	6.20	(2.69)	5.67	(0.34)	4.92	(1.27)	1.9-6.2
Na	42.52	(33.25)	68.73	(45.16)	56.07	(34.43)	44.49	(29.61)	
K	17.78	(9.30)	28.13	(21.34)	97.54	(88.49)	42.57	(63.05)	
Mn	0.79	(0.43)	0.67	(0.27)	0.55	(0.36)	1.13	(0.32)	
Cr	2.10	(0.29)	1.81	(0.23)	1.68	(0.69)	0.31	(0.07)	1.1-4.3
Ni	0.95	(0.39)	1.43	(0.58)	1.11	(0.44)	0.92	(0.39)	
D (amph/ol)									
Ti	19.38	(13.29)	n.a.		35.00	(15.10)	31.83	(17.50)	
Mn	0.68	(0.22)	n.a.		0.65	(0.49)	1.05	(0.29)	1.2-1.7
Cr	9.11	(2.28)	n.a.		10.38	(3.76)	2.33	(0.88)	
Ni	0.28	(0.11)	n.a.		0.30	(0.10)	0.29	(0.12)	
D (cpx/opx)									
Ti	2.96	(0.15)	3.14	(0.39)	2.78	(0.59)	2.80	(0.42)	
Al	1.26	(0.08)	1.48	(0.16)	1.34	(0.32)	1.32	(0.18)	
Na	5.52	(4.31)	11.58	(7.60)	9.79	(6.01)	13.60	(8.57)	
K	0.53	(0.27)	0.72	(0.52)	1.26	(1.13)	1.57	(2.32)	
Mn	0.83	(0.39)	0.91	(0.23)	0.66	(0.14)	0.64	(0.15)	
Cr	1.54	(1.47)	1.49	(1.86)	1.66	(1.99)	1.40	(1.53)	
Ni	0.70	(0.12)	0.59	(0.30)	0.78	(0.36)	0.54	(0.24)	

Standard deviations are in parentheses. Values from the literature were collated by Gilbert *et al.* (1982).

Comparison with natural rocks

As the aim of this project is to model the conditions above a subducting slab, it is instructive to compare the minerals formed in these experiments with minerals in natural amphibole peridotites. Amphiboles have been found in a number of mantle xenoliths both from within-plate localities (Boettcher *et al.*, 1979) and at plate-collision margins such as Japan (Aoki, 1970) or Alaska (Francis, 1976a,b). Although pargasites and titanian pargasites are the most common, potassium richterites and kaersutites have also been found (see review by Dawson & Smith (1982)). However, detailed petrological and textural studies have revealed that in many cases the

amphiboles are not primary[7]. Primary amphiboles from five xenoliths are shown in Table 5.13.

Table 5.13: Amphiboles from mantle xenoliths.

NATURAL AMPHIBOLES	a	b	c	d	e	f
SiO_2	44.73	49	45.7	43.17	45.99	55.4
TiO_2	0.29	0.9	0.01	0.18	0.08	0.46
Al_2O_3	12.58	7.5	11.1	14.81	12.91	0.99
Cr_2O_3	2.37	2.8	2.64	4.07	3.42	0.48
FeO	19.17	20.8	11.1	18.37	18.45	2.25
MgO	10.95	9.6	20.2	11.55	9.07	22.9
CaO	3.84	4.1	3.2	3.17	4.79	6.74
Na_2O	0.43	1	1.34	0.9	0.92	3.82
K_2O	0.11	0.06	0.18	0.05	0.07	4.63
MnO	2.43	2.1	2.1	1.47	3.14	
NiO			0.36			
Fe_2O_3	1.1					
TOTAL	98	97.9	97.93	97.74	98.84	97.67

a - sodian pargasitic hornblende in a lherzolite xenolith in an alkali basalt from Ataq, South Yemen (Varne, 1970); b - subcalcic sodian edenite in lherzolite nodule from Engaruka, Tanzania (Dawson & Smith, 1982); c - edenitic hornblende in harzburgite nodule in kimberlite from Monastery mine (Dawson & Smith, 1975); d - pargasite in lherzolite from Eifel, West Germany (Stosch & Seck, 1980); e - magnesio-taramite in lherzolite from Nunivak Island, Alaska (Francis, 1976); f - K richterite, average of twenty-two samples from the Bultfontein kimberlite, South Africa (Dawson & Smith, 1982).

In many respects the experimentally-produced amphiboles are similar in composition to mantle amphiboles (Fig. 5.14) although the experimental amphiboles have higher Mg nos., higher TiO_2 contents and lower alkalis (Fig. 5.15). These discrepancies are less marked for the subsolidus amphiboles.

[7]Often the amphiboles appear to have formed after the other minerals, during ascent of the rock or as a result of metasomatism by alkali-rich fluids (e.g. Wilshire *et al.*, 1980). In other cases amphibole is interpreted to be the remains of an intercumulus liquid (Dawson & Smith, 1982). The amphiboles whose compositions are reported in Table 5.13 are thought to be primary.

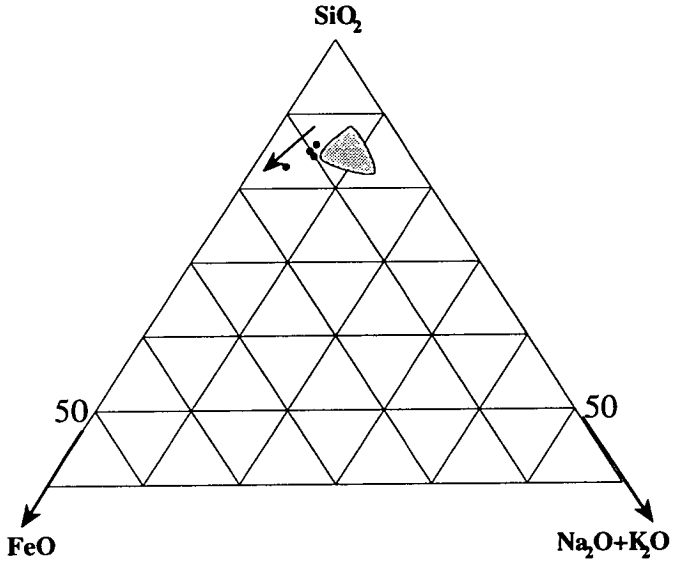

Figure 5.14: Triangular diagram showing a comparison between natural and experimental amphiboles. Natural amphiboles (shaded area) are xenolithic, thought to have formed under mantle conditions; experimental amphiboles were produced in forward experiments at 1.8 GPa. The arrow indicates the change in composition with increasing temperature.

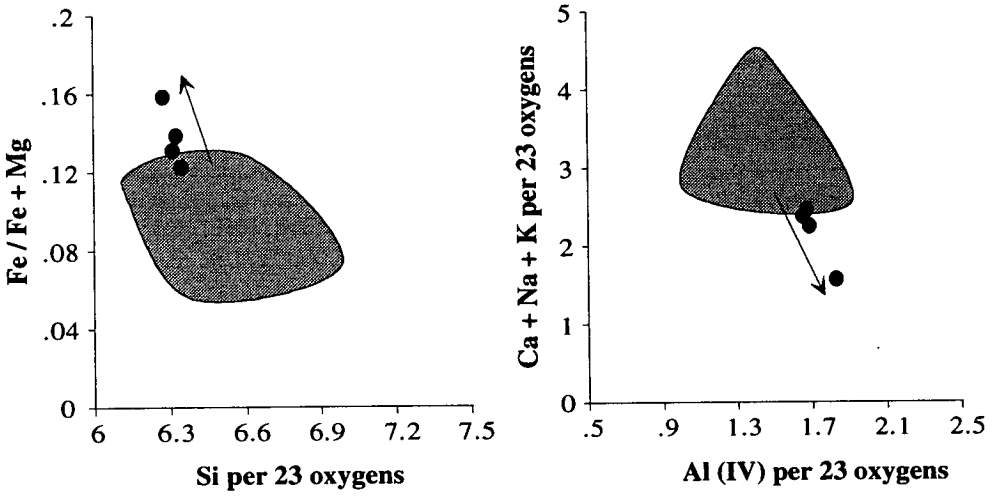

Figure 5.15: A comparison between natural and experimental (1.8 GPa) amphiboles. See caption to Figure 5.14.

Pyroxenes in equilibrium with the natural amphiboles considered above are also similar in composition to the experimentally produced pyroxenes (Fig. 5.16).

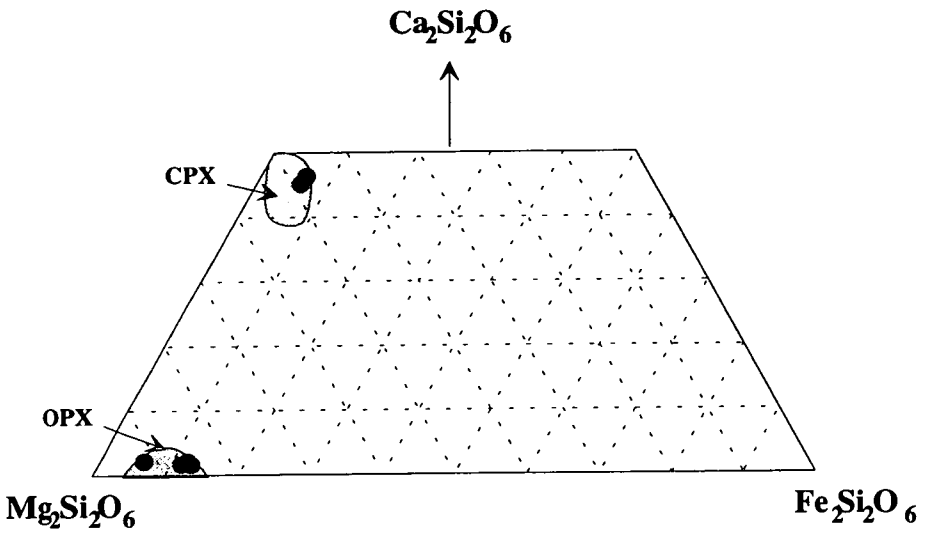

Figure 5.16: Pyroxene quadrilateral showing the compositions of orthopyroxene and clinopyroxene from the forward experiments at 1.8 GPa (black dots) and the range in compositions of pyroxenes found in amphibole-bearing mantle xenoliths.

The range in composition of spinels from xenoliths is shown in Figure 5.17. Again, the experimentally-produced spinels fall within the natural range.

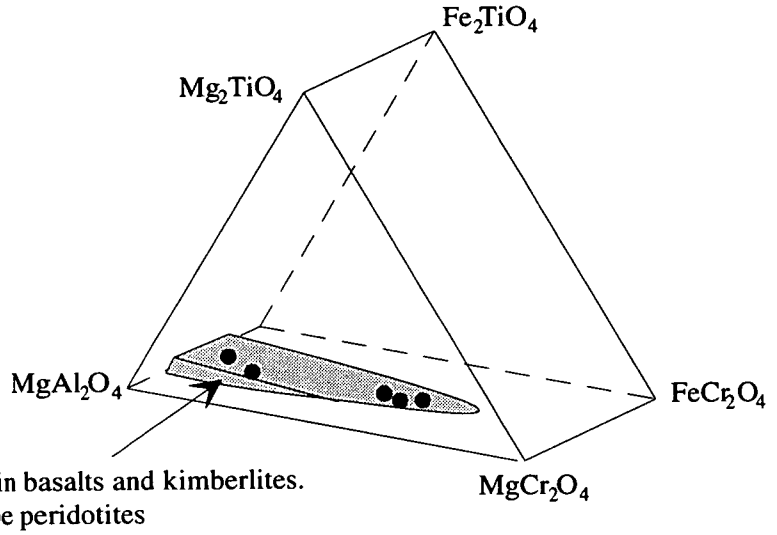

Figure 5.17: Spinel prism (see text) showing spinels produced in forward experiments at 1.8 GPa (black dots) and a range of spinels found in mantle xenoliths and alpine-type peridotites. After Haggerty (1976).

To conclude, it has been shown that the minerals produced in these forward experiments at 1.8 GPa were formed at equilibrium and resemble their natural mantle equivalents. The melt composition from these experiments is discussed overleaf.

5.2.4 Melt composition

Determination of melt composition

The problems encountered in the determination of melt composition have been discussed fully in Chapter 3. It is known that during quenching of an experiment, the composition of the interstitial melt can be modified as a result of quench growth. Thus, the remaining interstitial glass does not necessarily reflect the equilibrium melt composition and cannot be used to predict that composition. In this study, the method of Odling *et al.* (*submitted*) was used in an attempt to overcome these problems. This method involves the production during the experiment of synthetic melt inclusions, which can be analysed subsequently by EPMA, in an olivine crystal. In the present experiments, each capsule contained a single crystal of olivine, drilled to form a bucket into which the starting material was loaded. During the experiment, melt migrates into the olivine crystal along microfractures, and isolated inclusions form as these fractures anneal. During the quenching process, small olivine crystals or platelets precipitate on the walls of the inclusion. This is facilitated by the expansion of the olivine phase field with the concurrent decrease in pressure experienced during the quenching process. Furthermore, it is thought that the walls of the inclusion will act as nucleation sites for the growth of olivine crystals. Assuming that this is an equilibrium process, the composition of these crystals can be predicted by the Fe-Mg exchange relationship of Roeder & Emslie (1970).

$$X_{Fe\,/\,Mg}^{Ol\,/\,Liq} = \left(\frac{X^{Fe^{2+}}}{X^{Mg}}\right)_{Ol} \Big/ \left(\frac{X^{Fe^{2+}}}{X^{Mg}}\right)_{Liq} = \text{constant} \qquad (5.9)$$

Experiments on anhydrous systems performed by Roeder & Emslie (*op. cit.*) indicated that the value of the constant ranged from 0.26 to 0.36 with a mean of 0.3, although more recent work has implied that it may be higher for hydrous systems (see the discussion in Section 5.3.2). Using the relationship shown above (and estimating the value of the constant), the composition of olivine (composition O1) in equilibrium with the melt inclusion (composition L1) is calculated. This olivine composition is then added numerically to the inclusion composition in a small increment (0.01 wt%) to form a new liquid composition (L2). The composition of olivine in equilibrium with the new liquid composition is then calculated using

Equation 5.9, and 0.01 wt% of this new olivine composition (O2) is added to the liquid composition (L2) to form a new liquid composition (L3). This process is repeated, with the calculated olivine composition becoming more forsteritic until its Mg no. equals that of the equilibrium olivine. At this point, it is considered that the liquid composition in equilibrium with this is the composition of the equilibrium melt during the experiment. Mote that in some experiments, particularly those that involve small-degree partial melting, analyses of some small melt inclusions contain more olivine component than the equilibrium melt, due to overlap of the electron beam onto the olivine bucket. Olivine is subtracted from these analyses incrementally until the chosen value for the constant in Equation 5.9 is achieved.

There are a number of inherent assumptions in this technique, discussed below:

1. It is assumed that the only crystals to quench in the melt inclusions are olivines. No quench crystals have been identified in melt inclusions in this study. Using a scanning electron microscope, melt inclusions from anhydrous experiments were examined using a scanning electron microscope (Odling, *pers. comm.*) and although no quench crystals have been identified it was inferred that a thin layer of olivine platelets had quenched onto the walls of the inclusion. Addition of water to the peridotite system causes the olivine phase field to expand (Chapter 3), and therefore it is likely that in the hydrous experiments performed in this study, olivine will have precipitated from hydrous melt inclusions on quenching.
2. It is assumed that the formation of quench crystals is an equilibrium process. This is the only way in which we can predict the composition of the quench olivine.
3. A value must be assumed for the Fe-Mg exchange coefficient of Roeder & Emslie (1970). Roeder & Emslie (*op. cit.*) determined experimentally, a range of values with an average of 0.3. More recent work (Nicholls, 1974) has indicated that the value may be higher (up to 0.4) for hydrous experiments. In this study, a value of 0.3 was assumed, but results of reversal experiments will show that it may be more appropriate to use a value of 0.4. As the value assumed for the exchange coefficient increases, more olivine must be added to the melt inclusion composition in order to derive the equilibrium melt composition. Therefore melt compositions calculated assuming a value of 0.4 for the exchange coefficient are more olivine rich than the compositions calculated assuming a value of 0.3.
4. It is assumed that all iron in the system is ferrous (Fe^{2+}). However, as the experiments are buffered to NNO, there will be some ferric iron present (Fe^{3+}), predominantly in the melt, as olivine does not accommodate Fe^{3+} easily. The Fe/Mg exchange coefficient used in the calculation of the equilibrium melt

composition is derived from the ratios of ferrous iron (Fe^{2+}) and magnesium in olivine and melt (Equation 5.9). If there is some Fe^{3+} in the melt then the Mg/Fe^{2+} ratio of the melt inclusion is underestimated by assuming that all Fe is Fe^{2+}. Therefore, the amount of olivine to be added to the melt inclusion composition is overestimated, and the true equilibrium melt composition should be less olivine rich than that calculated. Fortunately, any underestimation that may occur is not likely to be very significant. A value of 0.016 for the ratio of ferric to ferrous iron in a melt produced at 1020°C, buffered to NNO, and with the composition of a typical melt inclusion from ED143 has been calculated from the empirical relationship of Sack *et al.* (1980). The equilibrium melt has been recalculated from the melt inclusion compositions in this experiment, assuming this value for the ratio of Fe^{3+} to Fe^{2+}. Results show that the new predicted melt composition is approximately 0.1% less olivine rich than the old predicted melt composition.

5. This technique will only work if olivine does not take part in any reactions, i.e. if the system is olivine saturated. In these experiments, olivine is stable up to the liquidus. Furthermore, the Mg no, of the olivine bucket was chosen to be similar to the equilibrium olivine.

Most of the assumptions made will control the amount of olivine component added to or subtracted from the melt inclusion compositions, and therefore even if these assumptions are incorrect, it should be possible to derive the calculated melt composition by addition or subtraction of olivine component, using the results of reversal experiments to evaluate the accuracy of the first estimate.

The olivine buckets from the experiments were retrieved and mounted in epoxy resin. After grinding and polishing, a microscope was used to check for melt inclusions which are brown in colour. Care had to be taken not to confuse melt inclusions with fluid inclusions which are generally smaller and colourless. If necessary, samples were polished further to reveal inclusions beneath the surface. Melt inclusions were found in four of these forward experiments, although not in ED133 despite the presence of interstitial melt. They are generally cuspate in shape and ranged from approximately 5x10 μm at 1020°C to approximately 50 μm at 1150°C (Plate 5.2). Inclusions were analysed by EPMA using a beam current of 5 nA rastered over an area of 8x8 μm in order to minimise sodium mobilisation (see Section 4.8.2). In theory, the analysed area should consist of the evolved glass composition which is low in olivine component. However due to the relatively small size of many of the inclusions, in particular those formed during low degree partial melting, there was

PLATE 5.2

Back-scattered electron images showing melt inclusions within the olivine bucket from a) ED244 and b) ED101. Note that the very bright patches within the melt inclusions from ED101 are remains of the gold coat that was used for analyses by SIMS.

sometimes overlap onto the surrounding olivine bucket. In addition, the shape of the inclusion governs the surface area to volume ratio and consequently the extent of modification by quenching. Analyses therefore encompassed a range of compositions from extremely evolved glass to more olivine-rich compositions in which there is a large overlap onto the olivine bucket (Fig. 5.18). It should be noted that analyses that overlap onto the olivine bucket may be less accurate than analyses of glass alone, as the corrections used in EPMA (Section 4.8) are based on the assumption that the analysis is homogeneous.

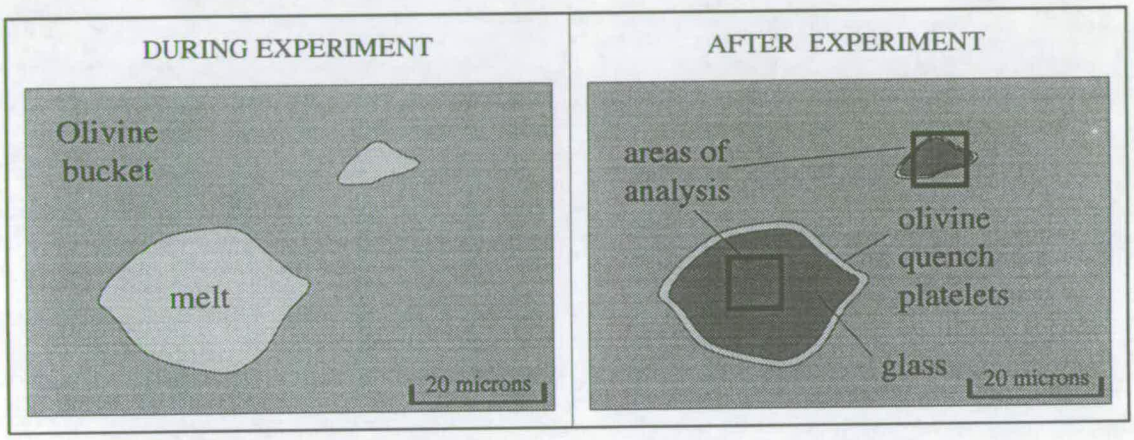

Figure 5.18: A cartoon illustrating melt inclusion formation. During the experiment, melt becomes trapped in the olivine crystal as fractures anneal out. During quenching, small undetectable platelets of olivine exsolve onto the inclusion walls, leaving a glass that is depleted in olivine component. Analysis of a large melt inclusion using a rastered electron beam (denoted by the black square in the right-hand cartoon) will yield a composition to which olivine must be added in order to derive the equilibrium melt composition. However, in analysing a small melt inclusion, the rastered beam may overlap onto the olivine bucket and thus yield an analysis from which olivine must be subtracted.

Results

The methods and results of this technique are illustrated with reference to two experiments: ED143 at 1020°C in which the melt inclusions were relatively small, and ED91 at 1150°C which experienced a much higher degree of melting and consequently formed larger melt inclusions. Seven analyses from ED143 are shown in Table 5.14. The original totals average approximately 80%, due to the presence of an undetermined amount of water in the glass.

Table 5.14: Selected melt inclusion analyses (normalised to 100%) from ED143, the equilibrium melt composition calculated from each melt inclusion analyses, and the average melt.

MELT FROM ED143

Melt inclusions (normalised to 100%)									
SiO_2	56.69	56.01	53.81	54.53	52.51	51.80	53.62		
TiO_2	0.96	0.87	1.19	1.33	0.79	1.63	1.02		
Al_2O_3	22.68	23.63	22.09	22.66	23.04	21.18	19.20		
Cr_2O_3	0.00	0.02	0.04	0.00	0.01	0.00	0.04		
FeO	1.66	2.06	4.07	2.55	3.52	4.34	3.59		
MgO	0.74	1.45	4.66	3.42	5.97	8.85	9.73		
CaO	14.26	13.30	11.67	13.00	11.80	10.06	10.14		
Na_2O	2.31	2.09	1.68	1.87	1.68	1.07	1.96		
K_2O	0.52	0.40	0.56	0.45	0.50	0.69	0.46		
MnO	0.17	0.12	0.10	0.13	0.09	0.18	0.12		
NiO	0.01	0.05	0.13	0.06	0.09	0.20	0.12		
(Orig. total)	(85.06)	(82.29)	(77.13)	(81.20)	(81.90)	(83.92)	(88.00)		
Mg no.	44.3	55.6	67.1	70.5	75.1	78.4	82.9		
Calculated melt composition:								**Av. [22]**	s.d.
SiO_2	55.83	55.45	53.75	54.67	53.11	52.92	55.52	**53.63**	1.67
TiO_2	0.90	0.83	1.17	1.34	0.83	1.79	1.16	**1.42**	0.63
Al_2O_3	21.52	22.78	21.92	22.86	24.15	23.34	22.09	**22.69**	0.92
Cr_2O_3	0.00	0.01	0.03	0.00	0.00	0.00	0.04	**0.02**	0.02
FeO	2.43	2.51	4.13	2.47	3.20	3.84	2.92	**3.24**	0.84
MgO	2.96	3.05	5.00	3.02	3.90	4.67	3.55	**3.94**	1.01
CaO	13.53	12.82	11.59	13.13	12.37	11.09	11.67	**12.45**	1.64
Na_2O	2.19	2.00	1.66	1.88	1.75	1.18	2.25	**1.81**	0.55
K_2O	0.48	0.39	0.55	0.45	0.51	0.76	0.52	**0.58**	0.21
MnO	0.16	0.12	0.09	0.12	0.09	0.20	0.13	**0.13**	0.03
NiO	0.00	0.04	0.12	0.05	0.09	0.21	0.13	**0.08**	0.06
Mg no.	68.5	68.5	68.5	68.5	68.5	68.5	68.5	**68.5**	
% olivine added or subtracted	5.4	3.8	0.9	-1.0	-4.8	-9.8	-14.1		

The percentage olivine added to (positive numbers) or subtracted from (negative numbers) the analysis to calculate the equilibrium melt composition is shown.

Some oxide contents in the melt inclusions are fairly consistent, for example the Al_2O_3 content ranges from over 19% to under 24%; the SiO_2 content ranges from ~51% to ~57% (Fig. 5.19).

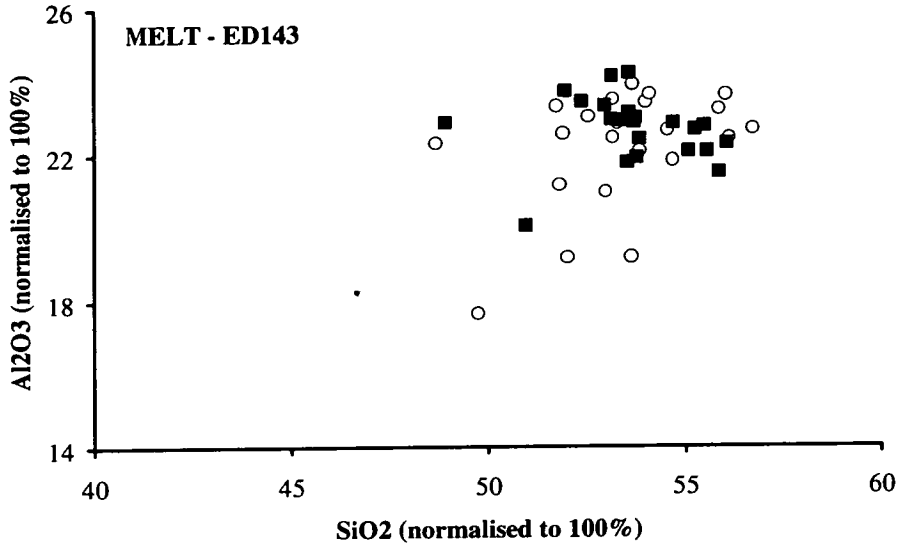

Figure 5.19: Al_2O_3 versus SiO_2 (normalised to 100% total) for melt inclusions (circles) and calculated melt (squares) from ED143.

However, the iron and magnesium oxide contents vary considerably: MgO content varies by over a factor of ten, presumably due to the diversity in olivine content of the areas analysed. In Figure 5.20 analyses fall on a rough mixing line between a low-MgO, low-FeO evolved melt and the equilibrium olivine composition. Four of these analyses are noticeably rich in olivine, probably because there was a large overlap onto the olivine bucket. These have not been used in the calculations. The average Mg no. of the equilibrium olivine in ED143 (Table 5.3) is 87.9. Assuming a value of 0.3 for the constant in Equation 5.9, the Mg no. of the equilibrium melt should be 68.5. Reference to Table 5.14 shows that the values of Mg no. for the analysed melt inclusions fall to either side of 68.5. In other words some analyses with low Mg no. contain less olivine component than the equilibrium melt, whilst other analyses have high Mg nos. and are richer in olivine than the equilibrium melt. Equilibrium melt compositions were calculated (see Table 5.14) from the melt inclusion analyses by incremental addition or subtraction of olivine compositions in equilibrium with the glass composition and with subsequent calculated liquid compositions, as described previously. In these initial calculations the constant in Equation 5.9 is taken to be 0.3 which is the average value derived by Roeder & Emslie (1970). The spread in composition exhibited by the melt inclusions, although still evident, has been much reduced (Figs. 5.19, 5.20).

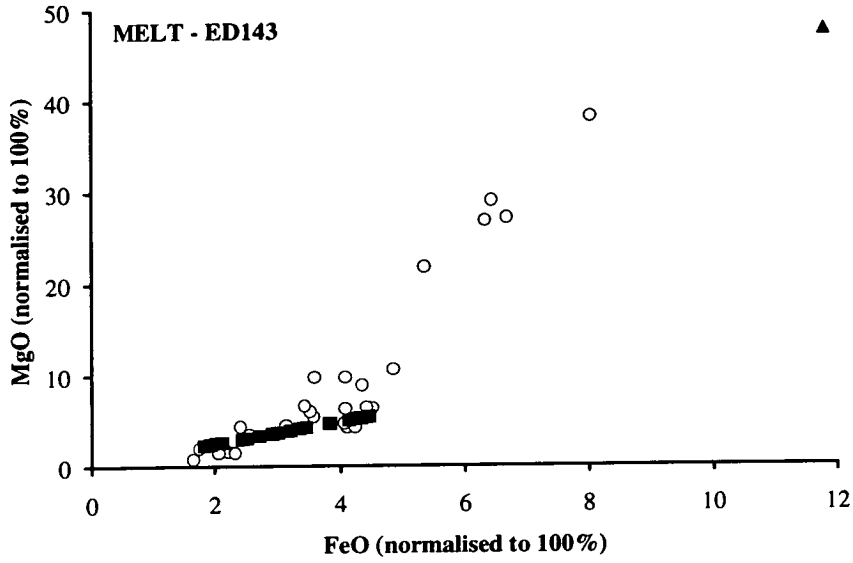

Figure 5.20: FeO versus MgO (normalised to 100% total) for melt inclusions (circles) and calculated melt (squares) from ED143. The equilibrium olivine composition is denoted by a triangle.

In the following discussions, the CIPW-normative compositions of melts and crystalline phases will be illustrated using projections within the basalt tetrahedron from diopside onto the (jadeite + Ca-tschermak's molecule)-olivine-quartz plane and from albite + anorthite onto the diopside-olivine-quartz plane (Fig. 5.21).

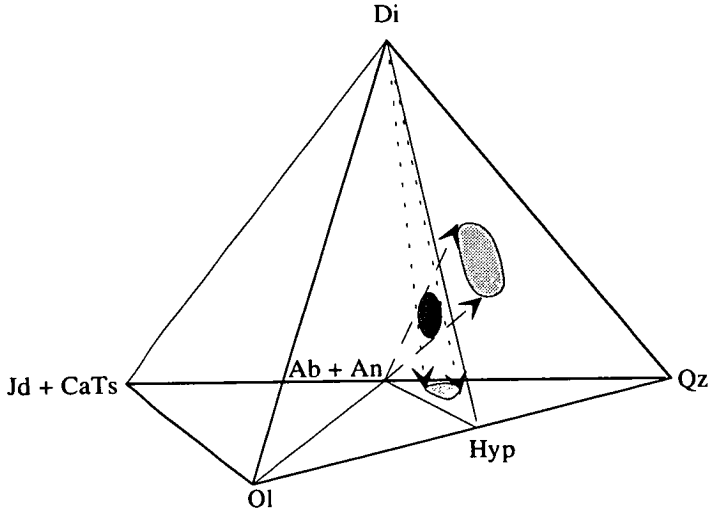

Figure 5.21: The basalt tetrahedron. An arbitrary composition (dark shading) is projected from diopside onto the (jadeite + Ca-tschermak's molecule)-olivine-quartz plane, and from albite + anorthite onto the diopside-olivine-quartz plane. The results of the projections are indicate by lighter shading. These projections will be used in following discussions.

The original melt inclusion compositions and the equilibrium melt compositions calculated from each melt inclusion analysis from ED143 are illustrated on normative projections in Figure 5.22. The calculated melt composition is quartz normative.

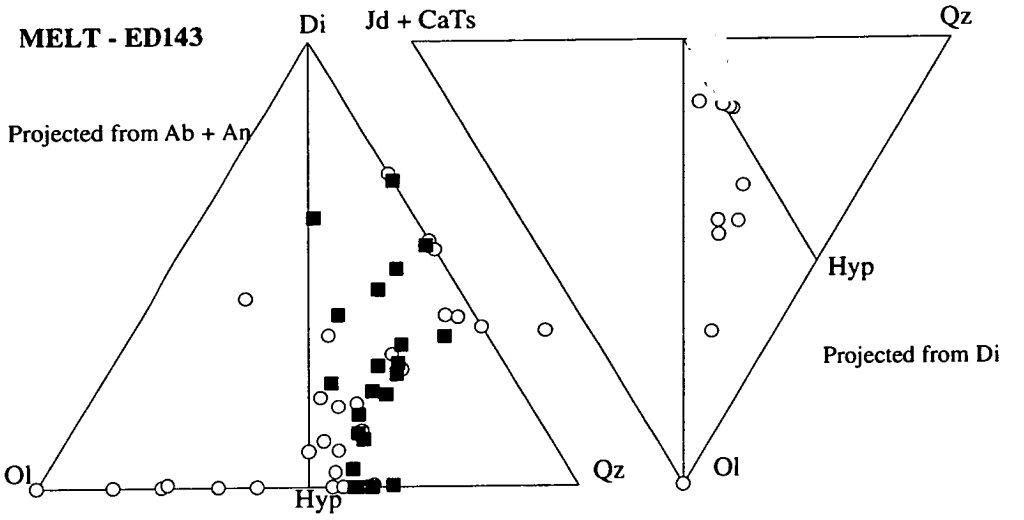

Figure 5.22: Melt inclusions (circles) and calculated melt compositions (squares) from ED143. The CIPW-normative composition are projected within the basalt tetrahedron (Fig. 5.21) from albite + anorthite onto the diopside-olivine-quartz plane, and from diopside onto the (jadeite + Ca-tschermak's molecule)-olivine-quartz plane.

The amount of olivine component added to or subtracted from the inclusion composition in order to derive the equilibrium melt is also shown in Table 5.14. As anticipated, there is a negative correlation between the initial Mg no. of the inclusion and the amount of olivine added, and a positive correlation between the Mg no. and the amount of olivine subtracted (Fig. 5.23).

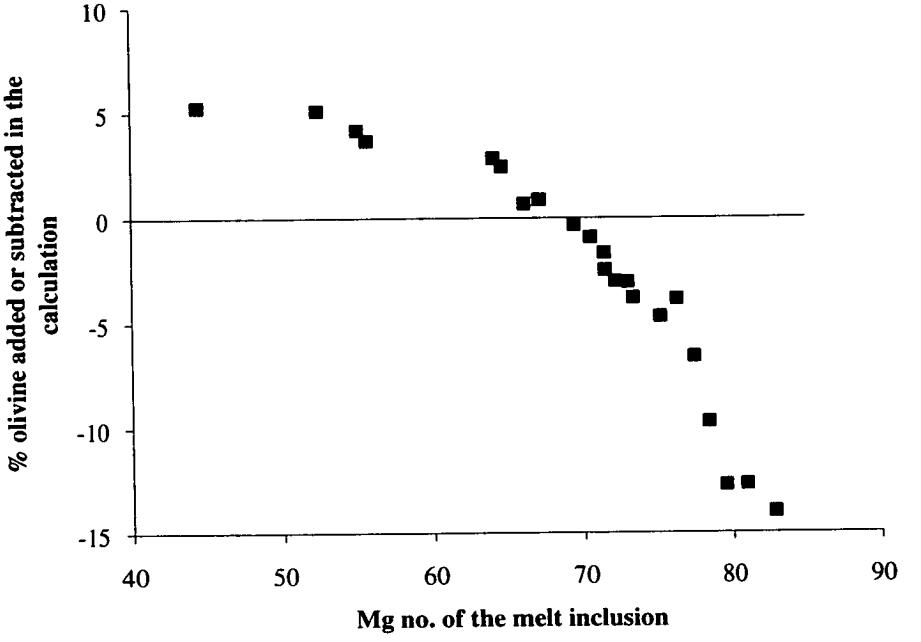

Figure 5.23: Percentage olivine added to (positive numbers) or subtracted from (negative numbers) the melt inclusion composition in order to derive the equilibrium melt composition, plotted against the Mg no. of the melt inclusion.

There is not an exact linear relationship as the amount of olivine added or subtracted is dependent on the absolute MgO and FeO content of the inclusions as well as the Mg no.

In Table 5.15 the average melt compositions calculated assuming different Mg nos. of olivine are shown. There is very little difference between the melt compositions calculated using the maximum, average and minimum values of Mg no. for the equilibrium olivine. Moreover, even when using more extreme values for olivine Mg no., the calculated melt composition does not alter significantly. Therefore, although extremely important, the accurate determination of the Mg no. of olivine is not crucial to the success of this technique.

Table 5.15: Average melt composition derived from melt inclusion analyses in ED143

AVERAGE MELT COMPOSITION FROM ED143

Olivine Mg no.	**86**		**87.64**		**87.85**		**88.06**		**90**	
	average	**s.d.**	**average**	**s.d.**	**average**	**s.d.**	**average**	**s.d.**	**average**	**s.d.**
SiO_2	53.86	(1.66)	53.63	(1.67)	53.60	(1.67)	53.27	(1.68)	53.66	(1.67)
TiO_2	1.45	(0.64)	1.42	(0.63)	1.42	(0.63)	1.38	(0.61)	1.43	(0.63)
Al_2O_3	23.09	(0.94)	22.69	(0.92)	22.64	(0.92)	22.04	(0.91)	22.75	(0.92)
Cr_2O_3	0.02	(0.02)	0.02	(0.02)	0.02	(0.02)	0.02	(0.02)	0.02	(0.02)
FeO	3.08	(0.81)	3.24	(0.84)	3.26	(0.84)	3.45	(0.87)	3.22	(0.84)
MgO	3.19	(0.84)	3.94	(1.01)	4.05	(1.04)	5.22	(1.32)	3.84	(1.00)
CaO	12.67	(1.64)	12.45	(1.64)	12.42	(1.64)	12.10	(1.66)	12.48	(1.64)
Na_2O	1.85	(0.55)	1.81	(0.55)	1.81	(0.54)	1.76	(0.53)	1.82	(0.55)
K_2O	0.59	(0.22)	0.58	(0.21)	0.58	(0.21)	0.56	(0.20)	0.58	(0.22)
MnO	0.13	(0.03)	0.13	(0.03)	0.13	(0.03)	0.12	(0.03)	0.13	(0.03)
NiO	0.08	(0.06)	0.08	(0.06)	0.08	(0.06)	0.08	(0.06)	0.08	(0.06)

Values were calculated assuming various Mg nos. for the equilibrium olivine and a value of 0.3 for the for the exchange relationship of Roeder & Emslie (1970). The shaded area represents the Mg no. of the equilibrium olivine ± 1 standard deviation.

Table 5.16 shows a selection of melt inclusion analyses from ED91, and the melt composition calculated from them.

Table 5.16: Selected melt inclusion analyses (normalised to 100%) from ED91, the equilibrium melt composition calculated from each melt inclusion analyses, and the average melt.

MELT FROM ED91

Melt inclusions (normalised to 100%)

SiO_2	65.28	65.72	65.74	65.54	63.40	56.46	66.70
TiO_2	1.41	1.56	1.71	2.07	1.45	0.84	2.01
Al_2O_3	13.85	14.26	14.03	13.28	13.34	20.05	12.07
Cr_2O_3	0.03	0.04	0.08	0.04	0.13	0.00	0.21
FeO	1.56	1.55	1.65	1.99	3.39	3.55	2.54
MgO	3.49	2.40	1.97	1.98	3.56	2.68	1.13
CaO	11.99	12.30	12.70	12.93	12.67	11.83	13.41
Na_2O	1.36	1.17	1.21	1.55	1.50	3.52	1.23
K_2O	0.50	0.46	0.44	0.41	0.39	0.92	0.45
MnO	0.17	0.23	0.16	0.13	0.18	0.14	0.22
NiO	0.36	0.30	0.32	0.06	0.00	0.02	0.02
(Orig. total)	(78.40)	(81.40)	(79.80)	(84.25)	(80.76)	(85.72)	(75.94)
Mg no.	80.0	73.4	68.0	63.9	65.2	57.4	44.2

Calculated melt composition:								**Av. [21]**	s.d.
SiO_2	65.29	64.93	64.4	63.58	60.63	53.78	62.06	**63.05**	2.76
TiO_2	1.4	1.5	1.61	1.9	1.27	0.7	1.65	**1.55**	0.34
Al_2O_3	13.83	13.78	13.25	12.2	11.68	16.6	9.91	**12.47**	1.55
Cr_2O_3	0.03	0.04	0.07	0.03	0.11	0	0.16	**0.06**	0.06
FeO	1.56	1.77	2.04	2.59	4.12	4.71	4.18	**2.91**	1.10
MgO	3.53	4.01	4.63	5.85	9.31	10.63	9.46	**6.59**	2.48
CaO	11.98	11.89	12	11.88	11.09	9.79	11.02	**11.35**	0.86
Na_2O	1.35	1.13	1.14	1.42	1.31	2.91	1.01	**1.28**	0.51
K_2O	0.5	0.44	0.41	0.37	0.34	0.75	0.37	**0.45**	0.09
MnO	0.17	0.23	0.14	0.12	0.15	0.12	0.17	**0.15**	0.05
NiO	0.36	0.29	0.3	0.05	0	0.01	0.01	**0.15**	0.14
MgO#	80.1	80.1	80.1	80.1	80.1	80.1	80.1	**80.1**	
% olivine added or subtracted	0.2	3.5	5.8	8.6	13.4	19	19.8		

The percentage olivine added to (positive numbers) or subtracted from (negative numbers) the analysis to calculate the equilibrium melt composition is shown.

The original totals are low, presumably due to an undetermined amount of water in the melt. Figures 5.24, 5.25, and 5.26 illustrate the range in composition of the analyses, recalculated to 100%.

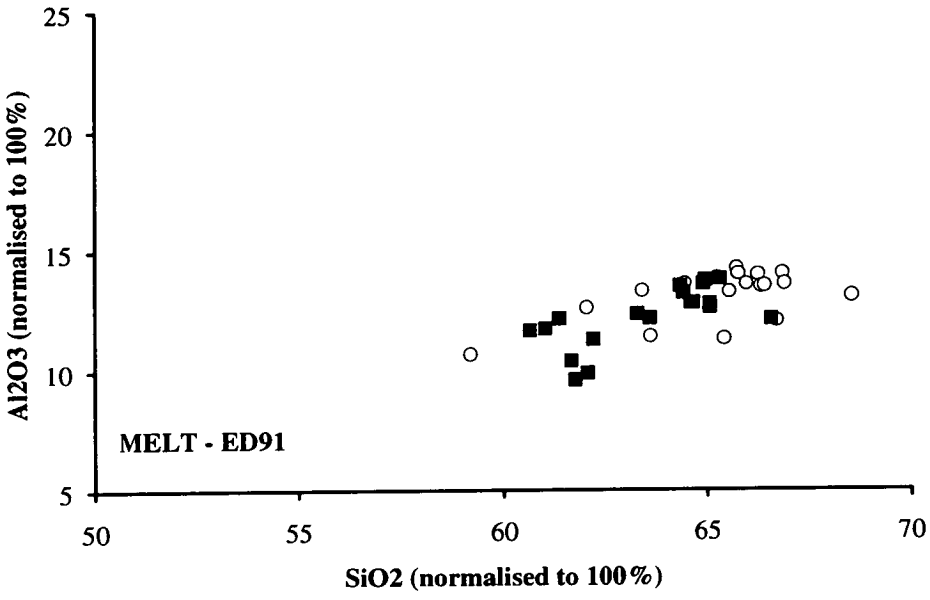

Figure 5.24: Al_2O_3 versus SiO_2 (normalised to 100% total) for melt inclusions (circles) and calculated melt (squares) from ED91.

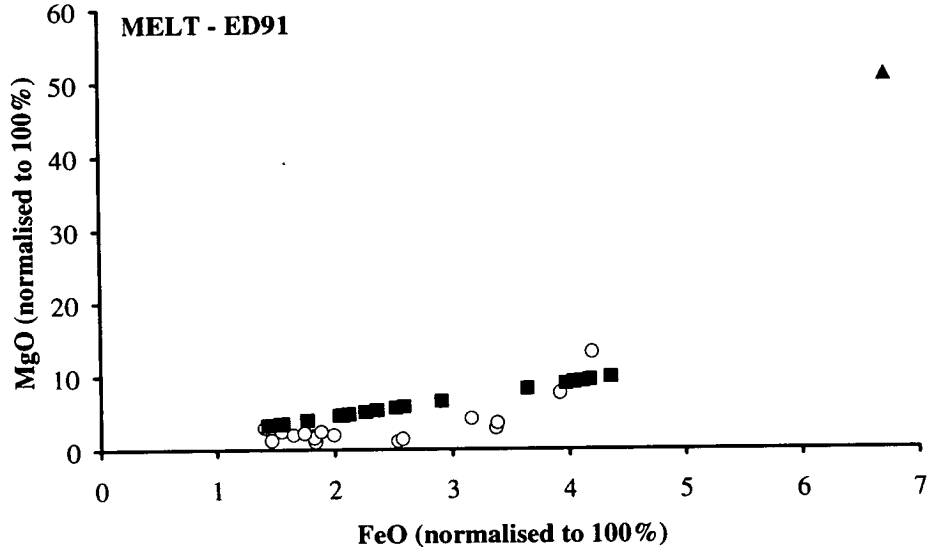

Figure 5.25: MgO versus FeO (normalised to 100% total) for melt inclusions (circles) and calculated melt (squares) from ED91.

The melt compositions, calculated from separate melt inclusions are quartz normative (Fig. 5.26).

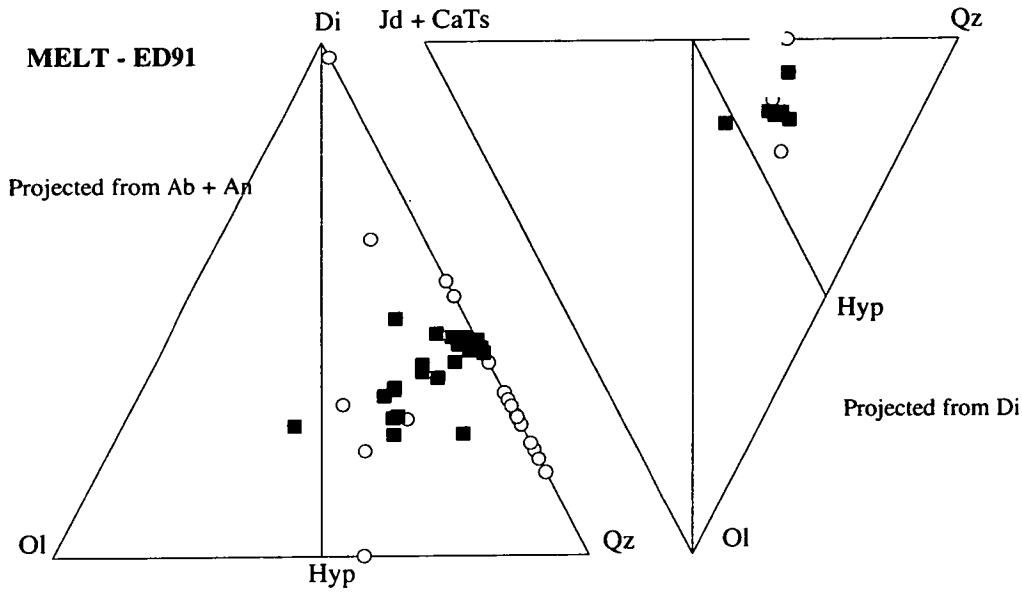

Figure 5.26: Melt inclusions (circles) and calculated melt compositions (squares) from ED91. The CIPW-normative composition are projected within the basalt tetrahedron (Fig. 5.21) from albite + anorthite onto the diopside-olivine-quartz plane, and from diopside onto the (jadeite + Ca-tschermak's molecule)-olivine-quartz plane.

In this experiment the inclusions are large (up to 50 μm) and consequently during analysis there is little if any overlap between the rastered beam and the olivine bucket. Hence all analyses require addition of olivine to reach the required Fe/Mg exchange ratio (Fig. 5.27). Again the calculated melts are less diverse in composition than the melt inclusions, particularly with regard to iron and magnesium oxides.

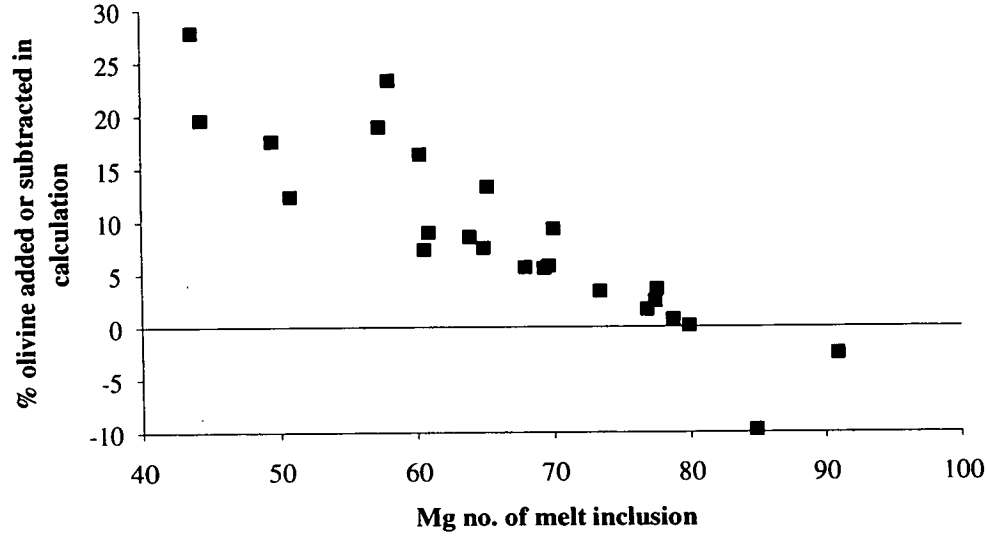

Figure 5.27: Percentage olivine added to (positive numbers) or subtracted from (negative numbers) the melt inclusion composition in order to derive the equilibrium melt composition, plotted against the Mg no. of the melt inclusion.

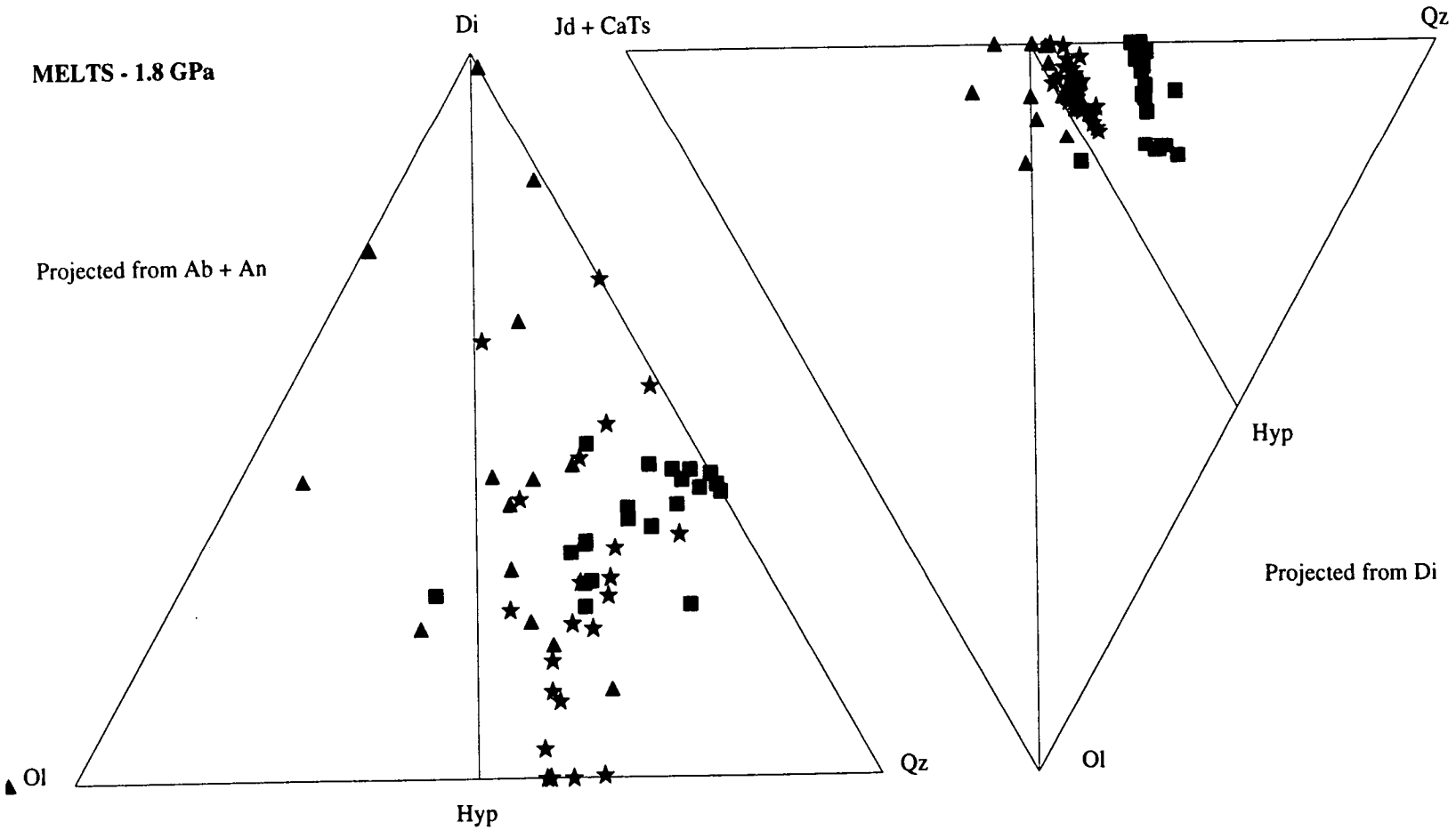

Figure 5.28: Melt compositions from three forward experiments at 1.8 GPa, calculated assuming a value of 0.3 for the Fe/Mg olivine/melt exchange coefficient of Roeder & Emslie (1970). ED143 (1020°C) = stars; ED137 (1032°C) = triangles; ED91 (1150°C) = squares.

The average melt composition for each experiment is calculated by averaging the melt composition predicted from each melt inclusion analysed. Results from three forward experiments are shown in Table 5.17 and Figure 5.28.

Table 5.17: Average melt compositions (and standard deviation) from three forward experiments at 1.8 GPa.

MELT COMPOSITIONS						
Expt.	**ED143**		**ED137**		**ED91**	
Temp.	**1020°C**		**1032°C**		**1150°C**	
	Av.	S.D.	Av.	S.D.	Av.	S.D.
SiO_2	53.63	(1.67)	50.64	(3.86)	63.05	(2.76)
TiO_2	1.42	(0.63)	1.55	(0.99)	1.55	(0.34)
Al_2O_3	22.69	(0.92)	21.68	(1.89)	12.47	(1.55)
Cr_2O_3	0.02	(0.02)	0.03	(0.04)	0.06	(0.06)
FeO	3.24	(0.84)	4.02	(1.18)	2.91	(1.10)
MgO	3.94	(1.01)	5.36	(1.58)	6.59	(2.48)
CaO	12.45	(1.64)	14.04	(3.08)	11.35	(0.86)
Na_2O	1.81	(0.55)	1.80	(0.42)	1.28	(0.51)
K_2O	0.58	(0.21)	0.64	(0.34)	0.45	(0.09)
MnO	0.13	(0.03)	0.13	(0.05)	0.15	(0.05)
NiO	0.08	(0.06)	0.11	(0.08)	0.15	(0.14)

Values were calculated from analyses of melt inclusions in olivine by incremental addition or subtraction of olivine using a value of 0.3 for the Roeder & Emslie (1970) Fe/Mg exchange relationship.

Before the implications of these data are discussed, it is necessary to assess the reliability of the compositions. One methods by which this can be done is by performing reversal experiments.

5.3 REVERSAL EXPERIMENTS

It was decided to test the calculated melt composition from ED143, because this experiment had produced coexisting amphibole and melt. Other phases produced in ED143 were olivine, orthopyroxene, clinopyroxene, spinel, rutile, and ilmenite. The calculated composition of the melt from this experiment was tested by performing several reversal experiments under various conditions. A reversal experiment is one in which the starting material is of the same composition as the calculated melt composition, and the P, T conditions are identical to the forward experiment. In

theory, the run product would consist of 100% melt. However, in practice a reversal experiment will produce mostly melt with a small number of crystals corresponding closely to the compositions of the minerals produced in the forward experiment. Not all of the original phases will be produced in a reversal experiment. For example, spinel is known to form a reaction relationship with melt whereby it produces other phases such as orthopyroxene and olivine.

The reversal experiments in this study were all designed to test the melt composition from ED143. They have been divided into two groups:

- Experiments run in olivine buckets, i.e. a similar capsule geometry to the forward experiment,
- Experiments run in gold capsules without olivine buckets, often containing added olivine component.

The experiments using olivine buckets were performed in 4 mm diameter platinum capsules in ½" talc/boron nitride cells. The starting materials were either sintered oxides or sintered oxide and gel mixtures (which were doped with trace elements). The reversal experiments without olivine buckets were executed, three capsules at a time, in 1 mm diameter gold capsules in ¾" salt cells. The starting materials were sintered oxide and gel mixtures, which had been doped with trace elements. For more details of the experimental procedure, see Chapter 4. The reversal experiments run in olivine buckets and those run without olivine buckets produced slightly different mineralogies and phase compositions, presented below.

5.3.1 Mineralogy

Reversal experiments in olivine buckets

The details of the experiments, and the phases found in run products are listed in Table 5.18.

The third reversal experiment (ED195) was not improved in terms of the reproduction of the phase assemblage of the forward experiment. Nevertheless the results of the subsequent reversals are worthy of note. These further experiments were performed for a number of reasons:

a) to produce fluid quench products (fq in Table 5.18) which could be analysed by EPMA and SIMS (see Chapter 7),
b) to grow large amphibole crystals (see Section 5.5),

c) to produce run products doped with trace elements (ED285 used a doped sintered oxide/gel mixture) with a view to analysing large amphiboles and calculating partition coefficients between amphibole and melt.

Table 5.18: mineralogy of reversal experiments of ED143 performed in olivine buckets.

Expt.	Mix	% H_2O	Temp.	Dur.	Mineralogy									
					melt	ol	opx	cpx	am	sp	ru	ilm	fq	gt
ED143	HAW		1020°C	24 hrs	•	•	•	•	•	•	•	•		
ED192	M3	50	1020°C	2 hrs	•	•	•	•					•	•
ED194	M3	30	1020°C	1 hr	•	•	•		•				•	•
ED195[1]	M3	30	1020°C	2 hrs	•	(•)	•	•	•				○	○
ED220[2]	M3	30	1020°C	24 hrs	•	•	•	•	•				•	•
ED223	M4	35	1020°C	24 hrs	•		•		•				•	•
ED234[3]	M4	57	1020°C	48 hrs	•			•		•			•	
ED238	M4	79	1015°C	48 hrs	•		•							
ED239	M4	63	1010°C	48 hrs			•						•	
ED285[4]	M5	36	1020°C	30 hrs	•		•							•

(melt, olivine, orthopyroxene, clinopyroxene, amphibole, spinel, rutile, ilmenite, fluid quench, garnet). Notes: [1]No olivine powder was used in reversal experiments after and including ED195; [2]nickel from the buffer contaminated the run products; [3]significant contamination by boron; [4]extreme contamination by boron. HAW is Hawaiian pyrolite - 40% olivine; M3 and M4 are sintered oxide starting mixtures of composition close to the calculated melt from ED143. M5 is a gel/sintered oxide mixture of similar composition. See Appendix B for details of the starting compositions.

Those experiments which contained more than 50 wt% initial water did not produce amphibole, possibly due to the dissolution of essential amphibole-forming elements[8]. With the exception of ED234 in which small spinel crystals were found, no reversal experiments produced the minor phases spinel, rutile or ilmenite. This in itself is not a cause for concern as it is probable that the melt reacts with these minerals.

The presence of garnet, however, in most of these reversal experiments is problematical as this was not present as an equilibrium phase in the original forward experiment. One possible explanation for this could have been the choice of a sintered oxide starting material. It is conceivable that the extremely refractory alumina component may have persisted during the experiment and acted as nucleation centres for garnet. However this idea was rejected after garnet was formed in ED285 which used a sintered oxide and gel mixture that was made in such a way that all alumina was in the gel. Therefore the presence of garnet is likely to be due to a miscalculation in the original melt composition.

Olivine was found in four reversal experiments, ED192, ED194, ED195 and ED220. In ED192 and ED194 there were large (up to 50x50 μm) euhedral olivine crystals

[8]Note that all experiments containing 50 wt% initial water or less produced amphibole with the exception of ED285 which contains large quantities of boron and is therefore unreliable.

present towards the top of the capsules. However, the composition of these crystals was similar to the composition of the San Carlos olivine used to make the olivine buckets and the olivine powder that was included at the top of the capsule. It was decided to exclude olivine powder from the remaining reversals. In ED195 small olivine crystals were found next to the walls of the bucket but none were present in the main part of the mix, suggesting that the crystals that were found in ED192 and ED194 had been either residual from the olivine powder or in equilibrium as a result of the modification of the starting material by the addition of the olivine powder. Large olivine crystals were present in ED220. However, as this experiment had been contaminated by the nickel from the buffer, the results were difficult to interpret.
The zoning of the mineralogy in the reversal experiments (particularly those which did not contain added olivine powder) is extremely striking and worthy of note. Plates 5.3 and 5.4 show back-scattered electron images of sections of run products from two reversal experiments, ED195 and ED285. The internal faces of the olivine buckets, generally fairly straight in run products from forward experiments, are irregular and embayed in places and appear to have been partially dissolved. Occasional small crystals (<5 μm wide) of olivine have grown in the embayments. The insides of the buckets are completely coated by a layer (approximately 20-40 μm thick) of radially-aligned orthopyroxene crystals. In ED195 this is followed by a layer of clinopyroxene and occasional amphibole crystals, with garnet restricted to the central part of the mix with the quench from the melt. This texture suggests that the olivine bucket plays an active role in these experiments. This is further supported by the fact that there is less of a zonation in mineralogy in those experiments in which olivine powder was included at the top of the charge. This could be because the olivine powder takes part in any olivine-consuming reaction, in preference to the olivine bucket.

The predicted melt composition from ED143 is quartz normative (Fig. 5.22) and therefore if this liquid is run in a reversal experiment it should not produce olivine. Figure 5.29 illustrates this: the liquid composition (A) lies on a peritectic in which diopside and enstatite can crystallise.

PLATE 5.4

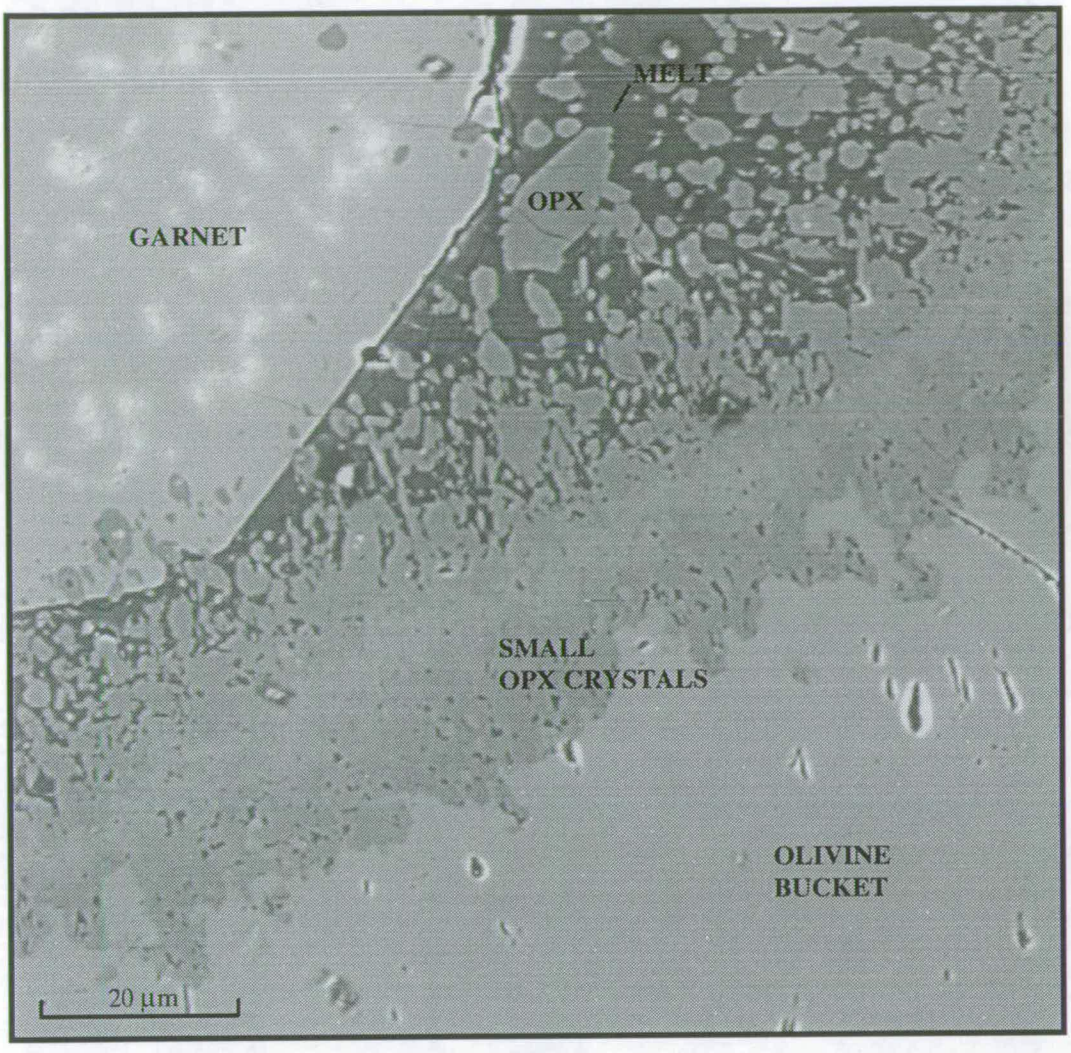

A back-scattered electron image of a polished section of ED285 showing the mineralogical zoning typical of many of the reversal experiments run in olivine buckets. Small crystals of orthopyroxene rim the internal edges of the olivine bucket, which appears to have been partially dissolved. A large crystal of garnet (containing inclusions of clinopyroxene and orthopyroxene) can also be seen.

PLATE 5.3

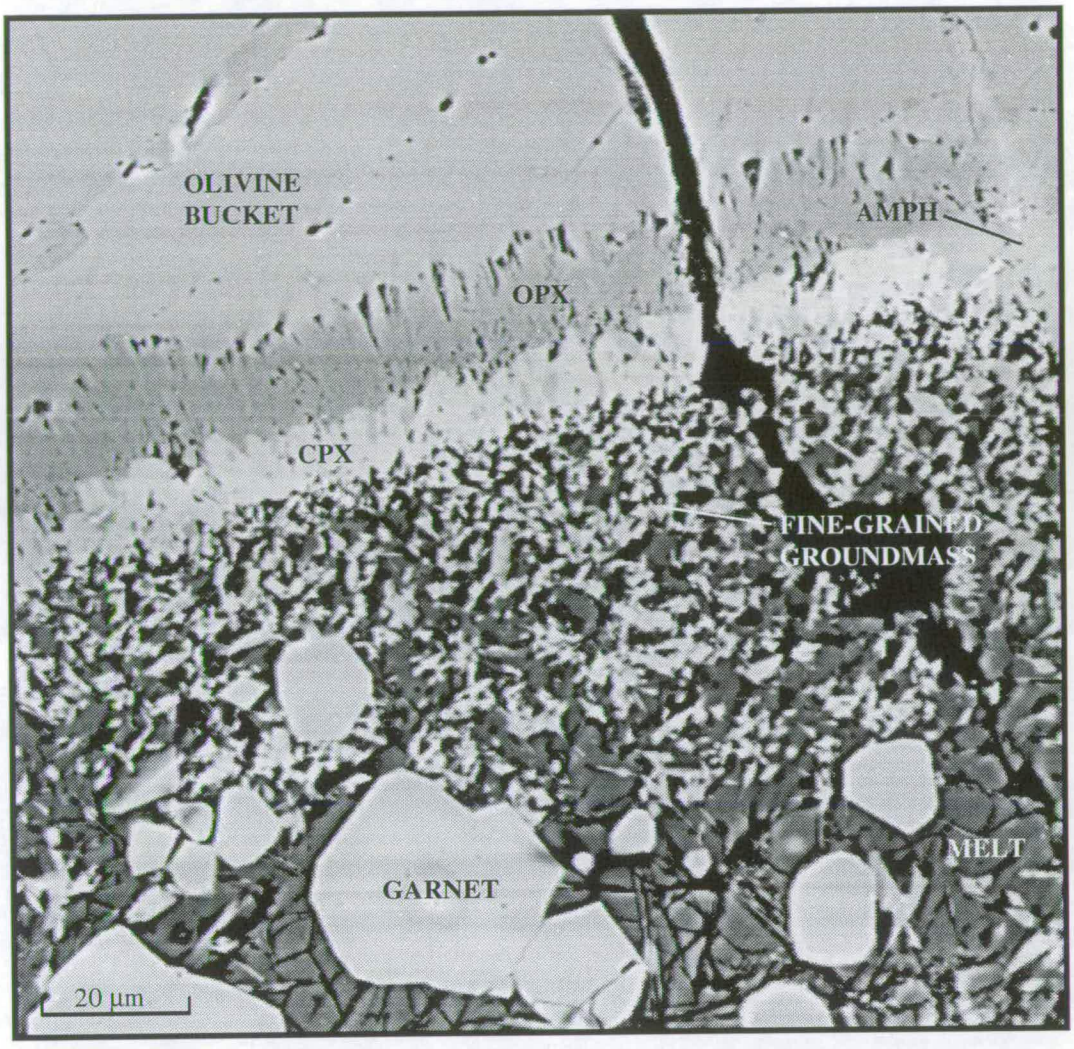

A back-scattered electron image of a polished transverse section of ED195 showing the mineralogical zoning typical of many of the reversal experiments run in olivine buckets. The internal edge of the olivine bucket is coated by a layer of orthopyroxene crystals followed by a layer of clinopyroxene crystals. In some areas, amphibole crystals are found with the clinopyroxene. The interior of the charge consists of a fine-grained groundmass (orthopyroxene, clinopyroxene, and amphibole), glass quenched from the melt, and euhedral crystals of garnet.

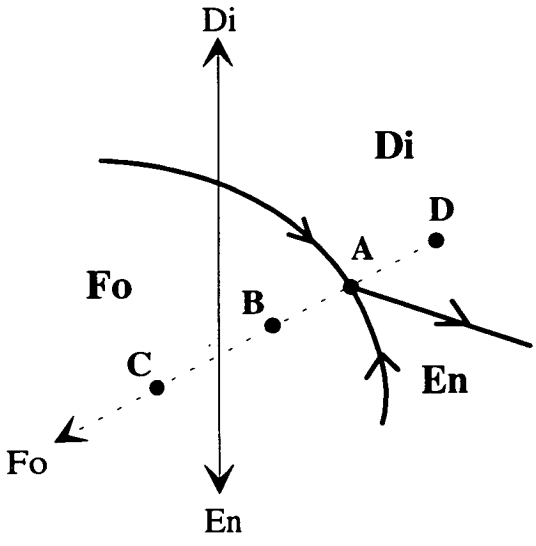

Figure 5.29: Schematic phases relations of system Fo-Di-SiO_2-H_2O (after Mysen & Kushiro, 1974; Nicholls, 1974). Composition A represents the initial liquid produced by partial melting of the peridotitic bulk composition. Compositions B and C represent this liquid composition plus some olivine (Fo_{90}) component. See text.

Theoretically liquid A would not crystallise anything if it were run on its own under identical conditions to the forward experiment. On quenching it would form a glass. However in these experiments the liquid is in equilibrium with an olivine bucket and therefore the peritectic reaction (5.10) can proceed:

Fo+Liq⇔En+Di (5.10)

This reaction proceeds until either of the two components on the left-hand side is consumed. The mineralogical zoning of the run products suggests that the reaction stops when the olivine bucket has been separated from the melt by the layer of orthopyroxene crystals coating it. In other words in these reversal experiments the olivine bucket reacts with the melt to produce enstatite (which coats the olivine) and diopside (which is found adjacent to the enstatite). The remaining liquid then crystallises more enstatite, diopside, amphibole and garnet. However, we might expect to see the same texture if the calculated melt composition had been too poor in olivine component (composition D). In this case the olivine would dissolve into the melt until the peritectic composition was reached after which reaction (1) would proceed as described above. Compositions B and C are rich in olivine component. If these were run in reversal experiments, olivine would be produced at equilibrium: this is not the case. Therefore, although these reversal experiments show that the calculated melt composition is not too rich in olivine, they do not prove that the calculated olivine component in the melt is correct.

Clearly, these experiments are not an adequate test of the assumptions which lead to the amount of olivine component added to or subtracted from the melt inclusion composition in order to derive the equilibrium melt. Therefore, more reversal

experiments were performed in which no olivine bucket was used. Instead, olivine (Fo_{90}) component was added to the original melt composition.

Reversal experiments without olivine buckets

The starting material (sintered oxide and gel mixtures of composition ED143M5 plus varying olivine (Fo_{90}) component) and water were sealed in gold capsules which were run in groups of three in a salt cell (see Section 4.4). Results from nine successful[9] reversal experiments are shown in Table 5.19.

Table 5.19: Mineralogy of reversal experiments not run in olivine buckets.

Expt.	% ol	% H_2O	Temp.	Dur.	Mineralogy									
					melt	ol	opx	cpx	am	sp	ru	ilm	fq	gt
ED143			1020°C	24 hrs	•	•	•	•	•	•	•	•		
ED317C2	0	30	1020°C	3 hrs	•								•	
ED327C2	10	30	1020°C	26 hrs	•			•					•	
ED327C3	20	30	1020°C	26 hrs	•	•		•					•	
ED332C1	0	30	1005°C	24 hrs	•								•	
ED332C2	10	30	1005°C	24 hrs	•			•	•				•	•
ED332C3	20	30	1005°C	24 hrs	•	•		•					•	•
ED348C1	0	10	1005°C	24 hrs	•			•						•
ED348C2	0	20	1005°C	24 hrs	•									
ED348C3	0	50	1005°C	24 hrs	•								•	

(melt, olivine, orthopyroxene, clinopyroxene, amphibole, spinel, rutile, ilmenite, fluid quench, garnet). The numbering system for the experiments refer to the run number (e.g. ED317) and the capsule no. (e.g. C1). Starting compositions consisted of ED143M5 plus 10 or 20 wt% olivine (Fo_{90}). All capsules contained water.

Two of the experiments (ED348C1 and ED348C2) did not contain sufficient water to render the conditions water saturated: there was no evidence of a free fluid phase at equilibrium. In all other experiments, conditions were water saturated and both melt and fluid were present at equilibrium. No crystals were produced at 1020°C from the melt composition alone (ED317C2). However after adding 10 wt% olivine (Fo_{90}) component, clinopyroxene became stable (ED327C2). The addition of a further 10 wt% olivine (Fo_{90}) produced equilibrium olivine crystals as well as clinopyroxene (ED327C3).

The absence of any crystals from the experiment with no added olivine could be explained in two ways:

- the liquidus temperature of the calculated melt composition is too low i.e. the true melt is actually more mafic;

[9]An experiment was deemed successful if no water was lost during the run.

- the nominal temperature of the reversal experiments run in salt cells is lower than that of the forward experiment (and reversals run in olivine buckets).

The latter hypothesis is supported by the fact that the potential discrepancy is in the same direction as that speculated earlier (Section 5.2.3) i.e. the nominal temperature in the forward experiments (and reversal run in olivine buckets) is too high. Therefore a similar experiment in a salt cell was conducted at the lower temperature of 1005°C, which is similar to the temperature of ED143 inferred from the two-pyroxene thermometer (Table 5.10). Again, no crystals were produced from the equilibrium melt composition alone. However, the addition of 10 wt% olivine (Fo_{90}) induced the precipitation of clinopyroxene, amphibole and garnet, suggesting that the following reaction may be occurring:

$$Fo+Liq \Leftrightarrow Di \quad (5.11)$$

Clinopyroxene, garnet and olivine were stable after the addition of a further 10 wt% olivine (Fo_{90}) component. Orthopyroxene is noticeably absent from any of these run products.

The interpretation of these results is complicated by the fact that the experimental set up is different to the forward experiments. In particular, the oxygen fugacity is thought to be lower in these experiments. Oxygen fugacity in salt cell runs is estimated to be 2 log units below QFM (see Section 4.4.5), whereas the oxygen fugacity in the forward experiments and the reversals in olivine buckets is buffered to NNO. This may have some bearing on the results. For example, olivine was observed to crystallise from a quartz tholeiite composition under water-saturated conditions with an fO_2 equal to the MW buffer whereas it did not crystallise under identical conditions with a higher fO_2 equal to the NNO buffer (Mysen & Kushiro, 1974). Any other differences between the capsules and cells should not, in theory, significantly affect the run products.

Results show that between 10 and 20 wt% olivine (Fo_{90}) component needs to be added to the melt composition in order to precipitate detectable olivine. A significant amount of olivine is produced by the addition of 20 wt% olivine (Fo_{90}) suggesting that this melt composition lies well into the olivine field. The experiment at 1005°C with 10 wt% added olivine (Fo_{90}) (ED332C2) most closely reproduces the original phase assemblage, producing melt, clinopyroxene, amphibole, garnet and fluid quench. However, orthopyroxene rather than garnet was stable in the original experiment.

Finally, it is worth noting that in addition to altering the starting composition of the experiments, the addition of olivine (Fo_{90}) to the melt composition is likely to increase its liquidus temperature. This could account for some of the differences in mineralogy and degree of crystallisation seen between runs with different amounts of olivine component.

5.3.2 Phase compositions in reversal experiments

Olivine

Table 5.20 shows the average composition of olivine from two experiments run in olivine buckets (ED192 and ED195) and two experiments without olivine buckets (ED327C3, ED332C3). Crystals in ED192 and ED195 are small, subhedral and with the exception of high Mg nos. are similar in composition to olivine in the initial forward experiment. However they are also close to the range of composition of the San Carlos olivine that makes up the bucket, and are therefore difficult to distinguish from these. More reliable are the olivine compositions from the experiments without olivine buckets. Olivines formed in these experiments resemble those from ED143 in terms of CaO and TiO_2 (Fig. 5.30).

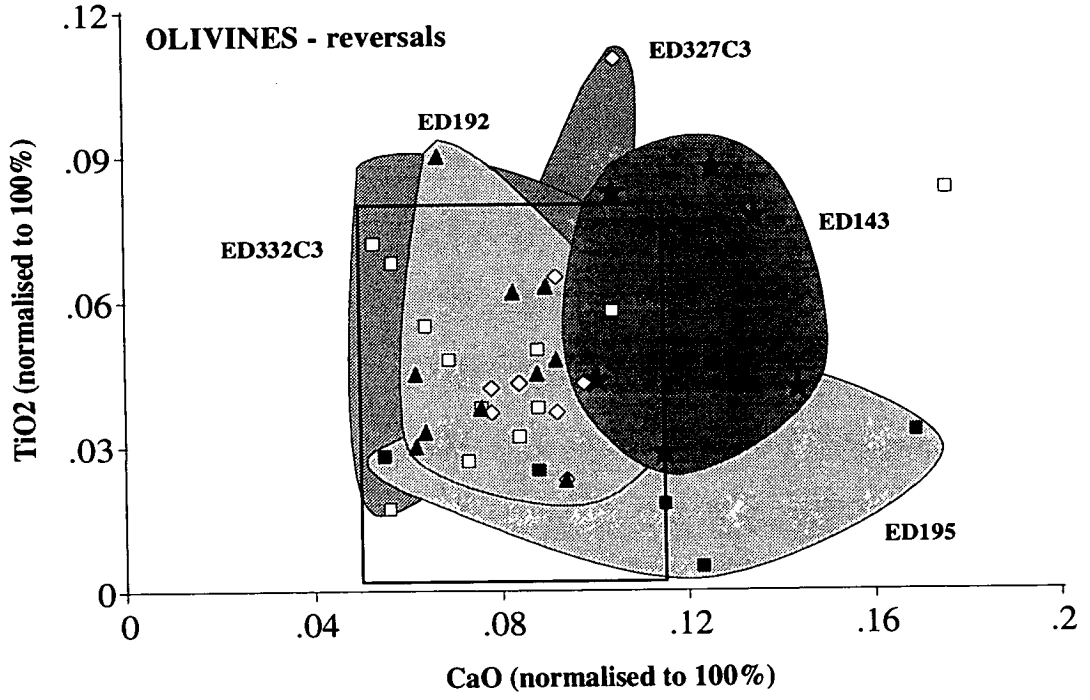

Figure 5.31: TiO2 versus CaO (normalised to 100% total) of olivines from ED143 and four reversal experiments. The range in composition of the olivine bucket is denoted by the box.

Table 5.20: Composition of olivines formed in reversals of ED143.

OLIVINE - reversal experiments

Expt.	ED143		ED192		ED195		ED327C3		ED332C3	
	[6]	s.d.	[12]	s.d.	[6]	s.d.	[10]	s.d.	[5]	s.d.
SiO_2	39.724	(0.141)	40.517	(0.648)	40.647	(0.927)	40.765	(0.237)	40.729	(0.900)
TiO_2	0.061	(0.026)	0.053	(0.026)	0.026	(0.014)	0.050	(0.027)	0.065	(0.038)
Al_2O_3	0.041	(0.022)	0.030	(0.019)	0.128	(0.176)	0.021	(0.007)	0.102	(0.038)
Cr_2O_3	0.072	(0.010)	0.033	(0.026)	0.034	(0.014)	0.051	(0.023)	0.045	(0.020)
FeO	11.762	(0.194)	8.207	(1.098)	9.285	(0.163)	9.026	(0.632)	8.380	(1.279)
MgO	47.705	(0.325)	50.833	(1.855)	49.151	(0.479)	49.729	(0.799)	50.069	(1.614)
CaO	0.121	(0.018)	0.084	(0.018)	0.113	(0.038)	0.090	(0.010)	0.255	(0.061)
Na_2O	0.011	(0.013)	0.013	(0.012)	0.026	(0.016)	0.009	(0.007)	0.015	(0.008)
K_2O	0.005	(0.008)	0.007	(0.009)	0.004	(0.005)	0.011	(0.003)	0.005	(0.005)
MnO	0.107	(0.044)	0.175	(0.036)	0.127	(0.022)	0.200	(0.010)	0.176	(0.021)
NiO	0.485	(0.033)	0.636	(0.360)	0.370	(0.048)	0.167	(0.174)	0.184	(0.296)
TOTAL	100.094	(0.252)	100.588	(1.647)	99.911	(1.219)	100.119	(0.299)	100.028	1.058
based on 4 oxygens:										
Si	1.00	(0.005)	0.985	(0.013)	0.996	(0.010)	0.996	(0.002)	0.992	(0.006)
Ti	0.002	(0.001)	0.001	(0.000)	0.000	(0.000)	0.001	(0.000)	0.001	(0.001)
Al	0.005	(0.003)	0.001	(0.001)	0.004	(0.005)	0.001	(0.000)	0.001	(0.001)
Cr	0.002	(0.001)	0.001	(0.001)	0.001	(0.000)	0.001	(0.000)	0.001	(0.000)
Fe	0.25	(0.003)	0.167	(0.024)	0.190	(0.005)	0.184	(0.014)	0.167	(0.029)
Mg	1.72	(0.007)	1.841	(0.040)	1.796	(0.023)	1.810	(0.020)	1.833	(0.034)
Ca	0.006	(0.001)	0.002	(0.000)	0.003	(0.001)	0.002	(0.000)	0.003	(0.002)
Na	0.002	(0.001)	0.001	(0.001)	0.001	(0.001)	0.000	(0.000)	0.001	(0.000)
K	0.000	(0.000)	0.000	(0.000)	0.000	(0.000)	0.000	(0.000)	0.000	(0.000)
Mn	0.003	(0.000)	0.004	(0.001)	0.003	(0.000)	0.004	(0.000)	0.004	(0.000)
Ni	0.011	(0.001)	0.012	(0.007)	0.007	(0.001)	0.003	(0.003)	0.004	(0.006)
TOTAL	3.00	(0.00)	3.014	(0.013)	3.002	(0.012)	3.003	(0.002)	3.006	(0.006)
Mg no.	87.26	(0.09)	91.694	1.212	90.417	0.156	90.753	0.722	91.634	1.449

The number of analyses are given in square brackets; s.d. is standard deviation.

However, the NiO content of these reversal olivines is lower, possibly due to a lack of NNO buffer (Fig. 5.31). Crystals are zoned with relatively iron-rich cores and iron-poor rims, (e.g. Mg no. ranges from 89.5 in the core to 92.8 in the rim), presumably an effect of iron loss to the gold capsules.

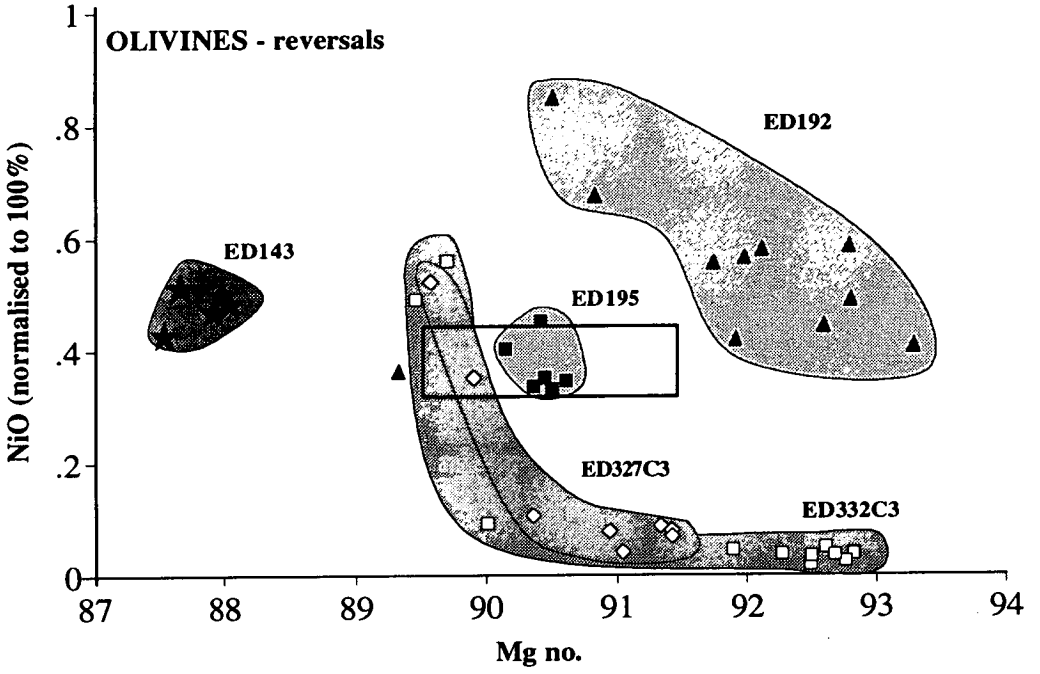

Figure 5.31: NiO versus Mg no. (normalised to 100% total) of olivines from ED143 and four reversal experiments. The range in composition of the olivine bucket is denoted by the box.

Orthopyroxene

Only those reversal experiments involving the use of olivine buckets produced orthopyroxene, present as small crystals coating the internal edges of the olivine buckets and larger crystals in the main part of the mix. Table 5.21 shows the average composition of orthopyroxene crystals in ED192 and ED195. These are classified according to Morimoto (1988) as aluminian enstatite and chromian aluminian enstatite, respectively i.e. broadly similar to the chromian aluminian enstatite formed in ED143. However the reversal orthopyroxenes are considerably richer in Al_2O_3, with higher Mg nos.

Clinopyroxene

This was formed in most reversals which used olivine buckets, and in the reversals without olivine buckets after the addition of 10 wt% olivine (Fo_{90}) component. The clinopyroxenes formed in reversals are chromian aluminian diopsides or aluminian

Table 5.21: Composition of orthopyroxenes formed in reversals of ED143.

ORTHOPYROXENE - reversal experiments

Expt.	ED143		ED192		ED195	
	[8]	s.d.	[6]	s.d.	[5]	s.d.
SiO_2	53.988	(0.240)	52.552	(0.685)	52.496	(1.055)
TiO_2	0.374	(0.015)	0.268	(0.058)	0.289	(0.032)
Al_2O_3	3.210	(0.446)	7.785	(0.459)	7.714	(0.837)
Cr_2O_3	0.448	(0.106)	0.215	(0.093)	0.058	(0.019)
FeO	8.113	(0.360)	4.966	(0.273)	6.344	(0.249)
MgO	31.919	(0.322)	32.497	(0.780)	31.888	(1.420)
CaO	0.912	(0.104)	0.831	(0.089)	1.061	(0.158)
Na_2O	0.042	(0.026)	0.032	(0.031)	0.030	(0.010)
K_2O	0.006	(0.005)	0.017	(0.008)	0.017	(0.010)
MnO	0.128	(0.022)	0.187	(0.020)	0.170	(0.009)
NiO	0.134	(0.034)	0.158	(0.065)	0.271	(0.063)
TOTAL	99.273	(0.330)	99.508	(1.022)	100.339	(0.975)
based on 6 oxygens:						
Si	1.902	(0.010)	1.819	(0.006)	1.815	(0.036)
Al (IV)	0.098	(0.010)	0.181	(0.006)	0.185	(0.036)
Total	2		2		2	
Al (VI)	0.035	(0.011)	0.137	(0.014)	0.130	(0.043)
Ti	0.010	(0.000)	0.007	(0.001)	0.008	(0.001)
Cr	0.013	(0.003)	0.006	(0.003)	0.002	(0.001)
Mg(M1)	0.943	(0.013)	0.850	(0.014)	0.861	(0.043)
Total	1		1		1	
Mg(M2)	0.733	(0.015)	0.826	(0.011)	0.783	(0.033)
Fe	0.239	(0.011)	0.144	(0.009)	0.183	(0.006)
Mn	0.004	(0.001)	0.005	(0.001)	0.005	(0.000)
Ca	0.034	(0.004)	0.031	(0.003)	0.039	(0.006)
Na	0.003	(0.002)	0.002	(0.002)	0.002	(0.001)
K	0.000	(0.000)	0.001	(0.000)	0.001	(0.000)
Total	1.014	(0.006)	1.009	(0.006)	1.013	(0.034)
TOTAL	4.017	(0.006)	4.014	(0.005)	4.020	(0.035)
Mg no.	87.52	(0.56)	92.097	(0.559)	89.954	(0.327)

The number of analyses are given in square brackets; s.d. is standard deviation.

diopsides (Morimoto, 1988), i.e. broadly similar to the chromian aluminian diopsides formed in ED143. There are some differences, notably the Na_2O and TiO_2 contents are lower in the crystals from reversal experiments whereas the Mg no. and the Al_2O_3 content are slightly higher (Table 5.22).

Table 5.22: Composition of clinopyroxenes formed in reversals of ED143.

CLINOPYROXENES - reversal experiments

Expt.	**ED143**		**ED195**		**ED327C2**		**ED327C3**		**ED332C3**	
	[10]	s.d.	[12]	s.d.	[5]	s.d.	[4]	s.d.	[7]	s.d.
SiO_2	50.551	(0.811)	51.111	(1.677)	51.909	(1.074)	51.751	(1.318)	51.358	(0.952)
TiO_2	1.041	(0.215)	0.661	(0.210)	0.512	(0.134)	0.664	(0.234)	0.485	(0.127)
Al_2O_3	4.286	(0.844)	6.676	(2.083)	4.637	(1.215)	5.288	(1.739)	4.553	(1.347)
Cr_2O_3	0.743	(0.238)	0.126	(0.070)	0.625	(0.227)	0.222	(0.078)	0.455	(0.128)
FeO	3.659	(0.217)	3.119	(0.158)	2.240	(0.099)	2.267	(0.097)	2.148	(0.142)
MgO	16.519	(0.594)	15.899	(1.117)	16.517	(0.706)	16.534	(0.889)	16.969	(0.703)
CaO	21.299	(0.648)	21.313	(0.317)	23.130	(0.145)	22.741	(0.278)	22.830	(0.284)
Na_2O	0.410	(0.053)	0.321	(0.059)	0.231	(0.027)	0.224	(0.042)	0.212	(0.045)
K_2O	0.007	(0.008)	0.020	(0.016)	0.011	(0.006)	0.004	(0.003)	0.009	(0.007)
MnO	0.084	(0.033)	0.171	(0.034)	0.140	(0.016)	0.137	(0.008)	0.109	(0.016)
NiO	0.105	(0.040)	0.272	(0.030)	0.023	(0.013)	0.019	(0.007)	0.006	(0.010)
TOTAL	98.703	(0.361)	99.688	(0.750)	99.977	(0.278)	99.849	(0.323)	99.133	(0.368)
based on 6 oxygens:										
Si	1.870	(0.025)	1.858	(0.051)	1.886	(0.032)	1.878	(0.043)	1.880	(0.034)
Al (IV)	0.130	(0.045)	0.142	(0.051)	0.114	(0.032)	0.122	(0.043)	0.120	(0.034)
Total	2		2		2		2		2	
Al (VI)	0.057	(0.014)	0.145	(0.043)	0.084	(0.021)	0.104	(0.032)	0.077	(0.024)
Ti	0.029	(0.006)	0.018	(0.006)	0.014	(0.004)	0.018	(0.006)	0.013	(0.003)
Cr	0.022	(0.007)	0.004	(0.002)	0.018	(0.007)	0.006	(0.002)	0.013	(0.004)
Mg(M1)	0.892	(0.019)	0.833	(0.049)	0.883	(0.030)	0.872	(0.040)	0.897	(0.031)
Total	1		1		1		1		1	
Mg(M2)	0.019	(0.021)	0.028	(0.016)	0.011	0.006	0.023	(0.010)	0.029	(0.009)
Fe	0.113	(0.007)	0.095	(0.004)	0.068	0.003	0.069	(0.003)	0.066	(0.004)
Mn	0.003	(0.001)	0.005	(0.001)	0.004	0.000	0.004	(0.000)	0.003	(0.001)
Ca	0.844	(0.026)	0.830	(0.014)	0.900	0.007	0.884	(0.012)	0.895	(0.011)
Na	0.029	(0.004)	0.023	(0.004)	0.016	0.002	0.016	(0.003)	0.015	(0.003)
K	0.000	(0.000)	0.001	(0.001)	0.001	0.000	0.000	(0.000)	0.000	(0.000)
Total	1.009	(0.034)	0.982	(0.011)	1.000	0.001	0.996	(0.002)	1.009	(0.002)
TOTAL	4.012	(0.002)	3.990	(0.011)	4.001	(0.001)	3.996	(0.002)	4.010	(0.002)
Mg no.	88.951	(0.381)	90.067	0.475	92.926	0.188	92.842	0.531	93.370	(0.335)

The number of analyses are given in square brackets; s.d. is standard deviation.

Amphibole

Amphiboles produced in experiments involving olivine buckets are euhedral and large (up to 15x60 μm in ED195), whereas those produced in ED327C2 are smaller (up to 8x15 μm) and consequently more difficult to analyse. They are classified as pargasitic hornblendes in ED195 and titanian pargasites in ED332C2, i.e. both are broadly similar to each other and to the pargasitic hornblende of ED143 (see Table 5.23). However, the reversal amphiboles are significantly more aluminous with most of the extra alumina occupying the Y site. Reversal amphiboles are also depleted in Cr_2O_3 and Na_2O relative to the amphibole in ED143. Again the Mg no. of the reversal amphiboles is higher than the Mg no. of the amphiboles in ED143.

Garnet

This was not formed in any of the forward experiments at 1.8 GPa. However, it was found as relatively large (up to 80 μm diameter) poikilitic, euhedral crystals in the reversal experiments in olivine buckets and as similarly large euhedral crystals in ED332C2 and ED332C3. Analysis was complicated by the presence of many small inclusions of other phases (such as orthopyroxene, clinopyroxene, olivine). In all experiments the garnet was predominantly pyrope with smaller amounts of grossular and almandine component (Table 5.24). This is very similar to the composition formed in mantle rocks (Deer *et al.*, 1992).

Melt

As well as glass quench mats, large melt inclusions were formed in those reversal experiments run in olivine buckets. These were analysed and corrected for quench fractionation by addition of olivine as described in Section 5.2.4. For reversal experiments the amount of olivine added to the melt inclusion analysis to achieve the Fe/Mg olivine/melt exchange relationship of Roeder & Emslie (1970) was small i.e. the large melt fraction was relatively unaltered during quenching. In all reversal experiments run in gold capsules, the majority of the charge is composed of glass quench mats with a ropy texture (Plate 5.5a). Note that the glass discussed in this chapter is considered to have quenched from the melt. Glass spheres quenched from the coexisting fluid phase are discussed in detail in Chapter 7. Crystals, where present, are generally of low abundance, clustered together in discrete groups. Glass adjacent to the crystals is of a smoother appearance (Plate 5.5b). There is a large spread in melt composition in some experiments, for example the MgO content (normalised to 100% total) in ED332C3 ranges from 0.6 wt% to 9.6 wt% (see Fig. 5.32).

Table 5.23: Composition of amphiboles formed in reversals of ED143.

AMPHIBOLES - reversal experiments

Expt.	ED143		ED195		ED332C2	
	[9]	s.d.	[9]	s.d.	[2]	s.d.
SiO_2	43.591	(0.568)	44.455	(1.089)	42.535	(0.956)
TiO_2	2.123	(0.096)	1.334	(0.131)	2.464	(0.019)
Al_2O_3	12.057	(0.929)	15.713	(1.393)	16.883	(3.246)
Cr_2O_3	0.751	(0.250)	0.108	(0.041)	0.018	(0.007)
FeO	5.204	(0.198)	3.791	(0.161)	4.083	(0.459)
MgO	18.143	(0.438)	17.353	(1.292)	16.267	(2.869)
CaO	10.935	(0.283)	11.488	(0.410)	10.947	(0.006)
Na_2O	2.348	(0.099)	1.947	(0.120)	1.829	(0.132)
K_2O	0.549	(0.078)	0.852	(0.072)	0.480	(0.078)
MnO	0.070	(0.044)	0.099	(0.016)	0.157	(0.029)
NiO	0.148	(0.045)	0.455	(0.083)	0.025	(0.013)
TOTAL	95.918	(0.406)	97.595	(1.019)	95.686	(0.125)
based on 23 oxygens:						
Si	6.326	(0.089)	6.270	(0.102)	6.104	(0.143)
Al (IV)	1.674	(0.089)	1.730	(0.102)	1.896	(0.143)
Total in Z	8		8		8	
Al (VI)	0.388	(0.077)	0.882	(0.171)	0.960	(0.403)
Ti	0.232	(0.010)	0.141	(0.013)	0.266	(0.002)
Mg	3.924	(0.094)	3.649	(0.275)	3.480	(0.617)
Mn	0.009	(0.005)	0.012	(0.002)	0.019	(0.004)
Fe (Y)	0.448	(0.043)	0.315	(0.112)	0.275	(0.209)
Total in Y	5		5		5	
Fe (X)	0.184	(0.052)	0.132	(0.107)	0.215	(0.154)
Ca	1.700	(0.045)	1.737	(0.076)	1.683	(0.003)
Na (X)	0.116	(0.026)	0.131	(0.085)	0.102	(0.157)
Total in X	2		2		2	
Na xs	0.545	(0.047)	0.402	(0.104)	0.407	(0.120)
K	0.102	(0.014)	0.153	(0.014)	0.088	(0.014)
Total in [A]	0.646	(0.055)	0.555	(0.105)	0.494	(0.106)
Cr	0.088	(0.029)	0.012	(0.005)	0.002	(0.001)
Ni	0.017	(0.005)	0.051	(0.010)	0.003	(0.002)
TOTAL	15.751	(0.039)	15.619	(0.110)	15.499	(0.107)
Mg no.	86.137	(0.465)	89.031	(0.979)	87.435	(3.156)

The number of analyses are given in square brackets; s.d. is standard deviation.

Table 5.24: Composition of garnets formed in reversals of ED143.

GARNET - reversal experiments

Expt.	ED192		ED195		ED332C2		ED332C3	
	[2]	s.d.	[6]	s.d.	[4]	s.d.	[6]	s.d.
SiO_2	41.823	(0.170)	40.060	(1.383)	40.818	(0.248)	40.812	(0.447)
TiO_2	1.073	(0.076)	1.127	(0.063)	1.058	(0.259)	0.743	(0.307)
Al_2O_3	22.772	(0.092)	21.615	(1.012)	22.437	(0.292)	22.103	(0.404)
Cr_2O_3	0.148	(0.064)	0.311	(0.143)	0.147	(0.036)	0.893	(0.163)
FeO	6.016	(0.397)	7.985	(0.152)	6.801	(0.348)	6.430	(0.550)
MgO	19.541	(0.212)	16.488	(0.753)	17.357	(0.312)	18.010	(0.824)
CaO	8.075	(0.245)	9.418	(0.427)	9.622	(0.109)	9.007	(0.656)
Na_2O	0.000	(0.000)	0.033	(0.014)	0.012	(0.001)	0.017	(0.006)
K_2O	0.004	(0.005)	0.006	(0.006)	0.006	(0.005)	0.013	(0.006)
MnO	0.529	(0.040)	0.605	(0.034)	0.612	(0.040)	0.504	(0.031)
NiO	0.014	(0.020)	0.059	(0.022)	0.000	(0.001)	0.015	(0.013)
TOTAL	99.993	(0.632)	97.706	(2.051)	98.867	(0.121)	98.547	(0.470)
based on 24 oxyens:								
Z-site								
Si	5.941	(0.002)	5.921	(0.064)	5.920	(0.018)	5.929	(0.018)
Al(IV)	0.059	(0.002)	0.079	(0.064)	0.080	(0.018)	0.071	(0.018)
Total	6		6		6		6	
Y-site								
Al(VI)	3.753	(0.028)	3.686	(0.136)	3.756	(0.045)	3.712	(0.054)
Cr	0.002	(0.002)	0.007	(0.003)	0.000	(0.000)	0.002	(0.001)
Ti	0.115	(0.008)	0.125	(0.009)	0.115	(0.029)	0.081	(0.034)
Total	3.869	(0.018)	3.818	(0.131)	3.871	(0.017)	3.796	(0.024)
X-site								
Mg	4.137	(0.060)	3.635	(0.184)	3.752	(0.055)	3.899	(0.155)
Fe	0.715	(0.045)	0.988	(0.023)	0.825	(0.045)	0.782	(0.072)
Mn	0.064	(0.005)	0.076	(0.006)	0.075	(0.005)	0.062	(0.004)
Ca	1.229	(0.033)	1.493	(0.092)	1.495	(0.022)	1.402	(0.111)
Total	6.144	(0.012)	6.192	(0.201)	6.148	(0.022)	6.145	(0.052)
TOTAL	16.031	(0.002)	16.058	(0.085)	16.041	(0.009)	16.052	(0.015)
Mg no.	85.27	(0.97)	78.61	(1.07)	81.97	(1.02)	83.28	(1.82)
% end-member								
Alm.	11.6	(0.7)	16.0	(0.6)	13.4	(0.7)	12.7	(1.1)
Gross.	20.0	(0.5)	24.1	(1.4)	24.3	(0.3)	22.8	(1.7)
Pyrope	67.3	(1.1)	58.7	(1.8)	61.0	(1.0)	63.5	(2.8)
Spess.	1.04	(0.09)	1.22	(0.07)	1.22	(0.08)	1.01	(0.06)

The number of analyses are given in square brackets; s.d. is standard deviation.

PLATE 5.5

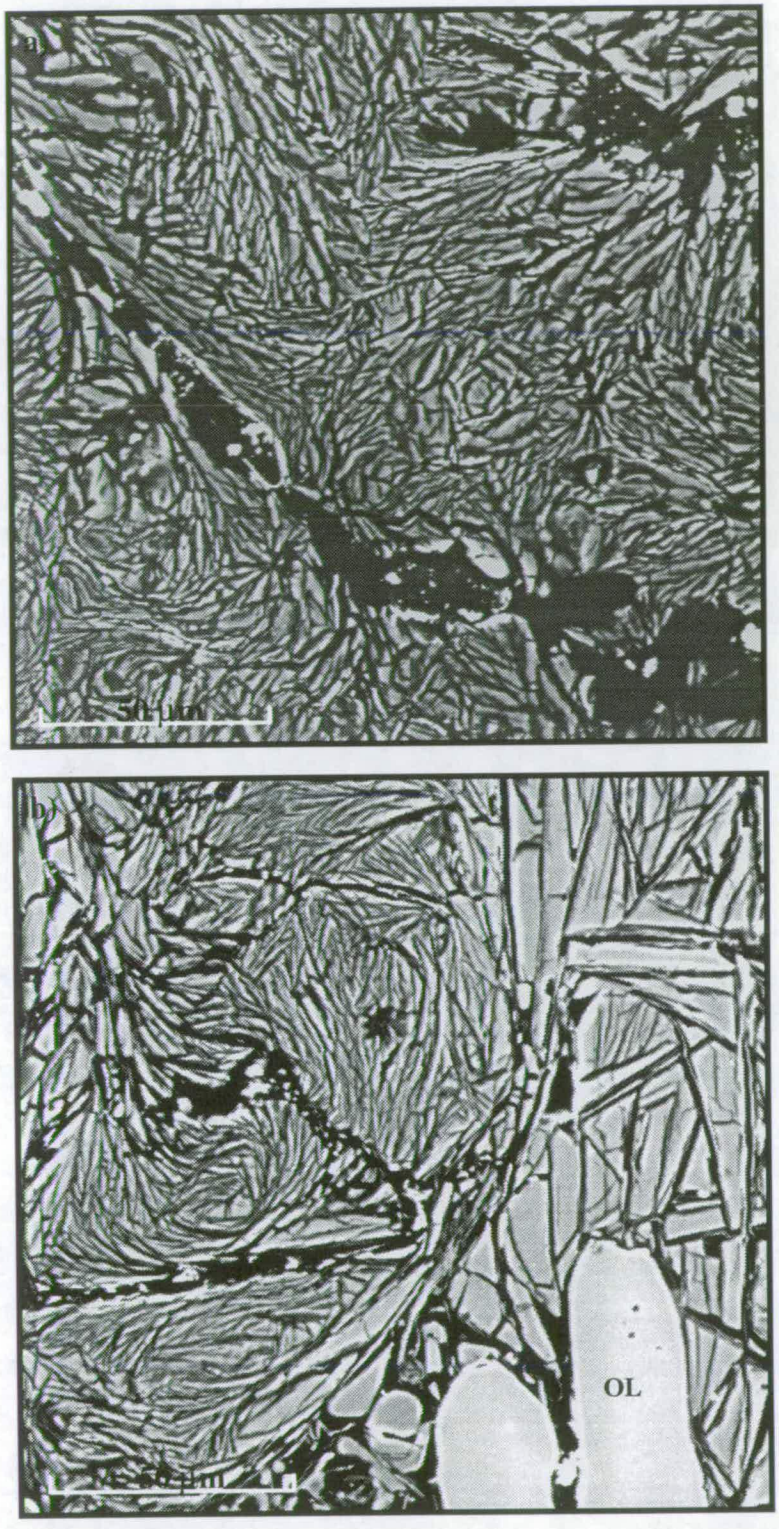

Back-scattered electron images of polished sections of run products. a) typical ropy-looking glass from ED332C3, b) From ED327C3: ropy-looking glass (left-hand side), smoother glass (right-hand side) and two olivine crystals.

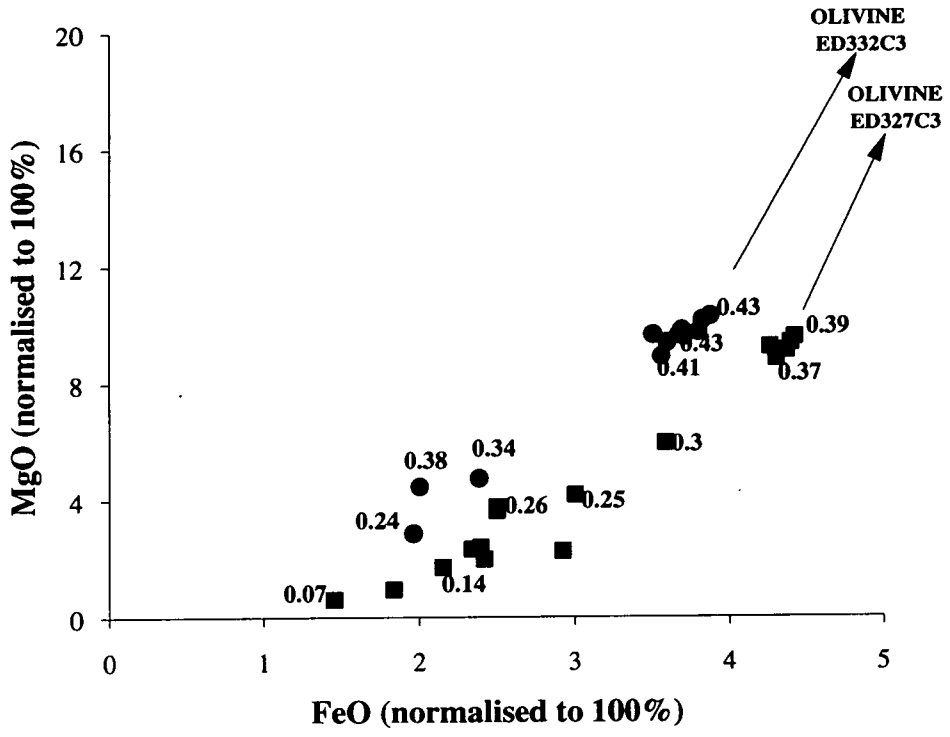

Figure 5.32: MgO versus FeO (normalised to 100% total) for glass from two reversal experiments run without olivine buckets. Circles denote ED332C3, squares denote ED327C3. The value of the Fe/Mg exchange coefficient between olivine and melt (Equation 5.9) is shown for selected analyses.

The cluster of high-MgO analyses in both ED327C3 and ED332C3 corresponds to the more abundant ropy glass, whereas the smoother glass adjacent to the crystals is much lower in MgO and FeO. This may be due to the extraction of olivine from the melt adjacent to the crystals (Figs. 5.32, 5.33), in which case the more homogeneous ropy glass would best represent the melt at equilibrium. Also shown for some glass compositions in Figure 5.32 is the Fe/Mg exchange coefficient (Equation 5.9), X, between the glass and the equilibrium olivine. The values of X for the smooth low-MgO glass are low and variable (e.g. 0.07, 0.15, 0.26) whereas the ropy glass gives more consistent higher values. Taking all analyses of the ropy glass, X is calculated to be 0.39±0.03 for ED327C3 and 0.43±0.08 for ED332C3. Although this is higher than that the value of 0.3 calculated by Roeder & Emslie (1970), it is consistent with more recent work involving experimentally-produced hydrous melts, e.g. a value of 0.4 was measured by Nicholls (1974); a value of 0.41 for coexisting melt and olivine at 2.0 GPa and 1100°C under water-saturated conditions (Green, 1976). Olivine was not found in any other of these experiments and hence similar distribution values could not be calculated. However, the composition of smooth glass in the run

products from ED327C2 and ED332C2 lies on a line of olivine extraction relative to the usual ropy glass (Fig. 5.33), suggesting that either:

a) equilibrium olivine is present but is too small to be noticed, or

b) there are small olivine quench crystals in the glass (too small to be detected).

Glass from those experiments in which there was no added olivine (ED317C2, ED332C2) is relatively homogenous.

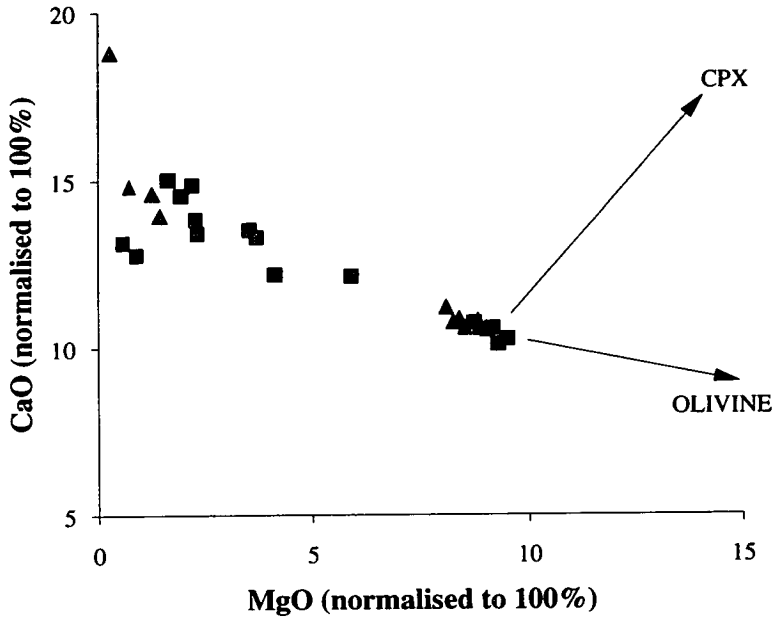

Figure 5.33: CaO versus MgO (normalised to 100% total) for glass from two reversal experiments run without olivine buckets. Triangles denote ED327C2, squares denote ED327C3. Note that in both experiments the glass compositions lie on an olivine control line.

In Table 5.25 melt compositions from reversals are compared with the melt from ED143. Most melts (including that from ED143) fall in the basaltic andesite field on a total alkali-silica diagram (after Le Maitre *et al.*, 1989) although the compositions become more mafic with added olivine (Fo_{90}) component. There is little difference between melt from ED327C2 (10% ol) and ED327C3 (20% ol), suggesting that olivine is near saturation in the former experiment. This is not the case, however, in ED332: melt composition becomes steadily more iron and magnesium rich with added olivine (Fo_{90}). Although no reversal experiments reproduced accurately the phase assemblage from ED143, the most exact were ED195 (in an olivine bucket) and ED332C2. The melts from these reversals (particularly ED332C2) and ED143 are extremely similar (Fig. 5.34).

Table 5.25: Melt compositions from forward (ED143) and reversal experiments at 1.8 GPa.

	ED143		ED192		ED195		ED317C2		ED327C2	
	[22]	s.d.	[4]	s.d.	[1]	s.d.	[11]	s.d.	[6]	s.d.
SiO_2	**53.631**	**(1.668)**	55.558	(2.046)	53.96	n.a.	54.982	(0.516)	52.066	(0.146)
TiO_2	**1.423**	**(0.630)**	0.940	(0.082)	0.77	n.a.	1.473	(0.091)	1.358	(0.035)
Al_2O_3	**22.695**	**(0.920)**	23.743	(1.242)	24.09	n.a.	23.102	(0.163)	20.881	(0.114)
Cr_2O_3	**0.019**	**(0.020)**	0.023	(0.017)	0	n.a.	0.038	(0.018)	0.052	(0.012)
FeO	**3.240**	**(0.837)**	2.100	(0.634)	2.07	n.a.	1.962	(0.466)	4.100	(0.068)
MgO	**3.944**	**(1.014)**	3.890	(1.164)	3.27	n.a.	1.302	(0.491)	8.437	(0.309)
CaO	**12.451**	**(1.642)**	11.943	(2.073)	13.56	n.a.	14.864	(0.497)	10.822	(0.230)
Na_2O	**1.812**	**(0.545)**	1.150	(0.130)	1.17	n.a.	1.681	(0.071)	1.570	(0.082)
K_2O	**0.578**	**(0.215)**	0.488	(0.034)	0.73	n.a.	0.394	(0.033)	0.541	(0.034)
MnO	**0.125**	**(0.031)**	0.118	(0.050)	0.22	n.a.	0.193	(0.041)	0.158	(0.020)
NiO	**0.080**	**(0.060)**	0.053	(0.059)	0.15	n.a.	0.010	(0.018)	0.016	(0.014)
						Original total	90.191	(0.813)	88.284	(0.411)

	ED327C3		ED332C1		ED332C2		ED332C3		ED348C3	
	[5]	s.d.	[16]	s.d.	[14]	s.d.	[9]	s.d.	[19]	s.d.
SiO_2	52.001	(0.212)	54.770	(0.629)	53.842	(0.341)	52.865	(0.533)	52.457	(0.242)
TiO_2	1.343	(0.040)	1.473	(0.033)	1.471	(0.061)	1.393	(0.039)	1.659	(0.048)
Al_2O_3	20.681	(0.070)	22.523	(0.151)	21.590	(0.187)	20.687	(0.176)	23.165	(0.107)
Cr_2O_3	0.043	(0.012)	0.057	(0.020)	0.028	(0.038)	0.030	(0.021)	0.059	(0.026)
FeO	4.341	(0.067)	2.560	(0.244)	2.782	(0.181)	3.689	(0.123)	2.379	(0.156)
MgO	9.209	(0.288)	4.012	(0.434)	7.213	(0.601)	9.669	(0.385)	4.434	(0.327)
CaO	10.365	(0.263)	11.845	(1.030)	10.715	(0.444)	9.226	(0.934)	14.197	(0.236)
Na_2O	1.213	(0.113)	1.758	(0.190)	1.631	(0.172)	1.578	(0.249)	1.125	(0.049)
K_2O	0.633	(0.054)	0.801	(0.300)	0.584	(0.049)	0.719	(0.150)	0.326	(0.025)
MnO	0.154	(0.015)	0.185	(0.047)	0.133	(0.067)	0.129	(0.028)	0.176	(0.041)
NiO	0.016	(0.019)	0.015	(0.022)	0.013	(0.015)	0.014	(0.016)	0.023	(0.022)
Original total	85.781	(2.881)	83.505	(2.253)	80.275	(3.106)	80.091	(3.870)	85.932	(0.241)

The number of analyses is shown in square brackets; s.d. is standard deviation. All compositions are normalised to 100%.

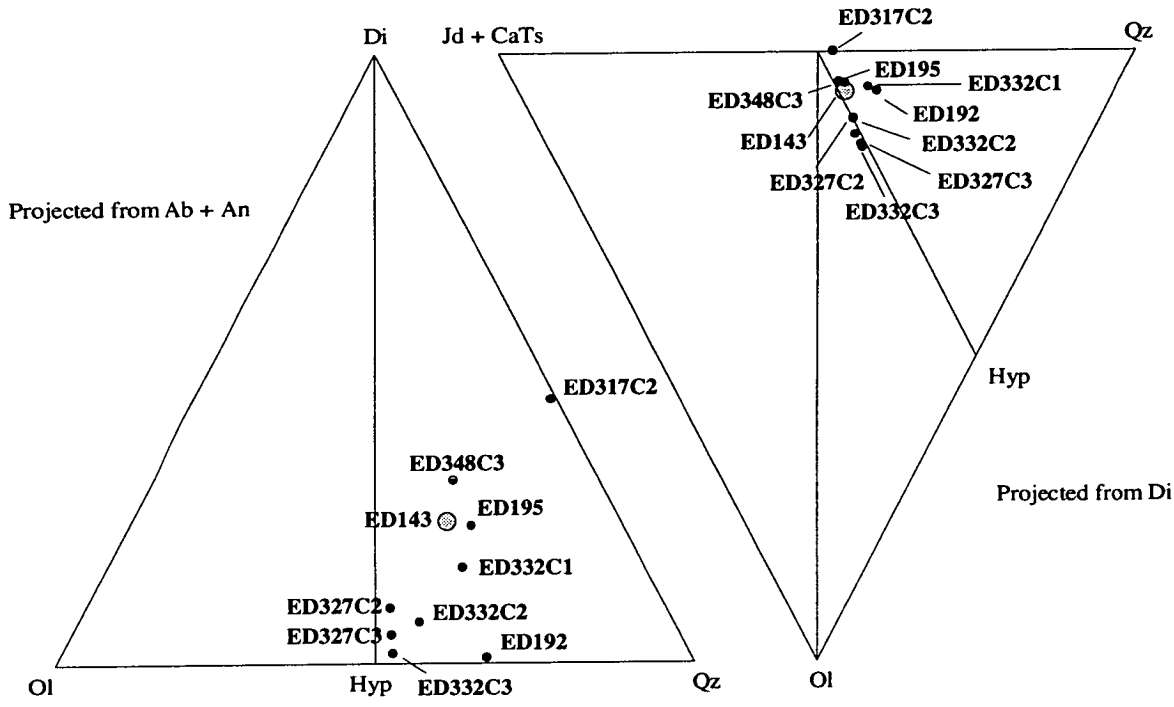

Figure 5.34: The calculated melt composition from ED143, and the average melt compositions from reversal experiments. The CIPW-normative composition are projected within the basalt tetrahedron (Fig. 5.21) from albite + anorthite onto the diopside-olivine-quartz plane, and from diopside onto the (jadeite + Ca-tschermak's molecule)-olivine-quartz plane.

Summary

The observations outlined above show that for many elements there is a consistent difference between the composition of phases formed in reversal experiments, and those formed in ED143. This is summarised below (Table 5.26).

Table 5.26: The relationship between the Mg no. and oxide contents of phases formed in reversal experiments relative to the same phase in ED143.

	Mg no.	TiO_2	Al_2O_3	Cr_2O_3	CaO	Na_2O	K_2O	MnO	NiO*
Olivine	high	-	-	low	-	-	-	high	low
Orthopyroxene	high	low	high	low	similar	low	high	high	-
Clinopyroxene	high	low	high	-	similar	low	-	high	low
Amphibole	high	-	high	low	similar	low	-	high	low
Melt (ED332C2)	high	similar	low	similar	low	low	similar	similar	low
starting compositions									
ED143M3				*high*				*high*	*high*
ED143M5				*high*		*high*		*high*	*high*

*The NiO content is taken from reversal experiments without olivine buckets.

The high MnO content of crystalline phases may be explained by the use of a starting material which had slightly more MnO than intended. However, this cannot be the reason for the other observations. Therefore, it would appear that the calculated melt composition should be richer in TiO_2, Cr_2O_3, Na_2O, NiO and poorer in Al_2O_3.

5.3.3 An appraisal of the reversal experiments

The results presented above could be used to argue either that the reversal experiments are a success i.e. the calculated melt composition is reasonably accurate, or that they are a failure i.e. the calculated melt composition is wrong:

- *success*: some phases from ED143 are reproduced: particularly encouraging is the presence of amphibole in ED195 and ED332C2. Furthermore, crystals in the reversal experiments are of a broadly similar composition to those in ED143 (Figs. 5.35, 5.36).
- *failure*: not all phases are reproduced, for example orthopyroxene is not found in reversal experiments without olivine buckets and garnet is formed in some reversals but is not present in ED143. The compositions of amphibole, clinopyroxene, olivine, orthopyroxene and melt are consistently different from the same phases in ED143, particularly in terms of Mg no., Al_2O_3 and certain minor elements.

In my view, although the experiments were not completely successful, the following observations and deductions can be made:

1. Olivine that was included in the form of a crystalline bucket or as powder appeared to play an active role in the experiments, reacting with the melt to form orthopyroxene and clinopyroxene. This observation, combined with knowledge of the phase relations of this system suggests that the olivine component in the calculated melt composition from ED143 is probably too low. The olivine addition experiments show that olivine saturation occurs after the addition of between 10% and 20% olivine (Fo_{90}) to the calculated melt composition from ED143.
2. All crystalline phases in the reversal experiments are substantially more aluminous than those in ED143; garnet is produced in most reversals; orthopyroxene is missing from reversals without olivine buckets.

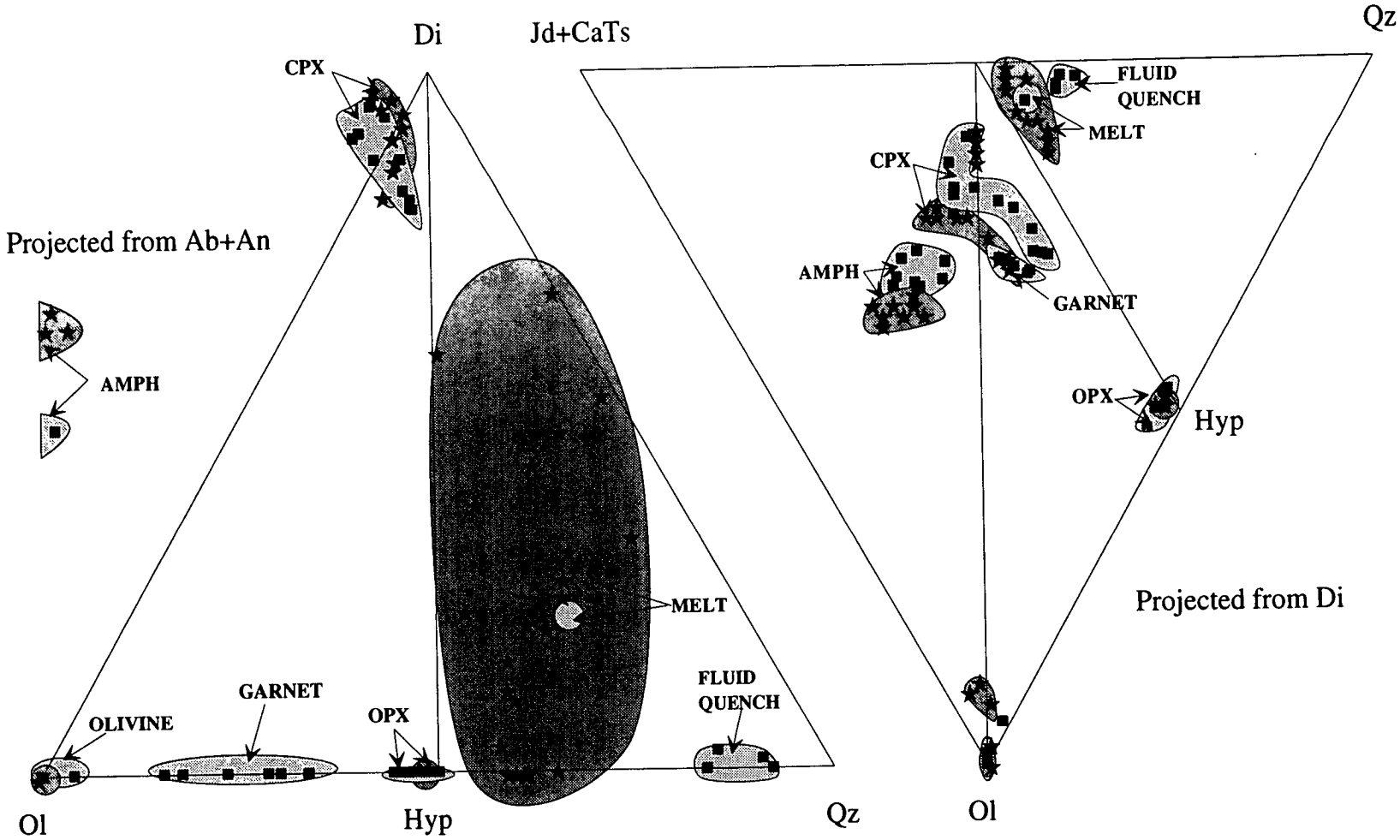

Figure 5.35 Comparison between phases produced in ED143 (stars, dark shading) and ED195 (squares, lighter shading). Note that amphibole is nepheline normative and lies outside the volume enclosed by (albite + anorthite), diopside, olivine, and quartz. Therefore, the projection of this composition from (albite + anorthite) falls outside the triangle enclosed by diopside, olivine, and quartz.

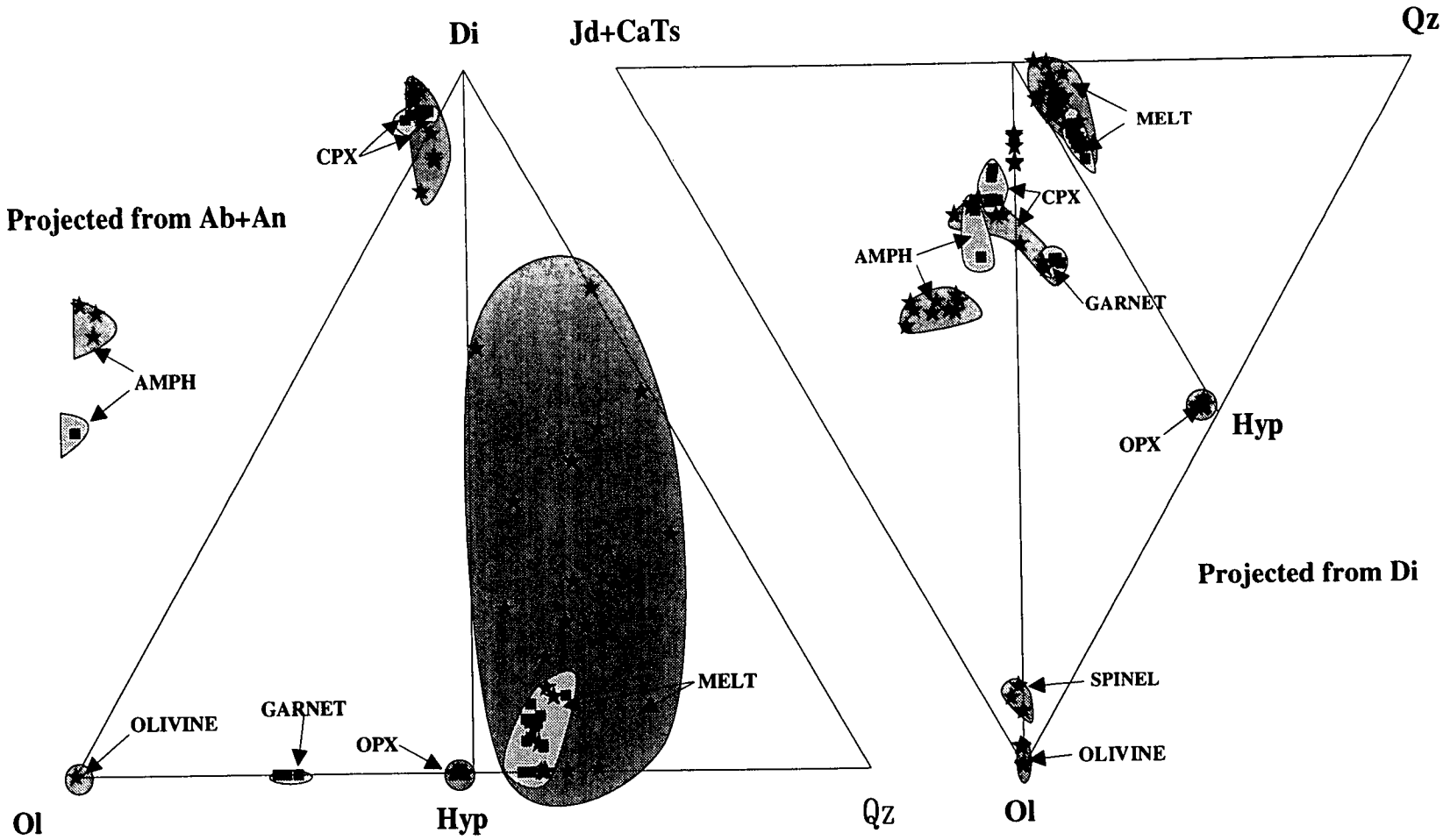

Figure 5.36: A comparison of phases produced in ED143 (stars, darker shading) and ED332C2 (squares, lighter shading)

3. The minor-element content of crystalline phases in the reversals is consistently different to those in ED143.

The calculated melt composition is therefore too poor in olivine component (by approximately 10%), slightly too poor in FeO and Na_2O, and substantially too rich in Al_2O_3.

This discrepancy requires a reconsideration of the technique used to calculate the original melt composition. In this technique, olivine component was added to the melt inclusion analyses until the Fe/Mg olivine/melt exchange coefficient (Equation 5.9) reached a value of 0.3. However, in experiments with no olivine buckets, measurement of this exchange coefficient yields numbers of approximately 0.4 (which is similar to the estimates derived from Nicholls (1974) and Green (1976)). Recalculation of melts using a value of 0.4 for the exchange coefficient involves the addition of a larger olivine component and yields compositions which are richer in iron and magnesium oxides, and poorer in all other oxides (Table 5.27). However this new melt composition is still less mafic than the composition formed by addition of 10% olivine (Fo_{90}) to ED143M5.

Table 5.27: Average melt compositions (and standard deviation) from ED143.

MELT COMPOSITIONS

Expt.	ED143		ED143		ED143M5 + 10% olivine (Fo_{90})
X	0.3		0.4		
	Av.	s.d.	Av.	s.d.	
SiO_2	53.63	(1.67)	53.02	(1.62)	50.04
TiO_2	1.42	(0.63)	1.36	(0.61)	1.35
Al_2O_3	22.69	(0.92)	21.64	(0.96)	20.83
Cr_2O_3	0.02	(0.02)	0.02	(0.02)	0.07
FeO	3.24	(0.84)	3.66	(0.89)	4.44
MgO	3.94	(1.01)	5.94	(1.43)	8.62
CaO	12.45	(1.64)	11.88	(1.64)	11.31
Na_2O	1.81	(0.55)	1.73	(0.53)	2.36
K_2O	0.58	(0.21)	0.55	(0.20)	0.66
MnO	0.13	(0.03)	0.12	(0.03)	0.18
NiO	0.08	(0.06)	0.08	(0.06)	0.14

The melt compositions were calculated from analyses of melt inclusions in olivine by incremental addition or subtraction of olivine using values of 0.3 and 0.4 for the Roeder & Emslie (1970) Fe/Mg exchange relationship. The composition formed by addition of 10% olivine (Fo_{90}) to ED143M5 is shown for comparison.

The low Na_2O content of the calculated melt is probably due to loss of sodium during analysis of melt inclusions, despite the use of a low beam current and a rastered beam. The high Al_2O_3 content is more problematical: one explanation may be that some of the alumina polishing compound became trapped in the melt inclusions. However, if this were the case then I would expect to see less consistency between results (from 22 analyses the calculated alumina content is 22.69±0.92). The inaccuracies in minor-element content of the calculated melt are small and relatively unimportant and probably due to a propagation of counting errors during analysis and weighing errors during the manufacture of the starting materials for the reversals.

Unfortunately there was no time to run further reversal experiments using a melt composition which is less aluminous and richer in olivine component. There is therefore considerable uncertainty regarding the composition of partial melts. This should be borne in mind in the following discussion.

5.4 DISCUSSION

The results of the reversal experiments have indicated that the melt composition calculated from ED143 (assuming that the value for the Fe/Mg olivine/melt exchange coefficient is 0.3) is too poor in olivine. It is considered that a better estimate can be made using a value of 0.4 for the exchange coefficient. However, the formation of garnet in preference to orthopyroxene in many reversal experiments, and the consistent difference in composition between the phases formed in ED143 and those formed in the reversal experiments can be used to argue that the calculated melt composition may be too enriched in alumina. Unfortunately, it has not proved possible for any experiment to reconstruct by mass balance the composition of the starting material from the inferred composition of the melt, and the compositions of the mineral phases. This may be partly because there was some loss of iron during the experiments, but it is more likely that this is a further indication that the calculated melt compositions are wrong. Nevertheless, the average calculated compositions of melts from three forward experiments (assuming a value of 0.4 for the exchange coefficient) are given in Table 5.28.

Table 5.28: Average melt compositions (and standard deviation) from three forward experiments at 1.8 GPa.

MELT COMPOSITIONS (X has a value of 0.4)						
Expt.	**ED143**		**ED137**		**ED91**	
Temp.	**1020°C**		**1032°C**		**1150°C**	
	Av.	s.d.	Av.	s.d.	Av.	s.d.
SiO_2	53.02	(1.62)	49.98	(3.59)	61.19	(2.44)
TiO_2	1.36	(0.61)	1.45	(0.94)	1.43	(0.28)
Al_2O_3	21.64	(0.96)	20.28	(1.94)	11.01	(1.64)
Cr_2O_3	0.02	(0.02)	0.03	(0.03)	0.06	(0.05)
FeO	3.66	(0.89)	4.55	(1.05)	3.57	(1.32)
MgO	5.94	(1.43)	8.09	(1.86)	10.76	(3.96)
CaO	11.88	(1.64)	13.12	(2.88)	10.24	(1.07)
Na_2O	1.73	(0.53)	1.69	(0.41)	1.07	(0.33)
K_2O	0.55	(0.20)	0.59	(0.32)	0.39	(0.07)
MnO	0.12	(0.03)	0.12	(0.05)	0.14	(0.04)
NiO	0.08	(0.06)	0.10	(0.07)	0.14	(0.13)
Mg no.	74.3		76.0		84.3	

Values were calculated from analyses of melt inclusions in olivine by incremental addition or subtraction of olivine using a value of 0.4 for the Fe/Mg olivine/melt exchange relationship (Roeder & Emslie, 1970).

The calculated melts from ED143 and ED91 are quartz normative, whereas the calculated melt from ED137 is hypersthene normative.

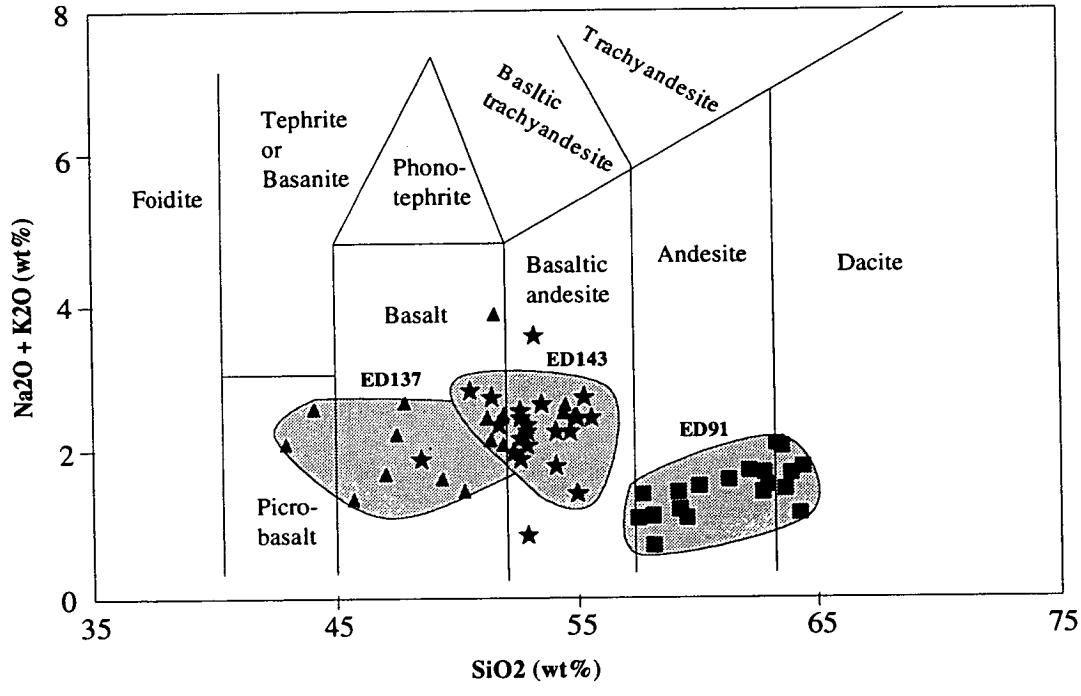

Figure 5.37: Average melt compositions from three forward experiments at 1.8 GPa, plotted on a total alkalis versus silica diagram (after Le Maitre *et al.*, 1989). Melts were calculated assuming a value of 0.4 for the Fe/Mg olivine/melt exchange coefficient (Equation 5.9).

In terms of total alkalis and silica, the calculated melt from ED143 is a basaltic andesite, that from ED137 is a basalt, and that from ED91 is an andesite (Fig. 5.37). The MgO content of the calculated melt from ED91, however, is far too high to represent an andesite. Instead, this melt composition more closely resembles a boninite. The nearest natural equivalents to the calculated melt compositions from ED143 and ED137 are found in subduction related settings (Fig. 5.38).

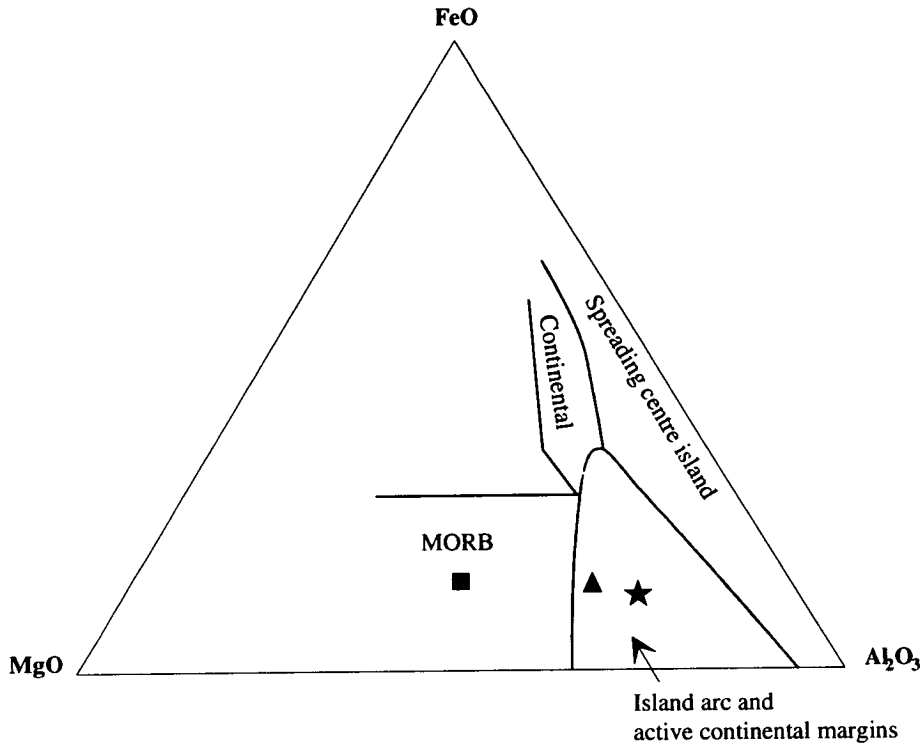

Figure 5.38: Average melt compositions from three forward experiments at 1.8 GPa, derived assuming a value of 0.4 for the Fe/Mg olivine/melt exchange coefficient (Equation 5.9). ED143 is a star, ED137 is a triangle, ED91 is a square. The boundaries from tectonic settings are from Pearce (1977).

Table 5.29 shows some estimates for the primary magma composition in island arcs, derived by a number of authors. Generally, primitive magmas are calculated from IAV by addition of fractionated phases until the calculated melt composition is in equilibrium with mantle mineralogy (e.g. Woodhead, 1988).

Table 5.29: The compositions of postulated primary melts in island arcs, and a boninite.

PRIMARY MELTS IN ISLAND ARCS?	a	b	c	d	e	f
SiO_2	50.07	48.94	52.69	49.4	48.9	57.23
TiO_2	0.72	0.7	0.81	0.52	0.5	0.12
Al_2O_3	15.92	16.01	18.14	12.1	11.4	10.61
FeO		7.95				8.80
MgO	10.1	11.42	4.21	12.6	14.7	12.27
CaO	10.12	10.89	10.2	10.8	10.3	9.69
Na_2O	2.35	2.21	2.68	1.97	1.84	0.87
K_2O	0.86	0.52	0.64	1.28	1.18	0.33
MnO	0.15	0.17	0.2	0.19	0.18	
Fe_2O_3	9.06	1.06	10.31	11.06	10.98	
Mg no.	69.0	69.6	45.0	69.5	72.8	68.2

Compositions are normalised to 100%. Data sources: a - Postulated primary magma for Okmok volcano, Aleutians (Miller *et al.*, 1992); b - primary basalt in equilibrium with forsteritic olivine from Okmok volcano, Aleutians (Nye & Reed, 1986); c - Postulated primary magma for the Mariana lavas, derived from addition of olivine and clinopyroxene to the parental magma composition (Woodhead, 1988); d, e - Picrites found in the Solomon islands, interpreted to be primary melts (Ramsay *et al.*, 1984); f - Boninite from the Bonin islands, Japan (Hickey & Frey, 1982).

In Figure 5.39 these estimates for the composition of primary magmas in island arcs are compared with the average calculated melt compositions from the three forward experiments (Table 5.28). Also illustrated are some estimates for the compositions of partial melts of hydrous peridotite made by previous workers (Table 3.1).

The diagram shows that to a first order approximation, there is a similarity between the melt compositions calculated from these experiments and possible primary melts of subduction zones. It can also be seen that the melt compositions calculated from these experiments are generally less olivine rich than those calculated by other authors. Unfortunately, until the estimated melt compositions have been verified and/or refined, no reliable conclusions that can be drawn from this.

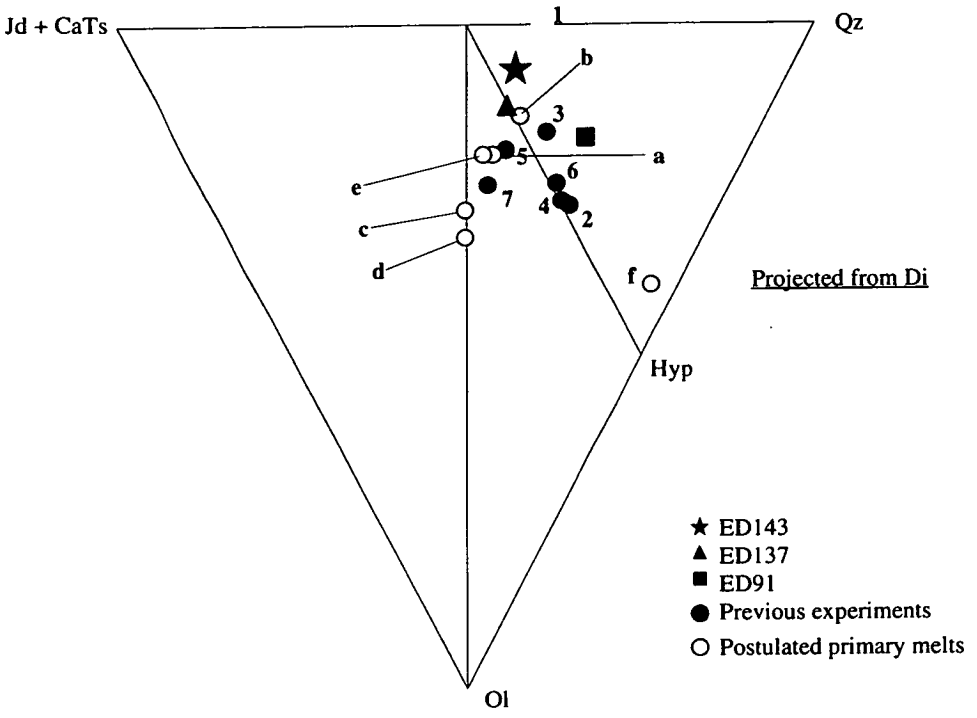

Figure 5.39: Projection from diopside onto the (jadeite+Ca-tschermak's molecule)-quartz-olivine plane showing the calculated composition of partial melts from ED143, ED137, and ED91 assuming that the value for the Fe/Mg exchange coefficient is 0.4. Also shown are the projections of the calculated melt compositions of hydrous peridotite from previous workers (numbered 1 to 7). The data were given in Table 3.1, and are derived from 1 - Kushiro *et al.* (1972); 2, 3 - Green (1976); 4, 5, 6, 7 - Kushiro (1990). Postulated primary melt compositions for island arcs are also shown along with a typical boninite. The labelling, a to f, refers to the columns in Table 5.29.

5.5 SIZE OF AMPHIBOLES

One of the main objectives of this study was to examine the role of amphiboles during partial melting of hydrous peridotite. There are little available data regarding the trace-element contents of amphiboles and coexisting melts and therefore efforts were made to produce supersolidus amphiboles which could be analysed by SIMS. To achieve this it was necessary to:

a) Discover the conditions under which both melt and amphibole coexist;

b) Dope the starting mixture with trace elements;

c) Produce large enough crystals. Although the optimum beam size of the ion probe is 15 μm in diameter, the sputtered volume is larger than this. In order to be confident that the beam does not overlap with any surrounding melt, crystals need to be >40x40 μm.

Coexisting amphibole and melt were produced in ED143 (see Section 5.2) and in many of the reversal experiments. In addition, a number of other experiments were performed in which the bulk composition was biased towards the amphibole and melt components. These are reviewed below. Initial efforts were directed towards growing large crystals using undoped sintered oxide starting mixtures. It was anticipated that once this had been achieved, a mixture could be made up which contained the necessary trace elements.

The amphiboles produced in ED143 are 10x10 μm on average, reaching a maximum size of 15x20 μm. Although still insufficient, crystals in the initial reversal experiments were larger (e.g. 15x50 μm in ED195 - see Plate 5.6a) suggesting that growth was facilitated by:

a) the high proportion of melt and/or

b) the larger initial water content.

Several further experiments were conducted, in which one or more of the following variables were changed: starting composition, run time, initial water content, and temperature. The results are shown in Table 5.30.

Table 5.30: Cross-sectional areas of the largest amphibole crystals found in run products.

	Mix	%H_2O	Temp[1]	Dur. (hrs)	Size of amph.
ED143	HAW	in HAW		24	10x15 μm
ED192	M3	50		2	none
ED194	M3	30		1	5x15 μm
ED195	M3	30		2	15x50 μm
ED201	W1	12		24	15x60 μm
ED204	W1	11		48	none
ED210	W1	11	1010°C	48	30x50 μm
ED213[2]	W2	14		46	10x20 μm
ED214	W2	10		24	20x30 μm
ED216	W2	10	1040°C	24	15x50 μm
ED217	HAW	in HAW	1150→1020°C	0.2→24	10x15 μm
ED220[3]	M3	30		24	15x25 μm
ED223	M4	35		24	25x80 μm
ED234	M4	57		48	none
ED238	M4	79	1015°C	48	none
ED239	M4	63	1010°C	48	none
ED285	M5	36		30	none

[1]All experiments were run at 1.8 GPa, 1020°C unless otherwise stated; [2]Temperature dropped during this experiment; [3]Nickel from the buffer contaminated run products. Starting mixtures: M3, M4, M5 are compositions similar to the calculated melt composition from ED143 (see Appendix B); W1 and W2 are weighted towards the amphibole and melt compositions from ED143. W1 (39% amph; 25% melt; 13% ol; 10% opx; 10% cpx; 2.6% others); W2 (43.5% amph; 36% melt; 10% opx; 5% cpx; 5% ol; 0.9% others).

PLATE 5.6

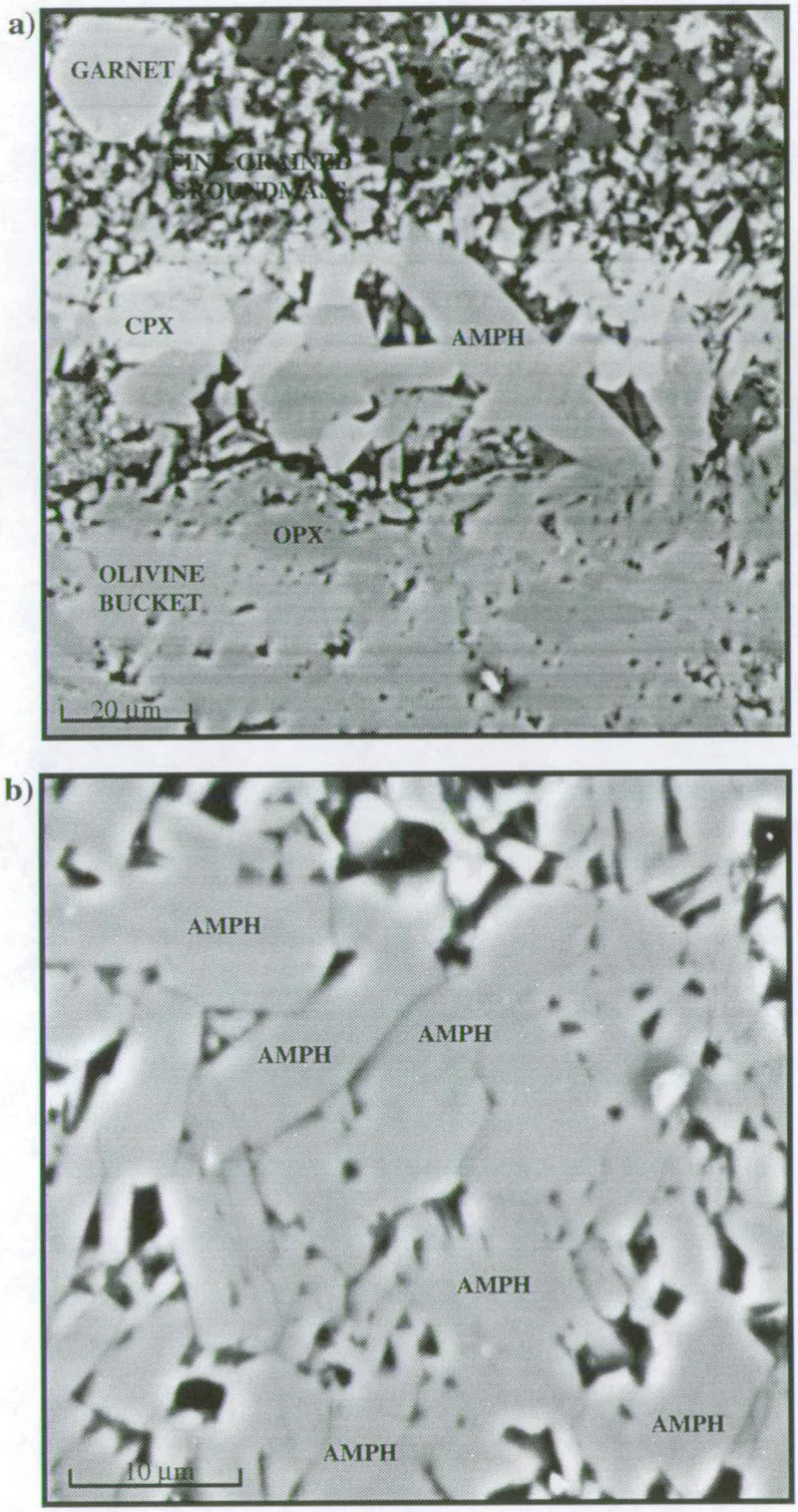

Back-scattered electron images. a) a large amphibole from ED195, b) several small amphiboles from ED214.

Despite many attempts, no crystals of the required size were produced. This approach was therefore abandoned. The results, nevertheless, show that:

- Biasing the starting compositions towards amphibole and melt compositions (W1, W2) yields more amphibole crystals, although they are not significantly larger (Plate 5.6b).
- Doubling the run time from one hour to two hours significantly increases the size of the crystals. However there is very little difference between crystals formed after two hours and those formed after 24 or 48 hours. Therefore it would have been futile to have attempted even longer experiments.
- The addition of more than 30% water to the melt composition precludes the formation of amphiboles, presumably due to the dissolution of essential amphibole-forming elements.
- Running experiments at slightly higher or lower temperatures has little effect on size of crystals. For reversal experiments using M4 as a starting composition, amphiboles were not formed in experiments at 1010°C and 1015°C. In ED217 the run temperature was approached from above, after the charge had been held at 1150°C for ten minutes. It was hoped that the melting of amphibole at the higher temperature would minimise the number of nuclei forming at run temperature, and consequently increase the size of those crystals that did form. Unfortunately this did not happen: crystals were the same size as those formed in the original forward experiment.

5.6 CONCLUSIONS

At the start of the project it was aimed to perform a set of partial melting experiments on a peridotite composition under hydrous conditions. It had been intended to document the major-element and trace-element compositions of partial melts over a range of pressures and temperatures. However, contamination of many experiments by boron, and its consequent effect on phase relations and phase compositions, ensured that many of the original aims could not be achieved. Nevertheless, major-element compositions of mineral phases produced from partial melting experiments at 1.8 GPa have been documented; major-element compositions of melts have been estimated; and an appraisal of the estimated melt composition from one experiment has been made from the results of a series of reversal experiments.

1. Forward experiments were performed in solid-media apparatus using 4 mm diameter platinum capsules. The starting material was Hawaiian Pyrolite - 40% olivine, and the conditions were water saturated and were buffered to an oxygen fugacity equivalent to NNO.
2. The mineralogy of forward experiments was consistent with Green (1973): the amphibole-out curve was encountered within approximately 40°C of the solidus, followed by the ilmenite-out, clinopyroxene-out, and orthopyroxene-out curves. These curves were, however, encountered at a higher nominal temperature than reported by Green (1973), possibly as a result of inter-laboratory differences.
3. The compositions of minerals produced in the forward experiments is strongly correlated with temperature. With increasing temperature, the most striking trends include increases in the Mg nos. of olivines and pyroxenes; a decrease in the Mg no. of amphibole; a decrease in CaO content in olivine; and an increase in Cr_2O_3 content in spinel. All mineral compositions are similar to their natural counterparts found in mantle xenoliths.
4. The melt composition was determined by a new technique in which the melt was trapped during the experiment in an *in situ* olivine crystal. Assuming that a) the only quench crystals to form in the melt inclusion are olivines, b) the formation of quench olivine crystals can be approximated as an equilibrium process, and c) the olivine bucket does not react with the starting material, it should be possible to reconstruct numerically the equilibrium melt composition from the melt inclusion composition by incremental addition of olivine until the Fe/Mg olivine/melt exchange coefficient of Roeder & Emslie (1970) is re-established. For the initial calculations, the value of this exchange coefficient was assumed to be 0.3.
5. The equilibrium melt compositions from three experiments were calculated from the melt inclusion analyses. The spread in compositions exhibited by the melt inclusions was lessened but not eradicated after addition or subtraction of olivine.
6. Several reversal experiments were performed using the average calculated melt composition from ED143. Encouraging results were obtained from reversal experiments run in olivine buckets: these yielded crystals of orthopyroxene, clinopyroxene, and amphibole, all of which were stable in the forward experiment. However, garnet, which had not been stable in the forward experiment, was also formed. Furthermore, it appeared from mineralogical textures, that the olivine bucket had reacted with the melt to form orthopyroxene and clinopyroxene. It was concluded that the calculated melt composition may have been too poor in olivine component.

7. Reversal experiments without the use of an olivine bucket were performed. Varying amounts of additional olivine component were included in some capsules. Results show that it required between 10 wt% and 20 wt% additional olivine to stabilise equilibrium olivine. The phase assemblage of the original experiment was not, however, reproduced. Further experiments were performed at a lower temperature to encourage crystallisation. However, although clinopyroxene and amphibole were formed after the addition of 10 wt% olivine, and olivine, clinopyroxene and garnet were formed after the addition of 20 wt% olivine, the phase assemblage from ED143 was not reproduced. In particular, no orthopyroxene was formed.
8. Phases formed in the reversal experiments were consistently more aluminous than those produced in the forward experiment, ED143. The Mg no. of all reversal phases was higher than those in ED143, and there were consistent differences between reversal experiments and the forward experiment in terms of Na_2O, NiO (both lower in the reversal experiment), and MnO (higher in the reversal experiments).
9. The results of the reversal experiments suggest that the true equilibrium melt composition is richer in olivine component than that originally estimated. Recalculation of the equilibrium melt composition from the melt inclusion compositions, assuming that the relevant value of the Fe/Mg olivine/melt exchange coefficient is 0.4, yields a more olivine-rich composition, and it is suggested that this is likely to be closer to the true melt composition. This is supported by results from reversal experiments that produced equilibrium olivine and melt, from which values for the Fe/Mg olivine/melt exchange coefficient of approximately 0.4 were inferred.
10. Melts from three experiments have been calculated assuming a value of 0.4 for the Fe/Mg olivine/melt exchange coefficient. Two relatively low-degree partial melts (both in equilibrium with amphibole) are similar to a basaltic andesite and a basalt. A much higher degree partial melt (in equilibrium with olivine and orthopyroxene) has a high-SiO_2, high-MgO composition similar to a boninite.
11. Further reversal experiments are required to establish the true melt composition from ED143. In particular, it would be instructive to run more experiments without an olivine bucket, possibly lowering the temperature to encourage crystallisation and using a starting composition more enriched in olivine component and less enriched in alumina. Until these experiments are performed, the melt compositions are by no means certain, and are not in my opinion sufficiently accurate to warrant use in modelling calculations.

12. It proved impossible to measure partition coefficients between amphibole and melt due to the small size of amphiboles formed. Comparison of the size of amphibole crystals between experiments indicated that their growth was facilitated by large melt fractions and high initial water content, although too much water appeared to dissolve the essential amphibole-forming elements and so preclude its formation. Crystals large enough to analyse successfully by SIMS were not formed.

CHAPTER 6

CONTAMINATION OF EXPERIMENTS BY BORON

CHAPTER 6: CONTAMINATION OF EXPERIMENTS BY BORON

6.1 INTRODUCTION

One objective of a perfect experiment is to equilibrate the starting mixture in a closed system. In practice, however, there may be fluxes into or out of the capsule, including loss of iron and/or nickel from the charge (Holloway & Wood, 1988; Hart & Davis, 1978), and diffusion of hydrogen through capsule walls (Holloway & Wood, *op. cit.*). In addition, there are potential contaminants from the cell. In many of the experiments in this study, the capsule is surrounded by boron nitride. It is now recognised that boron, which has a very small ionic radius, may be capable of diffusing through platinum (Holloway, *pers. comm.*). Any such contamination of experiments in the past is unlikely to have been discovered, as boron cannot be unequivocally detected by the electron microprobe[1]. Recently, though, it has become increasingly common to analyse run products by SIMS, by which boron can be readily detected. Chaussidon & Libourel (1993) used this technique to suggest that their run products had suffered no contamination from boron, despite its presence in the surrounding Pyrex. On the other hand, Hart & Dunn (1993) analysed experimental run products by SIMS, and found that their melt possessed a boron content which exceeded the expected value by a factor of ten. Clinopyroxene crystals were zoned in boron, with contents increasing towards the edges. The authors attributed these observations to progressive diffusion of boron from the surrounding Pyrex sleeve through the walls of the platinum capsule. Much more severe contamination by the surrounding medium is possible if a capsule bursts during a run, allowing the contents to escape and the surrounding material to enter, with serious implications for the results. Thus it is of utmost importance to ensure that a capsule has remained intact for the duration of the experiment. For water-saturated experiments, the retention of free water in the run product has generally been used as evidence that the capsule has remained intact during the experiment (e.g. Anderson & Burnham, 1965; Kitahara *et al.*, 1966; Holloway, 1971; Green, 1973; Sisson & Grove, 1993a). The majority of capsules in this study retained water (confirmed by loss of weight after piercing and heating) and were consequently

[1]Boron can only be detected when it is extremely abundant (e.g. >50% B_2O_3).

deemed successful. It was therefore assumed that there could not have been any major contamination of run products.

Surprisingly, analysis of the run products by SIMS has revealed that there are anomalously high levels of boron[2] in many experiments, with B_2O_3 occasionally present in major-element abundances. Analysis by SIMS has also shown that a bizarre mineral produced in three experiments is a borate, despite previous investigation by electron microprobe which failed to detect any boron. Because the contamination is so extensive, it is thought that the cause may be capsule failure rather than diffusion through the capsule walls. This inferred failure of capsules, which in many cases had retained their water contents, calls into question the assumption that an experiment is successful if water is present in the capsule at the end of the experiment.

In this chapter, the extent of the boron contamination is assessed, and possible reasons for its occurrence are discussed. As experiments have been contaminated to a variety of degrees, results will be used to establish, at least qualitatively, the effects of boron in this system. It will be shown that high levels of boron can sufficiently influence the phase relations and compositions of phases, to render many of these experiments invalid for their original purpose.

6.2 THE OCCURRENCE OF BORON IN RUN PRODUCTS

As it requires an ion probe to detect boron, and as ion-probe time is a precious and rare commodity, the problem of boron contamination was not discovered until approximately sixty experiments had been executed. In the run products of three of these experiments, a new mineral (nicknamed ignorite) had been detected. This has now been shown to be a borate, although previous analysis by electron microprobe had failed to detect boron.

[2]The starting mixture for the experiments contains boron in low concentrations (<10 ppm). The expected concentration of boron in a 10% partial melt is therefore <100 ppm.

6.2.1 Ignorite

A Mg, Cr, Ti, Al non-silicate mineral was discovered in the run product of ED242, a forward experiment at 1.8 GPa, 1060°C. The mineral occurs as large laths (up to 100 μm in length) and smaller subhedral clumps (Plate 6.1). Examination in transmitted light shows the crystals to be brown in colour, possibly pleochroic, with straight extinction and a faint cleavage parallel to length. The experiment was repeated four times, but the mineral was only produced in one of these repeated experiments (ED250), and in another experiment at 1040°C (ED253).

Major-element analyses performed by electron microprobe are shown in Table 6.1.

***Table 6.1*: A selection of analyses of ignorite from ED242, performed by EPMA.**

IGNORITE from ED242								
SiO_2	0.17	0.14	0.11	0.20	0.26	0.12	0.09	0.10
TiO_2	7.73	10.83	12.04	12.91	13.05	13.13	13.93	15.13
Al_2O_3	6.07	6.85	6.46	7.76	7.70	7.96	8.75	7.78
Cr_2O_3	25.85	18.91	18.48	15.36	15.10	14.91	11.71	11.26
FeO	4.80	5.21	5.30	5.61	5.60	5.38	5.48	5.86
MgO	30.54	32.91	32.92	32.57	32.83	32.64	33.32	33.91
CaO	0.02	0.03	0.03	0.04	0.04	0.03	0.04	0.04
Na_2O	0.00	0.04	0.02	0.01	0.01	0.02	0.02	0.01
K_2O	0.01	0.02	0.01	0.00	0.01	0.01	0.01	0.01
MnO	0.09	0.05	0.08	0.07	0.06	0.07	0.05	0.05
NiO	0.82	1.18	0.69	1.39	1.13	1.68	0.80	1.23
TOTAL	76.10	76.16	76.12	75.92	75.78	75.94	74.20	75.35
Cations assuming that shortfall is B_2O_3: based on 40 oxygens								
Si	0.0	0.0	0.0	0.0	0.1	0.0	0.0	0.0
Ti	1.4	1.9	2.2	2.3	2.3	2.3	2.4	2.7
Al	1.7	1.9	1.8	2.2	2.1	2.2	2.4	2.2
Cr	5.0	3.6	3.5	2.9	2.9	2.8	2.2	2.1
Fe	1.0	1.0	1.1	1.1	1.1	1.1	1.1	1.1
Mg	11.0	11.7	11.7	11.5	11.6	11.5	11.5	11.9
Ca	0.0	0.0	0.0	0.0	0.0	0.0	0.0	0.0
Na	0.0	0.0	0.0	0.0	0.0	0.0	0.0	0.0
K	0.0	0.0	0.0	0.0	0.0	0.0	0.0	0.0
Mn	0.0	0.0	0.0	0.0	0.0	0.0	0.0	0.0
Ni	0.2	0.2	0.1	0.3	0.2	0.3	0.1	0.2
B	10.0	9.8	9.8	9.9	9.9	9.8	10.3	10.0
TOTAL	30.3	30.4	30.3	30.2	30.2	30.2	30.1	30.2
Mg no.	91.89	91.84	91.72	91.19	91.27	91.53	91.55	91.17

The cation distribution has been calculated assuming that the missing 25 wt% represents B_2O_3.

PLATE 6.1

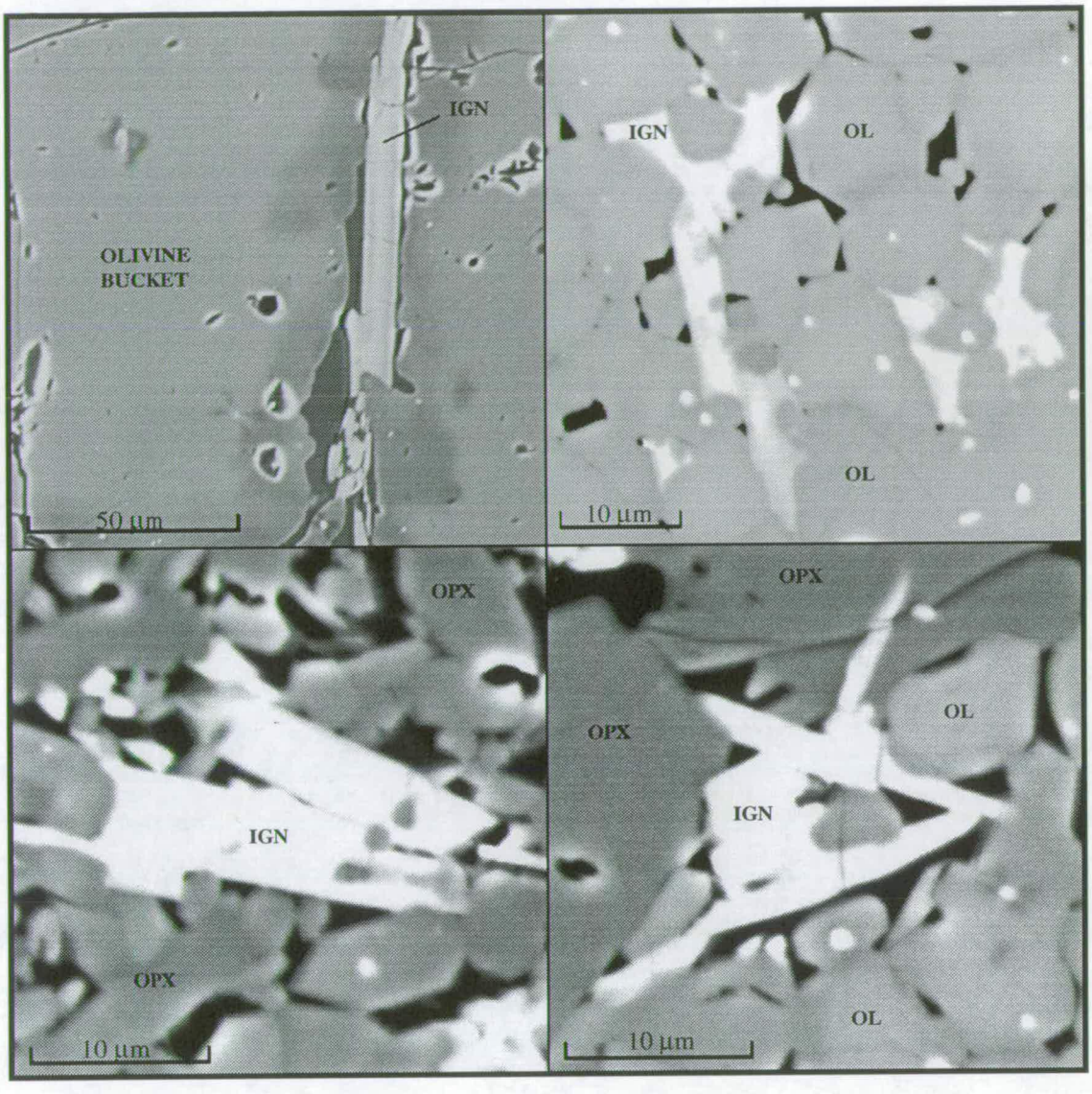

Back-scattered electron images of a polished section of ED242 showing crystals of olivine (OL), orthopyroxene (OPX), and ignorite (IGN).

MgO and Cr_2O_3 are predominant in this mineral, which also contains smaller amounts of Al_2O_3, TiO_2 and FeO, but negligible SiO_2, CaO or alkalis. There are distinct correlations between the major-element oxides within an experimental charge, with TiO_2 and Al_2O_3 decreasing as Cr_2O_3 increases (Fig. 6.1).

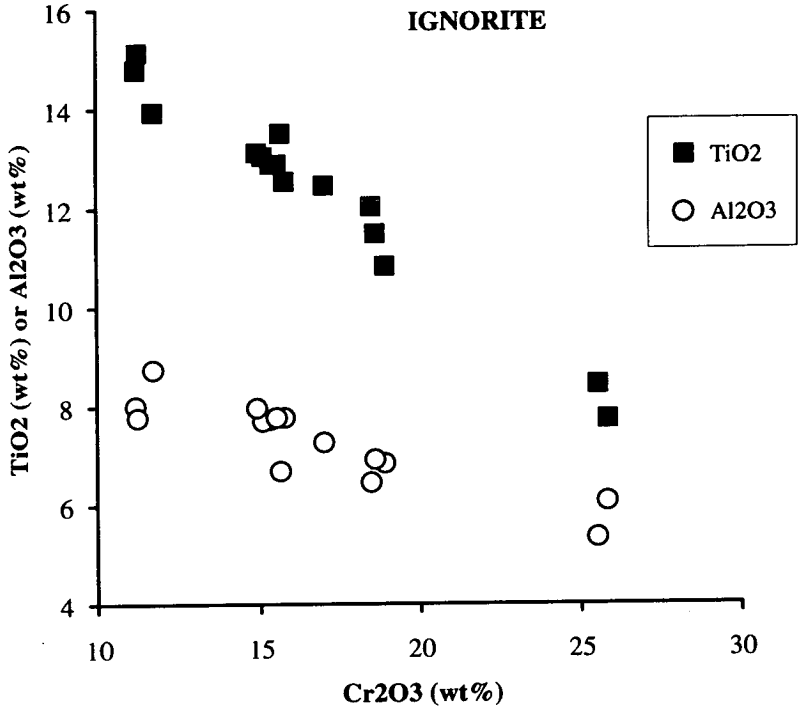

Figure 6.1: Composition of ignorite crystals from ED242 - the correlation between Cr_2O_3, TiO_2, and Al_2O_3.

The total (MgO+FeO) also changes, although less markedly. Careful examination using optical and electron microscopy refutes the possibility that the 'mineral' is composed of a fine intergrowth of two or more end members. It is therefore probable that there is extensive solid solution within the mineral. The oxide totals for all analyses fall between 73 and 77. These extremely low totals are not due to machine error, as the results were reproduced after all standard measurement were repeated and the counters were rebiased. Generally, low totals are caused by the presence of an unanalysed component such as a major-element oxide that has been overlooked or a light element or molecule such as carbon or water. All major-element oxides present in the starting mixture were included in the analysis, and therefore the only legitimate component that could have made up the shortfall was water. However, there is no record of a hydrous mineral of such composition, and moreover, the amount of water would have to have been unreasonably large to account for such low

totals. Another possible explanation for the low totals was contamination of the experiment. The Pc2 crystal was used to measure boron, carbon and nitrogen. No significant amounts of these elements were detected. Phosphorus was measured using a TAP crystal: again count rates were negligible.

In order to investigate further the crystallography of this seemingly new mineral, an attempt was made to synthesise it from a sintered oxide composition mid way between the end members, and water. The experiment, which was run under the same conditions as ED242, produced olivine, ilmenite and spinel, but no ignorite.

Analysis of the mineral by SIMS shows that it contained a substantial amount of boron: although no crystals are large enough to accommodate the entire beam, in one analysis which overlaps onto surrounding phases the extremely high count rate[3] from ^{11}B suggested that boron is present at major-element levels. ^{26}Mg, ^{30}Si, ^{42}Ca and ^{47}Ti count rates were recorded in addition to ^{10}B. Titanium was used as the reference element as it has a relatively high abundance in ignorite (approximately 12 wt%) relative to other phases. The boron content was calculated to be approximately 80,000 ppm (which is equivalent to 26 wt% B_2O_3). Therefore the low total oxide value in analyses by electron microprobe is due entirely to B_2O_3.

The mineral can most simply be described as $(Mg,Cr,Ti,Al,Fe)_2BO_4$. There appear to be a number of coupled solid solutions and consequently it is difficult to assign a more specific formula. The Cr-rich composition is best represented as $(Mg,Fe)_{12}(Cr,Al)_6Ti_2B_{10}O_{40}$; the Cr-poor composition is $(Mg,Fe)_{13}(Cr,Al)_4Ti_3B_{10}O_{40}$.

As well as raising questions about the detection of boron using the Pc2 crystal on the electron microprobe, this discovery shows that in at least three experiments there has been ingress of boron to such an extent that a borate phase has been produced.

6.2.2 Distribution of boron within one experiment

After the boron contamination was discovered, it was necessary to check as many run products as possible to assess the extent of the problem. Analyses of melt inclusions, fluid quench products (where present) and random areas of the mix were performed by SIMS. Silicon was chosen to be the reference element, and most analyses were calculated assuming a SiO_2 content of 50%. Errors inherent from this approximation are insignificant in comparison to the measured range of boron contents. Five melt inclusions from ED253 were analysed (Fig. 6.2). Boron contents range from under

[3]Boron was present in such high quantity that the counts from ^{11}B overloaded the electron multiplier. Consequently ^{10}B was measured in the analysis.

100 ppm to over 100,000 ppm. The high-boron inclusions are situated nearer to the internal edge of the olivine bucket, whereas the low-boron melt is further from the starting mixture.

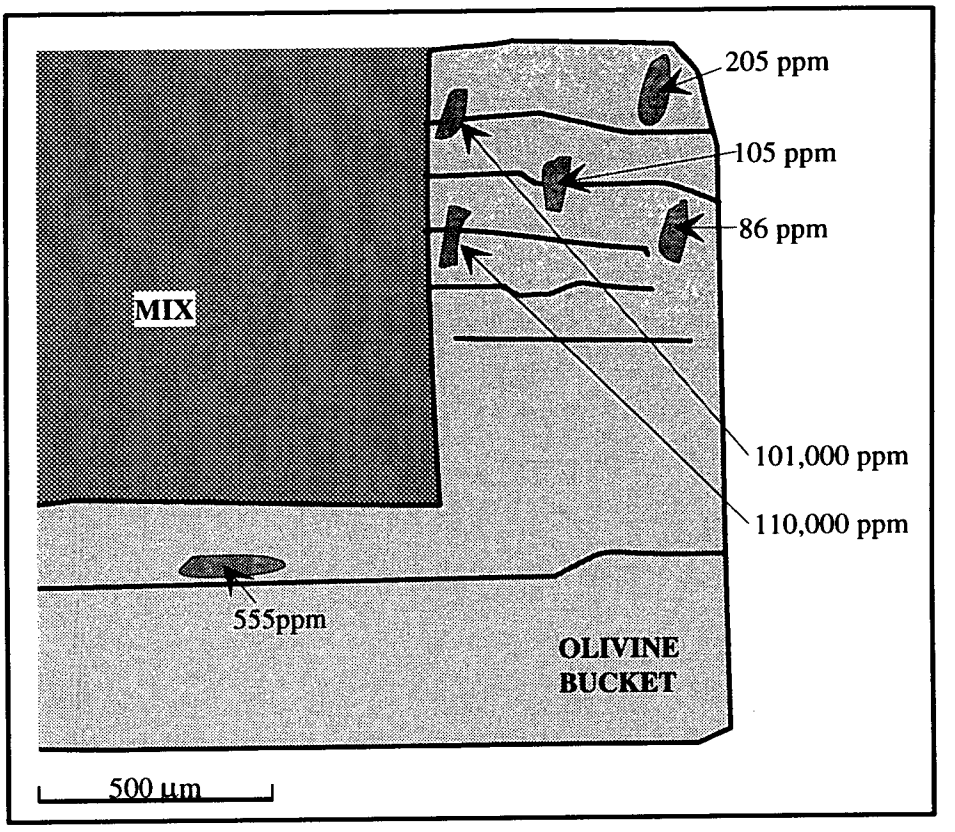

Figure 6.2: Cartoon showing melt inclusions in the olivine bucket from ED253. The boron content, measured by SIMS, is shown for each inclusion analysed.

It is possible that the first formed melt, which contained little boron, migrated further into the olivine bucket, whereas melt formed later on was highly contaminated and did not have time to migrate so far. There is similar variation in other run products: for example in ED279 the boron contents vary from approximately 380 ppm to 24,000 ppm in the mix, with values of up to 34,500 ppm in melt pools. The presence of ignorite testifies to very severe contamination by boron. However, in one melt inclusion from ED242 (the first experiment to produce ignorite), the boron content was measured as 191 ppm. Regardless of the cause, the extreme inconsistency in boron content makes it difficult to assess the extent of contamination, especially in those experiments for which there are few analyses.

6.2.3 Extent of boron contamination

Twenty-eight run products were analysed for boron. In most cases, several analyses were performed and the highest value was used to quantify the extent of boron contamination. However it should be remembered that boron contents in a single experiment can vary by several orders of magnitude and therefore if only a few analyses are performed, it is not always possible to detect contamination. Table 6.2 shows results from all experiments analysed. There is a wide range of maximum boron contents: many experiments appear to be severely affected with boron contents of several thousand parts per million. However, there are also run products in which only low levels of boron have been detected.

Table 6.2: Experimental conditions and maximum boron content of run products analysed by SIMS.

Expt.	P (GPa)	T (°C)	dur^n (hrs)	Max B (ppm)	H_2O (mg)	Expt.	P (GPa)	T (°C)	dur^n (hrs)	Max B (ppm)	H_2O (mg)
ED91	1.8	1150	24	70	x	**ED249**	1.8	1060	24	240	7.3
ED101	1.8	1125	24	670	x	**ED250***	1.8	1060	24	9,370	2.3
ED133	1.8	1010	24	200	x	**ED253**	1.8	1060	24	110,000	2
ED135	1.8	1065	<16	270	x	**ED257**	2.3	1040	24	57,200	1
ED143	1.8	1020	24	290	1.8	**ED258**	2.3	1020	24	40,900	0
ED192	1.8	1020	2	50	18	**ED259**	2.3	1000	24	180	x
ED194	1.8	1020	1	20	3.6	**ED260**	2.3	1060	24	86,800	0
ED195	1.8	1020	2	140	4.1	**ED278**	1.8	1050	25	1,870	2.1
ED201	1.8	1020	24	500	5.2	**ED279**	2.8	1040	24	34,600	0.6
ED223	1.8	1020	24	130	7.8	**ED283**	2.3	1010	24	13,100	0.9
ED231	1.8	1020	48	4450	6.6	**ED285**	1.8	1020	30	70,600	x
ED234	1.8	1020	48	980	0	**ED315**	2.3	1040	24	420	0
ED242*	1.8	1060	24	66,000	0.7	**ED339**	1.8	1060	24	100,000	0
ED244	1.8	1060	24	11,600	1.7	**ED340**	1.8	1040	24	43,300	0

Also shown is the mass of water retained in the capsule at the end of the experiment, measured by weight loss. An x indicates that this value was not measured. *Ignorite was produced in these experiments.

The mass of water lost from the retrieved capsule after piercing and heating is also shown in Table 6.2. Several experiments that retained some water had been contaminated by boron. For example, ED231, which released 6.6 mg of water, contained up to 4450 ppm boron; ED250 released 2.3 mg of water even though boron contamination had resulted in the formation of ignorite. There were several run

products which did not lose water after the experiment (e.g. ED258, ED260). Their mineralogy is not consistent with the loss of water during the experiment[4], and therefore it was assumed that the water had been lost during the quenching process. It is now clear that these experiments have been severely contaminated by boron. There is a crude negative correlation between the mass of water left in the capsule after the experiment and the extent of boron contamination (Fig. 6.3), suggesting that water escapes gradually with progressive ingress of boron.

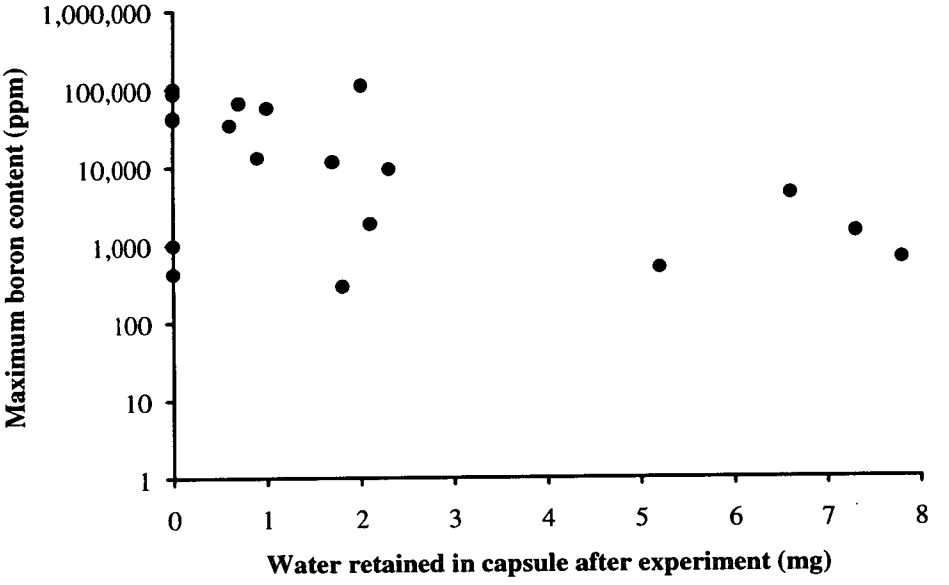

Figure 6.3: Boron content versus water retained in the capsule after the experiment. The maximum value of boron, measured by SIMS, is plotted. The amount of water retained in the capsule was determined by measuring the weight loss after piercing and heating the capsule.

6.3 BORON CONTAMINATION - DETERMINING FACTORS

It is clear that not all experiments have been contaminated to the same degree: indeed, several experiments appear to be relatively unaffected by boron. There are several potential reasons for this which are discussed overleaf.

[4]An experiment which loses its water during the run is expected to behave as anhydrous, i.e. it is unlikely that the solidus will be intersected, and therefore the mineralogy is expected to be consistent with a subsolidus anhydrous peridotitic assemblage.

6.3.1 Capsule geometry

Initial experiments involved capsules in which the bulky second crimp was at the top of the capsule (see Figure 4.1 in Chapter 4). After approximately twenty experiments performed in this way, the arrangement was changed so that the second crimp was at the bottom. The effect of this was to reduce the cushion of platinum between the alumina disc and the charge thereby bringing the starting mixture nearer to the thermocouple. However, this arrangement may also increase the possibility of the rigid olivine bucket puncturing the top of the capsule. Figure 6.4 shows that with two notable exceptions (ED242, ED253) the levels of boron in experiments using the first configuration are considerably lower than for the second configuration. Whilst this may be taken as good evidence that the top of the capsule in the second configuration is indeed too thin and easily punctured, there are other changes that occurred to the cell at this time, which may also account for the observations noted above.

6.3.2 Cell geometry

The ½" talc-boron nitride cell used in these experiments is described in Chapter 3. The main changes made to the cell during the course of the project are listed below, and the approximate times at which these changes occurred are indicated in Figure 6.4.

- Alumina discs were changed from soft to hard - although the timing of this corresponds more or less to a general increase in boron contamination in experiments, it is not clear whether there is any relationship between the two. It is conceivable that the use of a hard alumina disc will facilitate a puncturing of the platinum.
- Thermocouple sheaths were changed from pyrophyllite to mullite - this happened at approximately the same time as the change in alumina discs: again, there is no proven relationship between the thermocouple sleeving material and the extent of boron contamination.
- Boron nitride was packed in powder form as opposed to rigid sleeves - the boron contents of these experiments are no different from those experiments conducted immediately before or after this.

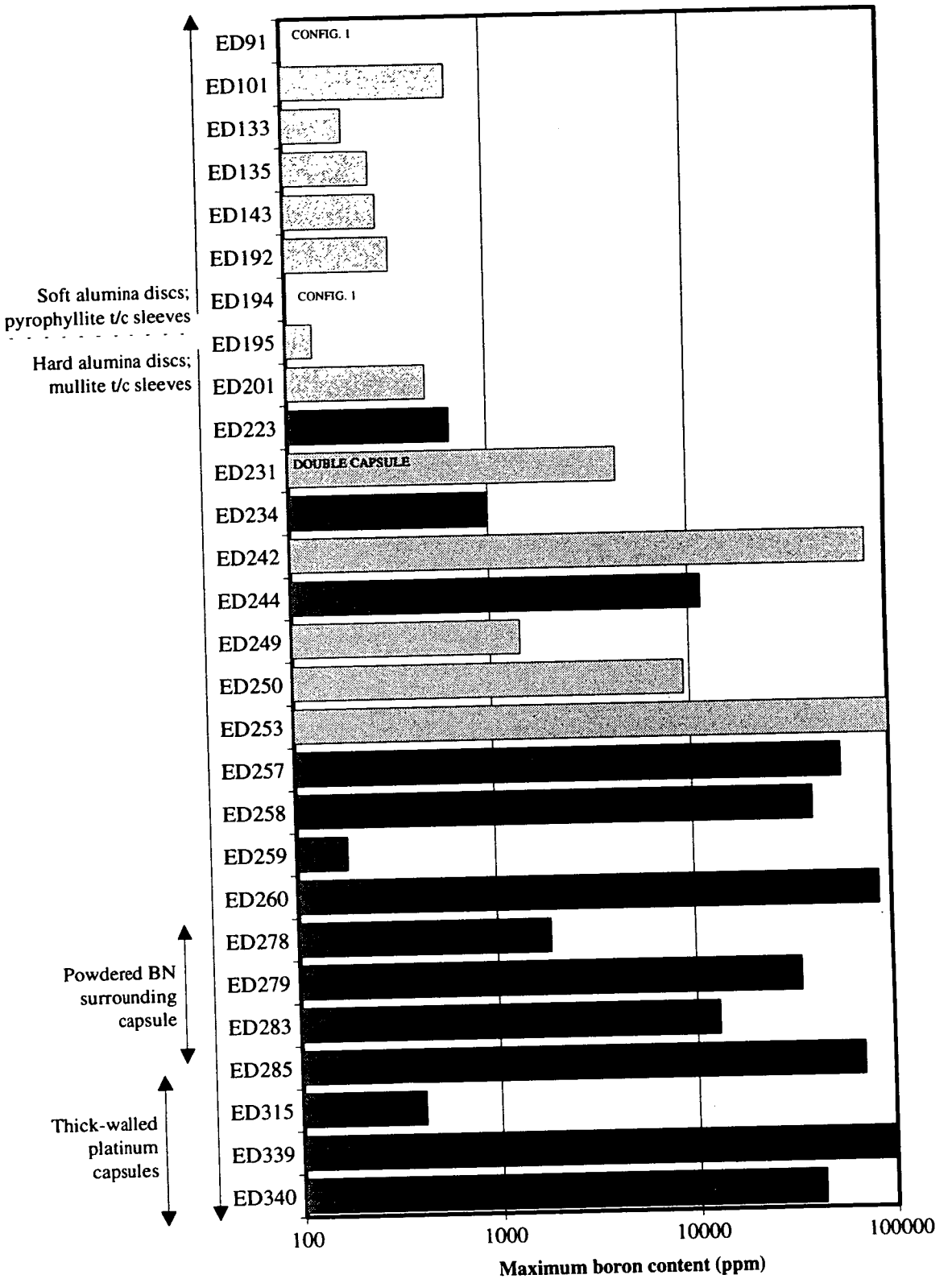

Figure 6.4: Maximum boron content (ppm) in all run products analysed. Light shading - capsule configuration 1; dark shading - capsule configuration 2. Experiments are shown in chronological order. To the left of the graph are indicated the points at which changes to the cell were executed.

- Thick-walled platinum tubing was used - this does not appear to have been successful in halting the ingress of boron into the capsules, despite the encouraging low values of boron measured in ED315 (see also Fig. 6.5).

6.3.3 Experimental conditions

The majority of runs analysed were performed at 1.8 GPa, with some at 2.3 GPa and 2.8 GPa. Temperature ranged from 1000°C to 1150°C, and run duration although normally 24 hrs, was 1 hr, 2 hrs, or 48 hrs for some experiments. In other words, there are several potential controls on the amount of boron in any particular experiment, and it is not an easy task to relate the amount of boron in a run product to the conditions at which the experiment was performed.

Pressure - There is no apparent correlation between the extent of boron contamination and the pressure of the experiment.

Run duration - Three analysed experiments were of a relatively short duration (1 hr and 2 hrs). There is considerably less than average boron in these run products. Those experiments which were run for longer than 24 hrs contain significant amounts of boron, although comparable to experiments run for 24 hrs.

Temperature - Any potential correlation between boron contamination and temperature of the run is obscured by other factors in the majority of experiments. However, for those experiments performed at 2.3 GPa using the same capsule geometry (configuration 2), there is a striking correlation between the maximum boron content and the temperature (Fig. 6.5). For ED259 (at 1000°C), random analyses of the mix show that the maximum boron content is low (180 ppm or 0.06 wt% B_2O_3). With increasing temperature the boron content rises steadily to a value of 87,000 ppm (or 28 wt% B_2O_3) at 1060°C, i.e. within the space of 60°C the boron content rises by a factor of almost five hundred.

Presence of free water - In the initial experiments, water was locked up in the hydrous starting material, whereas in reversal experiments and later forward experiments, free water was present in the capsule. As this coincided with a number of highly contaminated runs, it was postulated that the free water may in some way have caused the capsules to burst. However, this is unlikely as no free water was added to ED339 or ED340, both of which were highly contaminated by boron.

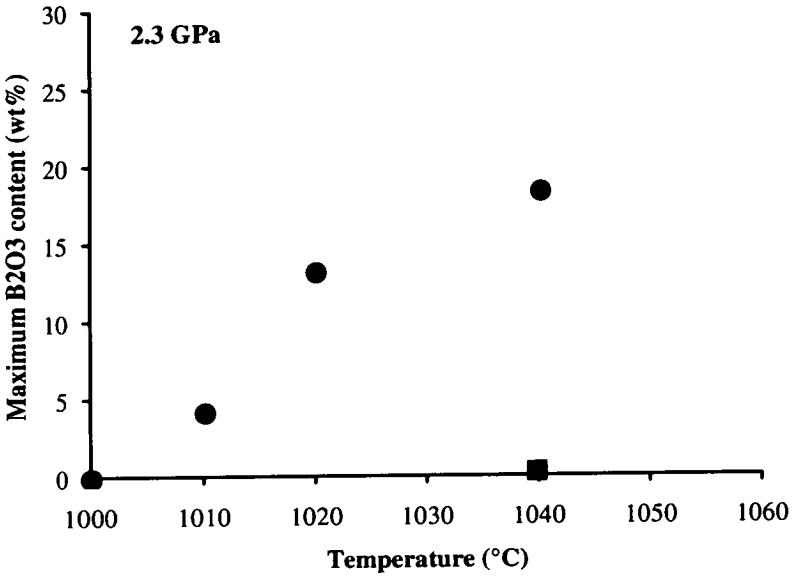

Figure 6.5: Maximum measured boron oxide content (wt%) from an experimental run product versus the temperature of the experiment. Data taken from experiments performed at 2.3 GPa using capsule configuration 2 (circles). The square represents ED315 which utilised thicker-walled platinum tubing.

6.3.4 Summary

The majority of experiments analysed contain more boron than is theoretically predicted, although contamination has occurred to a range of degrees. There does not appear to be any single specific factor controlling the large variation seen. Most of those experiments using capsule configuration 2 contain more boron than most experiments involving capsule configuration 1. The type of cell may also contribute to the extent of boron contamination: those experiments in which a hard alumina disc was used are generally more contaminated than the initial experiments which employed a softer alumina disc.

Although these factors may affect the susceptibility of cells to contamination, data suggest that the amount of boron in melts is dependent on the temperature of the run. It is not clear whether this is due to enhanced mobilisation of boron with increasing temperature, whether larger degree partial melts are more capable than smaller-degree partial melts of dissolving borate, or whether the increased temperatures lead to weakening of the capsule walls and consequent infiltration of boron.

6.4 MECHANICS OF BORON INFILTRATION

The boron is undoubtedly derived from boron nitride components in the cell (see Chapter 3). The material used is UCAR® Boron Nitride: hot pressed - grade HBN, which is claimed by the manufacturers to be at least 99% pure. X-ray diffraction of the powder used in these experiments shows that it is pure (to within the 5% detection limit of the instrument).

One method of ingress of boron could be by diffusion through the platinum. The presence of water in the run products of many experiments could be taken as supporting evidence for this hypothesis. Platinum from capsules affected by boron was analysed by SIMS and found to contain negligible boron. However, this does not preclude the possibility of some boron diffusion.

The extremely high levels of boron in many experiments (including those in which water was retained) suggest that another method of ingress of boron is in operation i.e. boron is leaking into the capsules through small holes or punctures. All capsules were tested before the experiment and are known to have been intact. Therefore any punctures form during the experiment, and in many cases are sealed to the extent that water cannot escape.

Capsules from each experiment were photographed and examined carefully for signs of rips or small holes. None were found[5], although in many cases the capsules are highly deformed. Of particular interest is the difference between the two capsule configurations. Plate 6.2 shows that for capsules with the long crimp at the top (configuration 1) the platinum from the top of the capsule is forced down into the olivine bucket. This also happens to capsules with the long crimp at the bottom (configuration 2), although in this case there is less platinum available to push down, and the walls at the top are often very thin (Plate 6.2). In two of these experiments, melt was found above the top of the capsule which proves that punctures can form in this area.

The position at which the nickel oxide reduces to nickel is worthy of note. In nearly all cases this occurs near the capsule walls directly underneath the olivine bucket, suggesting that hydrogen reaches this area of the bucket first. One possible explanation for this may be that the platinum in this area is particularly weak (possibly ripped) allowing hydrogen to diffuse through easily. This hypothesis is supported by the observation that the platinum often buckles in this area. However,

[5]This is not surprising as capsules were sectioned and mounted in epoxy resin prior to detailed examination and therefore the chances of intersecting any holes are relatively small.

PLATE 6.2

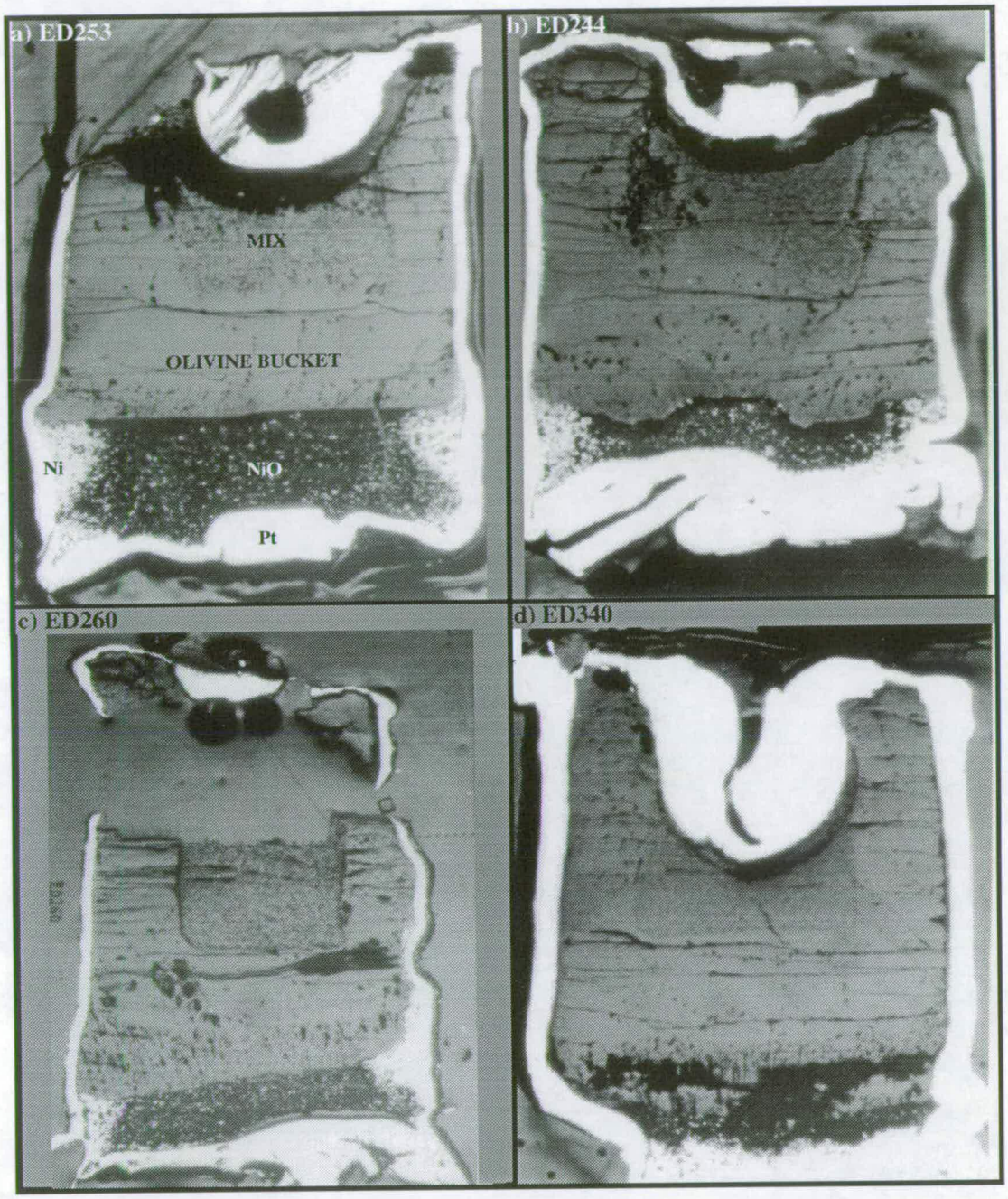

Reflected-light photomicrographs showing polished longitudinal cross sections of four run products: a) ED253, b) ED244, c) ED260, d) ED340. The capsule from ED253 is in configuration 1(Fig. 4.1), i.e. the long crimp is at the top. Capsules from ED244 and ED260 are in configuration 2 (Fig. 4.1), i.e. the long crimp is at the bottom, and in these run products the platinum at the top of the capsules is very thin. ED340 was performed using thick-walled platinum in configuration 2, and again, the platinum is very thin at the top of the capsule. All run products shown were highly contaminated by boron (Fig. 6.4).
The diameter of all capsules shown is 4 mm.

another valid explanation is that hydrogen from the top of the capsule migrates down the sides of the olivine bucket and reacts with the buffer.

The preceding observations suggest, but do not conclusively prove, that the rigid olivine bucket may rip the platinum capsule, possibly beneath the olivine bucket and certainly at the top in some cases. This would explain why capsules in configuration 2 are more often contaminated than capsules in configuration 1. The inter-experiment variation in boron contents may result from differences in the size of the holes. It is also possible that diffusion through the platinum is taking place simultaneously, which may explain the slightly elevated boron contents in some experiments (e.g. ED143).
The presence of water in many contaminated run products is still unexplained. I suggest that holes are sealed in some way, possibly by borate.

6.5 PHASE ASSEMBLAGE AND COMPOSITION - THE EFFECT OF BORON

6.5.1 Introduction

Boron is known to be an extremely effective flux: the introduction of B_2O_3 to SiO_2 causes its melting temperature to drop from 1600°C to 440°C (Levin *et al.*, 1965). Consequently, it is expected that significant levels of boron would cause a fluxing effect in these experiments, and produce phase assemblages and phase compositions that are typical of an experiment run at a higher temperature.
Interpretation is complicated by the fact that boron nitride in experimental charges has been found to establish oxygen fugacity at very low levels (Wendlandt *et al.*, 1982). They found that boron nitride reacts with oxygen to produce boric oxide and nitrogen according to the probable reaction:

$$2BN + 1½O_2 \leftrightarrow B_2O_3 + N_2$$

At high pressures this reaction establishes oxygen fugacity below QIF, i.e. extremely reducing. In their experiments, nickel oxide and iron oxide in the vicinity of boron nitride were both reduced to metal.

In this section, results are presented from forward experiments that have been contaminated by boron. Included are all experiments conducted at 2.3 GPa and 2.8 GPa, and several experiments conducted at 1.8 GPa. Where possible, connections are drawn between the mineralogy and phase compositions, and the extent of boron contamination. This is particularly significant for experiments at 1.8 GPa, for which uncontaminated experiments are available as controls. For the higher temperature experiments there are few uncontaminated analogues and therefore interpretation of results is less straightforward.

6.5.2 Experiments at 1.8 GPa

Results from forward experiments not contaminated by boron have already been presented in Chapter 4 (see Table 4.1 for a summary of mineralogy). Subsequently, experiments were performed at 1040°C and 1060°C. Because of the presence of ignorite in these run products, the experiments were repeated a number of times (Table 6.3) with inconsistent results. Analysis by SIMS shows that all of these run products have been contaminated by boron.

Table 6.3: Mineralogy of forward experiments at 1.8 GPa, contaminated by boron.

Expt.	T(°C)	melt	ol	opx	cpx	amph	sp	ru	ilm	fq	ignorite	Boron ppm
ED256	1040	•	•	•			•				•	80,000
ED340	1040	•	•	•	•		•					43,300
ED242	1060	•		•							•	80,000
ED244	1060	•		•								11,600
ED250	1060	•		•							•	80,000
ED253	1060	•	•	•	•		•					110,000
ED339	1060	•	•	•	(•)		•			•		100,000

(melt, olivine, orthopyroxene, clinopyroxene, amphibole, spinel, rutile, ilmenite, fluid quench, ignorite). The maximum boron content (ppm) is also shown.

Extrapolation of results from the uncontaminated experiments suggests that the phases produced at 1040°C and 1060°C should consist of melt, olivine, orthopyroxene, clinopyroxene, and spinel with or without amphibole, ilmenite or rutile. This is found to be the case for some experiments (ED253, ED256, ED339, ED340) although clinopyroxene was not formed in other experiments performed under identical conditions. Three experiments produced ignorite in equilibrium with

orthopyroxene, melt (and olivine in ED256). Thus the same conditions have yielded a number of different combinations of phases, which suggests that the presence of boron can affect the phase relations. However, there is no apparent correlation between phases produced and maximum boron content in the experiment.

The compositions of the minerals produced will now be examined and compared to those in experiments which have been relatively unaffected by boron.

Olivine

Olivine was found in some but not all of these experiments. The reason for its apparent absence in ED242, ED244, ED250 is not clear: there is no evidence of significantly higher boron levels in these experiments. In ED253 and ED339 (both at 1060°C) large (up to 50x100 μm) olivine crystals are present towards the top of the capsule (Plate 6.3) in addition to the relatively small (10x15 μm) crystals in the main part of the charge. In some cases the long axes of the larger crystals appear to be aligned. Analyses by electron microprobe show that these two groups of olivines are of slightly different compositions. The larger olivines at the top of the charge contain less CaO and NiO and possess a higher Mg no. (Table 6.4).

Table 6.4: Average compositions of small and large olivine crystals from ED253 and ED339.

OLIVINES

	ED253				ED339			
	small		large		small		large	
	[5]	s.d.	[3]	s.d.	[5]	s.d.	[4]	s.d.
SiO_2	40.718	(0.199)	41.111	(0.184)	40.449	(0.170)	40.882	(0.198)
TiO_2	0.058	(0.008)	0.055	(0.006)	0.057	(0.009)	0.054	(0.015)
Al_2O_3	0.055	(0.043)	0.053	(0.004)	0.014	(0.014)	0.024	(0.001)
Cr_2O_3	0.236	(0.237)	0.254	(0.113)	0.075	(0.006)	0.132	(0.013)
FeO	7.647	(0.948)	5.281	(0.686)	8.879	(0.911)	5.552	(0.315)
MgO	50.827	(1.625)	53.811	(0.747)	49.782	(0.765)	52.406	(0.315)
CaO	0.058	(0.014)	0.037	(0.002)	0.078	(0.008)	0.056	(0.007)
Na_2O	0.013	(0.012)	0.001	(0.002)	0.004	(0.008)	0.016	(0.006)
K_2O	0.009	(0.008)	0.006	(0.001)	0.001	(0.002)	0.015	(0.004)
MnO	0.089	(0.006)	0.085	(0.018)	0.129	(0.009)	0.114	(0.006)
NiO	0.316	(0.030)	0.248	(0.070)	0.332	(0.043)	0.259	(0.024)
TOTAL	100.026	(1.015)	100.942	(0.565)	99.801	(0.277)	99.510	(0.178)
Mg no.	92.20	(1.08)	94.78	(0.70)	90.90	(0.97)	94.39	(0.33)

See text. The number of analyses is shown in square brackets; s.d. is standard deviation.

PLATE 6.3

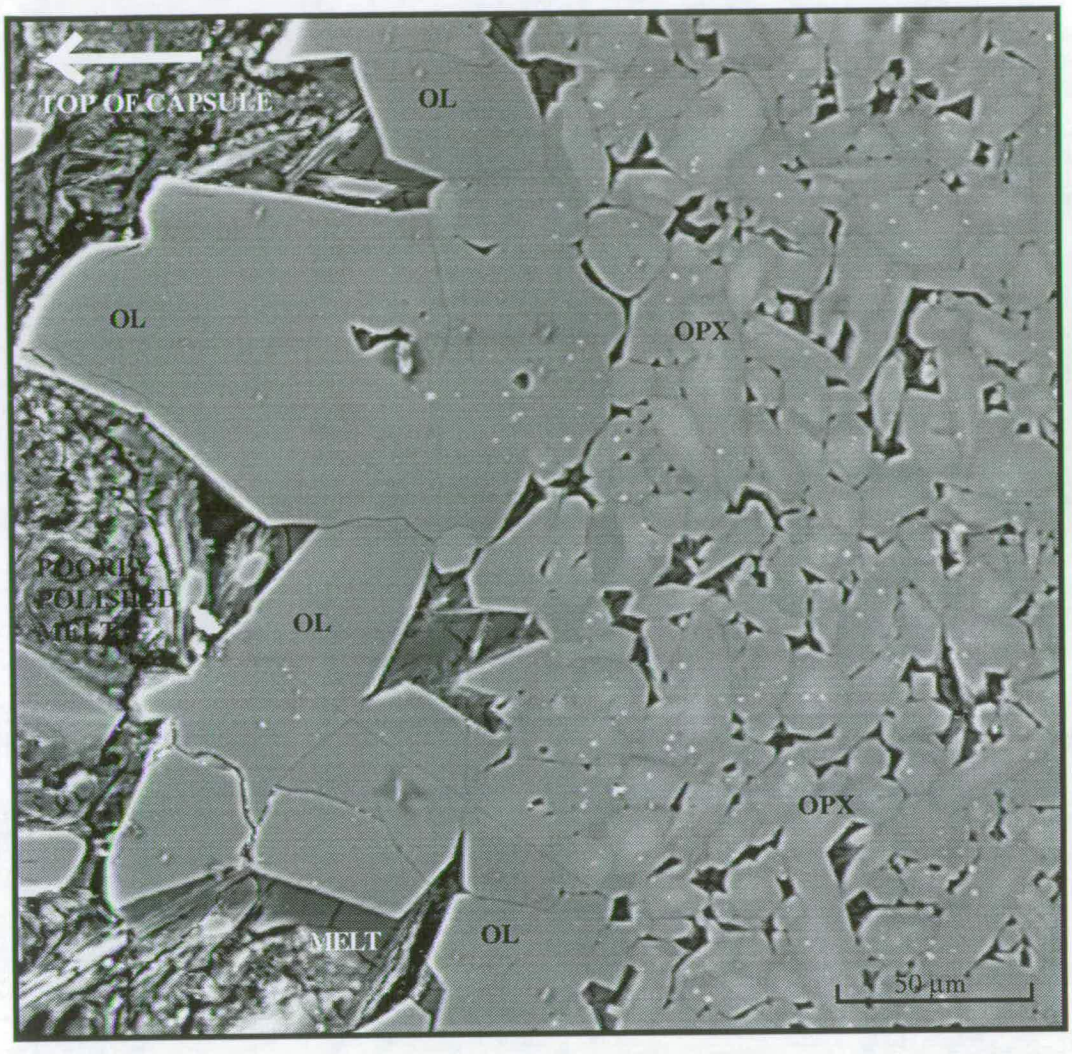

A back-scattered electron image of a polished section of ED339 showing the large olivine crystals (OL) at the top of the capsule, above smaller, zoned crystals of orthopyroxene (OPX).

The average compositions of the small olivines from these experiments lie in the composition-temperature trend inferred from the former experiments (Fig. 6.6). However the larger olivines more closely resemble those from higher temperature experiments such as ED91 at 1150°C.

a)

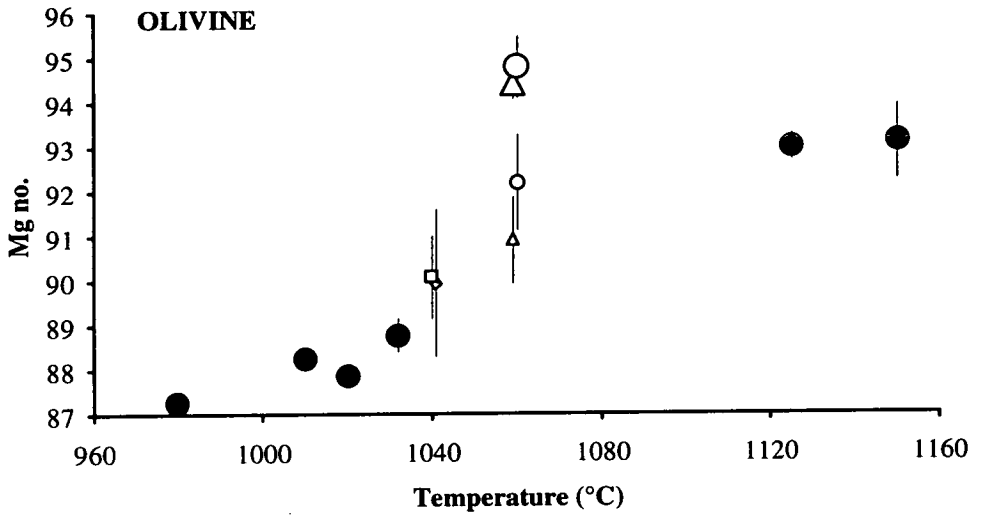

b)

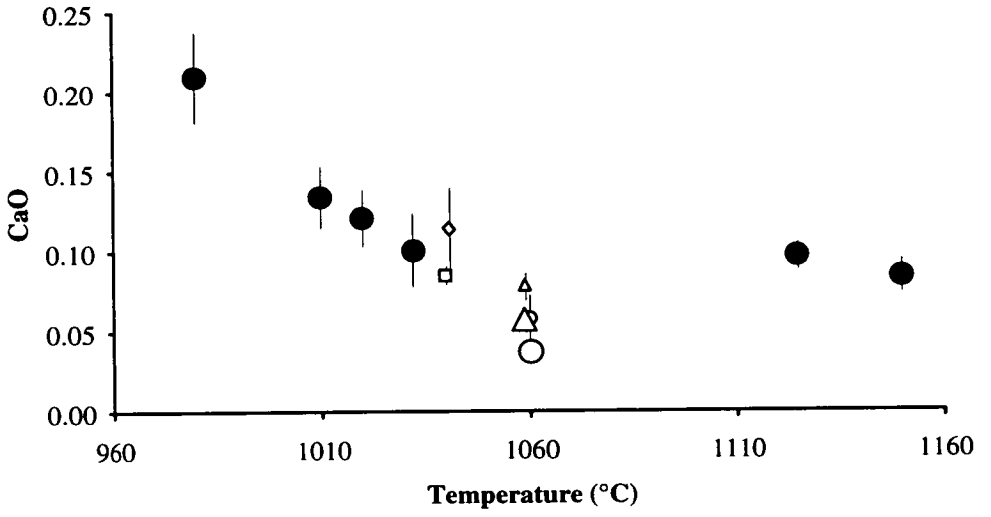

Figure 6.6: Composition of olivines versus temperature from experiments at 1.8 GPa. a) Mg no., b) CaO content. The large filled circles denote the uncontaminated experiments; the open symbols denote the boron-contaminated experiments (see Table 6.3 for levels). ED256 is a square, ED340 is a diamond, ED253 is a circle, ED339 is a triangle. Larger symbols represent the large olivine crystals at the top of some capsules. Large crystals from boron-contaminated experiments have apparently higher Mg nos. and lower CaO contents than the expected values derived by interpolation from the uncontaminated experiments.

PLATE 6.4

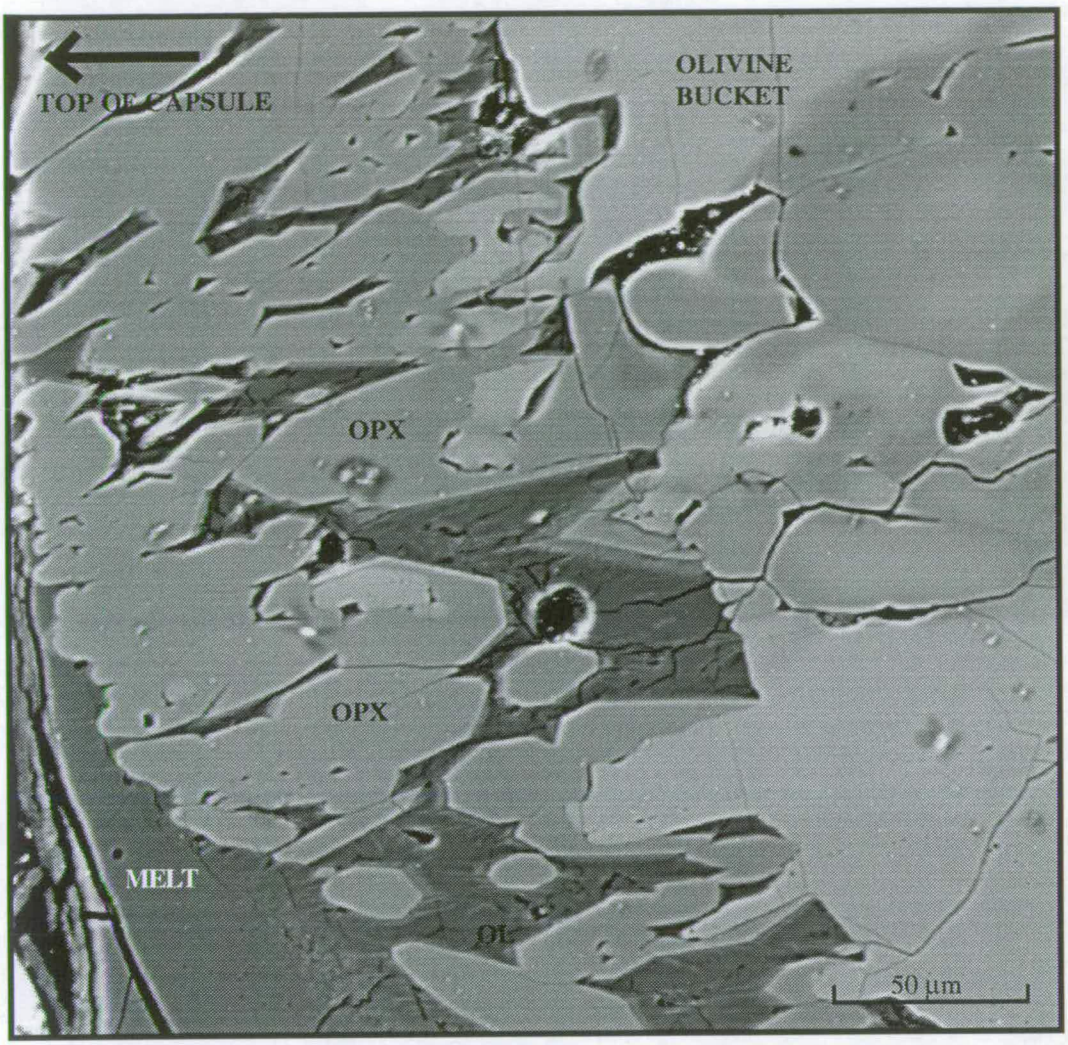

A back-scattered electron image of a polished section of ED339 showing the large orthopyroxene crystals (OPX) at the top of the capsule above the olivine bucket.

Table 6.5: Average compositions of small and large orthopyroxene crystals from ED340 and ED243.

ORTHOPYROXENES

	ED340 (1040°C)				ED253 (1060°C)			
	small		large		small		large	
	[12]	s.d.	[4]	s.d.	[8]	s.d.	[6]	s.d.
SiO_2	54.287	(0.552)	56.825	(0.510)	55.730	(0.824)	58.290	(0.540)
TiO_2	0.399	(0.037)	0.117	(0.019)	0.248	(0.062)	0.076	(0.010)
Al_2O_3	3.226	(0.472)	2.488	(0.526)	2.298	(0.812)	1.202	(0.567)
Cr_2O_3	0.742	(0.092)	0.130	(0.051)	1.033	(0.262)	0.581	(0.354)
FeO	6.938	(0.899)	2.038	(0.067)	4.820	(0.227)	2.486	(0.210)
MgO	32.108	(0.831)	37.137	(0.205)	34.742	(0.783)	38.177	(0.343)
CaO	0.933	(0.110)	0.094	(0.008)	0.946	(0.153)	0.164	(0.030)
Na_2O	0.030	(0.012)	0.013	(0.003)	0.004	(0.009)	0.016	(0.009)
K_2O	0.007	(0.006)	0.013	(0.005)	0.008	(0.005)	0.006	(0.003)
MnO	0.129	(0.013)	0.075	(0.008)	0.125	(0.008)	0.056	(0.008)
NiO	0.096	(0.024)	0.043	(0.013)	0.096	(0.015)	0.135	(0.019)
TOTAL	98.896	(0.396)	98.972	(0.281)	100.050	(0.584)	101.187	(0.250)
based on 6 oxygens:								
Si	1.909	(0.012)	1.941	(0.013)	1.920	(0.027)	1.956	(0.017)
Al(4)	0.091	(0.012)	0.059	(0.013)	0.080	(0.027)	0.044	(0.017)
Total(4)	2		2		2		2	
Al(6)	0.043	(0.008)	0.041	(0.008)	0.013	(0.020)	0.003	(0.005)
Ti	0.011	(0.001)	0.003	(0.000)	0.006	(0.002)	0.002	(0.000)
Cr	0.021	(0.003)	0.004	(0.001)	0.029	(0.007)	0.016	(0.010)
Mg (M1)	0.926	(0.009)	0.952	(0.010)	0.951	(0.023)	0.979	(0.014)
Total	1		1		1		1	
Mg (M2)	0.757	(0.030)	0.939	(0.004)	0.833	(0.016)	0.930	(0.006)
Fe	0.204	(0.027)	0.058	(0.002)	0.139	(0.006)	0.070	(0.006)
Mn	0.004	(0.000)	0.002	(0.000)	0.004	(0.000)	0.002	(0.000)
Ca	0.035	(0.004)	0.003	(0.000)	0.035	(0.006)	0.006	(0.001)
Na	0.002	(0.001)	0.001	(0.000)	0.000	(0.001)	0.001	(0.001)
K	0.000	(0.000)	0.001	(0.000)	0.000	(0.000)	0.000	(0.000)
Total	1.002	(0.003)	1.004	(0.002)	1.011	(0.017)	1.008	(0.002)
TOTAL	4.005	(0.003)	4.005	(0.002)	4.013	(0.017)	4.012	(0.002)
Mg no.	89.18	(1.49)	97.01	(0.08)	92.78	(0.25)	96.47	(0.31)

Both experiments were contaminated by boron. The number of analyses is shown in square brackets; s.d. is standard deviation.

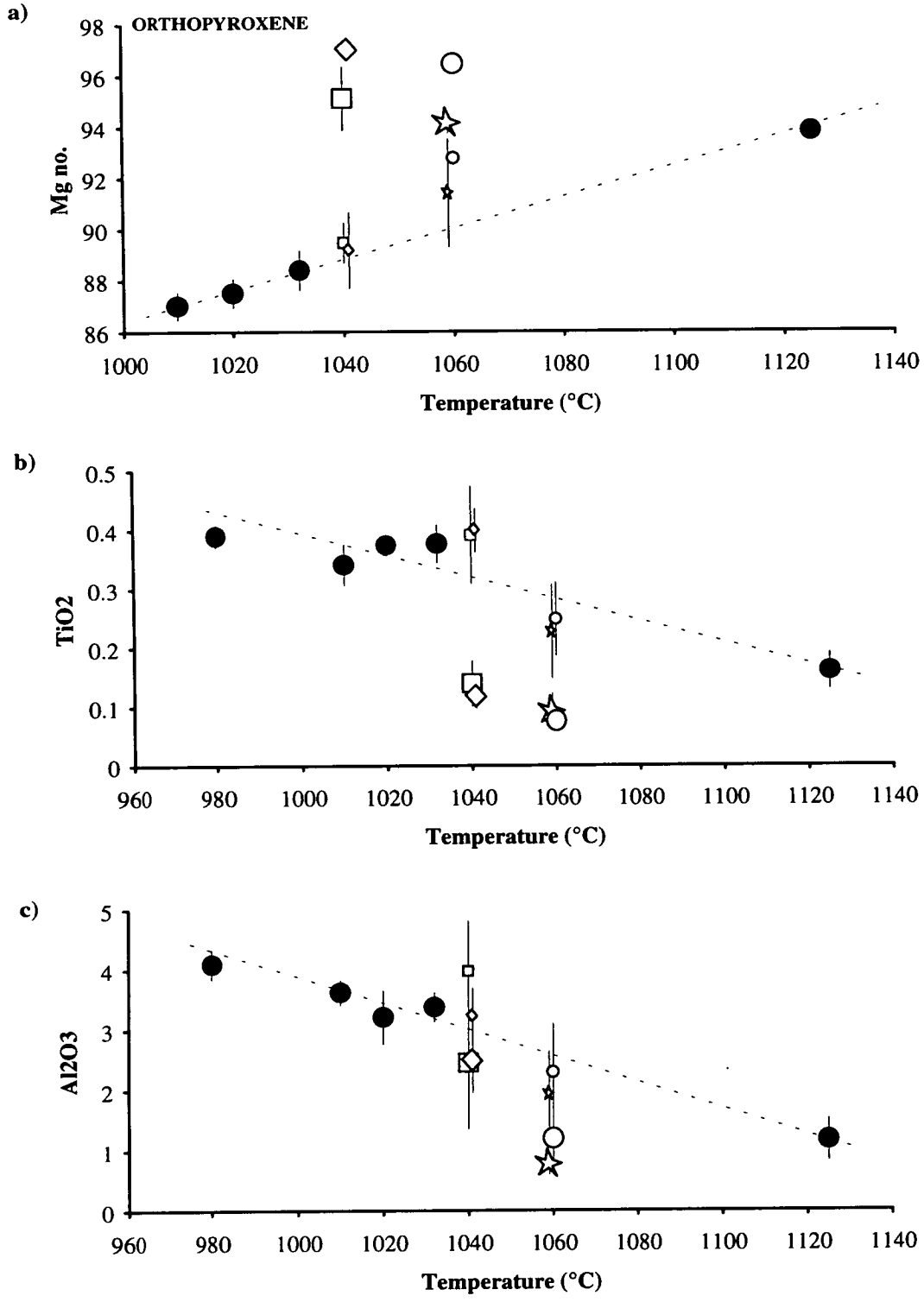

Figure 6.7: Composition of orthopyroxenes versus temperature from experiments at 1.8 GPa. a) Mg no.; b) TiO2 content; c) Al2O3 content (%). The large filled circles denote the uncontaminated experiments; open symbols denote boron-contaminated experiments. ED256 is a square; ED340 is a diamond; ED253 is a circle; ED242 is a star. Larger symbols represent the large orthopyroxenes at the top of some capsules. Contamination appears to produce higher Mg nos., lower TiO2, and lower Al2O3 contents.

Orthopyroxene

This was produced in all of these experiments; in some cases there are two distinct groups of orthopyroxenes - large aligned crystals (up to 100x200 μm) at the top of the capsule (Plate 6.4) and smaller crystals (10x20 μm) in the main body of the charge. The larger crystals have higher Mg nos. (average of 97 in ED340) and lower TiO_2, Al_2O_3, Cr_2O_3, and MnO (Table 6.5). In some experiments, the rims of smaller orthopyroxene crystals are similar in composition to the larger crystals. Although the compositions of the smaller crystals are not entirely consistent with the trends observed in earlier experiments (Fig. 6.7) they are close to the expected compositions. The larger crystals more closely resemble those from the higher temperature experiment, ED101 (at 1125°C).

Clinopyroxene

Clinopyroxene was produced in three of these experiments[6]. In contrast to olivine or orthopyroxene, only one population of clinopyroxene crystals was found in each run product. These crystals possess higher Mg nos. than crystals formed in uncontaminated experiments (Fig. 6.8a) possibly as a result of the higher temperatures. However the striking increase in Na_2O content with temperature (Fig. 6.8b) is not continued in these experiments: Na_2O contents in clinopyroxenes from ED339 and ED253 are similar to those of crystals from ED143 (1020°C).

a)

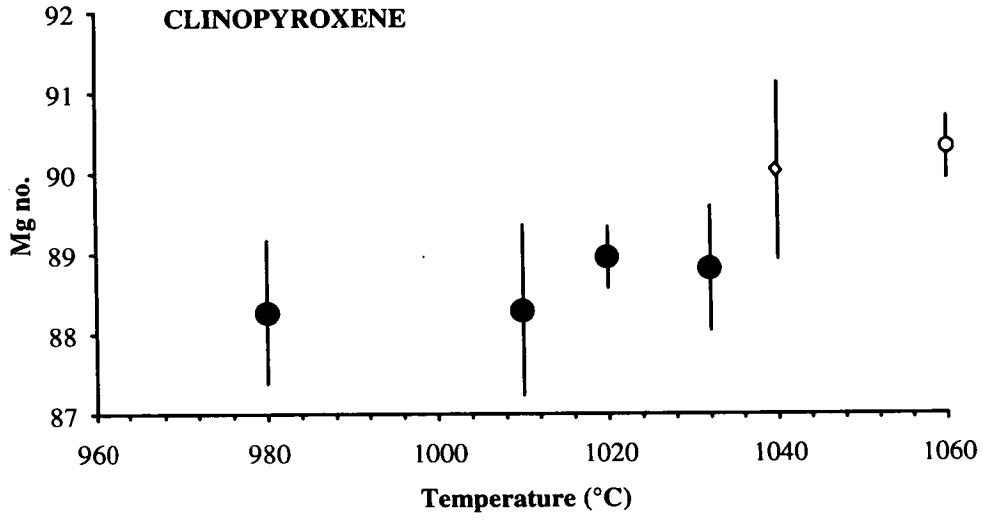

Figure 6.8a (see overleaf for caption)

[6]Crystals in ED339 were very small and in the cores of orthopyroxene. Consequently analyses could not be obtained.

b)

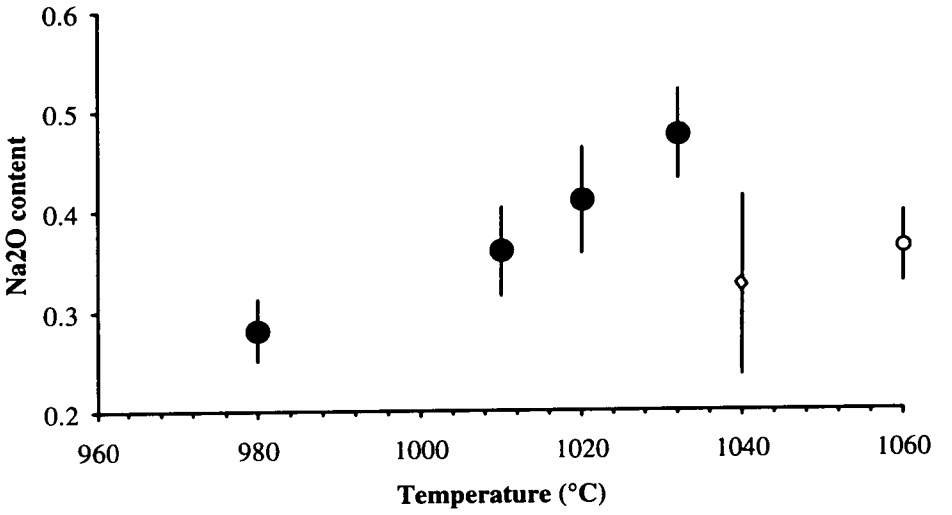

Figure 6.8: Composition of clinopyroxenes versus temperature from experiments at 1.8 GPa. a) Mg no., b) Na_2O content. The large filled circles denote the uncontaminated experiments; the open symbols denote the boron-contaminated experiments (see Table 6.3 for levels). ED340 is a diamond, ED253 is a circle.

Spinel

The presence of spinel appears to mirror that of olivine - both phases were produced in all but three of these experiments. Spinel, when present, is of a composition consistent with the temperature trends observed in uncontaminated experiments (Fig. 6.9).

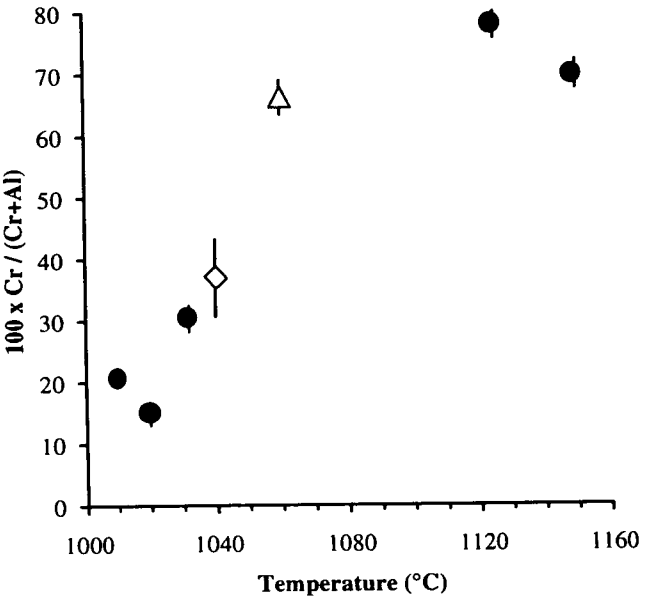

Figure 6.9: Cr / (Cr + Al) value of spinels versus temperature from experiments at 1.8 GPa. The large filled circles denote the uncontaminated experiments; the open symbols denote the boron-contaminated experiments (see Table 6.3 for levels). ED340 is a diamond, ED339 is a triangle.

Ignorite

This was produced in three experiments. In ED242 and ED250 all nickel oxide in the buffer has been reduced to nickel, and the mix contains small (1-2 μm wide) patches of nickel-iron alloy of approximate composition $Ni_{97}Fe_3$, suggestive of an extremely low oxygen fugacity during the experiment. The buffer from ED256 had been substantially but not completely reduced, implying that the establishment of low oxygen fugacity is not a prerequisite of ignorite formation, but that the reduction of the buffer is a result of the extremely high levels of boron necessary to form this mineral.

Discussion

The introduction of boron clearly causes a change in the phases produced and the compositions of those phases.

The data show that the minerals developed in the main body of the charges are of a composition that is consistent with the temperature of the experiment (from extrapolating trends displayed by boron-free experiments). However the rims of the crystals (in particular orthopyroxene) and some large crystals at the top of the charge are of different compositions, similar to crystals formed at higher temperature.

I suggest that as boron enters the capsule, the crystals change in composition in a manner that is consistent with an increase in temperature and consequently with an increase in the degree of melting. This produces more magnesian olivine and orthopyroxene and lower contents of incompatible elements such as TiO_2, Al_2O_3, and Na_2O. In other words, boron is acting as a flux. There is also evidence that experiments which have been contaminated by boron, have produced some extremely large crystals.

6.5.3 Experiments at higher pressure

2.3 GPa

Six forward experiments were performed at 2.3 GPa. Table 6.6 shows the results of these experiments and the maximum boron content measured from each run product. With the exception of ED315, there are systematic changes in mineralogy as temperature increases: the solidus is encountered between 1000°C and 1010°C, followed by the amphibole-out curve (approximately 1010°C), the rutile-out and the garnet-out curves (both inferred to occur between 1040°C and 1060°C). ED315, an experiment in which thick-walled platinum was used, contains substantially less

boron than does ED257 which was performed at the same temperature. These two experiments yielded different results: whilst ED257 produced melt, ED315 is subsolidus. This is consistent with the hypothesis that boron fluxes an experiment and causes mineralogical changes expected from an increase in temperature (and melting).

Table 6.6: Mineralogy of forward experiments at 2.3 GPa.

Expt.	T(°C)	melt	ol	opx	cpx	gt	amph	sp	ru	ilm	fq	Boron ppm
ED259	1000		•	•	•	•	•	•	•			180
ED283	1010	•	•	•	•	•	(•)		•			13,100
ED258	1020	•	•	•	•	•			•			40,900
ED257	1040	•	•	•	•	•		•	•		•	57,200
ED260	1060	•	•	•	•			•				87,000
ED315	1040		•	•	•	•	•		•	•		400

(Melt, olivine, orthopyroxene, clinopyroxene, garnet, amphibole, spinel, rutile, ilmenite, fluid quench). Also shown is the maximum boron content, measured by SIMS.

The compositions of minerals in ED315 are also distinct from those minerals in ED257. For example, the olivines from ED315 possess relatively lower Mg nos. and higher CaO contents (Fig. 6.10) and the orthopyroxenes from ED315 are of a lower Mg no. and higher Al_2O_3 content than those from ED257 (Fig. 6.11). In both cases the minerals from ED315 are more similar in composition to those from lower temperature experiments such as ED259 at 1000°C. The same conclusion can be drawn from clinopyroxenes: crystals from ED315 have lower Na_2O contents[7] than crystals from ED257 i.e. ED315 resembles an experiment run at a lower temperature (Fig. 6.12).

In more general terms, minerals from within any experiment at 2.3 GPa display a wider range of composition relative to the same mineral from an uncontaminated experiment at 1.8 GPa (this is manifested by the larger error bars on Figures 6.10-6.12). The crystals are often zoned; in particular orthopyroxenes have Mg-poor, Al-rich cores and Mg-rich, Al-poor rims. In two experiments, large orthopyroxene crystals of composition similar to the rims of smaller crystals (Fig. 6.13), are present at the top of the charge.

The higher pressure complicates interpretation as it is difficult to divorce the effects of the experimental conditions from the effects of high boron content. Nevertheless,

[7]Clinopyroxenes from experiments at 1.8 GPa show a strong positive correlation between Na_2O content and temperature.

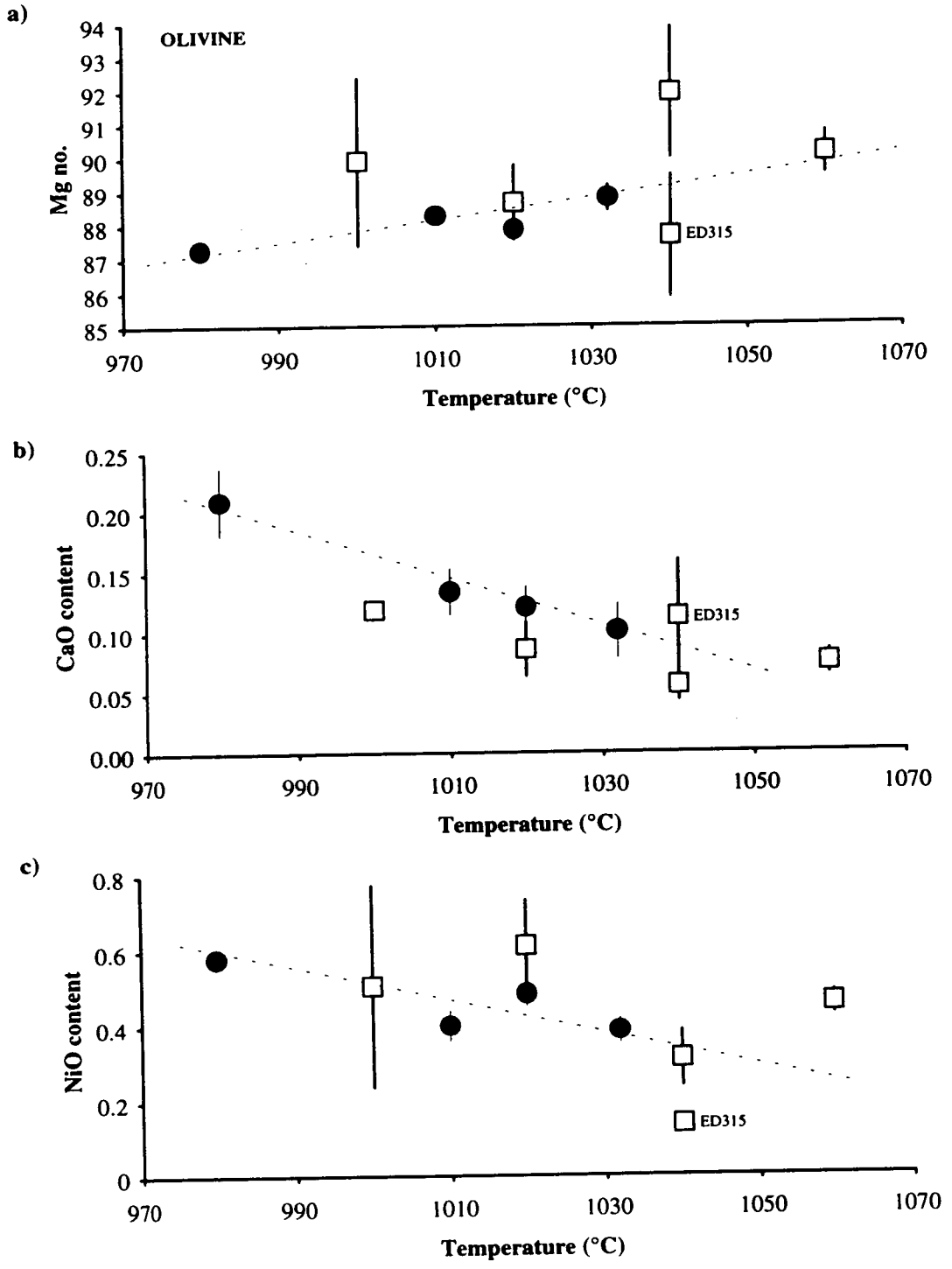

Figure 6.10: Composition of olivines versus temperature: a) Mg no.; b) CaO content; c) NiO content (%). Olivines from 2.3 GPa are denoted by squares, olivines from 1.8 GPa are denoted by circles. The marked correlations between composition and temperature observed for the experiments at 1.8 GPa (dashed line) are not seen to the same extent for the experiments at 2.3 GPa, presumably due to contamination of the latter experiments by boron. The olivine crystals from ED315, which was uncontaminated, possess lower Mg nos., higher CaO and lower NiO contents than the olivine crystals from the contaminated experiment performed at the same pressure and temperature.

it seems clear that the boron has affected the results of the experiments and has obscured the strong correlations between composition and temperature which were evident from uncontaminated experiments at 1.8 GPa. One corollary of this is that it is not possible to deduce any relationship between pressure and composition.

a)

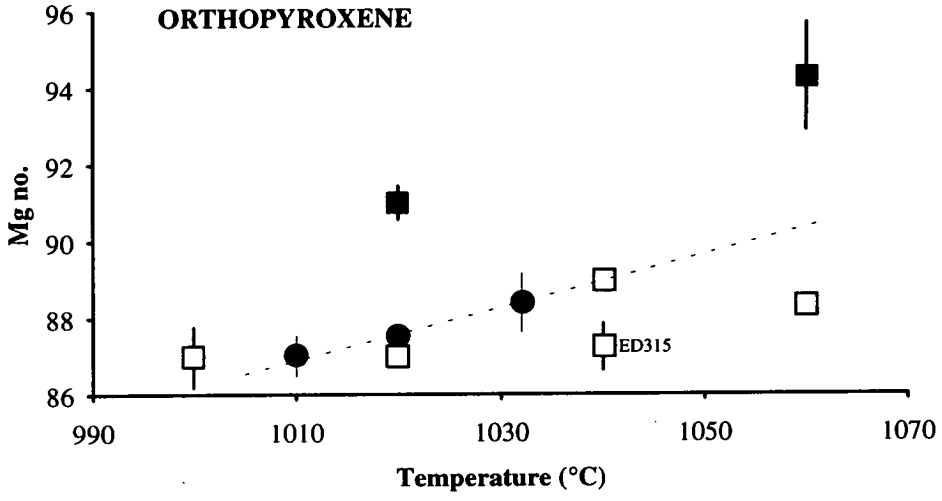

b)

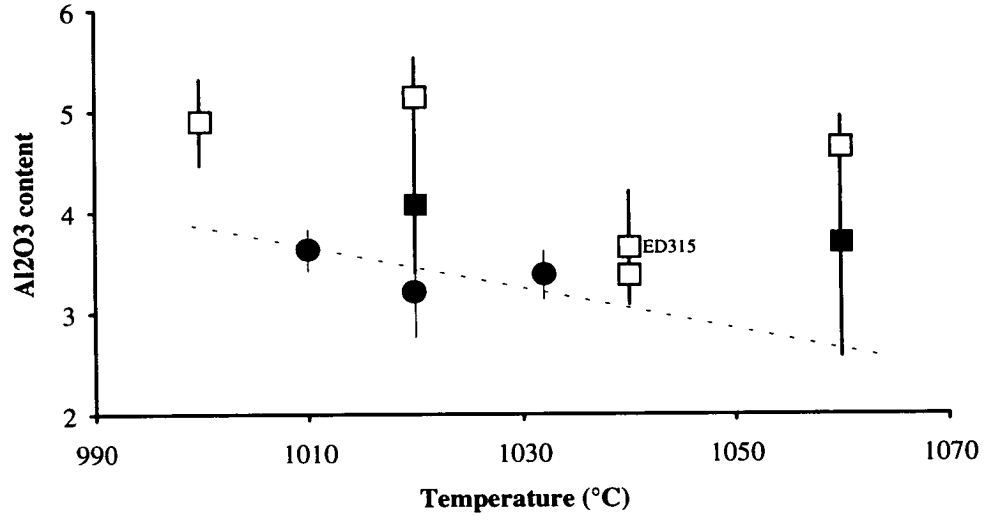

Figure 6.11: Composition of orthopyroxene crystals versus temperature: a) Mg no., b) Al_2O_3 content. Orthopyroxenes from 2.3 GPa are denoted by open squares (small crystals) and filled squares (large crystals at the tops of some capsules). Orthopyroxenes from 1.8 GPa are denoted by filled circles. The marked correlations between composition and temperature observed for the experiments at 1.8 GPa (dashed line) are not seen to the same extent in the experiments at 2.3 GPa, presumably due to contamination of the latter experiments by boron. The orthopyroxene crystals from ED315, which was not contaminated by boron, possess lower Mg nos., higher CaO contents, and lower NiO contents than the orthopyroxene crystals from the contaminated experiment performed at the same pressure and temperature.

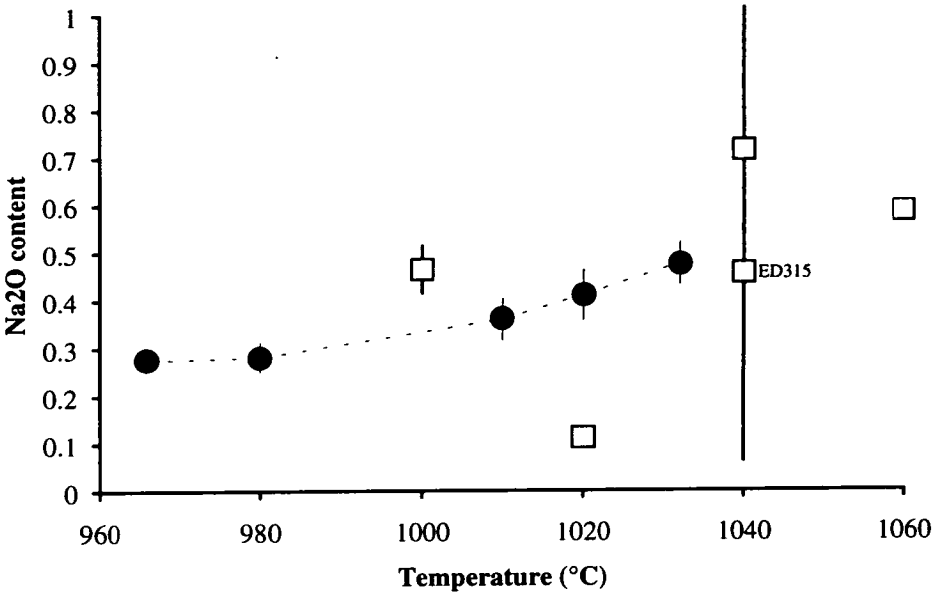

Figure 6.12: Na_2O content of clinopyroxene crystals versus temperature. Clinopyroxenes from 2.3 GPa are denoted by open squares, clinopyroxenes from 1.8 GPa are denoted by filled circles. The marked correlation between Na_2O content and temperature observed for the experiments at 1.8 GPa (dashed line) is not seen in the experiments at 2.3 GPa, presumably due to contamination of the latter experiments by boron. The clinopyroxene crystals from ED315, which was not contaminated by boron, possess lower Na_2O contents than the clinopyroxene crystals from the contaminated experiment performed at the same pressure and temperature.

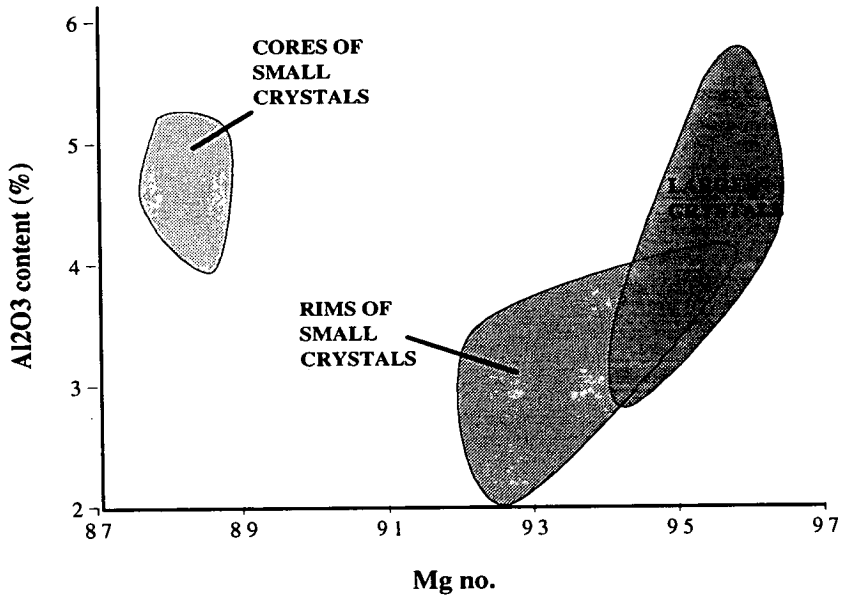

Figure 6.13: Al_2O_3 versus Mg no. of orthopyroxene crystals from ED260 (2.3 GPa, 1060°C). The range in composition of large crystals at the top of the charge, and cores and rims of smaller crystals are shown. Note that the large crystals are similar to the rims of the small crystals.

2.8 GPa

One experiment performed at 2.8 GPa was analysed by SIMS and proved to be contaminated. However, as the strong mineral zoning characteristic of boron contamination was observed in all three experiments conducted at 2.8 GPa, it is suggested that all three experiments have been contaminated by boron. Although all mineral phases were analysed for major elements by electron microprobe, it is not considered that the results are useful as the contamination will have obscured any relationships between pressure, temperature and composition, and there appear to be no boron-free experiments at this pressure which could be used as controls in an investigation into the effects of boron.

Table 6.7: Mineralogy of forward experiments at 2.8 GPa.

Expt.	T(°C)	melt	ol	opx	cpx	gt	amph	sp	ru	ilm	fq	Boron ppm
ED282	1020		•	•	•	•			•	•		n.a.
ED279	1040	•	•	•	•	•			•			24,100
ED280	1060	•	•	•	(•)	•			•			n.a.

(melt, olivine, orthopyroxene, clinopyroxene, garnet, amphibole, spinel, rutile, ilmenite, fluid quench). Also shown is the maximum boron content from ED279. ED282 and ED280 were not analysed by SIMS. Note that the nominal pressure of these experiments is 2.8 GPa. After correction for friction, the pressure is calculated to be ~2.7 GPa.

6.6 CONCLUSIONS

Many experiments conducted in this study were found, in retrospect, to have been contaminated by boron. The extent of contamination varies within one charge and between experiments, with boron contents reaching up to several thousand parts per million in many cases. In three experiments a borate mineral was produced.

Boron, derived from the boron nitride components in the cell, probably enters the capsule through rips or holes formed in the platinum during the experiment. There is some evidence to show that high temperatures increase the extent of the ingress. As boron enters, it is sometimes possible for water to escape, although in many cases some or all water is retained in the capsule throughout the experiment. The holes may have formed as a result of the rigid olivine bucket puncturing the platinum capsule. This hypothesis is supported by the observation that capsules in which there

is a large platinum crimp separating the olivine bucket from the top of the capsule appear to have suffered less from boron contamination. In addition, in a few experiments melt has been observed outside the capsule.

Comparisons between contaminated and uncontaminated run products indicate that boron acts as a flux, promoting melting of the charge and changing the composition of minerals in the same way as would an increase in temperature. The data are not sufficient to quantify these findings. However they do show us that these experiments are not reliable analogues for the melting of peridotite under hydrous conditions.

Some experiments appear to have suffered only minor contamination. For example the maximum boron content in ED143 is 290 ppm, which is not considered to be significant. I have assigned a cut-off point of 1000 ppm (or 0.32 wt% B_2O_3): the results from experiments which contain greater than 1000 ppm boron are not used. Therefore, experiments reviewed in Chapter 5 are deemed relatively uncontaminated whereas the majority of experiments reviewed in this chapter are contaminated.

6.6.1 The solution?

Unfortunately, time constraints prevented the development of a new technique and the repeating of these experiments. It was hoped that thick-walled platinum would solve the problem. However, this was not the case. If I were to attempt to repeat these experiments I would use an olivine bucket which had been thoroughly rounded, possibly with a smaller hole in the top to prevent the collapse of the top of the capsule.

6.6.2 Wider Implications

Many experimentalists in the past have used boron nitride or Pyrex components in solid-media cells.

Whilst it does not appear that the presence of boron in these experiments is directly relevant to other work - it was probably the presence of the rigid olivine bucket in these experiments that was the cause of the problem - there are two conclusions which have come from this study that are of particular significance.

1. Boron cannot be detected by the electron microprobe - the electron probe failed to detect boron even when it was present in major element levels. Past run

products were seldom analysed by SIMS and therefore it is likely that boron contamination would have remained undiscovered.

2. Water does not always escape from contaminated capsules - traditionally the retention of water during an experiment has been adequate proof that the capsule remained intact and that the experiment was a success (e.g. Green, 1973). However in this study there were many capsules in which water was retained that were found to contain significant levels of boron. This method of judging a capsules success is therefore fallible.

This study has shown that boron contamination can significantly affect the mineralogy and phase compositions of a run product. Any undetected contamination in the past may have led to erroneous results.

CHAPTER 7

PARTITIONING OF TRACE ELEMENTS INTO HYDROUS FLUID

CHAPTER 7: PARTITIONING OF TRACE ELEMENTS INTO HYDROUS FLUIDS

7.1 INTRODUCTION

Results from many experimental and theoretical studies provide support for the current view that melting in the mantle wedge is triggered by the influx of fluid from the downgoing slab. Preferential transport of mobile trace elements by such fluids is one possible explanation for the characteristic trace-element signature seen in IAV. On the other hand, it has been argued that a slab-derived fluid would be incapable of producing the inferred changes, which are better explained by interaction of the mantle with a slab-derived melt. Chapter 1 summarises the evidence for and against the theories for the production of melt in subduction zones. In order to assess the validity of these theories it is essential to quantify the chemical characteristics of fluids in equilibrium with the slab and the mantle under pertinent conditions. Although there have been some measurements of mobility of trace elements in fluids and of partitioning of trace elements between a fluid phase and coexisting minerals (see Chapter 3), relatively few experimental studies have been performed at high pressures, and moreover there are many important trace elements for which data are unavailable. Some workers (e.g. Hawkesworth *et al.*, 1993a) have estimated D (rock/fluid) for several trace elements by extrapolating the relationship between partition coefficient and ionic radius (Brenan & Watson, 1991). Thus, B and Be, which are very small, are inferred to be extremely insoluble in the fluid: a prediction at odds with other evidence that indicates that these elements are highly mobile in slab-derived fluids (Morris *et al.*, 1991). Clearly, experimental data are needed to solve this apparent paradox and to extend the data base.

The aim of this section of the project was to measure partition coefficients between fluid, melt and coexisting phases for a range of trace elements (encompassing Li, Be, B, Na, K, Ti, Rb, Sr, Y, Zr, Nb, Cs, Ba, REE, Hf, Ta, Pb, U) at high pressures. In contrast to the methods employed in previous studies (see Chapter 3), the fluid composition was derived from direct analyses of fluid quench products. The experiments from which the data are taken include forward experiments (with peridotite starting material), reversal experiments (with a basaltic starting material)

and some more complex experiments involving the use of double capsules; all performed at approximately 2.0 GPa. This chapter contains a description of the occurrence, appearance and major- and trace-element composition of fluid quench products from a number of experiments. This information will be used to justify the assumption that the composition of fluid quench is representative of the fluid at equilibrium. Partition coefficients between fluid, melt and olivine will then be presented using estimates of the water content of all phases at equilibrium.

7.2 EXPERIMENTAL RESULTS

Previous workers have noted that in many fluid-saturated experiments, a separate fluid phase has been produced, which quenches to form small glass spheres (Kushiro, 1969; Nicholls & Ringwood, 1973; Nicholls & Ringwood, 1974; Mysen & Boettcher, 1975) described as "fish roe" by Holloway (1971). Cloudy amorphous matter and small glass fragments in run products have also been attributed to a fluid phase (Holloway, 1971; Millholen *et al.*, 1974). The glass spheres were analysed by Holloway (1971) and found to be extremely rich in SiO_2 and Al_2O_3. In this project, small glass spheres (but no amorphous glass matter) were found in the run products of many experiments, including forward and reversal runs. Experiments with large water contents were performed subsequently in order to maximise the amount of fluid phase. The occurrence, appearance and composition of the glass spheres are documented below.

7.2.1 Occurrence and appearance of glass spheres

The sectioning procedure for all run products is described in Chapter 4. Essentially, run products were impregnated with epoxy resin, sectioned, mounted in epoxy resin, and polished. Fluid quench products, where present, usually appear as small circles of glass surrounded by epoxy resin. For the purposes of this discussion, the size of the sphere is defined as the diameter apparent from the polished section. Note that this is likely to be less than the true diameter of the sphere.

Forward experiments

ED91 (Table 7.1) contains the first identified glass spheres, located near the top of the capsule (now surrounded by epoxy resin), and in a large inclusion within the olivine bucket (Plate 7.1). The polished section contains fewer than twenty glass spheres, each less than 10 μm. ED249 and ED257 yielded similar-sized glass spheres. The apparent absence of fluid quench in the majority of forward experiments is possibly due to a low initial water content, but it is more likely that only a few spheres are produced in forward runs, and are therefore difficult to find.

Reversal experiments using olivine buckets

The majority of run products contain some glass spheres of similar size to those from ED91. They are situated mostly at the top of the capsules above the olivine bucket (Plate 7.1b), although in some experiments there are occasional glass spheres between the sides of the olivine bucket and the capsule walls. None were found within inclusions in the olivine bucket.

Table 7.1: Details of a forward run and a reversal from which data are presented.

Experiment	*Type*	*Pressure, Temp., Duration*	*Run products*						
ED91	Forward	1.8 GPa, 1150°C, 24 hrs	MELT	FQ	OL	OPX		GT	SP
ED234	Reversal in olivine bucket	1.8 GPa, 1020°C, 48 hrs	MELT	FQ			CPX		SP

where FQ represents quench products from the fluid phase.

Reversal experiments in salt cells

These experiments were designed to maximise the amount of fluid quench recovered, and to investigate the liquidus behaviour of the melt composition calculated from ED143 (Chapter 5). The capsules contained a mix of basaltic composition, and water. No internal buffer was used (see Chapter 4 for details of the experimental technique). Experiments were run at three temperatures (Table 7.2). Fluid quench was found in all run products with the exceptions of ED348C1 and ED348C2 which had initial water contents of 10 wt% and 20 wt%, respectively, and did not become water saturated. All run products contain large areas of a 'ropy'-looking melt quench (hereafter referred to as melt) which appears to have a higher surface tension than the capsule walls i.e. the melt has formed large globules (Plate 7.2). Many small (< 10 μm) glass spheres were found, situated in the top half of the capsule and also present

PLATE 7.1

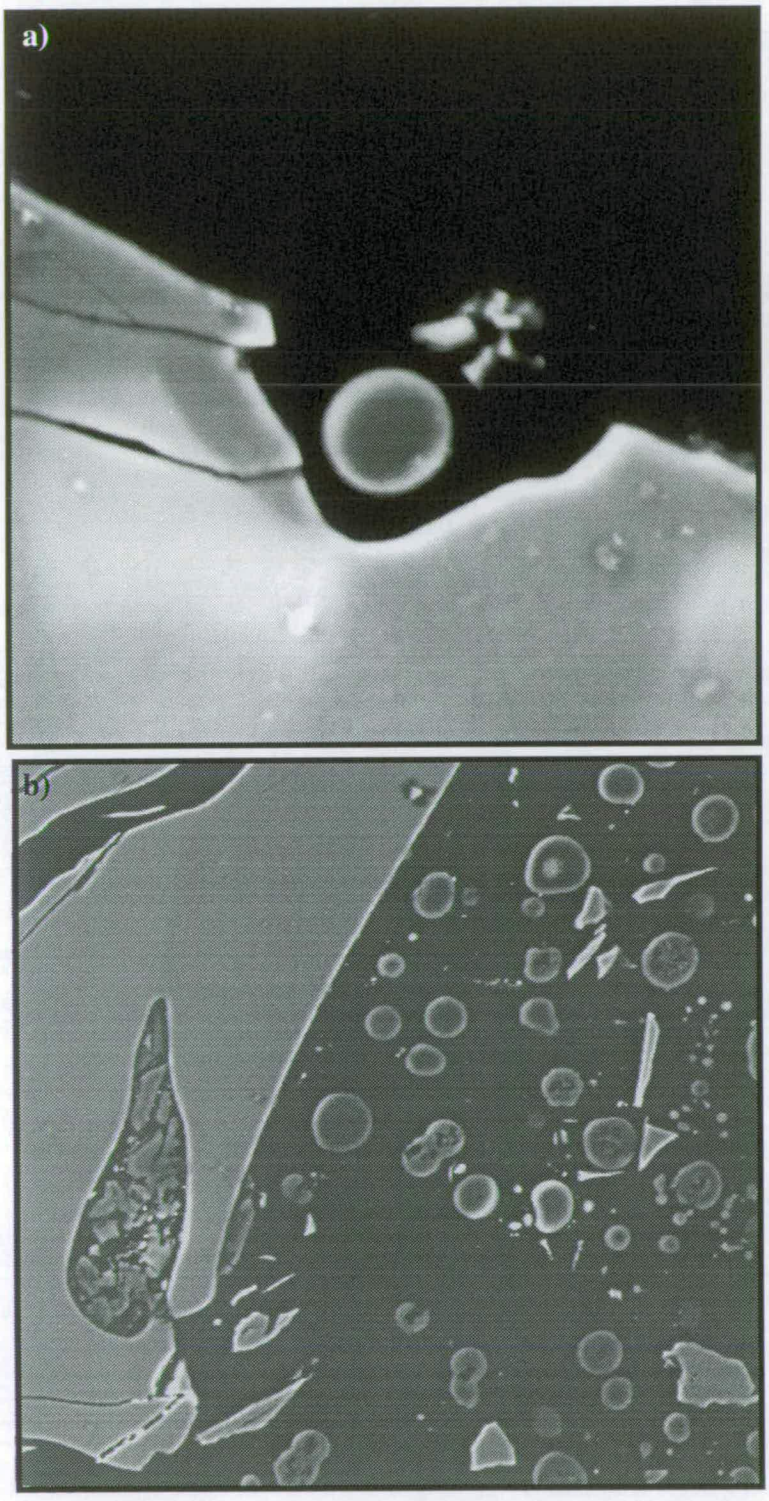

Back-scattered electron images of polished sections of run products. a) ED91 showing the olivine bucket and one glass sphere b) ED234 showing the olivine bucket, a melt inclusion, and several glass spheres quenched from the fluid.

PLATE 7.2

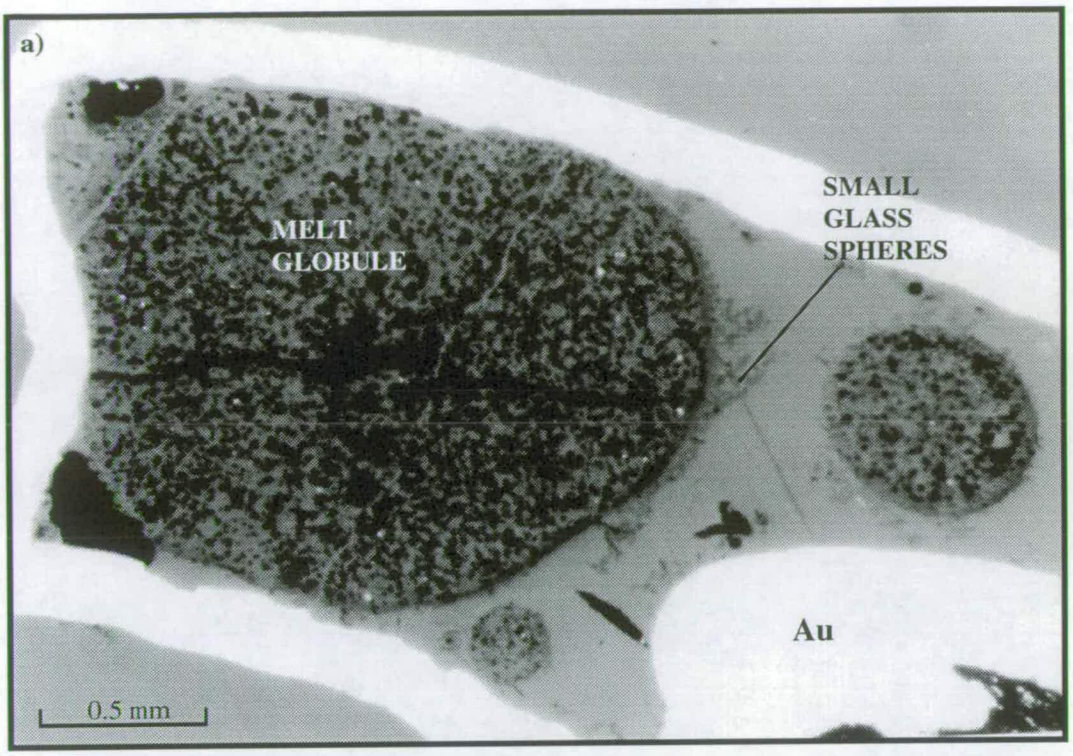

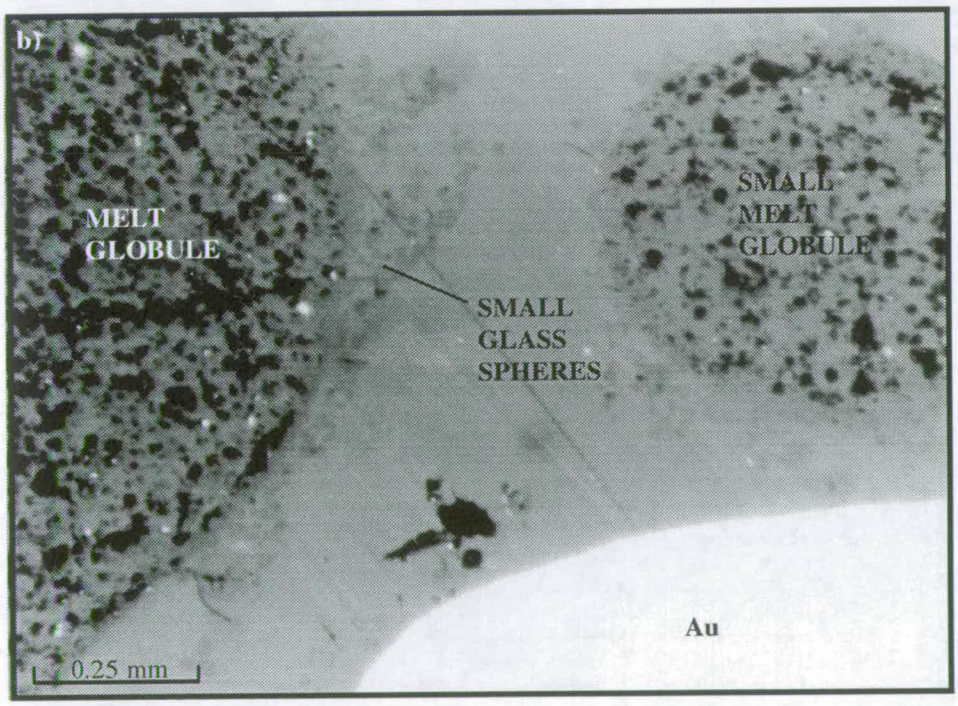

Reflected-light photomicrographs of the polished section of ED348C3 showing a) the gold capsule, melt globules and fluid quench material embedded in epoxy resin b) a close up of two melt globules. The small light-coloured circles near the rims of the melt globules are glass spheres quenched from the fluid.

in the folded gold at the top of the capsules (Plates 7.3 and 7.4). In addition to these, there are distinctive larger spheres (30 μm - 100 μm). Polished cross sections of these larger spheres reveal a heterogeneous internal structure: the edges generally polish to a featureless surface whereas the interiors appear to be of an uneven texture, similar to the coexisting melt. In some run products there are very large glass spheres (up to 200 μm) with an obvious break in texture and composition between the smoother-looking edges and the more ropy-looking centres (Plate 7.5).

Table 7.2: Details of reversal experiments run in salt cells.

Experiment	Temp. (°C)	Duration (hrs)	Starting mix	Initial H_2O content (wt%)	Run products					
ED317C2	1020	3	A	30	MELT	FQ				
ED317C3 *	1020	3	B	30	MELT	FQ	GT	AM	CPX	
ED327C2	1020	24	B	30	MELT	FQ	GT	AM	CPX	
ED327C3	1020	24	C	30	MELT	FQ			CPX	OL
ED332C1	1005	24	A**	30	MELT	FQ				
ED332C2	1005	24	B	30	MELT	FQ	GT	AM	CPX	
ED332C3	1005	24	C	30	MELT	FQ	GT		CPX	OL
ED348C1	1005	24	A	10						
ED348C2	1005	24	A	20	MELT					
ED348C3	1005	24	A	50	MELT	FQ				

* This capsule lost its water during the run.
** Starting mix was additionally doped with U, Pb, Cs, Be, Li.

Starting mix A is a basaltic composition (see Chapter 4). Mixes B and C consist of mix A plus 10% and 20% forsterite component, respectively.

ED348C3 contained more initial water (50 wt%) than other experiments. The run product consists of several large melt globules, up to 1.5 mm in diameter, which appear to be fringed by small glass spheres. Larger glass spheres are also present. Generally there is less distinction between the melt globules and the large glass spheres in this experiment, which suggests that there may be some form of gradation (either mechanical or chemical) between fluid quench and melt.

Double-capsule experiment

ED231 is a double-capsule experiment, similar to those of Schneider & Eggler (1986). A perforated inner capsule (Ag-Pd) containing the starting mix, and approximately 50 wt% water were sealed into an outer platinum capsule (see Chapter 4 for details). The rationale of this was to prevent any melt or crystalline material escaping from the inner capsule, whilst allowing the fluid phase to circulate freely throughout both capsules. In theory, it should have been possible to separate both

PLATE 7.3

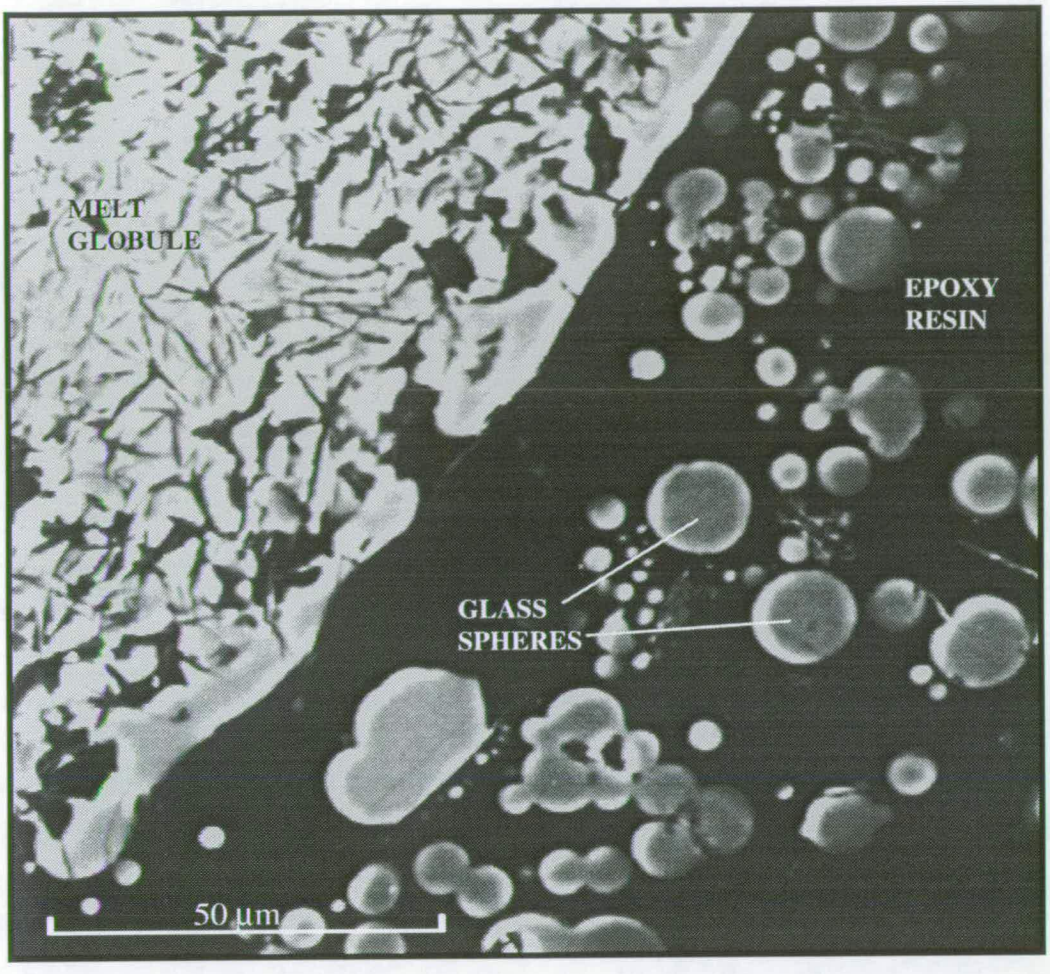

Back-scattered electron image of the polished section of ED348C3 showing a melt globule and several glass spheres embedded in epoxy resin.

PLATE 7.4

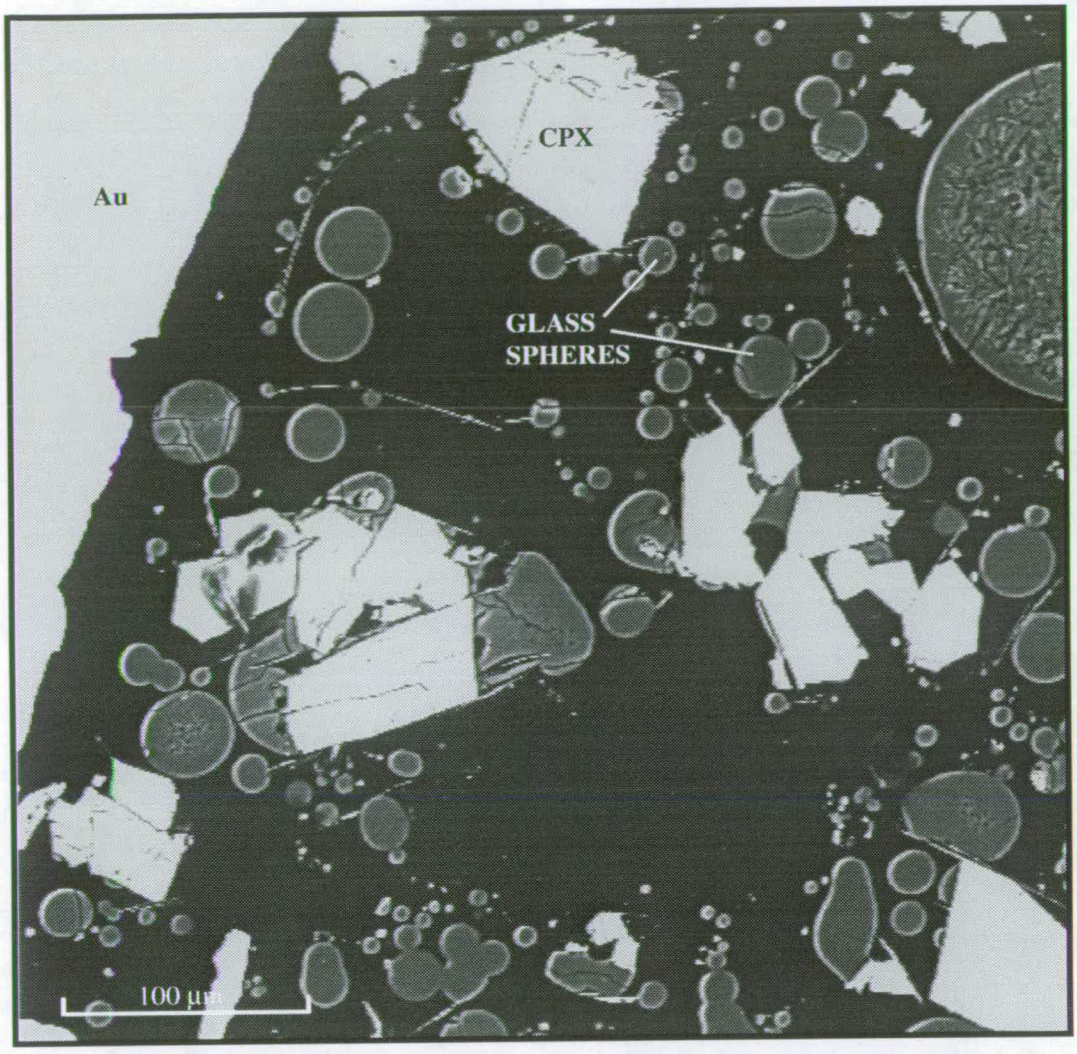

A back-scattered electron image of a polished section of ED332C3 showing glass spheres and clinopyroxene crystals embedded in epoxy resin.

PLATE 7.5

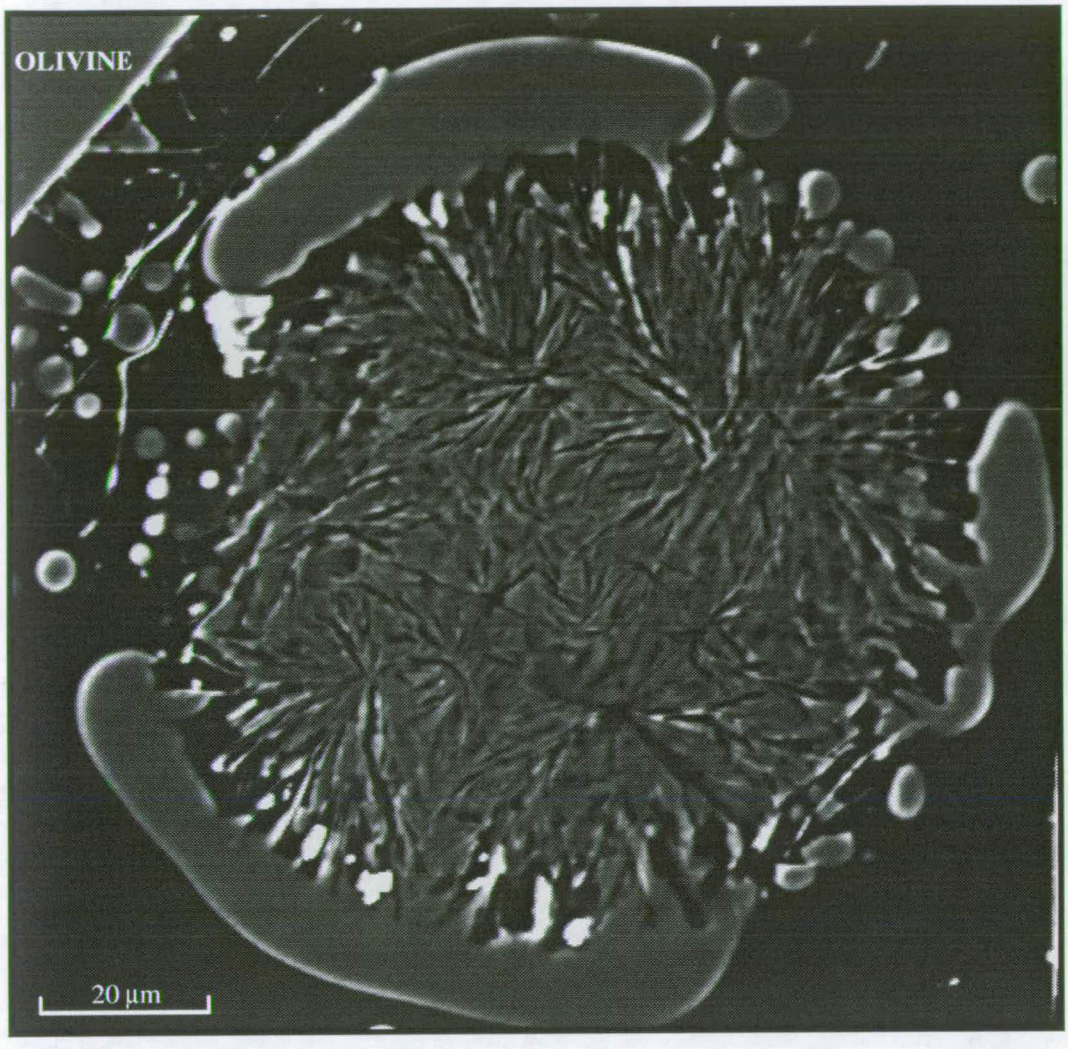

A back-scattered electron image of a polished section of ED327C3 showing a large glass sphere. The interior resembles the ropy-looking melt seen elsewhere in the capsules (see Plate 5.5) whereas the rims of the large glass sphere are closer in appearance to the small glass spheres from other experiments (see Plate 7.1).

capsules after the experiment, collect the fluid solute from between the capsules, and analyse it. However, this proved impossible because the capsules had partly pressure-welded together during the run (see Chapter 4, Plate 4.2). A further attempt using gold capsules run in a salt cell also failed for the same reasons. Although this approach was abandoned, it was still possible to examine the fluid quench after impregnating the capsules with epoxy resin. Results showed that most of the space between the two capsules contains small glass spheres (15 μm or less - Plate 7.6).

ED312

This experiment, which contained equal parts of a basaltic composition and water, was run in a large Pt bucket within a Ti sleeve according to the method of Ayers *et al.* (1992). A separate Pt lid pressure welded to the capsule and sealed it (see Chapter 4 for details). The run product, which was impregnated with epoxy resin and sectioned, consisted of melt which appeared to be wetting the walls of the Pt capsule, some crystals at the bottom of this melt, and a large number of glass spheres in the middle (Plate 7.7).

In summary, there is no apparent evidence that the fluid quench contains any material other than glass spheres, which are generally small (<15 μm) and are homogeneous in texture. In reversal experiments with high water:silicate ratios, there are large glass spheres which are texturally zoned with ropy-looking glass interiors rimmed by a smoother-looking glass. The interiors resemble the coexisting melt whereas the rims are similar in appearance to the smaller glass spheres.

7.2.2. Composition of glass spheres - major elements

Glass spheres were analysed for major elements using the electron microprobe. The remobilisation of alkalis during analysis was minimised by use of a rastered beam (6 x 6 μm), a low beam current (< 7 nA) and shortened count times for Na and K (see Chapter 4 for details). Despite these precautions, there was still some drop off with time in Na and K count rates. Therefore measured values of these elements should be treated with caution. Major-element compositions of glass spheres are variable, although all glass spheres are rich in SiO_2 and Al_2O_3, and poor in TiO_2 and FeO, with high alkalis relative to the starting material (Table 7.3).

PLATE 7.6

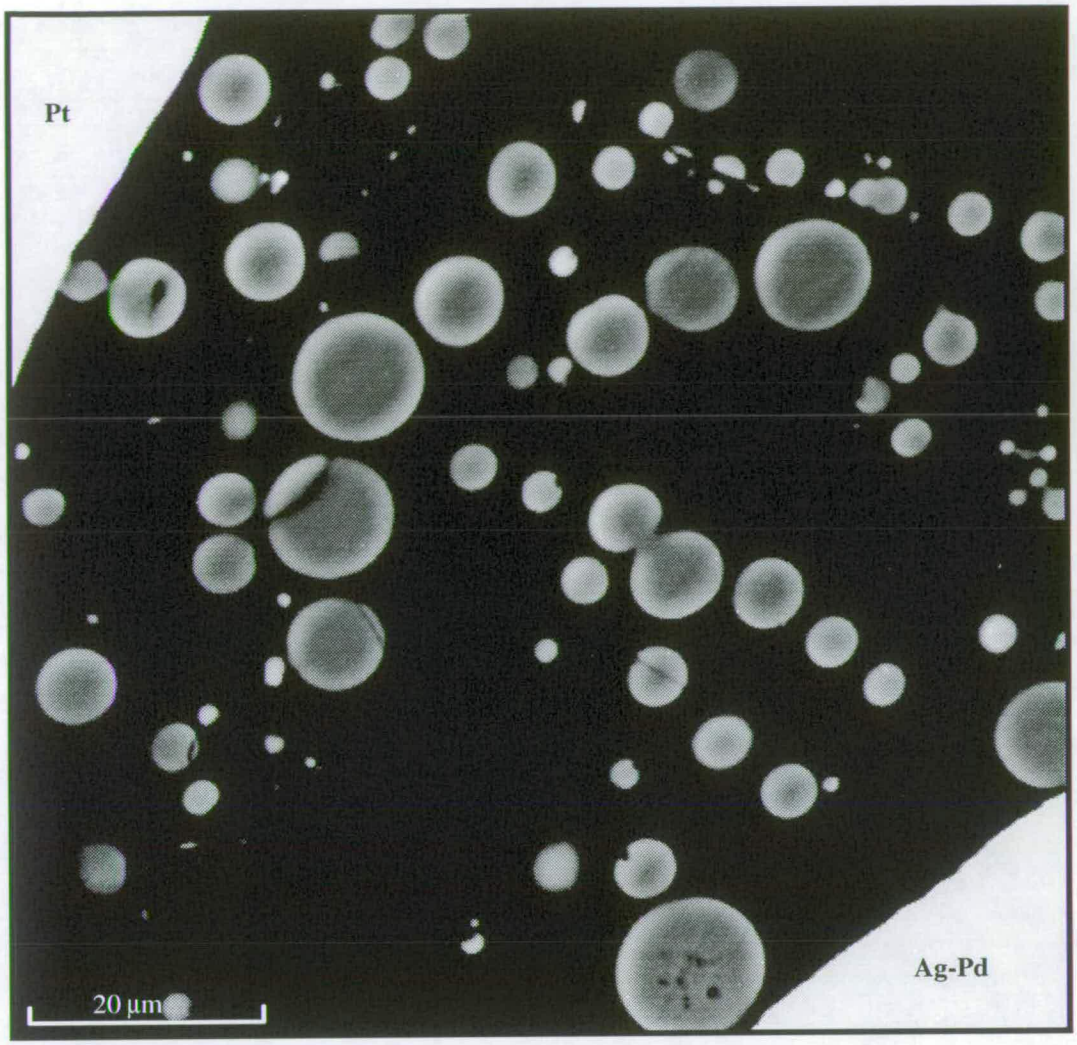

A back-scattered electron image of a polished section of ED231 showing the material trapped between the outer and the inner capsules.

PLATE 7.7

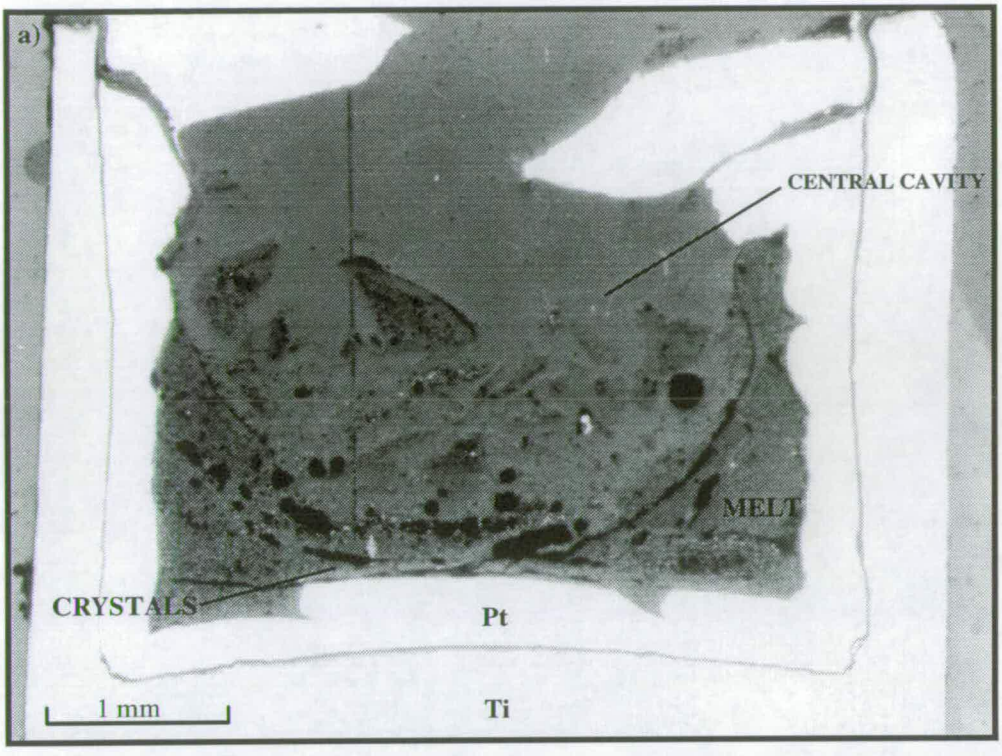

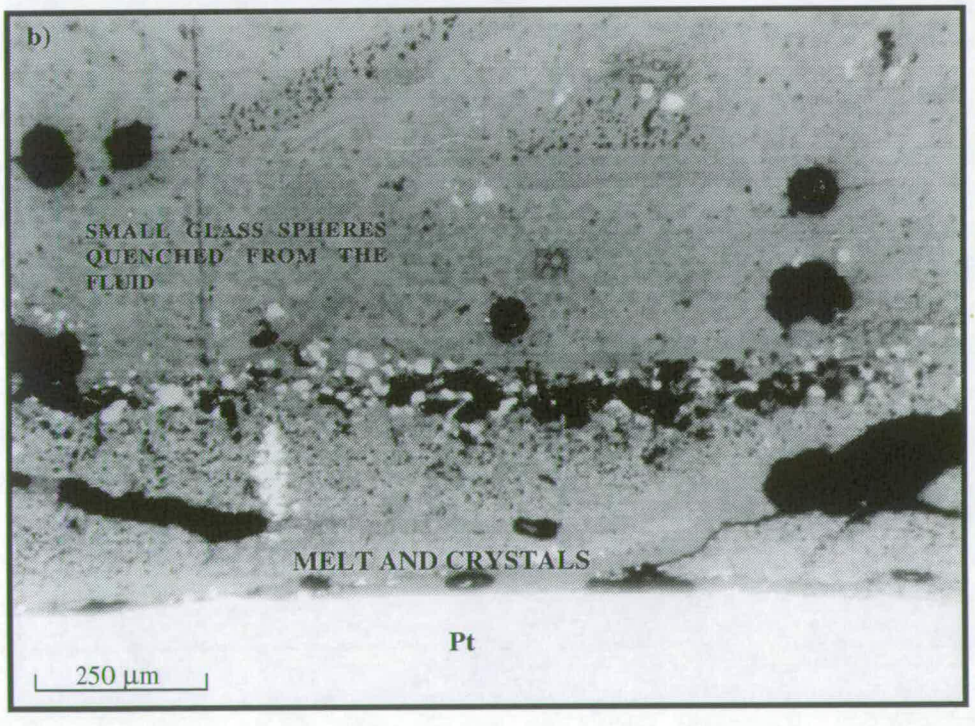

Reflected light photomicrographs of a polished section of ED312. a) The bright materials are the titanium bucket and the platinum capusle. Inside the capsule, the quenched melt can be seen. The meniscus separates melt from the cavity in the centre of the capsule (now represented by epoxy resin). Within this cavity are fragments of melt which have fallen from above, as well as quench from the fluid. b) a close-up showing the melt and crystals at the bottom, and hundreds of small glass spheres within the cavity.

Table 7.3: Representative electron-probe analyses of glass spheres from ED332C1 and ED348C3.

		ED332C1					*ED348C3*				
	starting comp.	*glass sphere*	*glass sphere*	*glass sphere*	*glass sphere*	*average melt*	*glass sphere*	*glass sphere*	*glass sphere*	*glass sphere*	*average melt*
SiO_2	51.0	53.59	58.93	55.95	55.07	**45.73**	60.21	57.40	59.31	53.74	**45.08**
TiO_2	1.5	0.29	0.40	0.74	0.90	**1.23**	0.23	0.60	0.44	0.82	**1.43**
Al_2O_3	23.1	13.35	16.11	18.03	19.08	**18.81**	14.46	17.04	16.38	17.87	**19.91**
FeO	3.9	0.38	0.50	1.20	1.29	**2.14**	0.15	0.28	0.39	1.37	**2.04**
MgO	4.1	0.46	0.73	1.61	1.93	**3.35**	0.17	0.33	0.65	2.39	**3.81**
CaO	12.6	3.89	3.58	5.36	3.83	**9.88**	1.65	4.21	2.49	5.70	**12.20**
Na_2O	2.6	0.93	1.66	2.19	1.93	**1.47**	2.64	2.83	1.05	2.31	**0.97**
K2O	0.7	1.05	1.59	1.52	2.49	**0.67**	2.83	2.19	2.80	2.12	**0.28**
MnO	0.2	0.01	0.04	0.08	0.10	**0.15**	0.04	0.04	0.06	0.06	**0.15**
Cr_2O_3	0.1	0.00	0.03	0.02	0.03	**0.05**	0.01	0.00	0.00	0.03	**0.05**
NiO	0.2	0.05	0.00	0.02	0.02	**0.01**	0.00	0.00	0.00	0.04	**0.02**
TOTAL	100	74.00	83.57	86.70	86.65	**83.50**	82.39	84.91	83.56	86.44	**85.93**
Mg no.		68.21	72.32	70.64	72.65	**73.6**	66.82	67.83	74.66	75.63	**76.9**

Run conditions are shown in Table 7.2.

The spread in composition within each experiment is systematic: the MgO and FeO contents of all glass spheres lie on a tie line between two end members, one of which is similar in composition to the average melt, and the other is extremely depleted in FeO and MgO (Fig. 7.1). The glass spheres have been divided into two groups, based on their apparent diameter: the majority of small glass spheres (10 μm or less) have lower MgO and FeO contents than the larger spheres (> 10 μm).

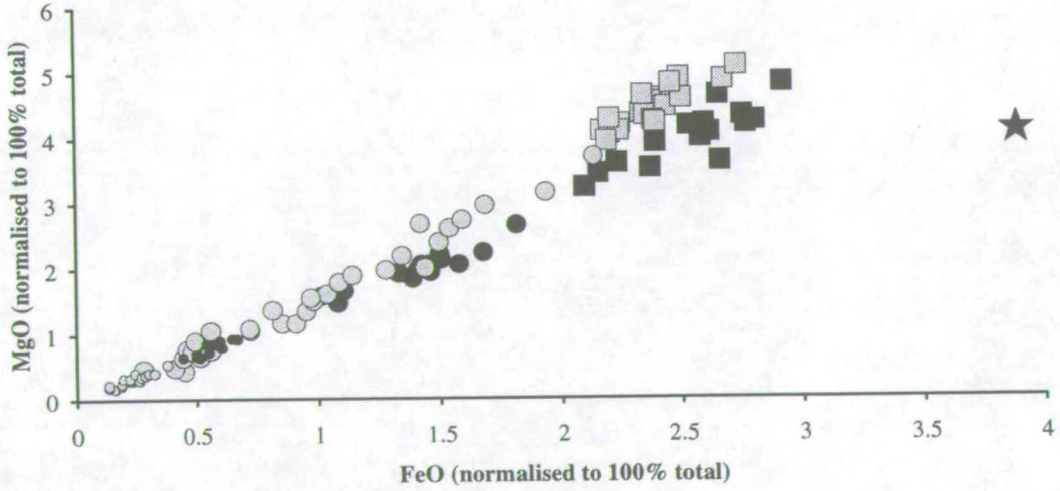

Figure 7.1: MgO versus FeO content of glass spheres and melt from ED332C1 (dark circles and squares, respectively) and ED348C3 (light circles and squares, respectively). Smaller spheres (10 μm or less) are represented by smaller circles. Values are normalised to a total of 100%. The bulk composition of the starting material is indicated by a star.

The distinction between these two groups persists when we examine other major element contents: the larger spheres plot nearer to the melt-like end of the trend than do the smaller spheres (Figs. 7.2, 7.3). The correlation between size and composition is not so clear for the alkalis (Fig. 7.4), although this may be a result of alkali loss during analysis.

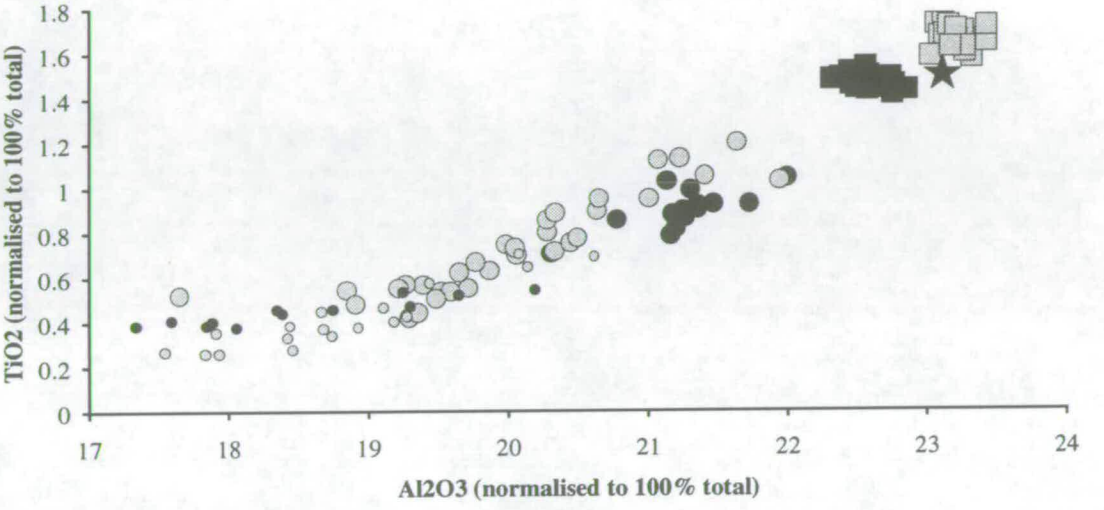

Figure 7.2: TiO_2 versus Al_2O_3 content of glass spheres and melt from ED332C1 (dark circles and squares, respectively) and ED348C3 (light circles and squares, respectively). Smaller spheres (10 μm or less) are represented by smaller circles. Values are normalised to a total of 100%. The bulk composition of the starting material is indicated by a star.

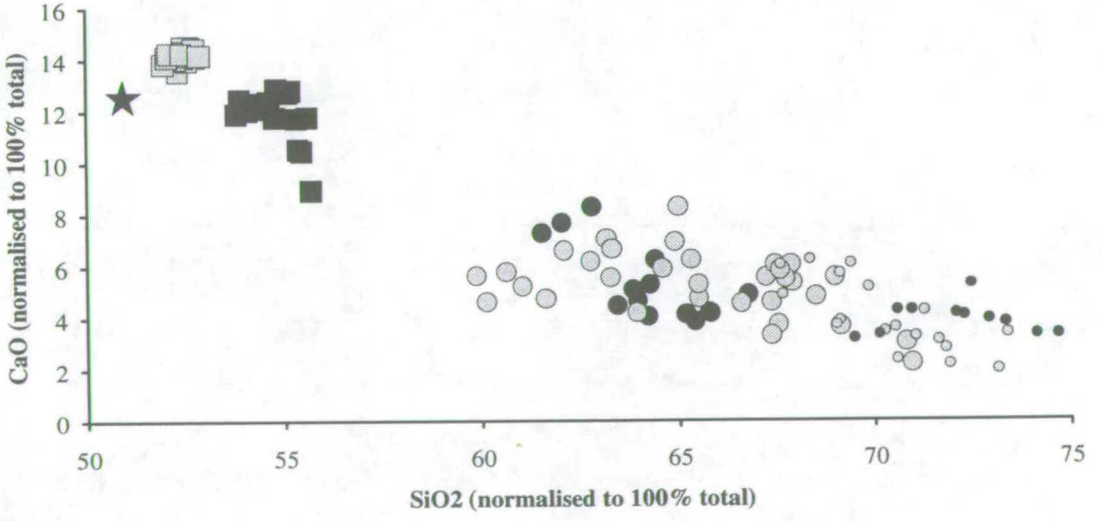

Figure 7.3: CaO versus SiO_2 content of glass spheres and melt from ED332C1 (dark circles and squares, respectively) and ED348C3 (light circles and squares, respectively). Smaller spheres (10 μm or less) are represented by smaller circles. Values are normalised to a total of 100%. The bulk composition of the starting material is indicated by a star.

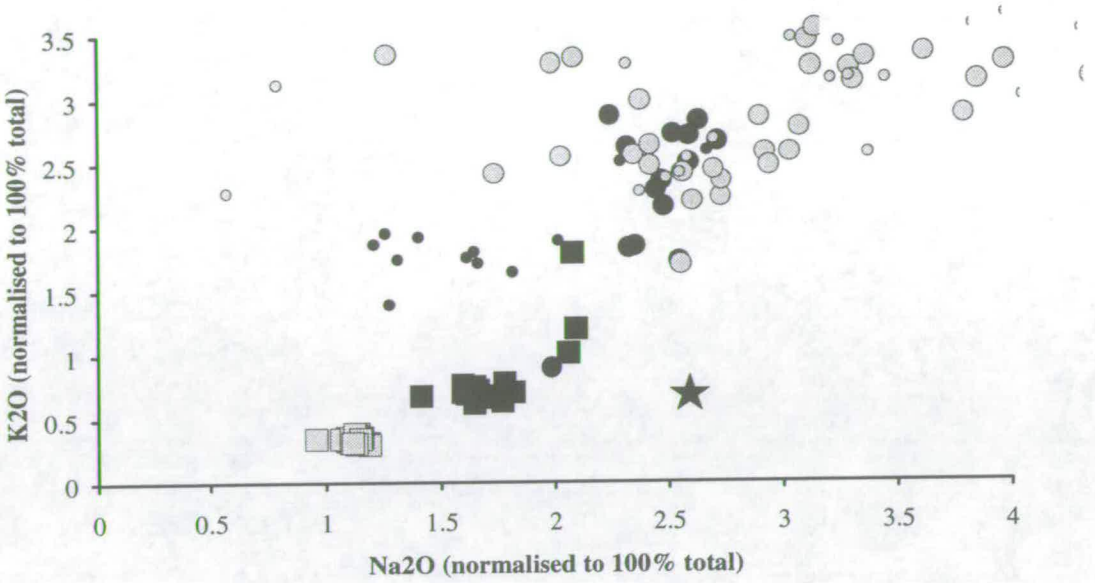

Figure 7.4: K_2O versus Na_2O content of glass spheres and melt from ED332C1 (dark circles and squares, respectively) and ED348C3 (light circles and squares, respectively). Smaller spheres (10 μm or less) are represented by smaller circles. Values are normalised to a total of 100%. The bulk composition of the starting material is indicated by a star.

The run products from both ED332C1 and ED348C3 consist entirely of melt and fluid quench. Assuming that the bulk composition remains constant during the experiment, it should be possible to combine the composition of the fluid quench products and the melt to form the starting composition. However, the starting composition is substantially more Fe rich than the run products (Fig. 7.1), presumably due to Fe loss during the experiment. It is interesting to note that ED348C3 appears to have suffered marginally more Fe loss than ED332C1, probably due to the larger water content in ED348C3. Fe loss also has the effect of increasing the percentage contents of the other major elements, and may contribute to the high SiO_2 content of the run products relative to the starting material (Fig. 7.3).

The compositions of glass spheres from ED234 (a reversal experiment in an olivine bucket) also lie on a trend verging towards the melt composition (Fig. 7.5).

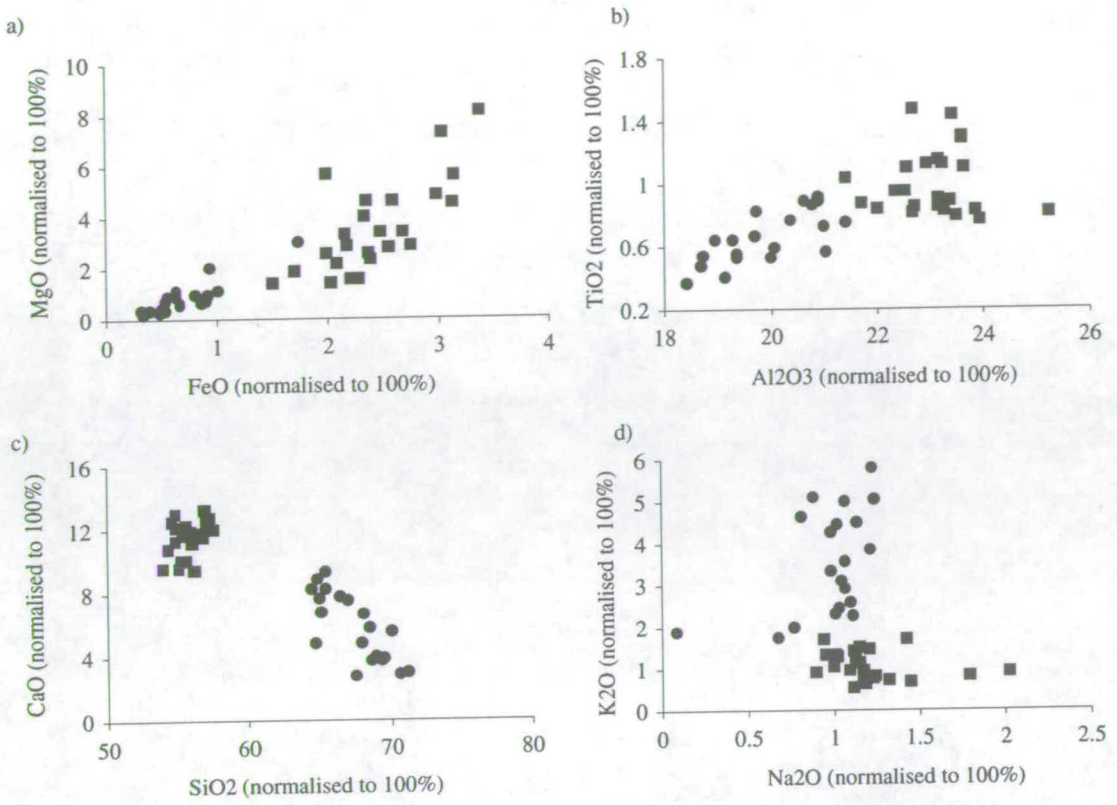

Figure 7.5: Composition of glass spheres (circles) and melt (squares) from ED234. All values are normalised to a total of 100%. a) MgO vs. FeO; b) TiO_2 vs. Al_2O_3; c) CaO vs. SiO_2; d) K_2O vs. Na_2O.

Zoning of melt globules and large glass spheres

Figure 7.6 shows the variation in composition across a melt globule from ED348C3. Most elements are extremely homogeneous throughout the melt globule, with the exception of the outer 10-20 μm. The composition of the edge is richer in SiO_2, Na_2O, and K_2O, lower in TiO_2, Al_2O_3, CaO, MgO, and FeO than the centre, and lies on a tie line between the melt and a small glass sphere.

There is also significant variation in major-element composition within some of the larger glass spheres. A traverse across a large glass sphere from ED327C3 (see Plate 7.5) reveals that there is a sharp distinction in SiO_2, TiO_2, MgO, FeO contents between the edge and the centre (Fig. 7.7). The change in Na_2O and K_2O contents is more gradational. For all elements, the centre is closer in composition to the melt, and the edge is similar to the small glass spheres.

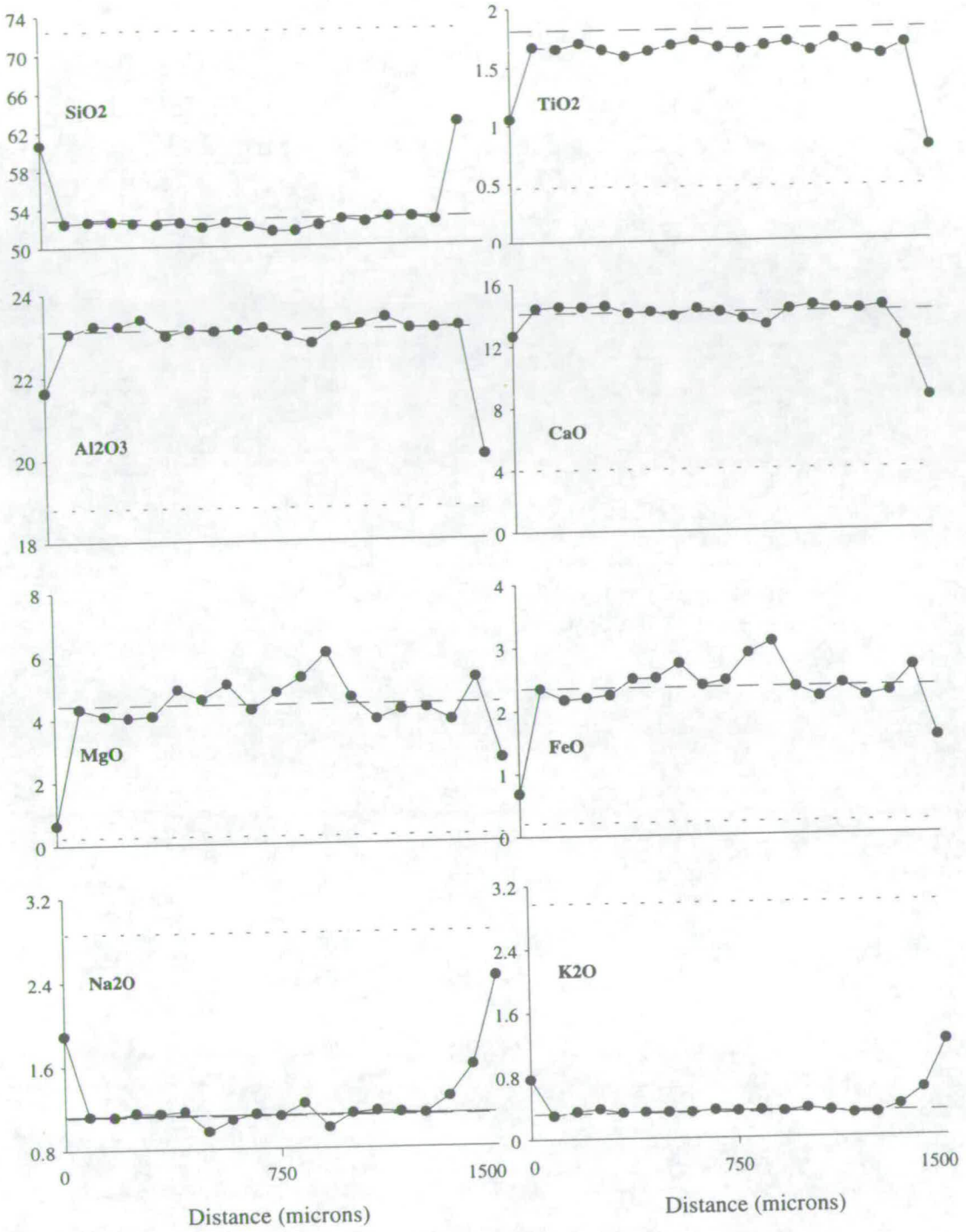

Figure 7.6: Variation in major-element composition (normalised to 100% total) across a large melt globule from ED348C3. Also shown are the average compositions of the melt (dashed line) and small glass spheres (dotted line).

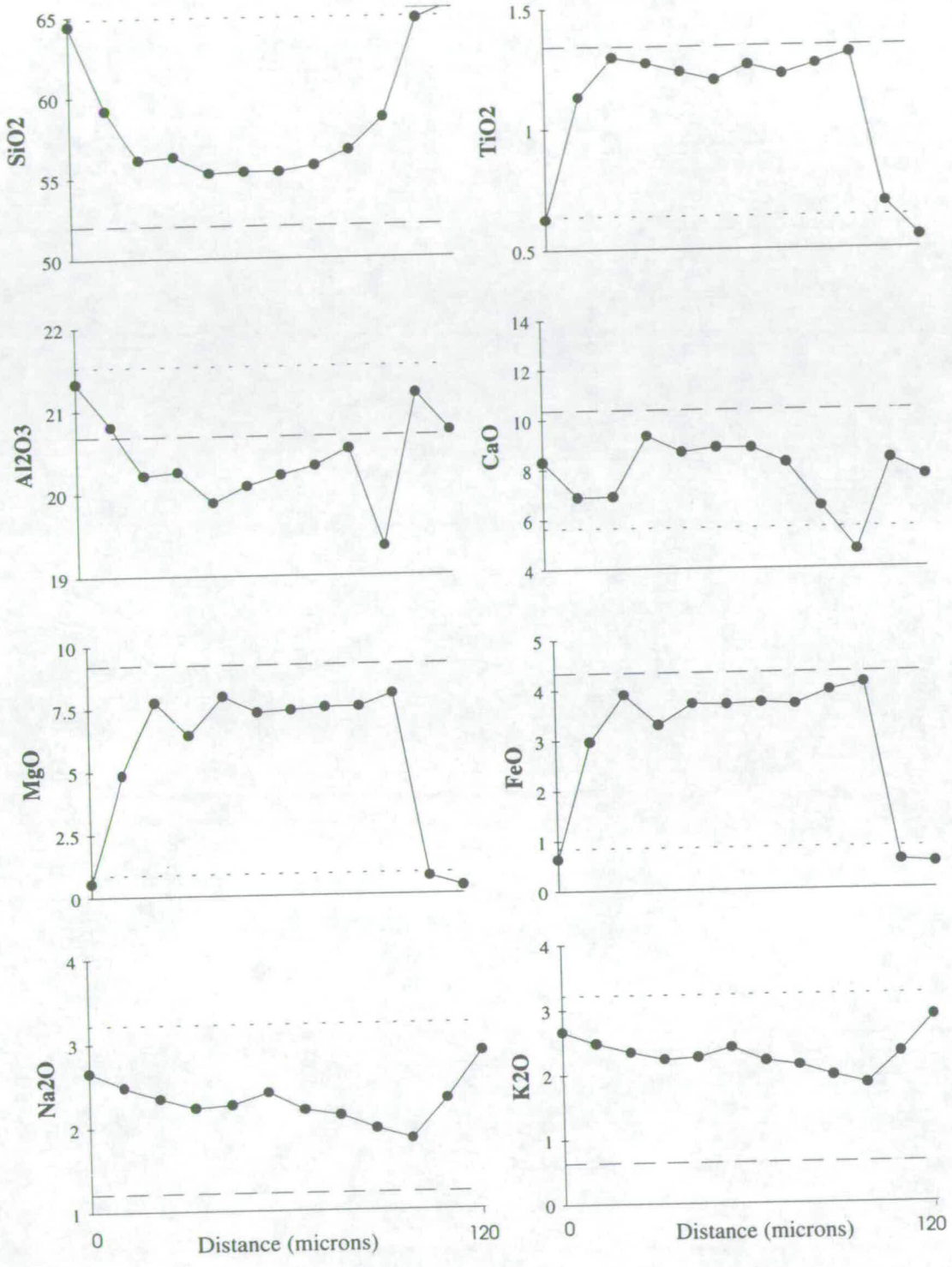

Figure 7.7: Major-element composition (normalised to 100%) from edge to edge across a large glass sphere from ED327C3. See Plate 7.5. Also shown are the average compositions of the melt (dashed line) and glass spheres (dotted line).

7.2.3 Composition of glass spheres - trace elements

The ion probe was used to analyse coexisting glass spheres and melt for a range of trace elements (B, Na, K, Ti, Rb, Sr, Y, Zr, Nb, Ba, REE, Hf, Ta). In addition, ED332C1, which had been further doped with beryl and uraninite (see Chapter 4), was analysed for Li, Be, Cs, Pb, U. Unfortunately, although uraninite should contain some Th, levels of this element were not sufficiently high to enable accurate analysis. When analysing small glass spheres, the beam (which was typically 10 - 15 μm in diameter) overlapped onto epoxy resin. This did not cause a problem as epoxy resin contains insignificant concentrations of trace elements or silica. However, the relatively large beam size coupled with the poor optics on the instrument ensured that the larger glass spheres were sampled preferentially. All ion yields were ratioed to the SiO_2 content (normalised to 100%) of a typical glass sphere. Errors inherent in this process are discussed later.

Results from two experiments are listed in Table 7.4. There is a large spread in trace-element composition within an experiment, with the concentrations of some elements varying by up to a factor of 10. Nevertheless, it can be seen that glass spheres are typically enriched in Rb, Cs, and B and depleted in all other elements relative to the bulk. This is illustrated in Figures 7.8 and 7.9 in which the composition of glass spheres, normalised to bulk, are plotted in order of decreasing ionic radius (the ionic radii values are given later in Table 7.13). For both experiments, values for all glass spheres decrease with increasing ionic radius to a minimum for Yb and then gradually increase again. The extent of the difference in normalised trace-element content between each element varies from one glass sphere to another.

Table 7.4: Representative ion-probe analyses of glass spheres (fl), melt, and bulk starting material.

	ED332C1					*ED348C3*				
	fl3	*fl4*	*fl9*	*melt*	*bulk*	*fl5*	*fl11*	*fl20*	*melt*	*bulk*
Be	260	263	214	310	350	n.d.	n.d.	n.d.	n.d.	n.d.
B	101	103	94	28	132	9.1	15	15	7.6	8.7
Rb	2731	1468	2524	438	537	1679	4618	3792	407	211
Sr	90	173	77	290	300	230	70	193	289	316
Y	12	22	5.0	112	111	34	0.43	3.4	115	126
Zr	44	65	16	216	223	94	0.69	9.4	217	248
Nb	63	66	42	104	109	76	23	43	91	105
Cs	72	48	82	11	11	n.d.	24	18	1.9	n.d.
Ba	61	130	63	210	211	256	39	135	212	261
La	71	138	31	740	721	227	2.2	23	758	844
Ce	14	27	6.3	140	139	44	0.44	4.7	143	160
Pr	2.6	4.8	1.2	26	25	8.1	0.054	0.80	26	29
Nd	31	64	13	336	321	99	1.0	10	341	378
Sm	2.8	6.0	1.4	36	33	11	0.16	0.79	38	40
Eu	14	32	11	111	108	46	2.9	17	113	125
Gd	2.5	5.3	1.0	27	25	6.3	0.046	n.d.	29	31
Tb	2.5	4.9	1.2	28	26	8.1	0.10	0.85	29	32
Dy	3.1	6.5	1.1	33	26	10	0.13	1.0	31	35
Ho	5.8	10	2.3	58	54	17	0.21	1.6	58	65
Er	2.6	6.1	1.2	33	28	8.6	0.36	0.59	34	35
Tm	2.7	4.9	1.1	29	26	n.d.	n.d.	n.d.	28	n.d.
Yb	3.4	5.9	1.2	33	30	9.2	0.13	0.93	32	35
Lu	4.4	7.9	1.7	43	40	n.d.	n.d.	n.d.	43	n.d.
Hf	n.d.	37	9.3	140	127	54	0.29	3.5	137	162
Ta	n.d.	6.3	2.5	31	15	13	0.26	1.3	30	33
Pb	19	11	7.2	178	35	n.d.	n.d.	n.d.	n.d.	n.d.
U	250	509	162	2498	2092	n.d.	n.d.	n.d.	n.d.	n.d.

Values in ppm. Undetermined values are denoted n.d. Individual glass spheres are labelled fl1, fl2, fl3 etc.

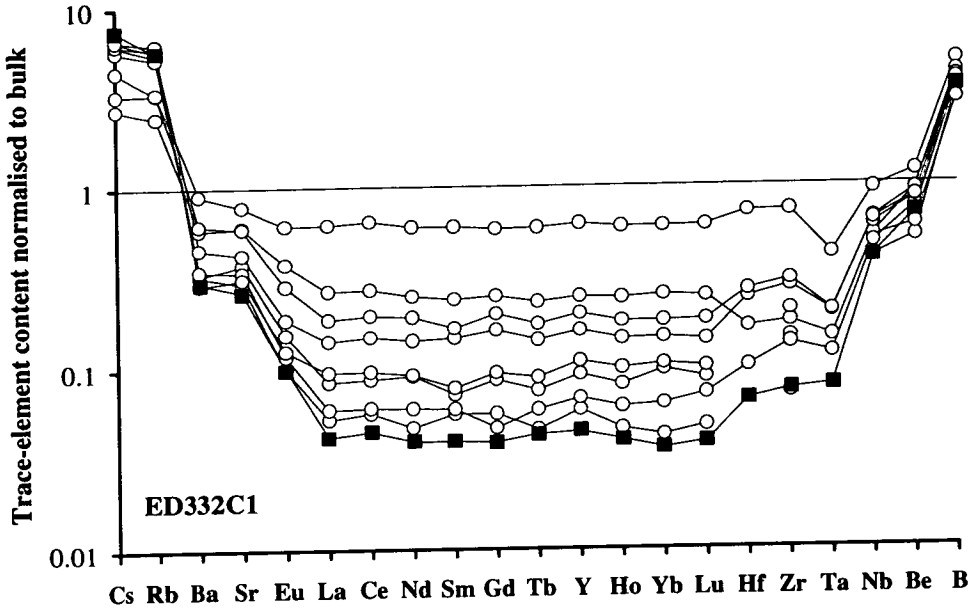

Figure 7.8: Trace-element content of glass spheres from ED332C1, normalised to the bulk composition, plotted in order of decreasing ionic radius. fl9 (referred to in Section 7.4.2) is indicated by filled squares.

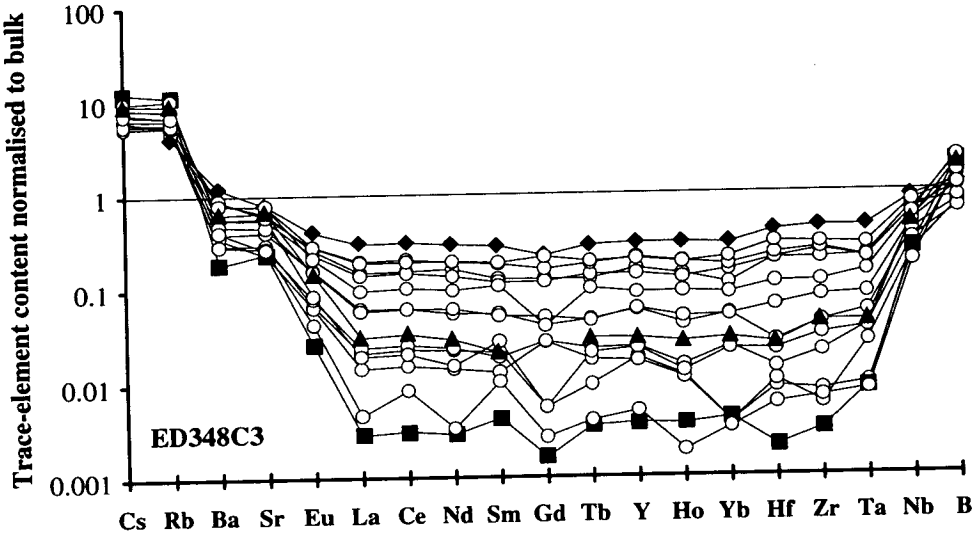

Figure 7.9: Trace-element content of glass spheres from ED348C3, normalised to the bulk composition, plotted in order of decreasing ionic radius. Symbols: squares - fl11; triangles - fl20; diamonds - fl5. These analyses are referred to in Section 7.3.2.

Scaling each analysis to the same Nd value allows easier comparison (Fig. 7.10), and highlights the difference between individual glass spheres. However, despite this variation, all glass spheres display the same basic trend of decreasing normalised trace-element content from Cs to Yb, followed by an increase from Hf to B.

a)

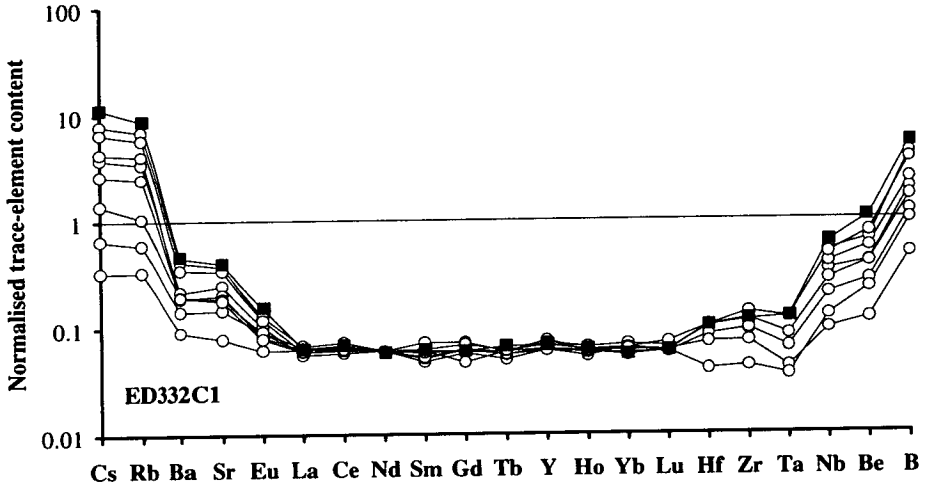

b)

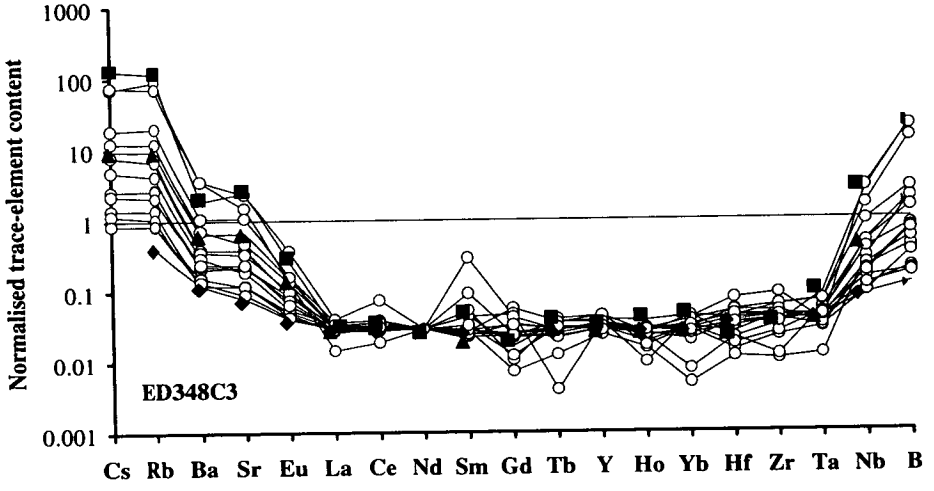

Figure 7.10: Trace-element content of glass spheres normalised to bulk composition, normalised to an arbitrary Nd content. a) from ED332C1, b) from ED348C3. For key to symbols, see caption to Figures 7.8 and 7.9.

This trend is seen in all experiments studied (Fig. 7.11), including those with basaltic bulk compositions (ED317, ED327, ED332, ED348) and peridotitic bulk composition (ED91).

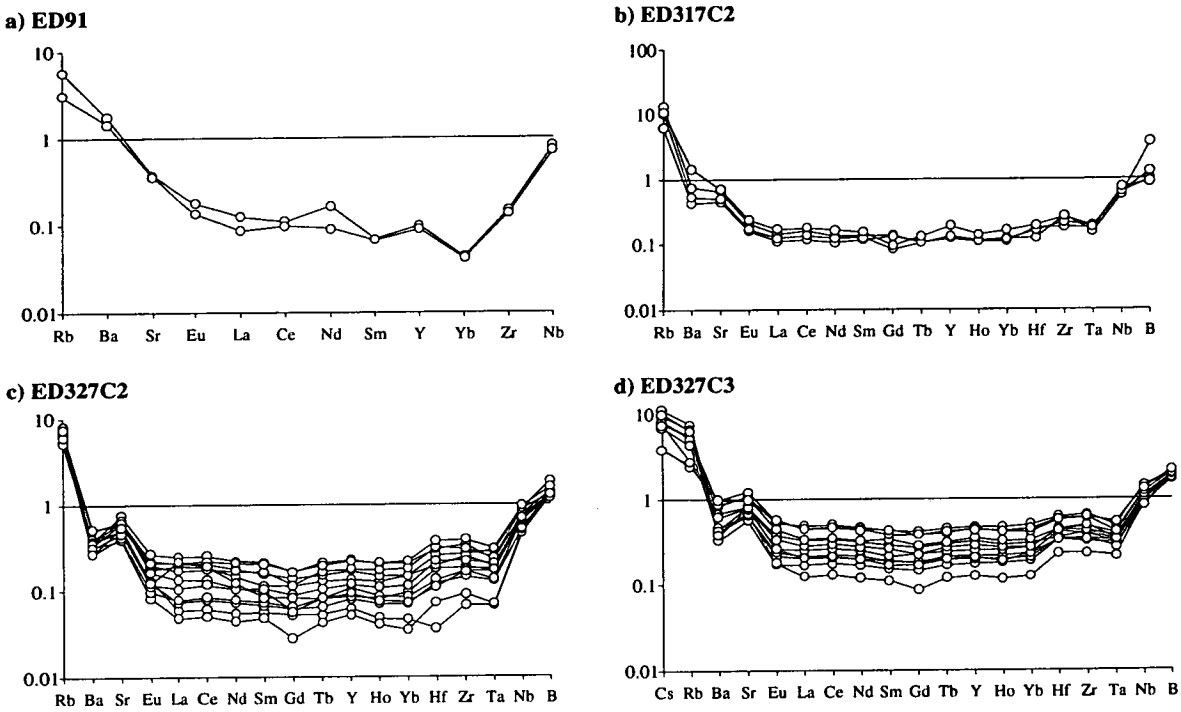

Figure 7.11: Trace-element contents of glass spheres normalised to bulk composition from a) ED91; b) ED317C2; c) ED327C2; d) ED327C3.

The compositions of all glass spheres, although highly variable, lie on a tie line between two end members, one of which is melt-like in composition, and the other is a Rb-rich, Cs-rich, REE-poor composition (Figs. 7.12, 7.13). In general, the correlation between trace-element concentration and glass sphere size is similar to that between major-element concentration and size i.e. the larger glass spheres fall nearer to the melt-like end member. For these reversal experiments, the composition of the starting material lies at the melt-like end of the tie line for nearly all elements. A notable exception is Pb, in which the run products are depleted relative to the starting material. This is probably due to loss of Pb to the capsule walls during the experiment. The Ta content of run products is also lower than in the starting material.

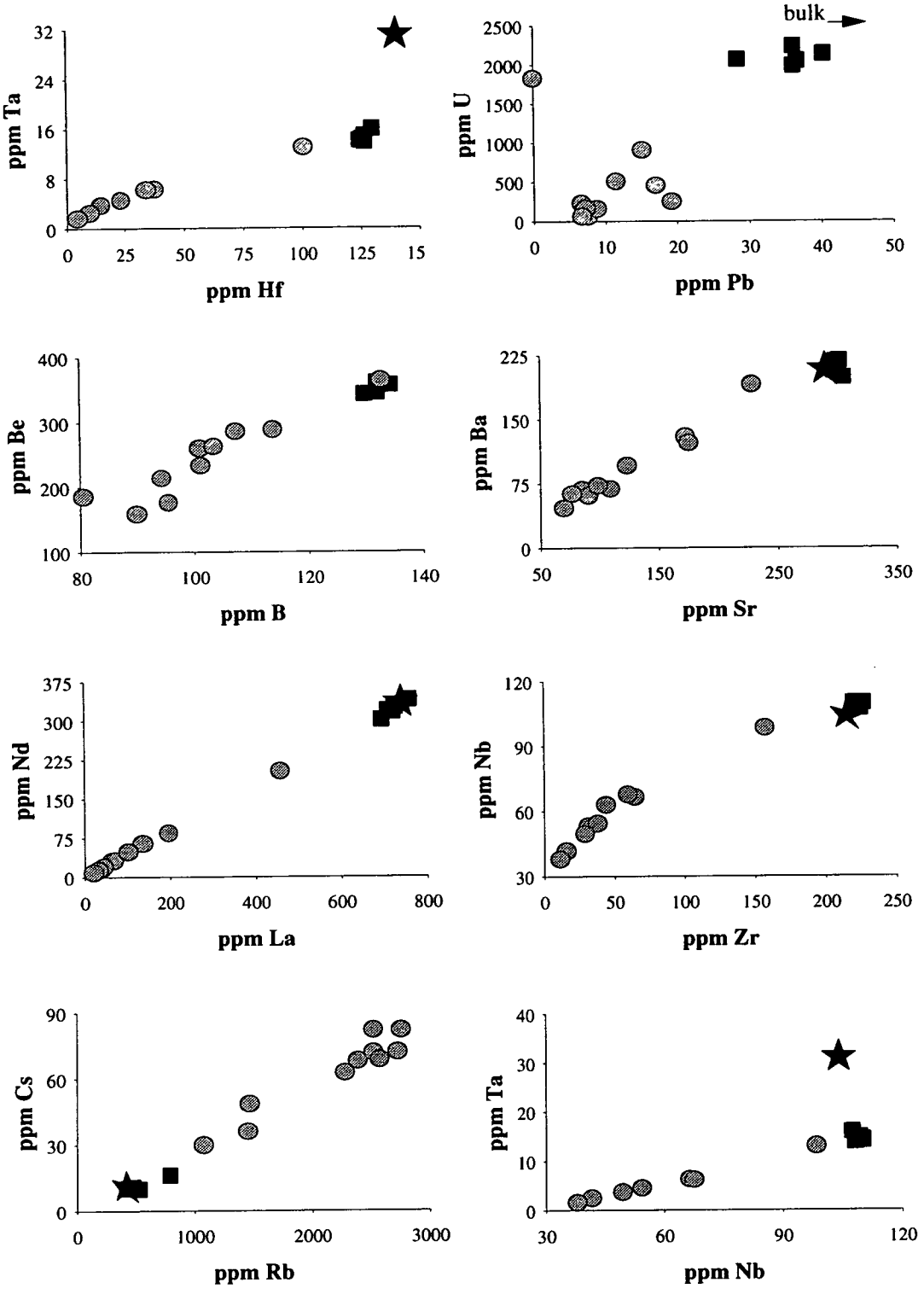

Figure 7.12: Trace-element contents of glass spheres (circles) and melt (squares) from ED332C1. The bulk composition of the starting material is represented by a star.

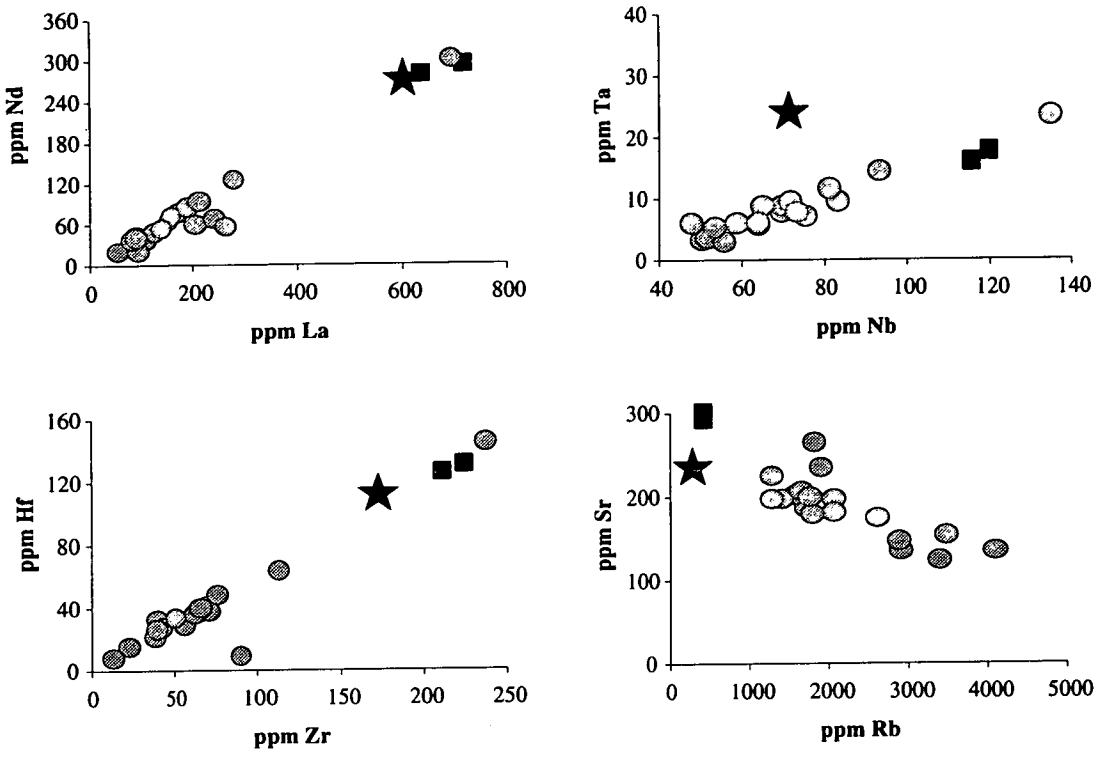

Figure 7.13: Trace-element contents of glass spheres (circles) and melt (squares) from ED332C3. The composition of the starting material is denoted by a star.

Zoning of melt globules and large glass spheres

Traverses across melt globules from ED348C3 show these to be relatively homogeneous in terms of the trace elements analysed (Fig. 7.14). However, the very edges of the melt globules are relatively enriched in Cs and Rb, and depleted in REE, Sr, Y, Zr, Ba. Large glass spheres also exhibit zonation in trace-element contents, with a relatively abrupt transition from a more melt-like composition in the interior to a LILE-rich, REE-poor composition at the edge. Figure 7.15 shows that the edge of the large glass sphere from ED327C3 (Plate 7.5) is similar in composition to a typical small glass sphere (i.e. high Rb, Cs; low Zr, La, Nb). The inner area is similar, but not identical to the average melt composition: Rb content equals that of the melt, but the contents of other elements (e.g. Zr, Nb, La) are slightly lower in the centre of the glass sphere than they are in the melt. Although the large beam size precludes high spatial accuracy, it appears that the compositional transition between the edge and the centre is very abrupt. These conclusions are similar to those drawn from the major-element traverse of this large glass sphere (see Figure 7.7).

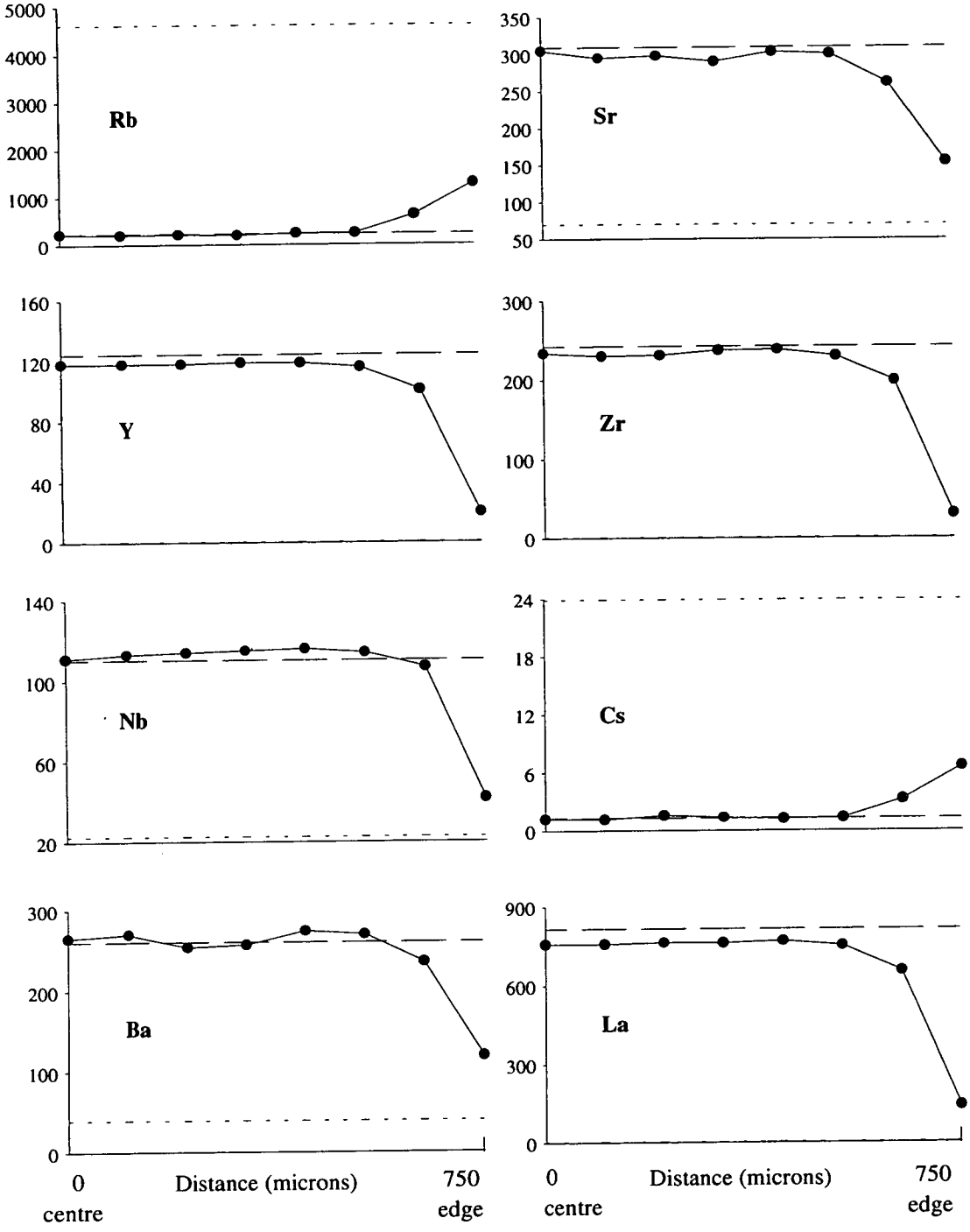

Figure 7.14: Variation in trace-element contents from the centre to the edge of a melt globule from ED348C3. Values are in ppm. Also shown are the average compositions of the melt (dashed line) and glass spheres (dotted line).

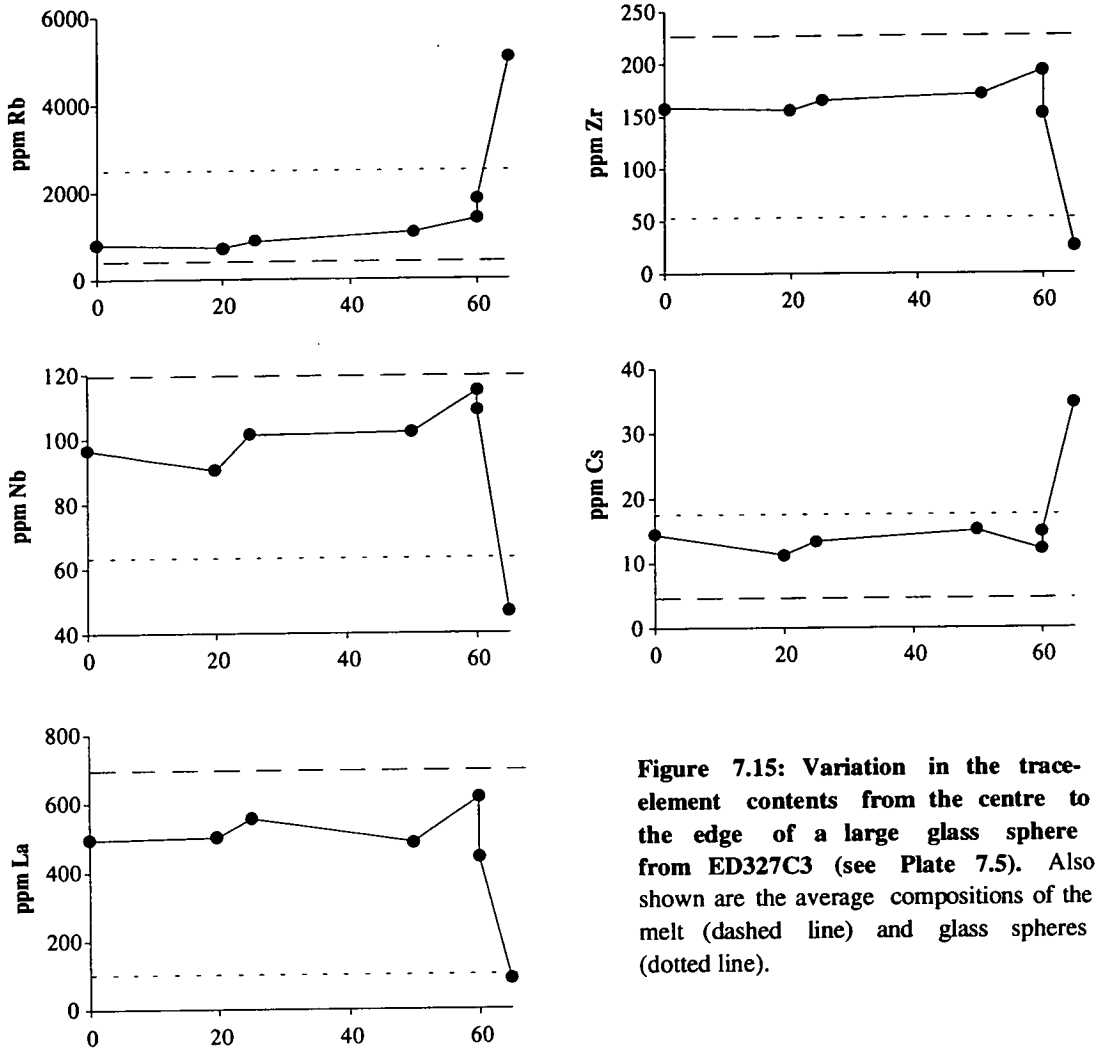

Figure 7.15: Variation in the trace-element contents from the centre to the edge of a large glass sphere from ED327C3 (see Plate 7.5). Also shown are the average compositions of the melt (dashed line) and glass spheres (dotted line).

7.2.4 Composition of glass spheres - summary

Both major- and trace-element compositions of glass spheres from within an experiment fall onto a well-defined trend between two end members:

End member 1	Melt-like in terms of major elements and trace elements
End member 2	High SiO_2, K_2O, Na_2O; low MgO, FeO, TiO_2, Al_2O_3, CaO. High Cs, Rb; low Ba, Sr, REE, Ta, Nb, Zr.

The proportion of end member 1 increases with the size of the glass sphere. In very large glass spheres and melt globules, the cores are similar to end member 1 and the rims are close to end member 2.

7.3 THE FORMATION OF FLUID QUENCH

Before the partition coefficients can be calculated, it is necessary to produce a model for the formation of the fluid quench, and so to decide at which point in the spectrum of compositions the true equilibrium fluid is most closely represented. In an ideal experiment, all equilibrium phases would quench to produce identical compositions at room temperature. Thus, ideally, the fluid quench would be an anhydrous representation of the fluid at equilibrium. However, in practise this may not always happen. Significant difficulties have been experienced by previous workers measuring the composition of hydrous melts (Chapter 3), primarily because of quench modification of the liquid during cooling, a process which may be in operation in the experiments in this study. For simplicity, I shall consider the experiments in which only melt and fluid were produced at equilibrium (ED332C1 and ED348C3). The quench products consist of 1) a ropy glass which is extremely abundant and is assumed on textural and compositional grounds to have quenched from the melt, 2) glass spheres of various sizes and compositions, and 3) water. It is assumed that at room temperature the water contains negligible dissolved material. The two models considered are illustrated in Figure 7.16. For clarity, the phase diagrams used to illustrate the models are extremely schematic.

Model 1. Mechanical mixing of melt and fluid quench

In this model, the equilibrium melt has a high surface tension and therefore tends to form globules, whereas the fluid has a much lower surface tension and wets the melt and the capsule. On quenching, the melt freezes into globules of sizes ranging from a few μm to 1000 μm in diameter. The melt globules then act as nucleation sites for exsolution of solute from the fluid, leading to the formation of rims of fluid overgrowth. The remaining vapour phase cools to form water. According to this model, the fluid quench product which is most representative of the equilibrium fluid composition is one in which there is no melt nucleus, i.e. the smallest glass sphere analysed.

a) Model 1

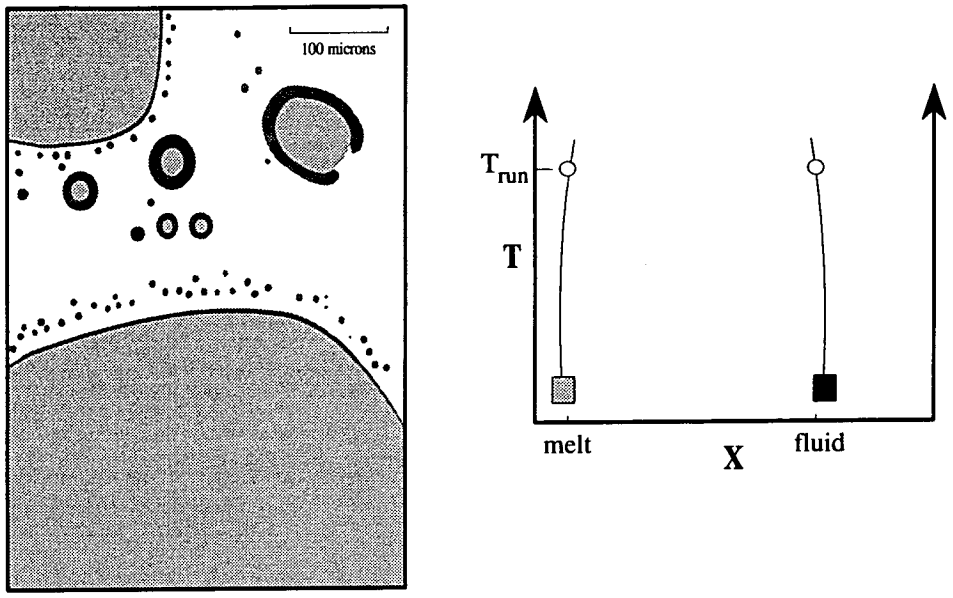

b) Model 2

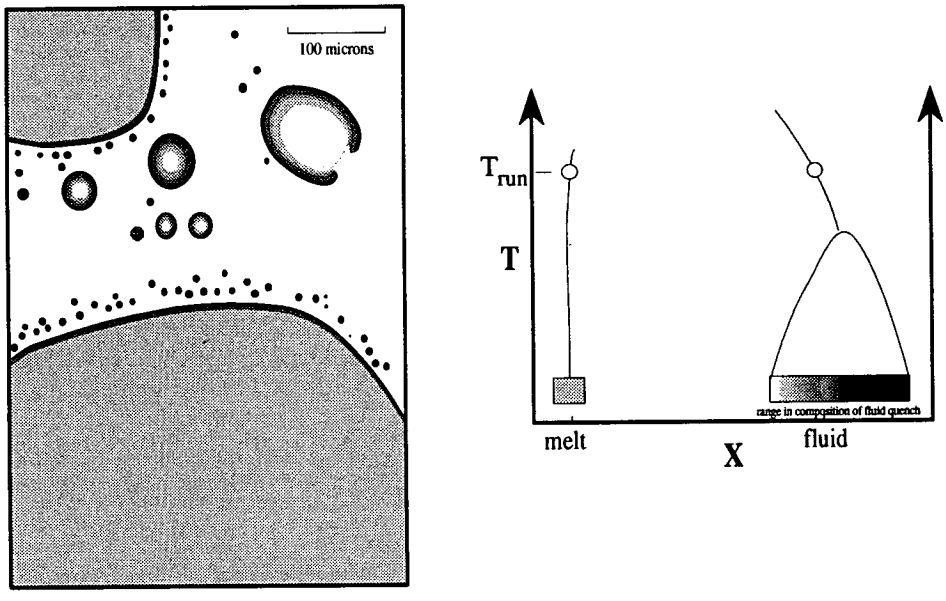

Figure 7.16: Cartoon to illustrate models for the formation of fluid quench (see text). The left-hand diagrams show a hypothetical polished section of an experimental charge containing melt globules and large and small glass spheres. On the right are schematic temperature-composition diagrams to show the position of the solvus relative to the compositions of the quench materials.
a) Model 1: Upon quenching, the melt and the fluid freeze to distinct compositions, which are illustrated on the T-X diagram. The melt globules and the centres of the large glass spheres are of a melt-like compositions, whereas the smaller glass spheres and the rims of the large glass spheres are of the fluid composition.
b) Model 2: As the temperature drops, the melt quenches to a single composition, but the fluid quenches to a range of compositions (shown as a colour zonation on the diagram). In the run product, the fluid quench has a corresponding range in composition.

Model 2. Fractionation on the fluid on quenching

In this model, the melt quenches first to form homogeneous mats. Fluid solute then quenches out of the vapour, but not as one composition: it fractionates into a continuous range of compositions, whose end members lie on either side of the true fluid composition. The first to quench is the more melt-like composition, followed by decreasingly melt-like compositions. The last solute formed is a highly evolved glass, present on the rims of the larger spheres and as very small spheres. In this case the fluid quench product which is most representative of the equilibrium fluid composition would be somewhere near the middle of the range of compositions of the glass spheres. The small glass spheres would represent a highly evolved fluid fractionation product.

7.3.1 Zoning of glass spheres

An important line of evidence for the method of formation of the fluid quench lies in the nature of the 'hybrid' large glass spheres. Model 1 would predict that there is a very abrupt jump in composition from a melt composition in the middle to a composition equivalent to a small glass sphere at the edge. Model 2 predicts that there is a more gradational change encompassing a range of compositions on either side of the true fluid composition. Texturally, the large glass spheres appear to be composed of two separate phases, and some major elements (SiO_2, TiO_2, MgO, FeO) show a distinct jump from the centre to the edge. However, the change appears to be more gradational for Na_2O and K_2O. Although the spatial resolution on the trace-element traverses (measured by ion probe) is poorer than for the major-element traverses (measured by electron probe), there does appear to be an abrupt rather than a gradual change in composition from the interior to the edge. This favours model 1. However, not all element contents in the centre of large glass spheres are exactly the same as the average melt. For example, the La content in the melt from ED327C3 is 710 ppm whereas it is only 620 ppm in the centre of a large glass sphere (Fig. 7.15).

7.3.2 Mass balance

Two experiments, ED332C1 and ED348C3 produced only fluid quench and melt, and can be used to test the two models. If a particular glass sphere composition is truly representative of the equilibrium fluid composition then it should be possible to combine its composition with an amount of melt to reproduce the bulk composition. I have used the starting bulk composition in these calculations, although there will be some error introduced owing to Fe loss during the experiment. For each element analysed, I have calculated the inferred proportions of the two end members (melt and glass sphere) according to the simple equation:

$$\mathbf{x[melt]} + (1 - \mathbf{x})\mathbf{[glass\ sphere]} = \mathbf{[bulk]} \qquad (7.1)$$

where x is the proportion of melt in the charge, and [phase] is the concentration of an element in the phase.

Table 7.5 shows the result of this calculation for ED348C3 assuming that one particular glass sphere (fl11) represents the fluid end member. The percentage melt values derived from all elements (with the exception of Nb and Rb) are fairly similar, ranging from 87.7% (Zr) to 92.9% (Sm). Rb, the only element more concentrated in the glass sphere than the melt, yields a slightly higher value of 96% melt in the bulk. The reason for the anomalous value for Nb is not known, but may be due to an inaccurate determination of the bulk Nb content.

Table 7.5: Trace element composition of the starting material (bulk), melt and a glass sphere (fl11) from ED348C3. The percentage melt in the bulk composition is also shown, calculated by mass balance for each element in turn.

	bulk	*melt*	*end-member: fl 11*			*bulk*	*melt*	*end-member: fl 11*	
	ppm	*ppm*	*ppm*	***% melt in bulk***		*ppm*	*ppm*	*ppm*	***% melt in bulk***
Rb	407	211	4618	**95.6**	**Sm**	38	40	0.16	**92.9**
Sr	289	316	70	**89.2**	**Eu**	113	125	2.9	**90.6**
Y	115	126	0.43	**91.2**	**Gd**	29	31	0.046	**91.1**
Zr	217	248	0.69	**87.7**	**Tb**	29	32	0.10	**89.9**
Nb	91	105	23	**82.9**	**Dy**	31	35	0.13	**90.3**
La	758	844	2.2	**89.9**	**Ho**	58	65	0.21	**88.4**
Ce	143	160	0.44	**89.3**	**Yb**	32	35	0.13	**91.4**
Pr	26	29	0.054	**89.2**	**Ta**	30	33	0.26	**90.3**
Nd	341	378	1.0	**90.0**					

In the preceding calculations, the fluid end member was assumed to be one of the least melt-like glass spheres (which is consistent with model 1). If we take a more melt-like glass sphere to represent the fluid end member (model 2), then the inferred percentage melt in the bulk should be lower (in Figure 7.17 a bulk composition described as a mixture of melt and fl 5 should contain less melt than one described as a mixture of melt and fl 11). Figure 7.9 shows the trace-element contents of glass spheres from this experiment. This can be seen quantitatively in Table 7.6. For example, taking the average of the result from eighteen elements, the proportion of melt in the bulk is calculated to be 93%, 91%, and 87% given fluid end members fl11, fl20, fl5, respectively. The percentage error on these values is highest for the most melt-like end member (fl5) and lowest for the least melt-like end member (fl11).

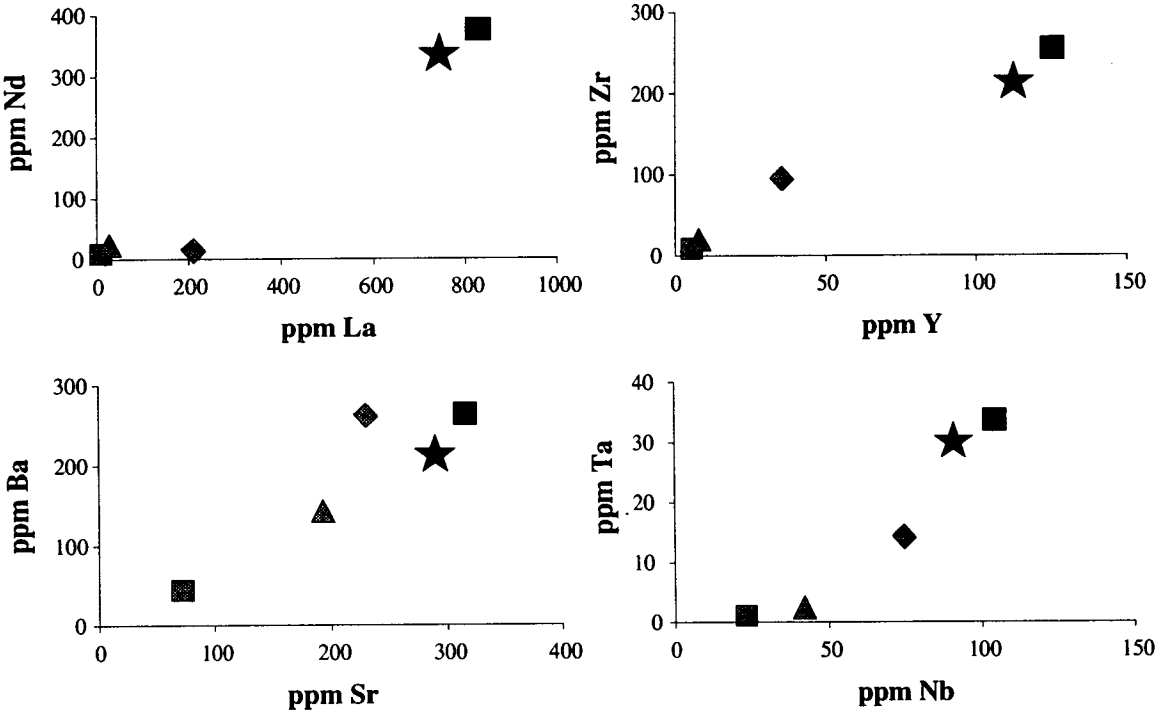

Figure 7.17: Trace-element contents of glass spheres fl5 (diamond), fl11 (square), fl20 (triangle), and average melt (large square) from ED348C3. The bulk composition is indicated by a star. See Table 7.6.

Table 7.6: The percentage melt in the bulk composition of ED348C3, calculated (see text) assuming that the end members consist of melt and fl11 (or fl20 or fl5).

	bulk	*melt*	*end member: fl11*		*end member: fl20*		*end member: fl5*	
	ppm	*ppm*	*ppm*	*% melt in bulk*	*ppm*	*% melt in bulk*	*ppm*	*% melt in bulk*
Rb	407	211	4618	**95.6**	3792	**94.5**	1679	**86.7**
Sr	289	316	70	**89.2**	193	**78.5**	230	**69.3**
Y	115	126	0.43	**91.2**	3.4	**91.0**	34	**87.9**
Zr	217	248	0.69	**87.7**	9.4	**87.3**	94	**80.3**
Nb	91	105	23	**82.9**	43	**77.2**	76	**50.1**
La	758	844	2.2	**89.9**	23	**89.6**	227	**86.2**
Ce	143	160	0.44	**89.3**	4.7	**89.0**	44	**85.3**
Pr	26	29	0.054	**89.2**	0.80	**88.9**	8.1	**85.2**
Nd	341	378	11	**90.0**	9.8	**89.8**	99	**86.5**
Sm	38	40	0.16	**92.9**	0.79	**92.8**	11	**90.5**
Eu	113	125	2.9	**90.6**	17	**89.4**	46	**85.5**
Gd	29	31	0.046	**91.1**	n.d.		6.3	**88.9**
Tb	29	32	0.10	**89.9**	0.85	**89.7**	8.1	**86.5**
Dy	31	35	0.13	**90.3**	1.0	**90.0**	10	**86.7**
Ho	58	65	0.21	**88.4**	1.6	**88.1**	17	**84.3**
Yb	32	35	0.13	**91.4**	0.93	**91.2**	9.2	**88.4**
Hf	137	162	0.29	**84.8**	3.5	**84.5**	54	**77.4**
Ta	30	33	0.26	**90.3**	1.3	**90.0**	13	**84.5**
		Average % melt		**89.9**		**88.3**		**82.8**
		standard deviation		**3.1**		**4.5**		**9.5**
		% error		**3**		**5**		**11**

If model 1 *is* in operation, we should expect to be able to describe fl5 in terms of two components: melt and fl11. However, the percentage melt component calculated using different elements is not consistent (Table 7.7).

Table 7.7: Percentage melt component in fl5 calculated by mass balance assuming that fl5 can be described as a mixture of melt and fl11.
From ED348C3.

	% melt		*% melt*		*% melt*
Rb	67	**Ce**	28	**Tb**	26
Sr	67	**Pr**	28	**Dy**	28
Y	27	**Nd**	27	**Ho**	27
Zr	38	**Sm**	27	**Yb**	26
Nb	61	**Eu**	37	**Hf**	35
La	28	**Gd**	21	**Ta**	40

7.3.3 Summary and implications

From the results of the mass-balance calculations using the most 'fluid-like' spheres, and from the optical observations, we can be reasonably confident that only glass spheres are quenching from the fluid. However, the exact mechanism for the formation of glass spheres is not clear from the evidence available. The traverses across large glass spheres suggest that these are composed of melt-like cores and small-glass-sphere-like rims. However, mass balance calculations to prove this are only partially successful, indicating that another factor is in operation.

In summary, I think that the abrupt change in composition within the large glass spheres is good evidence that Model 1 is in operation. The centres of the large glass spheres are very similar in composition to the melt and may represent melt nuclei. However, as it is not possible to reproduce by mass balance the composition of a large glass sphere from the compositions of a small glass sphere and melt, it seems likely that some of the range in composition within the glass spheres is due to fractionation during quenching. Furthermore, there is no abrupt change in alkali element concentrations within a large glass sphere, suggesting that for these elements at least, there is considerable exchange between the melt quench and the fluid quench. Using the evidence presented above, I have decided to select the least melt-like analysed glass sphere to be representative of the fluid. As very small glass spheres (< 15 μm) could not be accurately analysed by SIMS, in practice the glass spheres chosen to be representative of the fluid are approximately 15μm.

Although there is considerable uncertainty surrounding the choice of a glass sphere composition representative of the equilibrium fluid composition, this is not critical to the results as all glass spheres have similar inter-element ratios (Figs. 7.8 - 7.11).

7.4 CALCULATION OF PARTITION COEFFICIENTS

The Nernst partition coefficient (D) between two phases, x and y is defined by:

$$D(x/y) = \frac{[x]}{[y]} \qquad (7.2)$$

where [x] is the concentration of the element in phase x.
In this section, the trace-element contents of glass spheres, melt and olivine will be used to calculate D (fluid/melt) and D (olivine/fluid).

7.4.1 Water and solute contents

Water content in the melt
In order to calculate the partition coefficients between melt and fluid at equilibrium, it is necessary to estimate the water contents in both phases. Although there have been some experimental studies to investigate this, data at 2.0 GPa are relatively scarce. Water contents were not measured explicitly in the present study. However, it is possible to infer the required information from the experimental results, using established techniques.
One method of determination of the solubility of water in melts is by the weight-loss method (e.g. Hamilton & Oxtoby, 1986), in which known amounts of mix and water are equilibrated at run conditions to form water-saturated melt. After quenching, the amount of dissolved water remaining in the capsule is determined by weight loss after piercing and heating to 110°C. From this information it should be possible to calculate the percentage water necessary to saturate a melt. In the present study, the experiments appropriate for this method include ED317C2, ED332C1 and ED348C3, which were all water saturated. Results (Table 7.8) however, are not consistent: it appears that the water solubility in melt from ED348C3 greatly exceeds that of melt from ED317C2 or ED332C1. This may be because water has come out of solution to varying extents during the quenching process; a common problem especially at high water contents (Holloway, 1981; McMillan & Holloway, 1987). An additional

potential problem is that water solubility may be overestimated as a result of entrapment of water in bubbles in the melt.

Table 7.8: Weight percent water retained in capsule after quenching.

Experiment	P (GPa)	T (°C)	wt % water at beginning	wt % water dissolved in run product
ED317C2	1.74	1020	30	10.0
ED332C1	1.85	1005	30	8.4
ED348C3	1.85	1005	50	17.8

All experiments produced melt and fluid quench.

Another common method for determination of water contents is by phase equilbria studies i.e. determination of the water content necessary to saturate a melt and produce a fluid phase. In general this method is accurate but low in precision (McMillan & Holloway, 1987). Experiments in the present study were conducted with initial water contents of 10 wt%, 20 wt%, 30 wt% and 50 wt%. Remains of a fluid phase were detected in runs with 30 wt% and 50 wt% H2O, but not in runs with 10 wt% or 20 wt% H2O, which suggests that the solubility of water in the melt is between 20 wt% and 30 wt%.

The solubility of water in melt in these experiments is therefore 25±5 wt%.

A more accurate estimate taken from existing literature is not possible due to the scarcity of high-pressure data and of adequate thermodynamic models for this extremely complex system. However, it is of interest to compare the value derived from the present study with estimates from the literature. Hamilton *et al.* (1964) measured water solubility from experiments performed at pressures up to 0.6 GPa. A projection of their data to 1.85 GPa (the pressure of ED348C3) gives a value between 21 and 23 wt% water. Eggler & Rosenhauer (1978) recorded water solubility of 17-20 wt% in diopside melt produced at 2.0 GPa and ~1250°C.

Solute content in the fluid

It is now possible to derive an estimate for the value of the solute content in the fluid.

For ED348C3:

Mass of mix = 6.67 mg

Mass of initial H_2O = 6.63 mg

mass balance from ED348C3 (using fl11 as the glass sphere representative of the fluid at equilibrium - see Table 7.5) suggests that melt and fluid solute (both

normalised to anhydrous compositions) are present in proportions 89.9 and 10.1 wt%, respectively.

$\therefore$ Mass of melt (anhydrous) = 0.899 X 6.67 = 5.99 mg

Mass of fluid solute (anhydrous) = 0.101 X 6.67 = 0.68 mg

Solubility of water in melt = 25 wt%

$\therefore$ Mass of water in melt = 2.00 mg

Mass of water in fluid = 6.63 - 2.00 = 4.63 mg

$\therefore$ Weight % solute in fluid = 100 X 0.68 / (0.68 + 4.63) = **12.73 wt%**

The three main sources of error in this calculation are:

1. proportion of melt in the charge (89.9±3.1% i.e. a 3.5% relative error),
2. proportion of fluid solute in the charge (10.1±3.1% i.e. a 30.7% relative error),
3. solubility of water in the melt (25±5 wt% i.e. a 20% relative error).

Propagation of these errors yields a relative error of 32.2% on the value of percent solute in the fluid.

The amount of solute dissolved in the fluid in these experiments is 12.73±4.1%

This result is consistent with the measured value of 11.9 wt% solute in a fluid in equilibrium with phlogopite peridotite at 1.7 GPa and 1080°C (Schneider & Eggler, 1986).

From the trace-element contents (normalised to 100% anhydrous) of the melt and of a glass sphere representative of the equilibrium fluid composition, the trace-element contents of the melt and fluid at equilibrium can be calculated:

$$[\textbf{melt at equilibirum}] = [\textbf{melt}] \times \frac{75}{100} \qquad (7.3)$$

$$[\textbf{fluid at equilibirum}] = [\textbf{glass sphere}] \times \frac{12.73}{100} \qquad (7.4)$$

7.4.2 Partition coefficients

D (fluid/melt)

The partition coefficients between fluid and melt at equilibrium were calculated from Equations 7.3, 7.4 and 7.2 using the trace-element contents of the average melt and fl9 from ED332C1 (Fig. 7.8). Glass sphere fl9 was chosen to represent the equilibrium fluid as it is one of the least melt-like compositions and has relatively small analytical errors. The Li, Na, and K contents were measured at a later time. For these elements a similar small glass sphere was chosen after ensuring that its composition is consistent with fl9. Results are given in Table 7.9 and are compared with results from other experiments in Figure 7.18.

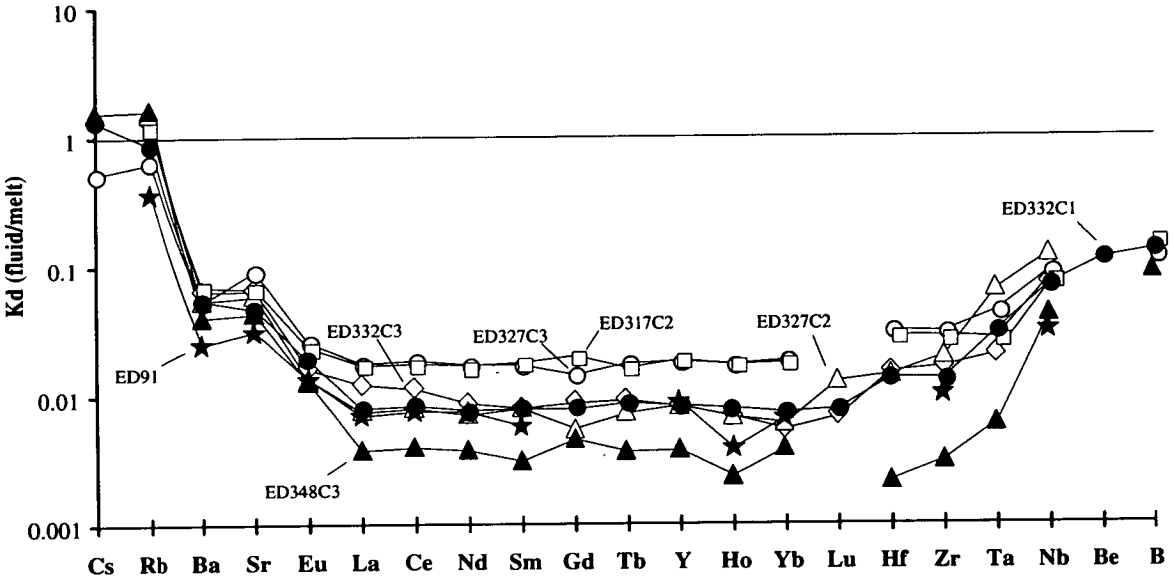

Figure 7.18: Comparison of D (fluid/melt) from all experiments analysed. For each experiment, results are derived from analyses of the average melt and of a small glass sphere considered to be representative of the fluid at equilibrium. Elements are plotted in order of decreasing ionic radius.

The generally higher absolute partition coefficients (for the majority of elements including the REE) derived from ED317C2 and ED317C3 may be due to a small amount of melt in the analyses of the glass spheres analysed from these experiments. Conversely, it is conceivable that the glass spheres analysed from ED348C3 may have contained less of a melt component and therefore yielded lower absolute values of partition coefficient. Despite these differences, results from all experiments are remarkably similar. Note that ED91, a forward experiment, gives results very close to those from ED332C1, ED327C3 and ED327C2. This is particularly significant as the glass spheres analysed from this experiment were formed in a fluid inclusion

Table 7.9: D (fluid/melt) and error calculated from compositions of a glass sphere and the average melt from ED332C1.

ppm	*Glass sphere (anhydrous)*	*Average melt*	***D (fluid/melt)***	***ERRORS (%)***					
				1	*2*	*3*	*5*	*6*	*Total*
Li	2.6	3.4	**0.13**	1.3	5.3	15.8	20	32.2	41
Be	233	350	**0.11**	0.13	5.3	2.3	20	32.2	38
B	103	132	**0.13**	0.37	5.3	1.2	20	32.2	38
Na	16403	13156	**0.21**	0.04	5.3	5.1	20	32.2	39
K	20329	6131	**0.56**	0.04	5.3	10	20	32.2	40
Ca	19348	75064	**0.044**	0.24	5.3	4.2	20	32.2	39
Ti	3167	8833	**0.061**	7.1	0	3.5	20	32.2	39
Rb	2748	537	**0.87**	0.18	5.3	27	20	32.2	47
Sr	83	300	**0.047**	0.54	5.3	1.0	20	32.2	38
Y	5.4	111	**0.0083**	1.7	5.3	3.0	20	32.2	38
Zr	18	223	**0.013**	1.7	5.3	1.1	20	32.2	38
Nb	45	109	**0.071**	1.1	5.3	1.1	20	32.2	38
Cs	89	11	**1.33**	1.3	5.3	24	20	32.2	45
Ba	69	211	**0.055**	0.96	5.3	4.0	20	32.2	38
La	34	721	**0.0080**	1.1	5.3	3.3	20	32.2	38
Ce	6.8	139	**0.0084**	2.7	5.3	3.6	20	32.2	39
Pr	1.3	25	**0.0088**	5.6	5.3	3.2	20	32.2	39
Nd	14	321	**0.0076**	4.8	5.3	4.4	20	32.2	39
Sm	1.6	33	**0.0079**	13	5.3	3.6	20	32.2	41
Eu	12	108	**0.019**	2.4	5.3	4.0	20	32.2	39
Gd	1.1	25	**0.0078**	10	5.3	9.2	20	32.2	41
Tb	1.3	26	**0.0087**	5.3	5.3	3.0	20	32.2	39
Dy	1.2	26	**0.0077**	11	5.3	5.1	20	32.2	40
Ho	2.5	54	**0.0079**	4.3	5.3	3.9	20	32.2	39
Er	1.3	28	**0.0077**	8.3	5.3	4.5	20	32.2	39
Tm	1.2	26	**0.0081**	5.5	5.3	3.0	20	32.2	39
Yb	1.3	30	**0.0074**	13	5.3	5.6	20	32.2	41
Lu	1.8	40	**0.0077**	5.6	5.3	2.9	20	32.2	39
Hf	10	127	**0.014**	8.4	5.3	1.6	20	32.2	39
Ta	2.7	15	**0.031**	7.4	5.3	5.7	20	32.2	39
Pb	7.8	35	**0.037**	24	5.3	12	20	32.2	47
U	177	2092	**0.014**	0.8	5.3	4.6	20	32.2	39

The errors are derived from:
1 - The analysis of the glass sphere, *2* - Estimation of the SiO_2 content of the glass sphere (note that this is not relevant for the Ti content which was measured by electron probe; note also that the Ca content was measured by ion probe), *3* - Error in the average melt composition. *5* - Error in the estimate of the water content in the melt, *6* - Error in the estimate of the amount of solute in the fluid. See Section 7.4.1.

inside the olivine bucket, and are therefore unlikely to have been modified by quenching of any crystalline phases other than olivine (see Chapter 5). The values of D (fluid/melt) used in future calculations are taken from ED332C1 as this was doped with the greatest number of trace elements.

D (olivine/fluid) and D (olivine/melt)

In two experiments (ED332C3 and ED327C3), large crystals of olivine were formed (Plate 7.8), thus allowing analysis by ion probe, and hence calculation of partition coefficients between olivine, coexisting melt and fluid. The olivine is slightly zoned with respect to some major elements, ranging from Fo90 in the centre to Fo93 at the edge (Table 7.10). Despite this zonation, which is probably due to iron loss during the experiment, the major-element composition is consistent with an equilibrium olivine.

Table 7.10: Major-element composition from the centre to the edge of an olivine from ED332C3.

	Centre	to	Edge
SiO_2	40.10	40.37	41.47
TiO_2	0.06	0.08	0.04
Al_2O_3	0.05	0.10	0.03
FeO	10.19	9.89	7.18
MgO	48.48	48.28	51.64
CaO	0.10	0.18	0.09
Na_2O	0.01	0.02	0.01
K2O	0.00	0.01	0.01
MnO	0.20	0.20	0.16
Cr_2O_3	0.06	0.06	0.03
NiO	0.49	0.56	0.03
TOTAL	99.74	99.74	100.69
Mg no.	89.5	89.7	92.8

Several olivine crystals were analysed using the ion probe. Although the crystals are up to 100 μm wide, and the ion beam is 15 μm in diameter, there is still some chance of overlap onto the surrounding melt. The most Rb-poor analysis of olivine was considered to be the purest, as Rb is an extremely incompatible element. The Nernst partition coefficients (Equation 7.2) between olivine and fluid, and between olivine and melt were calculated from compositions of olivine, melt and a glass sphere from ED332C3, using values for water and solute content in fluid and melt calculated in Section 7.4.1. Results are given in Tables 7.11 and 7.12.

PLATE 7.8

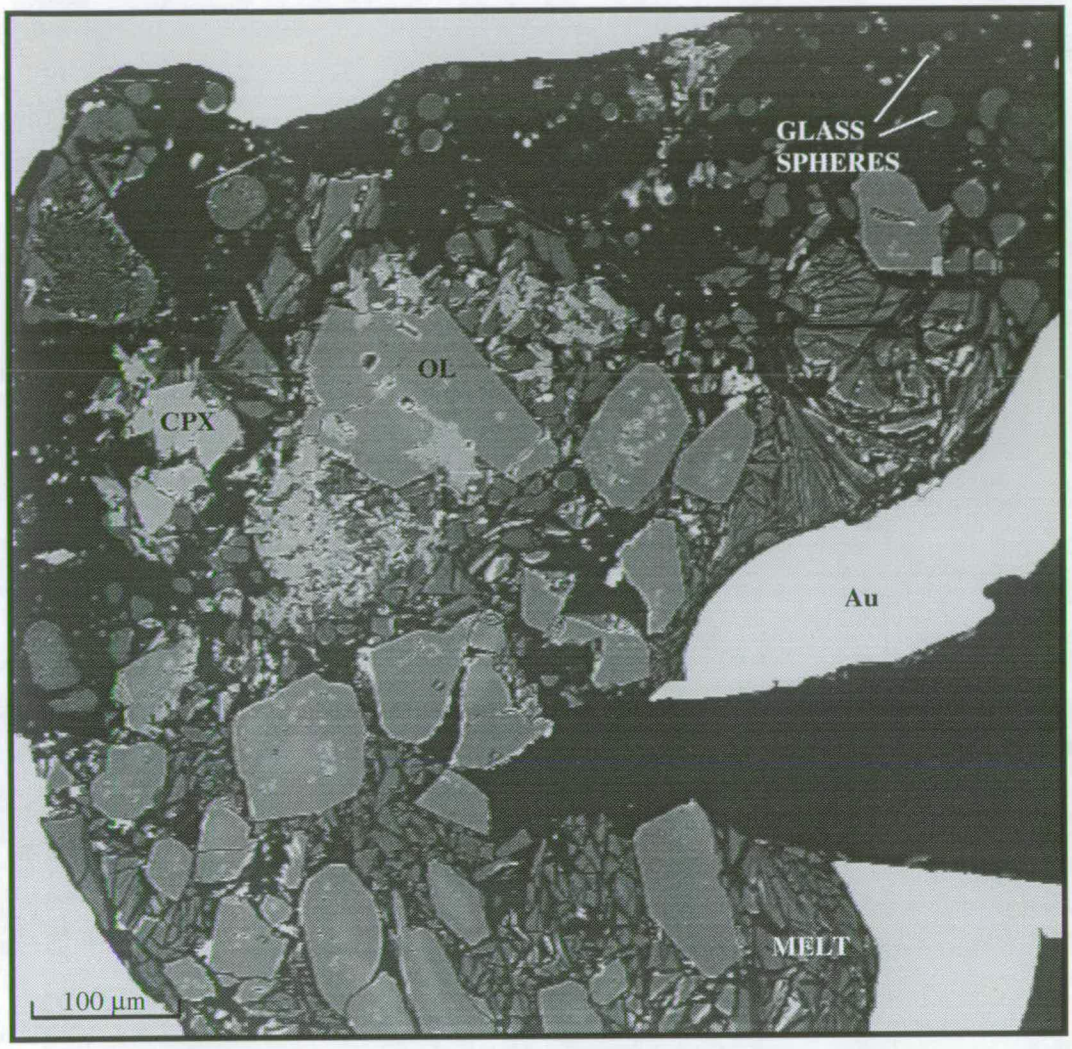

A back-scattered electron image of a polished section of ED327C3 showing melt, glass spheres, large crystals of olivine and smaller crystals of clinopyroxene embedded in epoxy resin.

Table 7.11: D (olivine/fluid) and error, calculated from compositions of an olivine crystal and a glass sphere from ED332C3.

ppm	*Olivine (anhydrous)*	*Glass sphere*	*D (olivine/fluid)*	*ERRORS (%)*				
				1	*2*	*4*	*6*	*Total*
Na	98	15461	0.050	28.5	0	60.4	32.2	74
Al	226	115300	0.015	3	0	88.8	32.2	95
K	43	12897	0.026	29.4	0	87	32.2	97
Ca	4043	15875	2.0	0.32	6.9	0.32	32.2	33
Ti	348	5331	0.51	38.4	0	65.5	32.2	82
Cr	285	187	12	96.5	0	47	32.2	112
Mn	1342	613	17	70.5	0	12	32.2	78
Ni	1472	102	113	111.5	0	157.9	32.2	196
Rb	0.83	3325	0.0020	0.25	6.9	2.71	32.2	33
Sr	0.014	114	0.0010	0.62	6.9	25	32.2	41
Y	0.18	4	0.34	1.94	6.9	5.83	32.2	33
Zr	0.13	21	0.048	1.77	6.9	12.3	32.2	35
Nb	0.026	50	0.0041	1.44	6.9	20	32.2	39
Ba	0.0024	79	0.00023	1.12	6.9	100	32.2	105
La	0.0016	50	0.00026	1.06	6.9	100	32.2	105
Ce	0.0019	9	0.0017	2.55	6.9	100	32.2	105
Pr	0.0015	2	0.0075	5.69	6.9	100	32.2	105
Nd	0	15	nd					
Sm	0	2	nd					
Eu	0.010	9	0.0088	2.75	6.9	50	32.2	60
Gd	0.0085	1	0.060	9.76	6.9	100	32.2	106
Tb	0.013	1	0.085	5.61	6.9	35.4	32.2	49
Dy	0.018	2	0.090	9.49	6.9	70.7	32.2	79
Ho	0.090	2	0.42	4.88	6.9	13.7	32.2	36
Er	0.085	1	0.56	8.98	6.9	30.2	32.2	46
Tm	0.15		nd					
Yb	0.23	1	3.0	14.7	6.9	19.2	32.2	41
Lu	0.54	1	4.3	6.87	6.9	6.62	32.2	34
Hf	0.049	11	0.034	8.67	6.9	70.7	32.2	78
Ta	0.014	3	0.039	8.8	6.9	40.8	32.2	53

The errors are derived from:
1 - The analysis of the glass sphere, *2* - Estimation of the SiO_2 content of the glass sphere (note that this is not relevant for those elements analysed by elctron probe), *4* - The analysis of olivine *6*- Error in the estimate of the amount of solute in the fluid. See Section 7.4.3.

Table 7.12: D (olivine/melt) and error, calculated from compositions of an olivine crystal and average melt from ED332C3.

ppm	*Olivine (anhydrous)*	*Melt*	*D (olivine/melt)*	*ERRORS (%)*			
				4	*3*	*5*	*Total*
Na	98	11711	0.011	60	16	20	66
Al	226	109520	0.0028	89	0.9	20	91
K	43	5969	0.010	87	21	20	92
Ca	4043	60950	0.088	0	1.6	20	20
Ti	348	8351	0.056	66	2.8	20	69
Cr	285	203	1.87	47	70	20	87
Mn	1342	1001	1.79	12	21	20	32
Ni	1471	112	17	158	113	20	195
Rb	0.83	425	0.0026	3	1.4	20	20
Sr	0.014	295	0.000065	25	1.7	20	32
Y	0.18	85	0.0028	6	6.7	20	22
Zr	0.13	220	0.00078	12	3.5	20	24
Nb	0.026	119	0.00029	20	2.4	20	28
Ba	0.0024	208	0.000015	100	0.8	20	102
La	0.0016	697	0.0000031	100	7.6	20	102
Ce	0.0019	135	0.000019	100	6.8	20	102
Pr	0.0015	24	0.000082	100	6.0	20	102
Nd	0	301	0		8.7	20	22
Sm	0	33	0		5.8	20	21
Eu	0.010	98	0.00014	50	6.3	20	54
Gd	0.0085	22	0.00052	100	6.3	20	102
Tb	0.013	23	0.00077	35	7.8	20	41
Dy	0.018	23	0.0010	71	10	20	74
Ho	0.090	42	0.0029	14	7.3	20	25
Er	0.085	21	0.0055	30	11	20	38
Tm	0.15	17	0.011		5.7	20	21
Yb	0.23	19	0.016	19	4.9	20	28
Lu	0.54	25	0.029	7	10	20	23
Hf	0.049	128	0.00052	71	2.4	20	74
Ta	0.014	23	0.00081	41	49	20	67

The errors are derived from:
4 - Analysis of olivine, *3* - Averaging the melt composition, *5* - Error in the estimate of water content of melt. See Section 7.4.3.

7.4.3 Errors

There is an inherent error associated with the choice of a glass sphere composition representative of the fluid at equilibrium. It was argued (Section 7.3) that the glass sphere most representative of the fluid is one which is the least melt like in composition. However, it is conceivable that even the least melt-like glass sphere may contain a certain amount of melt component. Fortunately, the unintentional incorporation of some melt component into the analysis will not have a large effect on the *relative* partition coefficients, although it will result in an overestimate of the trace element contents of the fluid (and hence an overestimate of D (fluid/melt)) and a slight underestimate of the difference between D (fluid/melt) for individual trace elements (see Fig. 7.8). It is not possible to quantify this error.

For each element, the error on the value of the partition coefficient has been calculated by propagating the individual errors described below (see Appendix C for details of the formulae used for error propagation). Results are given in Tables 7.9, 7.11, and 7.12.

1. The analysis of the glass spheres. Instrument errors range from very small (e.g. 0.04% for Na, 0.4% for B) to relatively large (e.g. 24.3% for Pb). Errors are prohibitively large for some minor elements analysed using the electron probe (e.g. 134% for Cr, 2182% for Ni).
2. Estimation of the SiO_2 content of the anhydrous glass sphere composition, used for conversion of ion counts to concentration. The value of this error is derived from the spread in composition of small glass spheres analysed by electron probe, and is equal to 5.3% for glass spheres from ED332C1 and 6.9% for glass spheres from ED332C3.
3. Standard deviation on the average melt composition. This is generally small, but is large for some elements (e.g. for melt from ED332C1 the error is 27.3% for Rb, 12.2% for Pb).
4. The analysis of olivine. The error is extremely high for some elements as a result of the low levels of these elements in olivine. Errors for the REE are particularly large (e.g. 100% for La, Ce, Pr, Gd). Levels of Nd and Sm are below the detection limits for the ion probe.
5. The amount of water dissolved in the melt. Experimental results suggest that the value is 25±5% i.e. a relative error of 20%.
6. The amount of solute dissolved in the fluid. Calculations (Section 7.4.1) give a value of 12.73±4.1 wt% i.e. a relative error of 32.2%.

7.4.4 Summary

The values of D (fluid/melt), D (olivine/fluid) and D (olivine/melt) and the errors associated with each calculation are given in Tables 7.9, 7.11 and 7.12, respectively. The main source of the error in the calculation of D (fluid/melt) arises from the uncertainty in the amount of solute in the fluid at equilibrium. As this will affect each element equally, the relative error between elements is considered to be smaller than that suggested by the final error. In contrast, the main source of error in the calculations of D (olivine/fluid) and D (olivine/melt) arises from the analysis of the olivine, and thus the large error bars may be real. An indication of the reliability of results can be gleaned from a comparison of these values of D (olivine/melt) with others taken from the literature (Fig. 7.19). Values of D (olivine/melt) from the present study are very similar to those measured by Kelemen *et al.* (1992) from ion probe analyses on experimental olivine/melt pairs. The disparity between these results and the data complied by McKenzie & O'Nions (1991) is possibly because McKenzie & O'Nions (*op. cit.*) took their data from studies performed under a variety of conditions and using less reliable analytical techniques (e.g. Hanson, 1980; Ulmer, 1989).

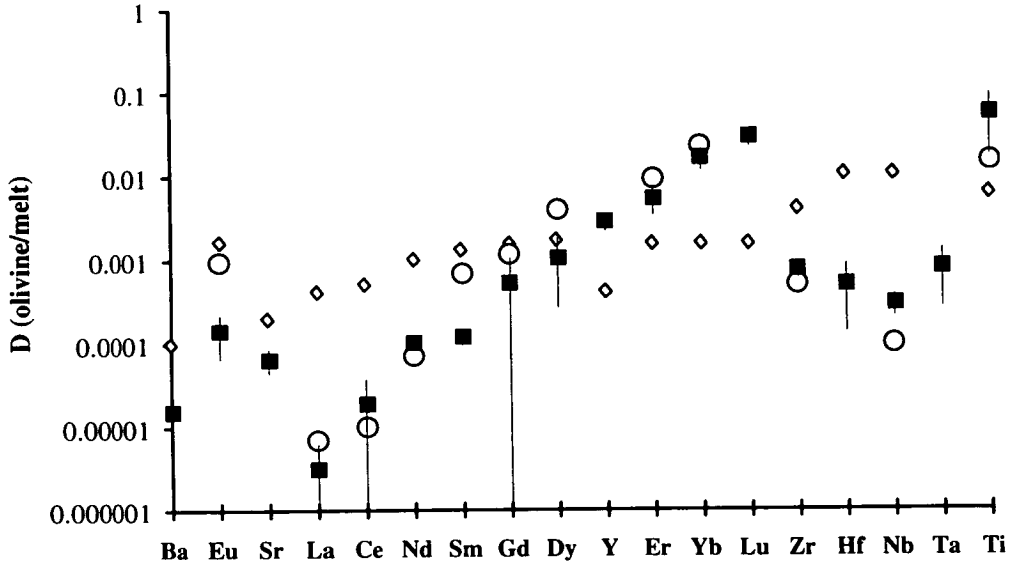

Figure 7.19: Comparison of D (olivine/melt) derived from the present study (filled squares and error bars), with values measured by Kelemen *et al.*, 1992 (open circles), and values compiled by McKenzie & O'Nions, 1991 (open diamonds).

7.5 IMPLICATIONS OF PARTITION COEFFICIENTS

Previous studies have shown that there is often a relationship between ionic radius, ionic charge and D (mineral/melt) (Philpotts, 1978; Colson *et al.*, 1988). This has been explained in terms of the energy needed to fit an element into the mineral lattice, which is dependent on the temperature and pressure of the system as well as the properties of the element (Colson *et al.*, 1988; Blundy & Wood, 1991; Beattie, 1994). Evaluation of these complex relationships would be invaluable as this could enable prediction of partition coefficients for additional elements. In Section 7.2.3 it was shown that the trace-element contents (normalised to bulk) of a glass sphere are correlated with ionic radius, with large ions and small ions more concentrated in the fluid. In this section the relationship between ionic radius, ionic charge and partition coefficient is investigated in more detail. D (olivine/fluid) and D (fluid/melt) are considered. Results are then compared with previous work.

7.5.1 Onuma diagrams

The relationships between ionic radius, ionic charge and partition coefficient can be illustrated on an Onuma diagram (Onuma *et al.*, 1968). This is a plot of the log of the partition coefficient against ionic radius. Previous studies have shown that ions of the same charge generally plot onto a parabolic curve with the maximum value of D (mineral/melt) corresponding to the optimum ionic radius for the mineralogical site occupied by ions of that charge. As the discrepancy increases between an element's ionic radius and the optimum ionic radius for a site, it requires more energy to force the element into the site and hence the D (mineral/melt) decreases. An Onuma diagram for garnet (Philpotts, 1978) illustrates the principal features (Fig. 7.20).

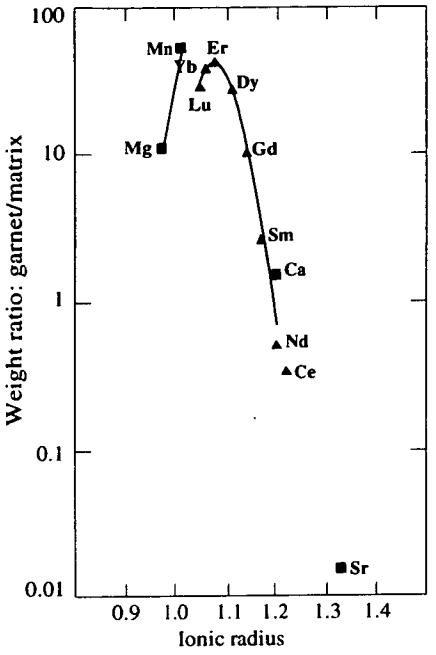

Figure 7.20: Onuma diagram for garnet.
From Philpotts (1978).

Ionic radii

For the purposes of the present study, the values of ionic radii compiled by Whittaker & Muntus (1970) are used (Table 7.13).

Table 7.13: Ionic radii

Element	*Charge*	*IR (Å)*	*Element*	*Charge*	*IR (Å)*	*Element*	*Charge*	*IR (Å)*
Li	+1	0.82	**Sr**	+2	1.21	**Dy**	+3	0.99
Be	+2	0.35	**Y**	+3	0.98	**Ho**	+3	0.98
B	+3	0.2	**Zr**	+4	0.80	**Er**	+3	0.97
Na	+1	1.10	**Nb**	+5	0.72	**Tm**	+3	0.96
Mg	+2	0.8	**Cs**	+1	1.78	**Yb**	+3	0.95
Al	+3	0.61	**Ba**	+2	1.44	**Lu**	+3	0.94
Si	+4	0.48	**La**	+3	1.13	**Hf**	+4	0.79
K	+1	1.46	**Ce**	+3	1.09	**Ta**	+5	0.72
Ca	+2	1.08	**Pr**	+3	1.08	**Pb**	+2	1.26
Ti	+4	0.69	**Nd**	+3	1.06	**Pb**	+4	0.86
Cr	+3	0.81	**Sm**	+3	1.04	**Th**	+4	1.08
Mn	+2	0.75	**Eu**	+2	1.25	**U**	+4	1.08
Fe	+2	0.69	**Eu**	+3	1.03	**U**	+6	0.81
Ni	+2	0.77	**Gd**	+3	1.02			
Rb	+1	1.57	**Tb**	+3	1.00			

From Whittaker & Muntus (1970). All ionic radii (IR) relate to ions in six-fold coordination except for B^{3+}(IV), U^{4+}(VIII). Mn^{2+}, Fe^{2+} and Cr^{3+} are low-spin.

These are not dissimilar to estimates by other workers (e.g. Weast, 1975, Shannon, 1976). Ionic radius is correlated negatively with oxidation state and correlated

positively with coordination number (Shannon, 1976). It is thus important to predict the oxidation state and coordination number of each ion. Table 7.13 gives the expected oxidation states of all ions under the conditions of the experiments in the present study (see Chapter 4 for details of oxygen fugacity). There is some doubt regarding the oxidation states of Eu, Pb and U. Two options are considered for these elements. Coordination number is less easy to predict: in the absence of any other constraints I have opted to choose the ionic radii relating to six-fold coordination where possible (Table 7.13).

D (olivine/fluid)

The logs of the partition coefficients between olivine and fluid are plotted versus ionic radius in Figure 7.21. Major-element partition coefficients, calculated from the average compositions of olivine and small glass spheres analysed by electron probe, are included. The largest value of D (olivine/fluid) is exhibited by Mg (Fig. 7.22). Other major elements (Fe, Mn, Si, Cr, Ni) also possess relatively high values of D (olivine/fluid), although the errors associated with measurement of Cr and Ni are extremely high. There is a strong correlation between D (olivine/fluid) and ionic radius, particularly for the ions with +2, +3, and +4 charges.

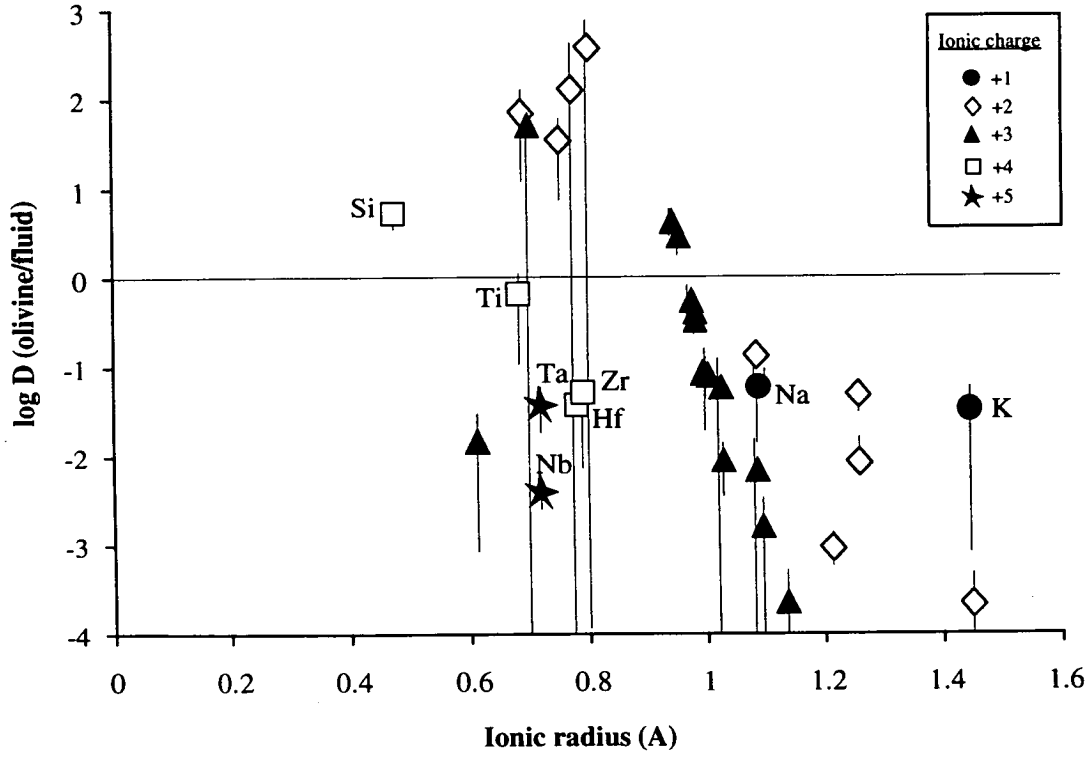

Figure 7.21: Onuma diagram for D (olivine/fluid). Ions with +1, +4, and +5 charges are annotated. Ions with +2 and +3 charges are shown in detail in Figure 7.22.

Figure 7.22 shows that the trivalent ions fall on a fairly well-defined parabola, with a maximum at about 0.8 Å. The remarkably well-defined correlation between D (olivine/fluid) and ionic radius, allows an accurate estimate of the values of D (olivine/fluid) for additional elements. For example, Nd and Sm, which are both present in olivine at levels below detection, are inferred to possess values of D (olivine/fluid) of approximately 0.016 and 0.045, respectively. The ionic radius of Th^{4+} is 1.08 (Table 7.13). Extrapolation of the trend for the +4 ions to this ionic radius suggests that the partition coefficient for Th lies between 0.001 and 0.0001 i.e. Th partitions strongly into the fluid relative to olivine.

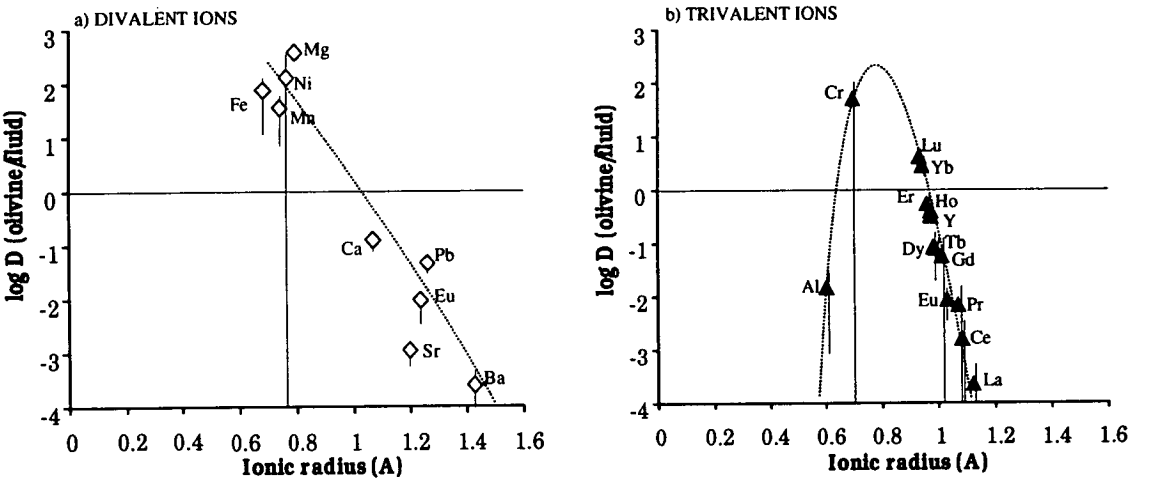

Figure 7.22: Detail of Onuma diagram for D (olivine/fluid). a) divalent ions, b) trivalent ions

D (fluid/melt)

The Onuma diagram (Fig. 7.23) illustrates the complex relationship between ionic charge, ionic radius and D (fluid/melt). Clearer correlations are displayed by ions of similar charge (Fig. 7.24). For the monovalent ions, D (fluid/melt) increases steadily with ionic radius. However, ions of higher charge do not display this trend: divalent ions possess fairly constant D (fluid/melt), perhaps lying on a broad inverted parabola. D (fluid/melt) for the trivalent ions exhibits a roughly negative correlation with ionic radius, with the REE and Y possessing extremely low values, and Cr, Al, and B possessing higher values. There is a similar negative correlation among the 4+ ions.

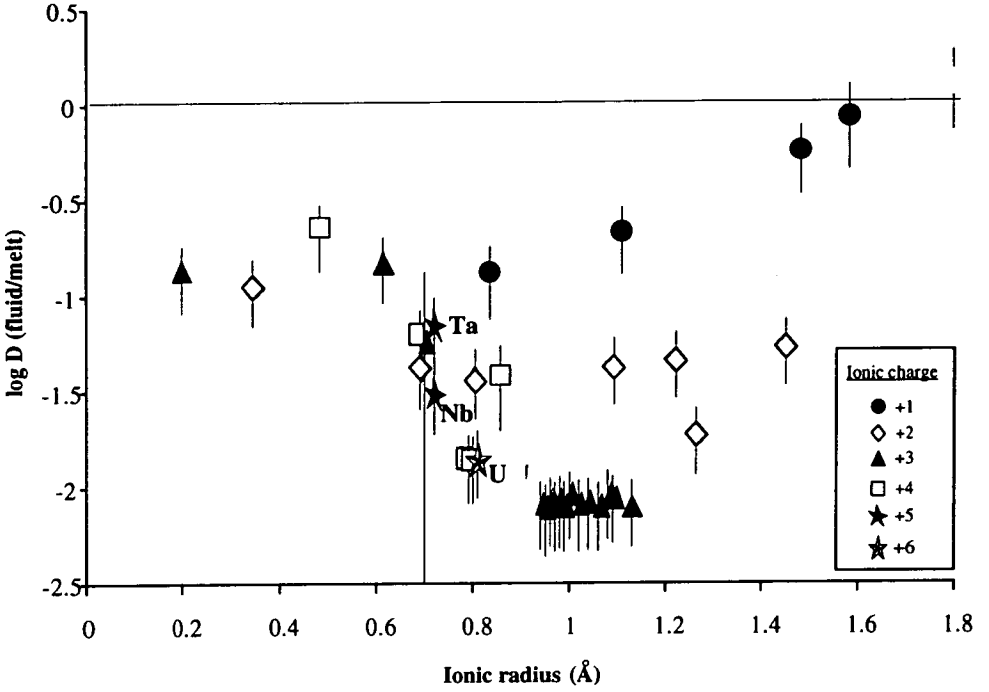

Figure 7.23: Onuma diagram for D (fluid/melt). Ions with +5 and +6 charges are annotated. Ions with +1, +2, +3, and +4 charges are shown in detail in Figure 7.24.

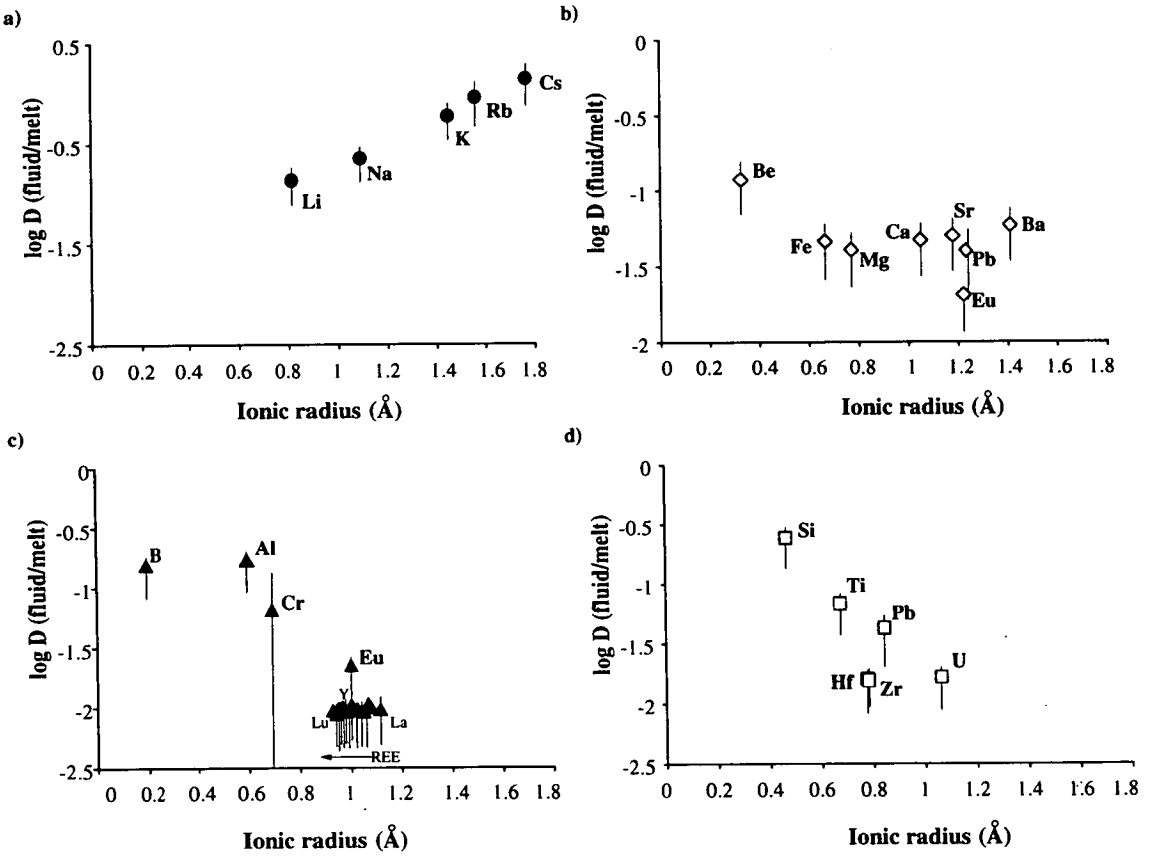

Figure 7.24: Detail of Onuma diagram for D (fluid/melt). a) +1 ions, b) +2 ions, c) +3 ions, d) +4 ions.

Eu does not fall onto the trend for either divalent or trivalent ions: its measured partition coefficient lies below the expected value for the divalent ion, and above the expected value for the trivalent ion. This intermediate partition coefficient can be explained if Eu is present in two valence states. Results of a calculation using the measured D (olivine/fluid) of Eu, and the predicted values for Eu^{2+} and Eu^{3+}, suggests that there is 49% Eu^{2+} and 51% Eu^{3+} in the run product from which the partition coefficients were measured. It is not, unfortunately, a simple matter to use the inferred ratio of $Eu^{3+}$to Eu^{2+} to calculate the oxygen fugacity of a system, as this ratio is dependent on many factors including temperature and melt composition as well as fO_2 (Möller & Muecke, 1984). A rough calculation based on experimental results concerning the valence of Eu in melts in equilibrium with plagioclase at ~1200°C and 1 atm pressure (Drake, 1975) suggests that the fO_2 in ED332C3 was $\sim 10^{-9}$. Although it is acknowledged that there will be a large uncertainty due to the pressure discrepancy (ED348C3 was performed at 1.85 GPa) this oxygen fugacity translates to just above the NNO curve at 2.0 GPa. The extremely large uncertainties surrounding the calculation of this oxygen fugacity, however, render the result fairly meaningless. D (olivine/fluid) for Pb is slightly lower than the expected value for the divalent ion and slightly higher than the expected value for the 4+ ion, suggesting that Pb is present as both Pb^{2+} and Pb^{4+}. No trend is obvious from the 5+ ions, as these include only two examples (Nb and Ta). U may be present as U^{4+} or U^{6+} (both options are illustrated). The consistent trends for each valence allow determination of unmeasured partition coefficients, although extrapolation to values much removed from the existing data should be treated with caution. This method suggests that Th (which has a charge of +4 and an ionic radius of 1.08 Å) has a D (fluid/melt) of approximately 0.006.

7.5.2 Comparison with previous studies

There have been few explicit measurements (e.g. Cullers *et al.*, 1973) of partition coefficients between fluid and coexisting melt. Rather, experimental studies have focused on measurement of partition coefficients between fluid and residual minerals (e.g. Cullers *et al.*, 1973, Mysen, 1979, Brenan & Watson, 1991) or of mobility of elements in a fluid phase released from hydrous minerals (Tatsumi *et al.*, 1986). See Chapter 3 for a summary of the results of these studies. A possible deduction from these limited data is that the partitioning of an element into a fluid is governed by its ionic radius, with large ions partitioning preferentially into the fluid phase. Several

authors (e.g. Hawkesworth *et al.*, 1993a; Stolper & Newman, 1994) have used this assumption to infer partition coefficients for unmeasured elements.

The present study has shown that the relationship between partition coefficient and ionic radius is much more complicated than that suggested previously. This is probably a consequence of the determination of data from a more extensive range of trace elements, as the positive correlation between D (olivine/fluid) and ionic radius inferred by Brenan & Watson (1991), using data from Cs, Ba, Sr, Na, Ce, Gd, Yb, is also apparent in the present study (Fig. 7.25). The slope on the trend inferred from the present study, however, is steeper and the absolute values of D (olivine/fluid) are lower than those measured by Brenan & Watson (*op. cit.*).

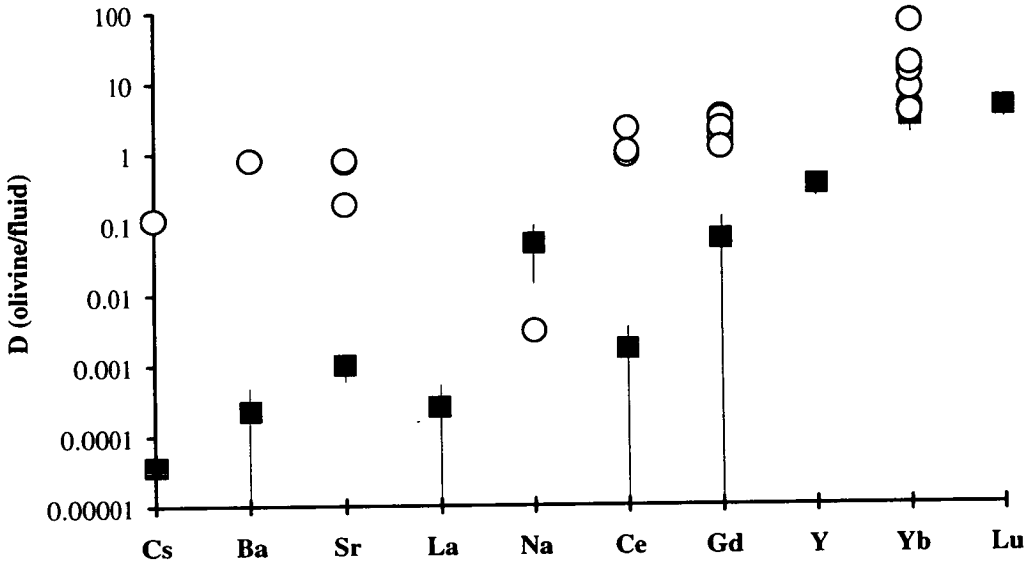

Figure 7.25: Comparison of D (olivine/fluid) derived from the present study (filled squares and error bars) and from Brenan & Watson, 1991 (open circles). Elements are plotted in order of decreasing ionic radius.

There are few data regarding elements with small, highly charged ions (e.g. Zr, Ta, Nb, Ti, Be, B). Tatsumi *et al.* (1986) claimed that Nb is highly immobile in a fluid phase. However, results from the present study support the conclusions of solubility studies (e.g. Ayers & Watson, 1991) which suggest that HFSE (e.g. Zr, Ta, Nb, Ti) are more soluble than REE in hydrous fluids. Tatsumi & Isoyama (1988) measured the mobility of Be in fluid released from serpentine, and concluded that it was more mobile than Ti, but less mobile than Yb or Sr. Results from this study, however, suggest that Be is substantially more mobile in the fluid than Yb, and slightly more mobile than Sr. B is also inferred to be mobile in a fluid phase, with values of

D (fluid/melt) for B greater than those for REE, HFSE, Be, Sr, Ba. This is consistent with data from fluid at low pressure (Fig. 7.26).

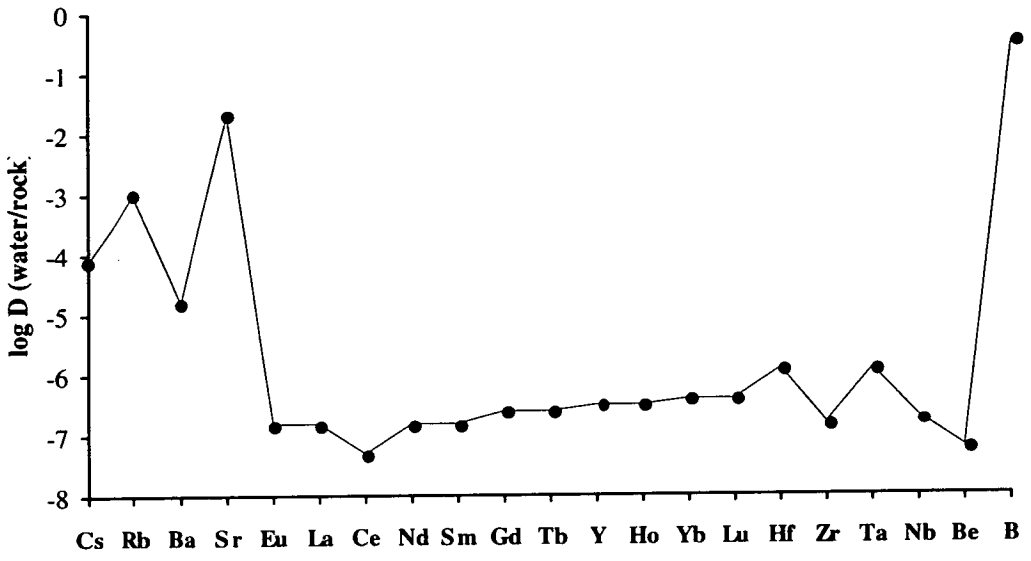

Figure 7.26: Partition coefficients between meteoric water and the upper crust (from Taylor & McLennan, 1985). Plotted in order of decreasing ionic radius.

7.5.3 Summary

This study has shown that there is a complex relationship between ionic charge, ionic radius and the partition coefficient between fluid and melt (or fluid and olivine). For studies of D (mineral/melt) such trends are often interpreted in terms of the size and valence of mineralogical sites. Using this approach, the values of D (olivine/melt) derived from the present study imply that there is a trivalent site in olivine which accommodates ions of radius approximately 0.8 Å, and a divalent site with a similar radius. Thus the partition coefficients between olivine and fluid are governed by the crystal structure of olivine. The sites in a fluid and a melt are less easy to conceive. Singly-charged ions exhibit a clear positive correlation between D (fluid/melt) and ionic radius, and in general they partition more favourably than multiply charged ions into the fluid phase. Thus it is inferred that there is a large singly-charged "site" in the fluid phase. There also appears to be a small, multiply-charged "site" in the fluid phase, which could account for the high values of D (fluid/melt) exhibited by Si, Be, B, Al, Nb, Ta etc. There appears to be no "site" which can accommodate significant REE in the fluid phase.

7.6 CONCLUSIONS

1. In many of the water-saturated experiments performed in this study, separate melt and hydrous fluid have coexisted at equilibrium. The melt phase quenches to a glass, which is often ropy in appearance; the fluid phase quenches to form glass spheres ranging in diameter from approximately 5 μm to 100 μm. No other fluid quench material has been detected.
2. The small glass spheres (< 15 μm) are rich in silica and alumina, and relatively rich in Cs, Rb, and B; whereas the larger glass spheres are closer in composition to the melt. The variation in composition across the large glass spheres, coupled with their texture, suggests that they are composed of two phases with compositions similar to the melt and to a small glass sphere. This observation is supported by mass-balance calculations. It is concluded that the cores of large glass spheres are composed of melt, which has acted as a nucleation site for the overgrowth of fluid quench. The small glass spheres are assumed to be free of a melt core and are taken to be representative of the fluid composition at equilibrium. It is acknowledged that this is an oversimplification as there is some evidence for exchange of elements (particularly the alkalis) between the melt and the fluid quench.
3. The amount of water in the melt at equilibrium, inferred from the results of liquidus experiments with varying initial water contents, is 25±5 wt%. This value has been used in conjunction with mass-balance results to calculate that there is 12.7±4.1 wt% solute in the fluid at equilibrium. These results are consistent with estimates derived from previous experimental studies.
4. Combining the calculated water contents with the trace-element contents of the average melt and of a small glass sphere, the partition coefficients between fluid and melt have been determined. For the elements measured, only Cs has a partition coefficient greater than 1. There is a rough correlation between partition coefficients and ionic radius, with large ions (e.g. Cs, Rb) and small ions (e.g. B, Be, Si, Nb) partitioning more readily than intermediate ions (e.g. REE, Y) into the fluid. Clearer correlations with ionic radius are exhibited by ions of equal charge. Results from individual experiments are extremely consistent. For the purposes of modelling (Chapter 8), the partition coefficients calculated from ED332C1 will be used, as this experiment was doped with the greatest number of trace elements.

5. Large olivine crystals were grown in two experiments. An analysis of olivine has been combined with an analysis of a small glass sphere to calculate partition coefficients between olivine and fluid. The relationships between D (olivine/fluid) and ionic radius exhibited by the divalent and the trivalent ions are very marked and can be explained in terms of the lattice sites of olivine.
6. The satisfactory agreement between the results of the present study and of previous studies provides further justification for the technique employed.

CHAPTER 8

MODELS OF MELT PRODUCTION IN SUBDUCTION ZONES

CHAPTER 8: MODELS OF MELT PRODUCTION IN SUBDUCTION ZONES

8.1 INTRODUCTION

Many previous studies of the geochemistry of IAV (see Chapter 2) have indicated that there are at least two sources involved in the genesis of magmas in subduction zones. That one of these sources lies in the subducting slab is implied unequivocally by the isotopic composition of the volcanics. It is now fairly well established that melting takes place in the mantle wedge, triggered by influx of fluid derived from the subducting slab. However, there is still much disagreement concerning the exact processes involved in melt generation. In particular, it is not clear by what process the slab component is transferred to the mantle wedge or to what extent melting takes place in the mantle wedge. There are also uncertainties surrounding the compositions of the mantle wedge and of the slab at depth. Many models for the generation of melt in subduction zones have been proposed to account for the characteristic geochemical signatures seen in the erupted products (see Chapter 2).

After making a few assumptions and simplifications it is possible to test a proposed model by comparing the composition of the melt predicted by the model with the compositions of actual melts (or their volcanic equivalents) produced. Given the composition and mineralogy of the source, and the partition coefficients between the melt and the residual phases, estimates of the trace-element contents of melts can be made by applying simple melting equations. The two end-member melting processes are:

- Batch melting, in which the partial melt continuously reacts with the matrix until the moment of segregation, and the bulk composition of the system remains constant.
- Fractional melting, in which the partial melt is continuously removed from the system as it is formed, and the bulk composition of the system is continuously changing.

The exact melting process in operation is not known, partly as there is considerably uncertainty surrounding the ability of a melt to separate from its matrix. I have chosen to model the batch melting process. However, results using fractional

melting models are very similar, especially for highly incompatible elements such as the ones considered here. The modal batch melting equation (Shaw, 1970) is given by:

$$\frac{C_L}{C_0} = \frac{1}{X + (1-X)\bar{D}} \qquad (8.1)$$

where C_0 is the original mantle composition and C_L is the melt composition; X is the proportion of melt generated. $\bar{D}$ is the bulk partition coefficient between the melt and the **residual** mantle phases. However, as the degree of melting is increased, the aluminous phases and clinopyroxene become less abundant in the residue, and the bulk partition coefficients will consequently change. This effect is accounted for by using the non-modal batch melting equation:

$$\frac{C_L}{C_0} = \frac{1}{\bar{D} + X + \bar{P}X} \qquad (8.2)$$

$\bar{P}$ is effectively a bulk partition coefficient weighted towards the minerals entering the melt. It can be calculated from the proportions and partition coefficients of minerals in the source, assuming that clinopyroxene and the aluminous phases disappear at a certain melt fraction, X_1. The following algorithms are used:

$$\bar{P} = \sum_{n=1}^{N} P_n D_n \qquad (8.3)$$

$$p_n = F_n^0 / X_1, \quad n \geq 3 \qquad (8.4)$$

$$p_n = \left(1 - \sum_{m=1}^{N} p_m\right) F_n^0 \Big/ \left(F_1^0 + F_2^0\right), \quad n < 3 \qquad (8.5)$$

where F_n^0 are the proportions by weight of the N minerals initially present, each with a partition coefficient D_n, with n=1 being olivine and n=2 being orthopyroxene. p_n are the proportions of minerals entering the melt. A value of 0.3 was assumed for X_1 (McKenzie & O'Nions, 1991).

For assumed mantle mineralogies of amphibole peridotite and garnet peridotite, there is some difference between the melts calculated by non-modal and modal batch

melting equations. For these mantle mineralogies, melts calculated from the non-modal melting equation will be presented, as it is considered that this equation most closely represents the true scenario, with the residual mineralogy becoming more olivine and orthopyroxene rich with increasing amounts of melting. For an assumed mantle mineralogy of spinel peridotite, the compositions of melts calculated using the non-modal and modal batch melting equations are very similar (Figure 8.5). For this mantle mineralogy, results using modal melting equations will be presented. This is because for some trace elements (B, Be, Li) partition coefficients for individual minerals, which are required in the non-modal melting equation, are not known, whereas the bulk partition coefficients for these elements have been estimated, and consequently the modal melting equation is easiest to implement.

Devolatilization of metamorphic rocks can be modelled in an analogous manner to melting: there are two end-member processes - batch devolatilization and fractional devolatilization (Valley, 1986). In general, the release of fluids from a system is thought to take place more easily than the release of melts, and therefore it is considered appropriate to model dehydration of the slab as fractional devolatilization. The trace-element composition of a fluid released from the slab can be determined by the following equation:

$$\frac{C_f}{C_0} = \frac{1}{\bar{D}_f}(1-X)^{\left(1/\bar{D}_f - 1\right)} \qquad (8.6)$$

where C_f and C_0 are the concentration of an element in the fluid and the rock respectively, $\bar{D}_f$ is the bulk partition coefficient between the rock and the fluid, and X is the fraction of fluid removed from the system.

Although I will investigate the effects of changing the value of X, it is not possible to make an accurate estimate for this, and thus in the majority of cases I will assume the limiting case where X approaches zero, and the composition of the fluid is given by:

$$C_f = \frac{C_0}{D_f} \qquad (8.7)$$

Thus, it is possible to predict the trace-element compositions of mantle- and slab-derived melts and fluids. It is also possible to predict the trace-element compositions of melts produced by more complicated models, e.g. melting of more than one

source, or melting of a mantle wedge that has already been metasomatised by a slab-derived fluid. However, the success of such modelling depends on the accurate selection of input parameters (e.g. compositions, mineralogies and partition coefficients). The selection of appropriate partition coefficients is extremely important in these modelling calculations, and it has been a lack of such data that has provided the main obstacles to previous workers. In particular, prior to this project there were very few data concerning the partitioning of trace elements between fluid and coexisting phases at high pressure (Chapter 3).

Two of the aims of this project were to measure partition coefficients between 1) partial melts of hydrous peridotite and coexisting phases, and 2) hydrous fluid and coexisting phases. Unfortunately, due to experimental problems (Chapter 6) it was not possible to achieve the former aim. However, partition coefficients between fluid and basaltic melt, and fluid and olivine have been measured (Chapter 7). In this chapter, values of D (fluid/melt) and D (olivine/fluid) are combined with published values of D (mineral/melt) to derive D (fluid/mineral), and from this, the partition coefficients of trace elements between hydrous fluid and the slab are estimated (Section 8.3.2). In addition, published values of D (mineral/melt) are used to estimate the partitioning of trace elements between mantle-derived melts and residual mantle mineralogy. With this information, various models of melt production in subduction zones will be tested.

Before testing the more complicated models, the trace-element compositions of melts produced from unmetasomatised hydrous mantle will be calculated. Subsequently, four models of melt production in subduction zones will be investigated. The models are labelled depending on the incorporation of either slab-derived fluid (SF), slab-derived melt (SM) or mantle-derived fluid (MF) to the mantle wedge (and the mantle-derived melt (MM)). The four models are summarised as follows:

MF/MM Melt of a mantle that has been metasomatised by mantle-derived fluid

SM/MM Mixture of slab-derived and mantle-derived melts

SF1/MM Melt of a mantle that has been metasomatised by slab-derived fluid

SF2/MM Melt of a mantle that has been metasomatised by slab-derived fluid after the slab has lost a substantial proportion of its mobile-element budget.

Three of these models involve metasomatism of the source region by fluids. Although this may be a complex process involving many stages of hydration and subsequent dehydration (e.g. Davies & Bickle, 1991), in this chapter metasomatism is envisaged as simple mixing between the mantle and small amounts of fluid.

The composition of melts predicted by these models will be compared to a range of compositions of IAV, which have been taken from the literature, and were chosen primarily because the analyses encompassed a wide range of trace elements. I have attempted to select a set of compositions which reflect the variety of basalts erupted in the volcanic fronts of several arcs (Table 8.1, see also Section 2.2.2).

Results of the modelling will be presented in tabular form and as spidergrams ratioed to MORB (MORB composition of Hofmann, 1989). There are many ways of ordering the elements on the abscissa (Wilson, 1989). I have chosen to follow the method of Pearce (1983) in which elements are split into mobile and immobile groups depending on the ratio of their ionic radius to charge (i.e. their ionic potential). Elements which possess high and low values of ionic potential are termed mobile whereas those elements with intermediate ionic potential are immobile. Mobile elements are plotted on the left-hand side of the diagram in order of increasing compatibility in garnet lherzolite. Immobile elements are plotted on the right-hand side in order of decreasing compatibility. The reasons for this choice of plotting order were given in Section 2.2.2. For reasons of clarity I have not shown all elements for which there are data. Figure 8.1 summarises the logic behind the plotting order, and displays the IAV compositions used in this study.

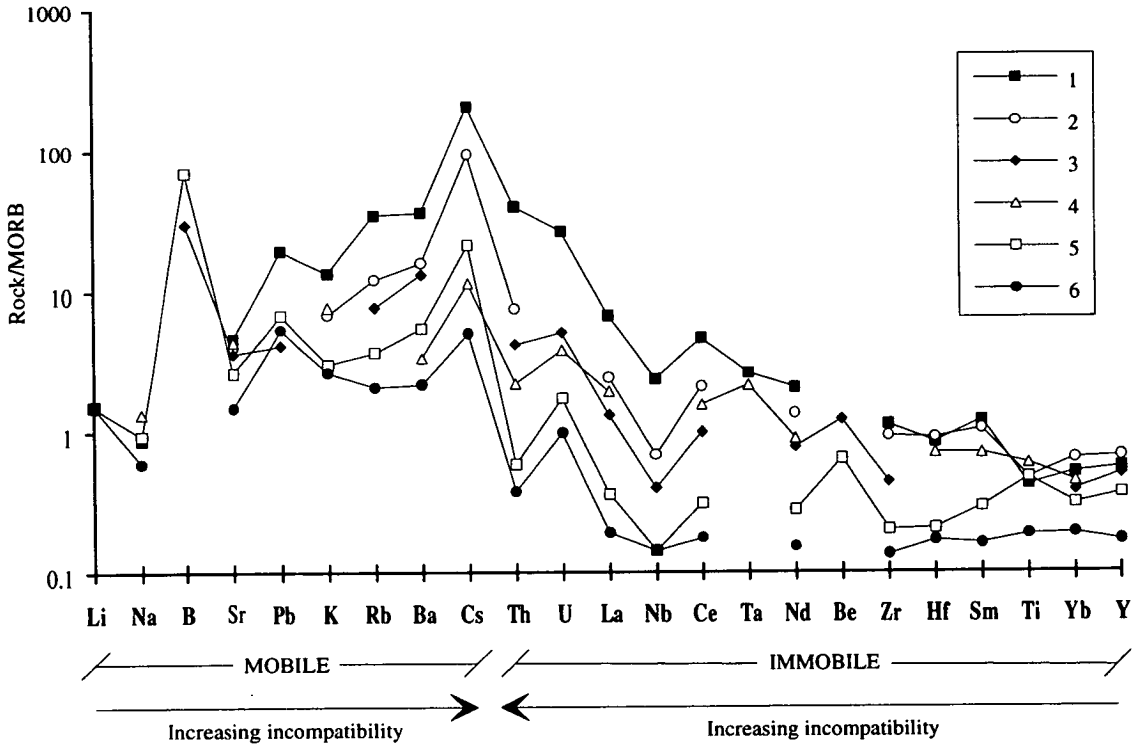

Figure 8.1: Typical IAV compositions used for comparison purposes. See caption to Table 8.1 for key to data sources.

Table 8.1: Typical IAV compositions used for comparison purposes.

values in ppm	*1*	*2*	*3*	*4*	*5*	*6*	*7*
Be	-	-	-	-	0.29	-	0.64
B	-	-	-	-	35	-	5.5
Na	17139	-	-	26561	18400	11723	22258
K	11866	6010	-	6804	2655	2323	3402
Ti	4076	-	-	5754	4555	1798	8571
Rb	44	15.3	9.7	-	4.6	2.6	6.2
Sr	518	451	407	497	297	167	213
Y	20	24	18	-	13	6	30
Zr	117	97	46	-	21	14	98
Nb	8.3	2.4	1.4	-	<1	<1	4
Cs	2.9	1.32	-	0.16	0.3	0.07	0.16
Ba	503	220	183	46	75	30	55
La	26	9.44	5.1	7.49	1.4	0.74	5.3
Ce	55	25	11.9	18.6	3.7	2.1	15
Pr	5.5	-	-	-	0.55	0.31	2.3
Nd	23	15	8.7	10	3.1	1.7	12
Sm	4.5	3.91	-	2.66	1.1	0.6	3.8
Eu	1.1	1.3	-	0.85	0.5	0.26	1.4
Gd	2.8	-	-	-	1.5	0.86	4.6
Tb	0.58	0.68	-	0.51	0.28	0.16	0.81
Dy	4.5	-	-	-	1.8	1	5.3
Ho	0.68	-	-	-	0.42	0.24	1.2
Er	1.9	-	-	-	1.3	0.73	3.6
Yb	2	2.52	1.5	1.74	1.2	0.74	3.5
Lu	-	0.4	-	0.257	-	-	-
Hf	2.5	2.7	-	2.11	0.61	0.5	2.4
Ta	0.5	-	-	0.41	-	-	-
Pb	9.5	-	2	-	3.3	2.6	2.5
Th	7.5	1.4	0.78	0.41	0.11	0.07	0.59
U	1.9	-	0.36	0.27	0.12	0.07	0.27

Key: ***1*** - Basalt from Stromboli, Aeolian Arc (Francalanci et al., 1994); ***2*** - Basalt from Southern Volcanic Zone, Andes (Hickey et al., 1986); ***3*** - Average arc basalt (Hawkesworth et al., 1991); ***4*** - Basalt from Aleutians (Yogodzinski et al., 1994); ***5, 6*** - Basalts from the front of the New Britain Arc, Papua New Guinea (Woodhead & Johnson, 1993; B and Be data from Morris et al., 1990). ***7*** - Volcanics from New Britain Arc lying 415-540 km above the WBZ from Woodhead & Johnson (1993) and Morris et al. (1990). This composition is not typical and will not be used for general comparison purposes. However, it will be investigated further in Section 8.7. Not shown: Li values for IAV (~6.5 ppm) from Ryan & Langmuir (1988).

It is acknowledged that the true scenario is likely to be very much more complicated than is modelled in this chapter. For example, it is assumed here that the mantle melts at one point, although in reality the mantle may melt over a large depth range. In addition, it is assumed that the melt source within the mantle wedge is homogeneous, which is unlikely given the complexity of a subduction zone. However, it is considered that more complicated models than are presented here are not warranted by the limited data.
Finally, it is noted that any comprehensive model of melt production in subduction zones must reproduce the major-element as well as trace-element compositions of melts. This will not be attempted here, due to lack of experimental data, but it remains an important task for the future.

8.2 THE CHOICE OF INPUT VALUES

The input into these models consists of the compositions of the slab and the mantle as well as the partition coefficients between melts, fluids and residual minerals in the slab and the mantle. This project has provided partition coefficients between fluid and melt, and some values for partition coefficients between olivine and melt. The natural compositions and the remaining partition coefficients are taken from the literature.

8.2.1 Slab composition

The composition of fluid released from the slab will be calculated using partition coefficients between hydrous fluid and an estimated slab mineralogy, and assuming a homogeneous trace-element composition of the slab.
For comparative simplicity I will restrict this discussion to the subduction of oceanic crust, which although less complex than continental crust is nevertheless highly variable. Typical oceanic crust consists of serpentinised ultramafic rocks, altered basalts and gabbros, fresh MORB, and oceanic sediments. In addition to this there are occasional seamounts and hot-spot related rocks. Dehydration of the slab is thought to play an important role in the generation of melts in subduction zones. Although there may be some fluid derived from the ultramafic part of the slab, it

would be virtually impossible to distinguish between the role of these slab ultramafics and the overlying mantle. Therefore, for the purposes of modelling, I will assume that the slab from which fluid is derived is composed solely of altered MORB and oceanic sediments.

Alteration of MORB is a complex process and can take a variety of forms. General chemical changes include the uptake of alkalis, sometimes accompanied by losses in Ca, Na, Fe, Mg (Alt *et al.*, 1992). Unfortunately there are no published analyses of altered MORB which include data for all elements of interest in this study. Therefore data have been selected from more than one source ensuring where possible that the amalgamated composition is internally consistent, i.e. that the relative concentrations of trace elements in the amalgamated composition are similar to those in the constituent data sets. See Table 8.2.

It has become increasingly apparent that the composition of sediments entering a subduction zone can greatly affect the trace-element composition of the resulting volcanics (e.g. Plank & Langmuir, 1993). The selection of an appropriate sediment composition is therefore extremely important. The composition of oceanic sediments at any one place is dependent on many factors including the sea-floor age and depth, the proximity of continental sediment sources, the organic productivity etc. Generally, sediments consist of biogenic silica, calcareous oozes, and a detrital component. The most appropriate sediment composition for the purposes of this modelling is a weighted mean of the entire sedimentary column. This calculation has been performed using sediments from an ODP hole adjacent to the Australian margin (Plank & Ludden, 1992). The resultant composition is very similar to an Australian shale that has been diluted by relatively trace-element free biogenic material. As shale compositions are fairly constant worldwide (Taylor & McLennan, 1985) it is considered that this estimate for sediment composition is applicable to a general model. Other estimates for average oceanic sediment composition (e.g. Hole *et al.*, 1984) are in close agreement. I will use data from Plank & Ludden (1992) with some extra sources for elements not analysed by them.

The relative proportions of sediments and altered MORB subducted to depth are thought to vary from arc to arc (Plank & Langmuir, 1993) depending on the thickness of the sedimentary column, the mode of accretion in the trench etc. The isotopic composition of the erupted products can be used to infer the proportions of the slab constituents: for example, the isotopic signature of the slab end member in the Sunda arc is suggestive of a slab composed of approximately 80% altered MORB and 20% oceanic sediment (Edwards *et al.*, 1993). This estimate of slab composition will be used in the majority of models in this chapter, although the effects of

Table 8.2: Chosen compositions of MORB, altered MORB and oceanic sediments, and calculated mantle compositions.

	MORB	*SLAB*		*MANTLE*		
ppm		altered MORB	oceanic sediments	MORB source	Depleted MORB Source	V Depleted MORB Source
Li	4.3	15	74	1.20	1.00	0.83
Be	0.45	0.45	0.73	0.06	0.03	0.007
B	0.5	47	40	0.05	0.03	0.005
Na	19735	15500	8160	2636	1405	420
K	884	6560	13280	89	45	8.91
Ti	9680	8392	2997	1814	1248	794
Rb	1.3	12	58	0.13	0.06	0.01
Sr	113.2	110	871	12.9	6.5	1.30
Y	35.8	42	21	5.48	3.25	1.46
Zr	104.2	100	106	12.42	6.26	1.33
Nb	3.5	2.8	7.4	0.36	0.18	0.035
Cs	0.014	0.14	3.7	0.0014	0.0007	0.0001
Ba	13.87	26	963	1.39	0.69	0.14
La	3.90	3.3	24	0.41	0.21	0.04
Ce	12.0	12.7	56	1.31	0.66	0.13
Pr	2.07	2.14	-	0.24	0.12	0.024
Nd	11.2	11.4	20	1.37	0.69	0.15
Sm	3.75	3.93	4.5	0.51	0.28	0.09
Eu	1.34	1.44	0.94	0.19	0.11	0.04
Gd	5.08	5.53	-	0.78	0.46	0.21
Tb	0.89	0.99	0.61	0.14	0.08	0.04
Dy	6.30	-	-	1.02	0.64	0.33
Ho	1.34	-	-	0.22	0.13	0.07
Er	4.14	-	-	0.67	0.41	0.21
Tm	0.62	-	-	0.11	0.07	0.04
Yb	3.90	3.78	2.1	0.70	0.47	0.28
Lu	0.59	0.65	0.33	0.11	0.08	0.05
Hf	2.97	2.86	3.1	0.41	0.22	0.07
Ta	0.19	0.2	0.67	0.02	0.01	0.002
Pb	0.49	0.3	14	0.05	0.02	0.005
Th	0.19	0.27	7	0.02	0.01	0.002
U	0.07	0.14	1.5	0.01	0.00	0.0007

Data from: **MORB** - all elements from Hofmann (1988) except Li (Sun & McDonough, 1979); Be (Ryan & Langmuir, 1988) and B (Chaussidon & Jambon, 1994). **Altered MORB** - all elements from Hole et al. (1984) except Li, B, Na, K, Ti (Donnelly, 1979); Pb, U (McCulloch & Gamble, 1991); Be, Cs, Pr, Gd, Hf (interpolated). **Oceanic sediments** - all elements from Plank & Ludden (1992) except Li (Leggett, 1982); B (Karl et al., 1992); Be (inferred from B/Be ratio from Morris et al., 1990); Pb (Ben Othman et al., 1989).

MORB-source was calculated assuming derivation of MORB by 10% melting of spinel peridotite. The depleted MORB-source compositions consist of mixtures of residue after MORB extraction, and MORB source (50% and 10% MORB source in Depleted MORB Source and Very Depleted MORB Source, respectively).

changing the proportions of altered MORB and oceanic sediment will be investigated.

In order to predict the partitioning of elements into slab-derived fluids and melts, it is necessary to assume a mineralogy for the downgoing slab at the pressures and temperatures of interest. This, however, is far from easy, for a number of reasons. Firstly, it is difficult to specify the pressure and temperature of interest, partly due to the large variation in temperature regimes between subduction zones and partly due to uncertainty surrounding the behaviour of slab-derived fluid. Fluid is released by a number of reactions, in the meta-sediment, metabasic, and possibly meta-ultramafic portions of the slab (see Chapter 2). It has been suggested (Tatsumi, 1989) that fluid may be released into the mantle wedge from the slab at pressures lower than those of the sub-arc slab, and that this fluid may be dragged down by convection induced by the slab until it reaches the sub-arc mantle. If this is the case then the pressure at which the slab transfers its signature to the mantle wedge may be lower than 3.0 GPa which is the approximate pressure at the top of the sub-arc slab. At 2.0 GPa, the temperature at the top of a typical slab can range from approximately 200°C to 700°C, depending on the angle and rate of subduction, the age of the subducting crust etc. (Peacock *et al.*, 1994). The temperature is higher at 3.0 GPa. The mineralogy of metabasic and metasedimentary rocks between 2.0 GPa and 3.0 GPa, and 200°C and 1000°C is not well known. Ultra high pressure metamorphic rocks are distinguished by the presence of omphacitic pyroxene and garnet. However, there are many other minerals that may be present, depending on the precise pressure and temperature conditions, and the composition of the rock. These include amphibole (glaucophane, or hornblende at higher temperatures), quartz, rutile, kyanite, sphene (Yardley, 1989) as well as many others (Mottana *et al.*, 1990). However, those rocks that have been obducted to the Earth's surface may not be typical representatives of a subducting oceanic slab, which in normal situations is eventually assimilated by the mantle. In theory, a more reliable method by which to predict the mineralogy of the slab is from experiments. However, the low temperatures involved can cause considerable difficulties in reaching equilibrium. There are therefore no good estimates for the mineralogy of the slab at pressures and temperatures appropriate for the transfer of slab material to the sub-arc mantle.

The approach adopted here is to model the slab as a mixture of five minerals: garnet, clinopyroxene, amphibole, rutile, and sphene.

- *Garnet* - this is abundant in eclogites and is undoubtedly present in the subducting slab. Evidence from metamorphic rocks suggests that it is likely to be pyrope poor (~30% pyrope).
- *Clinopyroxene* - Omphacitic pyroxene is abundant in eclogites.
- *Amphibole* - This may either be hornblende or glaucophane depending on the P, T conditions. As hornblende is one likely candidate for the source of slab-derived fluid (Tatsumi, 1989), the modelled slab will contain a substantial proportion of hornblende.
- *Rutile, sphene* - these may also be present. It has been suggested that the retention of rutile in the slab during melting or dehydration may be the cause of the low HFSE contents in IAV. This possibility will be investigated by modelling melt compositions produced with and without residual rutile in the slab.

In the majority of models in this chapter, Slab Mineralogy 1 (Table 8.3) will be assumed. This consists of 50% garnet; 22.5 % clinopyroxene; 22.5% amphibole and accessory rutile and sphene and is similar in modal mineralogy to rocks from the paleosubduction zone exposed in Catalina, Southern California (Sorenssen & Grossman, 1988). The influence of the slab mineralogy will be investigated in a later section by reducing the proportions of rutile, amphibole and cpx (Slab Mineralogies 2, 3, 4, respectively).

Table 8.3: Chosen mineralogies of the slab.

	Garnet	*Clinopyroxene*	*Amphibole*	*Rutile*	*Sphene*
Slab mineralogy 1	0.5	0.225	0.225	0.025	0.025
Slab mineralogy 2	0.5	0.25	0.25	-	-
Slab mineralogy 3	0.5	0.4	0.05	0.05	-
Slab mineralogy 4	0.5	0.1	0.35	0.025	0.025

The proportions by weight of constituent minerals are shown.

It is acknowledged that these estimates are inexact, and that there will undoubtedly be other phases present in the slab. However, in the absence of more detailed information, it was decided to use relatively simple estimates of the slab mineralogy. Furthermore, as the mineralogy of the slab will be combined with known partition coefficients to derived bulk partition coefficients between melt, fluid, and the slab, it would be pointless to assume a more complicated slab mineralogy involving minerals for which there are no good partitioning data. In the future however, given more experimental data or thermodynamic predictions of the slab mineralogy, and

more accurate partition coefficients between slab phases and melt, it may be possible to model the process of melt production in subduction zones using a more complex, or realistic, slab mineralogy.
Although this is clearly an area of uncertainty in the present study, results in this chapter will show that the modelled melt compositions are not particularly sensitive to the mineralogy of the slab (Fig. 8.17).

8.2.2 Change in slab composition with increasing metamorphism

There is a growing wealth of evidence from metamorphic rocks to suggest that the composition of the slab will not be the same at depth as it was at the surface. Studies in the Catalina Schist indicate that Cs and B are particularly mobile in hydrous fluids released from the subducting slab (Bebout *et al.*, 1993; Bebout *et al.*, *in prep.*). Results suggest that between conditions of 0.5 GPa, 300°C and 1.1 GPa, 750°C, the slab will have lost approximately 75% of its total B and Cs. These elements are thought to be expelled back through the accretionary complex (You *et al.*, 1993) or into the shallow mantle, thus preventing their possible recycling by incorporation into arc magmas. No evidence was found from these rocks of enhanced mobility of other LILE (K, Ba, Rb) although this does not rule out the possibility that they are lost under different conditions. In a similar study, Domanik *et al.*, (1993) found that although substantially less mobile than boron, beryllium is also transported by aqueous fluids in subduction zones. Sighinolfi & Gorgoni (1978) showed that LILE are progressively depleted with increasing metamorphism, consistent with the release of hydrous fluids (Rb > K > Pb). These results should be considered when modelling the transfer of elements from the slab to the mantle.

8.2.3 Mantle composition

I have chosen to use a MORB-source mantle composition for the majority of the models. Although the similarity in isotopic and trace-element composition between IAV and OIB has led some authors to suggest that they are derived from the same source as each other, it is the opinion of the majority of workers that this observation can be better explained by the addition of a subduction component to MORB-source mantle (see Chapter 2). Results of modelling calculations will show that it is indeed possible to model IAV by using a MORB-source mantle as the starting point, thus

providing support for this assumption. In order to create an internally consistent model, I have calculated the composition of the MORB source from the MORB composition (Table 8.2) of Hofmann (1988), assuming that MORB is produced by 10% batch melting of spinel peridotite[1] (mineralogy and partition coefficients presented later). The calculated concentrations of most trace elements are slightly higher than the concentrations suggested by McKenzie & O'Nions (1991), although the interelement ratios are very similar to those of McKenzie & O'Nions (*op. cit.*).

The very low levels of HFSE in some arcs may be indicative of a mantle source depleted by prior melt extraction (e.g. McCulloch & Gamble, 1991; Defant *et al.*, 1993; Woodhead *et al.*, 1993; Pearce *et al.*, 1994). To test this hypothesis, depleted mantle compositions have been calculated assuming that convection within the mantle wedge has mixed varying proportions of residue after MORB extraction, with fresh asthenospheric mantle of MORB-source composition. Two depleted mantle compositions are given in Table 8.2 and are termed Depleted MORB Source and Very Depleted MORB Source.

As a starting point three mantle mineralogies are used: spinel peridotite, amphibole peridotite and garnet peridotite (from McKenzie & O'Nions, 1991). See Table 8.4.

Table 8.4: Mineralogy of spinel, amphibole and garnet peridotite

	Olivine	*Orthopyroxene*	*Clinopyroxene*	*Spinel*	*Amphibole*	*Garnet*
Spinel peridotite	0.578	0.270	0.119	0.033	-	-
Amphibole peridotite	0.599	0.247	0.038	-	0.116	-
Garnet peridotite	0.598	0.211	0.076	-	-	0.115

The proportions by weight of constituent minerals are shown (from McKenzie & O'Nions, 1991).

8.2.4 Partition coefficients

The selection of relevant partition coefficients is critical to the successful modelling of igneous processes. Unfortunately the data are highly variable. This can be illustrated by comparison of the sets of partition coefficients chosen by previous workers for the purposes of modelling melt production in subduction zones (e.g. McKenzie & O'Nions, 1991; Kelemen *et al.* 1992; Hawkesworth *et al.*, 1993a; Stolper & Newman, 1994). Before selecting partition coefficients it is wise to examine the methods by which they were calculated and the conditions under which the rock was formed or the experiment was run. There are three main ways of

[1]This assumption is not strictly true, as there is evidence to suggest that some melting takes place in the garnet field (McKenzie & Bickle, 1988). However for these purposes the assumption is sufficient.

measuring partition coefficients: by analysing natural rocks, from experimental studies, or by thermodynamic calculations. The last method may be the most accurate in the future but at present the models are relatively unconstrained. Compositions of natural rocks (including volcanics and xenoliths) form the basis for many values in the literature. However, care has to be taken to ensure that melt and mineral are in equilibrium. Furthermore, large uncertainties can arise due to the very low levels of some trace elements in natural crystals. These problems can be surmounted in experimental studies in which the element of interest can be artificially added to the starting material. In early studies, partition coefficients were often calculated from analyses by electron microprobe. For many trace elements this is not as precise or as accurate as analysis by SIMS (e.g. Hart *et al.*, 1991) or proton microprobe (e.g. Green *et al.*, 1989).

The conditions at which the experiment was run or the rock was formed are critical. Experimental studies have shown that there are many factors which can affect partition coefficients (Rollinson, 1993) , the most important of which are:

- Composition - a general rule is that the partition coefficient between mineral and melt increases with the silica content of the melt.
- Temperature - whilst not completely quantified, and perhaps confused by the coincident change in melt composition with temperature, there is generally a negative relationship between temperature and partition coefficient i.e. as temperature increases, elements partition more into the melt.
- Pressure - there is a clear increase in partition coefficient with increasing pressure. One important aspect of this pressure effect is that high-level phenocryst/liquid pairs may not be a suitable analogue for deep level partitioning behaviour.

Whenever possible I have selected partition coefficients measured by an accurate and precise analytical technique, appropriate to the pressure and temperature conditions of interest (roughly 2.0 GPa to 3.0 GPa and <1200°C), and relating to basaltic melt compositions. Another important consideration is that for the full set of trace elements the chosen values are as mutually consistent as possible. The majority of partition coefficients between olivine and melt are taken from this study (see Chapter 7). All chosen data are shown in Table 8.5, and a brief description of the methods by which they were measured is given in the caption to Table 8.5.

Table 8.5: Selected partition coefficients, with data sources indicated by numbers 1-14 (see next page for figure caption)

	D (olivine/melt)		*D (opx/melt)*		*D (cpx/melt)*		*D (amph/melt)*		*D (garnet/melt)*		*D (spinel/melt)*		*D (rutile/melt)*	
Li					0.59	8								
Be					0.047	8								
B	0.034	1	0.027	1	0.117	1					0.08	1		
Na	0.00001	2	0.05	2	0.2	2	0.53	2	0.04	2				
K	0.00018	2	0.00001	3	0.0072	8	1.2	2	0.00001	3	0.0001	2		
Ti	0.015	3	0.14	3	0.384	8	1.5	2	0.6	3	0.15	3	38.8	14
Rb	0.00018	2	0.0006	2	0.001	9	0.2	2	0.0007	2	0.0005	13		
Sr	0.000065	4	0.00019	2	0.1283	8	0.64	7	0.0011	2	0.0005	13		
Y	0.0028	4	0.005	6	0.467	8	1	2	10.5	10	0.01	13		
Zr	0.0008	4	0.014	3	0.1234	8	0.5	2	0.3	3	0.07	3		
Nb	0.0003	4	0.003	3	0.0077	8	0.8	2	0.03	10	0.01	3	26.5	14
Cs	0.00005	2	0.0001	2	0.0002	2	0.14	2	0.0002	2	0.0001	2		
Ba	0.000015	4	0.0001	2	0.00068	8	0.76	2	0.0005	2	0.0001	2		
La	0.000003	4	0.0005	3	0.0536	8	0.17	7	0.001	3	0.0006	3		
Ce	0.00002	4	0.0009	3	0.0858	8	0.26	7	0.004	3	0.0006	3		
Pr	0.00008	4	0.005	5	0.1329	5	0.35	11	0.031	5	0.0006	5		
Nd	0.00010	5	0.009	3	0.1873	8	0.44	7	0.057	3	0.0006	3		
Sm	0.00012	5	0.02	3	0.291	8	0.76	7	0.5	3	0.0006	3		
Eu	0.00014	4	0.03	3	0.35	8	0.88	7	1	3	0.0006	3		
Gd	0.00052	4	0.04	3	0.4	8	0.86	7	2	3	0.0006	5		
Tb	0.00077	4	0.05	5	0.414	5	0.83	7	2.22	5	0.0006	3		
Dy	0.0010	4	0.06	3	0.442	8	0.78	7	2.5	3	0.0015	3		
Ho	0.0029	4	0.065	5	0.405	5	0.73	11	2.75	5	0.002	5		
Er	0.0055	4	0.07	3	0.387	8	0.68	7	3	3	0.003	3		
Tm	0.011	4	0.09	5	0.409	5	0.64	11	3.49	5	0.004	5		
Yb	0.016	4	0.1	3	0.43	8	0.59	7	4	3	0.0045	3		
Lu	0.029	4	0.12	5	0.433	8	0.51	7	5.46	5	0.0054	5		
Hf	0.0005	4	0.04	7	0.256	8	0.38	7	0.44	6				
Ta	0.0008	4	0.005	6	0.013	10	0.38	7	0.09	10			44	14
Pb	0.0001	2	0.0013	2	0.01	2	0.1	2	0.0005	2	0.0005	2		
Th	0.0001	2	0.0001	2	0.00026	9	0.038	7	0.0001	2	0.001	2		
U	0.0001	2	0.0001	2	0.00036	2	0.08	12	0.0001	2	0.001	2		

Table 8.5: Selected partition coefficients between minerals and melt. Data were taken from the following sources:

1 Chaussidon & Libourel (1993), from partial melting experiments using natural peridotites.
2 McKenzie & O'Nions (submitted), compiled results from natural rocks and experimental studies.
3 Kelemen *et al.* (1992), compiled results from ion probe analyses on experimental charges.
4 This study, ion probe results on an experimental olivine/basalt pair produced at 1.9 GPa, 1005°C.
5 Interpolated value.
6 Ulmer (1989), electron probe analyses of experimental cpx, opx, garnet and calc-alkaline picrobasalt produced at 2.8 GPa, 1330°C.
7 Irving & Frey (1984), megacrysts of cpx, opx and amphibole in host basalts.
8 Hart & Dunn (1993), ion probe analyses of cpx/melt from an alkali olivine basalt at 3.0 GPa, 1380°C.
9 Hawkins *et al.* (1990), compiled from volcanic rocks and experimental results.
10 Green *et al.* (1989), analyses by proton microprobe of experimental charges run at 2.5 GPa, 1100°C with 10 wt% H_2O.
11 McKenzie & O'Nions (1991), compiled and interpolated results from natural rocks and experimental studies.
12 Lemarchand *et al.* (1987), from analyses of crystals and glass in basaltic lavas.
13 Hawkesworth *et al.* (1993a), compiled from previous work.
14 Green & Pearson (1986), electron probe analyses of experimental rutile and andesitic liquid.

Although some of the partition coefficients presented in Table 8.5 have been derived from melts and residual phases from basaltic starting materials, the majority of chosen values are appropriate to melting of the mantle. There are substantial differences between the compositions of minerals in the subducting oceanic crust and in the mantle. For example, the Mg nos. of slab amphiboles and garnets are lower than their mantle counterparts; the pyroxene in the slab is omphacitic whereas diopside is present in the mantle. In addition, melts (where present) in equilibrium with the slab are more silicic than melts in equilibrium with the mantle at similar pressure (Helz, 1976). Ideally, partition coefficients relevant to slab-melt and slab-fluid equilibria should be used to model the compositions of slab-derived melts and fluids. However, it was decided to use the same set of partition coefficients for both the mantle equilibria and the slab equilibria, for the following reasons:

1. Partition coefficients between minerals and melts more relevant to slab equilibria were compiled from the literature, but in general, due to the techniques used in their derivation, they are not considered to be as reliable as those presented in Table 8.5.
2. The fluid partitioning data used in this modelling are in the form of partition coefficients between fluid and *basaltic* melt. For consistency, partition coefficients between minerals and *basaltic* melt will be used to calculate D (mineral/fluid).

As the equilibrium between slab and melt is at a lower temperature than that between mantle and melt; and as melt (where present) in equilibrium with the slab is more

siliceous than that in equilibrium with the mantle, the true partition coefficients between slab and melt are likely to be higher than those adopted here. The implications of this will be addressed qualitatively in Section 8.6.

8.3 PARTITIONING BETWEEN MELTS, FLUIDS AND RESIDUAL PHASES

The selected mineral/melt partition coefficients can be used to infer bulk partition coefficients between mantle and melt, and between slab and melt, once mineralogies for the mantle and the slab have been chosen. These values can be combined with measured partition coefficients between fluid and melt (Chapter 7) to calculate bulk partition coefficients between the mantle, the slab, and fluids in equilibrium with both. The bulk partition coefficient, $\bar{D}$, is defined by the expression

$$\bar{D}_i = F_1D_1 + F_2D_2 + F_3D_3 \ldots\ldots \qquad (8.8)$$

where $\bar{D}_i$ is the bulk partition coefficient for element *i*, and F_1 and D_1 etc. are the percentage proportion of mineral 1 in the rock and the partition coefficient for element *i* in mineral 1 respectively.

For three elements (Li, Be and B) there are insufficient mineral/melt partitioning data to calculate bulk partition coefficients. I have therefore used estimates of bulk partition coefficients appropriate to the production of MORB (Ryan & Langmuir, 1987, 1988, 1993).

The bulk partition coefficient between fluid and rock can be calculated from $\bar{D}$ (bulk/melt) and D (fluid/melt) in the following manner:

$$\bar{D}(\text{bulk/fluid}) = \frac{\bar{D}(\text{bulk/melt})}{D(\text{fluid/melt})} \qquad (8.9)$$

Unfortunately D (fluid/melt) for Th was not calculated from this study due to the low concentration of this element in experiments.

8.3.1 Partitioning between fluids, melts and the mantle

The partition coefficients between basaltic melt, fluid and peridotite are given in Table 8.6. Three mantle compositions were investigated: spinel peridotite, garnet peridotite and amphibole peridotite (see Table 8.4). A comparison of $\bar{D}$ (bulk/melt) and $\bar{D}$ (bulk/fluid) for each composition is shown in Figure 8.2.

8.3.2 Partitioning between fluids, melts and the slab

The bulk partition coefficients between melts, fluids and slab were calculated in the manner described above. Table 8.6 shows the bulk partition coefficient assuming Slab Mineralogy 1. A comparison of $\bar{D}$ (bulk/melt) and $\bar{D}$ (bulk/fluid) is shown in Figure 8.3, for all four slab mineralogies.

8.4 MELTING WITH NO SLAB INVOLVEMENT

Before incorporating the downgoing slab into any models, it is useful to examine the compositions of predicted melts given no input, other than pure water, from the slab. The composition of partial melts of the mantle are shown in Figure 8.4 and 8.5. In Figure 8.4 a comparison is made between a 10% partial melt of spinel, amphibole and garnet peridotite. Melts containing garnet in the residue are predicted to be depleted in HREE and Y. This is not a characteristic of IAV and therefore it seems unlikely that garnet is a residual phase (see also McKenzie & O'Nions, 1991). Amphibole peridotite yields a melt that is generally more depleted than melt in equilibrium with spinel or garnet peridotite. Small relative depletions in the HFSE (Nb, Ta, Zr, Ti) are evident, perhaps suggesting that residual amphibole may be in the source of IAV. However other elements such as Na, Sr, K, Ba are also relatively depleted in the melt.

Table 8.6: Bulk partition coefficients between mantle and melt; mantle and fluid; slab and melt; and slab and fluid.

	MANTLE							
	---------- $\bar{D}$ (bulk/melt)---------			---------- $\bar{D}$ (bulk/fluid)----------			$\bar{D}$ (bulk/melt)	$\bar{D}$ (bulk/fluid)
Mineralogy	*sp per*	*gt per*	*amph per*	*sp per*	*gt per*	*amph per*	*Slab*	*Slab*
Li	0.20	0.20	0.20	1.55	1.55	1.55	0.20	1.55
Be	0.03	0.03	0.03	0.27	0.27	0.27	0.03	0.27
B	0.01	0.01	0.01	0.05	0.05	0.05	0.01	0.05
Na	0.037	0.030	0.081	0.176	0.143	0.385	0.184	0.871
K	0.001	0.001	0.140	0.002	0.001	0.248	0.272	0.48
Ti	0.097	0.137	0.232	1.60	2.25	3.82	1.98	32.52
Rb	0.0004	0.0004	0.023	0.0005	0.0004	0.027	0.046	0.052
Sr	0.015	0.010	0.079	0.33	0.21	1.68	0.173	3.68
Y	0.059	1.25	0.137	7.12	150.76	16.54	5.58	675.3
Zr	0.021	0.047	0.067	1.59	3.55	5.00	0.29	21.8
Nb	0.002	0.005	0.094	0.031	0.068	1.33	0.95	13.4
Cs	0.0001	0.0001	0.016	0.0001	0.0001	0.012	0.032	0.024
Ba	0.0001	0.0001	0.088	0.002	0.003	1.60	0.17	3.11
La	0.007	0.004	0.022	0.82	0.54	2.75	0.051	6.39
Ce	0.010	0.007	0.034	1.26	0.86	4.03	0.080	9.56
Pr	0.017	0.015	0.047	1.94	1.66	5.31	0.12	14.0
Nd	0.025	0.023	0.060	3.24	2.98	7.90	0.17	22.2
Sm	0.040	0.084	0.104	5.07	10.60	13.17	0.49	61.5
Eu	0.050	0.148	0.123	2.64	7.85	6.51	0.78	41.2
Gd	0.059	0.269	0.125	7.52	34.47	16.03	1.28	164.4
Tb	0.063	0.298	0.125	7.26	34.23	14.32	1.39	159.7
Dy	0.069	0.334	0.123	9.04	43.54	15.98	1.52	198.6
Ho	0.068	0.362	0.118	8.58	46.06	14.98	1.63	207.2
Er	0.068	0.392	0.114	8.90	51.20	14.89	1.74	227
Tm	0.078	0.458	0.118	9.69	56.52	14.54	1.98	244.8
Yb	0.088	0.523	0.119	11.92	71.21	16.21	2.23	303.3
Lu	0.102	0.704	0.123	13.13	90.92	15.93	2.94	379.9
Hf	0.042	0.079	0.064	3.06	5.80	4.71	0.36	26.7
Ta	0.003	0.013	0.046	0.108	0.41	1.48	1.50	48.1
Pb	0.002	0.001	0.012	0.043	0.031	0.330	0.03	0.67
Th	0.0001	0.0001	0.005	-	-	-	0.01	-
U	0.0002	0.0001	0.009	0.011	0.008	0.65	0.02	1.27

Three mantle mineralogies were used: spinel peridotite (sp per), garnet peridotite (gt per), and amphibole peridotite (amph per) (see Table 8.4). Slab Mineralogy 1 was used (Table 8.3).

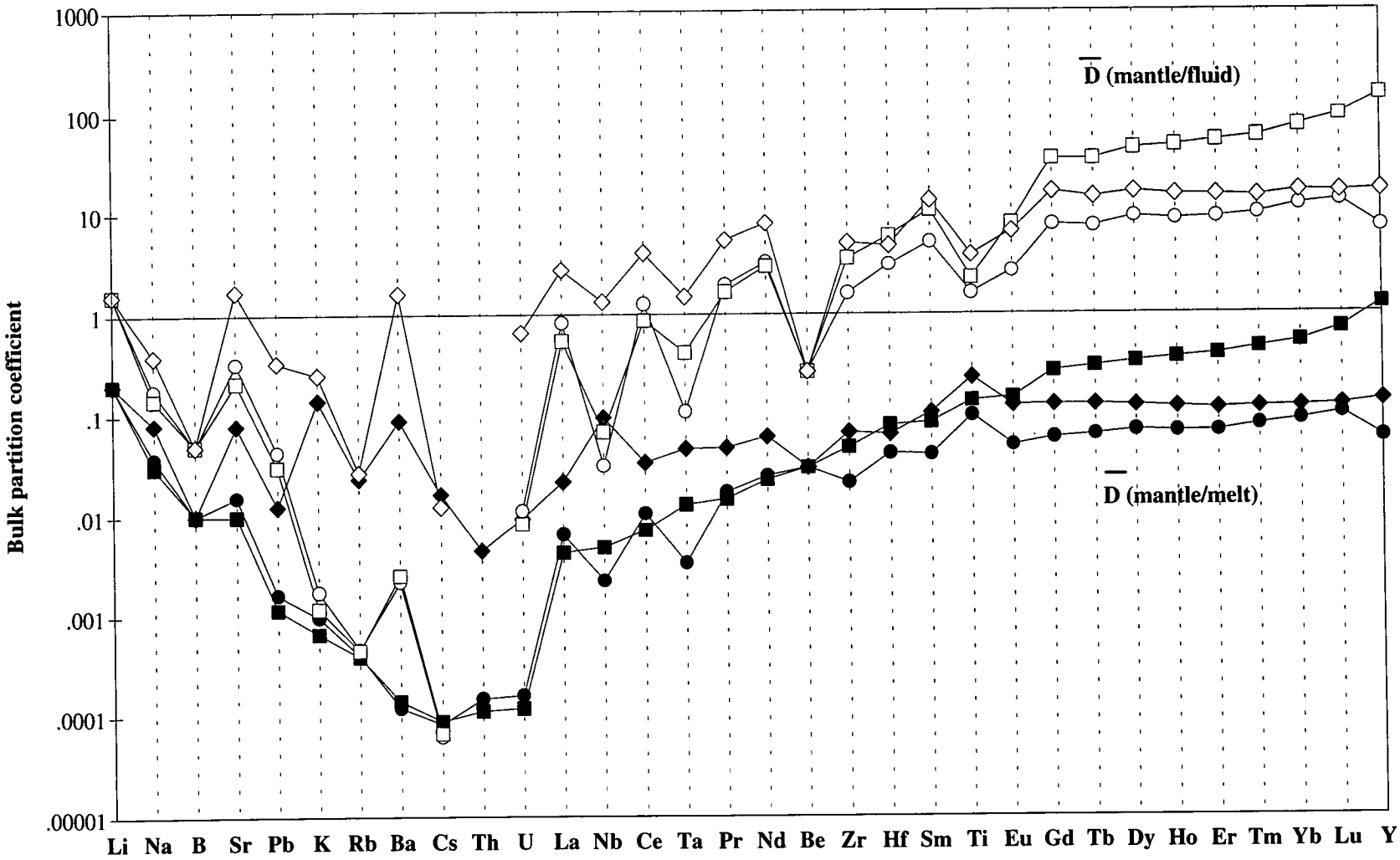

Figure 8.2: Partition coefficients between mantle and melt; and mantle and fluid. Symbols: squares - garnet peridotite; circles - spinel peridotite; diamonds - amphibole peridotite. See Table 8.6 for data.

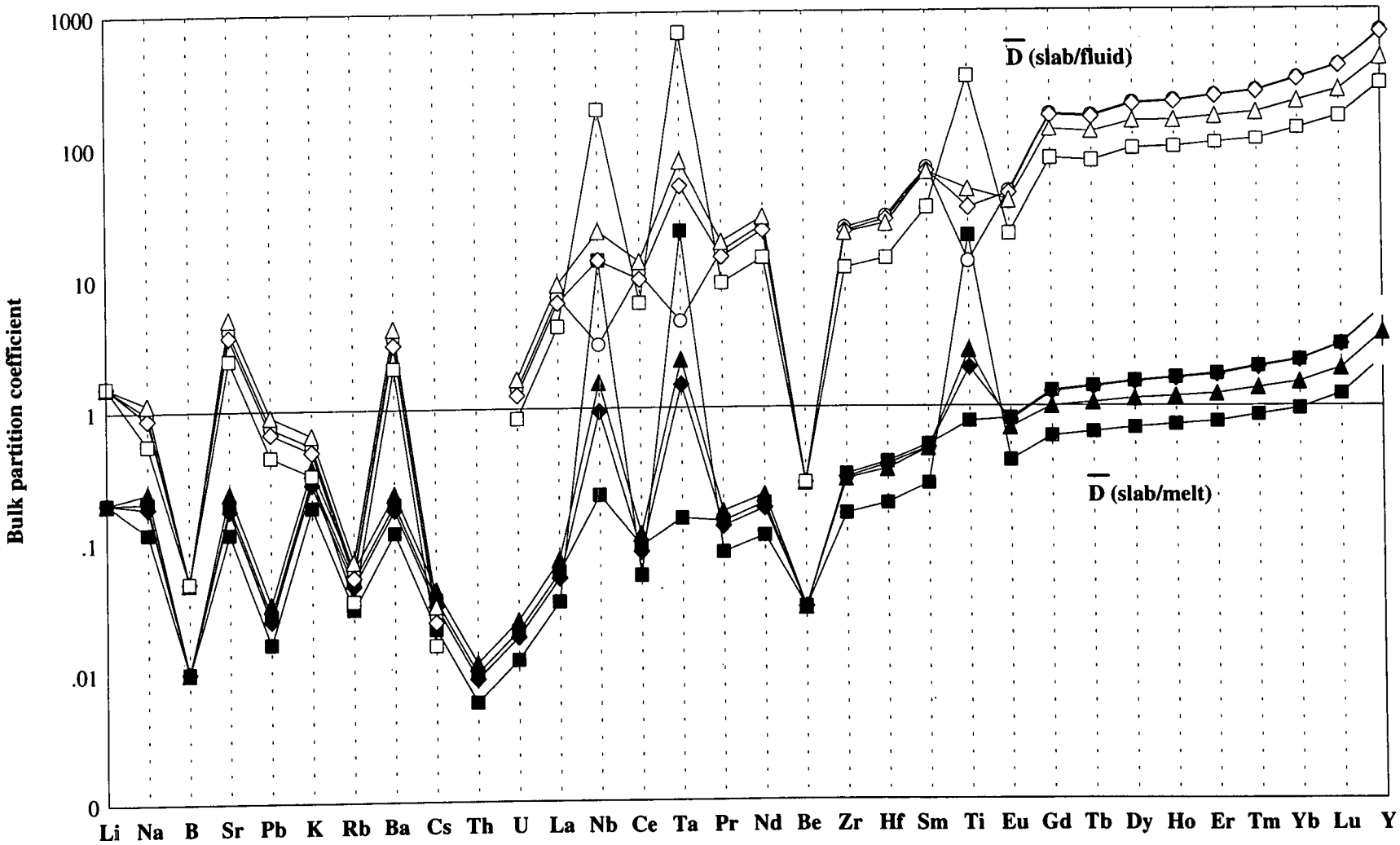

Figure 8.3: Partition coefficients between slab and melt; and slab and fluid. Symbols: circles, diamonds, triangles, squares represent Slab Mineralogies 1, 2, 3, 4, repectively. See Table 8.6 for data.

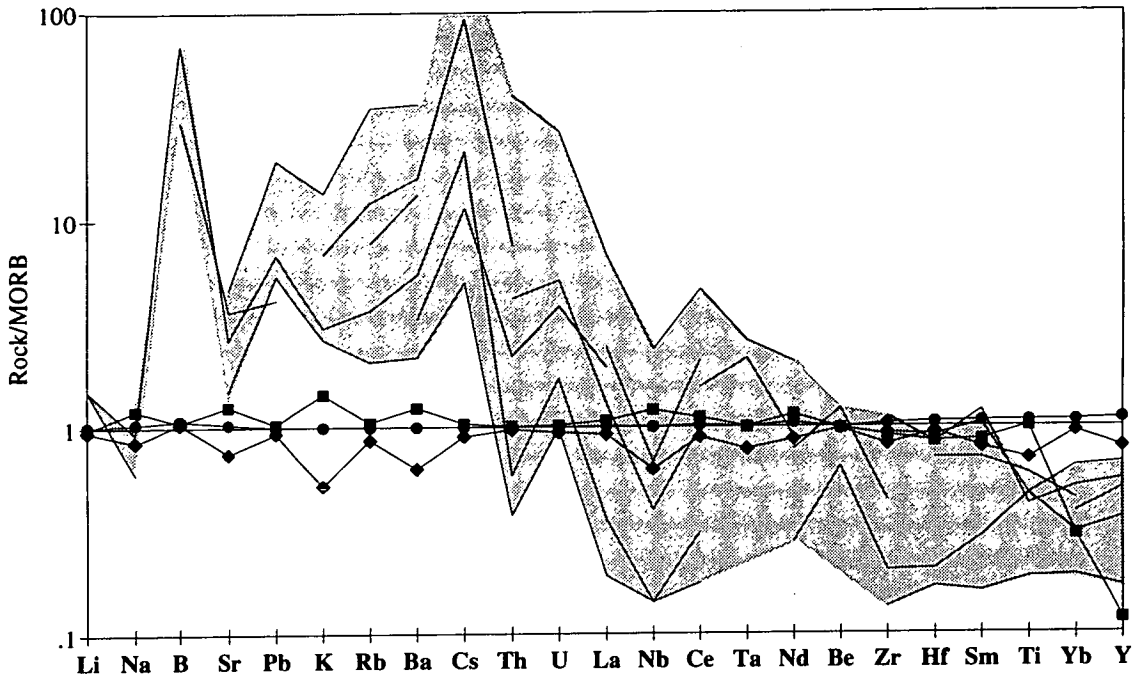

Figure 8.4: Trace-element concentrations in calculated melts of the mantle, for three mantle mineralogies (assuming 10% non-modal batch melting of a MORB-source composition). Symbols: squares - garnet peridotite; circles - spinel peridotite; diamonds - amphibole peridotite. As in all future figures of this type, the thin black lines represent individual IAV compositions and the shaded area represents a range of IAV compositions (Table 8.1).

With increasing degrees of melting the overall concentration of trace elements decreases (Fig. 8.5).

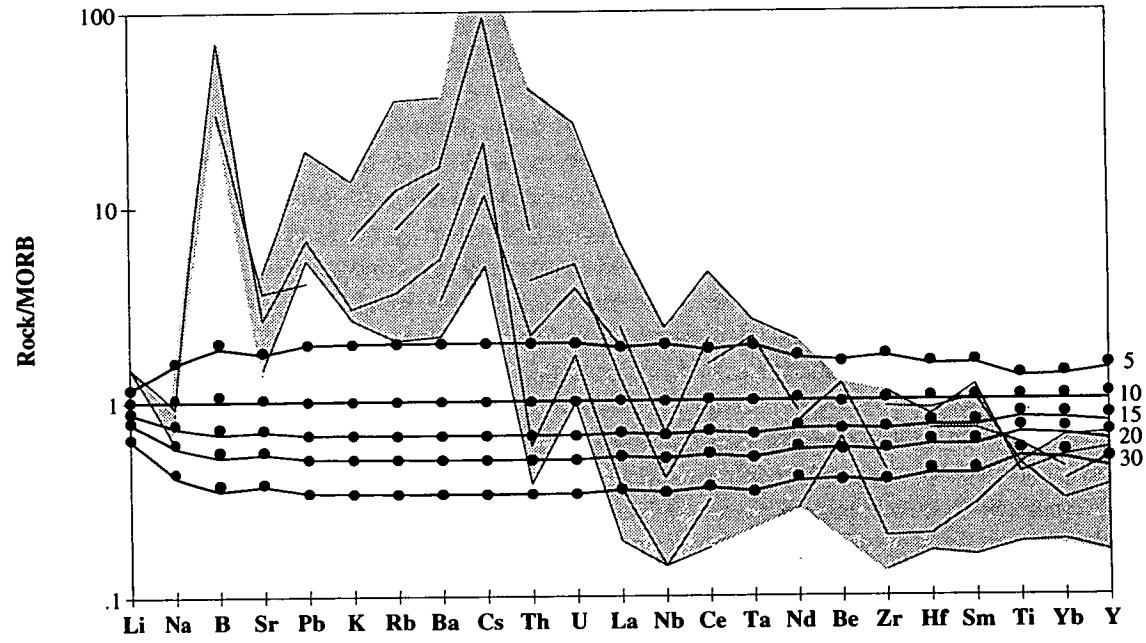

Figure 8.5: Trace-element concentrations in partial melts of the mantle, assuming spinel peridotite mineralogy of the MORB-source composition. Caption continued overleaf

Figure 8.5 (caption, continued). The melt compositions calculated from the modal batch melting equation (Equation 8.1) are shown as thick lines. The filled circles represent the compositions of partial melts calculated from the non-modal batch melting equation (Equation 8.2). There is little difference between the compositions of melts calculated by using the modal and the non-modal melting equations. However melts calculated by the non-modal melting equation are slightly richer in Ti, Yb, and Y. The percentage melting is indicated to the right of the diagram.

Figure 8.6 shows the predicted changes in partial melt composition with increasing degrees of melting of amphibole peridotite. With small-degree melting, a sharp Nb trough is predicted, which becomes less marked as melting increases. These melt compositions were calculated using the non-modal batch equation (Equation 8.2). It was assumed (after McKenzie & O'Nions, 1991) that amphibole and clinopyroxene were present in the residue, although becoming less abundant with progressive melting, until 30% melting in which they disappeared. However, the results of previous partial melting studies of hydrous peridotite, and the results of the present study (Chapter 5) suggest that amphibole will disappear at a much lower temperature than clinopyroxene. Therefore, I do not believe that the influence of residual amphibole, i.e. the Nb trough, will be seen in partial melts produced by more than, say, 10% melting.

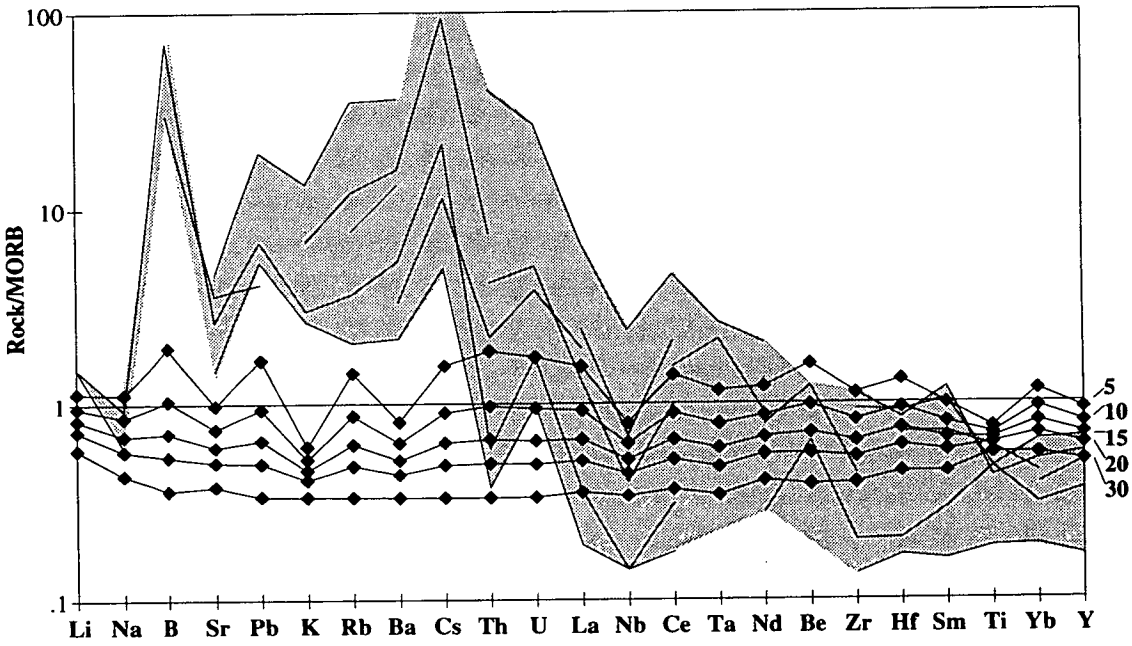

Figure 8.6: Trace-element concentrations in partial melts of the mantle, assuming the initial mineralogy is amphibole peridotite and the composition is identical to the MORB source. Melt compositions were calculated from the non-modal batch equation (Equation 8.3). The degree of melting is indicated to the right of the diagram.

In order to reproduce the low immobile element concentrations (right-hand side of the spidergram) of IAV it is necessary to invoke fairly large degrees of melting (over 40% in some cases). An alternative explanation for the low concentrations of immobile elements in IAV is that the source had been depleted by previous melt extraction. Melts of a depleted mantle (e.g. Depleted MORB source of Table 8.2) contain lower concentrations of trace elements relative to melts of MORB-source mantle (Figure 8.7).

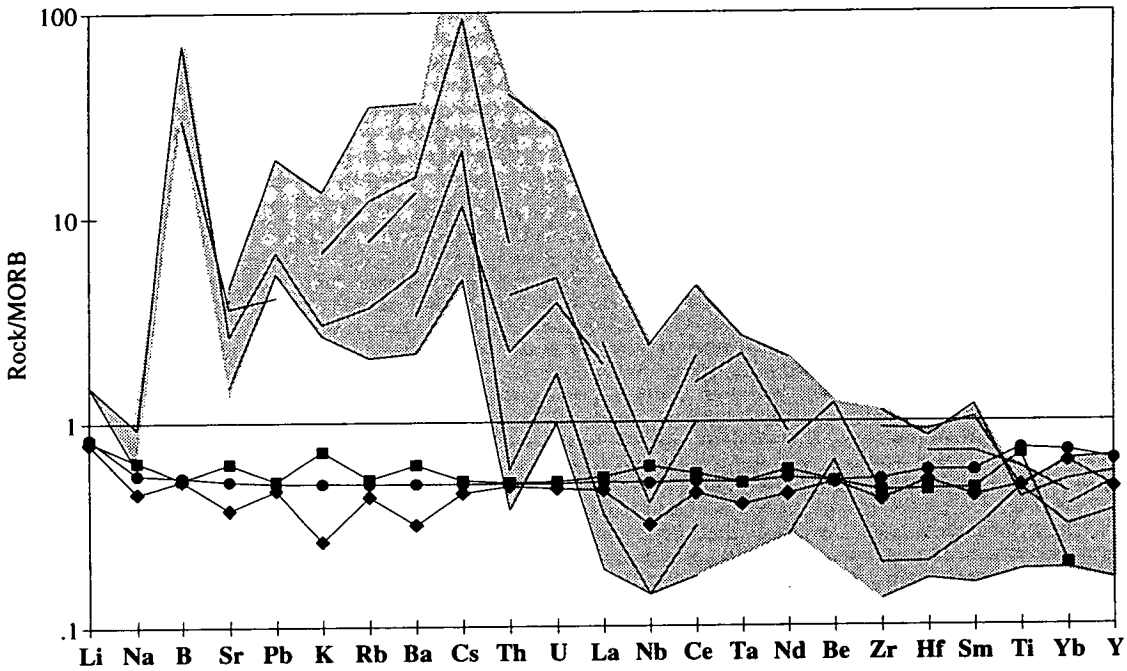

Figure 8.7: Trace-element concentrations in calculated melts of mantle already depleted by prior melt extraction, for three mantle mineralogies (assuming 10% batch melting of a mantle composed of a mixture of 50% MORB source and 50% residue after 10% melting of MORB source, see Table 8.2). Symbols: squares - garnet peridotite; circles - spinel peridotite; diamonds - amphibole peridotite.

However, even for this depleted source, relatively high degrees of melting (approx. 30%) are required to account for the very low concentrations of immobile elements in some arcs. With such high degrees of melting, amphibole and garnet would again no longer be present (see Chapter 3). Amphibole is therefore unlikely to be a residual phase during the production of much of the IAV found worldwide. This is consistent with the geochemistry of IAV which indicates that in the majority of cases amphibole is not stable in the residue after melting. There is, however good evidence to suggest that *some* small-degree partial melts may have been in equilibrium with amphibole (e.g. Thirlwall *et al.*, 1994). For future calculations I will assume that the source region of melts is spinel peridotite (Table 8.4). In this way, the problems

associated with the use of non-modal batch melting equations to model melting of amphibole peridotite will be avoided.

The most striking feature of these diagrams, however, is that these simple models have failed to generate the familiar LILE enrichment and HFSE depletion of IAV relative to mantle melt. Clearly an additional component is required to explain these observations. Possible sources of this subduction component include mantle-derived fluids.

MODEL MF/MM. Melt of a mantle metasomatised by mantle-derived fluid.

In this scenario, pure water is released from the slab and in traversing the mantle wedge scavenges relatively mobile elements. The metasomatism of the source region is envisaged as simple mixing between mantle and fluid.

The composition of fluid in equilibrium with mantle has been calculated assuming the limiting case for fluid devolatilization (Equation 8.7) and is given in Table 8.7. The fluid is extremely enriched in Cs, Rb, K and Ba with high concentrations of U, Nb, Pb, B, Ta and Be. Melts of a mantle metasomatised by this fluid (in varying amounts) are shown in Figure 8.8. This process can sufficiently increase the concentrations of certain elements in the resultant melts. In particular it can cause large enrichments in B, K, Rb, Ba, Cs, U and Be. However it cannot explain the relative enrichments in Li, Sr, Pb or the LREE seen in IAV, and furthermore, metasomatism of the melt source by a fluid in equilibrium with the mantle is predicted to **increase** the Nb and Ta concentrations. Therefore in order to produce the trace-element chemistry of IAV a more complex model is necessary. It is time to consider the role of the slab.

8.5 THE INFLUENCE OF THE DOWNGOING SLAB

Although wholesale melting of the slab to produce IAV has been largely ruled out (Chapter 2) there are still some authors who invoke a role for this process, albeit in conjunction with melting of the mantle (e.g. Plank & Langmuir, 1992; Yogodzinski *et al.*, 1994). Figure 8.9 shows the predicted composition of small degree partial melts of the slab. The resulting melts resemble IAV in terms of their relative trace-

Table 8.7: Calculated compositions of fluids in equilibrium with the mantle and the slab (altered MORB, oceanic sediments, or a combination of both).

	MANTLE			*SLAB*		
ppm	MORB source	Depleted MORB Source	V Depleted MORB Source	altered MORB	oceanic sediments	slab (20% sediments)
Li	0.78	0.64	0.56	9.68	47.7	17.3
Be	0.21	0.11	0.05	1.69	2.74	1.90
B	1.07	0.54	0.21	954	812	926
Na	14955	7970	3780	17811	9374	16123
K	51884	25942	10377	13581	27507	16367
Ti	1137	782	569	258	92	225
Rb	274	137	55	229	1106	404
Sr	39.5	19.8	7.9	29.9	237	71.3
Y	0.77	0.46	0.27	0.06	0.03	0.06
Zr	7.80	3.93	1.61	4.59	4.87	4.65
Nb	11.38	5.69	2.28	0.21	0.55	0.28
Cs	22.6	11.3	4.5	5.9	155	35.8
Ba	637	319	127	8.3	309	68.5
La	0.50	0.25	0.10	0.52	3.76	1.16
Ce	1.05	0.52	0.21	1.33	5.86	2.24
Pr	0.12	0.06	0.02	0.15	-	-
Nd	0.42	0.21	0.09	0.51	0.90	0.59
Sm	0.10	0.05	0.03	0.06	0.07	0.07
Eu	0.07	0.04	0.02	0.03	0.02	0.03
Gd	0.10	0.06	0.04	0.03	-	-
Tb	0.02	0.01	0.01	0.01	0.004	0.01
Dy	0.11	0.07	0.04	-	-	-
Ho	0.03	0.02	0.01	-	-	-
Er	0.08	0.05	0.03	-	-	-
Tm	0.01	0.01	0.00	-	-	-
Yb	0.06	0.04	0.03	0.01	0.01	0.01
Lu	0.01	0.01	0.00	0.002	0.001	0.002
Hf	0.13	0.07	0.04	0.11	0.12	0.11
Ta	0.18	0.09	0.04	0.004	0.01	0.01
Pb	1.15	0.57	0.23	0.45	20.95	4.55
U	0.64	0.32	0.13	0.11	1.19	0.33

Fluid compositions were calculated assuming the limited case for fluid devolatilization (Equation 8.7). Assumed mineralogies are spinel peridotite for the mantle (Table 8.4) and Slab Mineralogy 1 (Table 8.3). The mantle and slab compositions are given in Table 8.2.

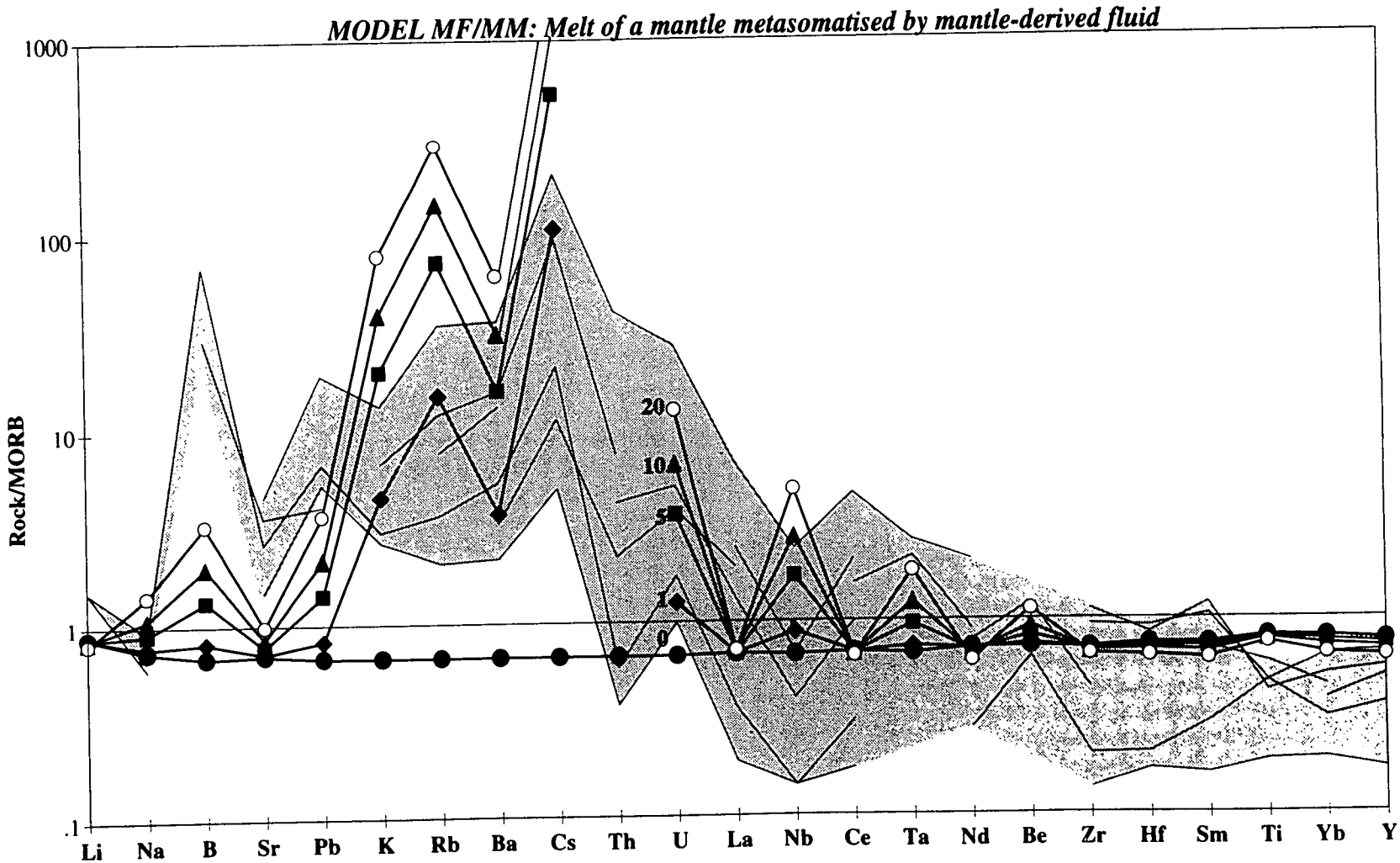

Figure 8.8: Trace-element contents of melts predicted by Model MF/MM (see text), assuming the limiting case for fluid devolatilization (Equation 8.7); mixing between fluid (percentage fluid indicated in figure) and mantle (spinel peridotite of MORB-source composition) followed by 15% melting of the resultant metasomatised mantle.

element concentrations. This resemblance increases with the amount of sediment component included. The melts on their own are, however, too enriched to represent IAV.

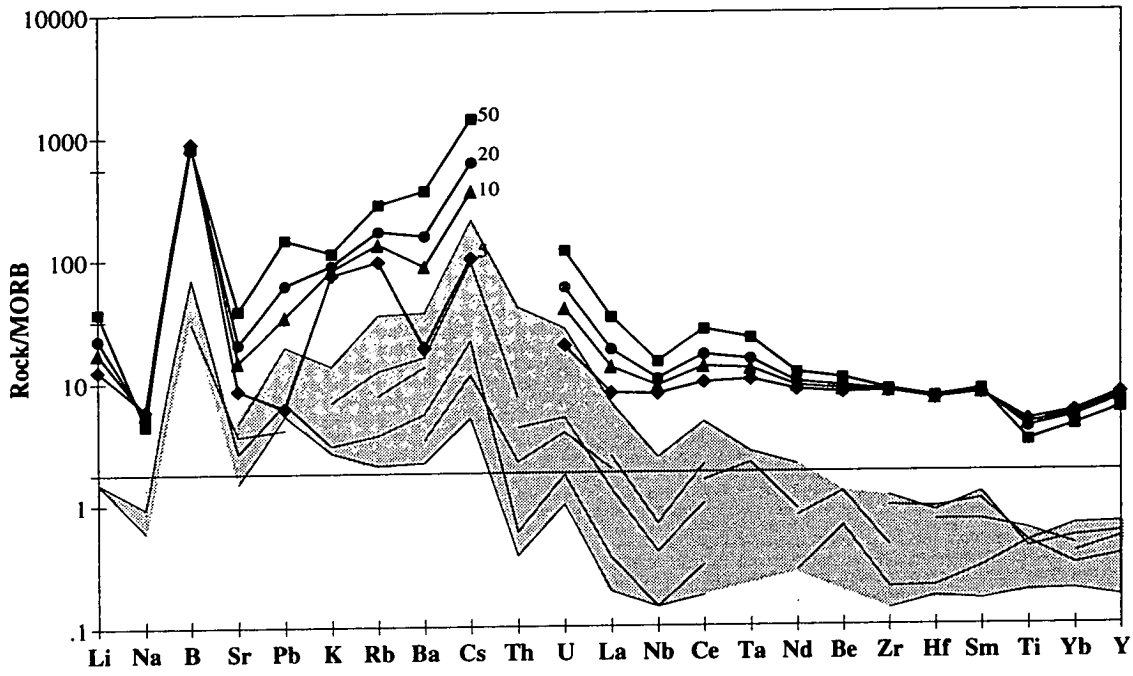

Figure 8.9: Trace-element composition of 10% partial melts of the slab (percentage sediments in slab are indicated) assuming Slab Mineralogy 1 (Table 8.2). The melt compositions was calculated from the non-modal batch melting Equation (Equation 8.1).

MODEL SM/MM. A mixture of slab-derived and mantle-derived melts.

In this scenario the slab dehydrates and partially melts. Liberated water (present as a free phase and/or within the slab-derived melt) acts as a trigger for production of partial melts of the mantle which mix with the slab-derived melt. This model deliberately ignores any transport of elements via the fluid in order to focus on the potential of a combination of unmodified slab and mantle melt to account for IAV compositions.

Figure 8.10 shows the final melt compositions predicted by this model. In this example the slab composition is set at 20% sediments, 80% altered MORB; and 15% partial melting of the mantle (spinel peridotite with MORB-source concentrations) is assumed. The resulting melt is remarkably similar to IAV i.e. enrichment of LILE and enhanced LREE/HREE. Relative depletion in Nb and Ta is also predicted

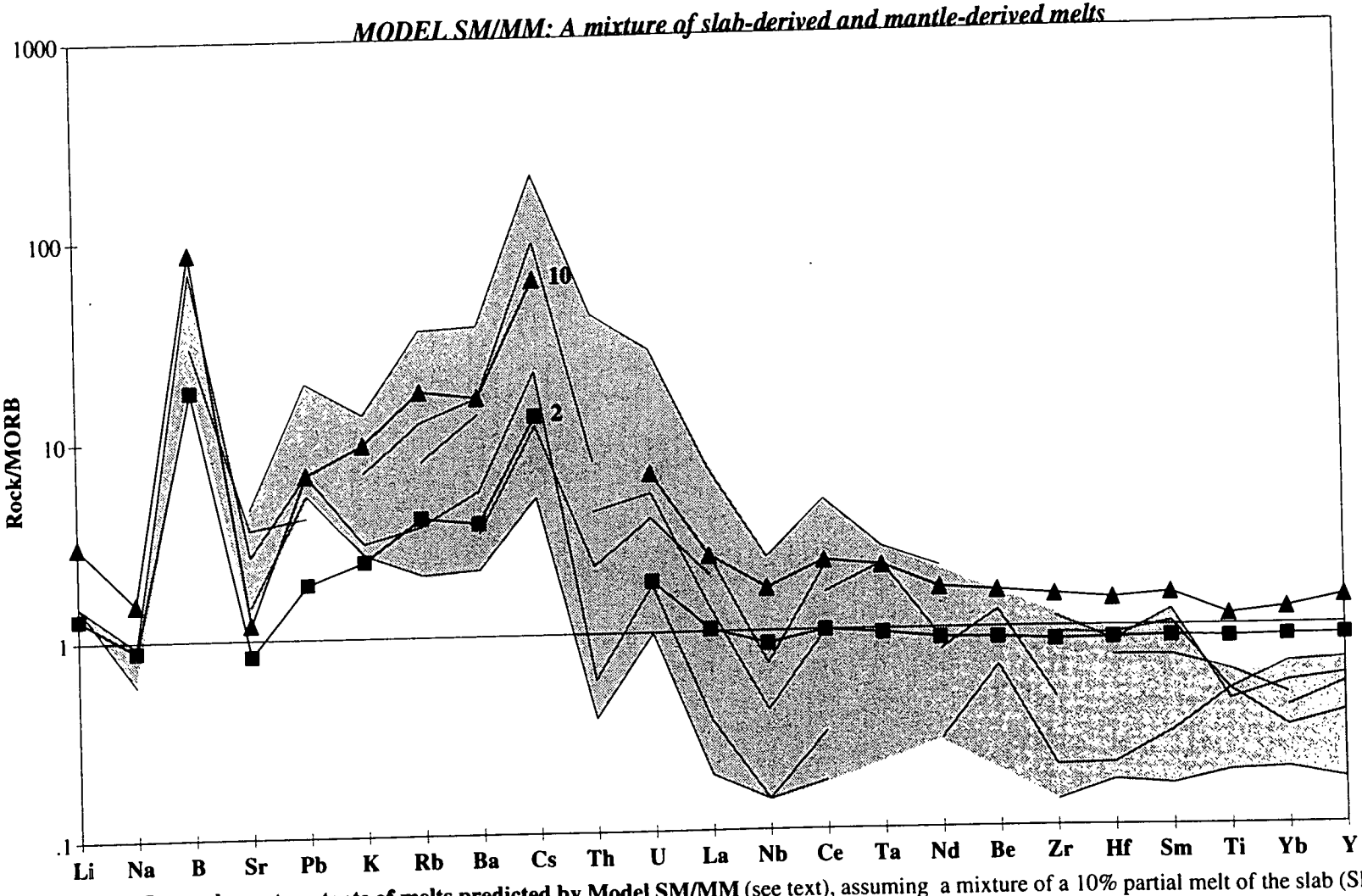

Figure 8.10: Trace-element contents of melts predicted by Model SM/MM (see text), assuming a mixture of a 10% partial melt of the slab (Slab Mineralogy 1; 20% sediments, 80% altered MORB) and a 15% partial melt of the mantle (spinel peridotite with MORB-source composition). The percentage slab melt in the final product is indicated.

although to a lesser extent than in IAV. However this may be due to an underestimate of the amount of residual rutile in the slab.

Although this model seemingly reproduces many of the characteristics of IAV, there are some strong arguments against it:

- Numerical modelling of the temperature regime of subduction zones suggests that the slab will not melt unless it is very young and hot (e.g. Davies & Stevenson, 1992; Peacock *et al.*, 1994). This conclusion is based upon comparison of the calculated temperature regime with the melting point of sediments and basalt. However, others have suggested that a combination of sediments and basalt may have a lower melting point than either end member, and so melting could be possible (e.g. Kelemen *et al.*, 1992).
- Geophysical evidence suggests that there is not a layer of melt above the slab (Matsuzawa *et al.* 1986).

Another serious problem is that the composition of the slab is likely to have changed by the time it reaches the zone of dehydration and/or melt generation (see discussion in Section 8.2.2). If, for example the slab had already lost 75% of its Cs and B (as inferred from metamorphic studies e.g. Bebout *et al.*, 1992) then the melts predicted by these models will be too low in B and Cs to represent IAV. The calculated B/La and Cs/La ratios are shown in Table 8.8.

Table 8.8 Mobile/immobile element ratios in melts predicted by Model 2, involving a) a slab from which there has been no previous loss of mobile elements, and b) a slab from which 75% of Cs and B has been lost previously.

		a) No loss of Cs, B			b) 75% loss of Cs, B		
	IAV	altered MORB	sediments	modelled melt	altered MORB	sediments	modelled melt
B/La	0.79-49.1	14.24	1.67	1.65-2.71	3.56	0.42	0.46-0.69
Cs/La	0.14	0.04	0.15	0.08-0.13	0.01	0.04	0.02-0.03

For a slab which has not previously lost B or Cs, Model 2 predicts B/La ratios which are at the bottom end of the range of values measured in arc rocks. The predicted Cs/La ratio is very similar to the measured value. However, using a more realistic composition for the slab (after loss of the extremely mobile B and Cs) the model severely underestimates the B/La and Cs/La ratios of IAV.

The cause of the striking similarity in composition between the Model 2 melts and IAV must be investigated before discarding this model. In my opinion this is due to the compositional similarity between the oceanic sediments and IAV (Fig. 8.11).

Oceanic sediments contain a detrital component which is derived from continental crust (which itself has been created by subduction-related magmatism). This recycling process will be further exaggerated by the subduction of sediments sourced from the existing arc volcanics.

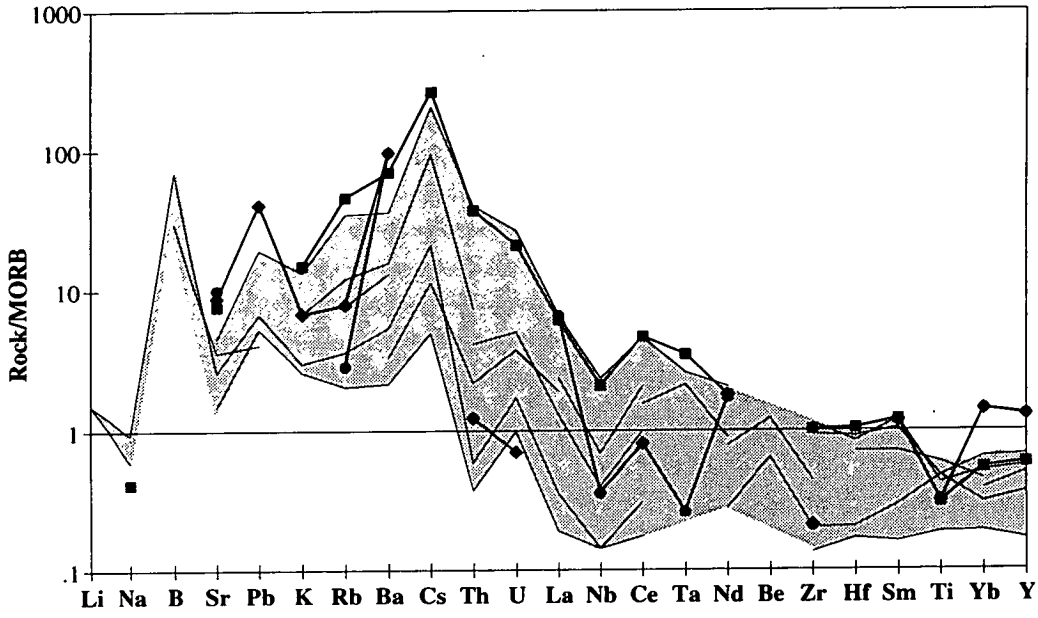

Figure 8.11: Trace-element composition of oceanic sediments (compared with a range of IAV compositions). Symbols represent sediment compositions: squares - Plank & Ludden (1992); circles - Hole *et al.* (1984); diamonds - McCulloch & Gamble (1991).

8.5.1 The role of fluids

Figure 8.12 shows the compositions of fluids in equilibrium with slab sediments and altered MORB. As a starting point, the composition of the slab is assumed to remain constant during metamorphism. Calculated fluid compositions are extremely depleted in HREE and Y, due to the retention of these elements in garnet. HFSE contents are also low and there are relative enrichments in LILE with pronounced enrichments in B, Rb and Cs. The differences between fluid from sediments and from altered MORB include the relatively high Pb content in the sediment-derived fluid and high K in the altered-MORB-derived fluid. The fluid compositions were calculated assuming the limiting case in which the fluid fraction released approaches zero (Equation 8.7). In reality, however, X will be greater than zero although likely to be very small due to the probable low water content in the slab by this stage. Figure 8.13 shows the effect of increasing the fluid fraction during fractional devolatilization of the slab (assuming a slab composed of 20% sediments and 80%

altered MORB). Large fluid fractions contain slightly less of the very fluid-compatible elements Cs, B, Rb, and Be.

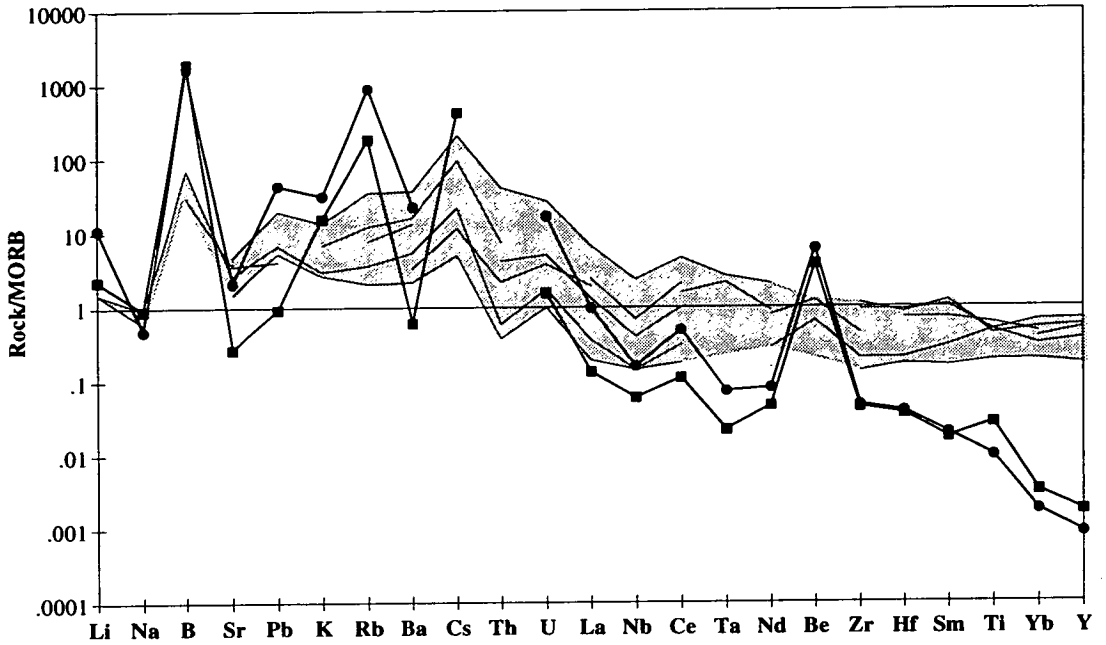

Figure 8.12: Trace element compositions of fluids in equilibrium with sediments and altered MORB, assuming the limiting case (Equation 8.7) for devolatilization of a slab with Slab Mineralogy 1 (see Table 8.3). Symbols: circles - sediments; squares - altered MORB. Symbols: circles - sediments; squares - altered MORB.

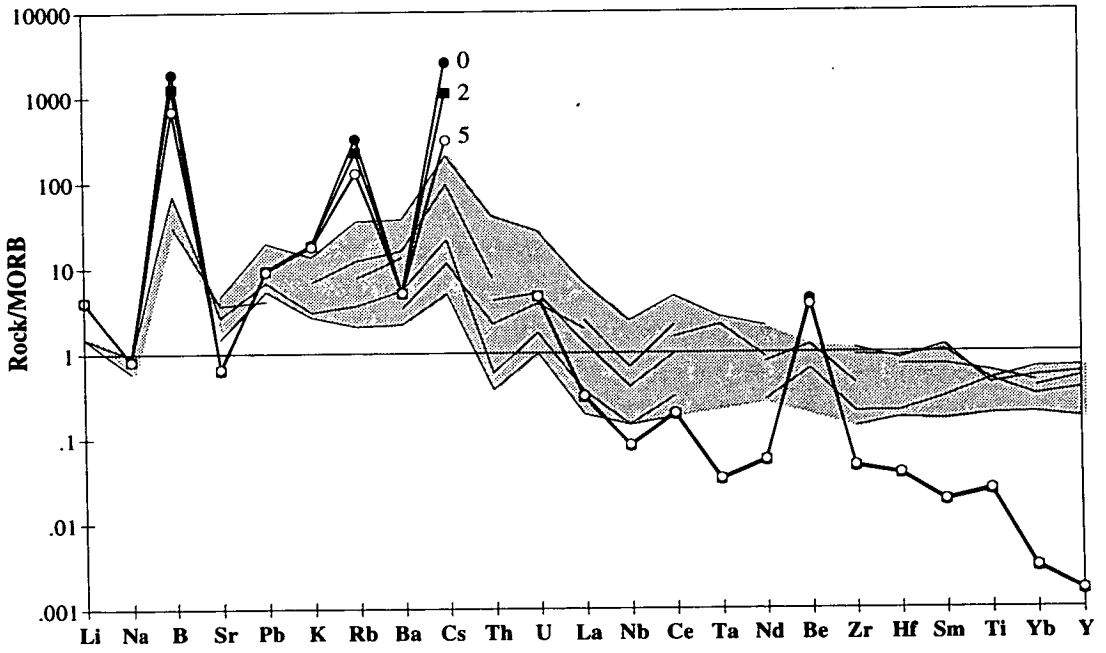

Figure 8.13: Trace element composition of fluid released from the slab by fractional devolatilization (20% sediments, 80% altered MORB with Slab Mineralogy 1; percentage fluid released is indicated in figure).

MODEL SF1/MM. Melt of mantle metasomatised by slab-derived fluid.

In this scenario, the slab retains its composition to depths at which fluid is released into the melting zone. The fluid metasomatises the mantle (by simple mixing) which then melts.

The predicted compositions of partial melts of a mantle metasomatised by slab-derived fluid are shown in Figure 8.14. In this example a slab composed of 25% sediments and 75% altered MORB was chosen. The fluid is released by 2% fractional devolatilization of the slab, and the mantle (spinel peridotite with a MORB-source composition) undergoes 15% partial melting. The predicted melt compositions show the elevated LILE characteristic of IAV. However they are far too enriched in B, Rb, K, Cs, Li and Be; and the predicted Nb, Ta depletion is not extreme enough to represent IAV.

If, however, the slab had already lost much of its mobile element budget during metamorphism, it may be possible to more accurately reproduce an IAV composition using this model.

MODEL SF2/MM. Melt of mantle metasomatised by a slab-derived fluid (after the slab has lost a proportion of mobile elements).

During the early stages of metamorphism, much of the mobile element budget of the slab is inferred to have been lost and therefore unable to be incorporated into the source region of arc magmas. Fluids released from the slab at depth infiltrate the mantle, metasomatising it and triggering melting as in Model SF1/MM.

The concentrations of the mobile elements in the downgoing slab have been numerically reduced until the resulting melts resemble a typical IAV. Assuming a fluid released (by 2% devolatilization) from the slab (composed of 25% sediments, 75% altered MORB) and a mantle with MORB-source composition, the percentage loss prior to the fluid reaching the subarc mantle necessary to reproduce the IAV composition is shown in Table 8.9. and the predicted melt composition is shown in Figure 8.15. The extent of metasomatism and melting is given in the figure caption.

Table 8.9. The inferred loss of mobile elements from the slab during metamorphism, necessary to produce a melt composition similar to a typical IAV (Fig. 8.15).

Element	Li	K	Rb	Cs	B	Be
% loss inferred	50	40	85	85	90	50

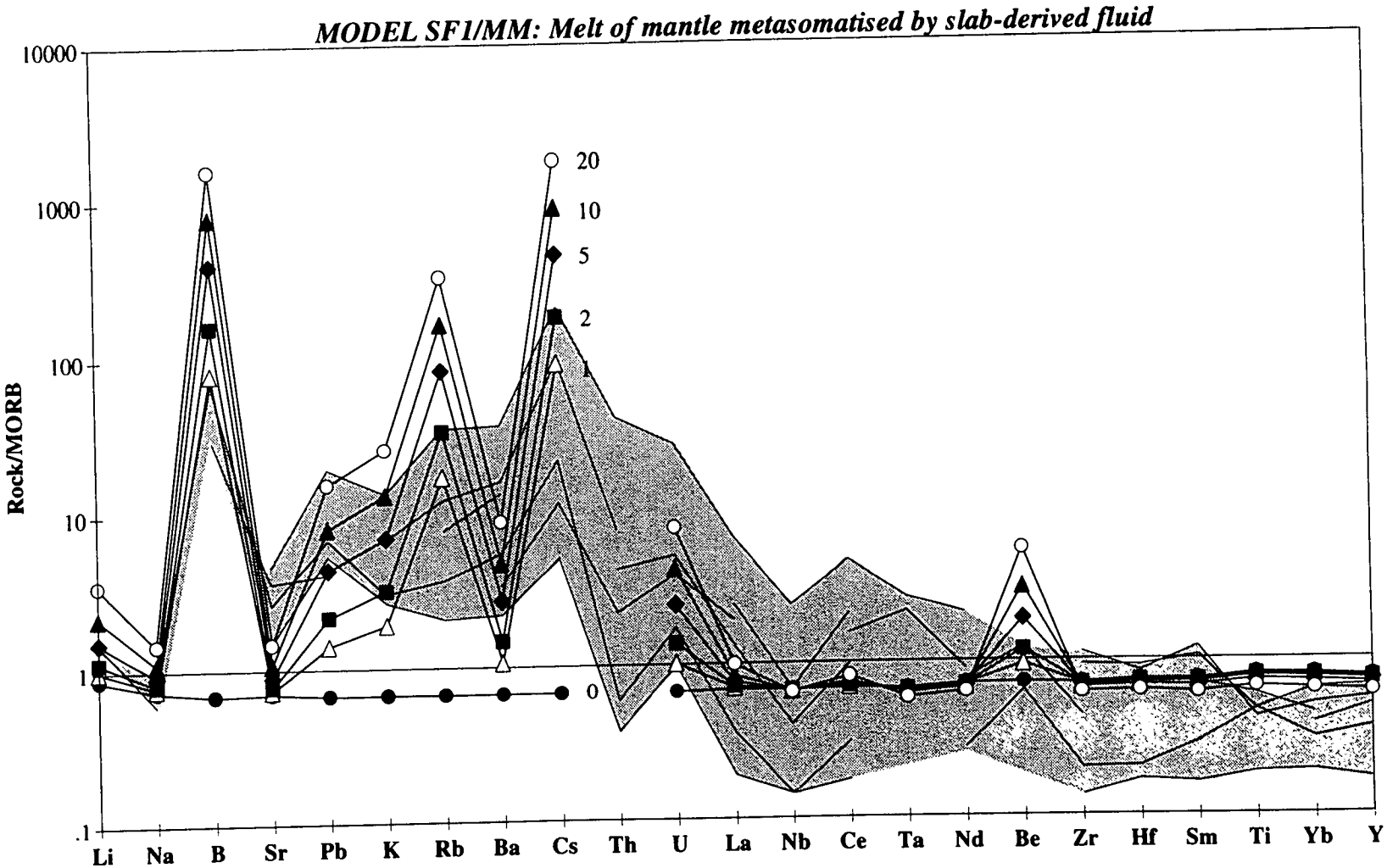

Figure 8.14: Trace-element contents of melts predicted by Model SF1/MM (see text), assuming 2% fractional devolatilization of the slab (Slab Mineralogy 1; 25% sediments, 75% altered MORB). This slab-derived fluid (percentage fluid shown in figure) mixes with the mantle (spinel peridotite; MORB-source composition) which undergoes 15% partial melting.

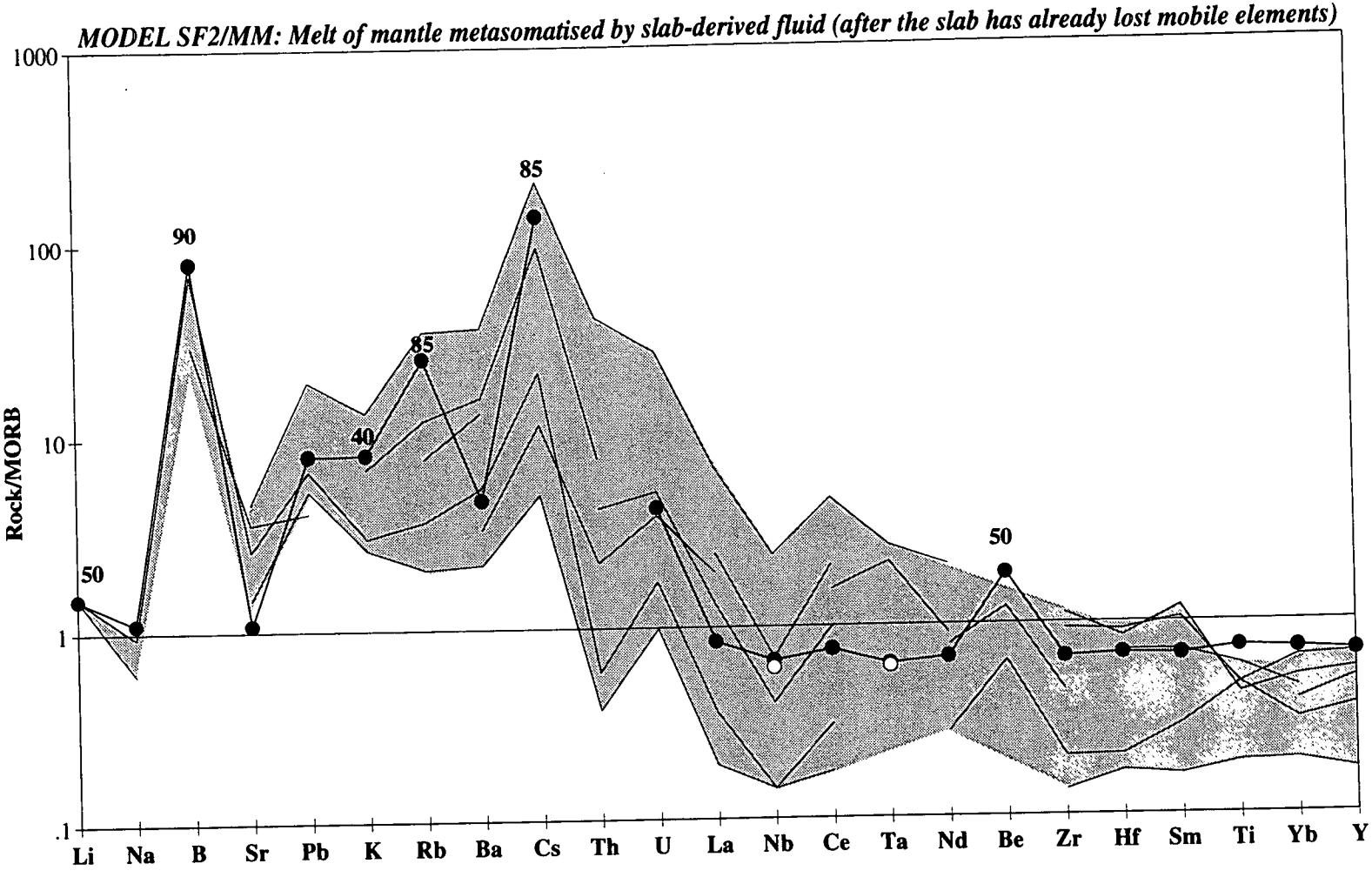

Figure 8.15: Trace-element contents of melts predicted by Model SF2/MM (see text). In this example the fluid from the slab (produced by 2% devolatilization of Slab Mineralogy 1 with 25% sediments, 75% altered MORB) metasomatises the mantle (10% fluid, spinel peridotite, MORB-source composition) which melts (15% melting). The slab had already lost much of its mobile-element budget. The percentage prior loss of elements is indicated in the figure (see also Table 8.9). The open circles represent the Nb and Ta contents in calculated melts assuming that slab-derived fluids contain no Nb or Ta.

The model suggests that there must have been considerable loss of B (90%) and Cs (85%), closely followed by Rb (85%), Li, K and Be. These values are probably not unreasonable given estimates of ~75% loss of B and Cs between 0.5 GPa, 300°C and 1.1 GPa, 750°C (Bebout *et al.*, 1992). According to Bebout *et al.* (*op. cit.*) Rb does not behave in such a manner. However other studies (e.g. Sighinolfi & Gorgoni, 1978) have shown that the Group 1 elements (including Rb) can be lost with increasing metamorphism. The melts predicted by Model SF2/MM resemble IAV in terms of the majority of trace elements. However the Ba content is noticeably low and the predicted Nb and Ta depletions are not particularly marked. Fluid compositions containing no Nb or Ta produce melts which are little different (Fig. 8.15). Therefore, according to this model the REE are not sufficiently mobile to produce the enrichments over HFSE *even if all HFSE are retained in the slab.* However if the mantle composition had already been depleted by prior melt extraction, it is possible to reproduce the Nb and Ta anomalies to some extent, although the depletions relative to the LREE are still not duplicated (Figure 8.16).

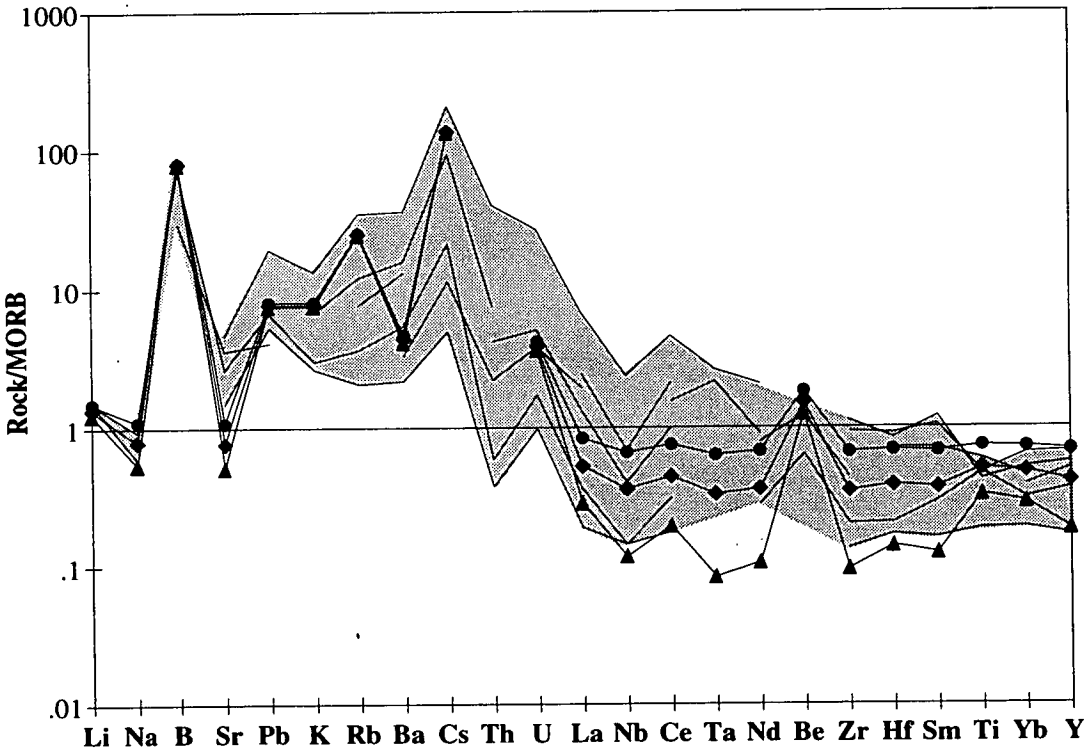

Figure 8.16: The influence of mantle compositions on the trace-element contents of melts predicted by Model SF2/MM. See caption to Figure 8.15 for assumptions used in this example. Three different mantle compositions were assumed (Table 8.2): circles - MORB-source mantle; diamonds - Depleted MORB Source (includes 50% residue after MORB extraction); triangles - Very Depleted MORB Source (includes 90% residue after MORB extraction). Note that as the mantle composition becomes more depleted, the Nb and Ta troughs in the final melt become more marked.

8.5.2 The influence of slab mineralogy

The mineralogy of the residue in the dehydrating slab is unknown. It is therefore necessary to evaluate qualitatively the importance of this uncertainty. Preceding calculations have assumed Slab Mineralogy 1 (Table 8.3) which consists of garnet (50%), cpx and amphibole (both 22.5%), and accessory rutile and sphene (both 2.5%). In Figure 8.17, the relative importance of these minerals is investigated by comparing melt compositions calculated assuming four different slab mineralogies (see Table 8.3).

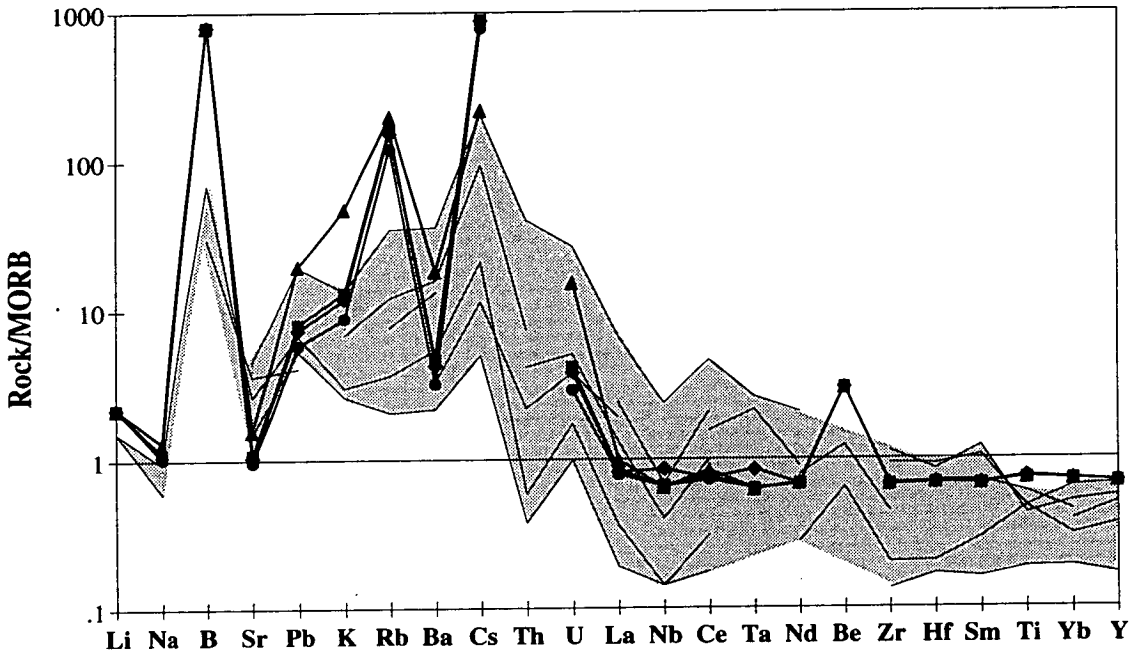

Figure 8.17: Trace-element compositions of melts predicted by Model SF1/MM given 15% melting of spinel peridotite metasomatised by 10% fluid released from the slab. Four different slab mineralogies have been used in the calculations: circles, diamonds, triangles, and squares represent Slab Mineralogy 1, 2, 3, 4, respectively (Table 8.3).

Results show that in general, the calculated melt compositions are not particularly sensitive to the mineralogy of the slab. In particular, the immobile elements (right-hand side of the spidergram) in calculated melts do not alter significantly with slab mineralogy. Decreasing the amphibole content in the model slab (Slab Mineralogy 3) does have some effect on the calculated melts: concentrations of Pb, K, Ba and U increase whereas the concentration of Cs decreases. Unfortunately in the absence of more precise estimates of the slab mineralogy at the pressures and temperatures of interest it must suffice to note that the uncertainty in slab mineralogy will introduce

an error, albeit relatively small, into the calculations. In the following discussions, Slab Mineralogy 1 is assumed.

8.5.3 HFSE anomalies

One popular hypothesis for the origin of the low HFSE contents in IAV is that these elements are retained in the residue after dehydration of the slab (e.g. Saunders *et al.*, 1980; Foley & Wheller, 1990; Hawkesworth *et al.*, 1991). However, in the last section it was shown that the fluid released from the slab is insufficiently rich in other elements to cause the necessary changes to the melt source region (assuming that the mantle is of MORB-source composition), even if *all* HFSE were retained in the slab. It *would*, however, be possible for this process to be responsible for the observed anomalies if the mantle were already sufficiently depleted.

I therefore propose that the HFSE anomalies seen in arc volcanics are a result of prior depletion of the mantle, coupled with addition of a slab-derived fluid phase enriched in LILE and, to a lesser extent, LREE. Calculations suggest that in order to produce the low HFSE contents seen in IAV, the mantle must be extremely depleted (approximately equivalent to a mixture of 80% residue after MORB extraction, and 20% MORB source). Support for this hypothesis includes the extremely depleted compositions of mantle xenoliths from the Southern Luzon Arc, Philippines (Vidal *et al.*, 1989; Defant *et al.*, 1991). Sm contents in these rocks range from 0.017 ppm to 0.2 ppm i.e. considerably more depleted than MORB source (Sm content of 0.51 ppm). Alternative explanations for Nb and Ta anomalies include:

- depletion in these elements by reaction with wall rock during the ascent of melts (Kelemen *et al.*, 1992),
- some input from rutile-saturated partial melts of the slab,
- some input from rutile-saturated partial melts of the mantle.

8.6 SUMMARY OF MODELS OF MELT PRODUCTION

The subducted sediment is similar to IAV in terms of its trace-element composition. Therefore models which invoke bulk recycling of sediment will give deceptively good results. However, evidence from metamorphic rocks suggests that the slab will

change composition as it is subducted, losing a large proportion of fluid-mobile elements. One method by which these elements can be added to the mantle wedge in sufficient quantities to account for the high-LILE signature of IAV is via a fluid phase which preferentially transports mobile elements. This method can successfully account for the concentrations of many trace elements in IAV although it will not explain the Nb and Ta depletion unless the mantle composition had been depleted by prior melt extraction.

The preferred model is thus Model SF2/MM in which the slab loses some of its mobile-element budget during metamorphism. At higher pressures, approaching those at which the slab is underneath the arc, fluid released from the slab infiltrates the mantle, carrying LILE, lesser amounts of LREE, and negligible HREE. The mantle is metasomatised and melts. In many cases, the mantle is inferred to have been depleted by prior melt extraction.
The extent of the loss of mobile elements from the slab during shallow-level metamorphism is not known, although there is evidence from metamorphic rocks to suggest that over 75% B and Cs, and lesser amounts of Be, Rb, K and Pb can be lost via fluids (Section 8.2.2). In the preceding section, the loss of mobile elements was inferred from the IAV composition, which, admittedly, is a somewhat circular argument. More information from metamorphic studies is therefore needed before this model can be developed further.

One major problem with this model is that the predicted Ba contents of melts are too low to represent IAV. This may be due to a number of reasons:

- The Ba content of sediments is highly variable and may have been underestimated in this model.
- The measured partition coefficient for Ba between fluid and melt is low relative to other LILE (e.g. K, Rb, Sr etc.). It is conceivable that in subduction zones there may be certain conditions or a different fluid composition which facilitate the transport of Ba.
- There may be some interaction with mantle-derived fluids which are relatively rich in Ba (Figs. 8.8 and 8.18). However, mantle fluids are predicted to increase the Ta and Nb contents of the source region and are therefore not thought to be the principal reason for the elevated LILE in IAV.

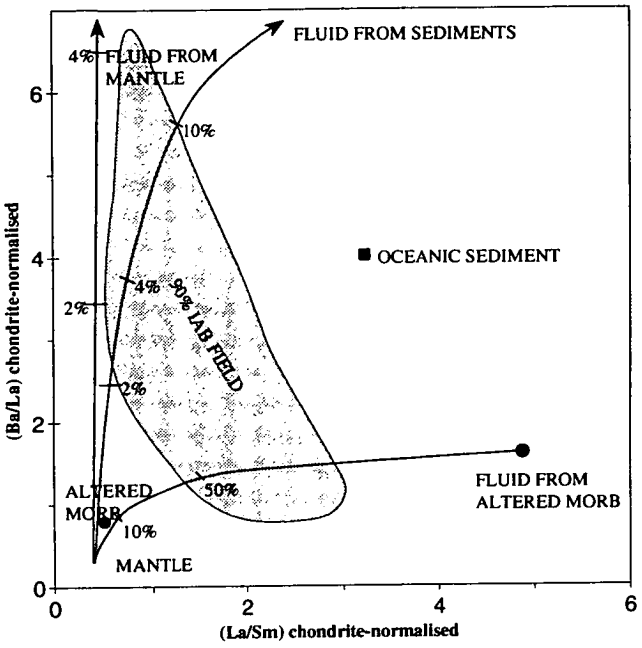

Figure 8.18: Chondrite-normalised Ba/La vs La/Sm plot. Normalising values are from Kay (1980). The field for IAB (>90%) is from Arculus & Powell (1986). Curves show mixing lines between fluid in equilibrium with mantle, with slab sediments or with altered MORB (values refer to percentage fluid).

It was stated at the outset (Section 8.2.4) that the slab/melt partition coefficients used in these calculations are likely to be overestimates (due to the low temperature of the slab and the siliceous nature of possible melts). As a consequence the calculated concentrations of trace elements in slab-derived fluids is almost certainly too high. A more realistic model will therefore invoke a larger proportion of slab-derived fluid in order to produce the changes seen.

In this section I have attempted to develop a general model for the derivation of the trace-element characteristics of IAV. There are many variables which will inevitably change from arc to arc and within an arc. These include the relative importance of subducted sediments in the slab, the amount of fluid released by dehydration, the extent of prior depletion of the mantle, and the percentage melting of the mantle.

8.7 VARIATION IN IAV COMPOSITION

In this section the model (Model SF2/MM) will be used to account for some of the variations in composition within an arc. I have chosen the New Britain Arc as an example.

Woodhead & Johnson (1993) documented the variation in composition of New Britain Arc volcanics overlying a wide range of depths to the Wadati-Benioff Zone

(WBZ). They found that the concentration of HFSE and the relative enrichment in LILE decrease with increasing distance from the arc front. Here, Model SF2/MM has been used in an attempt to account for this variation in composition. By changing four parameters (extent of prior loss of mobile elements from the slab, previous depletion of the mantle, extent of fluid infiltration, and extent of melting), I have modelled the compositions of volcanics from the arc front (~ 70-95 km above the WBZ) and from behind the arc (~ 415-540 km above the WBZ). See Table 8.1 for the compositions of the volcanics. Results (Fig. 8.19) show that the composition of the near-trench volcanics can be achieved by 15% metasomatism (by a slab-derived fluid) of a depleted mantle source followed by 20% melting, whereas the more distal volcanics may have been produced by less partial melting (10%) of a MORB-source mantle after metasomatism by 4% slab-derived fluid.

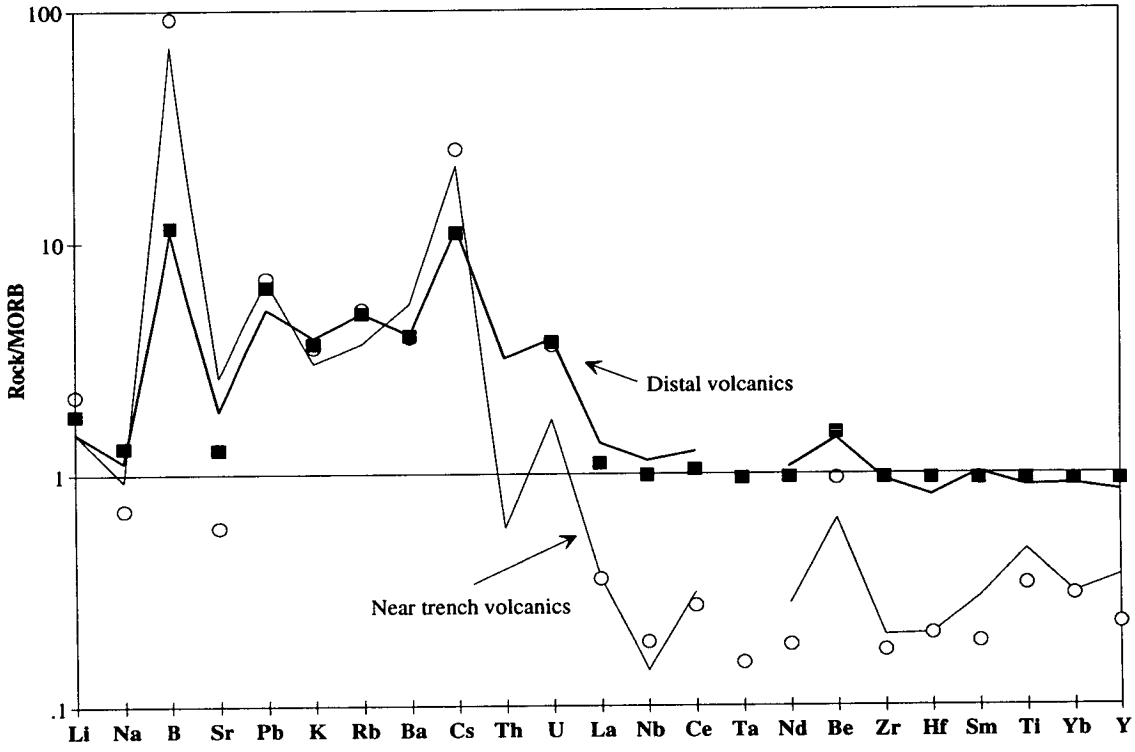

Figure 8.19: Trace-element contents in volcanics from the New Britain Arc (solid lines) compared with modelled melt compositions (symbols). The best-fit parameters (using Model SF2/MM) for both modelled melts are given in Table 8.10.

The inferred prior loss of mobile elements from the slab is consistent for both volcanics, with the exception of B and Cs which appear to be have further decreased in the slab beneath the distal volcanics. The best-fit parameters are shown in Table 8.10. With so many degrees of freedom there is inevitably some trade off between

parameters. Nevertheless, Table 8.10 illustrates the general trends with increasing distance above the WBZ.

Table 8.10: Best fit parameters used in modelling compositions erupted in the New Britain Arc

	Near trench volcanics	*Distal volcanics*
Height above WBZ	~ 70-90 km	~ 415-540 km
Mantle composition	70% residue[1], 30% MORB source	MORB source
Prior loss of elements from slab	70% Be, 75% K, 97% Rb 90% B, 97% Cs	70% Be, 75% K, 97% Rb 98.5% B, 98.5% Cs
% slab-derived fluid	15	6
% melting of the mantle	20	10

[1] residue after 10% melting of MORB source.

Although there are insufficient data to elucidate a rigorous model for melt production in this arc, results suggest that with increasing distance from the arc front, the melts are less slab-dominated. A consequence of less fluid reaching the source area is that the percentage melting is reduced. In addition, the mantle composition is inferred to be more depleted near the arc front, probably due to extensive melt production in this area.

8.8 CONCLUSIONS

In this chapter, models have been developed to account for the trace-element chemistry of IAV. Results show that it is possible to obtain compositions similar to IAV by mixing melts of the slab with melts of the mantle. Bulk entrainment of the slab followed by melting can also yield IAV-like compositions. However, these scenarios are physically unlikely; and the apparent success of these models is thought to be largely due to the similarity between sediments and IAV. Independent evidence from metamorphic rocks suggests that mobile elements are lost from the slab at high levels and are thus unable to be incorporated into the source of melts in subduction zones. Results from this study indicate that fluids released from the downgoing slab are capable of reversing this process by preferentially transporting these mobile elements. Thus these results provide a mechanism for enriching mobile elements in the volcanics despite their prior depletion in the slab.

Therefore, the preferred model for the formation of subduction-related melts involves release of fluids from the subducting slab (which has lost a proportion of its mobile-element budget during subduction) and metasomatism of the mantle wedge. In many cases, the mantle is inferred to have been depleted by prior melt extraction. The influx of fluids triggers melting. Although not quantified, there is a relationship between extent of metasomatism and extent of melting, with large degrees of melting triggered by a large influx of fluid from the slab. This could explain many of the variations seen along and across arcs.

Notwithstanding the limitations of the chosen model (such as the difficulty in constraining relevant partition coefficients, the uncertainties in the slab mineralogy) a number of problems raised by previous studies can be addressed:

- The models have assumed that the mantle composition is similar to or more depleted than the MORB source. The success of the models in generating IAV-like melt compositions is good evidence that the mantle wedge is not composed of the OIB source.
- A residual titaniferous phase in the mantle is not necessary to explain the HFSE anomalies seen in IAV. These results suggest that metasomatism by fluids from the slab (which contains accessory rutile) is capable of producing the requisite depletions in HFSE provided that the mantle had been depleted by prior melt extraction. The low HFSE contents relative to the LREE can be reproduced by addition of a LREE-rich slab-derived fluid to the depleted mantle. Retention of HFSE in a residual phase, such as amphibole, in some cases is not ruled out. For example, it is probable that amphibole is in the source region of some low-degree partial melts in the Lesser Antilles (Thirlwall *et al.*, 1994).
- Many authors have attempted to constrain the proportions of slab and mantle component in IAV, using the trace-element and isotopic compositions of the volcanics, the mantle and melts therefrom, and the subducted slab. Figure 8.20 shows the subduction component[2] in a melt (similar to an IAV from the front of the New Britain Arc) calculated from Model SF2/MM.

[2]The subduction component (Pearce, 1983) in the final melt is defined as the proportion of the trace-element content not derived from a melt of the mantle.

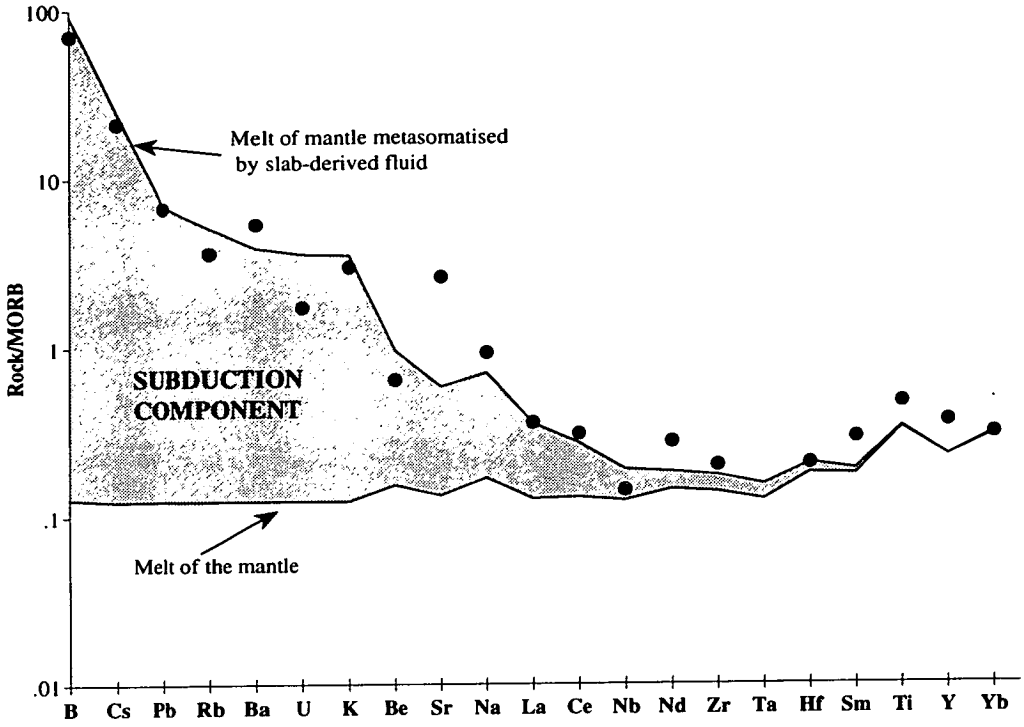

Figure 8.20: Trace-element content of a melt calculated from Model SF2/MM, plotted in order of decreasing subduction component. For each element the subduction component in the final melt is defined as the proportion which has been derived from the slab. See Table 8.11. The compositions of the actual IAV (from New Britain) is shown by the filled circles.

Table 8.11: Subduction component in the modelled melt of Figure 8.20

Element	*subduction component*	*Element*	*subduction component*	*Element*	*subduction component*
B	99.9	Be	84	Zr	20
Cs	99.5	Sr	77	Ta	19
Pb	98	Na	76	Hf	12
Rb	98	La	64	Sm	7
Ba	97	Ce	52	Ti	1
U	97	Nb	34	Y	0
K	96	Nd	22	Yb	0

values in per cent

The calculation shows (Table 8.11) that the LILE (e.g. Cs, Rb, Pb, Ba, U, K) and B are derived almost exclusively from the slab whereas the HREE and HFSE contain a larger proportion of mantle component.

One perplexing feature of IAV is that the slab component inferred from trace elements is much larger than that inferred from isotopes. Calculations using the Pb, Sr and Nd isotopic signatures of the various components suggest that the percentage

of these elements derived from the slab is ~50%, ~20% and ~15%, respectively (Hawkesworth *et al.*, 1991). See Figure 8.21.

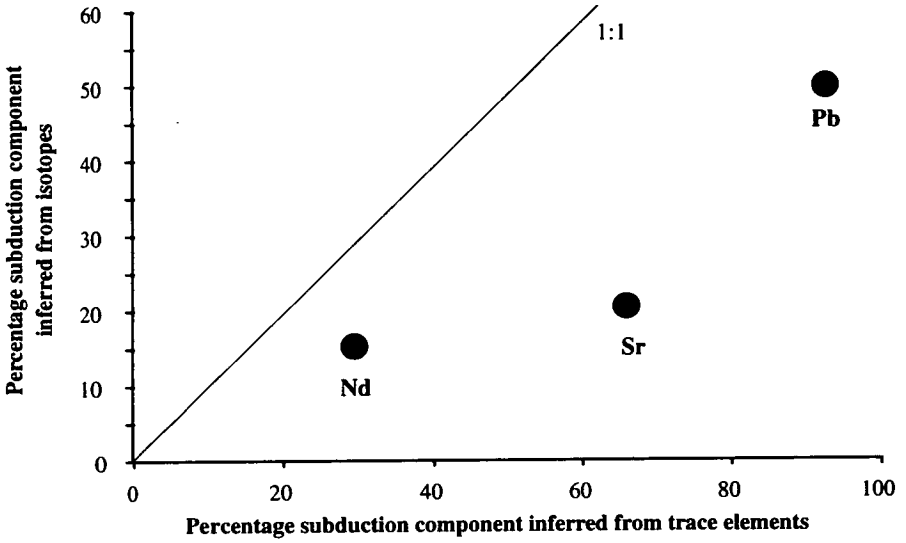

Figure 8.21: Comparison between average subduction component calculated from trace elements and from isotopes.

A possible explanation for this apparent anomaly may be that there is considerable isotopic exchange between fluids and the mantle wedge. Thus, the slab isotopic signature may have been diluted by the time it reaches the zone of melt generation.

- Many studies have concluded that the trace-element and isotopic signatures in IAV are decoupled (e.g. Lin *et al.*, 1990, Francalanci *et al.*, 1993). Within-suite variations often show little correlation between radiogenic isotopes and LILE, leading many authors to suppose that the component responsible for the radiogenic nature of melts is not responsible for the elevated LILE/HFSE. I propose that these observations can be partially explained by a model such as the one developed here in which the extent of melting is governed by the influx of fluids. This can be illustrated with reference to the negative relationship between radiogenic lead (Δ7/4) and Sr/Nd ratio, seen in many volcanics (Ellam & Hawkesworth, 1988).

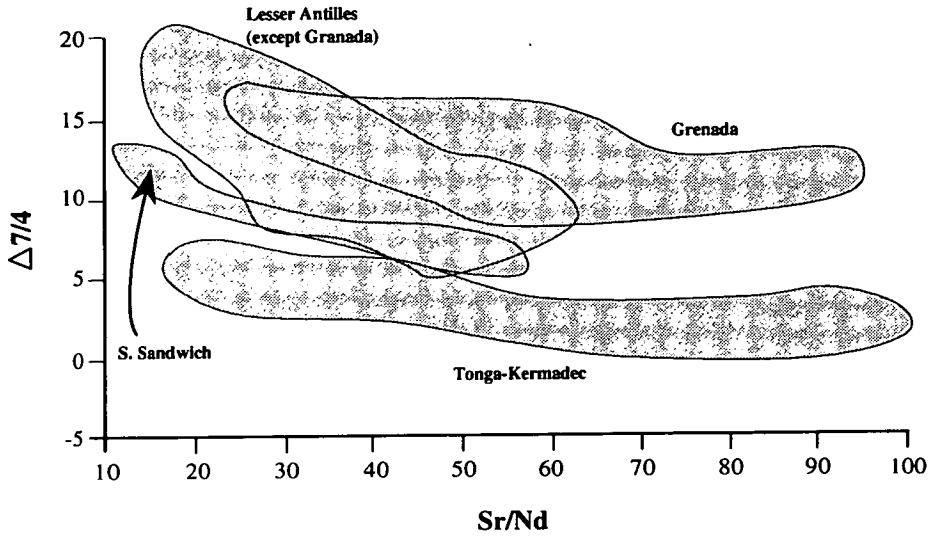

Figure 8.22: Δ7/4 versus Sr/Nd showing negative correlations for various island arcs. From Ellam & Hawkesworth (1988). Δ7/4 is the displacement to high $^{207}Pb/^{204}Pb$ above the Northern Hemisphere Reference Line (Hart, 1984).

Figure 8.23 shows a schematic mixing line between the mantle and a slab-derived fluid. The fluid is rich in LILE (e.g. Sr) and radiogenic lead in comparison to the mantle. Melting of this hypothetical metasomatised mantle will tend to decrease the Sr/Nd ratio whilst preserving the isotopic composition. If the extent of melting is governed by the influx of fluids then the more metasomatised source area (with high Δ7/4) will undergo more melting and so decrease in Sr/Nd to a greater extent than a more mantle-like source area.

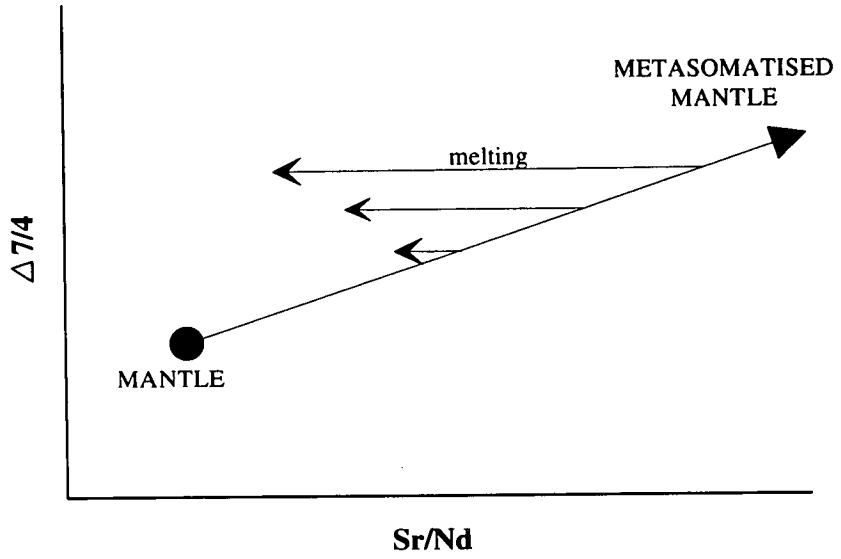

Figure 8.23: A schematic plot of Δ7/4 versus Sr/Nd to illustrate the effect on isotopic and trace-element compositions of calculated melts of increasing the amount of melting with increasing fluid infiltration.

It is conceivable that this, combined with a dilution of the subducted isotopic signature, may account for the observed negative correlation between radiogenic lead (Δ7/4) and Sr/Nd ratio.

- Hawkesworth *et al.* (1991) noted that the high LILE/HFSE ratios were best developed in arc volcanics which possessed low absolute values of HFSE. This observation can be explained with reference to Figure 8.16: the LILE abundances in modelled melts are relatively independent of the composition of the mantle whereas the HFSE abundances are higher in melts of more enriched mantle. Thus high LILE/HFSE ratios and low absolute HFSE contents are developed in volcanics sourced from depleted mantle.

In the discussion so far it has been assumed that hydrous fluid from the slab will reach the source area unaltered (except for its isotopic composition which will have been modified by exchange with mantle rocks). Clearly this assumption must be examined. One school of thought suggests that the mantle acts like an ion-exchange column (Navon & Stolper, 1987), separating trace elements according to their incompatibility. This approach has been combined with equations relating to the geometry of subduction zones (Spiegelman & McKenzie, 1987) to infer the behaviour of individual elements in a subduction zone melt or fluid. (See Chapter 2). The essential conclusion is that highly incompatible elements in the fluid or the melt will effectively travel with the fluid and will reach their destination unaltered, whereas the more compatible elements will effectively be swept down with the mantle and thus the melt or fluid will contain these elements in concentrations determined by the mantle wedge rather than the subducting slab. The value of the partition coefficient, $\bar{D}$(bulk/fluid) beyond which the element is swept down with the matrix, is defined as the critical value.
The results in this chapter can give some indication of the critical value of the partition coefficient during fluid/rock interaction. If, for example, the critical value of partition coefficient were approximately three, then all elements with $\bar{D}$ (bulk/fluid) greater than three would be swept down with the mantle, and would therefore not be capable of metasomatising the melt-source. Those elements with $\bar{D}$ (bulk/fluid) less than three would be capable of metasomatising the melt source. For this example the elements swept down with the matrix would include Ba, Sr, La, Ce. As these elements are clearly enriched in IAV, it is inferred that the critical value of $\bar{D}$ (bulk/fluid) is greater than three. Reference to Figure 8.20 shows that the only elements not enriched in IAV are the HREE and Y. These possess $\bar{D}$ (bulk/fluid)

values far in excess of those of other elements (Table 8.6) and may well be greater than the critical value. The critical value is thus inferred to fall between 60 (Sm) and 150 (Tb).

It is not claimed that this an exhaustive model for melt production in subduction zones. There may be many complicating factors in operation, such as possible melting of the slab in some arcs, bulk entrainment of the slab into the melting zone, or metasomatism by fluids in equilibrium with the mantle. However, in this chapter it has been shown that it is possible to explain many features of IAV by a model in which slab-derived fluids infiltrate the mantle causing enrichments in LILE and LREE, which are transferred to the mantle melts, and ultimately the IAV.

CHAPTER 9

CONCLUSIONS AND FUTURE WORK

CHAPTER 9: CONCLUSIONS AND FUTURE WORK

The origin of the distinctive trace-element signature displayed by IAV has been the subject of many geochemical studies. These have shown that there are at least two sources involved in the genesis of magmas in subduction zones, and that one of these sources is the subducting slab. There is good experimental, theoretical, and petrological evidence to suggest that the majority, at least, of melting in subduction zones takes place in the mantle, triggered by influx of fluid from the slab. It is not clear, however, to what extent these slab-derived fluids are the conduit for the slab component seen in the volcanics. Various authors have argued for the importance of either slab-derived fluids, slab-derived melts, or slab-derived carbonatite melts in the derivation of the high-LILE, low-HFSE signature of IAV. Alternatively, it has been suggested that the trace-element signature results from the retention of some elements, specifically the HFSE, in residual phases during melting of the hydrous mantle wedge. Prior to this project, one major obstacle to the development of models of magma genesis in subduction zones was a scarcity of experimental data relevant to the partitioning of trace elements between melts, fluids, and residual phases during melting or dehydration of the mantle or the slab. The aims of this project were to determine experimentally the major- and trace-element compositions of partial melts and coexisting phases of hydrous peridotite, and to calculate the partition coefficients between aqueous fluid and coexisting phases at high pressures and temperatures.

The project has involved the execution of partial melting and liquidus experiments using solid-media apparatus. Although a large proportion of runs were found to have been contaminated by boron derived from the experimental cell, there were fortunately some experiments that had not been contaminated. The results of the uncontaminated partial melting and reversal experiments make up a study into the compositions of partial melts and residual phases of peridotite under water-saturated conditions at 1.8 GPa. In addition, hydrous fluid compositions were investigated by performing a number of liquidus experiments on a basaltic composition, run in salt cells to avoid contamination by boron.

Three experimental studies have been reported in this thesis: the partial melting of hydrous peridotite, an investigation into the contamination of experiments by boron,

and experimental determination of the partitioning of trace elements between hydrous fluids and basaltic melt.

9.1 SUMMARY OF RESULTS

9.1.1 The determination of major-element compositions of partial melts of hydrous peridotite

Results were taken from a set of experiments performed at 1.8 GPa between 980°C and 1150°C using a hydrated peridotitic starting material. The conditions were water saturated, buffered to an oxygen fugacity of NNO. All phases were analysed for major elements by EPMA, and run products were analysed by SIMS to ensure that they had not been contaminated significantly by boron.

Although there have been many previous studies of partial melting of hydrous peridotite, results are still subject to much debate. In particular, there is disagreement over the major-element compositions of partial melts of water-undersaturated and water-saturated peridotite. This is due to the modification of the melt on quenching, and the consequent difficulty in inferring the equilibrium melt composition from the composition of the interstitial glass. In the present study, a new method for the determination of melt composition was employed. This involved the use of a single-crystal olivine bucket within the capsule. During the experiment, the melt migrates into fractures in the olivine bucket, which subsequently anneal to leave isolated melt inclusions. By assuming that a) the only quench crystals to form are olivine, b) the formation of olivine quench crystals is an equilibrium process, and c) the olivine bucket does not react with the starting material, melt compositions were reconstructed numerically from the melt inclusion compositions by incremental addition of olivine until the Fe/Mg olivine/melt exchange coefficient of Roeder & Emslie (1970) was re-established. For the initial calculations, the value of this exchange coefficient was assumed to be 0.3.

The equilibrium melt compositions from three experiments were calculated from melt inclusion analyses. The spread in compositions exhibited by the melt inclusions was lessened but not eradicated after addition or subtraction of olivine. Several reversal experiments were performed using the average calculated melt composition from ED143, which had been performed at 1.8 GPa, 1020°C, and had produced

olivine, orthopyroxene, clinopyroxene, amphibole, spinel, rutile, and ilmenite in addition to melt. Encouraging results were obtained from reversal experiments run in olivine buckets: these yielded crystals of orthopyroxene, clinopyroxene, and amphibole, all of which were stable in the forward experiment. However, garnet, which had not been stable in the forward experiment, was also formed. Furthermore, it appeared from mineralogical textures that the olivine bucket had reacted with the melt to form orthopyroxene and clinopyroxene. It was concluded that the calculated melt composition may have been too poor in olivine component. Reversal experiments without the use of an olivine bucket were therefore performed. Varying amounts of additional olivine (Fo_{90}) component were included in some capsules. Results show that it required between 10 wt% and 20 wt% additional olivine to stabilise equilibrium olivine. The phase assemblage of the original experiment was not, however, reproduced, despite lowering the run temperature to encourage crystallisation. Significantly, no orthopyroxene was formed in any of the reversal experiments performed without olivine buckets. In addition, phases formed in the reversal experiments were consistently more aluminous than those produced in the forward experiment; the Mg nos. of all reversal phases were higher than those in ED143; and there were consistent differences between phases formed in reversal experiments and those formed in the forward experiment in terms of Na_2O, NiO (both lower in the reversal experiments), and MnO (higher in the reversal experiments). The results of the reversal experiments therefore suggest that the true equilibrium melt composition is richer in olivine component than that originally estimated. Recalculation of the equilibrium melt composition from the melt inclusion compositions assuming that the relevant value of the Fe/Mg olivine/melt exchange coefficient is 0.4 yields a more olivine-rich composition, and it is suggested that this is likely to be closer to the true melt composition. This is supported by results from reversal experiments that produced equilibrium olivine and melt, from which values for the Fe/Mg olivine/melt exchange coefficient of approximately 0.4 were inferred.

Melts from three experiments have been calculated assuming a value of 0.4 for the Fe/Mg olivine/melt exchange coefficient. Two relatively low-degree partial melts (both in equilibrium with amphibole) are similar to a basaltic andesite and a basalt. A higher-degree partial melt (in equilibrium with olivine and orthopyroxene) has a high-SiO_2, high-MgO composition similar to a boninite.

Further reversal experiments are required to establish the true melt composition from ED143. In particular, it would be instructive to run more experiments without an olivine bucket, possibly lowering the temperature to encourage crystallisation, and

using a starting composition more enriched in olivine component and less enriched in alumina.

To conclude, the determination of partial melt compositions of peridotite from synthetic melt inclusions in olivine has yielded encouraging results in the water-saturated system, but to date the calculated melts compositions have not been verified and the method may need to be refined. Until further reversal experiments are performed, the melt compositions are by no means certain, and are not in my opinion sufficiently accurate to warrant use in modelling calculations.

9.1.2 Contamination of solid-media experiments by boron

Many experiments in this study were found, in retrospect, to have been contaminated by boron. The extent of contamination varies within each run product and between experiments, with boron contents reaching up to several thousand parts per million in many cases. In three experiments, ingress of boron had been so extensive that a new Mg,Cr,Ti,Al-borate mineral had been formed.

Comparison of experiments contaminated to different extents shows that boron acts as a flux, promoting melting and causing compositional changes expected from an increase in temperature (and consequent increase in the degree of melting). Evidence for this includes the higher than expected Mg nos. exhibited by the rims of orthopyroxenes and olivines, and by some large crystals of these minerals present at the top of contaminated charges. It is concluded that the effects of boron are sufficient to render the results from contaminated experiments unreliable.

The boron was derived from the boron nitride components in the cell and is thought to have entered through rips or holes in the capsule walls, caused by puncturing of the platinum by the rigid olivine bucket. Diffusion of boron through the platinum walls may also have occurred, although any effects are obscured by the more extensive contamination due to mechanical failure.

Many experimentalists in the past have used boron nitride or boron-bearing Pyrex components in solid-media cells. At first glance it may appear that the problems that have affected this study are not directly relevant to other work, as it is thought to be the rigid olivine bucket in these experiments that was the cause of the problem. However, the following observations may have important implications for other studies:

1. Boron cannot be detected by the electron microprobe - the electron probe failed to detect boron even when it was present in major-element levels. Past run

products were seldom analysed by SIMS and therefore it is likely that boron contamination would have remained undiscovered.

2. Water does not always escape from contaminated capsules - traditionally the retention of water during an experiment has been adequate proof that the capsule remained intact and that the experiment was a success (e.g. Green, 1973). However in this study there were many capsules which retained water, and were also found to contain significant levels of boron. This method of judging a capsule's success is therefore fallible.

Therefore, if capsule failure and contamination by boron had occurred in previous experiments, it may not have been detected. Any such contamination may have significantly affected results, causing more melting than would otherwise have occurred.

9.1.3 Partitioning of trace elements into hydrous fluids

In many of the water-saturated experiments performed in this study, melt and aqueous fluid coexisted at equilibrium. The quench products of these phases were easily distinguishable, and have been analysed by EPMA and SIMS.

The fluid quench products appear to consist entirely of glass spheres of various sizes (up to 125 μm in diameter), which are rich in silica and alumina, and relatively rich in Cs, Rb, and B. There is considerable variation in composition between glass spheres, with the larger spheres more typical of the melt composition. Within the largest glass spheres there is a variation in composition, which, coupled with their texture, suggests that they are composed of two phases with compositions similar to the melt and to a small glass sphere. This observation is supported by mass-balance calculations. It is concluded that the cores of large glass spheres are composed of melt, which has acted as a nucleation site for the overgrowth of fluid quench. The small glass spheres are assumed to be free of a melt core and are taken to be representative of the fluid composition at equilibrium. It is acknowledged that this is an oversimplification as there is some evidence for exchange of elements (particularly the alkalis) between the melt and fluid quench.

The amount of water in the melt at equilibrium, inferred from the results of liquidus experiments with varying initial water contents, is 25±5 wt%. This value has been used in conjunction with mass-balance results to calculate that there is 12.7±4.1 wt% solute in the fluid at equilibrium, which is consistent with estimates derived from previous experimental studies (e.g. Schneider & Eggler, 1986).

Combining the calculated water contents with the trace-element contents of the average melt and of a small glass sphere, the partition coefficients between fluid and melt, D (fluid/melt), have been determined. For the elements measured, only Cs (D = 1.33) has a partition coefficient greater than unity. Rb (D = 0.87) and K (D = 0.56) also possess relatively high values of D (fluid/melt) as do Na (D = 0.21), B (D = 0.13) and Be (D = 0.11). The REE (D < 0.009, except Eu for which D = 0.019) and Y (D = 0.0083) possess very low values of D (fluid/melt). The HFSE are intermediate with Nb and Ta possessing D (fluid/melt) values of 0.071 and 0.031, respectively. Previous studies had indicated that the mobility of an element in aqueous fluid at high pressure and temperature was positively correlated with its ionic radius (Tatsumi *et al.*, 1986; Brenan & Watson, 1991). Results from the present study, for the elements in common with those measured by Tatsumi *et al.* (*op. cit.*) and Brenan & Watson (*op. cit.*), show that there is indeed a positive relationship between D (fluid/melt) and ionic radius. However, the larger number of trace elements measured in the present study allow a more thorough investigation of this relationship. For the monovalent ions, D (fluid/melt) increases steadily with ionic radius. However, ions of higher charge do not display this trend: divalent ions possess fairly constant D (fluid/melt), perhaps lying on a broad inverted parabola. D (fluid/melt) for the trivalent ions exhibits a roughly negative correlation with ionic radius, with the REE and Y possessing extremely low values, and Cr, Al, and B possessing higher values. There is a similar negative correlation among the 4+ ions. No relationship between D (fluid/melt) and ionic radius can be seen for the 5+ ions as these include only two examples (Nb and Ta).

Results from individual experiments, including liquidus experiments with a basaltic starting material and a partial melting experiment with a perdidotitic starting material, are extremely consistent.

Large olivine crystals were produced in two experiments. An analysis of olivine has been combined with an analysis of a small glass sphere to calculate partition coefficients between olivine and fluid. The relationships between D (olivine/fluid) and ionic radius exhibited by the divalent and the trivalent ions are very marked and can be explained in terms of the lattice sites of olivine.

There is some uncertainty in the absolute values of the calculated partition coefficients. However, the relative fractionation between elements is independent of the choice of the absolute values, and is considered to be reliable.

9.2 IMPLICATIONS FOR SUBDUCTION-ZONE MAGMATISM

Although the major- and trace-element compositions of partial melts of hydrous peridotite were not considered reliable enough to merit use in modelling calculations, the trace-element partition coefficients between aqueous fluid and basaltic melt, and aqueous fluid and olivine have been used, together with published values of D (mineral/melt), to infer the partition coefficients between aqueous fluid and coexisting minerals. Using these values, the trace-element compositions of aqueous fluids in equilibrium with the slab and the mantle (of chosen compositions and mineralogies) have been calculated. Note that it was assumed for the purposes of modelling, that the slab was composed of altered MORB and oceanic sediment. Although there are many assumptions and simplifications involved, this method has enabled a more detailed prediction of the composition of slab-derived fluids than have been made by previous workers using the more limited experimental data available previously. Slab-derived fluids are estimated to be extremely rich in B, Rb, and Cs (all enriched relative to MORB by over a factor of 100). Pb, K, Ba, U, Li, and La are also predicted to be enriched in slab-derived fluids relative to MORB. LREE have higher contents than do HREE in the predicted fluid, although in general the REE are extremely poor in the fluid. The behaviour of the HFSE is partly dependent on the presence or absence of rutile as a residual phase, although even with rutile absent in the slab, the predicted contents of Nb and Ta in the fluid are low. The trace-element compositions of some IAV can be reasonably well reproduced by a model in which the slab-derived fluid mixes with the mantle (of the MORB-source composition) which subsequently melts (assuming non-modal batch melting of a spinel peridotite or amphibole peridotite mineralogy). However, some mobile elements (especially Cs, B, and Rb) are considerably higher in the calculated melts than they are in IAV. Independent evidence from metamorphic rocks (e.g. Bebout *et al.*, 1992; Moran *et al.*, 1992) has suggested that a large proportion of Cs and B in the slab may have been lost prior to it reaching subarc depths. A process such as this may account for the observed discrepancy between calculated melts and the volcanics. A model is therefore preferred whereby some of the mobile elements in the slab are lost prior to the recycling process. Fluids are released from the slab at subarc depths (or thereabouts) and metasomatise the mantle wedge which subsequently melts. Although this model can successfully reproduce some IAV compositions, it would require unreasonably large degrees of melting to reproduce the very low levels of immobile elements in many IAV compositions. Rather, it is

suggested that these compositions were formed by metasomatism and melting of a mantle that had already been depleted in incompatible elements by prior melt extraction.

It is suggested that the range in composition of IAV, both within suite and between suite, can be attributed to variations in the following parameters:

- The composition of the slab, i.e. the composition of the constituent sediments and altered MORB, and the relative proportions of these constituents subducted.
- The composition of the mantle wedge, i.e. the extent of depletion in incompatible elements by previous melt extraction, and the possible rare occurrence of OIB-source mantle.
- The extent of influx of fluid into the mantle wedge. This is probably controlled by the temperature regime within the subduction zone (Leeman *et al.*, 1994).
- The amount of melting undergone by the mantle wedge, which is likely to be a function of the fluid input.

As an example, the compositions of volcanics from the front of the New Britain arc (Woodhead & Johnson, 1993), and from behind this arc (i.e. volcanics erupted near the trench, and far from the trench) were modelled. It is suggested that the near-trench volcanics, which are very depleted in REE and enriched in LILE, were produced by melting of a source that had been severely depleted in incompatible elements by previous melt extraction, had been metasomatised by slab-derived fluid, and subsequently melted (20% melting). The more distal volcanics are less enriched in LILE and more enriched in the immobile elements (REE, HFSE). These are inferred to have been produced by melting of a less depleted mantle composition which had been metasomatised to a lesser extent by the slab-derived fluid, and had consequently undergone a smaller amount of melting (10%).

It is now possible to attempt to answer the questions posed at the beginning of this thesis (Chapter 2, p12).

Q How is material transported from the slab to the mantle melting zone? Can slab-derived fluids significantly modify the composition of the mantle wedge?

A Although slab-derived melts may be capable of producing the trace-element characteristics seen in IAV, it is not likely that the slab will melt in the majority of subduction zones (Peacock *et al.*, 1994; Matsuzawa *et al.*, 1986). Results from this study show that aqueous fluids are capable of transferring trace elements from the slab to the mantle wedge, and of causing significant modification of the mantle wedge, which becomes richer in LILE and LREE.

Q Why in some arcs is there an apparent decoupling between isotopic compositions and incompatible-element abundances and ratios (see Section 2.3.2)? Is there more than one slab component to account for this decoupling? Is part of the LILE signature derived from fluids in equilibrium with the mantle?

A It is possible that part of this apparent decoupling may be due to the variation of metasomatism and melting along an arc. In areas with high fluid fluxes, the mantle wedge will acquire an elevated LILE/REE signature, and will be isotopically shifted towards high $^{87}Sr/^{86}Sr$, low $^{143}Nd/^{144}Nd$ and high isotopic Pb ratios. However, another effect of the high fluid flux will be to produce relatively high-degree partial melts. A consequence of the differing compatibilities of elements during mantle melting is that as melting is increased, the LILE/REE ratios of melts decreases. In areas of low fluid flux, the isotopic composition of melts will be nearer to that of the unmodified mantle (i.e. relatively low $^{87}Sr/^{86}Sr$ and Pb isotopic ratios, and relatively high $^{143}Nd/^{144}Nd$). Although the LILE/REE ratio of the mantle wedge will be relatively low in areas of low fluid flux, there will be relatively low degrees of melting and consequently less decrease of LILE/REE in melts produced. Taking this argument to its extreme, melts from areas of high fluid flux will be isotopically enriched with low LILE/REE, whereas melts produced from areas of high fluid flux will be less isotopically enriched, with higher LILE/REE. This is not thought to be a comprehensive solution, and the possibility of other sources for the high-LILE signature has not been ruled out. These could include fluids from isotopically unenriched parts of the slab, or fluids in equilibrium with the mantle, which are predicted to be rich in LILE.

Q What is the composition of the mantle wedge? Is it more similar to the OIB source, the MORB source, or the MORB source which has been depleted in incompatible elements by previous melt extraction?

A Results have shown that it is possible to reproduce the IAV trace-element signatures assuming a MORB-source (or depleted MORB-source) mantle composition. In my view, this eliminates the need for the presence of OIB-source mantle in subduction zones, although this is not ruled out in special cases. Therefore the mantle wedge is of MORB-source composition, although it has been depleted in incompatible elements by previous melt extraction in many arcs.

Q Do the low HFSE contents in IAV reflect low HFSE contents in their source, or are they a result of retention of these elements in a residual phase during partial melting?

A There are strong geochemical arguments against the presence of a residual HFSE-bearing phase during melting to produce IAV. Unfortunately it did not prove possible to compare the trace-element contents of differing degrees of partial melts of hydrous peridotite. Neither was it possible to determine values of D (amphibole/melt), which are still needed for a thorough assessment of the influence of residual amphibole during melting of hydrous mantle. Nevertheless, results using values of D (fluid/melt) derived from the present study, indicate that it is possible to produce low Nb contents in IAV by the addition of a LILE-rich, LREE-rich fluid to a mantle which had been extremely depleted in incompatible elements by previous melt extraction. This method cannot, however, reproduce the very low HFSE/LREE ratios seen in some arcs. Another method must therefore be in operation to produce these compositions. Small amounts of rutile-saturated melts of the slab or of the mantle in addition to the large-degree melting of the mantle may be one solution. Another possibility is that the HFSE are removed by reaction between ascending melts and the surrounding mantle (Kelemen *et al.*, 1993).

9.3 FUTURE WORK

Melt generation in subduction zones is still poorly constrained, and there is much scope for future work. This could include further evaluation of the geochemical characteristics of IAV, concentrating in particular on the HFSE contents, and paying special attention to spatial and temporal variations in composition. Metamorphic studies such as those in the Catalina schist (Bebout *et al.*, 1992) have provided information regarding the mobility of trace elements in slab-derived fluids at pressures lower than those of the subarc slab. More information from such studies would be extremely useful, especially as the results of this project suggest that a large proportion of mobile elements must be lost from the slab prior to recycling of slab-derived material through the mantle wedge.

Experimental studies, however, can arguably provide the most significant information on this subject. In the present study, the trace-element composition of

aqueous fluid at 1.85 GPa was determined from analysis by SIMS of fluid quench products. The success of this method provides the opportunity for many similar studies of fluid composition. Further work could include similar experiments at higher pressure, as it is well known that pressure can affect solubility and partition coefficients (Mysen, 1979; Ayers & Watson, 1991). Another profitable set of experiments could be performed using a hydrous slab analogue as a starting material. Analysis of fluid quench products from subsolidus and supersolidus experiments could provide extremely relevant information regarding the composition of slab-derived fluids. This would also provide information regarding the mineralogy of the slab at depth.

One of the aims of this project was to determine the effect of water on the major- and trace-element compositions of partial melts of peridotite. Unfortunately this was not achieved in the time available. Consequently, in the modelling calculations, partition coefficients largely relating to the melting of anhydrous peridotite have been used. However, it is still considered important to investigate the major- and trace-element contents of partial melts of peridotite under water-saturated and water-undersaturated conditions. Before this can be achieved, it is necessary to refine the technique for the determination of melt composition using an olivine crystal to trap melt inclusions. To avoid puncturing of capsules and contamination of boron, olivine buckets should be thoroughly rounded, possibly with a very small hole to contain the starting mixture. Several reversal experiments must also be performed in order to evaluate the calculated melt compositions. In addition, it may be useful to perform similar experiments using crystals of other minerals to trap melt inclusions.

After performing the suggested experiments, it would be possible to model much more accurately the trace-element compositions of melts produced in subduction zones.

REFERENCES

REFERENCES

AKIMOTO, S. & AKAOGI, M. 1980. The system Mg_2SiO_4-MgO-H_2O at high pressures and temperatures- possible hydrous magnesian silicates in the mantle transition zone. *Phys. Earth Planet. Int.* **23**, 268-275.

ALLEN, J.C.; BOETTCHER, A.L. & MALAND, D.G. 1975. Amphiboles in andesite and basalt: I. Stability as a function of P-T-fO_2. *Am. Min.* **60**, 1074-1087.

ALT, J.C.; FRANCE-LANORD, C.; FLOYD, P.A.; CASTILLO, P. & GALY, A. 1992. Low-temperature alteration of jurassic ocean crust, site 801. *Init. Rep. DSDP* **129**, 415-427.

ANDERSON, R.N. & BURNHAM, C.W. 1965. The solubility of quartz in supercritical water. *Am. J. Sci.* **263**, 494-511.

ANDERSON, R.N.; DeLONG, S.E. & SCHWARZ, W.M. 1978. Thermal model for subduction with dehydration in the downgoing slab. *J. Geol.* **86**, 731-739.

ANDERSON, R.N.; UYEDA, S. & MIYASHIRO, A. 1976. Geophysical and geochemical constraints at converging plate boundaries- part I: dehydration in the downgoing slab. *Geophys. J. R. Astr. Soc.* **44**, 333-357.

ANDREWS, D.J. & SLEEP, N.H. 1974. Numerical modelling of tectonic flow behind island arcs. *Geophys. J. R. Astr. Soc.* **38**, 237-251.

AOKI, K. 1970. Petrology of kaersutite-bearing ultramafic and mafic inclusions in Iki Island, Japan. *Contrib. Mineral. Petrol.* **25**, 270-283.

AOKI, K.; FUJINO, K.; AKAOGI, M. 1976. Titanochondrodite and Titanoclinohumite derived from the Upper Mantle in the Buell Park Kimberlite, Arizona, USA. *Contrib. Mineral. Petrol.* **56**, 243-253.

ARCULUS, R.J. & POWELL, R. 1986. Source component mixing in the regions of arc magma generation. *J. Geophys. Res.* **91**, 5913-5926.

ARCULUS, R.J. & WILLS, K.J.A. 1980. The petrology of plutonic blocks and inclusions from the Lesser Antilles island arc. *J. Pet.* **21**, 743-799.

AYERS, J.C.; BRENAN, J.B.; WATSON, E.B. & WARK, D.A. 1992. A new Capsule Technique for Hydrothermal Experiments using the Piston-Cylinder Apparatus. *Am. Min.* **77**, 1080-1086.

AYERS, J.C. & WATSON, E.B. 1991. Solubility of apatite, monazite, zircon, and rutile in supercritical aqueous fluids with implications for subduction zone geochemistry. *Phil. Trans. R. Soc. Lond. A* **335**, 365-375.

BAKER, M.B. & STOLPER, E.M. 1994. Determining the composition of high-pressure mantle melts using diamond aggregates. *Geochim. Cosmochim. Acta.* **58**, 2811-2827.

BALLHAUS, C.; BERRY, R.F. & GREEN, D.H. 1990. Oxygen fugacity controls in the Earth's upper mantle. *Nature* **348**, 437-440.

BALLHAUS, C.; BERRY, R.F. & GREEN, D.H. 1991. High-pressure experimental calibration of the olivine-orthopyroxene-spinel oxygen geobarometer - implications for the oxidation state of the mantle. *Contrib. Mineral. Petrol.* **107**, 27-40.

BARSDELL, M. & BERRY, R.F. 1990. Origin and evolution of primitive island arc ankaramites from Western Epi, Vanuata. *J. Pet.* **31**, 747-777.

BEATTIE, P.; DRAKE, M.; JONES, J.; LEEMAN, W.; LONGHI, J.; McKAY, G.; NIELSON, R.; PALME, H.; SHAW, D.; TAKAHASHI, E. & WATSON, B. 1993. Terminology for trace-element partitioning. *Geochim. Cosmochim. Acta.* **57**, 1605-1606.

BEATTIE, P. 1994. Systematics and energetics of trace element partitioning between olivine and silicate melts: implications for the nature of mineral/melt partitioning. *Terra Abstacts* **6**, 3.

BEBOUT, G.E. 1991. Field-based evidence for devolatilization in subduction zones: implications for arc magmatism. *Science* **251**, 413-416.

BEBOUT, G.E. & BARTON, M.D. 1989. Fluid flow and metasomatism in a subduction zone hydrothermal system: Catalina Schist, California. *Geology* **17**, 976-980.

BEBOUT, G.E. & FOGEL, M.L. 1992. Nitrogen-isotope compositions of metasedimentary rocks in the Catalina Schist, California: implications for metamorphic devolatilization history. *Geochim. Cosmochim. Acta.* **56**, 2839-2849.

BEBOUT, G.E.; RYAN, J.G. & LEEMAN, W.P. 1993. B-Be systematics in subduction-related metamorphic rocks: characterization of the subducted component. *Geochim. Cosmochim. Acta.* **57**, 2227-2237.

BEBOUT, G.E.; RYAN, J.G.; LEEMAN, W.P. & BEBOUT, A.E. (*in prep.*). Fractionation of trace elements by subduction-zone metamorphism: significance for models of crust-mantle mixing.

BEN OTHMAN, D.; WHITE, W.M. & PATCHETT, J. 1989. The geochemistry of marine sediments, island arc magma genesis, and crust-mantle recycling. *Earth Planet. Sci. Lett.* **94**, 1-21.

BICKLE, M.J. & McKENZIE, D. 1987. The transport of heat and matter by fluids during metamorphism. *Contrib. Mineral. Petrol.* **95**, 384-392.

BLUNDY, J.D. & WOOD, B.J. 1991. Crystal-chemical controls on the partitioning of Sr and Ba between plagioclase feldspar, silicate melt, and hydrothermal solutions. *Geochim. Cosmochim. Acta.* **55**, 193-209.

BOETTCHER, A.L. 1973. Volcanism and orogenic belts - the origin of andesites. *Tectonophysics* **17**, 223-240.

BOETTCHER, A.L.; O'NEILL, J.R.; WINDOM, K.E.; STEWART, D.G. & WILSHIRE, H.G. 1979. In *The mantle sample: inclusions in kimberlites and other volcanic rocks* (eds. Boyd, F.I.F. & Meyer, H.O.A.), Am. Gephys. Union, Washington 173-182.

BÖHLKE, J.K.; HONNOREZ, J.; HONNOREZ-GUERSTEIN, B.-M.; MUEHLENBACHS, K. & PETERSON, N. 1981. Hetergeneous alteration of the upper oceanic crust: correlation of rock chemistry, magnetic properties, and O isotope ratios with alteration patterns in basalts from site 396B, DSDP. *J. Geophys. Res.* **86**, 7935-7950.

BOTTAZZI, P.; OTTOLINI, L. & VANNUCCI, R. 1991. SIMS analyses of REE in natural minerals and glasses: an investigation of structural matrix effects on ion yields. *SIMS VIII Abstracts*, 274.

BOYD, F.R. & ENGLAND, J.L. 1960. Apparatus for phase-equilibrium measurements at pressures up to 50 kilobars and temperatures up to 1750°C. *J. Geophys. Res.* **65**, 741-748.

BRENAN, J.M. & WATSON, E.B. 1991. Partitioning of trace elements between olivine and aqueous fluids at high P-T conditions: implications for the effect of fluid composition on trace-element transport. *Earth Planet. Sci. Lett.* **107**, 672-688.

BRIQUEU, L.; BOUGAULT, H. & JORON, J.L. 1984. Quantification of Nb, Ta, Ti and V anomalies in magmas associated with subduction zones: petrogenic implications. *Earth Planet. Sci. Lett.* **68**, 297-308.

BROPHY, J.G. 1990. Andesites from northeastern Kanaga Island, Aleutians: implications for calc-alkaline fractionation mechanisms and magma chamber development. *Contrib. Mineral. Petrol.* **104**, 568-581.

CARRINGTON, D.P. 1994. Partial melting and phase relations in metapelitic granulites. *Unpublished PhD thesis, University of Edinburgh.*

CAWTHORN, R.G.; CURRAN, E.B. & ARCULUS, R.J. 1973. A petrogenetic model for the origin of the calc-alkaline suite of Grenada, Lesser Antilles. *J. Pet.* **14**, 327-337.

CHAUSSIDON, M. & JAMBON. Boron content and isotopic composition of oceanic basalts: geochemical and cosmochemical implications. *Earth Planet. Sci. Lett.* **121**, 277-291.

CHAUSSIDON, M. & LIBOUREL, G. 1993. Boron partitioning in the upper mantle: an experimental and ion probe study. *Geochim. Cosmochim. Acta.* **57**, 5053-5062.

CHERNOSKY, Jr. J.V.; DAY, H.W. & CARUSO, L.J. 1985. Equilibria in the system MgO-SiO_2-H_2O: experimental determination of the stability of Mg-anthophyllite. *Am. Min.* **70**, 223-236.

CHOPIN, C. 1986. Phase relationships of ellenbergerite, a new high-pressure Mg-Al-Ti-silicate in pyrope-coesite-quartzite from the Western Alps. *Geol. Soc. Amer. Mem.* **164**, 31-42.

CHOU, I.M. 1987. Oxygen buffer and hydrogen sensor techniques at elevated pressures and temperatures. *In G.C. ULMER & H.L. BARNES, Eds., Hydrothermal experimental techniques p. 61-99. Wiley, New York.*

COLSON, R.O.; MCKAY, G.A. & TAYLOR, L.A. 1988. Temperature and composition dependencies of trace element partitioning: olivine/melt and low-Ca pyroxene/melt. *Geochim. Cosmochim. Acta.* **52**, 539-553.

CULLERS, R.L.; MEDARIS, L.G. & HASKIN, L.A. 1970. Gadolinium: distribution between aqueous and silicate phases. *Science* **169**, 580-583.

CULLERS, R.L.; MEDARIS, L.G. & HASKIN, L.A. 1973. Experimental studies of the distribution of rare earths as trace elements among silicate minerals and liquids and water. *Geochim. Cosmochim. Acta.* **37**, 1499-1512.

DAVIDSON, J.P. 1987. Crustal contamination versus subduction zone enrichment: Examples from the Lesser Antilles and implications for mantle source composition of island arc rocks. *Geochim. Cosmochim. Acta.* **51**, 2185-2198.

DAVIES, J.H. & BICKLE, M.J. 1991. A physical model for the volume and composition of melt produced by hydrous fluxing above subduction zones. *Earth. Planet. Sci. Lett. (submitted).*

DAVIES, J.H. & STEVENSON, D.J. 1992. Physical model of source region of subduction zone volcanics. *J. Geophys. Res.* **97**, 2037-2070.

DAWSON, J.B. & SMITH, J.V. 1975. *Phys. Chem. Earth* **9**, 339-350.

DAWSON, J.B. & SMITH, J.V. 1982. Upper-mantle amphiboles: a review. *Min. Mag.* **45**, 35-46.

DEER, W.A.; HOWIE, R.A. & ZUSSMAN, N.J. 1966. *An introduction to the rock forming minerals.*: Longmans.

DEFANT, M.J.; MAURY, R.C.; RIPLEY, E.M.; FEIGENSON, M.D. & JACQUES, D. 1991. An example of island-arc petrogenesis: geochemistry and petrology of the Southern Luzon Arc, Philippines. *J. Pet.* **32**, 455-500.

DEFANT, M.J. & DRUMMOND, M.S. 1990. Derivation of some modern arc magmas by melting of young subducted lithosphere. *Nature* **347**, 662-665.

DELANY, J.M.& HELGESON, H.C. 1978. Calculation of the thermodynamic consequences of dehydration in subducting oceanic crust to 100kb and > 800 °C. *Am. J. Sci.* **278**, 638-686.

DICKINSON, W.R. & HATHERTON, T. 1967. Andesite volcanism and seismicity around the Pacific. *Science* **157**, 801-803.

DOMANIK, K.J.; HERVIG, R.L. & PEACOCK, S.M. 1993. Beryllium and boron in subduction zone minerals: an ion microprobe study. *Geochim. Cosmochim. Acta.* **57**, 4997-5010.

DONNELLY, T.W.; THOMPSON, G. & SALISBURY, M.H. 1979. The chemistry of altered basalts at site 417, Deep Sea Drilling Project Leg 51. pp1319-1330. *In Donnelly, T.; J. Francheteau, W. Bryan, P. Robinson, M. Flower, M. Salisbury (eds). Initial Reports of the Deep Sea Drilling Project* **Vol. 51, 52, 53, Part 2,** U.S. Government Printing Office, Washington, D.C.

DRAKE, M.J. 1975. The oxidation state of europium as an indicator of oxygen fugacity. *Geochim. Cosmochim. Acta.* **39**, 55-64.

EDWARDS, C.M.H.; MORRIS, J.D. & THIRLWALL, M.F. 1993. Separating mantle from slab signatures in arc lavas using B/Be and radiogenic isotope systematics. *Nature* **362**, 530-533.

EGGLER, D.H. 1987. Discussion of recent papers on carbonated peridotiote, bearing on mantle metasomatism and magmatism: an alternative. *Earth. Planet. Sci. Lett.* **82**, 398-400.

EGGLER, D.H. & ROSENHAUER, M. 1978. Carbon dioxide in silicate melts. II. Solubilities of CO_2 and H_2O in $CaMgSi_2O_6$ (diopside) liquids and vapors at pressures to 40kb. *Am. J. Sci.* **278**, 64-94.

ELLAM, R.M. & HAWKESWORTH, C.J. 1988. Elemental and isotopic variations in subduction related basalts: evidence for a three component model. *Contrib. Mineral. Petrol.* **98**, 72-80.

FEIGENSON, M.D. & CARR, M.J. 1986. Positively correlated Nd and Sr isotope ratios of lavas from the Central American volcanic front, *Geology* **14**, 79-82.

FITTON, J.G. 1971. The generation of magmas in island arcs. *Earth Planet. Sci. Lett.* **11**, 63-67.

FITTON, J.G.; JAMES, D. & LEEMAN, W.P. 1990. Basic magmatism associated with late Cenozoic extension in the Western United States: compositional variations in space and time.

FODEN, J.D. 1983. The petrology of calcalklaline lavas of Rindjani volcano, East Sunda arc: a model for island arc petrogenesis. *J. Pet.* **24**, 98-130

FOLEY, S.F. & WHELLER, G.E. 1990. Parallels in the origin of the geochemical signatures of island arc volcanics and continental potassic igneous rocks: the role of residual titanites. *Chem. Geol.* **85**, 1-18.

FRANCALANCI, L.; TAYLOR, S.R.; McCULLOCH, M.T. & WOODHEAD, J.D. 1993. Geochemical and isotopic variations in the calc-alkaline rocks of Aeolian arc, southern Tyrrhenian Sea, Italy: constraints on magma genesis. *Contrib. Mineral. Petrol.* **113**, 300-313.

FRANCIS, D.M. 1976a. Amphibole pyroxenite xenoliths: cumulate or replacement phenomena from the Upper Mantle, Nunivak Island, Alaska. *Contrib. Mineral. Petrol.* **58**, 51-61.

FRANCIS, D.M. 1976b. The origin of amphibole in lherzolite xenoliths from Nunivak Island, Alaska. *J. Pet.* **17**, 357-378.

GILBERT, M.C.; HELZ, R.T.; POPP, R.K. & SPEAR, F.S. 1982. Experimental studies of amphibole stability. *Reviews in Mineralogy* **9B**, 229-353.

GILL, J.B. 1981. *Orogenic andesites and plate tectonics.* Berlin: Springer-Verlag, 358pp.

GOTO, A. & TATSUMI, Y. 1990. Stability of chlorite in the upper mantle. *Am. Min.* **75**, 105-108.

GREEN, D.H. 1973. Experimental melting studies on a model upper mantle composition at high pressure under water-saturated and water-undersaturated conditions. *Earth. Planet. Sci. Lett.* **19**, 37-53.

GREEN, D.H. 1976. Experimental testing of "equilibrium" partial melting of peridotite under water-saturated, high-pressure conditions. *Can. Min.* **14**, 255-268.

GREEN, D.H. & WALLACE, M.E. 1988. Mantle metasomatism by ephemeral carbonatite melts. *Nature* **336**, 459-462.

GREEN, T.H. & PEARSON, N.J. 1985. Rare earth element partitioning between clinopyroxene and silicate liquid at moderate to high pressure. *Contrib. Mineral. Petrol.* **91**, 24-36.

GREEN, T.H. & PEARSON, N.J. 1986. Ti-rich accessory phase saturation in hydrous mafic-felsic compositions at high P,T. *Chem. Geol.* **54**, 185-201.

GREEN, T.H. & PEARSON, N.J. 1987. An experimental study of Nb and Ta partitioning between Ti-rich minerals and silicate liquids at high pressures and temperature. *Geochim. Cosmochim. Acta.* **51**, 55-62.

GREEN, T.H.; SIE, S.H.; RYAN, C.G. & COUSENS, D.R. 1989. Proton microprobe-determined partitioning of Nb, Ta, Zr, Sr and Y between garnet, clinopyroxene and basaltic magma at high pressure and temperature. *Chem. Geol.* **74**, 201-216.

GUST, D.A. & PERFIT, M.P. 1987. Phase relations of a high-Mg basalt from the Aleutian Island Arc: implications for primary island arc basalts and high-Al basalts. *Contrib. Mineral. Petrol.* **97**, 7-18.

HAGGERTY, S.E. 1983. New metasomatic upper mantle minerals: example of Pandora's havoc. *EOS* **64**, 349.

HAMILTON, D.L.; BURNHAM, C.W. & OSBORN, E.F. 1964. The solubility of water and effects of oxygen fugacity and water content on crystallisation in mafic magmas. *J. Pet.* **5**, 21-39.

HAMILTON, D.L. & HENDERSON, C.M.B. 1968. The preparation of silicate compositions by a gelling method. *Min. Mag.* **36**, 832-838.

HAMILTON, D.L. & OXTOBY, S. 1986. Solubility of water in albite-melt determined by the weight-loss method. *J. Geol.* **94**, 626-630.

HANSON, G.N. 1980. Rare-earth elements in petrogenic studies of igneous systems. *Ann. Rev. Earth Planet Sci.* **8**, 371-406.

HART, S.R. & DAVIS, K.E. 1978. Nickel partitioning between olivine and silicate melt. *Earth. Planet. Sci. Lett.* **40**, 203-219.

HART, S.R. & DUNN, T. 1993. Experimental cpx/melt partitioning of 24 trace elements. *Contrib. Mineral. Petrol.* **113**, 1-8.

HASEBE, K.; FUJII, N. & UYEDA, S. 1970. Thermal processes under island arcs. *Tectonophysics* **10**, 335-355.

HAWKESWORTH, C. & ELLAM, R. 1989. Chemical fluxes and wedge replenishment rates along recent destructive margins. *Geology* **17**, 46-49.

HAWKESWORTH, C.J.; HERGT, J.M.; ELLAM, R.M. & McDERMOTT, F. 1991. Element fluxes associated with subduction related magmatism. *Spec. Publ. Roy. Soc. Lond.* **A335**, 393-405.

HAWKESWORTH, C.J.; GALLAGHER, K.; HERGT, J.M. & McDERMOTT, F. 1993a. Trace element fractionation processes in the generation of island arc basalts. *Phil. Trans. Roy. Soc. Lond.* **A342**, 179-191.

HAWKESWORTH, C.J.; GALLAGHER, K.; HERGT, J.M. & McDERMOTT, F. 1993b. Mantle and slab contributions in arc magmas. *Ann. Rev. Earth Planet Sci.* **21**, 175-204.

HAWKINS, J.W.; LONSDALE, P.F.; MACDOUGALL, J.D. & VOLPE, A.M. 1990. Petrology of the axial ridge of the Mariana trough back-arc spreading centre. *Earth. Planet. Sci. Lett.* **100**, 226-250.

HELZ, R.T. 1973 Phase relations of basalts in their melting ranges at P_{H_2O}=5kb as a function of oxygen fugacity. Part I. Mafic phases. *J. Pet.* **14**, 249-302.

HELZ, R.T. 1976 Phase relations of basalts in their melting ranges at P_{H_2O}=5kb. Part II. Melt compositions. *J. Pet.* **17**, 139-193.

HICKEY, R.L. & FREY, F.A. 1982. Geochemical charcateristics of boninite series volcanics: implications for their source. *Geochim. Cosmochim. Acta.* **46**, 2099-2115.

HICKEY, R.L.; FREY, F.A. & GERLACH, D.C. 1986. Multiple sources for basaltic arc rocks from the Southern Volcanic Zone of the Andes (31°-41°S): trace element and isotopic evidence for contributions from subducted oceanic crust, mantle and continental crust. *J. Geophys. Res.* **91**, 5963-5983.

HICKEY-VARGAS, R. 1992. A refractory HIMU component in the sources of island-arc magma. *Nature* **360**, 57-59.

HILDRETH, W. & MOORBATH, S. 1988. Crustal contributions to arc magmatism in the Andes of Central Chile. *Contrib. Mineral. Petrol.* **98**, 455-489.

HIROSE, K. & KUSHIRO, I. 1993. Partial melting of dry peridotites at high pressures: determination of compositions of melts segregated from peridotite using aggregates of diamond. *Earth. Planet. Sci. Lett.* **114**, 477-489.

HOFMANN, A.W. 1988. Chemical differentiation of the Earth: the relationship between mantle, continental crust, and oceanic crust. *Earth. Planet. Sci. Lett.* **90**, 297-314.

HOLE, M.J.; SAUNDERS, A.D.; MARRINER, G.F. & TARNEY, J. 1984. Subduction of pelagic sediments: implications for the origin of Ce-anomalous basalts from the Mariana Islands. *J. Geol. Soc. London* **141**, 453-472.

HOLLOWAY, J.R. 1971. Composition of Fluid Phase Solutes in a Basalt-H_2O-CO_2 System. *Geol. Soc. Am. Bull.* **82**, 233-238.

HOLLOWAY, J.R. 1981. Volatile interactions in magmas. In *Thermodynamics of minerals and melts* Newton, R.C.; Navrotsky, a. & Wood, B.J. (eds), 273-293. Springer-Verlag: New York.

HOLLOWAY, J.R. & WOOD, B.J. 1988. *Simulating the earth: experimental geochemistry.* Unwin Hyman: Boston.

HUNT, J.B. & HILL, P.G. 1993. Tephra geochemistry: a discussion of some persistent analytical problems. *The Holocene*, **3**, 271-278.

IRVING, A.J. 1978. A review of experimental studies of crystal/liquid trace element partitioning. *Geochim. Cosmochim. Acta.* **42**, 743-770.

IRVING, A.J. & FREY, F.A. 1984. Trace element abundances in megacrysts and their host basalts: constraints on partition coefficients and megacryst genesis. *Geochim. Cosmochim. Acta.* **48**, 1201-1221.

ITO, E. & STERN, R.J. 1985/86. Oxygen- and strontium-isotopic investigation of subduction zone volcanism: the case of the volcano arc and the Marianas Island arc. *Earth. Planet. Sci. Lett.* **76**, 312-320.

JENKINS, D.M. & CHERNOSKY Jr. J.V. 1986. Phase equilibria and crystallochemical properties of Mg-chlorite. *Am. Min.* **71**, 924-936.

JOHNSTON, A.D. & DRAPER, D.S. 1992. Near-liquidus phase relations of an anhydrous high-magnesia basalt from the Aleutian islands: implications for arc magma genesis and ascent. J. Volcanol. Geotherm. Res. **52**

JUREWICZ, A.J.G. & WATSON, E.B. 1988. Cations in olivine, part 1: calcium partitioning and calcium-magnesium distribution between olivines and coexisting melts, with petrologic applications. *Contrib. Mineral. Petrol.* **99**, 176-185.

KARL, S.M.; WANDLESS, G.A. & KARPOFF, A.M. 1992. 2. Sedimentalogical and geochemical characteristics of Leg 129 siliceous seposits. *Proc. ODP Sci. Results* **129**, 31-80.

KAY, R.W. 1980. Volcanic arc magmas: implications of a melting-mixing model for element recycling in the crust-upper mantle system. *J. Geol.* **88**, 497-522.

KAY, S.M. & KAY, R.W. 1985. Aleutian tholeiitic and calc-alkaline magma series I: the mafic phenocrysts. *Contrib. Mineral. Petrol.* **90**, 276-290.

KELEMEN, P.B. 1990. Reaction between ultramafic rock and fractionating basaltic magma I. Phase relations, the origin of calc-alkaline magma series, and the formation of discordant dunite.*J. Pet.* **31**, 51-98.

KELEMEN, P.B.; JOHNSON, K.T.M.; KINZLER, R.J. & IRVING, A.J. 1990. High-field-strength element depletions in arc basalts due to mantle-magma interaction. *Nature* **345**, 521-524.

KELEMEN, P.B.; JOYCE, D.B.; WEBSTER, J.D. & HOLLOWAY, J.R. 1990. Reaction between ultramafic rock and fractionating basaltic magma II. Experimental investigation of reaction between olivine tholeiite and harzburgite at 1150-1050°C and 5kb. *J. Pet.* **31**, 99-134.

KELEMEN, P.B.; SHIMIZU, N. & DUNN, T. 1993 . Relative depletion in niobium in some arc magmas and the continental crust: partitioning of K, Nb, La and Ce during melt/rock reaction in the upper mantle. *Earth. Planet. Sci. Lett.***120**, 111-134.

KITAHARA, S.; TAKENOUCH, I.S. & KENNEDY, G.C. 1966. Phase relations in the system MgO-SiO_2-H_2O at high temperatures and pressures. *Am. J. Sci.* **264**, 223-233.

KUSHIRO, I. 1969. The system forsterite-diopside-silica with and without water at high pressures. *Am. J. Sci.* **267-A**, 269-194.

KUSHIRO, I. 1990. Partial melting of mantle wedge and evolution of island arc crust. *J. Geophys. Res.* **95**, 15,929-15,939.

KUSHIRO, I.; SHIMIZU, N.; NAKAMURA, Y. & AKIMOTO, S. 1972. Compositions of coexisting liquid and solid phases formed upon melting of natural garnet and spinel lherzolites at high pressures: a preliminary report. *Earth. Planet. Sci. Lett.***14**, 19-25.

KUSHIRO, I.; SYONO, Y. & AKIMOTO, S-I. 1968. Melting of a Peridotite nodule at high pressures and high water pressures. *J. Geophys. Res.* **73**, 6023-6029.

LE MAITRE, R.W.; BATEMAN, P.; DUDEK, A.; KELLER, J.; LAMEYRE; LE BAS; M.J.; SABINE, P.A.; SCHMID, R.; SORENSEN, A.; WOOLEY, A.R. & ZANETTIN, B. 1989. *A classification of igneous rocks and glossary of terms.* Blackwell: Oxford.

LEAKE, B.E. 1978. Nomenclature of amphiboles. *Am. Min.* **63**, 1023-1052.

LEEMAN, W.P.; CARR, M.J. & MORRIS, J.D. 1994. Boron geochemistry of the Central American volcanic arc: constraints on the genesis of subduction-related magmas. *Geochim. Cosmochim. Acta.* **58**, 149-168.

LEGGETT, J.K. 1982. Geochemistry of Cocos Plate pelagic-hemipelagic sediments in hole 487, Deep Sea Drilling Project Leg 66. *Init. Rep. DSDP* **66**, 683-686.

LEMARCHAND, F.; VILLEMANT, B. & CALAS, G. 1987. Trace element distribution coefficients in alkaline series. *Geochim. Cosmochim. Acta.* **51**, 1071-1081.

LESHER, C.E. & WALKER, D. 1988. Cumulate maturation and melt migration in a temperature gradient. *J. Geophys. Res.* **93**, 10295-10311.

LEVIN, E.M.; ROBBINS, C.R. & McMURDIE, H.F. 1964. *Phase diagrams for ceramicists*. The American Ceramic Society, Columbus, Ohio.

LIN, P.N.; STERN, R.J.; MORRIS, J. & BLOOMER, S.H. 1990. Nd- and Sr-isotopic compositions of lavas from the northern Mariana and southern Volcano arcs: implications for the origin of island arc melts. *Contrib. Mineral. Petrol.* **105**, 381-392.

LIN, P.N.; STERN, R.J. & BLOOMER, S.H. 1989. Shoshonitic volcanism in the northern Mariana arc, 2. Large-ion lithophile and rare earth element abundances: evidence for the source of incompatible element enrichments in intraoceanic arcs. *J. Geophys. Res.* **94**, 4497-4514.

LINDSLEY, D.H. 1976. Experimental studies of oxide minerals. In Oxide minerals. Min. Soc. America, Short Course Notes, 3,

LIU, L-G. 1989. Water, low-velocity zone and the descending lithosphere. *Tectonophysics* **164**, 41-48.

MATSUZAWA, T.; UMINO, N.;HASEGAWA, A. & TAKAGI, A. 1986. Upper mantle velocity structure estimated from PS-converted wave beneath the north-eastern Japan arc. *Geophys. J. R. Astr. Soc.* **86**, 767-787.

MATTIOLI, G.S.; BAKER, M.B.; RUTTER, M.J. & STOLPER, E.M. 1989. Upper mantle oxygen fugacity and its relationship to metasomatism. *J. Geol.* **97**, 521-536.

MATTIOLI, G.S. & WOOD, B.J. 1988. Magnetite activities across the $MgAl_2O_4$-Fe_3O_4 spinel join, with application to thermobarometric estimates of upper mantle oxygen fugacity. *Contrib. Mineral. Petrol.* **98**, 148-162.

MAURY, R.C.; DEFANT, M.J. & JORON, J.L. 1992. Metasomatism of the sub-mantle inferred from trace elements in Philippine xenoliths. *Nature* **360**, 661-663.

McCULLOCH, M.T. & GAMBLE, J.A. 1991. Geochemical and geodynamical constraints on subduction zone magmatism. *Earth. Planet. Sci. Lett.* **102**, 358-374.

McDERMOTT, F. & HAWKESWORTH, C. 1991. Th, Pb & Sr isotope variations in young island arc volcanics and oceanic sediments. *Earth. Planet. Sci. Lett..* **104**, 1-15.

McGETCHIN, T.R. & SILVER, L.T. 1970. Compositional relations in minerals from kimberlite and related rocks in the Moses Rock Dike, San Juan County, Utah. *Am. Min.* **55**, 1738-1771.

McKENZIE, D. 1969. Speculations on the consequences and causes of plate motions. *Geophys. J. R. Astr. Soc.* **18**, 1-32.

McKENZIE, D. 1985. The extraction of magma from the crust. *Earth. Planet. Sci. Lett.* **74**, 81-91.

McKENZIE, D. 1989. Some remarks on the movement of small melt fractions in the mantle. *Earth. Planet. Sci. Lett.* **95**, 53-72.

McKENZIE, D. & BICKLE, M.J. 1988. The volume and composition of melt generated by extension of the lithosphere. *J. Pet.* **29**, 625-679.

McKENZIE, D. & O'NIONS, R.K. 1991. Partial melt distributions from inversion of rare earth element concentrations. *J. Pet.***32**, 1020-1091.

McKENZIE, D. & O'NIONS, R.K. 1994. The source regions of ocean island basalts *J. Pet.* (in press).

McMILLAN, P.F. & HOLLOWAY, J.R. 1987. Water solubility in aluminosilicate melts. *Contrib. Mineral. Petrol.* **97**, 320-332.

MEYER, J.W. & CHI-SUN YANG, J. 1962. Some observations in the system MgO-H_2O. *Am. J. Sci.* **260**, 707-717.

MILLER, D.M.; LANGMUIR, C.H.; GOLDSTEIN, S.L. & FRANKS, A.L. 1992. The importance of parental magma composition to calc-alkaline and tholeiitic evolution: evidence from Uninak Island in the Aleutians. *Journal Geophys. Res.* **97**, 321-343.

MILLHOLEN, G.L.; IRVING, A.J. & WYLLIE, P.J. 1974. Melting interval of peridotite with 5.7 per cent water to 30 kilobars. *J. Geol.* **82**, 575-587.

MÖLLER, P. & MUECKE, G.K. 1984. Significance of europium anomalies in silicate melts and crystal-melt equilibria: a re-evaluation. *Contrib. Mineral. Petrol.* **87**, 242-250.

MORAN, A.E.; SISSON, V.B. & LEEMAN, W.P. 1992. Boron depletion during progressive metamorphism: implications for subduction processes. *Earth. Planet. Sci. Lett.* **111**, 331-349.

MORIMOTO, N. 1988. Nomenclature of pyroxenes. *Min. Mag.* **52**, 535-550.

MORRIS, J.D. & HART, S.R. 1983. Isotopic and incompatible element constraints on the genesis of island arc volcanics from Cold Bay and Amak Island, Aleutians, and implications for mantle structure. *Geochim. Cosmochim. Acta.* **47**, 2015-2030.

MORRIS, J.D.; LEEMAN, W.P. & TERA, F. 1990. The subducted component in island arc lavas: constraints from Be isotopes and B-Be systematics. *Nature* **344**, 31-36.

MORRIS, J. & TERA, F. 1989. ^{10}Be and ^{9}Be in mineral separates and whole rocks from volcanic arcs: implications for sediment subduction. *Geochim. Cosmochim. Acta.* **53**, 3197-3206.

MOTTANA, A.; CARSWELL, D.A.; CHOPIN, C. & OBERHÄNSLI, R. 1990. Eclogite facies mineral paragenesis. *In Eclogite Facies Rocks* (ed. D.A. Carswell) Blackie: Glasgow & London.h

MYSEN, B.O. 1979. Trace-element partitioning between garnet peridotite minerals and water-rich vapour: experimental data from 5 to 30 kbar. *Am. Min.* **64**, 274-287.

MYSEN, B.O. & BOETTCHER, A.L. 1975A. Melting of a hydrous mantle: I. Phase relations of natural peridotite at high pressures and temperatures with controlled activities of water, carbon dioxide, and hydrogen. *J. Pet.* **16**, 520-548.

MYSEN, B.O. & BOETTCHER, A.L. 1975B. Melting of a hydrous mantle: II. Geochemistry of crystals and liquids formed by anatexis of mantle peridotite at high pressures and high temperatures as a function of controlled activities of water, hydrogen and carbon dioxide. *J. Pet.* **16**, 549-593.

MYSEN, B.O. & KUSHIRO, I. 1974. A possible mantle origin for andesitic magmas: Discussion of a paper by Nicholls and Ringwood, 1. Opening discussion and 3. Comments on the reply of Nicholls and Ringwood. *Earth. Planet. Sci. Lett.* **21**, 221-229.

NAVON, O. & STOLPER, E. 1987. Geochemical consequences of melt percolation: the upper mantle as a chromatographic column. *J. Geol.* **95**, 285-307.

NEWMAN, S.; MACDOUGALL, J.D. & FINKEL, R.C. 1984. ^{230}Th-^{238}U disequilibrium in island arcs: evidence from the Aleutians and the Marianas. *Nature* **308**, 268-270.

NEWTON, R.C. 1986. Metamorphic temperatures and pressures of Group B and C eclogites. *Geol. Soc. Amer. Mem.* **164**, 17-30.

NICHOLLS, I.A. 1974. Liquids in equilbrium with Peridotitic Mineral Assemblages at High Water Pressures. *Contrib. Mineral. Petrol.* **45**, 289-316.

NICHOLLS, I.A. & HARRIS, K.L. 1980. Experimental rare earth element partition coefficients for garnet, clinopyroxene and amphibole coexisting with andesitic and basaltic liquids. *Geochim. Cosmochim. Acta.* **44**, 287-308.

NICHOLLS, I.A. & LORENZ, V. 1973. Origin and crystallisation history of Permian tholeiites from the Saar-Nahe trough, SW Germany. *Contrib. Mineral. Petrol.* **40**, 327-344.

NICHOLLS, I.A. & RINGWOOD, A.E. 1973. Effect of water on olivine stability in tholeiites and the production of silica-saturated magmas in the island-arc environment. *J. Geol.* **81**, 285-300.

NICHOLLS, I.A. & RINGWOOD, A.E. 1974. A possible mantle origin for andesitic magmas: Discussion of a paper by Nicholls and Ringwood, 2. Reply to opening discussion and 4. Final reply. *Earth. Planet. Sci. Lett.* **21**, 221-229.

NORRISH, K. & CHAPPELL, B.W. 1977. X-ray fluoscence spectography. In *Physical Methods in Determinative Mineralogy (2nd edition),* J. Zussman (ed.), 201-272. Academic press: London.

NYE, C.J. & REID, M.R. 1986. Geochemistry of primary and least fractionated lavas from Okmok Volcano, Central Aleutians: implications for arc magmagenesis. *Journal Geophys. Res.* **91**, 10,271-10,287.

O,NEILL, H.St.C. 1987. The free energies of formation of NiO, CoO, Ni_2SiO_4. *Am. Min.* **72**, 280-291.

O'NEILL, H.St.C. & WALL, V.J. 1987. The olivine-orthopyroxene-spinel oxygen geobarometer, the nickel precipitation curve, and the oxygen fugacity of the Earth's upper mantle. *J. Pet.* **28**, 1169-1191.

ODLING, N.W.A. (in press). A fusion method for preparing glass samples of peridotite and picritic rock compositions for bulk analysis. *Min. Mag.*

ODLING, N.W.A., GREEN, D.H. & HARTE, B. (accepted subject to minor revision). The determination of partial melt compositions of peridotitic systems by melt inclusion synthesis. *Contrib. Mineral. Petrol.*.

OLAFSSON, M. & EGGLER, D.H. 1983. Phase relations of amphibole, amphibole-carbonate and phlogopite-carbonate peridotite: petrologic constraints on the asthenosphere. *Earth. Planet. Sci. Lett.* **64**, 305-315.

ONUMA, N.; HIGUCHI, H.; WAKITA, H. & NAGASAWA, H. 1968. Trace element partitioning between two pyroxenes and the host lava. *Earth. Planet. Sci. Lett.* **5**, 47-51.

PALMER, M.R. 1991. Boron-isotope systematics of Halmahera arc (Indonesia)lavas: Evidence for involvement of the subducted slab. *Geology* **19**, 215-217.

PEACOCK, S.M. 1990 a. Fluid processes in subduction zones. *Science* **248**, 329-337.

PEACOCK, S.M. 1990 b. Numerical simulation of metamorphic pressure-temperature-time paths and fluid production in subducting slabs. *Tectonics* **9**, 1197-1211.

PEACOCK, S.M.; RUSHMER, T. & THOMPSON, A.B. 1994. Partial melting of subducting oceanic crust. *Earth Planet. Sci. Lett.* **121**, 227-244.

PEARCE, J.A. 1982. Trace element characteristics of lavas from destructive plate boundaries. In *Andesites: orogenic andesites and related rocks,* R. S. Thorpe (ed.), 525-548. Chichester: Wiley.

PEARCE, J.A. 1983. Role of the sub-continental lithosphere in magma genesis at active continental margins. In *Continental basalts and mantle xenoliths,* C.J. Hawkesworth & M.J. Norry (eds), 230-249. Nantwich: Shiva.

PEARCE, J.A.; ALABASTER, T; SHELTON; A.W. & SEARLE, M.P. 1981. The Oman ophiolite as a Cretaceous arc-basin complex: evidence and implications. *Phil. Trans. R. Soc. Lond.*, **A300**, 299-317.

PEARCE, J.A.; GORMAN, B.E. & BIRKETT, T.C. 1977. The relationship between major element chemistry and tectonic environment of basic and intermediate volcanic rocks. *Earth Planet. Sci. Lett.* **36**, 121-132.

PEARCE, J.A. & NORRY, M.J. 1979. Petrogenetic implications of Ti, Zr, Y, and Nb variations in volcanic rocks. *Contrib. Mineral. Petrol.* **69**, 33-37.

PEARCE, J.A.; PARKINSON, J.A. & PEATE, D.W. 1994. Geochemical evidence for magma generation above subduction zones. *Min. Mag.* **58A**, 701-702.

PEARCY, L.G.; DEBARI, S.M.; & SLEEP, N.H. 1990. Mass balance calculations for two sections of island arc crust and implications for the formation of continents. *Earth. Planet. Sci. Lett.* **96**, 427-442.

PERFIT, M.R.; GUST, D.A.; BENCE, A.E.; ARCULUS, R.J. & TAYLOR, S.R. 1980. Chemical characteristics of island-arc basalts: implications for mantle sources. *Chem. Geol.* **30**, 227-256.

PHILIPPOT, P. & SELVERSTONE, J. 1991. Trace element-rich brines in eclogitic veins: implications for fluid composition and transport during subduction. *Contrib. Mineral. Petrol.* **106**, 417-430.

PHILPOTTS, J.A. 1978. The law of constant rejection. *Geochim. Cosmochim. Acta.* **42**, 909-920.

PLANK, T. & LANGMUIR, C.H. 1988. An evaluation of the global variations in the major element chemistry of arc basalts. *Earth. Planet. Sci. Lett.* **90**, 349-370.

PLANK, T. & LANGMUIR, C.H. 1992. Sediments melt and basaltic crust dehydrates at subduction zones. *EOS* **73**, 637.

PLANK, T. & LANGMUIR, C.H. 1993. Tracing trace elements from sediment input to volcanic output at subduction zones. *Nature* **362**, 739-742.

PLANK, T. & LUDDEN, J.N. 1992. Geochemistry of sediments in the Argo Abyssal Plain at site 765: a continental margin reference section for sediment recycling in subduction zones. *J. N. Proc. ODP Sci. Res.* **123**, 167-189.

RAMSAY, W.R.H.; CRAWFORD, A.J. & FODEN, J.D. 1984. Field setting, mineralogy, chemistry, and genesis of arc picrites, New Georgia, Solomon Islands. *Contrib. Mineral. Petrol.* **88**, 386-402.

REAGAN, M.K. & GILL, J.B. 1989. Coexisting calcalkaline and high-niobium basalts from Turrialba Volcano, Costa Rica: implications for residual titanates in arc magma sources. *J. Geophys. Res.* **94**, 4619-4633.

REED, S.J.B. 1989. Ion microprobe analysis - a review of geological applications. *Min. Mag.* **53**, 3-24.

REED, S.J.B. 1993. *Electron microprobe analysis. Cambridge Monographs on Physics,* second edition. Cambridge University Press: Cambridge.

RINGWOOD, A.E. 1974. The petrological evolution of island arc systems. *Jl. geol. soc. Lond.* **130**, 183-204.

RINGWOOD, A.E. 1990. Slab-mantle interactions. 3. Petrogenesis of intraplate magmas and structure of the upper mantle. *Chem. Geol.* **82**, 187-207.

ROEDER, P.L. & EMSLIE, R.F. 1970. Olivine-liquid equilibrium. *Contrib. Mineral. Petrol.* **29**, 275-289.

ROLLINSON, H. 1993. *Using geochemical data: evaluation, presentation, interpretation.* Wiley: New York.

RYABCHIKOV, I.D. & BOETTCHER, A.L. 1980. Experimental evidence at high pressure for potassic metasomatism in the mantle of the Earth. *Am. Mineral.* **65**, 915-919.

RYABCHIKOV, I.D.; SCHREYER, W. & ABRAHAM, K. 1982. Compositions of aqueous fluids in equilibrium with pyroxenes and olivines at mantle pressures and temperatures. *Contrib. Mineral. Petrol.* **79**, 80-84.

RYAN, J.G. & LANGMUIR, C.H. 1987. The systematics of lithium abundances in young volcanic rocks. *Geochim. Cosmochim. Acta.* **51**, 1727-1741.

RYAN, J.G. & LANGMUIR, C.H. 1988. Beryllium systematics in young volcanic rocks: implications for ^{10}Be. *Geochim. Cosmochim. Acta.* **52**, 237-244.

RYAN, J.G. & LANGMUIR, C.H. 1993. The systematics of boron abundances in young volcanic rocks. *Geochim. Cosmochim. Acta.* **57**, 1489-1498.

RYERSON, F.J. & WATSON, E.B. 1987. Rutile saturation in magmas: implications for Ti-Nb-Ta depletion in island-arc basalts. *Earth. Planet. Sci. Lett.* **86**, 225-239.

SACK, R.O.; CARMICHAEL, I.S.E.; RIVERS, M. & GHIORSO, M.S. 1980. Ferric-ferrous equilibria in natural silicate liquids at 1 bar. *Contrib. Mineral. Petrol.* **75**, 369-376.

SAUNDERS, A.D.; TARNEY, J. & WEAVER, S.D. 1980. Transverse geochemical variations across the Antarctic Peninsula: implications for the genesis of calc-alkaline magmas. *Earth. Planet. Sci. Lett.* **46**, 344-360.

SCHNEIDER, M.E. & EGGLER, D.H. 1986. Fluids in equilibrium with peridotite minerals: implications for mantle metasomatism. *Geochim. Cosmochim. Acta.* **50**, 711-724.

SCHUBERT, G.; YUEN, D.A. & TURCOTTE, D.L. 1975. Role of phase transitions in a dynamic mantle. *Geophys. J. R. Astr. Soc.* **42**, 705-735.

SEKINE, T. & WYLLIE, P.J. 1983. Experimental simulation of mantle hybridisation in subduction zones. *J. Geol.* **91**, 511-528.

SEYFRIED, JR., W.E.; JANECKY, D.R. & MOTTL, M.J. 1984. Alteration of the oceanic crust: implications for geochemical cycles of lithium and boron. *Geochim. Cosmochim. Acta.* **48**, 557-569.

SHANNON, R.D. 1976. Revised effective ionic radii and systematic studies of interatomic distances in halides and chalcogenides. *Acta Cryst.* **A32**, 751-767.

SHAW, D.M. 1970. Trace element fractionation during anatexis. *Geochim. Cosmochim. Acta.* **34**, 237-243.

SIGHINOLFI, G.P. & GORGONI, C. 1978. Chemical evolution of high-grade metamorphic rocks - anatexis and remotion of material from granulite terrains. *Chem. Geol.* **22**, 157-176.

SIGMARSSON, O.; CONDOMINES, M.; MORRIS, J.D. & HARMON, R.S. 1990. Uranium and ^{10}Be enrichments by fluids in Andean arc magmas. *Nature* **346**, 163-165.

SISSON, T.W. & GROVE, T.L. 1993. Experimental investigations of the role of H_2O in calc-alkaline differentiation and subduction zone magmatism. *Contrib. Mineral. Petrol.* **113**, 143-166.

SISSON, T.W. & GROVE, T.L. 1993. Temperatures and H_2O contents of low-MgO high-alumina basalts. *Contrib. Mineral. Petrol.* **113**, 167-184.

SLODZIAN, G. 1980. Microanalysis using secondary ion emission. *Advances in Electronics and Electron Physics* **Supplement 13B**, 1-44.

SOBOLEV, N.V. & SHATSKY, V.S. 1990. Diamond inclusions in garnets from metamorphic rocks: a new environment for diamond formation. *Nature* **343**, 742-746.

SORENSSEN, S.S. & GROSSMAN, J.N. 1989. Enrichment of trace elements in garnet amphibolites from a paleo-subduction zone: Catalina Schist, southern California. *Geochim. Cosmochim. Acta.* **53**, 3155-3177.

SPIEGELMAN, M. & McKENZIE, D. 1987. Simple 2-D models for melt extraction at mid-ocean ridges and island arcs. *Earth. Planet. Sci. Lett.* **83**, 137-152.

STOLPER, E. & NEWMAN, S. 1994. The role of water in the petrogenesis of Mariana trough magmas. *Earth. Planet. Sci. Lett.* **121**, 293-325.

STOLZ, A.J.; VARNE, R.; DAVIES, G.R.; WHELLER, G.E. & FODEN, J.D. 1990. Magma source components in an arc-continent collision zone: the Flores-Lembata sector, Sunda arc, Indonesia. *Contrib. Mineral. Petrol.* **105**, 585-601.

STOSCH, H.-G. & SECK, H.A. 1980. Geochemistry and mineralogy of two spinel peridotite suites from Dreiser Weiher, West Germany. *Geochim. Cosmochim. Acta.* **44**, 457-470.

SUDO, A. & TATSUMI, Y. 1990. Phlogopite and K-amphobole in the upper mantle: implications for magma genesis in subduction zones. *Geophys. Res. Lett.* **17**, 29-32.

SUN, S.-S. 1980. Lead isotopic study of young volcanic rocks from mid-ocean ridges, ocean islands and island arcs. *Phil. Trans R. Soc. Lond.* **A297**, 409-445.

SUN, S.-S. & McDONOUGH, W.F. 1989. Chemical and isotopic systematics of oceanic basalts: implications for mantle composition and processes. *Geol. Soc. Spec. Publ.* **42**, 313-345. Magmatism in Ocean Basins, eds. A.D. Saunders & M.J. Norry.

TAMURA, Y. 1994. Genesis of island arc magmas by mantle-derived bimodal magmatism: evidence from the Sirahama group, Japan. *J. Pet.* **35**, 619-646.

TATSUMI, Y. 1989. Migration of fluid phases and genesis of basalt magmas in subduction zones. *Journal Geophys. Res.* **94**, 4697-4707.

TATSUMI, Y. 1991. Identification of subduction components in arc magma genesis: comtribution from phase petrology and geochemistry. *EOS* **72**, 239.

TATSUMI, Y.; HAMILTON, D.L. & NESBITT, R.W. 1986. Chemical characteristics of fluid phase derived from a subducted lithosphere and origin of arc magmas: evidence from high-pressure experiments and natural rocks. *Journal Volc. & Geotherm. Res.* **29**, 293-309.

TATSUMI, Y. & ISOYAMA, H. 1988. Transportation of beryllium with H_2O at high pressures: implication for magma genesis in subduction zones. *Geophys. Res. Lett.* **15**, 180-183.

TATSUMI, Y. & NAKAMURA, N. 1986. Composition of fluid from serpentinite in the subducted lithosphere. *Geochem. J.* **20**, 191-196.

TATSUMI, Y.; MURASAKI, M.; ARSADI, E.M. & NOHDA, S. 1991. Geochemistry of Quaternary lavas from NE Sulawesi: transfer of subduction components to the mantle wedge. *Contrib. Mineral. Petrol.* **107**, 137-149.

TAYLOR, L.A. & NEAL, C.R. 1989. Eclogites with oceanic crustal and mantle signatures from the Bellsbank kimberlite, South Africa, part 1: mineralogy, petrography, and whole rock chemistry. *J. Geol.* **97**, 551-567.

TAYLOR, S.R. & McLENNAN 1985. *The continental crust: its composition and evolution.* Blackwell scientific: Oxford.

TAYLOR, W.R. 1985. The role of C-O-H fluids in upper mantle processes: a theoretical, experimental and spectroscopic study. *Unpublished PhD thesis, University of Tasmania.*

TERA, F.; BROWN. L.; MORRIS, J.; SELWYN SACKS, I.; KLEIN, J. & MIDDLETON, R. 1986. Sediment incorporation in island-arc magmas: inferences from ^{10}Be. *Geochim. Cosmochim. Acta.* **50**, 535-550.

THIRLWALL, M.F.; SMITH, T.E.; GRAHAM, A.M.; THEODOROU, N.; HOLLINGS, P.; DAVIDSON, J.P. & ARCULUS, R.J. 1994. High field strength element anomalies in arc lavas: source or process? *J. Pet.* **35**, 819-838.

THOMPSON, A.B. 1992. Water in the Earth's upper mantle. *Nature* **358**, 295-302.

ULMER, P. 1989. Partitioning of high field strength elements among olivine, pyroxenes, garnet and calc alkaline picrobasalt: experimental results and an application. *Annual Report of the Director of the Geophysical Laboratory, Carnegie Instn. Washington, 1988-1989.* Geophysical Laboratory, Washington, D.C., 42-27, 1989.

VALLEY, J.W. 1986. Stable isotope geochemistry of metamorphic rocks. *Rev. Mineral.* **16**, 445-489.

VARNE, R. 1970. Hornblende lherzolite and the upper mantle. *Contrib. Mineral. Petrol.* **27**, 45-51.

VIDAL, P.; DUPUY, C.; MAURY, R. & RICHARD, M. 1989. Mantle metasomatism above subduction zones: trace-element and radiogenic isotope characteristics of peridotite xenoliths from Batan Island (Philippines). *Geology* **17**, 1115-1118.

WALKER, D.; SHIBATA, T. & DE LONG, S.E. 1979. Abyssal tholeiites from the Oceanographer Fracture Xone II. Phase equilibria and mixing. *Contrib. Mineral. Petrol.* **70**, 111-125.

WALLACE, M.E. & GREEN, D.H. 1988. An experimental determination of primary carbonatite magma composition. *Nature* **335**, 343-345.

WEAST, R.C. 1975. *Handbook of chemistry and physics. 56th edition 1975-1976.* CRC Press: Ohio.

WELCH, M.D. 1987. Experimental studies of selected amphiboles in the system Na_2O-CaO-MgO-Al_2O_3-SiO_2-H_2O-F_2 and its subsystems. *Unpublished PhD thesis, University of Edinburgh.*

WELLS, P.R.A. 1977. Pyroxene thermometry in simple and complex systems. *Contrib. Mineral. Petrol.* **62**, 129-139.

WENDLANDT, R.F.; HUEBNER, J.S. & HARRISON, W.J. 1982. Redox potential of boron nitride and implications for its use as a crucible material in experimental petrology. *Am. Min.* **67**, 170-174.

WHITE, W.M. & DUPRE, B. 1986. Sediment subduction and magma genesis in the Lesser Antilles: isotopic and trace element constraints. *Journal Geophys. Res.* **91**, 5927-5941.

WHITE, W.M. & PATCHETT, J. 1984. Hf-Nd-Sr isotopes and incompatible element abundances in island arcs: implications for mantle origins and crust-mantle evolution. *Earth. Planet. Sci. Lett.* **67**, 167-185.

WHITTAKER, E.J.W. & MUNTUS, R. 1970. Ionic radii for use in geochemistry. *Geochim. Cosmochim. Acta.* **34**, 945-956.

WILL, T.M.; POWELL, R. & HOLLAND, T.J.B. 1990. A calculated petrogenetic grid for ultramafic rocks in the system CaO-FeO-MgO-Al_2O_3-SiO_2-CO_2-H_2O at low pressures. *Contrib. Mineral. Petrol.* **105**, 347-358.

WILL, T.M.; POWELL, R.; HOLLAND, T. & GUIRAUD, M. 1990. Calculated greenschist facies mineral equilibria in the system CaO-FeO-MgO-Al_2O_3-SiO_2-CO_2-H_2O. *Contrib. Mineral. Petrol.* **104**, 353-368.

WILSHIRE, H.G.; NELSONPIKE, T.E.; MEYER, C.E. & SCHREYER, E.C. 1980. Amphibole-rich veins in lherzolite xenoliths, Dish Hill and Deadman Lake, California. *Am. J. Sci.* **280-A**, 576-593.

WILSON, M. 1989. *Igneous Petrogenesis.* London: Unwin Hyman.

WITT-EICKSCHEN, G. & SECK, H.A. 1991. Solubility of Ca and Al in orthopyroxene from spinel peridotite: an improved version of an empirical geothermometer. *Contrib. Mineral. Petrol.*

WOOD, B.J. & VIRGO, D. 1989. Upper mantle oxidation state: ferric iron contents of lherzolite spinels in ^{57}Fe Mössbauer spectroscopy and resultant oxygen fugacities. *Geochim. Cosmochim. Acta.* **53**, 1277-1291.

WOODHEAD, J. 1988. The origin of geochemical variations in Mariana lavas: a general model for petrogenesis in intra-oceanic island arcs? *J. Pet.* **29**, 805-830.

WOODHEAD, J. 1989. Geochemistry of the Mariana arc (western Pacific): source composition and processes. *Chem. Geol.* **76**, 1-24.

WOODHEAD, J.; EGGINS, S. & GAMBLE, J. 1993. High field strength and transition element systematics in island arc and back-arc basin basalts: evidence for multi-phase melt extraction and a depleted mantle wedge. *Earth. Planet. Sci. Lett.* **114**, 491-504.

WOODHEAD, J.D. & FRASER, D.E. 1985. Pb, Sr and ^{10}Be isotopic studies of volcanic rocks from the Northern Marianas Islands: implications for magma genesis and crustal recycling in the Western Pacific.*Geochim. Cosmochim. Acta.* **49**, 1925-1930.

WOODHEAD, J.D. & JOHNSON, R.W. 1993. Isotopic and trace-element profiles across the New Britain arc, Papua New Guinea. *Contrib. Mineral. Petrol.* **113**, 479-491.

WYLLIE, P.J. 1979. Magmas and volatile components. *Am. Min.* **64**, 469-500.

WYLLIE, P.J. 1982. Subduction products according to experimental prediction. *Geol. Soc. Am. Bull.* **93**, 468-476.

WYLLIE, P.J. 1987. Discussion of recent papers on carbonated peridotite, bearing on mantle metasomatism and magmatism. *Earth. Planet. Sci. Lett.* **82**, 391-397.

YARDLEY, B.W.D. 1989. *An introduction to metamorphic petrology.* Longman Scientific and Technical. Wiley: New York.

YOGODZINSKI, G.M.; VOLYNETS, O.N.; KOLOSKOV, A.V.; SELIVERSTOV, N.I. & MATVENKOV, V.V. 1994. Magnesian andesites and the subduction component in a strongly calc-alkaline series at Piip Volcano, Far Western Aleutians. *J. Pet.* **35**, 163-204.

YOU, C.F.; SPIVACK, A.J.; SMITH, J.H. & GIESKES, J.M. 1993. Mobilization of boron in convergent margins: implications for the boron geochemical cycle. *Geology* **21**, 207-210.

ZIELINSKI, R.A. & FREY, F.A. 1974. An experimental study of the partitioning of a rare earth element (Gd) in the system diopside-aqueous vapour. *Geochim. Cosmochim. Acta.* **38**, 545-565.

ZINNER, E. & CROZAZ, G. 1986. A method for quantitative measurement of rare earth elements in the ion microprobe. *Int. J. Mass Spectrom. Ion Phys.* **69**, 17-38.

APPENDICES

APPENDIX A

Run conditions and mineralogy (where determined) for all experiments (for more discussion of individual experiments see Chapters 5, 6, and 7). The starting compositions are given in Appendix B.

Expt	Type and aim	Start. comp.	Temp. (°C)	P (GPa)	Dur. (hrs)	Run history	Phases										Notes
							melt	ol	opx	cpx	amph	gt	sp	ru	ilm	fq	
ED91	Forward	HAW	1150	1.8	24	stable	•	•	(•)			(•)	•			•	
ED101	Forward	HAW	1125	1.8	24	stable	•	•	•	(•)			•				
ED111	Forward	HAW	966	1.8	24	OK		•		•			•	•	•		
ED116	Forward - failed	HAW															
ED117	Forward - failed	HAW															
ED121	Forward	HAW	980	1.8	24	OK		•	•	•	•			•	•		
ED130	Forward - failed	HAW															
ED132	Dummy capsule																
ED133	Forward	HAW	1010	1.8	24	Wobbly	•?	•	•	•	•		•				*amph v. small*
ED135	Forward	HAW	1065	1.8	10-23?	Failed	•	•	•	•	•		•	•	•		
ED137	Forward	HAW	1032	1.8	24	T/c extr?	•	•	•	•	•		•	•			*amph v. small*
ED142	Dummy capsule																
ED143	Forward	HAW	1020	1.8	24	T/c extr?	•	•	•	•	•		•	•	•		
ED192	Reversal	M3	1020	1.8	2	V. stable	•	•	•	•	•?	•				•	

Expt	Type and aim		Temp. (°C)	P (GPa)	Dur. (hrs)	Run history	Phases										Notes
							melt	ol	opx	cpx	amph	gt	sp	ru	ilm	fq	
ED194	Reversal - more water	M3	1020	1.8	1	Wobbly	•	•	•		•					•	
ED195	Reversal- no ol powder	M3	1020	1.8	2	Stable	•	•	•	•	•	•				•	
ED201	Weighted - doped	W1	1020	1.8	24	Stable	•	•	•	•	•		•			•	*REE acc.*
ED204	Weighted - doped	W1	1020	1.8	48	Stable	•	•	•?	•			•	•			*REE acc.*
ED210	Weighted - doped	W1	1010	1.8	48	Wobbly	•	•	•	•	•	•	•	•			*REE acc.*
ED213	Weighted	W2	1020	1.8	46	Low T		•	•	•	•		•				
ED214	Weighted	W2	1020	1.8	24	OK	•?		•	•	•			•			
ED216	Weighted	W2	1040	1.8	24	V. Good	•	•	•	•	•					•	
ED217	Forward - split temp.	HAW	1150, 1020	1.8		OK	•	•	•	•	•				•		
ED220	Reversal	M3	1020	1.8	24	OK	•	•	•	•	•	•				•	*Ni contam.*
ED223	Reversal	M4	1020	1.8	24	OK	•		•		•	•				•	*upside down?*
ED227	Reversal - failed																
ED228	Reversal - more water	M4	1020	1.8													
ED231	Double capsule	HAW	1020	1.8	24	V. Good	•	•	•	•			•	•		•	

Expt	Type and aim		Temp. (°C)	P (GPa)	Dur. (hrs)	Run history	Phases										Notes
							melt	ol	opx	cpx	amph	gt	sp	ru	ilm	fq	
ED234	Reversal	M4	1020	1.8	48	Wobbly	•			•			•			•	
ED237	Reversal - failed																
ED238	Reversal	M4	1015	1.8	48	quenched	•		•								
ED239	Reversal	M4	1010	1.8	48	V. Good			•							•	
ED242	Forward	HAW	1060	1.8	24	V. Good	•		•								*ignorite*
ED243	Forward - failed																
ED244	Forward (rpt ED242)	HAW	1060	1.8	24	V. Good	•		•								
ED249	Forward (rpt ED242)	HAW	1060	1.8	24	Wobbly		•		•			•	•		•	
ED250	Forward (rpt ED242)	HAW	1060	1.8	24	Wobbly											*ignorite*
ED253	Forward (rpt ED242)	HAW	1060	1.8	24	Stable	•	•	•	•			•				
ED255	Forward - failed	HAW															
ED256	Forward	HAW	1040	1.8	24	Stable	•	•	•				•				*ignorite*
ED257	Forward	HAW	1040	2.3	24	Stable	•	•	•	•		(•)		•		•	
ED258	Forward	HAW	1020	2.3	24	OK	•	•	•	•		•		•			

Expt	Type and aim		Temp. (°C)	P (GPa)	Dur. (hrs)	Run history	Phases										Notes
							melt	ol	opx	cpx	amph	gt	sp	ru	ilm	fq	
ED259	Forward	HAW	1000	2.3	24	Stable		•	•	•	•	•	•	•			
ED260	Forward	HAW	1060	2.3	24	V. Good	•	(•)	•	(•?)			•				*capsule failed*
ED276	Synthesis - failed																
ED277	Synthesis - failed																
ED278	Synthesis (ign)	ign	1050	1.8	25	V. Good		•					•		•		
ED279	Forward	HAW	1040	2.8	24	V. Good	•	•	•	•		•		•			
ED280	Forward	HAW	1060	2.8	24		•	•	•	(•)		•		•			
ED282	Forward	HAW	1020	2.8	24	V. Good		•	•	•		•		•	•		
ED283	Forward	HAW	1010	2.3	24	Stable	•	•	•	•	•?	•		•			
ED285	Reversal	M5	1020	1.8	30		•		•			•					
ED288	Boron test																
ED300	Reversal salt cell	M5	1020	1.95	25	V. Good	•			•	quench						
ED307	Reversal - double capsule	M5	1020	1.8	1		[qz cor gt ru amph?]										

Expt	Type and aim		Temp. (°C)	P (GPa)	Dur. (hrs)	Run history	Phases										Notes
							melt	ol	opx	cpx	amph	gt	sp	ru	ilm	fq	
ED312	Reversal - super capsule	M3	1020	1.8	3	OK	[qz cor melt fl sp Fe-Ti oxide]										
ED315	Forward thick Pt	HAW	1040	2.3	24	Good		•	•	•	•	•		•	•		
ED317	Reversal adding ol	M5	1020	1.75	3	Good											
	C2 no ol added						•									•	
	C3 10% ol added						•			•	•	•				•	*capsule failed*
ED327	Reversal adding ol	M5	1020	1.8	26	Good											
	C2 10% ol added						•			•						•	
	C3 20% ol added						•	•		•						•	
ED332	Reversal adding ol	M5	1005	1.85	24	Good											
	C1 no ol added						•									•	
	C2 10% ol added						•			•	•	•				•	
	C3 20% ol added						•	•		•		•				•	
ED339	Forward	HAW	1060	1.8	24	Good	•	•	•	(•)			•			•	
ED340	Forward	HAW	1040	1.8	24	Good	•	•	•	•			•			•	
ED348	Reversal	M5	1005		24	Good											
	C1 10 wt% water						•			•		•					
	C2 20 wt% water						•										
	C3 50 wt% water						•									•	

APPENDIX B

STARTING COMPOSITIONS FOR EXPERIMENTS

Major-element composition of starting materials

	HAW	ED143M3	ED143M4	ED143M5	ED143W1	ED143W2
SiO_2	47.9	53.0	52.8	51.0	48.7	49.2
TiO_2	5.9	1.4	1.4	1.5	1.8	1.9
Al_2O_3	8.1	22.6	22.8	23.1	11.5	14.4
FeO	29.8	3.8	3.7	3.9	6.2	5.4
MgO	5.2	4.1	4.6	4.1	18.4	15.2
CaO	0.94	12.1	12.1	12.6	10.2	10.6
Na_2O	0.22	1.9	1.8	2.6	1.7	2.0
K_2O	1.3	0.70	0.64	0.73	0.38	0.43
MnO	0.09	0.17	0.13	0.20	0.11	0.10
Cr_2O_3	0.49	0.05	0.03	0.07	0.62	0.52
NIO	0.06	0.11	0.13	0.15	0.51	0.17

Normalised to 100% total.

HAW is Hawaiian pyrolite - 40% olivine; ED143M3, ED143M4, and ED143M5 were used in reversal experiments of ED143 and they are similar to the estimated melt composition from ED143 (see Chapter 5). ED143W1 and ED143W2 were calculated from the compositions of phases produced in ED143 and are biased towards the amphibole and melt components. ED143W1 is 39.4% amphibole, 13% olivine, 10% orthopyroxene, 10% clinopyroxene, 2% spinel, 0.3% rutile, 0.3% ilmenite, 25% melt. ED143W2 is 43.5% amphibole, 5% olivine, 10% orthopyroxene, 5% clinopyroxene, 0.5% spinel, 0.3% rutile, 0.1% ilmenite, 35.6% melt.

The trace-element contents of ED143M5 are given in Table 4.3 (Chapter 4).

APPENDIX C

THE CALCULATION OF ERRORS

Analytical errors associated with the electron microprobe and the ion microprobe are discussed in Sections 4.8 and 4.9, respectively.
Where mineral compositions were averaged, errors were quoted as one standard deviation from the mean.

When summing or subtracting means, the standard deviation of the product was calculated as the square root of the sum of the squares of the standard deviations of the constituents.

When multiplying or dividing means, the percentage error (i.e. the standard deviation expressed as a percentage of the mean) was calculated as the square root of the sums of the squares of the percentage errors of the constituents.